

# STRUCTURE AND OPTICAL PROPERTIES OF NATURAL LOW DIMENSIONAL, SEMICONDUCTING, ORGANIC INORGANIC HYBRIDS

Robert Shewan Black

A thesis submitted to the Faculty of Science,  
University of the Witwatersrand, Johannesburg, in  
fulfillment of the requirements for the degree of  
Doctor of Philosophy

Johannesburg

2012

## Declaration

I declare that this thesis is my own, unaided work. It is being submitted for the Degree of doctor of Philosophy in the University of the Witwatersrand, Johannesburg. It has not been submitted before for any degree or examination in any other University.

---

(Signature of Candidate)

\_\_\_\_\_ day of \_\_\_\_\_ 2012

## Abstract

The aim of investigating the 2D  $\text{PbX}_6$  inorganic organic hybrids was to study octahedral distortions, short interlayer spacing's, and the effect of functionalized aliphatic's terminal halogen on idealizing or destabilizing the octahedral arrangements and their effect on the band gap of the single layer 2D hybrid systems. It was found that the  $\text{PbX}_6$  metal centred distortions do display some impact on the band gap, the greater the distortion experienced in the  $\text{I}_{\text{eq}}\text{-Pb-I}_{\text{eq}}$  cis bond angles, the wider the band gap, as we suspect a decrease in  $\text{I } 5p$  antibonding character which lowers the top of the valence band. The terminal halogen interaction specifically in  $(\text{BrC}_2)\text{PbI}_4$ , clearly displayed some  $\text{Br } 4p/s$  character at the bottom of the conduction band, which may further explain the reduction of the band gap of this compound. This in conjunction with the shorter interlayer spacing serve to stabilize more idealized bridging angles, as seen in both the lead iodide and bromide analogues. In the short interlayer spacing compounds large idealizations of the  $\text{Pb-X-Pb}$  bridging angles are observed however display a large metal centred octahedral distortions in order accommodate the spatial occupation of the lone pair on lead.

It was generally observed that the lead bromide hybrids appear to have a greater sensitivity to exciton lattice interactions, which give rise to red shifted emissions and absorptions with decreasing temperature. Structurally this behaviour is counterintuitive; because the structures increase in inorganic distortions with decreasing temperature and therefore a blue shift in the exciton absorption is expected. It should be noted that compounds displaying this phenomenon most,  $(\text{C}_4, \text{C}_6, \text{C}_7)\text{PbBr}_4$  do display a large amount of structural disorder in their lower temperature phases.

In the 1D systems investigated further structure to property correlations were made. Optically it was found that unlike the corner-shared perovskite type 1D wires of  $[\text{NH}_2\text{C(I)=NH}_2]_3\text{PbI}_5$  and  $[\text{CH}_3\text{SC(=NH}_2)\text{NH}_2]_3\text{PbI}_5$  the first exciton absorption of the octahedral face sharing wires of  $(\text{A})\text{PbI}_3$  appear to be largely insensitive to the inorganic structural distortions experienced as a result of the low temperature phase transitions. In one instance however a low temperature phase transition did result in a polaron emission which was directly related to a discontinuity in the inorganic wires. More generally experimental links between the STE luminescence emissions and the inter-wire spacing, organic dielectric constant, and the density of the crystal, were shown to influence the STE lattice interactions to a greater degree. This effect is increased through a decrease in crystal density and organic dielectric constant, with an associated increase in the inter-wire spacing. Therefore as the exciton lattice interactions increase, a red shift in the STE emissions is observed.

In another series of systems strong  $\text{I} - \pi$  and  $\pi - \pi$  interactions were present in particularly two 1D charge transfer compounds. It was noted that the inorganic wires promote  $\pi - \pi$  interactions between the organic templates as has also been established in literature. Structurally it was also observed that the CT transitions of these compounds begin to largely coincide with the STE emission arising from the inorganic wire. Even though the CT compounds structurally have strong  $\pi - \pi$  interactions the current experiments do not ascertain to what degree this interaction assists in electron transport. It was also established that as intermolecular  $\pi - \pi$  interactions are absent in previously published MV and Et compounds with the dominant CT interaction was the  $\text{I} \dots \text{N}$  interaction which functions over a large range ( $4.9\text{\AA}$ ). This long distance is substantiated from the strong covalent character of the  $\text{I} \dots \text{N}$  interaction observed in IR experiments completed on  $(\text{MV})\text{Pb}_2\text{I}_6$ . It was also observed in our compounds that the position of the LUMO of the organic cation relative to the valence band of the inorganic wires appears to be largely dependent on the  $\text{N} \dots \text{I}$  distance and largely independent of the electron accepting templates HOMO-LUMO gap.

The increased wire thickness observed in these compounds does appear to display a pronounced effect on the PL emissions as seen in three chain wide wires produced. The thicker chains begin to allow higher energy emission's to occur i.e. the desired first exciton emission begins to become favored due to the relaxing of the wires spatial confinement on the electron-hole's orbit. Further investigations are needed into even thicker chain wires, in order to ascertain the ideal size of the wire to obtain the desired high energy first exciton emission. To date the wire thickness that does give rise to the first exciton emission appears to still need at least six coordinated  $\text{PbI}_6$  octahedral units.

## Acknowledgments

I would firstly like to acknowledge my supervisor Prof. Dave Billing for giving me the wonderful opportunities in attending 3 conferences, one local and two international. This definitely helped shape my view of research and gave me many useful ideas and experiences. From a technical point of view thanks for letting me break many an instrument on my initial learning curve, and for the useful talks on diffraction both powder and single crystal. I would also like to thank him for the many laughs and coffee sessions over the years, thanks for your friendship.

A special thanks Dr Manuel Fenandes for helping me with some ideas in solving the more difficult crystal structures, keeping the APEX running, and for showing me how to fix many instrumental issues. Also thanks for helping me to build a fully functional Linux machine - what would Wits chemistry do without you? And lastly, thanks for all the many discussions on the random but interesting topics over the years.

To Dr Rudolph Erasmus, a special thanks to you for the photoluminescence and UV-Vis optical absorption measurements. Thanks for all of the useful discussions your knowledge and input is greatly appreciated.

To Prof Demi Levendis thanks for the discussions on symmetry and the visits to Jan Boeyens. I sincerely hope you manage to find your blue key.

To my office mates Matt and Roy, thanks for the good laughs and many random discussions, many of which I'd prefer to forget.

A special thanks to my Dad, thanks for all the encouragement over the years and for the opportunity to study in the first place. I aspire to be like you. I would also like extent thanks to my mom and remaining family for all your support.

Most importantly I would like to thank my wife for all her encouragement to finish my thesis and for standing by me since my first year at varsity. I know sometimes we do things to simply prove others wrong. Thanks for helping me to stop caring what other people think. Your love and support have been nothing short of spectacular. I love you dearly my angel.

*To my Father in Heaven, you make all things clearer over time. My life in your hands. All things for your Glory. To You my Dad and my wife I dedicate this thesis.*



## Posters and Presentations

### Posters

Robert S. Black and David G. Billing, *Structure and properties of selected organic-inorganic hybrid perovskites namely R, S, And R&S, [C<sub>6</sub>H<sub>5</sub>C<sup>\*</sup>(H)(CH<sub>3</sub>)NH<sub>3</sub><sup>+</sup>]<sub>2</sub>SnI<sub>4</sub>*. Carmen Physical Chemistry Symposium, V&A Waterfront, Cape Town, (2007). (Awarded poster prize)

Robert S. Black and David G. Billing, *Structure and properties of selected organic-inorganic hybrid perovskites namely R, S, And R&S, [C<sub>6</sub>H<sub>5</sub>C<sup>\*</sup>(H)(CH<sub>3</sub>)NH<sub>3</sub><sup>+</sup>]<sub>2</sub>SnI<sub>4</sub>*. Post graduate symposium, University of the Witwatersrand. (2008)

Robert S. Black and David G. Billing, *Structure and photoluminescence of chiral tin and lead inorganic-organic hybrid perovskites*. International Union of Crystallography (IUCr) 2008 Osaka Japan. *Acta Cryst.* (2008) **A64**, C455-C456

Robert S. Black and David G. Billing, *Structure and photoluminescence of chiral tin and lead inorganic-organic hybrid perovskites*. Post graduate symposium, University of the Witwatersrand. (2009)

Robert S. Black, David G. Billing and Rudolph E. Erasmus, *Structure and Optical Properties of Natural 1D Quantum Wires*. European Crystallographic Meeting (ECM) Darmstadt Germany. (2010)

David G. Billing, Robert S. Black, *Structure and Optical Properties of Natural 2D Quantum Wells*. European Crystallographic Meeting (ECM) Darmstadt Germany. (2010)

### Presentations

Robert S. Black and David G. Billing, *Structure and photoluminescence of tin and lead inorganic-organic hybrid perovskites*. **SACI** young chemists symposium, University of the Witwatersrand, Chemistry Department. (2008)

Robert S. Black and David G. Billing, *Structure and optical properties of natural low dimensional semiconductors*. Chem. Soc. Post graduate Colloquium, University of the Witwatersrand, Chemistry Department. (2010)

Robert S. Black and David G. Billing, *Structure and optical properties of natural low dimensional semiconductors*. Materials Physics Research Institute Centre of Excellence in Strong Materials

(MPRI), University of the Witwatersrand, Physics Department. (2010) (Won student prize for best talk in 2010)

## Preface

The thesis is comprised two distinct sections, namely the section A which comprises of the background theory, literature survey, and experimental section, and section B which comprises the results and discussions sections. The entire thesis is written in a uniform style, with the exception of chapter 6. As chapter 6 was intended for non linear optical investigations, and therefore it is written with its own theory and brief literature survey section.

The introduction and background theory section (chapter 1) was intended to establish a foundation of the fundamentals of semiconductor devices. Chapter 2 follows on from this by giving the background literature of low dimensional inorganic organic hybrids. The results chapters (4-6) investigated SC-XRD, and optical property investigations of 44 different low dimensional organic inorganic hybrids. Only 29 of the structures are new, however the other structures investigated formed the basis of the optical investigations. It was the intention in this work to correlate structure to optical property relationships, and therefore SC-XRD structural determinations were either revisited or completed at multiple temperatures for most of the compounds investigated. The previously published structures were revisited to ensure direct optical to property correlations could be made without worry of polymorphism (as will be established in the literature survey).

All of the relevant structure files as well as an electronic copy of this thesis are supplied on the disc under the relevant chapter numbers.

<b>Table of Contents</b>	<b>Page</b>
<b>Abstract</b>	iii
<b>Acknowledgements</b>	iv
<b>Posters and Presentations</b>	v
<b>Preface</b>	vii
<b>Table of contents</b>	viii
<b>List of figures</b>	xii
<b>List of tables</b>	xxii
<b>List of schemes</b>	xxiv

### ***Section A: Background Theory and Literature Survey***

<b>Chapter 1: Introduction and Theory</b>	<b>1</b>
1.1 Introduction	1
1.2 Brillouin zones and reciprocal space	2
1.3 Energy bands in semiconducting solids	5
1.4 Density of States (DOS)	9
1.5 General properties of semiconductors	13
1.5.1 Recombination processes	13
1.5.2 Carrier densities	14
1.5.2 Carrier transport	15
1.6 Optical processes and excitons in semiconductors	16
1.7 Confinement of excitons through dimensional reduction	20
1.7.1 The 3D case	21
1.7.2 The 2D case	22
1.7.3 The 1D case	23
1.7.4 The 0D case	25
1.8 Aims	26
1.9 Bibliography	27
<b>Chapter 2: Literature Survey</b>	<b>28</b>
2.1 Introduction	28
2.2 3D organic inorganic hybrid perovskites	28
2.2.1 Optical properties of 3D organic inorganic hybrid perovskites	31

2.2.2 Comparison of 3D and 2D electronic states .....	33
2.3 <100> 2D hybrid perovskites and their relative orientations.....	35
2.3.1 Size of the cation and the effect on the dimensionality and topology of the <100> hybrids.....	38
2.3.2 <100>, <110> and <111> 2D orientations .....	42
2.3.3 Group 14(IVA) <100> hybrids and the $ns^2$ lone pair stereo chemical activity .....	46
2.3.4 The effect of structural distortions on the stereo chemical activity of the $ns^2$ lone pair of <100> (A) <sub>2</sub> SnI <sub>4</sub> hybrids.....	49
2.3.5 Electrical transport of <100> and <110> tin iodide based hybrid perovskites .....	53
2.3.6 The <110> orientation and the effect on the band gap of lead based hybrids .....	55
2.4 Different motifs generated through varying the M/X and cation ratio's.....	58
2.5 Optical properties and Photoluminescence of <100> 2D hybrids.....	63
2.5.1 Optical properties of lead bromide and chloride 2D hybrids.....	71
2.6 Phase changes of the <100> 2D hybrids.....	78
2.6.1 Enthalpy and entropy energies from CnMX <sub>4</sub> phase transitions .....	88
2.6.2 Unusual phase behavior of the short alkylammonium hybrids of (C <sub>3</sub> )MCl <sub>4</sub> .....	91
2.7 1D hybrids and their optical properties .....	93
2.7.1 Charge transfer effects between wires and spacers .....	103
2.8 Optical nonlinearity in organic inorganic hybrids.....	107
2.9 Electroluminescent devices and the use of chromophores in 2D hybrids .....	110
2.10 Summary and conclusions .....	113
<b>Chapter 3: Experimental</b> .....	<b>114</b>
3.1 Synthesis.....	114
3.1.1 Slow cooling method .....	114
3.1.2 Slow evaporation method .....	115
3.1.3 Schemes of compounds investigated with relevant chapter numbers.....	116
3.2 Single Crystal X-ray diffraction (SC-XRD) .....	120
3.2.1 References.....	121
3.3 Powder X-ray diffraction (P-XRD) .....	122
3.3.1 References.....	122
3.4 Photoluminescence .....	123
3.5 UV-Vis .....	123
3.6 Thermal analysis (DSC) .....	124

3.7 Elemental analysis.....	124
-----------------------------	-----

## ***Section B: Results and Discussion***

### **Chapter 4: The structure and optical properties of <100> 2D lead halide quantum wells.....125**

#### 4.1 The Structure and Phase transitions of $(C_nH_{2n+1}NH_3)_2PbBr_4$ where $n = 4-7$ .....125

##### 4.1.1 Introduction .....125

##### 4.1.2 Results and Discussion .....129

##### 4.1.3 Thermal analysis studies of the $(Cn)PbBr_4$ where $n = 4-7$ .....134

##### 4.1.4 The structures and phases of $(Cn)PbBr_4$ where $n = 4-7$ .....137

##### 4.1.5 Conclusions .....142

#### 4.2 The Structure and Phase transitions of $(HOC2, BrC3, BrC4, BrC5)_2PbBr_4$ .....143

##### 4.2.1 Introduction .....143

##### 4.2.2 Results and Discussion .....145

##### 4.2.3 Thermal analysis .....146

##### 4.2.4 The structure and phases of $(HOC2, BrC3, BrC4, BrC5)_2PbBr_4$ .....150

##### 4.2.5 Conclusions .....159

#### 4.3 Optical properties of $(C_nH_{2n}NH_3)_2PbX_4$ where $n = 4-7$ , and $(HOC_2H_4NH_3)_2PbX_4$ , where $X = Br$ and $I$ and $(BrC_nH_{2n}NH_3)_2PbBr_4$ where $n = 3-5$ and $(IC_nH_{2n}NH_3)_2PbI_4$ where $n = 2-6$ and $(BrC_2H_4NH_3)_2PbI_4$ . .....160

##### 4.3.1 Introduction .....160

##### 4.3.2 Results and Discussion .....164

##### 4.3.3 Structural Summary of the lead iodide analogues.....165

##### 4.3.4 Optical absorption and photoluminescence of $(Cn)PbX_4$ and $(ZCn)PbX_4$ .....169

##### 4.3.5 Structure and optical property correlation of the lead iodide series .....172

##### 4.3.6 Lead halide substitution and the effect on the exciton absorption .....181

##### 4.3.7 Conclusions .....183

### **Chapter 5: Structure and optical properties of lead iodide quantum wires .....185**

#### 5.1 The structures, phase transitions and optical properties of the natural 1D organic inorganic quantum wire hybrids of $(A)PbI_3$ .....185

##### 5.1.1 Introduction .....185

##### 5.1.2 Results and Discussion .....187

##### 5.1.3 Powder diffraction investigations.....192

##### 5.1.4 Thermal analysis studies (DSC) .....193

##### 5.1.5 The structure and phase transitions of $(Py)PbI_3$ , $(PD)PbI_3$ , and $(Az)PbI_3$ .....195

5.1.6 The structures of (Pyr)PbI <sub>3</sub> , [(n-But) <sub>4</sub> N]PbI <sub>3</sub> and [(Et) <sub>3</sub> NH]PbI <sub>3</sub> .....	202
5.1.7 Structural conclusions .....	203
5.1.8 Optical properties of compounds 1-6 .....	206
5.1.9 Structure and optical property conclusions .....	211
5.2 The structures and phases of the solvated 1D xDMF.(A)PbI <sub>3</sub> compounds, where distortions of the periodicity of the wire generates an alternative PL emission pathway.....	212
5.2.1 Introduction.....	212
5.2.2 Results and Discussion .....	213
5.2.3 Photoluminescence and optical absorption.....	215
5.2.4 The variable temperature structures of (DPBD)Pb <sub>2</sub> I <sub>6</sub> and (EPPA)PbI <sub>3</sub> .....	217
5.2.5 Conclusions.....	219
5.3 Structure and optical properties of thick chain 1D lead iodide wires, and the Charge transfer effects between the wires and spacers.....	221
5.3.1 Introduction.....	221
5.3.2 Results and Discussion .....	224
5.3.3 Powder Diffraction investigations .....	231
5.3.4 Optical properties.....	232
5.3.5 Conclusions.....	237
<b>Chapter 6: Chiral organic inorganic hybrid materials and their potential for NLO properties .</b>	<b>238</b>
6.1 Theoretical background.....	238
6.1.1 The physical origin of optical nonlinearities.....	238
6.1.2 Non-resonant nonlinearities .....	242
6.1.3 Resonant nonlinearities.....	244
6.1.4 Phase matching and optical birefringence (briefly) .....	246
6.1.5 Symmetry conditions for second order effects.....	247
6.1.6 Brief literature survey of NLO hybrid materials .....	248
6.2 Introduction.....	254
6.2.1 Results and discussion (2D) .....	255
6.2.2 Variable temperature photoluminescence of compounds 4-8.....	266
6.2.3 Conclusions.....	275
6.3 Structure and optical properties of the 1D compounds .....	276
6.3.1 Results and discussion (1D) .....	276
6.3.2 Crystal structures .....	276

6.3.3 Luminescence .....	282
6.3.4 Conclusions 1D.....	285
<b>Chapter 7: Conclusion .....</b>	<b>286</b>
7.1 Concluding remarks .....	286
7.2 Future work.....	289
<b>Chapter 8: References .....</b>	<b>290</b>
<b>Appendix.....</b>	<b>298</b>
Appendix A.....	298
Appendix B .....	304
Appendix C .....	308

## List of figures

## Page

<b>Figure 1.1:</b> Brillouin Zone generation in a) a cubic Bravais lattice and b) in a hexagonal Bravais lattice. (This image was reused under the GNU public licence from <a href="http://en.wikipedia.org/wiki/Brillouin_zone">http://en.wikipedia.org/wiki/Brillouin_zone</a> ).	1
<b>Figure 1.2:</b> The First Brillouin Zone of a face centred cubic lattice where the labels in red represent the critical points (points of high symmetry) and $\Gamma$ is the zone centre (0, 0, 0). (This image was reused under the GNU public licence from <a href="http://en.wikipedia.org/wiki/Brillouin_zone">http://en.wikipedia.org/wiki/Brillouin_zone</a> ).	5
<b>Figure 1.3:</b> a) The free electron model representation of an $\epsilon_k$ vs $k$ diagram, i.e. with no periodic boundary conditions included. b) A new $\epsilon_k$ vs $k$ diagram with periodic boundary conditions included. What becomes evident is that at the zone boundaries $\pm n\pi/a$ for a linear system, band gaps begin to arise. Diagram obtained from (Kittel C, 1996).	6
<b>Figure 1.4:</b> a) The variation potential energy of a conduction electron in a linear lattice a in a field of ion cores. b) The probability density wavefunctions of the travelling waves $ \psi(+)^2 $ and $ \psi(-)^2 $ . Where the positive probability wavefunction piles up positive charge around the ion cores, and the negative probability wavefunction piles up negative charge in the interstitial regions. (Diagram obtained from Kittel. C, 1996).	7
<b>Figure 1.5:</b> The first diagram displays the $\epsilon_k$ vs $k$ diagram of the Kronig-Penney model where the band gaps arise at the Brillouin zone boundaries $\pm n\pi/a$ where $n$ is an integer. The Black curves are the Kronig-Penney model and the green curves are the free electron model. a) is the $\epsilon_k$ vs $k$ diagram only b) is the $\epsilon_k$ vs $k$ diagram combined with the reduced zone diagram, and c) is the $\epsilon_k$ vs $k$ diagram of the reduced zone diagram only or the band structure diagram of the First Brillouin zone. (ref: <a href="http://ecee.colorado.edu/~bart/book/welcome.htm">http://ecee.colorado.edu/~bart/book/welcome.htm</a> Chapter 2)	8
<b>Figure 1.6:</b> The overlaid band structure of GaAs and Ge show the difference between a direct and indirect band gap of a band structure. Where GaAs has a direct bad gap of $E_g = 1.519\text{eV}$ at room temperature, and Ge has an indirect band gap of $0.7437\text{eV}$ .	9
<b>Figure 1.7:</b> Density of states for bulk (3D blue), quantum well (2D red), quantum wire (1D green) and quantum Dot (0D black) (Diagram obtained from: <a href="http://britneyspears.ac/physics/dos/dos.htm">http://britneyspears.ac/physics/dos/dos.htm</a> ). Functions are described in the text.	12
<b>Figure 1.8:</b> An exciton which is a bound electron hole pair. An illustration of a Mott-Wannier type exciton with an effective Bohr radius equivalent to or greater than the unit cell dimensions.	16



**Figure 1.9:** Energy subbands generated from excitons with various quantum numbers  $n$ , the lowest excitons energy level has the largest orbiting radius, binding energy, and lowest emission energy associated with  $n=1$ . (Diagram obtained from Kittel. C, 1996).

17

**Figure 1.10:** a) Shows the excitonic absorption of very pure GaAs at 1.2K. From the absorption spectra, one is able to experimentally observe three of the excitonic subband energy levels. b) Shows the temperature effect on GaAs absorption spectrum. It is evident that the excitons absorption line only becomes evident at lower temperatures. The dashed line shows the calculated band gap with decreasing temperature. (Diagrams obtained from Fox M, 2008).

19

**Figure 1.11:** The eigenenergy of the bound states may be seen in the above plot. These eigenenergies show that for  $d = 1$  the odd ( $2p$ ) and even ( $2s$ ) parity  $n = 2$  energy levels are fairly evenly spaced just below the conduction band and converge to  $-E_R^*$  at  $x_0 = 0$ . However what is observed is that as the wire length is shortened ( $x_0 \rightarrow 0$ ) the eigenenergy of the lowest energy state  $n = 1$  diverges to negative infinity. This is where the 1D model begins to break down, and or the wire is at the limit of being a wire, and should now be treated as a quantum dot. (Diagram obtained from: Ogawa T, Kanemitsu Y., 1995).

24

**Figure 1.12:** A representation of the effect of the dielectric constant ratio of the wire and the barrier, and its enhancement of the coulomb potential with increasing dielectric mismatch. The dashed line represents the bare coulomb potential. Essentially one may say that the more negative the coulomb potential, the greater the increase on the binding energy of the exciton. (Diagram obtained from: Ogawa T, Kanemitsu Y., 1995).

25

**Figure 2.1:** The perovskite structure ( $\text{CaTiO}_3$ ) which holds the general formula  $\text{ABO}_3$ , however for the Organic inorganic hybrid perovskites the formula is changed to  $\text{AMX}_3$  where A is the organic cation, M the metal, and X is any halogen.

28

**Figure 2.2:** The low temperature absorption spectra both obtained from the reflectance and Kramers-Kronig relationship. a) Displays the 5K absorption spectrum of  $(\text{CH}_3\text{NH}_3)\text{PbBr}_3$  obtained from (Tanaka K, et al, 2003) b) Displays the 4.2K absorption spectrum of  $(\text{CH}_3\text{NH}_3)\text{PbI}_3$  obtained from (Hirasawa M, et al, 1994).

32

**Figure 2.3:** The UPS spectra and the calculated density of states, of a) The 3D Hybrid perovskite  $(\text{CH}_3\text{NH}_3)\text{PbI}_3$ , and b) the 2D hybrid perovskite  $(\text{C}_4\text{H}_9\text{NH}_3)_2\text{PbI}_4$  (Umebayashi T, et al, 2003).

33

**Figure 2.4:** a) The 3D structure of  $(\text{CH}_3\text{NH}_3)\text{PbI}_3$  and b) the 2D structure of  $(\text{C}_4\text{H}_9\text{NH}_3)_2\text{PbI}_4$  (Umebayashi T, et al, 2003).

34

**Figure 2.5:** The results of the band structure calculations of a)  $(\text{CH}_3\text{NH}_3)\text{PbI}_3$  and b)  $(\text{C}_4\text{H}_9\text{NH}_3)_2\text{PbI}_4$ . The critical points in the first Brillouin zone of c) the cubic phase crystal structure of  $(\text{CH}_3\text{NH}_3)\text{PbI}_3$ , d) the orthorhombic phase of  $(\text{C}_4\text{H}_9\text{NH}_3)_2\text{PbI}_4$  (Umebayashi T, et al, 2003).

35

**Figure 2.6:** As the R group increases in size the 3D perovskite motif is changed, as the octahedral vertically separate. This separation may increase with increasing length of the R group.

36

**Figure 2.7:** a) Eclipsed arrangement of the  $\langle 100 \rangle$  layers. b) Staggered arrangement of  $\langle 100 \rangle$  layers.

37

**Figure 2.8:** The hydrogen bonding configurations observed in the  $\langle 100 \rangle$  oriented 2D hybrids. a) The bridging halide configuration i.e. two hydrogen bonds to the bridging halides and one hydrogen bond to the terminal halogen. b) The terminal halogen configuration, where there is now one bridging halide hydrogen bond, and two terminal halide hydrogen bonds.

37

**Figure 2.9:** The primary cyclic amine templates used to ascertain at which point the bulkiness of the template forces a new templated motif.

38

**Figure 2.10:** The Lead iodide and Lead bromide series form the same basic motif with the cycloheptyl ammonium template. a) The cycloheptyl ammonium cation with lead bromide, produces 1D double layer corner sharing octahedral chains. b) The side view displays the chain motif which resembles the  $\langle 110 \rangle$  2D layer motif (Billing D. G, and Lemmerer A, 2009).

39

**Figure 2.11:** The Lead Chloride cycloheptyl ammonium hybrid forming inorganic bilayers in the crystal may be an intermediate dimension between 1D and 2D (Billing D. G, and Lemmerer A, 2009).

39

**Figure 2.12:** When the template ring size increases from cycloheptyl ammonium to the cyclooctyl ammonium cation for lead Bromide, a new type of bilayer motif is formed as in the lead chloride cycloheptyl ammonium case. The difference between them is observed when studying the bilayer topology. Instead of only corner sharing octahedra as seen in the lead chloride case, some of the  $\text{PbBr}_6$  octahedra only have two corner sharing halides instead of four. This motif alternates on the top and bottom edges as seen in the picture above (Billing D. G, and Lemmerer A, 2009).

40

**Figure 2.13:** Lead Chloride with the cyclooctyl ammonium cation, which produced 2D layers unlike the smaller cycloheptyl ammonium cation, however a very unexpected topology arises (Billing D. G, and Lemmerer A, 2009). 40

**Figure 2.14:** The cyclooctyl ammonium template with lead iodide producing 1D single chain face sharing octahedra (Billing D. G, and Lemmerer A, 2007). 41

**Figure 2.15:** 2D layered perovskite orientations. a)  $\langle 100 \rangle$  oriented  $(R-NH_3)_2A_{n-1}M_nX_{3n+1}$ , b)  $\langle 110 \rangle$  oriented  $(R-NH_3)_2A_nM_nX_{3n+2}$ , and c)  $\langle 111 \rangle$  oriented  $(R-NH_3)_2A_{n-1}M_nX_{3n+3}$  (Mitzi D. B, 2004). 43

**Figure 2.16:** Comparison of the two  $\langle 110 \rangle$  oriented perovskites a) N-(3-aminopropyl)imidazole in PbBr b) Methyl ammonium and Iodoformamidinium in SnI, the diagram reference from (Mitzi D. B, et al, 1998; Li Y, et al 2006) respectively. 45

**Figure 2.17:** The  $\langle 111 \rangle$  orientation i.e.  $(R-NH_x)_2A_{n-1}M_nX_{3n+3}$ , here we seen an example of the  $n = 1$  case, which gives rise to isolated  $SnCl_6$  octahedra, the ideal 0D case (Ben Ghazlen M. H, et al, 1981). 45

**Figure 2.18:** Luminescence emission of a)  $(C_4H_9NH_3)_2GeI_4$  b)  $(C_4H_9NH_3)_2SnI_4$  c)  $(C_4H_9NH_3)_2PbI_4$ , figure adapted from (Mitzi D. B, 1996). 48

**Figure 2.19:** Schematic of 2D perovskite sheets which shows the (a) undistorted lattice, (b) in-plane distortion, (c) out-of-plane distortion, and (d) combined in- and out-of-plane distortion. The green box highlights the unit cell that describes each lattice (Knutson J. L, et al, 2005). 50

**Figure 2.20:** Plot of the top of the valence band and the bottom of the conduction band upon in plane (solid lines) and out of plane (dashed lines) distortions to the  $SnI_4^{2-}$  perovskite type lattice (Left). A plot of the band structure of the 2D tin iodide hybrid perovskite showing the relevant band contributions (Knutson J. L, et al, 2005). 51

**Figure 2.21:** Temperature (T) Vs Resistivity ( $\rho$ ) of measurements of  $[NH_2C(I)=NH_2]_2(CH_3NH_3)_mSn_mI_{3m+2}$  where  $m = 1$  generates corner sharing single 1D chain systems, and  $m = 2$  generates the  $\langle 110 \rangle$  2D topology. Furthermore measurements of  $(C_4H_9NH_3)_2(CH_3NH_3)_{n-1}Sn_nI_{3n+1}$  are also displayed. For  $n = 1$  the common  $\langle 100 \rangle$  topology is generated. (Mitzi D. B, et al, 1995a; Mitzi D. B, et al, 1994). 53

**Figure 2.22:** The schematic diagram of the melt processed organic inorganic field effect transistor OIFET, based on a silicon substrate. The inset displays a magnified view of the orientation of the hybrid perovskite with the kapton sheet on the top of the processed layer (Mitzi D. B, et al, 2002). 54

**Figure 2.23:** Temperature vs Resistivity ( $\rho$ ) for IPy (2-I-pyridine), C4 (Butylamine), AEPI ( $C_5H_{10}NHC_2H_4NH_3$ ), GABA ( $HOCC_3H_6NH_3$ ), IC4 ( $I-C_4H_8NH_3$ ), TRA ( $HOCC_6H_{10}CH_2NH_3$ ), PEA ( $C_6H_5C_2H_4NH_3$ ), and C5di ( $H_3NC_5H_{10}NH_3$ ) in  $(A)_2SnI_4$  hybrid perovskites. The discontinuity of C4 is the result of a phase change as the sample is being cooled. Furthermore the resistivity measurement are sensitive to the preparation method, hence great care should be taken when preparation and measurement take place (Takahashi Y, et al, 2007). 55

**Figure 2.24:** The charge transfer mechanism proposed by (Li Y, et al, 2006). The first absorption emission diagram is for the API.2HBr crystal, the second is the new mechanism for the hybrid perovskite crystal. 56

**Figure 2.25:** The crystal packing of (2-(aminoethyl)isothiourea)PbBr<sub>4</sub> viewed along the 001 axis a) where the octahedra are largely distorted, and adopt a staggered arrangement, where as the (API)PbBr<sub>4</sub> adopts an eclipsed arrangement. b) Crystal packing view along 010 axis (Li Y, et al, 2008b). 57

**Figure 2.26:** The cystamine cations ability to template various lead iodide structural motifs with the general formula  $Pb_nI_{(4n+2)}^{(2n+2)-}$  (Mercier N, et al, 2009). 61

**Figure 2.27:** Important intermolecular interactions considered when growing hybrid materials. A and B represent an addition or subtraction of an inorganic unit. An addition of a “solvent/(anionic and cationic included)” molecule may give rise to a newly defined inorganic subunit (A and C). Intermolecular interactions need to be considered in order to stabilize surface interactions between the inorganic interfaces, as well as with other organic moieties present in the crystal (D and E) (Mercier N, 2009). 62

**Figure 2.28:** The Optical absorption for a) 3D  $(CH_3NH_3)PbI_3$ , b) 2D  $(C_9H_{19}NH_3)_2PbI_4$ , c) 1D  $(NH_2C(I)=NH_2)_3PbI_5$  and d) 0D  $(CH_3NH_3)_4PbI_6 \cdot H_2O$  crystals (Papavasiliou G. C, 1997). 64

**Figure 2.29:** Height of Inorganic layer = 6.36 Å ; interlayer spacing  $c/2 = 21.25 \text{ Å}$  of  $(C_{10}H_{21}NH_3)_2PbI_4$  (Ishihara T, et al, 1990). 67

**Figure 2.30:** Lattice constant c (o) and barrier width ( $\Delta$ ) as a function of chain length of  $(C_nH_{2n+1}NH_3)_2PbI_4$  where the interlayer distance is  $c/2$  (Ishihara T, et al, 1990). 67

- Figure 2.31:** The calculated exciton binding energies for lead iodide. (Elleuch S, et al, 2010) Blue curve is the increase in well thickness as the barrier is kept constant; conversely the red and black curves are constant inorganic well thickness as a function of the barrier length i.e.  $\epsilon_w/l_b$  as  $l_w$  is kept constant. 68
- Figure 2.32:** The optical absorption and photoluminescence emission of  $(C_{12}H_{25}NH_3)_2PbI_4$  a) displays the inorganic distortion as a result of the phase change, the reason for the optical shift. B) optical absorption, c) photoluminescence emission (Pradeesh K, et al, 2009b). 70
- Figure 2.33:** Optical density measurements of  $(RNH_3)_2Pb(Br_xI_{4-x})$  and  $(RNH_3)_2Pb(Cl_xBr_{4-x})$  with  $x = 0, 1, 2, 3, 4$ , displaying the optical shift with the change in halogen (Kitazawa N, 1997). 71
- Figure 2.34:** Photoluminescence of  $(C_4)_2PbBr_4$  displaying the biexciton emission generated from a pulsed excitation source at 10K (Kato Y, et al, 2003) a) and the continuous wave excitation luminescence displaying the excitonic fine structure at 1.5K (no biexciton emission is observed with CW excitation) (Ema K, et al, 2006). 74
- Figure 2.35:** The 1s exciton energy level has a fine structure which is split into three fine structure energy levels. These are the purely triplet state  $\Gamma_1^-$ , the triplet dominant  $\Gamma_2^-$  and the singlet dominant state  $\Gamma_5^-$ . As may be seen in a)  $\Gamma_5^-$  decays into  $\Gamma_2^-$  and  $\Gamma_1^-$  through a spin relaxation, as well as a spin flip decay b) as may be seen in c) (Ema K, et al, 2006). 75
- Figure 2.36:** The temperature dependant PL spectra for a)  $PhCH_2NH_3$  displaying fine structure splitting at low temperature. b)  $PhC_4H_8NH_3$  displaying very little fine structure splitting at low temperature (Kitazawa N, et al, 2010b). 76
- Figure 2.37:** The geometric parameters assigned to the alkyl ammonium cation in order to describe the relevant angles associated from phase change behavior. The angles are described in the text (Billing D. G, Lemmerer A, 2007). 80
- Figure 2.38:** The two ammonium head group positions associated with the phase transformations. The green parallelogram depicts two arrangements (a) the ammonium head resides within the obtuse angle of the parallelogram and the hydrogen bonding configuration forms an equilateral triangle. The arrangement (b) situates the ammonium head in the acute angle of the green parallelogram, and the hydrogen bonding formation forms a right angled triangle. It is observed that the obtuse arrangement is associated with the low temperature phase, and the acute arrangement with the higher temperature phases. The high temperature disordered phases result in the ammonium group being in the centre of the parallelogram (Billing D. G, Lemmerer A, 2007; 2008; Lemmerer A, 2007; Lemmerer A, Billing D. G, 2011). 81
- Figure 2.39:** The top image displays the multiple phase transitions of  $C10PbI_4$ , which proceeds from the low temperature monoclinic P phase to two middle orthorhombic P phases, and finally to the disordered orthorhombic C state. The bottom image of  $C8PbI_4$  displays the same mechanism however with one less orthorhombic P phase. Both compounds highest temperature phases display the aliphatic as disordered over two position, i.e. illustrating the mechanism which suggest that the aliphatic undergoes a quasi-melting transition before the entire compound melts at a higher temperature (Lemmerer A, 2007; Lemmerer A, Billing D. G, 2011). 82
- Figure 2.40:** The high temperature phase of  $C10CdCl_4$  displaying the evidence of the disordered arrangement of the decylammonium cation obtained from the electron density map (Kind R, et al, 1979). 83
- Figure 2.41:** The above diagrams are the two types of tilting experienced from the decylammonium cation with  $C10MnCl_4$  and  $C10CdCl_4$  respectively (Ciajolo M. R, et al, 1976; Kind R, et al, 1979). 85
- Figure 2.42:** Chain length of  $CnPbI_4$  vs the quasi melting phase change enthalpy for the heating run. This quasi-melting enthalpy generally increases in a linear fashion with increasing chain length.  $n = 6$  (Billing D. G, and Lemmerer A, 2007);  $n = 7-10$  (Lemmerer A, 2007);  $n = 12, 14, 16, 18$  (Billing D. G, and Lemmerer A, 2007). 90
- Figure 2.43:** The DSC results from  $(Cn)CdCl_4$ . The general graph represents a schematic of the DSC phase transition runs, where the lines pointing up are the endotherms for the increasing temperature run, and the lines pointing down are the exotherms for the decreasing temperature run. The insert in the top left is the enthalpies for the quasi-melting transitions for increasing chain lengths (Shenk K. J and Chapuis G, 1988). 90
- Figure 2.44:** The  $C3CdCl_4$  disordered low temperature phase III and high temperature phase I (Chapuis, G, 1978). 92
- Figure 2.45:** The unit cell information for the phases of  $C3CdCl_4$  and the relevant phase transformation temperatures (Chapuis, G, 1978; Doudin B, and Chapuis G, 1988). 92

<b>Figure 2.46:</b> The phase sequence of C3MnCl <sub>4</sub> (Depmeier and Mason S. A, 1978; 1983; Harris, <i>et al</i> , 1994).	92
<b>Figure 2.47:</b> The room temperature structural diagram of (piperdimium)PbI <sub>3</sub> displaying the face sharing octahedral chains of lead iodide.	93
<b>Figure 2.48:</b> a) One photon absorption spectrum of (PD)PbI <sub>3</sub> E.Lc, and b) E//c. c) The two photon absorption spectrum of (PD)PbI <sub>3</sub> displaying the odd parity absorbed exciton state (H). (Fukumoto T, <i>et al</i> , 2000) d) Photoluminescence emission of (PD)PbI <sub>3</sub> at 37K with the peak centred at 2.1eV (Nagami A, <i>et al</i> , 1996).	94
<b>Figure 2.49:</b> a) The PL emission as the hydrostatic pressure, b) a plot of the PL peak blue shift with an increase in pressure, which is due to exciton phonon coupling increasing with increasing pressure (Fukumoto T, <i>et al</i> , 2000).	95
<b>Figure 2.50:</b> The luminescence decay time vs 1/T a) and the plot of the luminescence integrated intensity vs 1/T b) (Akimoto I, <i>et al</i> , 2004).	96
<b>Figure 2.51:</b> Reflectivity measurement of (PD)PbBr <sub>3</sub> . The first exciton peak arises at 3.9eV. Band assignments are explained in the text (Azuma J, <i>et al</i> , 2002a).	97
<b>Figure 2.52:</b> a) The contour map of the luminescence of (PD)PbBr <sub>3</sub> with increasing temperature. The temperature dependence of the luminescence may be seen in the luminescence intensity plot of b). The mechanism of the emission may be seen in c) as the temperature increases, the V state flows into the R2 state through thermal transfer. The V state is generated from a free exciton, and the R state is generated through the polaron formation (explained in text). Adapted from (Azuma J, <i>et al</i> , 2002a).	98
<b>Figure 2.53:</b> Calculated band structures and DOS of both (PD)PbX <sub>3</sub> where X = I and Br. The notations for C,B, A,B, N.B, B, are conduction band, antibonding, nonbonding, and bonding, respectively.	100
<b>Figure 2.54:</b> a) The optical absorption and photoluminescence of [NH <sub>2</sub> C(I)=NH <sub>2</sub> ] <sub>3</sub> PbI <sub>5</sub> respectively b) The optical absorption and photoluminescence of [CH <sub>3</sub> SC(=NH <sub>2</sub> )NH <sub>2</sub> ] <sub>3</sub> PbI <sub>5</sub> respectively. The large shift in optical absorption of the two compounds is due to the large distortions experienced in [CH <sub>3</sub> SC(=NH <sub>2</sub> )NH <sub>2</sub> ] <sub>3</sub> PbI <sub>5</sub> compared with the idealized wires in [NH <sub>2</sub> C(I)=NH <sub>2</sub> ] <sub>3</sub> PbI <sub>5</sub> .	101
<b>Figure 2.55:</b> Optical absorption and photoluminescence spectra at 4K. Photoluminescence spectra at various excitation wavelengths (Fujisawa J and Ishihara T, 2004).	103
<b>Figure 2.56:</b> Charge transfer mechanism for (MV)Pb <sub>2</sub> I <sub>6</sub> as proposed by (Fujisawa J and Ishihara T, 2004), details explained in the text.	104
<b>Figure 2.57:</b> Infrared spectra recorded for a) (MV)Cl, b) (MV)Cl <sub>2</sub> c) (MV)I <sub>2</sub> , d) (MV)Pb <sub>2</sub> I <sub>6</sub> (Fujisawa J, <i>et al</i> , 2007).	106
<b>Figure 2.58:</b> Schematic representation of the conformational change of the organic diamine in the {[NH <sub>3</sub> (CH <sub>2</sub> ) <sub>2</sub> SS(CH <sub>2</sub> ) <sub>2</sub> NH <sub>3</sub> ]PbI <sub>5</sub> }H <sub>3</sub> O hybrid system at 75°C (Mercier N, <i>et al</i> , 2006).	109
<b>Figure 2.59:</b> The use of the Chromophore 5,5'''-bis(aminoethyl)-2,2':5',2'':5'',2'''-quaterthiophene (AEQT) with in (AEQT)PbX <sub>4</sub> , where X = Cl, Br, and I (Mitzi D. B, <i>et al</i> , 2001c).	111
<b>Figure 2.60:</b> (Top) Electroluminescent device of the chromophore hybrid (AEQT)PbCl <sub>4</sub> , (Bottom) the UV-Vis absorption spectrum of (AEQT)PbCl <sub>4</sub> . The 331nm peak associated with the PbCl <sub>4</sub> layers and the broad 400nm peak with the AEQT dye (Mitzi D. B, <i>et al</i> , 2001c).	112
<b>Figure 3.1:</b> The Bruker Apex II single crystal diffractometer with Mo K <sub>α</sub> radiation, with attached Oxford cryostream cooler Series 700.	120
<b>Figure 3.2:</b> The Bruker D8 Advance powder diffractometer with the Vantec super-speed MIKROGAPTM detector, and Cu K <sub>α</sub> 1, K <sub>α</sub> 2 spectral lines, as K <sub>β</sub> was suppressed using a Ni filter.	122
<b>Figure 3.3:</b> The experimental set up used for the photoluminescence measurements. The UV laser had to pass outside the original optics, as the instrument was not UV optics capable. Hence a set of mirrors redirected the beam to avoid the internal optics, and onto the sample to excite the compound in order to measure the photoluminescence response. The sample is mounted in the cryostat and cooled down with liquid nitrogen to 77K through a temperature controller.	123
<b>Figure 4.1.1:</b> The geometric parameters assigned to the alkyl ammonium cation in order to describe the relevant angles associated from phase change behaviour. The angles are described in the text, adapted from (Billing D. G, Lemmerer A, 2007).	129

**Figure 4.1.2:** The two ammonium head group positions associated with the phase transformations. The green parallelogram depicts two arrangements (a) the ammonium head resides within the obtuse angle of the parallelogram and the hydrogen bonding configuration forms an equilateral triangle. The arrangement (b) situates the ammonium head in the acute angle of the green parallelogram, and the hydrogen bonding formation forms a right angled triangle. It is observed that the obtuse arrangement is associated with the low temperature phase, and the acute arrangement with the higher temperature phases. The high temperature disordered phases result in the ammonium group being in the centre of the parallelogram. (Billing D. G, Lemmerer A, 2007; 2008; Lemmerer A, 2007) 130

**Figure 4.1.3:** The DSC graphs displaying the reversible high temperature phase transitions for compounds 1 a), 2 b), 3 c), and 4 d). 135

**Figure 4.1.4:** The DSC thermal graphs for (C4)PbBr<sub>4</sub> a) and (C6)PbBr<sub>4</sub> b) run between 123K and 473K, displaying the low temperature thermal stability of (C4)PbBr<sub>4</sub>, however b) displays all four phases present in (C6)PbBr<sub>4</sub>, the additional two low temperature phases are evidenced here (Tabuchi Y, et al, 2000). 136

**Figure 4.1.5:** Chain length of (Cn)PbI<sub>4</sub> Vs the quasi melting phase change enthalpy for the heating run. This quasi-melting enthalpy generally increases in a linear fashion with increasing chain length. Values obtained for n = 4-6 (Billing D. G, and Lemmerer A, 2007); n = 7-10 (Lemmerer A, 2007); n =12, 14, 16, 18 (Billing D. G, and Lemmerer A, 2007). 137

**Figure 4.1.6:** Conformational change of the alkyl ammonium chain C5, from the gauche to anti-clinal, between phase III and II. This conformational change and the increase in the alpha and phi tilts account for the large increase of interlayer spacing between phase III and II. 138

**Figure 4.1.7:** The disordered phase II of (C4)PbBr<sub>4</sub>, a) a front view of the disordered C4 alkyl ammonium chain where the dark shaded atoms represent the disordered component of the alky chain. The disordered alkyl chains are both coplanar for the measurement of the  $\angle_{\alpha}$  tilt angle. b) The side view of the disordered chain, displaying the low degree of distortion out of the alpha (blue) plane. 140

**Figure 4.1.8:** The disordered phase IV of (C6)PbBr<sub>4</sub>, a) a front view of the disordered C6 alkyl ammonium chain with the where the dark shaded atoms represent the disordered component of the alky chain. b) The side view of the disordered chain, displays the plane only passing through N1-C1-C2-C3, with atoms C4-C5-C6 tilting out of the alpha plane. 140

**Figure 4.2.1:** The DSC graphs displaying the reversible high temperature phase transitions for compounds 5 a), 6 b), 7 c), and 8 d). 147

**Figure 4.2.2:** The lead bromide octahedra, depicting the distortion angles around the lead atom. The Br<sub>ap</sub>-Pb-Br<sub>ap</sub> and X<sub>eq</sub>-Pb-X<sub>eq</sub> angles which deviate significantly from 180°. The adjacent angles of the equatorial X<sub>eq</sub>-Pb-X<sub>eq</sub>'s which deviate from 90°. And the bridging angle Pb-Br-Br which deviate from 180°. 152

**Figure 4.2.3:** Phase III of (BrC4)PbBr<sub>4</sub> displaying the all trans conformation of N1-C4, and the kink of the Br atom out of the alpha plane of the alkyl ammonium chain. 154

**Figure 4.2.4:** The packing diagram of (HOC2)PbBr<sub>4</sub> displaying the dimer between the layers, forming an R<sup>2</sup><sub>2</sub>(10) hydrogen bonded ring. 157

**Figure 4.3.1:** a) The molecular orbital diagram of an isolated lead iodide PbI<sub>6</sub> cluster (OD), displaying the anti-bonding orbital's of the  $\pi$ -antibonding Pb 6p – I 5p and the  $\sigma$ -antibonding Pb 6p – I 5s at the bottom of the conduction band (BCB). The top of the valence band (TVB) is comprised of the Pb 6s – I5p  $\sigma$ -antibonding (nonbonding) orbitals, below which are the nonbonding I 5p states. Further below are the  $\pi$ -bonding Pb 6p – I 5p and the  $\sigma$ -bonding Pb 6p – I 5s orbitals in the bottom state. b) The 3D and 2D states are extrapolated from the OD case, where the 3D case remains similar to the OD system. However the 2D system the I1 and I2 states split due to the two dimensional nature, where the (I1)  $\pi$ -antibonding Pb 6p – I 5p and the  $\sigma$ -antibonding Pb 6p – I 5s show greater dispersion than the (I2)  $\sigma$ -antibonding Pb 6p – I 5s orbital. This is due to the loss of  $\pi$  character as a result of the separation of the layers. The top of the valence band still remains with mainly the Pb 6s, as well as the I 5p  $\sigma$ -antibonding orbital's. (Umebayashi T, et al, 2003) 162

**Figure 4.3.2:** The photoluminescence (Blue) stokes shifted (26meV) from the exciton absorption peak (Red). Both spectra were measured at 77K, and were able to obtain the approximated binding energy for (IC6)PbI<sub>4</sub> of (260meV). 171

**Figure 4.3.3:** The continuous excitation photo-luminescence emissions at 77K of (IC5)PbI<sub>4</sub> (left) displaying the multiple emission lines. The main peak (2.341eV) corresponds to the free exciton absorption at 77K, however the small peak at 2.520eV (right) may be the direct band to band recombination, as the separation of the main peak and the blue shifted emission are 179meV apart, however decay kinetics experiments would need to be carried out to further ascertain the origin of the peak. The photoluminescence emission of (IC4)PbI<sub>4</sub> (77K) also displays two emission peaks, where the main peak (2.531eV) corresponds to the free exciton optical absorption peak at 77K. The pronounced but secondary peak (2.402eV) which is still present in the 293K spectra may be assigned as a deeply bound exciton trapped at an impurity centre (Ishihara T, *et al*, 1990). 172

**Figure 4.3.4:** A plot of the exciton absorption against the Br-Pb-Br bridging angle. The compounds are coloured accordingly: red (BrC2), light red (HOC2), bright green (IC2), white (IC3), yellow (IC4), Light yellow (IC5), orange (IC6), purple (C4), light orange (C5), olive green (C6), and light Blue (C7). 174

**Figure 4.3.5:** A plot of the exciton absorption against the interlayer spacing. The compounds are colored accordingly: red (BrC2), light red (HOC2), bright green (IC2), white (IC3), yellow (IC4), Light yellow (IC5), orange (IC6), purple (C4), light orange (C5), olive green (C6), and light Blue (C7). 175

**Figure 4.3.6:** Photoluminescence emission of a single crystal of (BrC2)PbI<sub>4</sub> at 77K with a FWHM of the main peak 15meV. The main peak is from the usual exciton recombination, the smaller peak is sample dependant, and is hence assigned as a shallow bound exciton emission. (Sharp lines at ~1.8eV are plasma lines) 177

**Figure 4.3.7:** a) The total and partial density of states, of (BrC2)<sub>2</sub>PbI<sub>4</sub> b) (IC2)<sub>2</sub>PbI<sub>4</sub>. The band structure plots of (BrC2)<sub>2</sub>PbI<sub>4</sub> c) and (IC2)<sub>2</sub>PbI<sub>4</sub> d). The atomic contributions in the DOS are as follows: Blue Pb, Red I, Black Br, Green N. 178

**Figure 4.3.8:** A plot of the exciton absorption against the Br-Pb-Br bridging angle. The compounds are colored accordingly: red (HOC2), yellow (BrC3), orange (BrC4), Sky Blue (BrC5), purple (C4), light orange (C5), green (C6), and light Blue (C7). 181

**Figure 4.3.9:** A plot of the exciton absorption against the interlayer spacing. The compounds are coloured accordingly: red (HOC2), yellow (BrC3), orange (BrC4), Sky Blue (BrC5), purple (C4), light orange (C5), green (C6), and light Blue (C7). 183

**Figure 5.1.1:** The rietveld refinement of the room temperature powder diffraction pattern of (Py)PbI<sub>3</sub>. Where  $R_{\text{Bragg}}$ : 6.586  $R_{\text{exp}}$ : 12.65,  $R_{\text{wp}}$ : 19.99,  $R_p$ : 15.62, GOF: 1.58  $R_{\text{exp}}$ : 18.65,  $R_{\text{wp}}$ : 29.47,  $R_p$ : 26.98, DW: 0.97. The remaining PXRD patterns may be found in appendix B. 192

**Figure 5.1.2:** The DSC graphs displaying the reversible high temperature phase transitions for compounds **1** a), **2** b), **3** c), and **5** d). Compounds **3** and **6** displayed no thermal event within the measured temperature range and their DSC graphs may be found in appendix B. 194

**Figure 5.1.3:** A plot of the unit cell volumes of compounds **1-6** against temperature (100-293K). Most of the volumes were obtained from only unit cells indexed from SC-XRD experiments collected on between 50-250 reflections. All new phase's volumes however, were obtained from full SC-XRD data sets which are included in the graph. The experiment displays the relative thermal stability of compounds **4-6** despite the existence of a minor phase change in **5**. Gaps in the temperature range are due to the results from the DSC experiments which showed no existence of a new phase in that temperature region. Compounds **1-3** show the large unit cell volume changes as a result of the crystal systems changing with decreasing temperature. 195

**Figure 5.1.4:** The crystal packing viewed along (010) axis of the ordered Phase III of (Py)PbI<sub>3</sub> (a) and the disordered envelope conformation shown from the side and above (b, c), where the dark grey atoms represent the disordered component. 196

**Figure 5.1.5:** The conformations of the cyclohexane type ring of pyrrolidinium cation through the four phase changes present in the compound (PD)PbI<sub>3</sub>. The most unfavoured twist chair conformation exists in the higher temperature phases II and I, where the more idealized conformations of the twist boat and chair conformer exist in the low temperature phases III and IV respectively. Note in phase III-I the nitrogen is disordered over two positions, where in phase I the nitrogen is no longer disordered. 196

**Figure 5.1.6:** The conformations of the cycloheptane type ring of the azepanium cation through the four phases of the compound (Az)PbI<sub>3</sub>. The low temperature phases IV and III are the most thermodynamically favoured conformations, whereas the twist and bent transition states in phases II and I respectively, are the least favoured conformers. 197

<b>Figure 5.1.7:</b> Phase I of (PD)PbI <sub>3</sub> disordered nitrogen's hydrogen bonding between the adjacent wires (a). The hydrogen bonding may be described by a hydrogen bonding interaction with the concave face generated by the octahedral face sharing of adjacent octahedra. The ammonium cation displays an N-H...I H-bond interaction with the edge and bottom of the concave face. The hydrogen bonding motif only alters in phase IV (b), where the N-H...I H-bonds now also occur with the top of the concave face in addition to the edge and bottom H-bonds. The H-bonds between the wires also become unsymmetrical in IV.	198
<b>Figure 5.1.8:</b> Disorder of [(Et <sub>3</sub> )NH]PbI <sub>3</sub> shown in black	202
<b>Figure 5.1.9:</b> The space filling view of Phase II (a) void shown in orange, which decreases in volume in phase III (b) as the C5-C6-C7-C8 torsion angle changes.	203
<b>Figure 5.1.10:</b> Optical absorption of (PD)PbI <sub>3</sub> at room temperature (red) and 77K (blue). The first excitation peak at 3.324eV at room and displays a minor blue shift upon cooling to 3.397eV at 77K. The remaining optical absorption of <b>1</b> , <b>5</b> , and <b>6</b> , may be found in appendix B.	206
<b>Figure 5.1.11:</b> The optical absorption of (Az)PbI <sub>3</sub> (a) and (Pyr)PbI <sub>3</sub> (b), displaying the large substructure peak at 2.7eV.	207
<b>Figure 5.1.12:</b> The photoluminescence emission from the self trapped exciton generated in from the 1D photo-excited states of compounds <b>1-6</b> .	207
<b>Figure 5.1.13:</b> The photoluminescence emission against the inter-wire spacing defined by the closest I...I contact (a), and the organic dielectric constant against the photoluminescence emission (b). Orange [(n-But) <sub>4</sub> N]PbI <sub>3</sub> , Light Blue [(Et <sub>3</sub> )NH]PbI <sub>3</sub> , Blue (Py)PbI <sub>3</sub> , Purple (Pyr)PbI <sub>3</sub> , Red (Az)PbI <sub>3</sub> , Green (PD)PbI <sub>3</sub> .	210
<b>Figure 5.1.14:</b> The STE emission against the crystal density. The decreasing crystal density increases exciton lattice interactions. This sees an associated red shift of the STE emission. Orange [(n-But) <sub>4</sub> N]PbI <sub>3</sub> , Light Blue [(Et <sub>3</sub> )NH]PbI <sub>3</sub> , Blue (Py)PbI <sub>3</sub> , Purple (Pyr)PbI <sub>3</sub> , Red (Az)PbI <sub>3</sub> , Green (PD)PbI <sub>3</sub> .	210
<b>Figure 5.2.1:</b> Photoluminescence spectra of (DPBD)Pb <sub>2</sub> I <sub>6</sub> and (EPPA)PbI <sub>3</sub> displaying the STE luminescence at 123K and 77K respectively. However at 77K (DPBD)Pb <sub>2</sub> I <sub>6</sub> displays an additional emission blue shifted to the STE emission. The excitation energy laser power was maintained at both 77K and 123K.	216
<b>Figure 5.2.2:</b> Optical absorption spectra of (DPBD)Pb <sub>2</sub> I <sub>6</sub> and (EPPA)PbI <sub>3</sub> at both room temperature and 77K	216
<b>Figure 5.2.3:</b> The hydrogen bonding and disorder (dark grey) of (EPPA)PbI <sub>3</sub> viewed along the (100) axis.	217
<b>Figure 5.2.4:</b> The packing motif of phase I and II of (DPBD)Pb <sub>2</sub> I <sub>6</sub> which shows the organic packing motif which remains the same in both phases, however the unit cell volume has doubled from phase I to II.	218
<b>Figure 5.2.5:</b> Phase I and II of (DPBD)Pb <sub>2</sub> I <sub>6</sub> the lead iodide wire viewed down the (100) direction in phase I, shows the regularity of the wire, in phase II the unit cell origin shifts, and the lead atoms now arrange in a wave like fashion in the (001) direction. This distortion has been attributed to the new PL emission at 77K.	218
<b>Figure 5.3.1:</b> The inorganic 1D "sheets" and the arrangement of the edge sharing lead iodide octahedra for compounds <b>1-5</b> . All five compounds display a similar surface topology on the "top" of the wire. Compounds <b>2</b> (b), <b>4</b> and <b>5</b> (d) display identical wire topologies as seen in b) and d) where the wire color represents the compounds crystal color. In compound ( <b>1</b> ) a) the octahedra are offset from one another, unlike the remaining compounds, and compound ( <b>3</b> ) c) displays the same topology as <b>2</b> , <b>4</b> , and <b>5</b> , however has an additional chain of lead iodide octahedra.	226
<b>Figure 5.3.2:</b> a) The packing diagram of 2.DMSO.(BP)Pb <sub>2</sub> I <sub>6</sub> viewed along (100) axis. b) The packing diagram of (EEDP)Pb <sub>2</sub> I <sub>6</sub> viewed along the (100) axis. c) The packing diagram of 2DMSO.(PDP)Pb <sub>3</sub> I <sub>8</sub> viewed along the (001) axis. (The wire colors represent the crystal color).	227
<b>Figure 5.3.3:</b> a) The packing diagram of <b>4</b> (MDA)Pb <sub>2</sub> I <sub>6</sub> viewed along (001) axis. b) The packing diagram of <b>5</b> (BD)Pb <sub>2</sub> I <sub>6</sub> viewed along the (100) axis.	230
<b>Figure 5.3.4:</b> The rietveld refined P-XRD data of (PDP)Pb <sub>3</sub> I <sub>8</sub> ( <b>3</b> ). R <sub>Bragg</sub> 5.507, R <sub>exp</sub> 12.80, R <sub>wp</sub> 18.71, R <sub>p</sub> 4.50, GOF 1.46, R <sub>exp</sub> 19.53, R <sub>wp</sub> 28.55, R <sub>p</sub> 24.87, DW 1.05.	231
<b>Figure 5.3.5:</b> The optical absorption measurements for (PDP)Pb <sub>3</sub> I <sub>8</sub> (a) and (BP)Pb <sub>2</sub> I <sub>6</sub> (b) at both room temperature and 77K. Both compounds display the distinct first exciton absorption peak at 3.21eV and 3.27eV for a) and b) respectively. However a substructure peak at 2.7eV is present in b) and the broad CT absorption band from 2.0-2.8eV is present in a).	234
<b>Figure 5.3.6:</b> The 77K photoluminescence emission of (PDP)Pb <sub>3</sub> I <sub>8</sub> (a), (BP)Pb <sub>2</sub> I <sub>6</sub> and (EEDP)Pb <sub>2</sub> I <sub>6</sub> (c). Emission profiles are explained in the text. Plasma lines are present in all the spectra as we did not have the correct band pass filter.	234

**Figure 5.3.7:** Charge transfer mechanism between the wires and spacers. Included are the previously investigated samples of (EV)Pb<sub>2</sub>I<sub>6</sub> and (MV)Pb<sub>2</sub>I<sub>6</sub> from which this mechanism is adapted from (Fujisawa J and Ishihara T, 2004; Fujisawa J and Tajima N, 2005; Fujisawa J, *et al*, 2007). (not to scale)

**Figure 6.1:** a) A view of compound **1** along the 001 axis. The hydrogen bonding of the compound adopts the acute right angled hydrogen bonding configuration within the void of the parallelogram formed between the four metal iodide octahedral. We notice for this compound an elongation of the sides of the parallelogram where the methyl group is positioned. This coincides with Sn-I<sub>eq</sub> bond length elongations (methyl position) and compressions (ammonium position) along the length of the obtuse angled side of the parallelogram. b) The view of **1** in its space group *P*2<sub>1</sub>2<sub>1</sub>2<sub>1</sub> along the 010 axis showing the staggered arrangement of the inorganic layers.

**Figure 6.2:** The weak interactions present in compound **7** (left) are representative of compounds **1-3** and **6-8** and compound **5b** (right) weak interactions, which is representative of compounds **4** and **5**.  $\pi$ - $\pi$  interactions shown in green,  $\sigma$ - $\pi$  interactions shown in light blue.

**Figure 6.3:** The variable temperature photoluminescence of (R&S-PhMetNH<sub>3</sub>)<sub>2</sub>PbI<sub>4</sub>. Two peaks are present at low temperature, the main excitonic emission, and a shoulder peak which displays much greater temperature dependence than the excitonic emission. The excitonic shift with temperature may be modeled using the varshni model as described in the test, with a  $\beta$  value of 780 and an alpha value of  $3.19 \times 10^{-4}$ . The FWHM of the main Eex peak has also been plotted against temperature and displays the expected liner increase with temperature (although not shown here the shoulder peak displays a similar linear increase with temperature). It should be noted that the main excitonic peak was fitted with a Gaussian peak profile with a minor amount of lorentzian character, while the shoulder peak showed a more lorentzian peak profile.

**Figure 6.4:** The variable temperature photoluminescence of (R-PhMetNH<sub>3</sub>)<sub>2</sub>PbI<sub>4</sub>. Two peaks are present at low temperature, the main excitonic emission, and a shoulder peak which displays much greater temperature dependence than the excitonic emission. The excitonic shift with temperature may be modeled using the varshni model as described in the test, with a  $\beta$  value of 780 and an alpha value of  $2.8 \times 10^{-4}$ . The FWHM has also been plotted against temperature and displays the expected liner increase with temperature (although not shown here the shoulder peak displays the same linear increase with temperature). It should be noted that the main excitonic peak was fitted with a Gaussian peak profile with a minor amount of lorentzian character, while the shoulder peak showed a more lorentzian peak profile.

**Figure 6.5:** The variable temperature photoluminescence of (R-MeOPhMtNH<sub>3</sub>)<sub>2</sub>PbI<sub>4</sub>. Two peaks are present at low temperature, the main excitonic emission, and a shoulder peak which displays much greater temperature dependence than the excitonic emission. The excitonic shift with temperature may be modeled using the varshni model as described in the test, with a  $\beta$  value of 500 and an alpha value of  $2.94 \times 10^{-4}$ . The FWHM has also been plotted against temperature and displays the expected liner increase with temperature. It should be noted that the main excitonic peak was fitted with a Gaussian peak profile with a minor amount of lorentzian character, while the shoulder peak showed a more lorentzian peak profile.

**Figure 6.6:** The 1s exciton energy level has a fine structure which is split into three fine structure energy levels. These are the purely triplet state  $\Gamma_1^-$ , the triplet dominant  $\Gamma_2^-$  and the singlet dominant state  $\Gamma_5^-$ . As may be seen in a)  $\Gamma_5^-$  decays into  $\Gamma_2^-$  and  $\Gamma_1^-$  through a spin relaxation, as well as a spin flip decay b) as may be seen in c). (Ema K, et al, 2006)

**Figure 6.7:** The energy difference between the main sharp excitonic peak, and the shoulder peak present in the emission spectrum. The shoulder peak positions have been plotted for each compound

**Figure 6.8:** The variable temperature photoluminescence of (S-MeOPhMtNH<sub>3</sub>)<sub>2</sub>PbI<sub>4</sub>. Three peaks are present at 100K, the main excitonic emission, the similar shoulder peak observed for the all of the 2D lead iodide systems, and a higher energy shoulder peak visible in the temperature range 77-150K. In this compound the Eex could not be empirically fitted with the Varshni model, however the FWHM plotted against temperature displays the expected liner increase with temperature. It should be noted that the main excitonic peak was fitted with a Gaussian peak profile with a minor amount of lorentzian character, while the shoulder peaks showed a more lorentzian peak profile.



**Figure 6.9:** Compound **9** on the left with compound **11** on the right. As seen from the diagrams above we notice the difference in the arrangement of the organic template relative to the inorganic metal halide's face sharing octahedral wires of compounds **9** and **11**. In both compounds the wires propagate along the (100) axis. We also notice that the hydrogen bonding motif between both compounds is almost identical. 280

**Figure 6.10:** The Variable temperature PL spectrum is of the R enantiomer 1D  $\text{PbI}_3$  wires, and follows a similar increase in temperature as observed for the  $\text{PbI}_3^-$  wires shown in the diagram on the right. (Sharp emission lines from the plasma lines from the laser, were present as we did not have the correct band pass filter). Bad crystal quality lead to the exclusion of the luminescence data of the S enantiomer. 283

**Figure 6.11:** The characteristic STE luminescence emission found in the 1D  $\text{SnI}_3$  compounds. What is evident from the temperature dependence experiments is that both the R and S enantiomer have similar STE shifts as the temperature increases, however at 200K, the S enantiomer exhibits a large shift, whereas the R enantiomer does not. The variable temperature PL is of (R) $\text{SnI}_3$  on the left and (R) $\text{SnI}_3$  on the right. (The sharp lines are plasma lines due to the lack of a band pass filter in for the UV laser). 284

**Figure A.1:** (HOC2) $\text{PbI}_4$  the optical absorption and photoluminescence. Please note as no band pass filter was used, the plasma lines are still present in the PL spectra 298

**Figure A.2:** (BrC2) $\text{PbI}_4$  the optical absorption and photoluminescence. Please note as no band pass filter was used, the plasma lines are still present in the PL spectra 298

**Figure A.3:** (IC2) $\text{PbI}_4$  the optical absorption and photoluminescence at 77K. Please note as no band pass filter was used, the plasma lines are still present in the PL spectra. 298

**Figure A.4:** (IC3) $\text{PbI}_4$  the optical absorption and photoluminescence at 77K. Please note as no band pass filter was used, the plasma lines are still present in the PL spectra. 299

**Figure A.5:** (IC4) $\text{PbI}_4$  the optical absorption and photoluminescence at 77K. Please note as no band pass filter was used, the plasma lines are still present in the PL spectra. 299

**Figure A.6:** (IC5) $\text{PbI}_4$  the optical absorption and photoluminescence at 77K. Please note as no band pass filter was used, the plasma lines are still present in the PL spectra. 299

**Figure A.7:** (IC6) $\text{PbI}_4$  the optical absorption and photoluminescence at 77K. Please note as no band pass filter was used, the plasma lines are still present in the PL spectra. 300

**Figure A.8:** The optical absorption of (C4) $\text{PbI}_4$  (left) and (C5) $\text{PbI}_4$  (right) at 77K 300

**Figure A.9:** The optical absorption of (C6) $\text{PbI}_4$  (left) and (C7) $\text{PbI}_4$  (right) at 77K 300

**Figure A.10:** The optical absorption of (C4) $\text{PbBr}_4$  (left) and (C5) $\text{PbBr}_4$  (right) at 77K 301

**Figure A.11:** The optical absorption of (C6) $\text{PbBr}_4$  (left) and (C7) $\text{PbBr}_4$  (right) at 77K 301

**Figure A.12:** The optical absorption of (HOC2) $\text{PbBr}_4$  (left) and (BrC3) $\text{PbBr}_4$  (right) at 77K 301

**Figure A.13:** The optical absorption of (BrC4) $\text{PbBr}_4$  (left) and (BrC5) $\text{PbBr}_4$  (right) at 77K 302

**Figure A.14:** The DSC scans of (BrC2) $\text{PbI}_4$  (left) and (HOC2) $\text{PbI}_4$  (right) 302

**Figure A.15:** The DSC scans of (IC2) $\text{PbI}_4$  (left) and (IC3) $\text{PbI}_4$  (right) 302

**Figure A.16:** The DSC scans of (IC4) $\text{PbI}_4$  (left) and (IC5) $\text{PbI}_4$  (right) 303

**Figure A.17:** The DSC scans of (IC6) $\text{PbI}_4$  303

**Figure B.1:** The DSC scans of (Pyr) $\text{PbI}_3$  (left) and  $[(\text{Et})_3\text{NH}]\text{PbI}_3$  (right). The small peaks in (Pyr) $\text{PbI}_3$  are sample dependant. 304

**Figure B.2:** The powder diffraction pattern and rietveld refinement of (PD) $\text{PbI}_3$  where RBragg: 3.635 Rexp : 17.41, Rwp : 19.77, Rp : 15.30, GOF : 1.14, Rexp` : 30.83, Rwp` : 35.01, Rp` : 31.85, DW : 1.56. Refined unit cell parameters for C2221 a = 8.7083(23) Å, b = 18.4196(50) Å, c = 8.1241(22) Å, V = 1303.15(61) Å<sup>3</sup>, refinement range: 5-60° 2θ 304

**Figure B.3:** The powder diffraction pattern and rietveld refinement of (Az) $\text{PbI}_3$  where RBragg: 8.801 Rexp : 11.18, Rwp : 18.36, Rp : 14.37, GOF : 1.64, Rexp` : 16.20, Rwp` : 26.61, Rp` : 23.86, DW : 0.84. Refined unit cell parameters for C2221 a = 8.75506(92) Å, b = 19.6060(21) Å, c = 8.20201(93) Å, V = 1407.89(26) Å<sup>3</sup>, refinement range: 7-60° 2θ 304

**Figure B.4:** The powder diffraction pattern and rietveld refinement of (Pyr) $\text{PbI}_3$  where RBragg: 3.502 Rexp : 7.52, Rwp : 11.71, Rp : 9.04, GOF : 1.56, Rexp` : 10.25, Rwp` : 15.95, Rp` : 13.24 DW : 0.92. Refined unit cell parameters for Pnma a = 14.9702(11) Å, b = 8.09842(60) Å, c = 9.89108(74) Å, V = 1199.15(15) Å<sup>3</sup>, refinement range: 8-60° 2θ 305

<b>Figure B.5:</b> The powder diffraction pattern and rietveld refinement of [(n-But)4N]PbI3 where RBragg: 5.735, Rexp : 10.87, Rwp : 16.68, Rp : 13.01, GOF : 1.53, Rexp` : 17.11, Rwp` : 26.26, Rp` : 24.07, DW : 1.05. Refined unit cell parameters for I-42d a = 24.5855(16) Å, b = 8.38275(63) Å, V = 5066.91(76) Å <sup>3</sup> , refinement range: 5-60° 2θ	305
<b>Figure B.6:</b> The powder diffraction pattern and rietveld refinement of [(Et)3NH]PbI3 where RBragg: 5.868, Rexp : 14.64, Rwp : 19.79, Rp : 15.90, GOF : 1.35, Rexp` : 24.64, Rwp` : 33.32, Rp` : 30.89, DW : 1.24. Refined unit cell parameters for Pnma a = 18.4833(24) Å, b = 8.0652(11) Å, c = 20.3529(26) Å, V = 3034.01(69) Å <sup>3</sup> , refinement range: 8-60° 2θ	305
<b>Figure B.7:</b> The optical absorption of (Py)PbI3 (left) and [(Et)3NH]PbI3 (right) at both 77K and room temperature.	306
<b>Figure B.8:</b> The optical absorption of [(n-But)4N]PbI3~ at both 77K and room temperature.	306
<b>Figure B.9:</b> The powder diffraction pattern and rietveld refinement of 2.DMSO(BP)Pb2I6 where RBragg : 6.004, Rexp : 11.52, Rwp : 15.53, Rp : 12.01, GOF : 1.35, Rexp` : 18.79, Rwp` : 25.33, Rp` : 22.19, DW : 1.24. Refined unit cell parameters for P21212 a = 8.10947(49) Å, b = 23.6548(12) Å, c = 33.0516(16) Å, V = 6340.21(59) Å <sup>3</sup> , refinement range: 5-60° 2θ.	306
<b>Figure B.10:</b> The powder diffraction pattern and rietveld refinement of 2H2O.(BD)Pb2I6 where RBragg : 2.318, Rexp : 4.73, Rwp : 7.79, Rp : 6.12, GOF : 1.65, Rexp` : 13.63, Rwp` : 22.46, Rp` : 26.19, DW : 0.88. Refined unit cell parameters for Fdd2 a = 25.3445(17)Å, b = 43.1408(27)Å, c = 4.53537(35) Å, V = 4958.88 (60) Å <sup>3</sup> , refinement range: 5-60° 2θ.	307
<b>Figure B.11:</b> The powder diffraction pattern and rietveld refinement of (MDA)Pb2I6 where RBragg : 19.447, Rexp : 2.71, Rwp : 12.13, Rp : 8.72, GOF : 4.48, Rexp` : 4.33, Rwp` : 19.41, Rp` : 16.46, DW : 0.26. Refined unit cell parameters for P21/c a = 4.521(67)Å, b = 13.216(65)Å, c = 22.636(11)Å, V = 1352.76(46) Å <sup>3</sup> , refinement range: 5-60° 2θ.	307
<b>Figure B.12:</b> The optical absorption of 2H2O.(BD)Pb2I6 (left) and (MDA)Pb2I6 (right) at both 77K and room temperature.	307
<b>Figure C.1:</b> The DSC scans of (R-C6H5C*(H)CH3NH3)2SnI4 (left), (S-C6H5C*(H)CH3NH3)2SnI4 (right) and (R&S-C6H5C*(H)CH3NH3)2SnI4 (bottom), compounds 1-3 respectively.	308
<b>Figure C.2:</b> The DSC scans of (R-MeOC6H4C*(H)CH3NH3)2PbI4 (left), (S-MeO-C6H4C*(H)CH3NH3)2PbI4 (right) compounds 4-5 respectively.	308
<b>Figure C.3:</b> The DSC scans of (R-C6H5C*(H)CH3NH3)2PbI4 (left), (S-C6H5C*(H)CH3NH3)2PbI4 (right) and (R&S-C6H5C*(H)CH3NH3)2PbI4 (bottom), compounds 6-8 respectively.	309
<b>Figure C.4:</b> The DSC scans of (R-C6H5C*(H)CH2CH3NH3)2PbI4 (left), (S-C6H5C*(H)CH2CH3NH3)2PbI4 (right), compounds 9-10 respectively.	309

## List of tables

<b>Table 2.1:</b> Crystal structure data for the Cubic (CH3NH3)PbX3 where X = Cl, Br, and I.	31
<b>Table 2.2:</b> The <100> orientation reported cases for Sn and Pb based hybrid perovskites with layers greater than 1.	44
<b>Table 2.3:</b> The structures studied by (Knutson J. L, et al, 2005) (not all these materials have been fully characterized crystallographically).	52
<b>Table 2.4:</b> All dimensions of lead and tin iodide shown as a I/M ratio, with the simplest MI formula unit reported (Mercier N, et al, 2009).	59
<b>Table 2.5:</b> All dimensions of bismuth and antimony iodide shown as a I/M ratio, with the simplest MI formula unit reported (Mercier N, et al, 2009).	59
<b>Table 2.6:</b> CSD search for lead iodide hybrids (Nov 2009).	60
<b>Table 2.7:</b> Table of lead iodide hybrids generated from the cystamine cation.	62
<b>Table 2.8:</b> The binding energies, optical absorption and Photoluminescence emissions at various temperatures, of some PbI based hybrids.	65
<b>Table 2.9:</b> The binding energies, optical absorption and Photoluminescence emissions at various temperatures, of some PbBr based hybrids.	73
<b>Table 2.10:</b> 2D lead chloride hybrids optical properties.	77
<b>Table 2.11:</b> Remaining lead halide crystal structures.	77

<b>Table 2.12:</b> Summary of the multiple phases of the alkyl ammonium cadmium chloride hybrid perovskites.	86
<b>Table 2.13:</b> Summary of the multiple phase changes of all the alkyl ammonium Lead Iodide hybrids.	87
<b>Table 2.14:</b> Phase Change enthalpies for the various phase changes for the aliphatic (Cn)PbI <sub>4</sub> hybrids.	89
<b>Table 2.15:</b> Reference of single chain 1D lead hybrids investigated structurally, and the few papers investigating the optical and electronic properties.	102
<b>Table 4.1.1:</b> Crystallographic structural tables. Experiments were carried out with Mo K $\alpha$ radiation using a Bruker APEX-II CCD diffractometer	131
<b>Table 4.1.2:</b> The enthalpy measurements from the DSC experiment of the phase transitions.	136
<b>Table 4.1.3:</b> Summary of the important geometrical parameters for the multiple phases of the (Cn)PbBr <sub>4</sub> series of compounds.	141
<b>Table 4.1.4:</b> The interlayer spacing and lattice constants for (Cn)PbBr <sub>4</sub> where n =4-7, obtained through thin film powder diffraction measurements.	142
<b>Table 4.1.5:</b> The lead bromide octahedral bond lengths and angles, displaying the distortions around metal centre.	142
<b>Table 4.2.1:</b> The enthalpy measurements from the DSC experiment of the phase transitions of (HOC2)PbBr <sub>4</sub> and (BrCn)PbBr <sub>4</sub> where n = 3-5, and (Cn)PbBr <sub>4</sub> where n = 4-7.	147
<b>Table 4.2.2:</b> Crystallographic structural tables Experiments were carried out with Mo K $\alpha$ radiation using a Bruker APEX-II CCD diffractometer.	148
<b>Table 4.2.3:</b> Important geometrical parameters associated with the phase transitions, and halogen bonding interactions.	158
<b>Table 4.2.4:</b> Inorganic distortions of the bond lengths and angles for the respective compounds and their phases.	159
<b>Table 4.3.1:</b> Important geometrical parameters of the (X-Cn)PbI <sub>4</sub> series where X = I for n =2-6 and X = OH and Br for n = 2. (This data is from our own structural (SC-XRD) experiments however the structures are reported by (Mercier N, <i>et al</i> , 2004 (9); Sourisseau S, <i>et al</i> , 2007a 10-11; Lemmerer A, Billing D. G, 2010 9-15).	165
<b>Table 4.3.2</b> The important geometrical parameters relating to the inorganic distortions for the Pb-I bond distances (Å) and the relevant octahedral angles (°).	166
<b>Table 4.3.3:</b> Important geometrical parameters of (Cn)PbI <sub>4</sub> where n = 4-7 (Values obtained exclusively from Billing D. G and Lemmerer A, 2007 16-18; Lemmerer A, 2007 19) Only low temperature and phases close to room temperature are quoted below, as our optical experiments did not investigate the high temperature forms.	168
<b>Table 4.3.4:</b> The important geometrical parameters relating to the inorganic distortions for the Pb-I bond distances (Å) and the relevant octahedral angles (°).	169
<b>Table 4.3.5:</b> The lead Iodide series summary of inorganic distortions, exciton optical absorptions, and estimated binding energies from the low temperature optical absorption measurements.	180
<b>Table 4.3.6:</b> The lead Iodide series summary of inorganic distortions, exciton optical absorptions, and estimated binding energies from the low temperature optical absorption measurements.	184
<b>Table 5.1.1:</b> Crystal structure data of compounds <b>1-6</b> , and their respective phases. Furthermore structures at both 173K and 293K are reported even if no phase transition was observed. Experiments were carried out with Mo K $\alpha$ radiation using a Bruker APEX-II CCD diffractometer. H-atom parameters were constrained.	189
<b>Table 5.1.2:</b> The enthalpy measurements of the phase transitions of compounds <b>1-3</b> and <b>5</b> for the heating runs only.	194
<b>Table 5.1.3:</b> Summary of the ranges of inorganic bond angles and bond lengths experienced in each compound.	201
<b>Table 5.1.4:</b> Summary of the ranges inorganic bond angles and bond lengths experienced in each compound.	204
<b>Table 5.1.5:</b> Hydrogen bonding tables of compounds <b>1-4</b> , and <b>6</b> .	206
<b>Table 5.1.6</b> The optical absorption and photoluminescence emissions summarized with the most important structural aspects of the compounds.	209
<b>Table 5.2.1:</b> The crystal structure data of the compound <b>1</b> and <b>2</b> completed at various temperatures. Experiments were carried out with Mo K $\alpha$ radiation. H-atom parameters were constrained.	213
<b>Table 5.2.2:</b> Summary of the inorganic bond lengths and bond angles.	219
<b>Table 5.2.3:</b> Table of hydrogen bonding interactions of compounds <b>1</b> and <b>2</b> at various temperatures.	220

<b>Table 5.3.1:</b> Experiments were carried out at 173 K with Mo $K\alpha$ radiation using a Bruker APEX-II CCD diffractometer. Absorption corrections were completed using the Integration method, <i>Bruker XPREP</i> (Bruker, 2005).	225
<b>Table 5.3.2:</b> Summary of the inorganic bond length and angle distortions ranges for compounds <b>1-5</b> .	227
<b>Table 5.3.3:</b> Hydrogen bonding interactions for compounds <b>1-5</b> .	230
<b>Table 6.1:</b> Crystal structure data of compounds <b>1-5</b> , and their respective phases. Structures at both 173K and 243K are reported even if no phase transition was observed. Experiments were carried out with Mo $K\alpha$ radiation using a CCD area detector diffractometer. Integration, <i>Bruker XPREP</i> (Bruker, 2005). H-atom parameters were constrained.	256
<b>Table 6.2:</b> Summary of excitonic emissions, and the relevant structural parameters for compounds <b>1-3</b> , which are compared with literature (references cited in the table), adapted from (Knutson J. L, <i>et al</i> , 2005).	260
<b>Table 6.3:</b> Summary of excitonic emissions, and the relevant structural parameters for the lead iodide compounds <b>4-8</b> , which are compared with work completed in chapter 4.	261
<b>Table 6.4:</b> Relevant inorganic bond lengths and angles and crystallographic data.	263
<b>Table 6.5:</b> The hydrogen bonding table of compounds <b>1-5</b> .	264
<b>Table 6.6:</b> The refined $\alpha$ and $\beta$ values for the empirical parameters of Varshni's model, for the 2D lead iodide compounds.	267
<b>Table 6.7:</b> For all structures: orthorhombic, $P2_12_12_1$ , $Z = 4$ . Experiments were carried out with Mo $K\alpha$ radiation using a CCD area detector diffractometer. Integration, <i>Bruker XPREP</i> (Bruker, 2005). Refinement was completed with 0 restraints. H-atom parameters were constrained. The absolute structure was obtained using Flack H D (1983), <i>Acta Cryst. A</i> 39, 876-881.	278
<b>Table 6.8:</b> Some selected inorganic bond lengths and angles for comparison between the structures. The labels have been rearranged for a direct comparison between each of the structures.	279
<b>Table 6.9:</b> Relevant organic torsion angles ( $^\circ$ ) for comparison between compounds.	281
<b>Table 6.10:</b> The hydrogen bonding table of compounds <b>9-12</b> .	281
<b>Table C1:</b> Summary of the melting point temperatures of compounds <b>1-10</b>	310

## List of schemes

## Page

<b>Scheme 4.1.1:</b> A summary of the phase transitions and the relative phase transformation temperatures for both heating and cooling runs for $(\text{Cn})\text{PbBr}_4$ . Estimates of the phase transformation temperatures were made for the transitions that occurred below the measuring capability of the differential scanning calorimeter, which were examined via SC-XRD cooling experiments.	128
<b>Scheme 4.2.1:</b> A summary of the phase transitions and the relative phase transformation temperatures for both heating and cooling runs for $(\text{BrCn})\text{PbBr}_4$ where $n = 3-5$ and $(\text{HOC2})\text{PbBr}_4$ . Estimates of the phase transformation temperatures were made for the transitions that occurred below the measuring capability of the differential scanning calorimeter, which were examined via SC-XRD cooling experiments.	145
<b>Scheme 4.2.2:</b> The phases of $(\text{BrC3})\text{PbBr}_4$ , moving from the disordered Phase IV, and increasing in order of the aliphatic proceeding to the less disordered phase II, and finally the ordered phase I. The disordered atoms have been shaded in dark grey to enhance clarity.	151
<b>Scheme 4.2.3:</b> The phases of $(\text{BrC5})\text{PbBr}_4$ , moving from the ordered Phase III, to the disordered phase II. The disordered atoms have been shaded in dark grey to enhance clarity.	156
<b>Scheme 5.1.1:</b> Polymeric schemes of the crystal structures of compounds <b>1-6</b> .	188
<b>Scheme 5.1.2:</b> A summary of the phase transitions and the relative phase transformation temperatures for both heating and cooling runs of the $(\text{A})\text{PbI}_3$ compounds. Estimates of the phase transformation temperatures were made for the transitions that occurred below the measuring capability of the differential scanning calorimeter, and were examined via VT-SC-XRD cooling experiments.	188
<b>Scheme 5.2.1:</b> The polymeric schemes of the crystal structures of <b>1</b> and <b>2</b> respectively.	213
<b>Scheme 5.3.1:</b> The polymeric schemes of the crystal structures of <b>1-5</b> respectively.	224
<b>Scheme 6.1:</b> The $\beta$ tensor vector possibilities of neighbouring polarizable molecules (Giffard M, <i>et al</i> , 2005).	252
<b>Scheme 6.2</b> Polymeric schemes of the chiral crystal structures and respective racemate structures of compounds <b>1-8</b> .	255



## ***Chapter 1: Introduction and Theory***

### ***1.1 Introduction***

Semiconductors have been an area of great interest for almost the past two centuries with the first reported case in 1833 by no other than Michael Faraday (Hirschfeld A. W, 2006). He observed an increase of silver sulphides' conductivity with increasing temperature which is most unlike that observed for copper. Semiconductor physics has drastically progressed since then with the full development of the theoretical background which includes the concept of electronic bands in solids, the density of states of a solid, and the various physical properties one may calculate using these functions. More recent developments have been the discovery of low dimensional semiconductors such as quantum wells, wires and dots, which have shown enhanced semiconducting properties especially in terms of highly efficient luminescence. These systems have been the subject of intensive research over the past three decades (Wang X. L, Voliotis V, 2006). To give an indication of how recent this field is, quantum dots were only discovered in the early 80's by Alexei Ekimov (Ekimov A. I, Onushchenko A. A, 1981) with the term "quantum dot" only later being coined by Mark Reed (Reed M. A, *et al*, 1988). The body of this thesis focuses particularly on the optical enhancements of natural low dimensional systems.

As is well established in solid state physics, when a semiconductor absorbs a photon with an energy  $E > E_g$ , it generates a coulomb correlated electron hole pair known as an exciton (or charge carrier). In this chapter we discuss the enhancement one may achieve by manipulating this particles property through dimensional reduction and quantum confinement. This is achieved by establishing the basic theoretical background followed by a theoretical description of excitonic and electronic states in low dimensional systems. This will establish a sound theoretical basis for the practical investigations carried out in the results chapters of this thesis.

In terms of fabrication of quantum confined semiconductors (wells, wires and dots), various methodologies have been employed. By far the most common technique used is the growth by advanced epitaxial techniques in nanocrystals produced by chemical methods or by ion implantation, or in nanodevices made by state of the art lithographic techniques (Wang X. L, Voliotis V, 2006; Delerue C, Lannoo M, 2004). Alternate approaches have been used specifically in the formation of quantum dots which are formed by generating, colloidal suspensions of the semiconductor, growth of quantum dots from viral assembly (Lee S. W, *et al*, 2002) and various electrochemical techniques.

In later chapters we expand the idea of the formation of crystalline quantum structures, through organically templating the inorganic semiconductor component into the desired dimensional motif. These motifs are grown through solution processing techniques. This branch of crystalline compounds is formally known as organic inorganic hybrids. Hybrid structures such as these have a distinct advantage over traditional fabrication techniques. The low dimensional structures are readily formed and are generally grown at the lower size limit of the well, wire or dot, and are easily solution processed into thin films. These compounds are therefore excellent candidates for investigating the fundamental excitonic enhancements occurring at these levels.

The main focus of this thesis has therefore been on both the fabrication of the low dimensional crystalline semiconductors (hybrids), and the measurement of their optical absorption and luminescent responses. As the hybrid systems can form single crystals, their structures have been fully characterized, with structure to optical property correlations being developed where possible. In many cases the low dimensional structures were found to undergo phase transitions because of the flexible nature of the organic template. As excitonic behaviour is largely studied at low temperature, all of the low temperature phases of the structures were characterized, to ensure that if any structure to optical property correlation was made, it would be correct (chapters 4 and 5).

Chapter 6 was written differently from chapters 4 and 5, as the focus of the chapter was on nonlinear optical properties. The results in that section began as an investigation into the use of chiral templates to ensure the symmetry condition would be met for efficient second order nonlinear effects to occur. A theoretical basis for NLO generation will therefore be covered in chapter 6 as it forms a related but somewhat separate piece of work from the work completed on dimensional reduction. It should be noted that most of the theory summarized in this chapter comes from a handful of sources, therefore only a bibliography is given at the end of this chapter as a separate reference list to the one in chapter 8.

## ***1.2 Brillouin zones and reciprocal space***

In order to describe the electronic structure of solids in low dimensional systems, we first need to describe the most fundamental tool, in which the rest of these theories use to describe themselves i.e. the crystal lattice, reciprocal space which is also known as  $k$  space, and the First Brillouin Zone (or Irreducible Brillouin Zone). As crystallographers work with reciprocal space when obtaining a diffraction pattern, from either a single crystal or powder diffraction

techniques, the  $k$  space description the spectroscopist uses should not be too difficult for them to grasp.

Brillouin zones may be described as polyhedra in reciprocal space in crystalline materials. They are geometrically equivalent to the Wigner-Seitz cells in real space. The first Brillouin zone (FBZ) or the irreducible Brillouin zone boundaries correspond to intersecting Bragg planes which uniquely describe the first Brillouin zone, and may be individually defined for each space group ([http://www.cryst.ehu.es/cryst/get\\_kvec.html](http://www.cryst.ehu.es/cryst/get_kvec.html)). One may also crudely think of it as the reciprocal lattice version of the asymmetric unit of the crystal structure in real space which describes the remainder of the unit cell through symmetry. However, the question still remains why is it necessary to describe the reciprocal lattice? Well, the crystal lattice in real space is used to describe the periodic structure, while the reciprocal lattice is used to describe the periodic structures interaction with waves. Obviously this point helps us realize why the reciprocal lattice is so important, as the electronic structure of any periodic material is described using some form of wave function. Furthermore the interaction of waves being reflected from planes in the reciprocal lattice is what gives rise to a diffraction pattern of a crystal in real space.

To fully describe the first Brillouin zone one must describe the reciprocal lattice from a set of wave vectors  $k$  that yield plane waves with the specific Bravais lattice periodicity. Mathematically one may say that  $k$  belongs to the reciprocal lattice of a Bravais lattice with real space lattice points of  $\mathbf{R}$  provided that the relationship

$$e^{ik(\mathbf{R}+\mathbf{r})} = e^{ik(\mathbf{r})} *$$

Holds for any  $\mathbf{r}$ , and all  $\mathbf{R}$  in the Bravais lattice. In this equation

$$\mathbf{k} = h\mathbf{b}_1 + k\mathbf{b}_2 + l\mathbf{b}_3$$

Where

$$\mathbf{b}_1 = 2\pi \frac{\mathbf{a}_2 \times \mathbf{a}_3}{\mathbf{a}_1 \cdot \mathbf{a}_2 \times \mathbf{a}_3}; \quad \mathbf{b}_2 = 2\pi \frac{\mathbf{a}_3 \times \mathbf{a}_1}{\mathbf{a}_1 \cdot \mathbf{a}_2 \times \mathbf{a}_3}; \quad \mathbf{b}_3 = 2\pi \frac{\mathbf{a}_1 \times \mathbf{a}_2}{\mathbf{a}_1 \cdot \mathbf{a}_2 \times \mathbf{a}_3}.$$

Are the reciprocal lattice vectors and  $hkl$  are the miller indices, with

$$\mathbf{R} = x\mathbf{a}_1 + y\mathbf{a}_2 + z\mathbf{a}_3$$

being the real space vectors. After defining these equations one can see that the periodicity of the first Brillouin zone describes the entire reciprocal lattice from the periodic condition in \*. For a graphical explanation of the first Brillouin zone (FBZ) we look at figure 1.1 where we have a



diffraction pattern of a single crystal in a cubic crystal system (figure 1.1a). To generate the FBZ a vector may be drawn from the centre diffraction spot to the nearest neighbour diffraction spot. This vector is then bisected by a Bragg plane. Three more vectors are added, as they are equal in magnitude to the first vector, since this is a cubic diffraction pattern which will describe four nearest neighbour spots with the same condition. The other Bragg planes are then added that meet the first criterion. This generates the first Brillouin zone for the cubic system. To generate the second Brillouin zone the next nearest neighbour spot is then selected, the vector is then bisected by the Bragg plane and then the next zone is completed as the first. The area between the second zone and the first zone, describes the second Brillouin zone. The FBZ generation for a hexagonal system follows the same principal and a graphical representation may be seen in figure 1.1b.

A three dimensional representation of the FBZ for a FCC unit cell, as seen in figure 1.2 shows the polyhedral nature of the zone. The labels in red are high symmetry positions known as critical points. These critical points are important, as they are points of high symmetry in the (real space) crystal lattice. A mapping of the path from the zone centre along the critical points into a two dimensional plot of  $k$  vs energy (obviously after some electronic computations), will give us the band structure model of the material along that  $k$  point path. This will be discussed in greater detail in the next section.

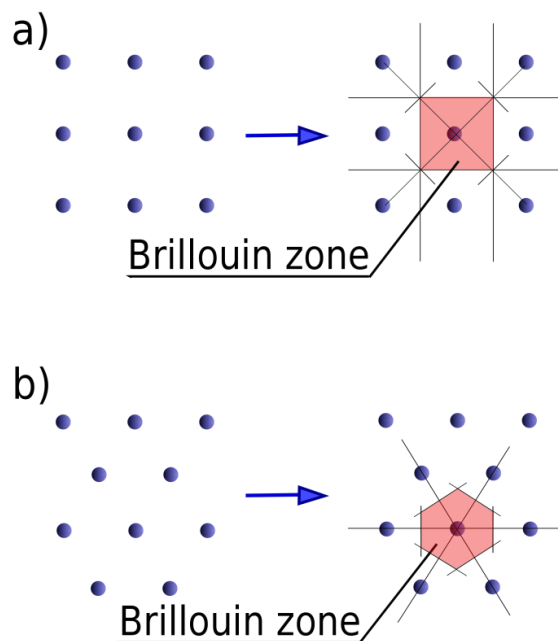


**Figure 1.1:** Brillouin Zone generation in a) a cubic Bravais lattice and b) in a hexagonal Bravais lattice. (This image was reused under the GNU public licence from [http://en.wikipedia.org/wiki/Brillouin\\_zone](http://en.wikipedia.org/wiki/Brillouin_zone)).

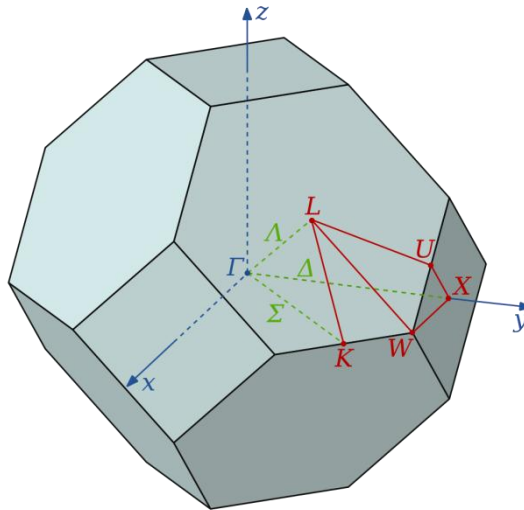


**Figure 1.2:** The First Brillouin Zone of a face centred cubic lattice where the labels in red represent the critical points (points of high symmetry) and  $\Gamma$  is the zone centre (0, 0, 0). (This image was reused under the GNU public licence from [http://en.wikipedia.org/wiki/Brillouin\\_zone](http://en.wikipedia.org/wiki/Brillouin_zone)).

### 1.3 Energy Bands in semiconducting solids

When we consider an atom in the gas phase, we know that there are multiple energy levels associated with the orbitals of the atom. However when these atoms crystallize in the solid state, they are in close proximity to one another, and the wave functions associated with the atoms electrons will overlap with its nearest neighbour. The solid state phase generates closely separated energy levels (Pauli's exclusion principle) which now form energy bands within the solid. The energy bands develop the framework needed to study the energy band gap associated with a semiconducting material.

The nearly free electron model is the first approximation that can be used to describe energy bands in solids. This model gives good calculated values to magnetic susceptibility, electrodynamics, heat capacity and thermal conductivity, especially in metals. However the free electron model fails to describe the occurrence of positive values of the Hall coefficients, the concept of conduction electrons in a metal to the valence electrons of free atoms and the transport properties. The lack of the ability to describe conduction electrons in metals, gives us the first indication that this model will be insufficient to describe semiconductors, semimetals and insulators. It also fails to describe energy gaps which exist at the Brillouin zone boundaries of these materials. The reason for this is that the free electron model uses a travelling wave description of an electrons motion, and does not take into account the periodicity of the lattice.

The periodicity condition is important because, firstly the first Brillouin zone may describe the entire reciprocal lattice through symmetry, and secondly, the FBZ boundary which is described by the irreducible region of intersecting Bragg planes, has the condition of the diffraction of waves at the zone boundary. This enables us to envisage the idea that a periodic function needs to be included in the electron model to accurately describe the conduction electrons in a periodic solid and the electron model in general.

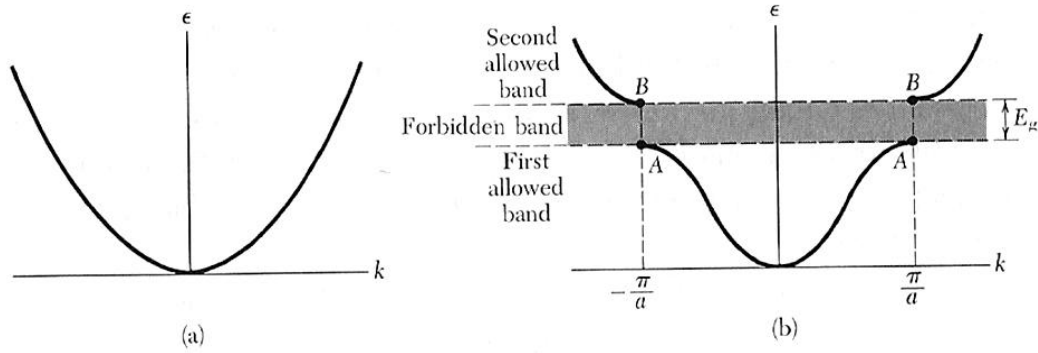


**Figure 1.3:** a) The free electron model representation of an  $\epsilon_k$  vs  $k$  diagram, i.e. with no periodic boundary conditions included. b) A new  $\epsilon_k$  vs  $k$  diagram with periodic boundary conditions included. What becomes evident is that at the zone boundaries  $\pm \frac{n\pi}{a}$  for a linear system, band gaps begin to arise. Diagram obtained from (Kittel C, 1996).

The physical proof of this may be seen in a plot of the  $\epsilon_k$  vs the free electron wave vector  $\mathbf{k}$ , and compared with the plot of the  $\epsilon_k$  vs the wavevector  $\mathbf{k}$  of a linear lattice of lattice constant ( $a$ ) where  $\epsilon_k = \frac{\hbar^2}{2m}(k_x^2 + k_y^2 + k_z^2)$ . In the linear lattice the Bragg reflection condition is included into the wavevector  $k$ , and from this we see the energy gaps that arise at the Brillouin zone boundary of  $\pm \frac{n\pi}{a}$  where  $n$  is an integer (figure 1.3). The Bragg imposed condition on the  $\epsilon_k$  vs  $k$  systems, becomes a standing wave, meaning that the original travelling wave is reflected at the zone boundaries, to the right at  $-\frac{\pi}{a}$  and to the left at  $+\frac{\pi}{a}$  which produces the standing wave. The standing wave, wave function now becomes

$$\psi(+) = 2\cos\left(\frac{\pi x}{a}\right) \text{ and } \psi(-) = 2i\sin\left(\frac{\pi x}{a}\right)$$

Where the + and – signs indicate if the wave has been reflected in the positive or negative direction.

By taking the probability density of both newly generated wave functions, i.e. a plot of  $|\psi(+)|^2$  and of  $|\psi(-)|^2$  against the potential energy  $U(x)$ , with ion cores situated along the linear lattice  $a$  where  $U(x)$  is the potential energy of an electron in a crystal at point  $x$  i.e.

$$U(x) = U \cos 2\pi a$$

It is then observed that the  $|\psi(+)^2|$  function piles up electrons or negative charge at ion cores, and the  $|\psi(-)^2|$  wavefunction concentrates electrons away from the ion cores (figure 1.4). This is the real reason for the energy gap development, as one may see that the valence electrons are centring around the ion cores, which is what should happen, and the other wavefunction centres the electrons in the interstitial regions, i.e. the conduction electrons. This implies that the difference of the two new wavefunctions will give rise to the band gap energy ( $E_g$ ). The final wave function that arises from this derivation is the Bloch function

$$\psi_r(r) = u_k(r)e^{(ik \cdot r)}$$

Where  $u_k(r)$  has the period of the crystal lattice included.

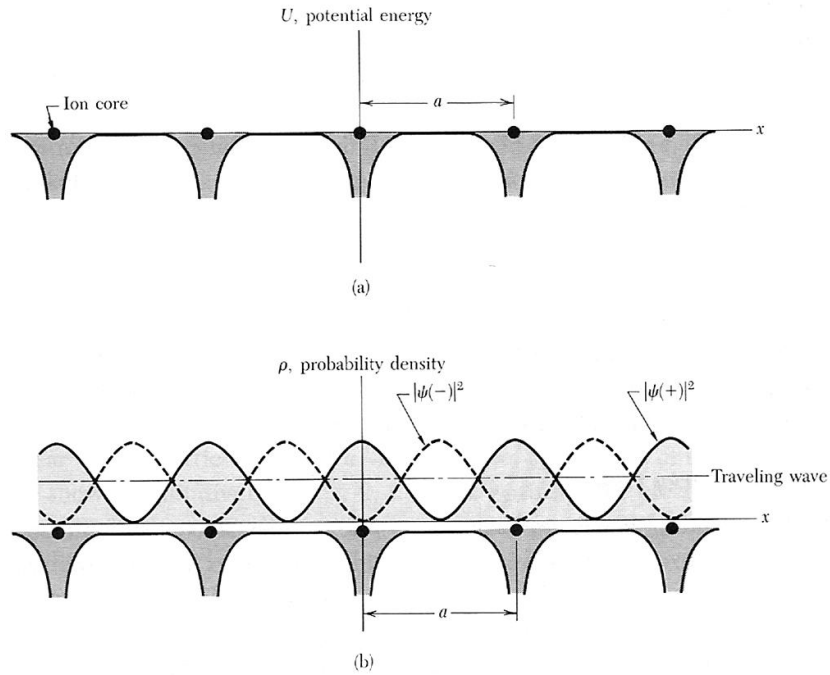


**Figure 1.4:** a) The variation potential energy of a conduction electron in a linear lattice  $a$  in a field of ion cores. b) The probability density wavefunctions of the travelling waves  $|\psi(+)|^2$  and  $|\psi(-)|^2$ . Where the positive probability wavefunction piles up positive charge around the ion cores, and the negative probability wavefunction piles up negative charge in the interstitial regions. (Diagram obtained from Kittel C, 1996).

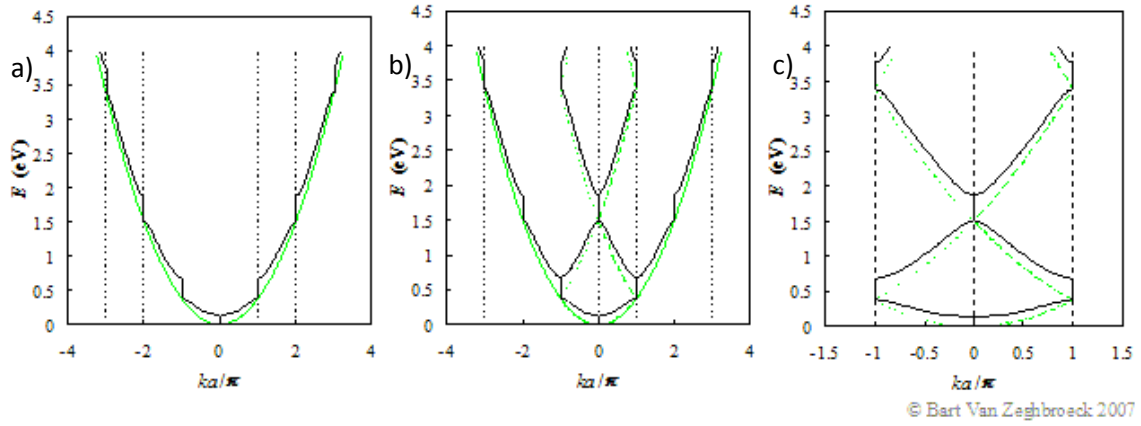


**Figure 1.5:** The first diagram displays the  $\epsilon_k$  vs  $k$  diagram of the Kronig-Penney model where the band gaps arise at the Brillouin zone boundaries  $\pm \frac{n\pi}{a}$  where  $n$  is an integer. The Black curves are the Kronig-Penney model and the green curves are the free electron model. a) is the  $\epsilon_k$  vs  $k$  diagram only b) is the  $\epsilon_k$  vs  $k$  diagram combined with the reduced zone diagram, and c) is the  $\epsilon_k$  vs  $k$  diagram of the reduced zone diagram only or the band structure diagram of the First Brillouin zone. (ref: <http://ecee.colorado.edu/~bart/book/welcome.htm> Chapter 2)

A representation of how this new functions works is represented in the Kronig-Penney model for a simple one dimensional periodic potential, which displays energy bands, as well as energy band gaps.

Figure 1.5 displays how the band structure of a linear lattice is generated. As the full band structure of a three dimensional lattice becomes rather complicated, the Kronig-Penney model serves as a simplified version to explain the band structure of a solid. We notice that band gaps are generated at the Brillouin zone boundaries  $\pm \frac{n\pi}{a}$ , where  $n$  is an integer (Figure 1.5a) and the Bragg reflection condition of the boundary holds. Because the periodic model uses standing waves, the band structure may be generated by moving the standing waves of the bands into the reduced zone (figure 1.5b). However band gaps are still evident at the zone boundaries, which means the band diagram may be further reduced into the irreducible Brillouin zone or the first Brillouin zone (figure 1.5c) which now shows us a clear picture of a direct gap semiconductors band structure, with the valence band edge at  $\sim 1.5\text{eV}$  and the conduction band edge just less than  $2\text{eV}$ .

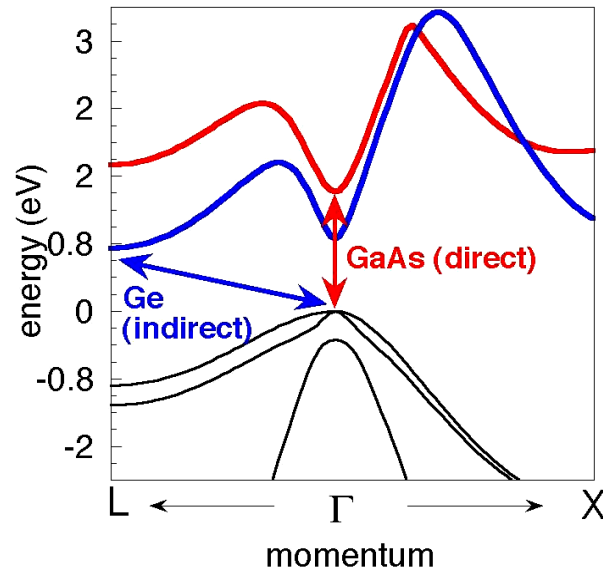


**Figure 1.6:** The overlaid band structure of GaAs and Ge show the difference between a direct and indirect band gap of a band structure. Where GaAs has a direct bad gap of  $E_g = 1.519\text{eV}$  at room temperature, and Ge has an indirect band gap of  $0.7437\text{eV}$ .

Figure 1.6 shows a band structure diagram of GaAs and of Ge. We notice that GaAs has a direct band gap as in figure 1.5 where Ge displays an indirect one. In a direct gap semiconductor a photon is absorbed with  $E > E_g$  which ejects an electron from the valence band directly into the conduction band. In an indirect band gap semiconductor a photon is absorbed with  $E > E_g$ , however the photon must also have a change in momentum in order for the electron to reach the conduction band. This process is assisted through the absorption of a phonon. It should be noted that indirect gap semiconductors tend to have very bad luminescence responses, as the change in momentum of the photon tends to yield large energy losses, causing the recombination to be inefficient, whereas a direct gap semiconductor is ideal for this process.

#### 1.4 Density of States (DOS)

Another important concept in solid state physics used to describe materials electronic properties is the concept of Density of States (DOS). The Density of States (DOS) of a crystalline material may be described as the statistical contribution of each energy level or state that is available to be occupied in a particular energy range. One may also think of it as the total electronic contribution of every atoms electronic structure to the overall energy of the crystal. For example, in a semiconductor, this means that one may see every atoms contribution to the valence and conduction bands i.e. the total DOS of a crystal. Furthermore, one must consider the fact that every electron in the crystal has a specific wavelength, and may propagate in one

direction, and the electron propagation be suppressed in another direction (confinement). The suppression of electrons propagation in any given direction will give rise to certain states being available for occupation, and certain energy states being unavailable for occupation. Moreover multiple electrons may also have the same wavelength, giving rise to the electrons having the same energy level/state, or being degenerate. It has been shown and will be shown here, that the density of states is dependent on the dimensional limits of the material itself. Here we will show the derivation of the DOS for a general material (3D), and then the density of states dependency on dimensional reduction (2D, 1D, 0D). The Density of States may be calculated for both Fermions (electrons, protons and neutrons) and Boson (phonon's and photons) systems. However we will restrict our description to the electronic model, and refer to properties that may be calculated for both types of systems.

In order to calculate the density of states for an electronic system, one must use the free electron model where we include the periodic boundary conditions. For the free electron model we set  $E = \frac{\hbar^2 k^2}{2m_e}$  where  $k = k_x + k_y + k_z$  and  $k_x = \pm \frac{2n_x}{L_x}$ ;  $k_y = \pm \frac{2n_y}{L_y}$ ;  $k_z = \pm \frac{2n_z}{L_z}$  where  $L_x, L_y, L_z$  are the limits of dimensions of the material in real space, and  $n_x, n_y, n_z$  are integer quantum numbers. Since the density of states is dependent on the volume of the material, we then need to define both the real and  $k$ -space volumes i.e. the volume of  $k$ -space per state is  $V_{k3} = (2\pi)^3 / (L_x L_y L_z)$  and the volume in real space is simply  $V_{r3} = (L_x L_y L_z)$ . If we wish to obtain a new energy state, we increase the value of  $n$ , which quantises the system since  $n$  is an integer. With this in mind the number of states  $N$  contained in a three dimensional system may then be described as

$$N = \frac{1}{(2\pi)^3} V_{k3} V_{r3}$$

To calculate the number of states for lower dimensional states we then only need to consider the area (2D) i.e.  $L_x L_y$  and the length,  $L_x$  (1D) of the respective systems. The  $N$  states can then be written for the 2 dimensional and 1 dimensional cases as follows:

$$N = \frac{1}{(2\pi)^2} V_{k2} V_{r2}; \quad N = \frac{1}{2\pi} V_{k1} V_{r1}$$

We now need to consider the number of states per real space unit volume ( $n$ ). This may be described by assuming that the  $k$ -space volume does not exceed the wavevector of magnitude  $|K|$  which will comprise a sphere of radius  $k = |K|$ . Manipulating the three dimensional  $N$  state equation by assuming  $V_{k3} = \frac{4}{3}\pi k^3$  we obtain  $n$  where

$$n = \frac{N}{V_{r3}} = \frac{1}{(2\pi)^3} \frac{4}{3} \pi k^3 = \frac{k^3}{6\pi^2}$$

Since we have a description for the number of states per real space unit volume, we can now obtain the density of states in  $k$  space where  $(k) \equiv \frac{dn}{dk} = \frac{k^2}{2\pi^2}$ . This derivation is important because we wish to obtain the density of states of  $E$  i.e.  $(E) \equiv \frac{dn}{dE} = \frac{dn}{dk} \frac{dk}{dE}$ . This means we must be able to differentiate all the terms in the energy expression. As mentioned previously,  $E = \frac{\hbar^2 k^2}{2m_e}$  which allows us to derive the three dimensional density of states as follows:

$$g(E) = \frac{1}{2\pi^2} \left( \frac{2m_e}{\hbar^2} \right)^{\frac{3}{2}} E^{\frac{1}{2}}$$

To obtain the 2D density of states we now take the area of a circle in  $k$  space instead of a sphere, i.e.  $V_{k2} = \pi k^2$  and multiplying by 2 to account for electron spin degeneracy. Surprisingly after derivation we obtain an energy independent term for  $g(E)$

$$g(E) = \frac{m_e}{\pi \hbar^2}$$

This implies that as the top of the energy gap is reached there is a large amount of states available. The density of states cannot be energy independent and must take into account the other energy levels in the quantum well. The function then becomes like a staircase function i.e.

$$g(E) = \frac{m_e}{\pi \hbar^2} \sum_i H(E - E_i)$$

Where  $\sum_i H(E - E_i)$  is the Heaviside function. This function equals one when  $E$  is greater than or equal to  $E_i$ , and it equals zero when  $E$  is less than  $E_i$ . A graphical representation may be seen in figure 1.7.

To then obtain the density of states for a one dimensional system through similar principals and taking spin degeneracy into account we may obtain  $g(E)$  for a 1D system

$$g(E) = \frac{1}{\pi} \left( \frac{2m_e}{\hbar^2} \right)^{\frac{1}{2}} \frac{1}{E^{\frac{1}{2}}}$$

However we must expand this term for energy levels greater than one, and  $g(E)$  now becomes

$$g(E) = \frac{1}{\pi} \left( \frac{2m_e}{\hbar^2} \right)^{\frac{1}{2}} \sum_i \frac{n_i H(E - E_i)}{(E - E_i)^{\frac{1}{2}}}$$



Where  $n_i$  is the integer quantum number, and  $\sum_i H(E - E_i)$  again is the Heaviside function with the same conditions which applied to the two dimensional case. Because more than one arrangement of confined states can be obtained in 1D and 0D cases, the quantum number must be included. For 0D states quantization now occurs in all directions, and only discrete energy levels exist within the quantum dot which may be described by a simple delta function. The graphical representation of all of the dimensional states may be seen in figure 1.7. We do notice the increase in the lowest energy states with decreasing dimensionality.

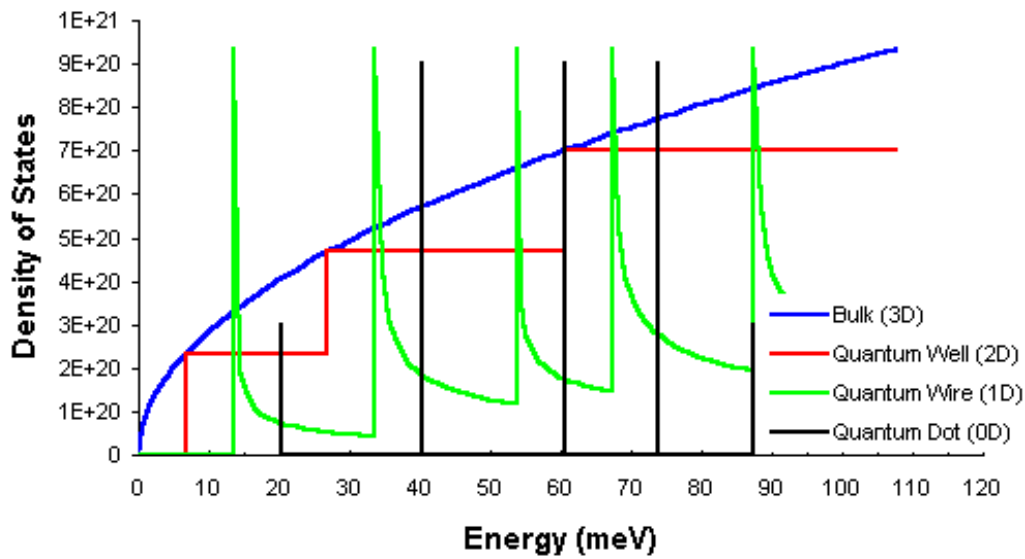


**Figure 1.7:** Density of states for bulk (3D blue), quantum well (2D red), quantum wire (1D green) and quantum Dot (0D black) (Diagram obtained from: <http://britneyspears.ac/physics/dos/dos.htm>). Functions are described in the text.

The density of states  $g(E)$  may be further combined with various distribution functions at thermal equilibrium to obtain various physical properties, such as the internal energy  $U$ , the density of particles  $n$ , specific heat capacity  $C$ , and thermal conductivity  $k$ . Remembering that a density of states may be generated for both Boson and Fermion particles, we will briefly discuss the two common distribution functions, used to calculate these physical properties.

Firstly the Fermi-Dirac distribution is used for Fermion particles (electrons, protons, and neutrons), which takes into account spin (obeys Pauli's exclusion principle). The distribution function may be described as follows:  $f_{FD}(E) = \frac{1}{\exp\left(\frac{E-\mu}{k_B T}\right) + 1}$  where  $\mu$  is the chemical potential  $k_B$

is the Boltzmann constant and  $T$  is the temperature in Kelvin. The Fermi-Dirac distribution function gives us insight into carrier concentrations and energy band gaps. The Bose-Einstein distribution equation on the other hand is for Boson particles i.e. phonons and photons. Boson particles do not have spin and or obey Pauli's exclusion principle. The distribution equation is

similar to the Fermi-Dirac equation i.e.  $f_{BE}(E) = \frac{1}{\exp\left(\frac{E-\mu}{k_B T}\right)-1}$ . It is necessary for both distribution functions for the calculation of the physical properties as both sets of particles are strongly correlated with these properties.

## **1.5 General properties of semiconductors**

In the previous sections we established the existence of electronic bands in metallic and semiconducting systems, with an emphasis on the properties one may readily calculate. The density of states has also shown the importance of spatial confinement on the electronic states in a material, and by combining the density of states with the correct distribution function one may readily describe the properties of bosons and or fermions of a particular material. In this next section we wish to briefly highlight the general properties semiconductors are used for before becoming more specific (optical processes) in the last two sections of this chapter.

### **1.5.1 Carrier generation and recombination processes.**

We generally know that semiconductor devices produce charge carriers, this process occurs when a semiconductor absorbs a photon  $E_{ph} > E_g$ , creating a positively charged hole in the valence band with the electron now residing in the conduction band creating a coulomb correlated electron hole pair, or a carrier (also known as an exciton, but in this section we are discussing the transport of charge in a semiconductor). The energy of the photon must be greater than the band gap energy so that the remaining excess energy is added to the electron hole pair to give the particle kinetic energy.

A coulomb correlated electron hole pair may also be generated via two other methods. The first method is known as the ionization process which occurs when a high energy beam of charged particles (for example electrons) generates a large amount of electron hole pairs. A mechanism similar to the method of the absorption of a photon except now, there are a greater amount of carriers available. The absorbed charged particle will eventually loose its energy, and in turn will stop producing carriers. Semiconducting materials which respond well to this process are used as nuclear particle counters. The second method is known as the impact ionization process, where an electron/hole pair with energy much larger or smaller than the band gap is accelerated in an electric field. This produces excess kinetic energy, whereby the excess energy is transferred

to another electron in the valence band. The amount of energy transferred is usually enough to then generate two more carriers. These two carriers still in the electric field will further produce four more carriers via the same mechanism, a  $n^2$  relationship. This process is known as the avalanche effect. Both electrons and holes contribute to the avalanche effect.

Carrier generation may also occur through a carrier recombination processes. There are different recombination processes that give rise to a photon, phonon or excess kinetic energy. These processes consist of a radiative recombination or annihilation through a band to band transition which give rise to a photon. There are also trap assisted radiative recombinations, where an electron falls into a trap which is created at an energy level in between the band gap energy, caused from a foreign atom or a structural defect or even a surface defect within the semiconductor. The electron further drops from the trap energy level into the hole in the valence band completing the recombination process with a lower energy photon being released from this process i.e. the emission is red shifted. This process is also known as the Shockley-Read-Hall (SRH) recombination. The last recombination process is known as an Auger recombination, which occurs when an electron recombines with the hole from the band to band transition, but instead of an immediate photon emission occurring, the energy is transferred to another electron or hole, i.e. generating another carrier. This is different from the normal band to band transition, because the final recombination rate of an Auger recombination is different (slower) from direct band to band recombination. The non-radiative recombination processes that also exist in semiconductors may occur via one or more phonon emissions, i.e. no photon will be emitted.

### **1.5.2 Carrier Densities**

Semiconductors properties may be altered in various ways, dimensional reduction being one of them, but there is still the traditional approach to altering semiconductors intrinsic properties. This is generally done through the addition of an impurity, otherwise known as doping. Doping may occur through either the addition of a few impurity atoms or through the addition of a stoichiometric amount of the impurity to enhance the general properties of the semiconductor. An example of this may be seen in the case of the addition of Boron atoms to silicon, where only a few Boron atoms substitute out silicon lattice atoms, thereby enhancing carrier mobility/conductivity substantially (1 Boron atom to  $10^5$  silicon atoms increases the conductivity by  $10^3$  at room temperature). The process of doping may occur through one of two

mechanisms, i.e. either adding an atom that when ionized in the crystal it donates an electron to the conduction band thereby creating a donor energy level just below the conduction band edge. This process is known as  $n$ -doping. The second process is when an atom is added to the lattice, which when ionized it is able to accept an electron at an energy level higher than that of the valence band edge. This process is known as  $p$ -doping. Doping is generally used to increase electrical conductivity and mobility of the semiconductor through the addition of electrons ( $n$ ) or holes ( $p$ ). In both cases ( $n$  and  $p$  doping) the band gap of the material is lowered. Doping with an impurity atom generally substitutes one of the semiconducting atoms out of the crystal lattice for itself, however the impurity atom may also sit within a void of the crystal, if the crystal structure permits this kind of substitution (Perovskite based materials are a good example of where this may occur).

### **1.5.3 Carrier transport**

As semiconducting materials are also extensively used for their conducting capabilities, a discussion of carrier transport will be briefly mentioned here. In semiconductors current is generated because of the motion of free carriers. Because these carriers are charged, motion may be induced from an electric field from an externally applied voltage. The transport mechanism is known as carrier drift. Another transport mechanism also exists, which is known as carrier diffusion. Carrier diffusion occurs in the semiconductor because there are regions that exist inside the material of different carrier densities. Diffusion occurs from the motion of areas of high density to low density. Furthermore carrier diffusion is also associated with thermal energy and the collisions of particles (phonons, other carriers, defects, impurities, etc) in the semiconductor. The measurement of the total current in the material is the sum of both drift and diffusion current.

When a semiconductor is in an applied electric field, the charged carriers are accelerated due to the electrostatic forces, and then reach a constant velocity, as thermal vibrations and lattice impurities begin to collide with the carriers. When this constant velocity is reached it is called the saturation velocity. Saturation velocity generally occurs in high electric fields. The ratio between the applied electric field and carrier velocity is called the mobility of a semiconductor. However it must be mentioned that semiconductors with high surface areas have lower carrier mobility's. This is due to the carriers being scattered by surface or interface scattering mechanisms.

### 1.6 Optical processes and excitons in semiconductors.

Semiconductors have energy gaps which stop the free flow of electrons as in conducting materials. Generally an absorption of either heat or light (in the form of photons) gives sufficient energy for electrons to “make the leap” into the conduction band. This energy gap is very useful because the energy associated to make this jump spans from deep infrared (semi-metals) to deep UV wavelengths (insulators) regarding photon absorption and or photon emission. The applications of these materials may immediately be envisaged (which has obviously spawned current modern day technology). The deep infrared semiconductors may be used in IR-detectors, and for thermal imaging devices. The wider gap materials are commonly used in LED’s, colour displays, lasers, fibre optics, and various types of detectors.

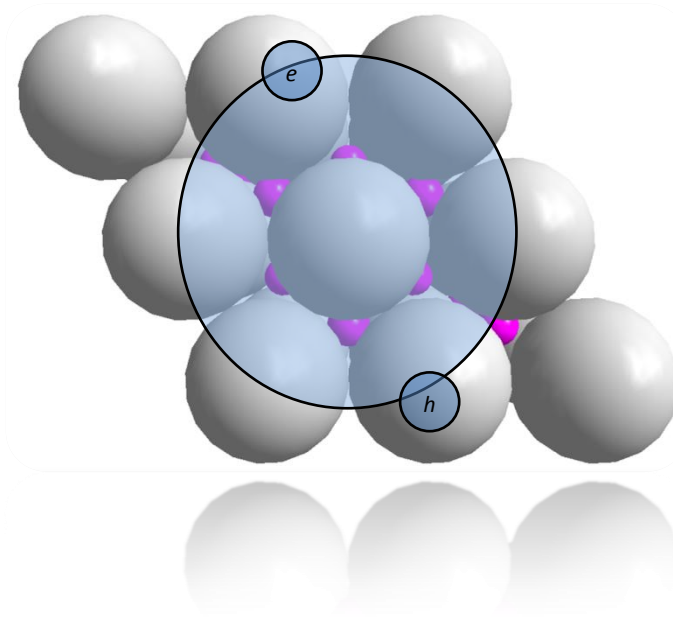


**Figure 1.8:** An exciton which is a bound electron hole pair. An illustration of a Mott-Wannier type exciton with an effective Bohr radius equivalent to or greater than the unit cell dimensions.

The process involved after an absorption of a photon with  $E > E_g$ , will cause the electron to leave the valence band, leaving behind a positively charged hole. With the electron now sitting in the conduction band, this newly generated system becomes a bound electron hole pair where the electron and hole have the same  $k$  vector and are attracted to each other through columbic forces. This new particle is known as an exciton (carrier in the previous section). Excitons typically exist only in direct gap semiconductors, this is because the group velocity of an electron in a band, given by  $v_g = \frac{1}{\hbar} \frac{\partial E}{\partial k}$ , implies that  $v_e = v_h$ . This condition can only be met if the gradient of the valence and conduction bands are the same at the relative point in the FBZ where the transition occurs. The excitons generated through this process are electrically neutral,

and are able to transport energy without transporting any net charge. The electron and hole do have parallel or anti-parallel spins which essentially means that relativistic effects and fine structure are still associated with excitons as they are with electrons. Furthermore the columbic attractive forces experienced between the electron and hole, makes excitons slightly more stable than just an uncorrelated electron and hole, which gives excitons a lower stabilization energy. This implies that excitons have energy sub-band levels that will exist below the conduction band of a given semiconductor.

Excitons exist in two different forms. The first is the Mott-Wannier exciton, which has a large exciton effective Bohr radius  $a_B$  (figure 1.8) (hydrogenic Schrödinger wave function), with a spatial movement much larger than that of the dimensions of the unit cell. It is also weakly bound (i.e. a binding energy  $E_b$  ranging from a few  $meV$  to  $300meV$ ), which means a recombination process can take place fairly easily although they are generally quite unstable. The second type is the Frenkel exciton, which is a tightly bound electron hole pair (i.e. a  $E_b$  greater than  $1eV$ ) generally localized on an atom or defect site. The alkali halide crystals are the most well known examples that display Frenkel excitons. For all intensive purposes from here on we will only deal with Wannier exciton systems as they form the basis of the optical investigations in this thesis.

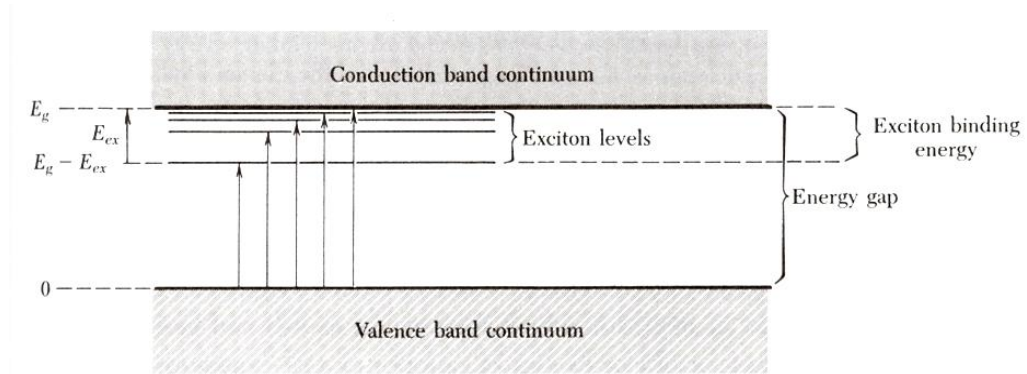


**Figure 1.9:** Energy subbands generated from excitons with various quantum numbers  $n$ , the lowest excitons energy level has the largest orbiting radius, binding energy, and lowest emission energy associated with  $n = 1$ . (Diagram obtained from Kittel. C, 1996).

After a Wannier exciton has been generated in a semiconductor, they form energy levels which exist as subbands below that of the conduction band as seen in figure 1.9 (excitonic fine structure). The energy difference between the conduction band and the lowest energy exciton band is known as the binding energy  $E_b$ . In bulk semiconductors excitonic effects are generally weak for Wannier excitons ( $E_b \sim 4meV$ ), and are only visible at very low temperatures ( $< 4K$ ). The general rule is that the binding energy of the exciton  $> k_b/T$  for excitonic emissions to be

observable, where  $k_b$  is the Boltzmann constant and  $T$  is temperature in Kelvin. Excitonic recombinations are advantageous because they give rise to sharp photoluminescence emission lines. This is very useful for applications in lasers because a narrow band emission is obviously advantageous for a focused beam line. One of the ways of enhancing excitonic effects in semiconductors displaying Wannier excitons is by changing the dimensionality of the system. For example changing structure from a 3 dimensional array into a 2D, 1D or 0D system, by introducing an insulating barrier around the semiconductor has been shown to drastically enhance these effects. However it must be said that the changing of the dimensionality must happen on the nanometre scale, i.e. confining the effective excitonic radius  $a_B$ , which is of the order of a few unit cells. A more accurate dimensional reduction guide is to be in the order of the de Broglie wave length  $\sim \lambda_B$  for a specified material. Where  $\lambda_B = h/mv$  where  $h$  is Planks constant,  $m$  is the particle in questions mass, and  $v$  is the particles speed. For example, for an electron moving at  $1.0 \times 10^6 \text{ m/s}$  with a rest mass of  $9.1 \times 10^{-31} \text{ kg}$ , has a de Broglie wavelength of  $\lambda_B = 7\text{\AA}$ . Hence dimensional reduction needs to occur in this regime for excitonic enhancements to occur for that specific material. Dimensional reduction plays a large part in the confining of excitons, which will be discussed in detail in the last section. For example the binding energy of an exciton of a 2D system will be four times as large than that of a 3D system. However it has also been shown in 2D systems that the larger the dielectric difference experienced between the quantum well and insulating barrier, far exceeds the enhancement of binding energy seen by simply reducing the dimensionality from 3D to 2D (Hong X, *et al*, 1992).

Figure 1.9 displays the excitons fine structure, just below the conduction band of a semiconductor. The binding energy of the subbands can be calculated, and we will show here for a 3D compound with uniform dielectric constant as follows:

$$E(n) = -\frac{\mu}{m_0} \frac{1}{\epsilon_r^2} \frac{R_H}{n^2}$$

Where  $\mu$  is the reduced mass of the electron and hole,  $m_0$  is the electron rest mass,  $\epsilon_r$  is the materials dielectric constant,  $R_H$  is the Rydberg constant and  $n$  is the principal quantum number. One should notice that an exciton may be treated as a hydrogenic system, i.e. make use of the Bohr model. This model takes into account the centre of mass motion (the kinetic energy of the system) and the relative motion, which determines the internal structure. Since this system behaves as a hydrogenic system, we should also be able to calculate the radius of the electron-hole orbit.

$$r_n = \frac{m_0}{\mu} \epsilon_r n^2 a_H = n^2 a_B$$

Where  $r$  is the excitonic radius for a given principal quantum number  $n$ ,  $a_H$  is the Bohr radius of the hydrogen atom, and  $a_B$  is the excitons effective Bohr radius for a given material. What becomes evident from these two equations is that, as the quantum number is increased, the binding energy decreases, with the excitonic Bohr radius increasing. Measurement of this phenomenon has been observed in low temperature (1.2K) optical absorption experiments of GaAs (figure 1.10a), where the multiple exciton energy levels are observed, and thus also can be calculated as follows:

$$E_n = E_g - \frac{\mu}{m_0} \frac{1}{\epsilon_r^2} \frac{R_H}{n^2}$$

Where  $E_g$  is the band gap, and the second term is the excitons binding energy for each principal quantum number  $n$ .

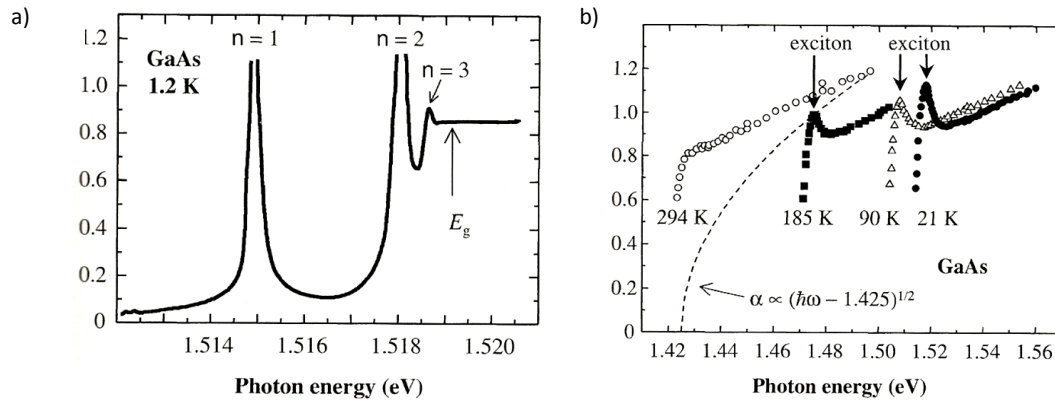


**Figure 1.10:** a) Shows the excitonic absorption of very pure GaAs at 1.2K. From the absorption spectra, one is able to experimentally observe three of the excitonic subband energy levels. b) Shows the temperature effect on GaAs absorption spectrum. It is evident that the excitons absorption line only becomes evident at lower temperatures. The dashed line shows the calculated band gap with decreasing temperature. (Diagrams obtained from Fox M, 2008).

After an exciton is generated they tend to not be totally free to orbit the crystal, i.e. an ideally free exciton. They generally tend to exist as self trapped excitons (STE), or quasi-free excitons (QFE) states. STE's and QFE's are known to be intrinsic properties of a crystal, and do not exist because of defects, dislocations, and impurities of the crystal. As mentioned previously a free exciton, may be described as the electron and hole being dependant of the wavevector  $k$  (for a direct gap semiconductor  $k_e = -k_h$ ). Keeping this concept in mind, these particles may be



defined as follows. A free exciton is delocalized and its energy is dependent on the wavevector  $k$ . A STE however is localized and its energy is not dependent on the wavevector  $k$ . A STE may have a lower energy state than that of a free exciton. A QFE is only different from a STE in the fact that its energy is dependent on the wavevector  $k$ ; however it is still localized as a STE. A QFE may also exist in a lower energy state than that of a free exciton (STE's the one's we have in our 1D systems (chapter 5)). The reason these STE's and QFE's are generated, is simply because free excitons couple with the phonon's generated from the vibrational modes of the crystal, both acoustic and optical phonons. The phonon contribution to the excitons state is able to add or subtract an energy term, making the STE or QFE either a lower or higher energy state than that of a free excitons energy state. Hence from this description we can ascertain that purely free excitons will be less common than STE's or QFE's as every crystalline material will have some phonon contribution that will arise from the natural modes of a given material (Singh J, Matsui A, 1987).

Another particle that may arise in a crystal is when an electron and a phonon interact with one another. In metals this effect may be seen in resistivity measurements, i.e. the higher the temperature the higher the resistivity of the metal. The increase in resistivity occurs because of an increase of electron phonon collisions causing electrons to lose energy. In the case of semiconducting/insulating materials this particle becomes known as a polaron. A polaron has an apparent increase in electron mass and is able to cause lattice deformations as it moves through the crystal. Polarons have a larger deformation effect in ionic crystals than in covalent neutral crystals because of the strong coulomb interaction between electrons and ions. However, they may still be present in covalent crystals and their excited state may create an energy level between the valence and conduction bands. To be able to distinguish a polaron from excitons (STE's, QFE's and free excitons) in a crystal, measurement of their luminescence decay kinetics, helps establish which particle is present, as both may occur simultaneously (Azuma J, *et al*, 2002a). Furthermore structurally the material may undergo a phase change to account for the lattice deformation caused through the generation of the polaron (chapter 5.2).

### **1.7 Confinement of excitons through dimensional reduction**

Now that we have discussed the density of states and dimensional reduction effect on the band gap, and that we have laid the foundation of band theory in solids, the generation of excitons, and further touched on the existence of excitonic subband energy levels. We need to embark on

the theoretical discussion of the confinement of Wannier excitons in low dimensional systems. In any given material a Wannier exciton has three degrees of freedom, i.e. a centre of mass motion, an electron hole relative motion and a spin configuration. The dimensionality of excitonic systems is highly dependent on the ratio of the effective Bohr radius ( $a_B$ ) and the geometrical confinement length. In the 3D case there are essentially no length limitations as described by  $L_x$ ,  $L_y$ , or  $L_z$  of the exciton. The centre of mass motion of our system in this case is well described by simply using a plane wave with a 3D wave vector. However in the lower dimensional cases new descriptions need to be generated in order to accurately describe these two parameters specifically i.e. the electron hole motion (binding energy) and the centre of mass motion of the exciton. This is obviously because the excitons motion is now confined in either one (2D), two (1D) or three (0D) dimensions and the plane wave wavevector needs to change accordingly. In order to simplify this problem the effective mass approximation is used, and exchange and spin orbit interactions will be neglected, therefore only the exciton spin singlet will be used.

### 1.7.1 The 3D case

The descriptions in the 3D case of the total energy of the Wannier excitons is given by  $E_k^{(3)} + E_v^{(3)}$ , where  $E_k^{(3)} = |K^{(3)}|^2/2(m_e^* + m_h^*)$  is the kinetic energy of the centre of mass motion and the  $E_v^{(3)}$  is the kinetic energy of the  $e - h$  relative motion (binding energy). The latter is the eigenvalue of the Schrodinger equation for the wavefunction  $\psi_v^{(3)}$  of an  $e - h$  relative motion i.e.

$$\Delta_3 \psi_v^{(3)}(r) + 2\mu[E_v^{(3)} - V^{(3)}(r)]\psi_v^{(3)}(r) = 0 \quad (\diamond)$$

With an index  $v$ . Here,  $r = (x, y, z)$  is equivalent to  $(x_e - x_h, y_e - y_h, z_e - z_h)$  is the relative coordinate of the  $e - h$  pair,  $\mu$  is the reduced mass of the  $e - h$  pair and  $\Delta_d$  is the Laplacian for the relative coordinate in 3 dimensions. With

$$V^{(3)}(r) = -e^2/(\varepsilon|r|)$$

Where  $V^{(3)}(r)$  is the unscreened Coulomb potential between an electron and a hole, and  $\varepsilon$  is the dielectric constant of the medium. To further describe the bound states of the exciton, and negative values of  $E_v^{(3)}$  (binding energy) a wavefunction needs to be generated for a three

dimensional system. Here we label eigenfunctions of  $(\diamond)$  with the quantum numbers  $v = (n, l, m)$  where  $[n = 1, 2, 3, \dots; l = 0, 1, 2, \dots, n - 1; |m| = 0, 1, 2, \dots, l;]$  as

$$\psi_v^{(3)}(r) = \psi_{nlm}^{(3)}(r) = N_{nl} F_{nl} \left( \frac{2r}{na_B^{(3)}} \right) Y_{lm}(\theta, \varphi),$$

where  $r = (r, \theta, \varphi)$ ,  $N_{nl}$  is the normalization constant,  $a_B^{(3)} = \varepsilon/\mu e^2$  is the effective Bohr radius of a 3D exciton, and  $Y_{lm}(\theta, \varphi)$  is the spherical harmonics of the orbital. Each bound state is  $n^2$ -fold degenerate except for the non-degenerate ground state ( $n = 1$ ) and its energy eigenvalue is independent of  $l$  and  $m$ , (remember  $l$  describes the subshell  $s, p, d, f$  and  $m$  is the specific orbital within the subshell, we have neglected spin in these descriptions) i.e., the  $e - h$  relative mass motion can be described as:

$$E_v^{(3)} = E_n^{(3)} = -\frac{E_R^*}{n^2},$$

Where  $E_R^* = \frac{\mu e^4}{2\varepsilon^2}$  is the effective Rydberg energy. For the  $n = 1$  i.e the binding energy of the 1s exciton  $E_1^{(3)} = -E_R^*$ . From this description the 3D case excitonic effects are much weaker than in lower dimensional cases.

### 1.7.2 The 2D case

In the two dimensional case the excitons motion is now confined in one direction, i.e. assuming confinement of  $L_{\perp z}$  where  $L_{\perp z} < a_B^{(3)}$ . Each exciton now forms larger subbands in the confinement potential. The electron and hole's motion of the exciton is only in the  $(x, y)$  plane for the ideal 2D case (assuming  $L_z = 0$  obviously  $L_z > 0$  in a real case but for a simplistic explanation we use this assumption), i.e. the Coulomb potential now becomes

$$V^{(2)}(x, y) = -\frac{e^2}{\varepsilon} \frac{1}{\sqrt{x^2 + y^2}}$$

Also the energy eigenvalues of the binding energy of  $E_v^{(2)} < 0$  and the wave functions of the bound states are characterized by two quantum numbers  $n$  and  $m$ ,  $v \equiv (n, m)$  becomes

$$E_v^{(2)} = E_n^{(2)} = -\frac{E_R^*}{\left(n - \frac{1}{2}\right)^2},$$

$$\psi_v^{(2)}(r, \vartheta) = \psi_{n,m}^{(2)}(r, \vartheta) = N_{n,m}^{(2)} e^{im\vartheta - \rho/2} \rho^{|m|} L_{n+|m|-1}^{2|m|}(\rho)$$

Where  $\rho \equiv 2r/[(n - \frac{1}{2})a_B^{(3)}]$  and  $r^2 = x^2 + y^2$  is the radius of the orbit. From this it can be seen that the binding energy from the lowest energy for the first exciton state,  $1s$  ( $n = 1$ ) is  $E_1^{(2)} = -4E_R^* = 4E_1^{(3)}$ . Essentially the binding energy of the 2D case of the  $1s$  exciton ( $n = 1$ ) should be four times that of the 3D case by simply reducing the spatial dimension. Also the effective Bohr radius for  $a_B^{(2)}$  reduces to  $a_B^{(2)} = \frac{1}{2}a_B^{(3)}$ .

### 1.7.3 The 1D case

In the one dimensional case both parameters i.e. the centre of mass motion and the relative motion of  $e - h$  are possible only along one axis, we assume  $x$  in our case. The description becomes a little more tricky when describing bound states ( $V^{(1)}(x)$ ). This is because in the lowest exciton state  $n = 1$  has a divergence of the binding energy and the violation of the non-degeneracy theorem for other bound states. Loudon and Elliot assumed the Coulomb potential to be

$$V^{(1)}(x) = -\frac{e^2}{\epsilon|x|},$$

However as can be seen for the  $|x| = 0$  results in divergence from the singularity around the origin. So in order to avoid the divergence, a regularized potential is added to obtain analytical solutions. The Coulomb potential then becomes

$$\tilde{V}^{(1)}(x; x_0) = -\frac{e^2 + 1}{\epsilon|x| + x_0}$$

Where  $x_0$  has  $a_B > 0$  cut-off. The wavefunctions of the bound states then become

$$\psi_v^{(1)}(x) = N_v^{(1)} \tilde{x} e^{-\frac{\tilde{x}}{2}} \Gamma(1 + \nu) [F(1 - \nu, 2; \tilde{x}) - G(1 - \nu, 2; \tilde{x})]$$

Where  $\tilde{x} = \frac{2(|x| + x_0)}{[va_B^{(3)}]}$ ,  $N_v^{(1)}$  is the normalization constant,  $\Gamma(z)$  is the gamma function,  $F(\alpha, \gamma, \tilde{x})$  and  $G(\alpha, \gamma, \tilde{x})$  are fundamental solutions to the confluent hypergeometric equation. The energy eigenvalue of the binding energy for  $E_v^{(1)} \equiv -E_R^*/\nu^2$  is determined by  $\nu$  which satisfies the additional constraints of:

$$\psi_v^{(1)}(\tilde{x}) \Big|_{\tilde{x}=2x_0/\nu a_B^{(3)}} = 0 \quad (\text{even parity state})$$

$$d\psi_v^{(1)}(\tilde{x})/d\tilde{x} \Big|_{\tilde{x}=2x_0/\nu a_B^{(3)}} = 0 \quad (\text{odd parity state})$$

Parity in this case is referring to the shape of the exciton energy level, for example  $1s$ ,  $2s$ ,  $3s$  are all even parity states, where as  $2p$ ,  $3p$ , etc, are odd parity states. The energy of the bound states can be seen in figure 1.11 below. As  $x_0 \rightarrow 0$  the lowest state becomes negatively infinite, i.e. the binding energy diverges. When  $x_0 = 0$  the  $n = 2$  bound states become doubly degenerate for both the odd ( $2p$ ) and even ( $2s$ ) parities at finite energies  $E_v^{(1)} \equiv -E_R^*/\nu^2$  with  $\nu = 2, 3, 4, \dots$ .

Measurement of the  $1s$  exciton absorption may be done simply through the one photon absorption process. However in order to measure the odd parity states Two Photon Absorption (TPA) experiments would be need to be carried out for the energy sub band to be seen.

Figure 1.12 shows a representation of the effect of the dielectric constant ratio of the wire and the barrier, and it's enhancement of the coulomb potential with increasing dielectric mismatch. These features suggest that the attractive force between the electron and the hole (binding energy) in the 1D case is much more effective than that of the 2D and 3D cases.

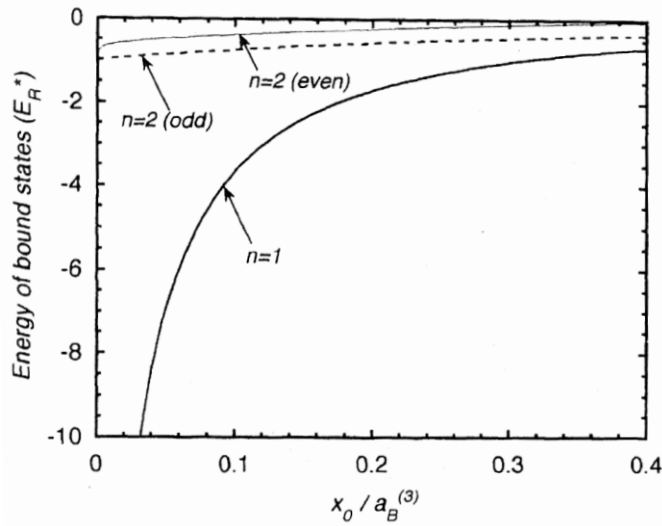


**Figure 1.11:** The eigenenergy of the bound states may be seen in the above plot. These eigenenergies show that for  $d = 1$  the odd ( $2p$ ) and even ( $2s$ ) parity  $n = 2$  energy levels are fairly evenly spaced just below the conduction band and converge to  $-E_R^*$  at  $x_0 = 0$ . However what is observed, is that as the wire length is shortened ( $x_0 \rightarrow 0$ ) the eigenenergy of the lowest energy state  $n = 1$  diverges to negative infinity. This is where the 1D model begins to break down, and or the wire is at the limit of being a wire, and should now be treated as a quantum dot. (Diagram obtained from: Ogawa T, Kanemitsu Y., 1995).

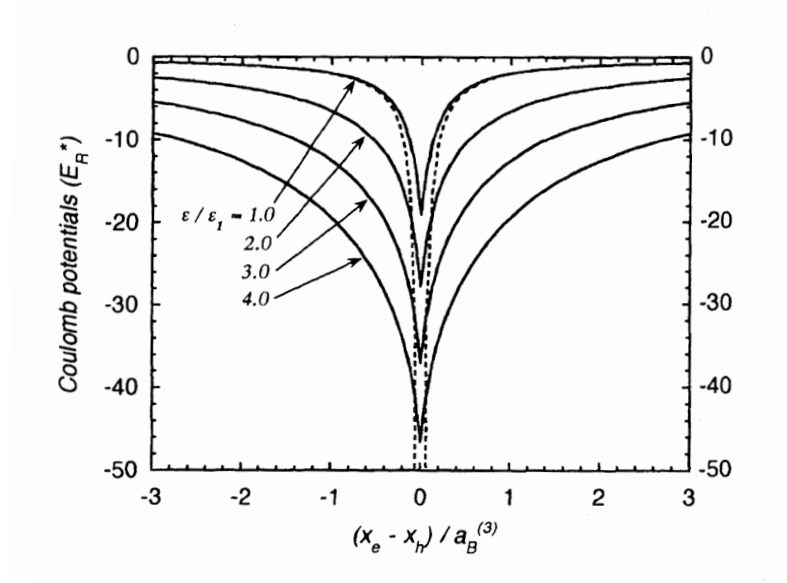


**Figure 1.12:** A representation of the effect of the dielectric constant ratio of the wire and the barrier, and its enhancement of the coulomb potential with increasing dielectric mismatch. The dashed line represents the bare coulomb potential. essentially one may say that the more negative the coulomb potential, the greater the increase on the binding energy of the exciton. (Diagram obtained from: Ogawa T, Kanemitsu Y., 1995).

#### 1.7.4 The 0D case

In the 0D case, the excitonic behaviour functions similar to that of the 3D case. However as in the 1D case there are two limiting situations. These cases are governed by the ratio of the characteristic length  $R$  representing the system size to the effective Bohr radius  $a_B^{(3)}$  of the exciton. The crossover between the two limiting cases is  $2 < R/a_B^{(3)} < 4$ .

The first case is where  $R/a_B^{(3)} \gg 1$ , and is called the *exciton confinement regime*. In this case the excitons character is conserved as in the 3D case, and the relative motion of the exciton is less restricted by the boundary conditions, as in 2D and 1D cases, however the centre of mass motion is still subject to quantum confinement effects and its kinetic energy does also suffer some increase. Hence in this case the total  $e - h$  relative motion energy (binding energy) is given by:

$$E_{total}^{(0)} \sim -E_R^* + \frac{\pi^2}{2(m_e^* + m_h^*)[R - \eta(\sigma)a_B^{(3)}]^2}$$

Where  $\sigma = m_h^*/m_e^*$  are the masses of the electron and hole and  $\eta(\sigma) \approx 1$  is an increasing function of  $\sigma$  of order of unity. The term  $\eta(\sigma)a_B^{(3)}$  corresponds to the dead layer. The centre of

mass motion in this case will effectively be static, because it will have to undergo a large deformation of the  $e - h$  orbit for it to reach the surface of the dot. Therefore if the Bohr radius is small enough (as in Frenkel excitons) the dead layer correction is unnecessary.

The second case is where  $R/a_B^{(3)} \ll 1$  and is called the *individual particle confinement regime*. The electron and hole primarily occupy an individual lowest eigenstate in a confinement potential that has little spatial correlation. Because the kinetic energy of the electron and hole becomes high in comparison to the Coulomb energy, no exciton (bound state) is formed. The squeezed wave function because of strong confinement becomes:

$$\psi^{(0)}(\vec{r}_e, \vec{r}_h) \sim N^{(0)}(1 - \alpha|\vec{r}_e - \vec{r}_h|)j_0\left(\frac{\pi r_e}{R}\right)j_0\left(\frac{\pi r_h}{R}\right)$$

Where  $N^{(0)}$  is the normalization constant  $j_0(x)$  is a spherical Bessel function of 0<sup>th</sup> order and  $\alpha = 0.498/a_B^{(3)}$ . Hence the total energy becomes:

$$E_{total}^{(0)} \sim \frac{\pi^2}{2\mu R^2} - 1.786 \frac{e^2}{\epsilon R} - 0.248 E_R^*$$

The final term is for the resonant excitonic effect.

## 1.8 Aims

In the introduction to this thesis I wanted to establish a good foundation regarding the optical and electronic properties of semiconductors, and how they may be manipulated and enhanced through the process of dimensional reduction, both in the increase in exchange energy with decreasing dimensionality, and with the enhancement of excitonic properties through the process of quantum confinement. This in itself will form a good background for the reader to understand the concepts of the rest of the thesis. In addition an introduction into the importance of increasing the dielectric mismatch between the well/wire and the barrier and how this process enhances the binding energy of the exciton (also to be covered in chapter 2). A brief discussion of excitonic effects and their interactions with the crystals lattice was also dealt with, as this is a core concept handled in chapter 5. And lastly excitonic fine structure is another important topic to be touched upon in both chapters 4 and 6.

Ultimately the aims of the project was to study two dimensional and one dimensional organic inorganic hybrid structures systematically in order to understand both the effects the organic

template has on the structure, and if we could correlate any structural influences directly to the optical absorption and or emissions for those particular set of compounds.

## 1.9 Bibliography

Azuma J, Tanaka K, Kan'no K., *J. Phys. Soc. Jpn.*, (2002) **71**, 971-977

Bilboa Crystallographic server (<http://www.cryst.ehu.es/cryst>)

Fox. M. *Optical Properties of Solids*. (2008). Oxford University Press Inc., New York

Kittel. C. *Introduction to Solid State Physics* 7<sup>th</sup> Ed., (1996). John Wiley & Sons, Inc.

Hirschfeld A. W, *The electric life of Michael Faraday*, Walker & company, (March 7 2006)

Hong X, Ishihara T, Nurmikko A. V, *Phys. Rev. B*. (1992) **45**, 6961-6964.

Loudon R., *Am. J. Phys.* (1959) **27**, 649; Elliot R. J, Loudon R., *J. Phys. Chem. Solids.*, (1959) **8**, 382; (1960) **15**, 196.

Ogawa T, Kanemitsu Y., *Optical Properties of Low-Dimensional Materials.*, *World Scientific Publishing Co Pte Ltd.*, 1995

<http://ecee.colorado.edu/~bart/book/welcome.htm> (online book: Principles of Semiconducting devices last accessed: 22 June 2010)

[http://www.doitpoms.ac.uk/tlplib/brillouin\\_zones/index.php](http://www.doitpoms.ac.uk/tlplib/brillouin_zones/index.php)

[http://phycomp.technion.ac.il/~nika/brillouin\\_zones.html](http://phycomp.technion.ac.il/~nika/brillouin_zones.html)

[http://en.wikipedia.org/wiki/Density\\_of\\_states](http://en.wikipedia.org/wiki/Density_of_states)

<http://britneyspears.ac/physics/dos/dos.htm>

Singh J, Matsui A. *Phys. Rev. B*, (1987) **36**, 6094-6098

Singleton. J. *Band Theory and Electronic Properties of Solids*. (2008). Oxford University Press Inc., New York



## Chapter 2: Literature Survey

### 2.1 Introduction

In this chapter we have covered the background literature regarding the origin of the organic inorganic hybrid perovskite structure, the concept of dimensional reduction, and its impact on the electronic properties of the material. A description of the two mechanisms that may be employed conceptually to create low dimensional systems namely, the traditional method developed from cutting various slices from the 3D perovskite motif, and the various inorganic motif types that can arise through altering I/M ratio's, organic weak interaction effects, and solvent effects will be discussed. In later sections more attention has been focussed on the excitonic behaviour in the 2D and 1D systems with discussions of the phase transitions that may arise through temperature fluctuations, as this forms the basis for the results discussed in chapters 4 and 5. Only a brief discussion on the literature on nonlinear optics of hybrid materials is presented, as this topic's background is developed more thoroughly in chapter 6. Lastly, a brief summary of electroluminescent devices developed from hybrid organic inorganic systems concludes this chapter, allowing us to see the applicability of the research for further device development.

### 2.2 3D organic inorganic hybrid perovskites

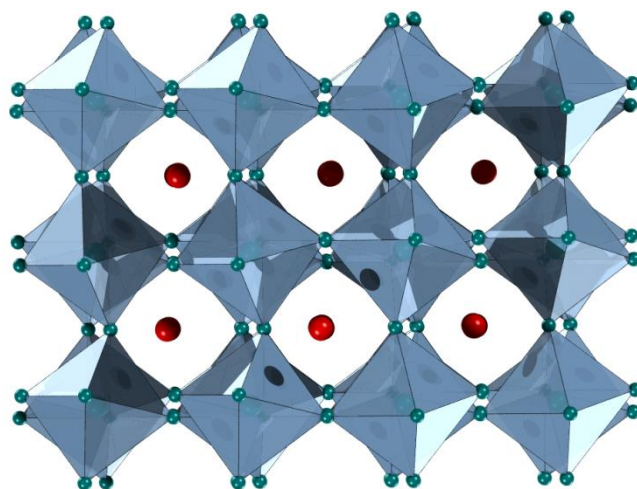


**Figure 2.1:** The perovskite structure ( $\text{CaTiO}_3$ ) which holds the general formula  $\text{ABO}_3$ , however for the Organic inorganic hybrid perovskites the formula is changed to  $\text{AMX}_3$  where A is the organic cation, M the metal, and X is any halogen.

The three dimensional organic inorganic halide hybrids are based on the traditional perovskite structure with the general formula  $ABO_3$  as seen in figure 2.1. The 3D hybrids adopt the same structure type but with the new general formula  $AMX_3$  where A is any monovalent cation, generally Li, Na, K, Rb, Cs, or may be replaced by an organic ammonium cation of suitable size, M is any M(II) metal and X = F, Cl, Br, or I. Many types of cations (A) may be incorporated into the void that is formed in the centre of the perovskite structure. However the cation must fall within the tolerance factor (t) in order to maintain the 3 dimensional perovskite structure type. To generate an ideal cubic perovskite crystal structure the tolerance factor must be  $t = 1$ . In order to accommodate larger cations the tolerance factor generally falls within the range  $0.8 < t < 0.9$ , with octahedral distortions occurring in order to accommodate the increase in cationic radii. This means that 3D perovskite structures that fall within this tolerance range adopt lower crystal symmetry to accommodate the distortions experienced in the structure (Mitzi, 1999).

The question then arises, how large can the cation A be, and still maintain the 3D perovskite structure type? A simple equation may be constructed in order to describe the atomic radii and all the constraints necessary to maintain the 3D structure type. To describe this equation let us consider the perfect cubic perovskite structure where  $t = 1$ , and we assume all the atoms are rigid spheres. The equation will then hold provided that each atom A, B and X's atomic radii are in contact, then  $(R_A + R_X) = t\sqrt{2}(R_B + R_X)$ . The use of this equation is illustrated when considering the largest atomic radii case of the 3D organic inorganic hybrid perovskite with the formula (A)PbI<sub>3</sub>. To maintain cubic symmetry, the value of  $R_A$  may not be larger than 2.6Å. In the organic inorganic systems the single bond length of C-N which is 1.45Å, should be the first constraint taken into consideration when choosing an organic ammonium cation. The cationic void parameter does severely limit our choice of organic cation suitable to template the 3D structure. Nevertheless a suitable candidate is readily found with the first obvious organic ammonium cation being methyl ammonium  $(CH_3NH_3)^+$ . This cation is predominantly found in most metal (II) halide 3D organic inorganic hybrids. Another suitable, marginally larger cation has been found to be the formidinium  $(NH_2CH=NH_2)$  cation which was successfully incorporated into the  $(NH_2CH=NH_2)SnI_3$  3D system (Mitzi D. B and Liang K, 1997). The unit cell parameters have been reported to be 1.2% larger than that of its methyl ammonium counterpart. In terms of further property discussions purposes we will limit ourselves to the  $(CH_3NH_3)PbX_3$  systems where X = Cl, Br, and I, as the 3D (A)SnI<sub>3</sub> case will be dealt with in the section on electrical transport.

As crystalline distortions or phase changes often occur as a result of the materials sensitivity to temperature. This sensitivity more often than not results in the altering of the physical/electronic properties of that material. Phase changes, specifically in the perovskite cases, may result in an increase or decrease of the crystallographic symmetry. This may cause a simple loss or gain of some form of crystallographic related physical properties, such as, non linear optics (SHG specifically) and piezoelectricity (non centrosymmetric crystals only), pyroelectricity, enantiomorphism and simple optical activity (Klapper H, Hann Th, 2002; Nye J, 1957). In other words a simple change in electronic dipole moment may result in a loss or gain of a very useful property as a result of the phase change. A reversible phase change in itself may be very useful as a temperature sensitive property on/off switch for crystallographic related properties. However if it is not desirable for the material to undergo a phase change, it is still then very useful to know the temperature stability range of that material for operational purposes. It should be noted that a phase change occurring at either high or low temperature, which falls outside the functional range of that material, should not deem the material unfit for practical use.

Moreover, phase changes may also result as a distortion of the metal centres site symmetry (as in the case for inorganic complexes). This generally has some effect on the electronic properties of the material itself, i.e., either red or blue shifting the optical absorption spectrum, Jahn teller distortions (well known in perovskites), drastically altering the magnetic properties (Meissner effect), superconductivity, and the Peierls transition (Kittel C, 1996). This also highlights the importance of knowing the thermal properties of any material under investigation.

When considering the structures of the 3D organic inorganic hybrids, one may routinely think that these systems would be stable as a cubic crystal system. This is not the case as there are three phases present for each of the halogenated  $(\text{CH}_3\text{NH}_3)\text{PbX}_3$  crystals, as reported by (Knop O, et al, 1990). Table 1 summarizes the temperature dependant phases and their stability ranges present for all three of the lead halogenated hybrids reported i.e. the Cl, Br, and I systems. Since the methyl ammonium cation does not obey the  $O_h$  site symmetry needed to maintain cubic symmetry, only the high temperature phases are cubic, as the methyl ammonium cation becomes isotropically disordered within the cationic void. Both NMR and nuclear quadrupole resonance (NQR) spectroscopies have confirmed this for all the  $(\text{CH}_3\text{NH}_3)\text{PbX}_3$  cubic phases (Knop O, et al, 1990).

**Table 2.1:** Crystal structure data for the Cubic (CH<sub>3</sub>NH<sub>3</sub>)PbX<sub>3</sub> where X = Cl, Br, and I.

X	Temperature (K)	Crystal System	Space Group	a (Å)	b (Å)	c (Å)	z
Cl	> 178.8	Cubic	<i>Pm3m</i>	5.675			1
	172.9-178.8	Tetragonal	<i>P4/mmm</i>	5.656		5.63	1
	<172.9	Orthorhombic	<i>P222<sub>1</sub></i>	5.673	5.628	11.182	2
Br	>236.9	Cubic	<i>Pm3m</i>	5.901(1)			1
	155.1-236.9	Tetragonal	<i>I4/mcm</i>	8.322(2)		11.832(7)	4
	149.5-155.1	Tetragonal	<i>P4/mmm</i>	5.894(2)		5.861(2)	1
	<144.5	Orthorhombic	<i>Pna2<sub>1</sub></i>	7.979(1)	8.580(2)	11.849(2)	4
I	>327.4	Cubic	<i>Pm3m</i>	6.3285(4)			1
	162.2-327.4	Tetragonal	<i>I4/mcm</i>	8.855(6)		12.659(8)	4
	<162.2	Orthorhombic	<i>Pna2<sub>1</sub></i>	8.861(2)	8.581(2)	12.620(3)	4

It should also be noted that, upon cooling the three different 3D hybrids, the methyl ammonium cations disorder undergo a dynamic disorder cooling effect, which results in structural phase changes. Upon cooling, the methyl ammonium cation becomes restricted, as the dynamical disorder is frozen out, and the  $O_h$  site symmetry may no longer be maintained. Therefore the overall crystal symmetry is lowered from cubic to tetragonal. Further cooling results in greater restrictions on the methyl ammonium cations disorder. The final phase change from tetragonal to orthorhombic, is a result of the rotation restrictions now imposed on the C-N axis, as the cation becomes completely “solidified”.

### 2.2.1 Optical properties of 3D organic-inorganic hybrid perovskites

As the (A)PbX<sub>3</sub> structures behave as semiconductors, the optical absorption spectra of the 3D systems are reported here as a comparison of firstly, the effect of halogen substitution on the band gap, and secondly, to serve as a reference for comparison with the lower dimensional organic inorganic hybrids (2D, 1D and 0D). As the 3D systems are not expected to have any quantum confinement effects, which results in observable excitonic effects at room temperature, the absorption spectra are reported at low temperature in order to thoroughly observe the exciton peak. The band gap of (CH<sub>3</sub>NH<sub>3</sub>)PbI<sub>3</sub> was obtained from the low temperature reflectance spectrum which was transformed through the Kramers Kronig relationship to obtain the absorption spectrum (Hirasawa M, *et al*, 1994). The absorption spectrum, as seen in figure 2.2, shows a very sharp 1s exciton absorption peak (I) at 1.633eV. The binding energy of

the exciton was estimated to be  $50\text{meV}$ , with an effective Bohr radius of  $22\text{\AA}$  and a reduced mass of  $0.15m_0$ .

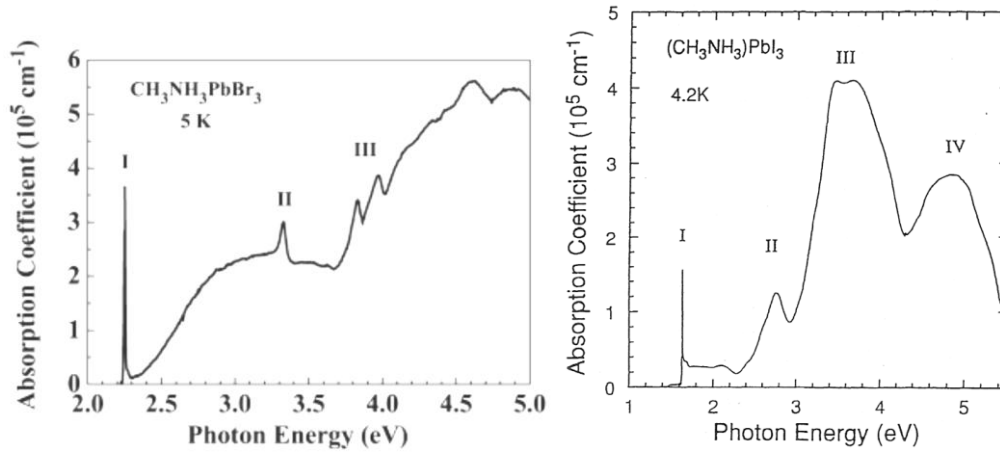


**Figure 2.2:** The low temperature absorption spectra both obtained from the reflectance and Kramers-Kronig relationship. a) Displays the  $5\text{ K}$  absorption spectrum of  $(\text{CH}_3\text{NH}_3)\text{PbBr}_3$  obtained from (Tanaka K, *et al*, 2003) b) Displays the  $4.2\text{ K}$  absorption spectrum of  $(\text{CH}_3\text{NH}_3)\text{PbI}_3$  obtained from (Hirasawa M, *et al*, 1994).

More recently the absorption spectrum for  $(\text{CH}_3\text{NH}_3)\text{PbBr}_3$  was obtained by (Tanaka K, *et al*, 2003) via the same method, where the sharp  $1s$  exciton absorption band was observed at  $2.258\text{eV}$  which is strongly blue shifted by comparison with its lead iodide analogue. The binding energy of the exciton is estimated at  $76\text{meV}$ , with an effective exciton Bohr radius of  $20\text{\AA}$  and a reduced mass of  $0.13m_0$ . The values quoted for  $(\text{CH}_3\text{NH}_3)\text{PbI}_3$  are the corrected values obtained from (Tanaka K, *et al*, 2003), as they believed the samples from (Hirasawa M, *et al*, 1994) were ill prepared when obtaining the magneto absorption spectra to determine the binding energy, effective Bohr radius, and the reduced mass. However more importantly, is the observed blue shift of the absorption spectrum with a substitution of the halogen from I to Br. This is also observed in the 2D and 1D cases, and will be discussed in greater detail in later sections.

### 2.2.2 Comparison of 3D and 2D electronic states

Here we report the electronic structure of  $(\text{CH}_3\text{NH}_3)\text{PbI}_3$  and  $(\text{C}_4\text{H}_9\text{NH}_3)_2\text{PbI}_4$  as carried out by (Umebayashi T, *et al*, 2003) and co-workers to further explore the effect of dimensional reduction on the electronic structure, and the electronic orbital's involved in the formation of the valence and conduction bands. Both ultraviolet photoelectron spectroscopy (UPS) and calculation (DFT) experiments were carried out to support one another's findings. The UPS spectra display's the experimental valence band of both the 3D and 2D hybrids in (figure 2.3). The first notable feature in the comparison of the spectra is that the 2D valence state has a narrower band width than that of the 3D state. Furthermore the calculated DOS displays broader peaks for the 3D with sharper and more localized peaks for the 2D hybrid. The experimental UPS and calculated density of states (DOS) both confirm that the dimensional reduction sharpens the density of states of the valence band. This feature is characteristic of the dimensional reduction process for semiconductors. Furthermore the narrower valence bands leads to an increase in the band gap, another expected feature of dimensional reduction. In addition, the basis for the localization of the electronic states in the 2D hybrid is purely because of the confinement of the DOS in the *c* axis (assuming the layers form in the *ab* plane). This is further evidenced through the analysis of the band structure of both systems.

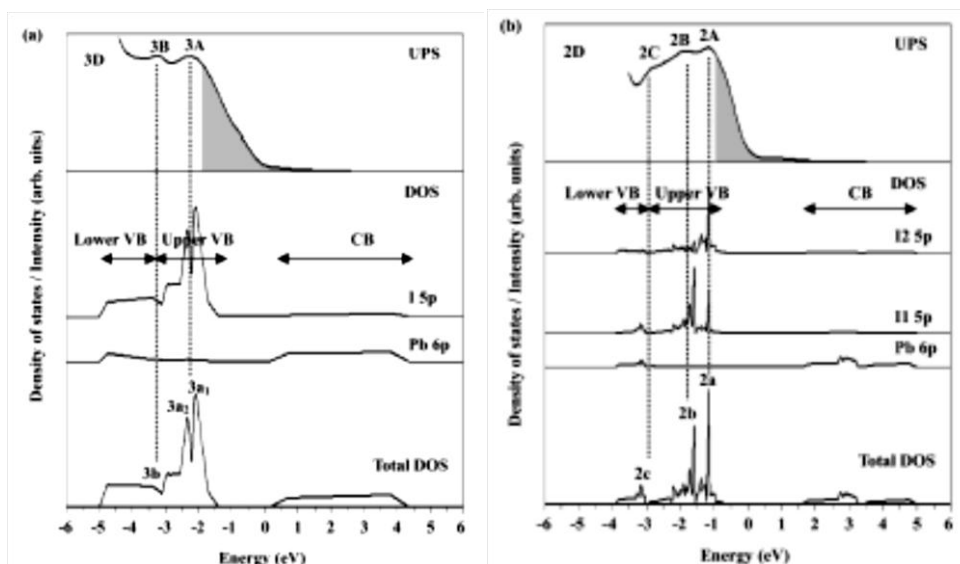


**Figure 2.3:** The UPS spectra and the calculated density of states, of a) The 3D Hybrid perovskite  $(\text{CH}_3\text{NH}_3)\text{PbI}_3$ , and b) the 2D hybrid perovskite  $(\text{C}_4\text{H}_9\text{NH}_3)_2\text{PbI}_4$  (Umebayashi T, *et al*, 2003).

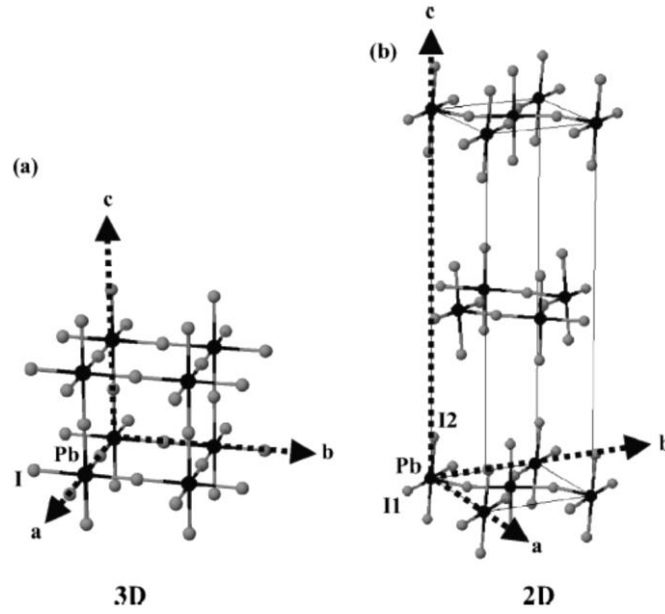


**Figure 2.4:** a) The inorganic sets only of the 3D structure of  $(\text{CH}_3\text{NH}_3)\text{PbI}_3$  and b) the 2D structure of  $(\text{C}_4\text{H}_9\text{NH}_3)_2\text{PbI}_4$  (Umebayashi T, *et al*, 2003).

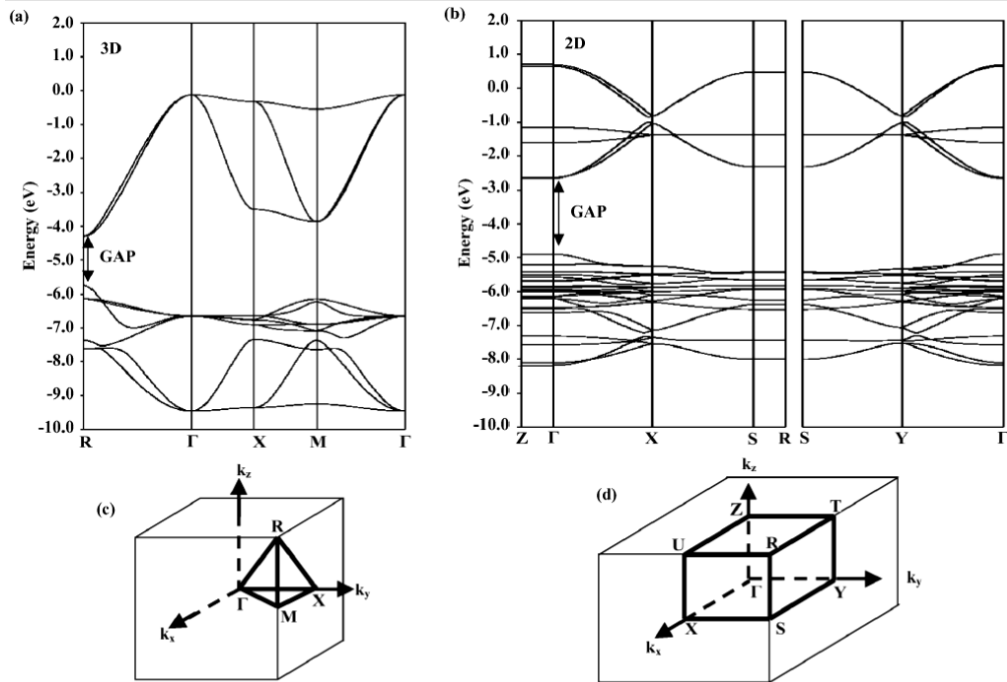


**Figure 2.5:** The results of the band structure calculations of a)  $(\text{CH}_3\text{NH}_3)\text{PbI}_3$  and b)  $(\text{C}_4\text{H}_9\text{NH}_3)_2\text{PbI}_4$ . The critical points in the first Brillouin zone of c) the cubic phase crystal structure of  $(\text{CH}_3\text{NH}_3)\text{PbI}_3$ , d) the orthorhombic phase of  $(\text{C}_4\text{H}_9\text{NH}_3)_2\text{PbI}_4$  (Umebayashi T, *et al*, 2003).

The structures of  $(\text{CH}_3\text{NH}_3)\text{PbI}_3$  and  $(\text{C}_4\text{H}_9\text{NH}_3)_2\text{PbI}_4$  may be seen in figure 2.4 above. The calculated band structures of both the 3D and 2D hybrids may be seen in figure 2.5 a) and b) with the critical points in  $k$ -space, for the generation of the band structure in the first Brillouin zone seen in figure 2.5 c) and d). From the band structure plots the first important aspect to scrutinize is the fact that the band dispersions in the vertical directions for the 2D crystal are

close to zero i.e.  $(\Gamma - Z; S - R)$ . The narrower 2D UPS spectra and the localization seen in the 2D DOS support this finding. These flat band structure bands, give a further justification for the observance of sharper absorption/emission spectra expected for a 2D system, as the momentum of the (electron)  $k_e$  and (hole)  $k_h$  have a flat band gradient giving rise to less absorption/emission broadening. In addition to the higher reduced masses and binding energies (386 meV for this 2D crystal) observed, the band structure plot also confirms a direct gap transition at the critical point  $R$  for the 3D hybrid, and  $\Gamma$  for the 2D hybrid. Finally the bonding, and anti-bonding states that contribute to the electronic structure are the Pb 6s and I 5p  $\sigma$ -antibonding states which form the top of the valence band, and the Pb 6p and I 5s  $\sigma$ -antibonding states contribute to the bottom of the conduction band, which was obtained from the DOS calculations (Umebayashi T, *et al*, 2003).

### **2.3 <100> 2D hybrid perovskites and the relative orientations.**

In the 2D layered hybrid perovskites, the hybrid layers may exist in various orientations. By far the most common orientation that exists is the <100>. This orientation is principally formed from a direct vertical separation of the octahedra of the 3D systems into single octahedral layers (figure 2.6). The vertical separation occurs as a result of the use of a larger cation (purely inorganic case  $K_2NiF_4$ ) or a longer R group as seen in figure 2.6. In organic inorganic hybrid perovskites a prerequisite for the formation of the <100> orientation, is the use of either a primary amine or primary diamine  $(R-NH_3)/(H_3N-R-NH_3)$  which allows the amine cation head to be able to hydrogen bond within the voids created between the octahedral layers. This means that there should be an extended arm (for example  $R-CH_2CH_2NH_3$ ) to allow enough space for the layers to form. If the R group on the cation does become too bulky, then either 1D chains, or some other motif will be generated (as will be discussed in later sections).



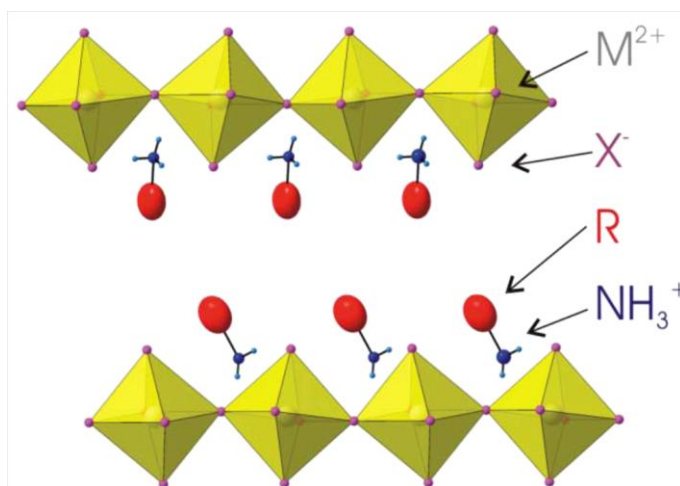


**Figure 2.6:** As the R group increases in size the 3D perovskite motif is changed, as the octahedra vertically separate. This separation may increase with increasing length of the R group.

In the  $\langle 100 \rangle$  orientation the inorganic layers may arrange in one of two orientations in the unit cell. They may arrange in either an eclipsed orientation, where the layers form directly over one another (figure 2.7 a), or the octahedral layers have slipped past one another and the axial halide position of the bottom layers octahedra now aligns with the centres of the voids created between the octahedral layers above it. This is known as the staggered arrangement (figure 2.7b). The eclipsed and staggered arrangements are also known as the monoclinic and orthorhombic arrangements respectively. Furthermore both arrangements may exist in the same hybrid at different temperatures, or phases. The monoclinic (eclipsed) phase is further known as the distorted or low symmetry form, and the orthorhombic (staggered) phase is known as the regular or high symmetry form (Mitzi D. B 1999). It should also be noted, an important parameter when discussing the properties of these compounds is the interlayer spacing. The interlayer spacing may be thought of as half the unit cell parameter,  $c$  for example where the layers form in the  $ab$  plane. The interlayer spacing is really a measure from a plane through the metal centres from one layer to a plane through the metal centres of the adjacent layer. This by definition is not the true interlayer spacing as the interlayer halogen to halogen contacts between the each layer is the true interlayer spacing value. However for single sheet 2D systems this is the simplest definition, and we will use it from here on out, unless otherwise specified.

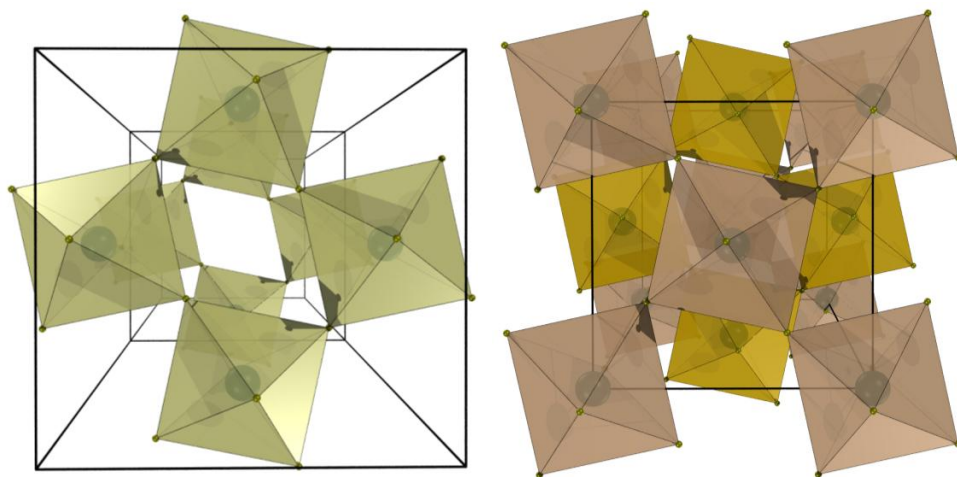


**Figure 2.7:** a) Eclipsed arrangement of the  $\langle 100 \rangle$  layers. b) Staggered arrangement of  $\langle 100 \rangle$  layers.

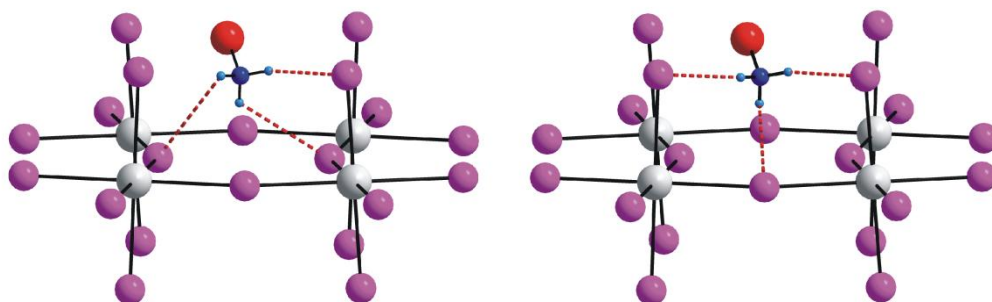


**Figure 2.8:** The hydrogen bonding configurations observed in the  $\langle 100 \rangle$  oriented 2D hybrids. a) The bridging halide configuration i.e. two hydrogen bonds to the bridging halides and one hydrogen bond to the terminal halogen. b) The terminal halogen configuration, where there is now one bridging halide hydrogen bond, and two terminal halide hydrogen bonds.

The  $\langle 100 \rangle$  orientation has a further convention of how the primary amine may hydrogen bond within the structure. The primary amine may hydrogen bond in one of two configurations, i.e. the terminal halogen configuration, or the bridging halogen configuration (Mitzi D, B 1999). The terminal halogen configuration may be defined as two terminal halogen hydrogen bonds which are formed from two of the individual hydrogen's on the ammonium cation, and one bridging halide hydrogen bond to the remaining hydrogen on the ammonium group. The bridging halogen configuration may be defined as two hydrogen bonds formed to the two bridging halides from two of the individual hydrogen's, and one terminal halide hydrogen bond to the remaining individual hydrogen of the ammonium group. There are additional definitions to this but will be further discussed in section 2.6

### 2.3.1 Size of the cation and the effect on the dimensionality and topology of <100> hybrids

A study of the effect of how bulky the R group may become, before forming an alternative motif from the <100> layers was conducted by (Billing D. G, and Lemmerer A 2007; 2009) for the Lead iodide and Lead Bromide and chloride series respectively. The primary ammonium templates used for this study were the primary cyclic ammonium groups, a series from cyclopropyl ammonium to cyclooctyl ammonium cations as seen in figure 2.9. What was observed in the Lead halogenated series was that the 2D <100> orientation was maintained from the cyclopropyl ammonium through to the cyclohexyl ammonium rings. However when the larger rings of the cycloheptyl ammonium template was used, different motifs were observed for all of the Lead halogen hybrids. For the Lead iodide and bromide cases, 1D double layer corner sharing chains, extending along the (100) direction, formed in preference to the <100> 2D layers as seen in figure 2.10. The motif however does strongly resemble the <110> type motif rarely observed in 2D layered systems. It must also be noted that the lead iodide and bromide cycloheptyl ammonium hybrids are not isostructural, they only adopt the same packing motif.

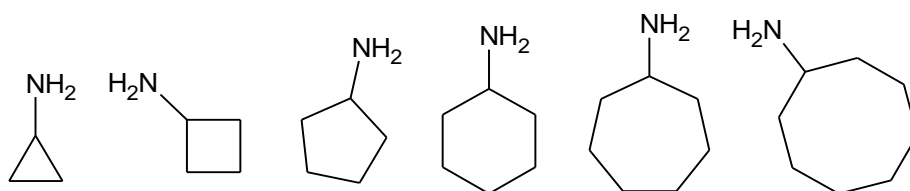


**Figure 2.9:** The primary cyclic amine templates used to ascertain at which point the bulkiness of the template forces a new templated motif.

The lead chloride cycloheptyl ammonium hybrid produced isolated bilayers, or one may broadly think of it as “wave like ribbons” as the authors describe it (Billing D. G, and Lemmerer A, 2009). These bilayers are not quite 1D or 2D and perhaps may be considered as an intermediate case (figure 2.11). However the bilayers of the octahedra are still connected in a regular corner sharing motif as seen in <100> 2D hybrids.

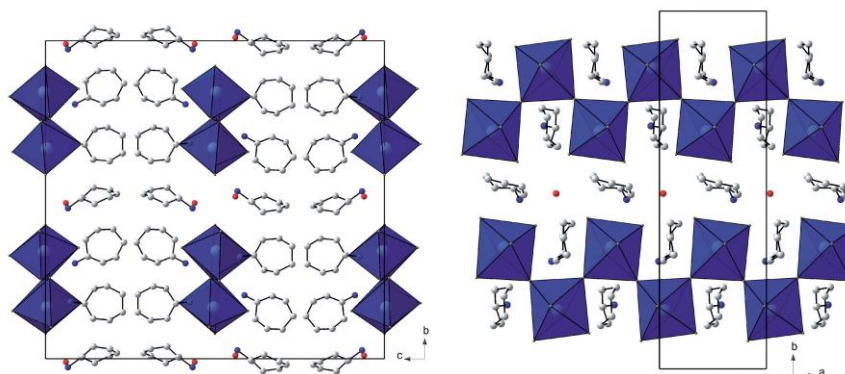


**Figure 2.10:** The Lead iodide and Lead bromide series form the same basic motif with the cycloheptyl ammonium template. a) The cycloheptyl ammonium cation with lead bromide, produces 1D double layer corner sharing octahedral chains. b) The side view displays the chain motif which resembles the  $\langle 110 \rangle$  2D layer motif (Billing D. G, and Lemmerer A, 2009).

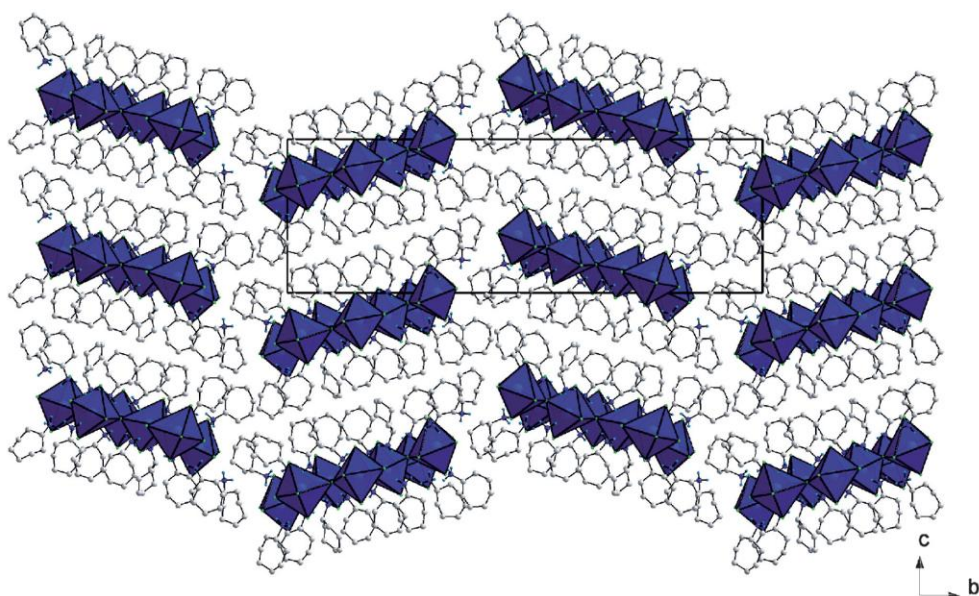


**Figure 2.11:** The Lead Chloride cycloheptyl ammonium hybrid forming inorganic bilayers in the crystal may be an intermediate dimension between 1D and 2D (Billing D. G, and Lemmerer A, 2009).

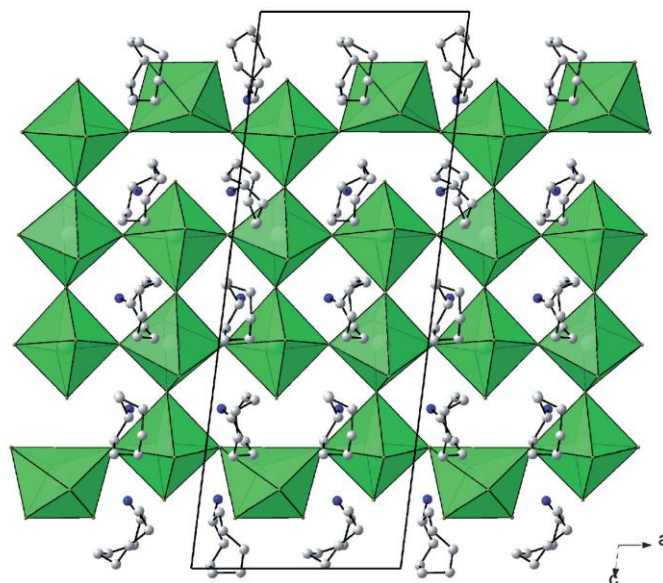


**Figure 2.12:** When the template ring size increases from cycloheptyl ammonium to the cyclooctyl ammonium cation for lead Bromide, a new type of bilayer motif is formed as in the lead chloride cycloheptyl ammonium case. The difference between them is observed when studying the bilayer topology. Instead of only corner sharing octahedra as seen in the lead chloride case, some of the  $\text{PbBr}_6$  octahedra only have two corner sharing halides instead of four. This motif alternates on the top and bottom edges as seen in the picture above (Billing D. G, and Lemmerer A, 2009).

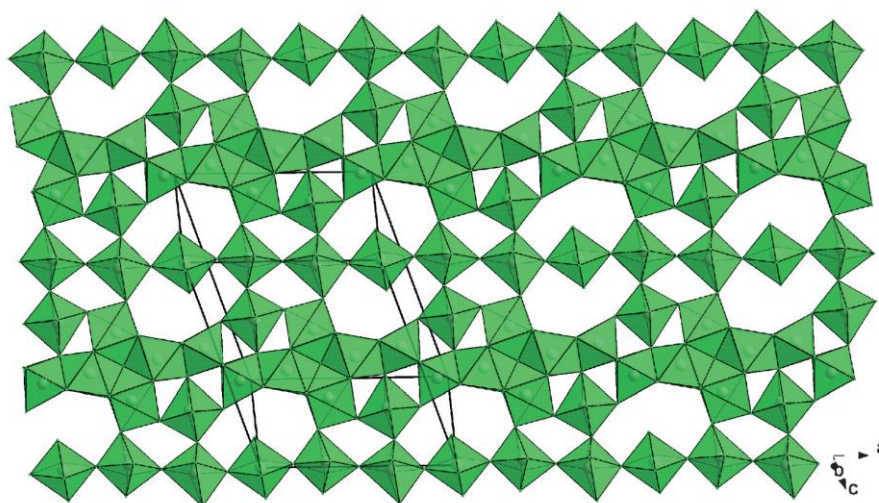


**Figure 2.13:** Lead Chloride with the cyclooctyl ammonium cation, which produced 2D layers unlike the smaller cycloheptyl ammonium cation, however a very unexpected topology arises (Billing D. G, and Lemmerer A, 2009).

As the organic cation increases with the size of the ring from the cycloheptyl ammonium to the cyclooctyl ammonium cation in the lead bromide hybrid, the hybrid forms bilayers, just like the (C7)PbCl based hybrid, with the exception that the bilayers are no longer regular corner sharing octahedra. The new bilayer topology may be seen in figure 2.12 where the  $\text{PbBr}_6$  octahedra now only have two corner sharing halides instead of four along the top and bottom edges of the



bilayer. The centre two rows of the bilayers octahedra still adopt the regular corner sharing motif type.

The final cyclooctyl ammonium lead chloride based hybrid, forms a completely unexpected fully 2D hybrid, with a complex layered topology as is seen in figure 2.13. This type of behaviour is difficult to rationalize especially when trying to reliably predict what the template will produce with respect to the inorganic motif. The final cyclooctyl ammonium lead iodide hybrid produces a 1D single chain system consisting of face sharing octahedral hybrid as seen in figure 2.14 below. The Lead Iodide hybrid series appears to follow a more reliable dimensional reduction scheme upon increasing the bulkiness of the cyclic ammonium template. In summary we note that all three halogenated C3-C6 ring templated hybrids, form  $\langle 100 \rangle$  2D layers. Both lead iodide and bromide form 1D  $\langle 110 \rangle$  based chains with the C7 ring. And finally the lead iodide forms single chain 1D hybrid with the cyclooctyl ammonium template where the lead bromide and chloride systems appear to revert to a more 2D type motif.

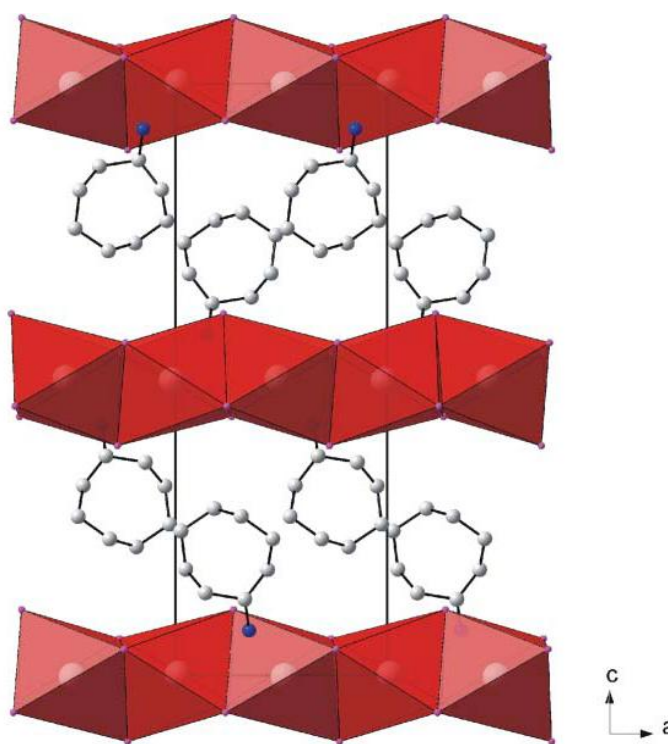


**Figure 2.14:** The cyclooctyl ammonium template with lead iodide producing 1D single chain face sharing octahedra (Billing D. G, and Lemmerer A, 2007).

### 2.3.2 <100>, <110> and <111> 2D orientations

We have discussed the origins of the <100> type orientations with the general formulae  $(\text{RNH}_3)_2\text{MX}_4$  or  $(\text{NH}_3\text{RNH}_3)\text{MX}_4$  depending on whether the ammonium ion is either a mono- or di-cation. These structures incorporate multilayered inorganic sheets, which are separated by the  $(\text{RNH}_3^+)$  ammonium cations. However there are other orientations that may be deduced from the basic 3D structure and separated into 2D layers similar to the <100> case. There are three different orientations that the 2D layered perovskites may adopt, these being <100>, <110>, and <111>. These orientations are defined as follows: at the terminating surface of the inorganic layer the <100> has one halide (a corner), <110> has two halides (an edge), and the <111> has three halides (a face) at the terminating surface (Mitzi D. B, 2001). If we look at figure 2.15 the orientation reduction from the bulk 3D orientation may be seen. For each orientation given that  $n = 1$  in each case, 2D layers are produced only in the <100> orientation. In the <110> orientation, corner sharing 1D chains are formed, and in the <111> isolated  $\text{MX}_6$  0D octahedral are formed.

From figure 2.15 let us briefly redefine the <100> orientation. The general formula for <100> single or multilayer oriented systems is  $(\text{RNH}_3)_2\text{A}_{n-1}\text{M}_n\text{X}_{3n+1}$  (where  $\text{A} = \text{CH}_3\text{NH}_3$  but may be any other small cation). When  $n = 1$ , a single inorganic layer is encountered. As  $n$  increases so does the thickness of the inorganic sheet (Figure 2.15a). Hence as  $n \rightarrow \infty$  the dimensionality  $\rightarrow 3\text{D}$ . The purpose of this process is to red shift the band gap and or increase the mobility of electrons within the layers. We will discuss this process and its impact on the physical properties in a later section. The <100> oriented systems have been extensively studied and the list of compounds that adopt this orientation for  $n = 1$  is very large. Table 2.2 only lists the compounds reported previously for Sn and Pb <100> orientations for  $n > 1$ .

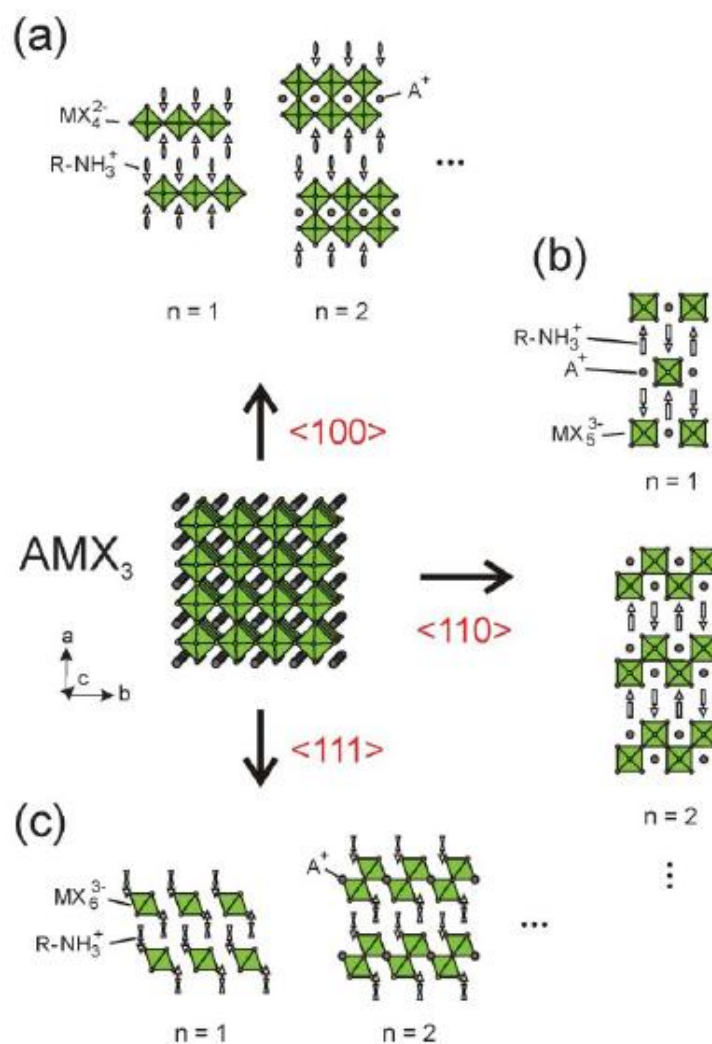


**Figure 2.15:** 2D layered perovskite orientations. a)  $\langle 100 \rangle$  oriented  $(R-NH_3)_2A_{n-1}M_nX_{3n+1}$ , b)  $\langle 110 \rangle$  oriented  $(R-NH_3)_2A_nM_nX_{3n+2}$ , and c)  $\langle 111 \rangle$  oriented  $(R-NH_3)_2A_{n-1}M_nX_{3n+3}$  (Mitzi D. B, 2004).

As already noted the  $\langle 100 \rangle$  orientation is the most common motif type however the  $\langle 110 \rangle$  orientation is also encountered but is much less common. The  $\langle 110 \rangle$  orientation as shown in (figure 2.15b) has the general formula  $(R-NH_3)_2A_nM_nX_{3n+2}$  where A is a small organic cation with the same criterion as in the 3D case i.e. the cation must fit inside a fully enclosed 3D cationic void. To generate the  $n = 2$  case a small organic cation is required however there does exist a compound that makes use of a diamine that forms the  $\langle 110 \rangle$  without the additional small amine cation  $(C_6H_{13}N_3)_2Pb_2Br_4$  (figure 2.16). Although this exception exists for the  $n = 2$  case, for  $n > 2$  cases, a second small cation of suitable size to fit inside the 3D cationic void must be readily available, as the structure grows in 3D character.



**Table 2.2:** The <100> orientation reported cases for Sn and Pb based hybrid perovskites with layers greater than 1.

Metal	Halide	First Amine	layers	Reference
Sn	I	C <sub>4</sub> H <sub>9</sub> NH <sub>3</sub>	2,3,4,5	Mitzi D. B, <i>et al</i> , 1994; 1995a,b
Pb	I, Br, Cl	C <sub>4</sub> H <sub>9</sub> NH <sub>3</sub>	2	Papavassillou G. C, <i>et al</i> , 1993
Pb	I	C <sub>5</sub> H <sub>11</sub> NH <sub>3</sub>	2	Elleuch S, <i>et al</i> , 2010
Pb	I	C <sub>6</sub> H <sub>13</sub> NH <sub>3</sub>	2, 3, 4	Tanaka K and Kondo T, 2003
Pb	I, Br, Cl	C <sub>8</sub> H <sub>17</sub> NH <sub>3</sub>	2	Papavassillou G. C, <i>et al</i> , 1993
Pb	I	C <sub>9</sub> H <sub>19</sub> NH <sub>3</sub>	2, 3, 4	Koutselas I. B, <i>et al</i> , 1996
Pb	Br	C <sub>9</sub> H <sub>19</sub> NH <sub>3</sub>	2	Koutselas I. B, <i>et al</i> , 1996
Pb,Sn(not Cl)	I, Br, Cl	C <sub>10</sub> H <sub>21</sub> NH <sub>3</sub>	2,{3(Pb I,Br)}	Papavassillou G. C, <i>et al</i> , 1993; 1995
Pb	I	CH <sub>3</sub> (CH <sub>2</sub> ) <sub>11</sub> NH <sub>3</sub>	2	Barman S, and Vasudevan S, 2009
Pb	I	CH <sub>3</sub> (CH <sub>2</sub> ) <sub>13</sub> NH <sub>3</sub>	2	Barman S, and Vasudevan S, 2009
Pb	I	CH <sub>3</sub> (CH <sub>2</sub> ) <sub>15</sub> NH <sub>3</sub>	2	Barman S, and Vasudevan S, 2009
Pb	I	CH <sub>3</sub> (CH <sub>2</sub> ) <sub>17</sub> NH <sub>3</sub>	2	Barman S, and Vasudevan S, 2009
Pb	I	C <sub>6</sub> H <sub>5</sub> C <sub>2</sub> H <sub>4</sub> NH <sub>3</sub>	2	Calabrese J, <i>et al</i> , 1991; Hong X, <i>et al</i> , 1992; Ishihara T, 1994; Kataoka T, <i>et al</i> , 1994
Pb	Br	C <sub>6</sub> H <sub>5</sub> C <sub>2</sub> H <sub>4</sub> NH <sub>3</sub>	2	Koutselas I. B, <i>et al</i> , 1996
Pb	I	HO <sub>2</sub> C(CH <sub>2</sub> ) <sub>3</sub> NH <sub>3</sub>	2	Mercier N, <i>et al</i> , 2005
Pb	I	C <sub>4</sub> H <sub>9</sub> SC <sub>2</sub> H <sub>4</sub> NH <sub>3</sub>	2	Zhu X. H, <i>et al</i> , 2002
Pb	I	I <sub>3</sub> .OC <sub>4</sub> H <sub>8</sub> NH <sub>2</sub>	2	Li H. H, <i>et al</i> , 2008
Pb	Br	H <sub>3</sub> CC <sub>6</sub> H <sub>4</sub> CH <sub>2</sub> NH <sub>3</sub>	3	Papavassillou G. C, <i>et al</i> , 2001
Pb	Br	C <sub>6</sub> H <sub>13</sub> NH <sub>3</sub>	2, 3	Tabuchi Y, <i>et al</i> , 2000
Pb	Br	C <sub>4</sub> H <sub>9</sub> NH <sub>3</sub>	2	Tabuchi Y, <i>et al</i> , 2000
Pb	Br	C <sub>3</sub> H <sub>7</sub> NH <sub>3</sub>	2	Tabuchi Y, <i>et al</i> , 2000
Pb	Br	C <sub>2</sub> H <sub>5</sub> NH <sub>3</sub>	2	Tabuchi Y, <i>et al</i> , 2000

The <110> orientation has only been reported for a handful of systems and we will discuss a few examples that have been found in literature. The tin iodide systems with the general formula (NH<sub>2</sub>C(I)=NH<sub>2</sub>)<sub>2</sub>(CH<sub>3</sub>NH<sub>3</sub>)<sub>n</sub>Sn<sub>n</sub>I<sub>3n+2</sub> where the structures of n = 1-4 have been reported (Mitzi D. B, *et al*, 1998). For the n = 1 case i.e. the 1D corner sharing hybrids case, the (NH<sub>2</sub>C(I)=NH<sub>2</sub>)<sub>3</sub>MI<sub>5</sub> for M = Sn and Pb, (Wang S, *et al*, 1995; Mitzi D. B, *et al*, 1998) and (NH<sub>3</sub>CSC(=NH<sub>2</sub>)NH<sub>3</sub>)PbI<sub>5</sub> (Mousdis G. A, *et al*, 1998) have also been reported. For the n = 2 case, where the second small A cation is replaced with a diamine, i.e. more correctly an imidazole in the compound (C<sub>6</sub>H<sub>13</sub>N<sub>3</sub>)<sub>2</sub>Pb<sub>2</sub>Br<sub>4</sub> (figure 2.16) or a 2-(aminoethyl)isothiurea to give the hybrid [2-(aminoethyl)isothiurea]PbBr<sub>4</sub>. These two compounds were reported fairly recently, as showing improved optical properties in comparison to those reported for the <100> orientations (Li Y, *et al*, 2006; 2008b).

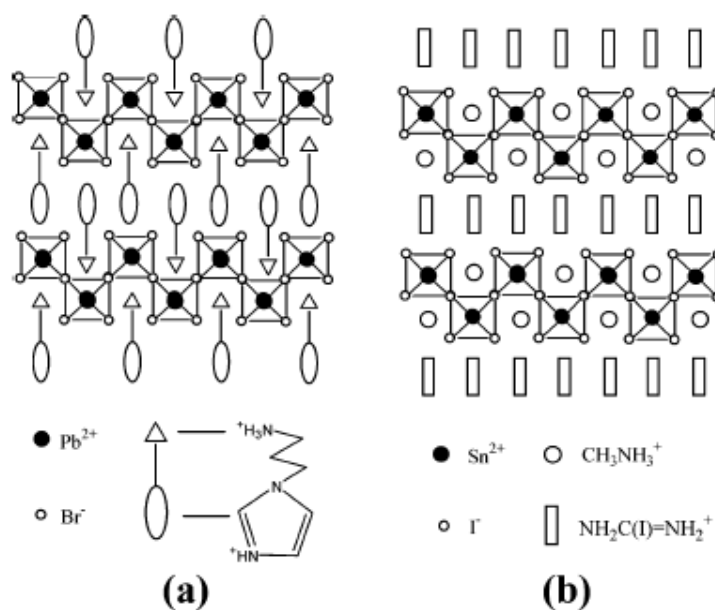


**Figure 2.16:** Comparison of the two  $\langle 110 \rangle$  oriented perovskites a) N-(3-aminopropyl)imidazole in PbBr b) Methyl ammonium and Iodoformamidinium in SnI, the diagram reference from (Mitzi D. B, et al, 1998; Li Y, et al 2006) respectively.

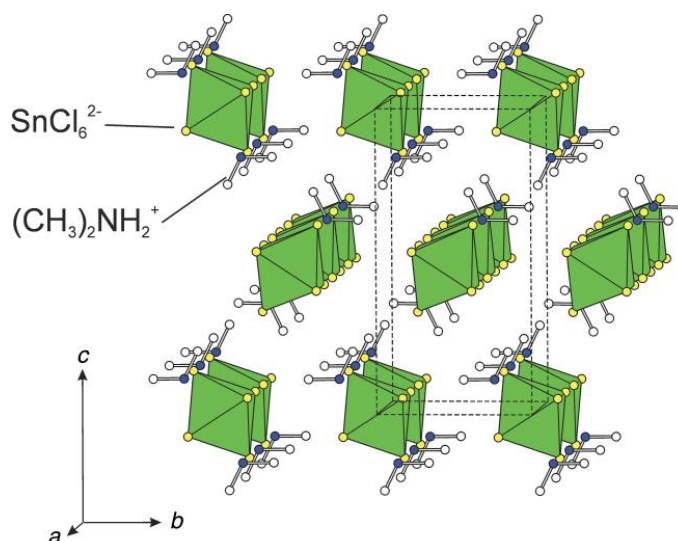


**Figure 2.17:** The  $\langle 111 \rangle$  orientation i.e.  $(R-NH_x)_2A_{n-1}M_nX_{3n+3}$ , here we seen an example of the  $n = 1$  case, which gives rise to isolated  $SnCl_6$  octahedra, the ideal OD case (Ben Ghazlen M. H, et al, 1981).

The  $\langle 111 \rangle$  orientation with the general formula  $(R-NH_x)_2A_{n-1}M_nX_{3n+3}$  have also been synthesized but are extremely rare (Mitzi D. B, 2001a). In the case where  $n = 1$  for the  $\langle 111 \rangle$  orientation, simply isolated  $MX_6$  octahedra would be expected [the OD case  $CH_3NH_3PbI_6 \cdot 2H_2O$  (Vincent B. R, et al, 1987)]. Essentially the  $n = 1$  case gives us the ideal OD hybrid. This system has been reported for a  $SnCl_6$  case, as seen in figure 2.17. Unfortunately for this orientation and for the  $n = 2$  stoichiometry to be maintained i.e.  $(R-NH_x)_2AM_2X_9$  the M oxidation state must be trivalent,

assuming A is a monovalent cation. Hence the compounds  $(\text{CH}_3\text{NH}_3)_3\text{Bi}_2\text{Br}_9$ ,  $[\text{NH}_2(\text{CH}_3)_2]_3\text{Sb}_2\text{Cl}_9$ , and  $[\text{NH}(\text{CH}_3)_3]_3\text{Sb}_2\text{Cl}_9$  are three examples that fit into  $n = 2$   $\langle 111 \rangle$  layers (Mitzi D. B, 2001a).

### **2.3.3 Group 14(IVA) $\langle 100 \rangle$ hybrids and the $ns^2$ lone pair stereo chemical activity**

With the various orientations of the 2D hybrid perovskites having now been defined, it is important to discuss the validity of going through so much effort to attain these various orientations. Therefore since the properties of the various orientations have only (to my knowledge) been reported for the lead, tin and Ge systems, we will only discuss their properties here. Although Bi and Sb hybrids may also fall in the  $\langle 111 \rangle$  2D class, they have by definition been denied true  $\langle 111 \rangle$  status and fall into a different structural motif class (Mitzi D. B, 2001a).

Before embarking on a discussion of the pros and cons of the various orientations, the electronic structure of the extensively investigated  $\langle 100 \rangle$  orientations should be reviewed. This will lay a foundation for further discussion of the properties associated with the group (IV) organic inorganic hybrid perovskites and their ability to be structurally tailored.

In the group 14 (IVA) metal halides, the metal cations which form 2D hybrid perovskites, exist in a divalent state. This gives rise to a nonbonding  $ns^2$  lone pair that sits on the metal which should result in the coordination geometry to be lowered from an octahedral arrangement to trigonal or square pyramidal in order to account for the lone pairs spatial occupation on the metal centre. However this is not the case as these metal halides readily form 2D hybrid perovskites with corner sharing octahedra, with of course the correct choice of organic cation. The nonbonding lone pair is important electronically, as the lone pair forms the top of the valence band in the group 14 (IVA) metal semiconductors. The stereo chemical activity of the nonbonding lone pair is important when tuning the band gap of the semiconductor. It is also important to note that the stereo chemical activity of the lone pair in group 14 has been found to increase in activity with the following trend,  $\text{Pb(II)} < \text{Sn(II)} < \text{Ge(II)}$ . The reason for this may be attributed to the increase of covalent character between the metal and the halide ligand (Mitzi D. B, 1996).

It should be brought to the readers attention that there are numerous reports of Pb and Sn (II) halide 2D perovskites, however only passing mention is made of the Ge(II) organic inorganic systems (Papavassiliou G. C, Koutselas I.B, 1995, Mitzi D. B, 1996). This is presumably because of

the decreasing stability of the group IVB Ge(II) oxidation state when moving up the group on the periodic table. The 3D perovskite family of  $\text{AGeX}_3$  ( $\text{A} = \text{Rb}, \text{Cs}$ ;  $\text{X} = \text{Cl}, \text{Br}, \text{I}$ ) however have been readily synthesized, and characterized structurally and electrically (Guen L *et al*, 1982; Thiele G, *et al*, 1987). It was found that  $\text{CsGeI}_3$  is of particular interest because it displays metallic character similar to some of the Sn(II) 3D derivatives (as will be discussed later).

Mitzi investigated three systems to ascertain the above mentioned stereo chemical activity model, namely  $(\text{C}_4\text{H}_9\text{NH}_3)_2\text{PbI}_4$ ,  $(\text{C}_4\text{H}_9\text{NH}_3)_2\text{SnI}_4$  and  $(\text{C}_4\text{H}_9\text{NH}_3)_2\text{GeI}_4$  hybrid perovskites. The Pb and Sn hybrids are basically isomorphous, and both metal halide systems crystallize in the orthorhombic space group *Pbca*. The Pb systems unit cell parameters are  $a = 8.8632(21) \text{ \AA}$ ,  $b = 8.6818(8) \text{ \AA}$  and  $c = 27.570(2) \text{ \AA}$ , with the Sn unit cell parameters being  $a = 8.8370(5) \text{ \AA}$ ,  $b = 8.6191(4) \text{ \AA}$ , and  $c = 27.562(2) \text{ \AA}$ . The Ge compound crystallizes in the space group *Pcmn*, with the unit cell parameters similar to the Pb and Sn systems, with  $a = 8.7220(5) \text{ \AA}$ ,  $b = 8.2716(4) \text{ \AA}$  and  $c = 28.014(1) \text{ \AA}$ , however it does not form an isomorphous crystal structure to that of the Pb and Sn systems.

The crux of this investigation is observed from the structural investigation of the bond angles and bond lengths of the metal halide octahedra. In the Ge-I case, the Ge-I bond lengths were observed to be greatly distorted, with Ge-I equatorial bond lengths of  $(3.217(2) \text{ \AA}$  and  $2.837(2) \text{ \AA})$  experiencing the greatest distortion whereas the axial Ge-I bond lengths of  $(3.016(3) \text{ \AA}$  and  $3.059(3) \text{ \AA})$  were much less so. A similar range of Ge-I bond lengths were observed in the rhombohedrally deformed room temperature perovskite structure of  $\text{CsGeI}_3$  (Thiele G, *et al* 1987). The 2D I-Ge-I bond angles also significantly deviated from  $90^\circ$  i.e. they ranged from  $81.18(6)^\circ$  to  $93.36(6)^\circ$ . These bond lengths and angles establish the highly distorted metal halide octahedra even with the use of a non bulky amine cation butylamine for  $\text{GeI}_4^{2-}$  hybrids.

The Pb and Sn systems displayed much smaller deviations in bond lengths in the  $\text{MI}_6$  octahedra than that of Ge structure. Where the M-I equatorial bond lengths were observed to be  $3.133(1) \text{ \AA}$  and  $3.138(1) \text{ \AA}$  for Sn-I and  $3.175(2) \text{ \AA}$  and  $3.177(2) \text{ \AA}$  for Pb-I which both display increased bond length distortions from their respective 3D  $(\text{CH}_3\text{NH}_3)\text{MI}_3$  analogues (Mitzi D. B, *et al*, 1995b; Knop O, *et al*, 1990). The axial bond lengths also showed only small deviations which are  $3.160(2) \text{ \AA}$  for Sn-I and  $3.200(2) \text{ \AA}$  for Pb-I. The I-M-I bond angles displayed no deviation for both Pb and Sn hybrids in the axial positions; however did display some deviation in the

equatorial positions which ranged from  $(86.97(4)^\circ$  to  $93.03(4)^\circ$  for Sn and  $86.32(5)^\circ$  to  $93.68(5)^\circ$  for Pb).

The bond angle that has been attributed to have the greatest impact on tuning the band gap for each individual metal, and impact the stereo chemical activity of the lone pair is the M-I-M bridging angle between the  $MI_6$  octahedra (Knutson J. L, *et al*, 2005). This angle is  $166.27(8)^\circ$  for Ge,  $159.61(5)^\circ$  for Sn and  $155.19(6)^\circ$  for Pb. This trend counters our original hypothesis of the increase of the lone pair's stereochemical activity with increased metal centred distortions as we proceed up the group. This relationship does however still hold, where the increase in the stereochemical activity of the lone pair increases as the covalent character of the ligand increases  $Pb(II) < Sn(II) < Ge(II)$ . However as the lone pair is better spatially accommodated as we proceed down the group the manifestation of an alternate distortion mechanism through the M-I-M bridging angle becomes the greater influence on the lone pair activity for the larger metals (Mitzi D. B, 1996).

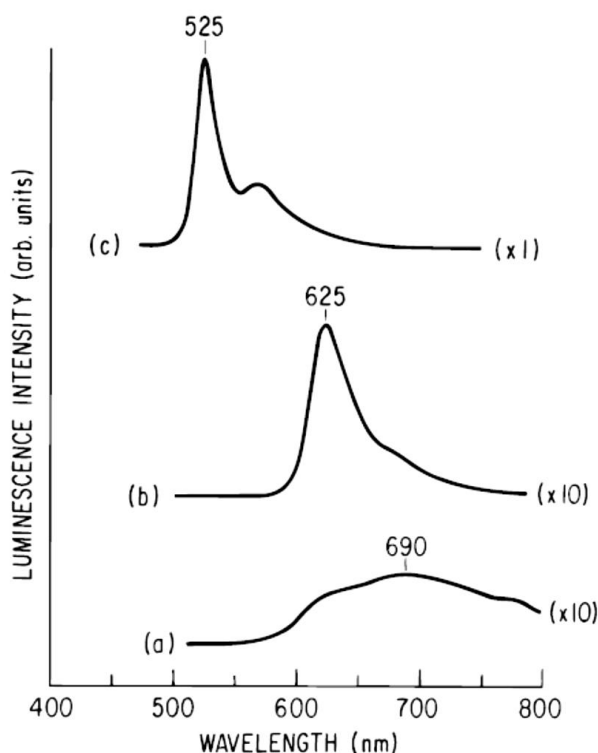


**Figure 2.18:** Luminescence emission of a)  $(C_4H_9NH_3)_2GeI_4$  b)  $(C_4H_9NH_3)_2SnI_4$  c)  $(C_4H_9NH_3)_2PbI_4$ , figure adapted from (Mitzi D. B, 1996).

In figure 2.18 the luminescence emissions of these three compounds may be seen where the emission blue shifts when proceeding down the group. To my knowledge this is the only reported case of optical characterization of a 2D Ge based hybrid. This is largely due to all of

these compounds being sensitive to oxidation, and need to be synthesized in an inert atmosphere. The stability of the compound toward degradation from oxidation follows the trend  $Ge < Sn < Pb$ , where Ge and Sn systems are only stable in air for a few minutes, whereas Pb is stable for much longer periods (Mitzi D. B, 1999). Mitzi also reported that the luminescence peak intensity decreased in the following order  $Pb(II) > Sn(II) > Ge(II)$  while the peak width increased and the peak shifted from 525nm to 625nm to 690nm respectively (Mitzi D. B, 1996).

#### **2.3.4 The effect of structural distortions on the stereo chemical activity of the $ns^2$ lone pair of $<100> (A)_2SnI_4$ hybrids.**

Knutson and co-workers (Knutson J. L, *et al*, 2005) studied 15 different tin iodide hybrid perovskites (table 2.3) to explain the distortions observed within the tin iodide octahedra. Extended Hückel tight binding band structure calculations were carried out to aid in the investigation, as well as a comparison with structural data (unpublished). It has been proposed (Mitzi D. B, 1999) that the shift in band gap may be largely correlated to the Sn-I-Sn bond angle between octahedra, away from the ideal undistorted angle of  $180^\circ$ . There are four cases of distortion that may occur within the layers. Firstly the undistorted, second in-plane distortion, thirdly out-of-plane distortion, and fourthly a combination of in- and out-of plane distortions (figure 2.19). To fully understand the affect that distortion has on the electronic structure, one has to consider the orbital overlap, and the band structure. The orbital based analysis of the electronic structure revealed that the main group halides dispersion will originate from  $\sigma^*$  interactions between the main group metal and the iodine  $p$  orbitals (Knutson J. L, *et al*, 2005).

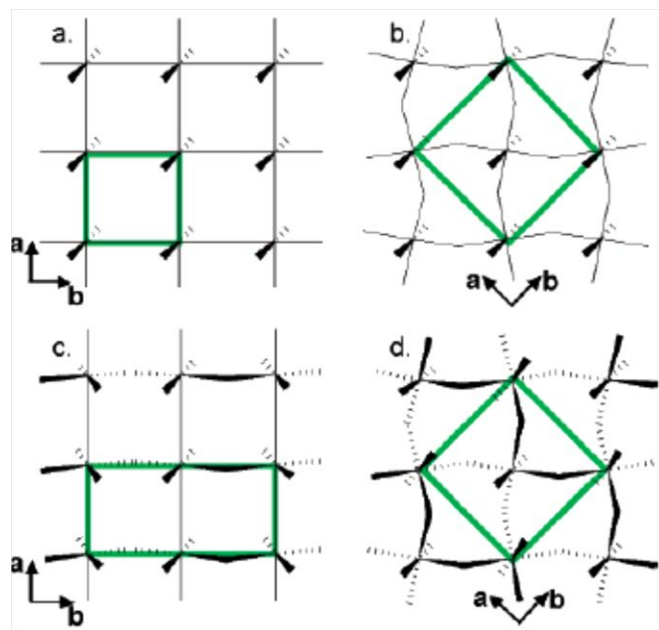


**Figure 2.19:** Schematic of 2D perovskite sheets which shows the (a) undistorted lattice, (b) in-plane distortion, (c) out-of-plane distortion, and (d) combined in- and out-of-plane distortion. The green box highlights the unit cell that describes each lattice (Knutson J. L, *et al*, 2005).

In the  $\text{Sn}^{2+}$  oxidation state, the highest-occupied orbitals will be localized on the Sn 5s orbitals, and thus, these orbitals are the origin of the top of the valence band of the extended lattice. The lowest-unoccupied orbitals, localized on the Sn 5p orbitals, are the origin of the conduction bands. In an octahedral  $\text{SnI}_6$  molecular fragment, both the Sn s and p orbitals will be destabilized by the  $\sigma$ -antibonding interactions by the iodine 5p and 5s orbitals. However, in the infinite lattice of the inorganic layers, the extent of the Sn-I antibonding interaction gives rise to the dispersion of the band structure (Knutson J. L, *et al*, 2005).

The conduction bands derived from the Sn 5p orbitals show much more distinct directional characteristics. The band derived from the Sn  $5p_z$  orbitals (in the axial direction) shows effectively no dispersion in the 2D perovskite because when using an alkyl ammonium cation to separate the tin iodide layers from one other, the  $\pi$ -type Sn-I interactions in the plane perpendicular to the long unit cell edge no longer interact. Then each of the Sn  $p_x$  and  $p_y$  bands display significant dispersions where strong antibonding with the iodine  $p_x$  and  $p_y$  orbitals occur, and much weaker antibonding interactions with the Is orbitals are also possible (Knutson J. L, *et al*, 2005).

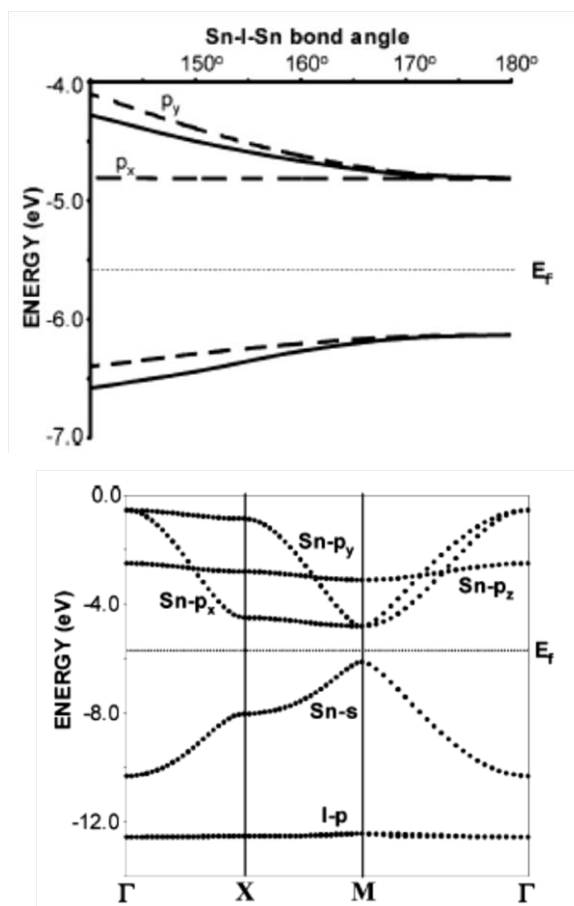


**Figure 2.20:** Plot of the top of the valence band and the bottom of the conduction band upon in plane (solid lines) and out of plane (dashed lines) distortions to the  $\text{SnI}_4^{2-}$  perovskite type lattice (Left). A plot of the band structure of the 2D tin iodide hybrid perovskite showing the relevant band contributions (Right) (Knutson J. L, et al, 2005).

In-plane distortions have a more drastic impact on the band gap than out-of-plane distortions. Bending the Sn-I-Sn bond angle away from  $180^\circ$ , where maximal orbital overlap is achieved, results in the loss of antibonding interactions between the Sn s orbitals and the I  $p_x$  and  $p_y$  orbitals and in so doing lowering the top of the valence band. This means that the more the Sn-I-Sn bond angle deviates from  $180^\circ$ , the larger the band gap becomes, as shown in (figure 2.20) (Knutson J. L, et al, 2005). This in-plane distortion is in part responsible for the lowering of the valence band (as mentioned), and raising the energy of the conduction band.

Out-of-plane distortions affect the Sn  $p_x$  orbitals from which the bottom of the conduction band is largely unchanged by distortion. The axial Sn-I bond distances also distort and determine the energy of the flat Sn  $p_z$  band, however they have no direct impact on the band gap. The hydrogen bonding to the axial iodides should have little impact on the band gap because the hydrogen bonding does not contribute to either the valence or conduction bands. Deviations of



the equatorial Sn-I bond distances do have a modest impact on the materials band gap. The shorter Sn-I distances result in the destabilization of the top of the valence band because of the increased anti-bonding while the nonbonding crystal orbitals of the bottom of the conduction band are not really affected by the variations of the Sn-I bond distances. This results in a red shifted band gap.

**Table 2.3:** The structures studied by (Knutson J. L, et al, 2005) (not all these materials have been fully characterized crystallographically).

<i>Metal</i>	<i>Halogen</i>	<i>Amine</i>	<i>Reference</i>
Sn	I	4-ClC <sub>6</sub> H <sub>5</sub> C <sub>2</sub> H <sub>4</sub> NH <sub>3</sub> <sup>+</sup>	i, iii, iv
Sn	I	2-ClC <sub>6</sub> H <sub>5</sub> C <sub>2</sub> H <sub>4</sub> NH <sub>3</sub> <sup>+</sup>	i, iii, iv
Sn	I	4-FC <sub>6</sub> H <sub>5</sub> C <sub>2</sub> H <sub>4</sub> NH <sub>3</sub> <sup>+</sup>	i, iii, iv
Sn	I	3-FC <sub>6</sub> H <sub>5</sub> C <sub>2</sub> H <sub>4</sub> NH <sub>3</sub> <sup>+</sup>	i, iii, iv
Sn	I	2-FC <sub>6</sub> H <sub>5</sub> C <sub>2</sub> H <sub>4</sub> NH <sub>3</sub> <sup>+</sup>	i, iii, iv
Sn	I	C <sub>6</sub> F <sub>5</sub> C <sub>2</sub> H <sub>4</sub> NH <sub>3</sub> <sup>+</sup>	i, v
Sn	I	C <sub>6</sub> F <sub>5</sub> C <sub>2</sub> H <sub>4</sub> NH <sub>3</sub> <sup>+</sup> & 2-C <sub>10</sub> H <sub>7</sub> C <sub>2</sub> H <sub>4</sub> NH <sub>3</sub> <sup>+</sup>	i, v
Sn	I	2-BrC <sub>6</sub> H <sub>5</sub> C <sub>2</sub> H <sub>4</sub> NH <sub>3</sub> <sup>+</sup>	i, iii, iv
Sn	I	2-(CF <sub>3</sub> )C <sub>6</sub> H <sub>5</sub> C <sub>2</sub> H <sub>4</sub> NH <sub>3</sub> <sup>+</sup>	I
Sn	I	C <sub>6</sub> H <sub>5</sub> C <sub>2</sub> H <sub>4</sub> NH <sub>3</sub> <sup>+</sup>	i, iii, viii
Sn	I	2-C <sub>10</sub> H <sub>7</sub> C <sub>2</sub> H <sub>4</sub> NH <sub>3</sub> <sup>+</sup>	i, iv
Sn	I	1-pyreneethylamine <sup>+</sup>	i, iv
Sn	I	C <sub>4</sub> H <sub>9</sub> NH <sub>3</sub> <sup>+</sup>	i, viii
Sn	I	C <sub>10</sub> H <sub>21</sub> NH <sub>3</sub> <sup>+</sup>	i, vi
Sn	I	(CH <sub>3</sub> ) <sub>3</sub> N <sup>+</sup> CH <sub>2</sub> CH <sub>2</sub> NH <sub>3</sub> <sup>+</sup>	i, ii

i) Knutson J. L, *et al*, 2005; ii) Xu Z, *et al*, 2003a; iii) Mitzi D. B, *et al*, 2001b ; iv) Xu Z, *et al*, 2003b; v) Xu Z, and Mitzi D. B, 2003c ; vi) Xu Z, and Mitzi D. B, 2003d ; vii) Mitzi D. B, 1996 ; viii) Papavassiliou G. C, *et al*, 1994

Interlayer I<sup>⋯</sup>I contacts have shown enhanced interaction between the layers (Xu Z, *et al*, 2003) when using a short dication. This apparently causes a substantial shift of the exciton state associated with the band gap toward lower energy, compared with other SnI<sub>4</sub> layered hybrids. This narrower band gap appears to be associated with the interlayer I<sup>⋯</sup>I Van der Waals contacts. The compound that has displayed this interaction is [(CH<sub>3</sub>)<sub>3</sub>NCH<sub>2</sub>CH<sub>2</sub>NH<sub>3</sub>]<sup>+</sup>SnI<sub>4</sub> (Xu Z, *et al*, 2003).

### 2.3.5 Electrical transport of <100> and <110> tin iodide based hybrid perovskites

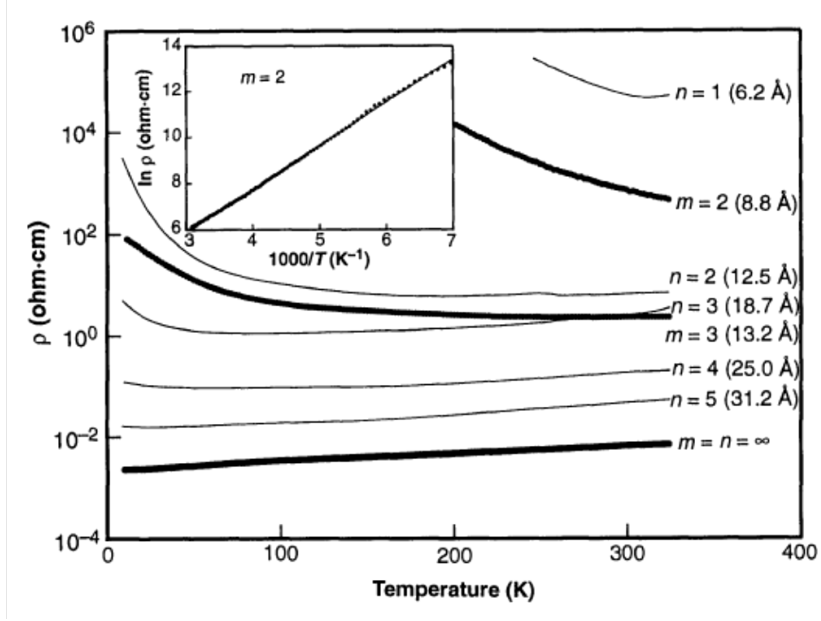


**Figure 2.21:** Temperature (T) Vs Resistivity ( $\rho$ ) of measurements of  $[\text{NH}_2\text{C}(\text{I})=\text{NH}_2]_2(\text{CH}_3\text{NH}_3)_m\text{Sn}_m\text{I}_{3m+2}$  where  $m = 1$  generates corner sharing single 1D chain systems, and  $m = 2$  generates the <110> 2D topology. Furthermore measurements of  $(\text{C}_4\text{H}_9\text{NH}_3)_2(\text{CH}_3\text{NH}_3)_{n-1}\text{Sn}_n\text{I}_{3n+1}$  are also displayed. For  $n = 1$  the common <100> topology is generated. (Mitzi D. B, *et al*, 1995a; Mitzi D. B, *et al*, 1994).

The hybrid material that has shown the most promising electrical transport properties have been the tin iodide based hybrids. As has been described in previous sections, there exists two main topologies i.e. the <100>  $(\text{C}_4\text{H}_9\text{NH}_3)_2(\text{CH}_3\text{NH}_3)_{n-1}\text{Sn}_n\text{I}_{3n+1}$  when  $n = 1$  we obtain the common 2D single layer hybrid, and the <110>  $[\text{NH}_2\text{C}(\text{I})=\text{NH}_2]_2(\text{CH}_3\text{NH}_3)_m\text{Sn}_m\text{I}_{3m+2}$  the less common 2D topology is obtained for  $m = 2$ . As displayed above in figure 2.21 a plot of temperature vs resistivity  $\rho$  has been done for both types of topologies for increasing  $n$  and  $m$  values respectively. An important point to note is the band gap of the <110> for  $m = 2$  case. Its band gap was calculated using the relationship  $\rho = A \exp(\frac{E_g}{2k_B T})$ . Taking the  $\ln$  of both sides of the equation and plotting  $1/T$  vs  $\ln(\rho)$  as seen in the top corner of figure 2.21 a straight line can be achieved. The gradient of the curve gives us the band gap, of  $E_g = 0.33(5)\text{eV}$ . The band gap for this topology is much lower than the lowest reported case for the  $n = 1$  <100> systems  $E_g = 1.97\text{eV}$ . However as  $n$  and  $m$  are increased to 3 the resistivity becomes comparable for both systems. Furthermore the electrical transport makes a semiconductor to metal transition at  $n = 4$  which corresponds to a well thickness of  $25\text{\AA}$ . For  $n$  and  $m = \infty$  the systems become fully three dimensional. The metallic transition occurs as a result of the dispersion of the Sn 5s hybridized with the I 5p valence orbital's, along the (111) direction in the cubic brillouin zone (special point

R) for the 3D  $\text{SnI}_3(\text{A})$  hybrid. The Sn 5s band slightly overlaps with the conduction Sn 5p band, giving rise to the semiconductor to metal transition (Mitzi D. B, *et al*, 1994; Mitzi D. B, *et al*, 1995a).

This property has been exploited in the  $\text{SnI}$  family of 2D hybrids, and has given rise to a large amount of literature published on the transport properties of  $(\text{A})_2\text{SnI}_4$  based hybrid perovskites. In addition the  $(\text{A})_2\text{SnI}_4$  systems have been deemed worthy systems for use as thin film field effect transistors (TFT's) with field effect mobility's of  $0.62\text{cm}^2/\text{V's}$  for  $(\text{C}_6\text{H}_5\text{C}_2\text{H}_4\text{NH}_3)_2\text{SnI}_4$ . Below in figure 2.22 a device built by (Kagan C. R, *et al*, 1999) that displays the high FET mobility's for this compound. Further work has been completed by (Mitzi D. B, *et al*, 2002) to compare thin film melt processing as an alternative to solution processing thin films, and the overall effect on the mobility of the tin iodide hybrid perovskites.

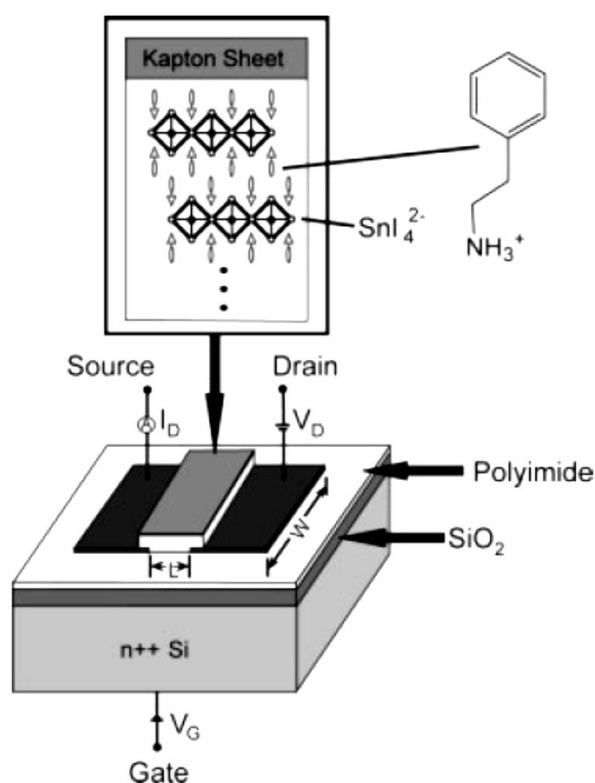


**Figure 2.22:** The schematic diagram of the melt processed organic inorganic field effect transistor OIFET, based on a silicon substrate. The inset displays a magnified view of the orientation of the hybrid perovskite with the kapton sheet on the top of the processed layer (Mitzi D. B, *et al*, 2002).

More Recently Takahashi and co-workers (Takahashi Y, *et al*, 2007) have shown the tuneable transport ability of the  $(\text{A})_2\text{SnI}_4$  hybrids, by merely tuning the band gap of the compound by varying the A template. The resistivity measurements are spread over a wide range of values as

the template is altered. The results are displayed below in figure 2.23. A simple discovery was made, that as the band gap of the material is decreased, the resistivity drastically decreases. However the important aspect to consider is that even though the band gaps of these materials are greater than 1eV, the resistivities of the compounds are still fairly low.

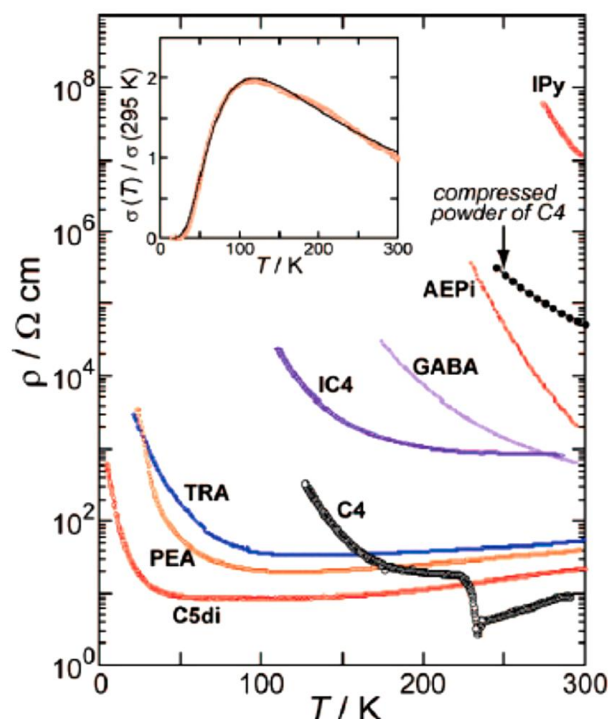


**Figure 2.23:** Temperature vs Resistivity ( $\rho$ ) for IPy (2-I-pyridine), C4 (Butylamine), AEPI ( $C_5H_{10}NHC_2H_4NH_3$ ), GABA ( $HOOC_3H_6NH_3$ ), IC4 ( $I-C_4H_8NH_3$ ), TRA ( $HOOC_6H_{10}CH_2NH_3$ ), PEA ( $C_6H_5C_2H_4NH_3$ ), and C5di ( $H_3NC_5H_{10}NH_3$ ) in  $(A)_2SnI_4$  hybrid perovskites. The discontinuity of C4 is the result of a phase change as the sample is being cooled. Furthermore the resistivity measurement are sensitive to the preparation method, hence great care should be taken when preparation and measurement take place (Takahashi Y, *et al*, 2007).

### 2.3.6 The <110> orientation and the effect on the band gap of lead based hybrids

To my knowledge there have been only three reported cases of the 2D <110> orientations for Pb and Sn hybrids. The first reported case is the  $[NH_2C(I)=NH_2]_2(CH_3NH_3)_2Sn_2I_8$  (Mitzi D. B, *et al*, 1995a) which has been discussed in the previous section. The two other reported cases are the lead bromide <110> systems of  $[N-(3\text{-aminopropyl})\text{imidazole}]PbBr_4$  i.e.  $[(API)PbBr_4]$  and the highly distorted layers of  $[2\text{-}(aminoethyl)\text{isothioure}]PbBr_4$  (Li Y, *et al*, 2006, 2008b). In the imidazole <110> hybrid case, the cation was chosen for one of two reasons. Firstly, it was probable that this template would arrange the inorganic component into the <110>

arrangement. And secondly, the imidazole ring is a good electron acceptor, in which a charge transfer interaction may take place between the inorganic layers and the imidazole ring.

The crystal structure of (API)PbBr<sub>4</sub> reveals that the important M-X-M bond angle (which has the greatest effect on the stereo chemical activity of leads lone pair of electrons) was found to be 162.68° and 171.85° in the vertical and horizontal directions respectively. Furthermore the Pb-Br bond lengths were quoted to range from 2.788 – 3.261Å which confirms the stereo chemical activity of the lone pair (Li Y, *et al*, 2006). However a fairly complex photoluminescence emission spectrum was obtained for (API)PbBr<sub>4</sub>, as a charge transfer interaction occurs between the layers and the API ligand. The sharp excitonic emission expected from the inorganic layers is still observed at 424nm, however it is accompanied by a broad emission at 503nm. This was assigned to a charge transfer interaction occurring from the inorganic layers to the imidazole electron acceptor rings. In the hybrids crystal structure, the imidazole rings of the API ligand in the hybrid were observed to have a  $\pi \rightarrow \pi$  stacking distance of only 3.558Å. Since it is generally considered that a  $\pi \rightarrow \pi$  stacking distance should range from 3.3 – 3.7Å, this short interaction should give rise to an acceptor band, between the band gap of the inorganic component, for the charge transfer interaction to occur. The charge transfer mechanism proposed by (Li Y, *et al*, 2006) may be seen below in figure 2.24.

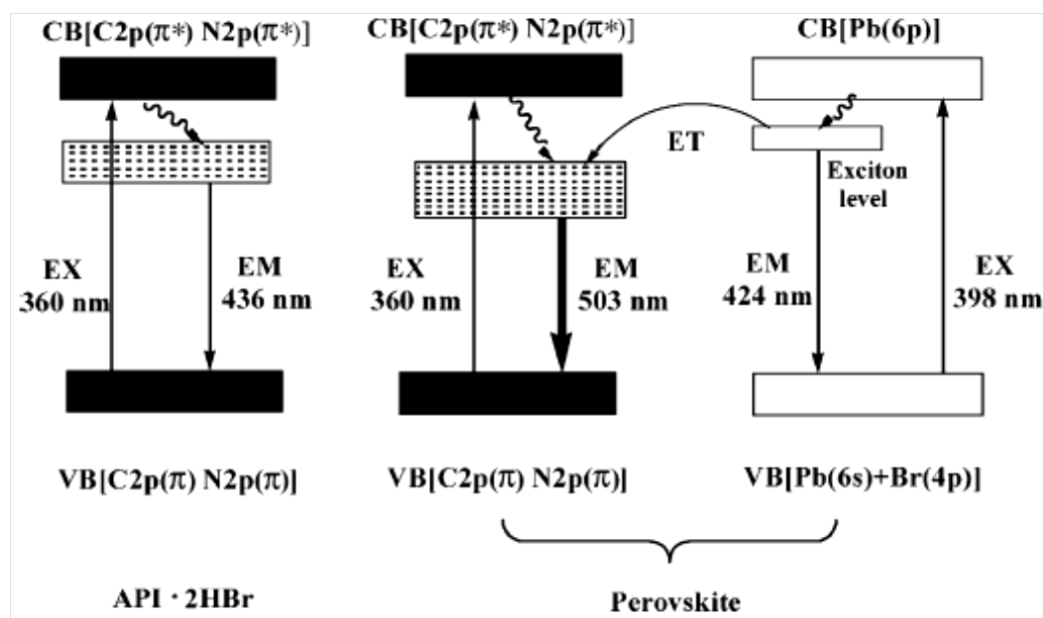


**Figure 2.24:** The charge transfer mechanism proposed by (Li Y, *et al*, 2006). The first absorption emission diagram is for the API.2HBr crystal, the second is the new mechanism for the hybrid perovskite crystal.

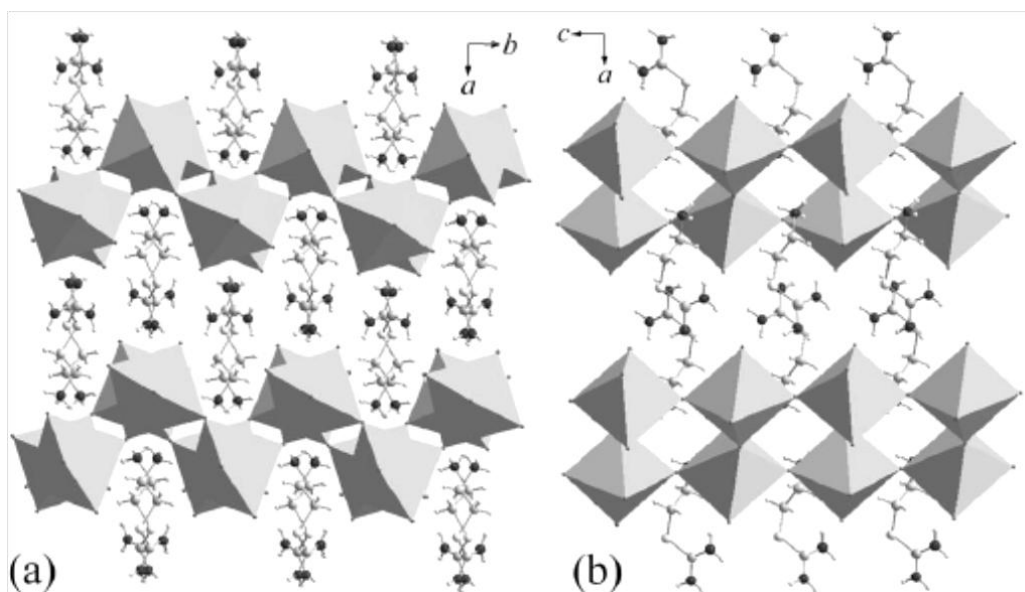


**Figure 2.25:** The crystal packing of (2-(aminoethyl)isothiourea)PbBr<sub>4</sub> viewed along the 001 axis a) where the octahedra are largely distorted, and adopt a staggered arrangement, whereas the (API)PbBr<sub>4</sub> adopts an eclipsed arrangement. b) Crystal packing view along 010 axis (Li Y, *et al*, 2008b).

The final <110> orientated 2D hybrid of [2-(aminoethyl)isothiourea]PbBr<sub>4</sub> was reported fairly recently (Li Y, *et al*, 2008b). The aim of using this new template was to suppress the charge transfer interaction observed in the previous case. However a highly distorted inorganic <110> layer was obtained, as seen in figure 2.25. The crystal structure reveals the Br-Pb-Br inter octahedral bond angle to range from 144.23(2)° and 170.54(2)° in the vertical and horizontal directions respectively. Furthermore the Pb-Br bond lengths range from 2.8440(6) – 3.1569(6) Å. The vertical Pb-Br-Pb bond angle of 144.23(2)° is highly distorted in comparison with vertical Pb-Br-Pb bond angle of 162.68° for (API)PbBr<sub>4</sub>. The Pb-Br bond lengths are less distorted than in the (API)PbBr<sub>4</sub> structure. As we know from the *ns*<sup>2</sup> stereo chemical activity, as the Pb-Br-Pb bond angle deviates from 180° the valence band drops in energy, causing an increase in the band gap. This is observed in the [2-(aminoethyl)isothiourea]PbBr<sub>4</sub> 1s exciton photoluminescence emission at 402nm, which is blue shifted, compared with (API)PbBr<sub>4</sub> PL emission of 424nm (due to the inorganic only).

There is only one significant advantage of the <110> orientation over the <100> orientation. This may be seen in the red shifted band gap seen in both the SnI and PbBr based hybrid cases. However large distortions of the inorganic layers make the band gap comparable with the band gaps reported for other PbBr <100> hybrids (Tabuchi Y, *et al*, 2000). An advantage of the single cation approach to synthesize the n = 2 <110> orientation, is that they may be readily solution processed into thin films for electroluminescent type displays (Li Y, *et al* 2006, 2008b), whereas

the two cation approach as seen in the tin iodide based hybrids thin films are a greater challenge to grow.

#### **2.4 Different motifs generated through varying M/X and cation ratio's**

We have now discussed the perovskite type orientational generation of 2D, 1D, and 0D hybrids from a dimensional reduction from the 3D perovskite various orientations. However there are other ways to generate low dimensional systems and unusual structural motifs which follow a different set of dimensional reduction rules. This has been discussed thoroughly in a recent review article from (Mercier N, *et al*, 2009). The hypothesis stands on the idea of varying the ratio of M/I to generate various clusters, ribbons, and layers, by altering the organic cation interaction with the surface of the inorganic component (Table 2.4 and 2.5). This is achieved through promoting intramolecular interactions such as hydrogen bonding,  $\pi - \pi$  interactions, weak Van der Waals interactions, S...S type interactions and lastly solvent influences (Mercier N, *et al*, 2009). Bulky cations have also been used in order to study 1D hybrids and 0D clusters. The extensively studied systems of Krautchild H, and co-workers, in the 90's and early 2000's have yielded some pleasing results and form the basis of the literature.

Tables 2.4 and 2.5 display the results of the I/M ratios of Pb/SnI and Bi/SbI based hybrids with the differing I/M ratios generating the various dimensions with Table 2.6 showing all the lead iodide hybrids quoted from the CSD Nov 2009. There are many other reported lead iodide hybrid cases, however their structure files don't seem to reach the CSD. The other structures and their properties will be discussed in later sections, specifically for the <100> 2D and 1D cases.

Referring to table 2.6 (Krautchild H, and Vielsack F, 1999) were the first authors who managed to synthesize the 0D clusters of:  $\text{Pb}_3\text{I}_{10}^{4-}$ ,  $\text{Pb}_7\text{I}_{22}^{8-}$ , and  $\text{Pb}_{10}\text{I}_{28}^{8-}$ . These clusters were synthesized with the bulky diammonium group of  $[(\text{Bu})_3\text{N}(\text{CH}_2)_4\text{N}(\text{Bu})_3]^{2+}$ . The cluster sizes were altered through varying the  $\text{I}^-$  stoichiometry (in the form of NaI), and the ratio of the solvents used for crystallization. The solvent contribution for cluster and ribbon formation is as important as the  $\text{I}^-$  ratio added to the solution. This was observed in the large amount of solvent incorporated into the crystal lattice of these structures (Krautchild H and Vielsack F, 1995; 1999).

**Table 2.4:** All dimensions of lead and tin iodide shown as a I/M ratio, with the simplest MI formula unit reported (Mercier N, *et al*, 2009).

Dimensionality				
I/M(II) Ratio	0D	1D	2D	3D
2.4		Pb <sub>5</sub> I <sub>12</sub> *	Pb <sub>5/6</sub> I <sub>2</sub> "	
2.44	Pb <sub>18</sub> I <sub>44</sub>			
2.57			Pb <sub>7</sub> I <sub>18</sub>	Pb <sub>7</sub> I <sub>18</sub>
2.67		Pb <sub>6</sub> I <sub>16</sub>	Sn <sub>3</sub> I <sub>8</sub>	
2.8	Pb <sub>10</sub> I <sub>28</sub>		Pb <sub>5</sub> I <sub>14</sub>	
3		MI <sub>3</sub> *	MI <sub>3</sub> *	MI <sub>3</sub> *(p)
3.14	Pb <sub>7</sub> I <sub>22</sub>			
3.2	Pb <sub>5</sub> I <sub>16</sub>			Pb <sub>5</sub> I <sub>16</sub>
3.33	Pb <sub>3</sub> I <sub>10</sub>	M <sub>3</sub> I <sub>10</sub> *	M <sub>3</sub> I <sub>10</sub> *(1p)	
3.5			Pb <sub>2</sub> I <sub>7</sub> *(1p)	
3.6			Pb <sub>5</sub> I <sub>18</sub>	
4		PbI <sub>4</sub>	MI <sub>4</sub> *(3p)	
4.4		Pb <sub>5</sub> I <sub>22</sub>		
4.5			Pb <sub>2</sub> I <sub>9</sub> (p)	
4.66		Pb <sub>3</sub> I <sub>14</sub>		
5		MI <sub>5</sub> *		
6	MI <sub>6</sub>			

M = Pb and Sn; \* structural isomers exist; "Deficient" PbI<sub>2</sub> Sheet; (p) perovskite network

**Table 2.5:** All dimensions of bismuth and antimony iodide shown as a I/M ratio, with the simplest MI formula unit reported (Mercier N, *et al*, 2009).

Dimensionality			
I/M(III) Ratio	0D	1D	2D
3.33		Sb <sub>3</sub> I <sub>10</sub> *	
3.5	M <sub>8</sub> I <sub>28</sub> *	M <sub>2</sub> I <sub>7</sub>	
3.6	M <sub>5</sub> I <sub>18</sub> *		
3.66	M <sub>6</sub> I <sub>22</sub> *	Bi <sub>3</sub> I <sub>11</sub>	
3.75	Bi <sub>8</sub> I <sub>30</sub>		
3.8	Bi <sub>5</sub> I <sub>19</sub>		
4	M <sub>4</sub> I <sub>16</sub> ; M <sub>3</sub> I <sub>12</sub> *	MI <sub>4</sub>	
4.5	M <sub>2</sub> I <sub>9</sub>		
5	M <sub>2</sub> I <sub>10</sub>	MI <sub>5</sub> *	
6	BiI <sub>6</sub>		M <sub>2/3</sub> I <sub>4</sub> "

M = Bi and Sb; \* structural isomers exist; "Deficient perovskite layer;



**Table 2.6:** CSD search for lead iodide hybrids (Nov 2009).

I/M ratio	Amine	I/M	Dimensionality	Reference
2.4	(C <sub>24</sub> H <sub>20</sub> P <sub>1</sub> ) <sup>+</sup>	Pb <sub>5</sub> I <sub>12</sub>	1D	Krautscheid H, et al, 1996
2.4	(C <sub>26</sub> H <sub>58</sub> N <sub>2</sub> ) <sup>2+</sup>	Pb <sub>10</sub> I <sub>24</sub>	1D	Krautscheid H, et al, 2001
2.4	(C <sub>8</sub> H <sub>4</sub> I <sub>2</sub> S <sub>6</sub> ) <sup>+</sup>	Pb <sub>5/6</sub> I <sub>2</sub>	2D	Devic T, et al, 2003
2.44	(C <sub>16</sub> H <sub>36</sub> N <sub>1</sub> ) <sup>+</sup>	Pb <sub>18</sub> I <sub>44</sub>	0D	Krautscheid H, Vielsack F, 1995
2.57	(C <sub>23</sub> H <sub>52</sub> N <sub>2</sub> ) <sup>2+</sup>	Pb <sub>7</sub> I <sub>18</sub>	2D	Krautscheid H, Vielsack F, 1999
2.57	(C <sub>12</sub> H <sub>32</sub> N <sub>2</sub> ) <sup>2+</sup>	Pb <sub>7</sub> I <sub>18</sub>	2D	Zhang Z. J, et al, 2008
2.8	(C <sub>28</sub> H <sub>62</sub> N <sub>2</sub> ) <sup>2+</sup>	Pb <sub>10</sub> I <sub>28</sub>	0D	Krautscheid H, Vielsack F, 1999
3	(C <sub>6</sub> H <sub>13</sub> N <sub>4</sub> ) <sup>+</sup>	PbI <sub>3</sub>	1D	Miyamae H, et al, 1988
3	(C <sub>9</sub> H <sub>24</sub> N <sub>2</sub> ) <sup>2+</sup>	Pb <sub>6</sub> I <sub>18</sub>	2D	Krautscheid H, Vielsack F, 1997
3	(C <sub>12</sub> H <sub>14</sub> N <sub>2</sub> ) <sup>2+</sup>	PbI <sub>3</sub>	1D	Tang Z, Guloy A. M, 1999
3	(C <sub>12</sub> H <sub>30</sub> N <sub>2</sub> ) <sup>2+</sup>	PbI <sub>3</sub>	2D	Krautscheid H, et al, 2001
3	(C <sub>12</sub> H <sub>26</sub> N <sub>2</sub> ) <sup>2+</sup>	PbI <sub>3</sub>	2D	Krautscheid H, et al, 2001
3	(C <sub>8</sub> H <sub>4</sub> I <sub>2</sub> S <sub>6</sub> ) <sup>+</sup>	PbI <sub>3</sub>	1D	Devic T, et al, 2004
3	(C <sub>10</sub> H <sub>16</sub> N <sub>1</sub> ) <sup>+</sup>	PbI <sub>3</sub>	1D	Li H. H, et al, 2004
3	(C <sub>14</sub> H <sub>18</sub> N <sub>2</sub> ) <sup>2+</sup>	PbI <sub>3</sub>	1D	Huang C. C, et al, 2004
3	(C <sub>18</sub> H <sub>19</sub> N <sub>4</sub> ) <sup>+</sup>	PbI <sub>3</sub>	1D	Sarker K. K, et al, 2006
3	(C <sub>8</sub> H <sub>22</sub> N <sub>2</sub> ) <sup>2+</sup>	Pb <sub>6</sub> I <sub>18</sub>	1D	Li H. H, et al, 2007
3	(C <sub>8</sub> H <sub>17</sub> N <sub>1</sub> O <sub>1</sub> ) <sup>2+</sup>	PbI <sub>3</sub>	1D	Sun L. G, et al, 2009
3.14	(C <sub>28</sub> H <sub>62</sub> N <sub>2</sub> ) <sup>2+</sup>	Pb <sub>7</sub> I <sub>22</sub>	0D	Krautscheid H, Vielsack F, 1999
3.2	(C <sub>14</sub> H <sub>30</sub> N <sub>2</sub> ) <sup>2+</sup>	Pb <sub>5</sub> I <sub>16</sub>	0D	Krautscheid H, Vielsack F, 2000
3.2	(C <sub>4</sub> H <sub>14</sub> S <sub>2</sub> N <sub>2</sub> ) <sup>2+</sup>	Pb <sub>5</sub> I <sub>16</sub>	3D	Louvain N, Mercier N, 2008
3.33	(C <sub>8</sub> H <sub>22</sub> N <sub>2</sub> ) <sup>2+</sup>	Pb <sub>3</sub> I <sub>10</sub>	1D	Krautscheid H, Vielsack F, 1997
3.33	(C <sub>9</sub> H <sub>24</sub> N <sub>2</sub> ) <sup>2+</sup>	Pb <sub>3</sub> I <sub>10</sub>	1D	Krautscheid H, Vielsack F, 1997
3.33	(C <sub>11</sub> H <sub>28</sub> N <sub>2</sub> ) <sup>2+</sup>	Pb <sub>3</sub> I <sub>10</sub>	0D	Krautscheid H, Vielsack F, 1999
3.33	(C <sub>28</sub> H <sub>62</sub> N <sub>2</sub> ) <sup>2+</sup>	Pb <sub>3</sub> I <sub>10</sub>	0D	Krautscheid H, Vielsack F, 1999
3.33	(C <sub>6</sub> H <sub>18</sub> N <sub>2</sub> ) <sup>2+</sup>	Pb <sub>3</sub> I <sub>10</sub>	1D	Corradi A.B, et al, 1999
3.33	(C <sub>6</sub> H <sub>16</sub> N <sub>2</sub> ) <sup>2+</sup>	Pb <sub>3</sub> I <sub>10</sub>	1D	Corradi A. B, et al, 2001
3.33	(C <sub>8</sub> H <sub>11</sub> N <sub>2</sub> S <sub>1</sub> ) <sup>+</sup>	Pb <sub>3</sub> I <sub>10</sub>	2D	Raptopoulou C. P, et al, 2002
3.33	(C <sub>10</sub> H <sub>12</sub> N <sub>1</sub> S <sub>3</sub> ) <sup>+</sup>	Pb <sub>3</sub> I <sub>10</sub>	1D	Zhu X. H, et al, 2003
3.33	(C <sub>15</sub> H <sub>14</sub> N <sub>1</sub> O <sub>2</sub> S <sub>1</sub> ) <sup>+</sup>	Pb <sub>3</sub> I <sub>10</sub>	1D	Maxcy K. R, et al, 2003
3.33	(C <sub>5</sub> H <sub>16</sub> N <sub>2</sub> ) <sup>2+</sup>	Pb <sub>3</sub> I <sub>10</sub>	1D	Billing D. G, Lemmerer A, 2004
3.33	(C <sub>9</sub> H <sub>14</sub> N <sub>1</sub> ) <sup>+</sup>	Pb <sub>3</sub> I <sub>10</sub>	2D	Billing D. G, Lemmerer A, 2006a
3.5	(C <sub>8</sub> H <sub>22</sub> N <sub>2</sub> ) <sup>2+</sup>	Pb <sub>2</sub> I <sub>7</sub>	2D	Krautscheid H, et al, 1998
3.5	(C <sub>5</sub> H <sub>8</sub> N <sub>1</sub> S <sub>1</sub> ) <sup>+</sup>	Pb <sub>2</sub> I <sub>7</sub>	2D (P)	Zhu X. H, et al, 2002
3.5	(C <sub>4</sub> H <sub>10</sub> N <sub>1</sub> O <sub>2</sub> ) <sup>+</sup>	Pb <sub>2</sub> I <sub>7</sub>	2D (P)	Mercier N, 2005
3.6	(C <sub>3</sub> H <sub>10</sub> N <sub>1</sub> ) <sup>+</sup>	Pb <sub>10</sub> I <sub>36</sub>	1D	Billing D. G, Lemmerer A, 2006b
4	(C <sub>9</sub> H <sub>22</sub> N <sub>1</sub> ) <sup>+</sup>	PbI <sub>4</sub>	2D (P)	Nagapetyan S. S, et al, 1988
4	(C <sub>12</sub> H <sub>18</sub> N <sub>2</sub> S <sub>4</sub> ) <sup>2+</sup>	PbI <sub>4</sub>	2D (P)	Zhu X. H, et al 2003
4	(C <sub>8</sub> H <sub>16</sub> N <sub>1</sub> ) <sup>+</sup>	PbI <sub>4</sub>	2D (P)	Billing D. G, Lemmerer A, 2006c
4.4	(C <sub>4</sub> H <sub>14</sub> S <sub>2</sub> N <sub>2</sub> ) <sup>2+</sup>	Pb <sub>5</sub> I <sub>22</sub>	1D	Louvain N, el al, 2007
4.5	(C <sub>2</sub> H <sub>10</sub> N <sub>2</sub> ) <sup>2+</sup>	Pb <sub>4</sub> I <sub>18</sub>	3D	Zhang Z. J, et al, 2006
4.5	(C <sub>4</sub> H <sub>10</sub> N <sub>1</sub> O <sub>1</sub> ) <sup>+</sup>	Pb <sub>2</sub> I <sub>9</sub>	2D (P)	Li H. H, et al, 2008
4.67	(C <sub>4</sub> H <sub>14</sub> S <sub>2</sub> N <sub>2</sub> ) <sup>2+</sup>	Pb <sub>3</sub> I <sub>14</sub>	1D	Louvain N, el al, 2007
5	(C <sub>10</sub> H <sub>12</sub> N <sub>1</sub> S <sub>3</sub> ) <sup>+</sup>	PbI <sub>5</sub>	1D	Zhu X. H, et al, 2004

6	(C <sub>1</sub> H <sub>6</sub> N <sub>1</sub> ) <sup>+</sup>	PbI <sub>6</sub>	0D	Vincent B. R, et al, 1987
6	(C <sub>3</sub> H <sub>12</sub> N <sub>2</sub> ) <sup>2+</sup>	PbI <sub>6</sub>	0D	Billing D. G, Lemmerer A, 2006d
6	(C <sub>12</sub> H <sub>16</sub> N <sub>2</sub> ) <sup>2+</sup>	PbI <sub>6</sub>	0D	Zheng Y. Y, et al, 2007
6	(C <sub>4</sub> H <sub>14</sub> S <sub>2</sub> N <sub>2</sub> ) <sup>2+</sup>	PbI <sub>6</sub>	0D	Louvain N, et al, 2008

Another example of this phenomenon was reported by (Krautschild H and Vielsack F, 1995). Again the use of a bulky ligand (Bu)<sub>4</sub>N<sup>+</sup> produced two different products by simply adjusting the NaI and solvent ratio's to produce either the large Pb<sub>18</sub>I<sub>44</sub><sup>8-</sup> 0D cluster, or the 1D face sharing octahedral chains of PbI<sub>3</sub><sup>-</sup>. Both methods were easily optimized in order to obtain 100% yields to generate their respective products. It was observed that as the NaI concentration was increased and or was in excess, the PbI<sub>3</sub><sup>-</sup> chains formed in complete preference over the large cluster formation. Hence in order to produce the large clusters, a stoichiometric amount of NaI was necessary. Furthermore the general trend as seen in table 2.4 (Mercier N, *et al*, 2009) and the CSD data base search in table 2.6, show that bulky ligands favour low I/M ratio's i.e. form large clusters or bulky ribbons. This was also observed with the lowest I/M ratio of 2.4 with 1D PbI ribbons of the quaternary phosphonium cation of (Ph)<sub>4</sub>P<sup>+</sup> reported by (Krautscheid H, *et al*, 1996).

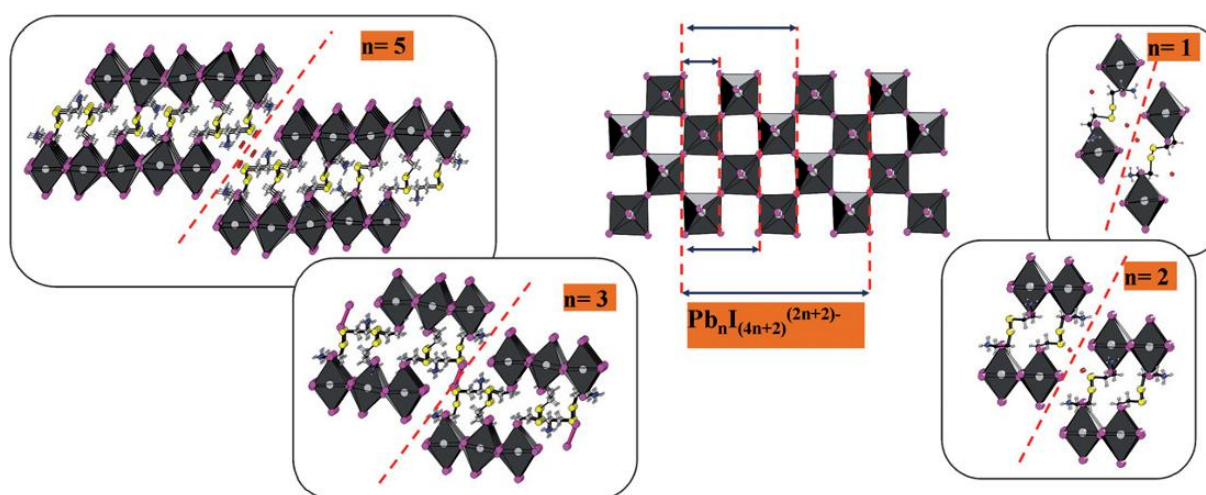


**Figure 2.26:** The cystamine cations ability to template various lead iodide structural motifs with the general formula  $\text{Pb}_n\text{I}_{(4n+2)}^{(2n+2)-}$  (Mercier N, *et al*, 2009).

Mercier and co-workers have found a different but similar trend using the cystamine (H<sub>3</sub>N(CH<sub>2</sub>)<sub>2</sub>S<sub>2</sub>(CH<sub>2</sub>)<sub>2</sub>NH<sub>3</sub>) cation, as seen in the figure 2.26. A group of 1D motifs reduced from the <100> type orientation, which incorporates either neutral H<sub>2</sub>O or I<sub>2</sub>, or the charged H<sub>3</sub>O<sup>+</sup> or I<sup>-</sup> into the hybrid crystal lattice in order to maintain a charge balance. The four compounds form 1D sheets generated from the general formula  $\text{Pb}_n\text{I}_{(4n+2)}^{(2n+2)-}$  for n = 1, 2, 3 and 5. However the

cystamine cation also generates the traditional 2D <100> hybrid perovskite, which was reported recently by (Lemmerer A, Billing D. G, 2010) and a pseudopolymorph of the  $n = 2$  structure, where the  $\text{H}_3\text{O}^+$  cation is replaced with the  $\text{I}^-$  anion. The overall formula changes in order to accommodate the new charge; however the structural motif remains the same. The reported structures formed by the cystamine cation generated with Pbl are listed in table 2.7. What has become apparent is the ability for the cystamine hybrids to generate pseudopolymorphs and various inorganic motifs. Furthermore this observation has been attributed to the ability of the cystamine cation to stabilize the various weak interactions needed to host various “solvent” molecules because of the S-S bridges intermolecular stabilizing effect (Mercier N, 2009).

**Table 2.7:** Table of lead iodide hybrids generated from the cystamine cation.

Hybrid Formula	Solvent	Anion	Dim	I/M ratio	Reference	n value
$(\text{H}_3\text{N}(\text{CH}_2)_2\text{S}_2(\text{CH}_2)_2\text{NH}_3)_2\text{PbI}_5\cdot\text{I}$	none	$\text{I}^-$	1D	5	Lemmerer A, Billing D. G, 2010	2'
$(\text{H}_3\text{N}(\text{CH}_2)_2\text{S}_2(\text{CH}_2)_2\text{NH}_3)\text{PbI}_5\cdot(\text{H}_3\text{O})$	$\text{H}_3\text{O}$	none	1D	5	Mercier N, <i>et al</i> , 2006	2''*
$(\text{H}_3\text{N}(\text{CH}_2)_2\text{S}_2(\text{CH}_2)_2\text{NH}_3)_2\text{PbI}_4$	none	none	2D (P)	4	Lemmerer A, Billing D. G, 2010	
$(\text{H}_3\text{N}(\text{CH}_2)_2\text{S}_2(\text{CH}_2)_2\text{NH}_3)\text{PbI}_6\cdot 2\text{H}_3\text{O}$	$\text{H}_3\text{O}$	none	0D	6	Louvain N, <i>et al</i> , 2008b	1
$(\text{H}_3\text{N}(\text{CH}_2)_2\text{S}_2(\text{CH}_2)_2\text{NH}_3)_4\text{Pb}_3\text{I}_{14}\cdot\text{I}_2$	none	$\text{I}_2$	1D	4.67	Louvain N, <i>et al</i> , 2007	3
$(\text{H}_3\text{N}(\text{CH}_2)_2\text{S}_2(\text{CH}_2)_2\text{NH}_3)_6\text{Pb}_5\text{I}_{22}\cdot 4\text{H}_2\text{O}$	$\text{H}_2\text{O}$	none	1D	4.4	Louvain N, <i>et al</i> , 2007	5''
$(\text{H}_3\text{N}(\text{CH}_2)_2\text{S}_2(\text{CH}_2)_2\text{NH}_3)_6\text{Pb}_5\text{I}_{22}\cdot 2\text{H}_2\text{O}$	$\text{H}_2\text{O}$	none	1D	4.4	Louvain N, <i>et al</i> , 2007	5''

' pseudopolymorphs, '' pseudopolymorphs, \*structural polymorph exists at high temperature

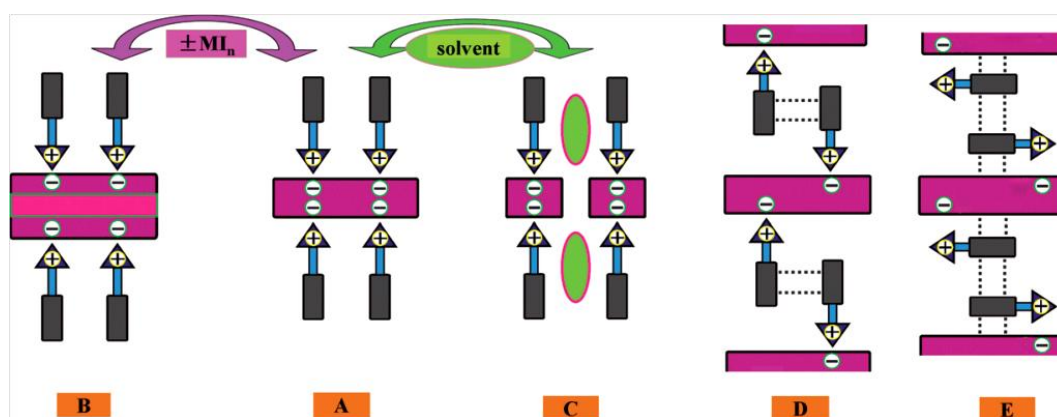


**Figure 2.27:** Important intermolecular interactions considered when growing hybrid materials. A and B represent an addition or subtraction of an inorganic unit. An addition of a “solvent/(anionic and cationic included)” molecule may give rise to a newly defined inorganic subunit (A and C). Intermolecular interactions need to be considered in order to stabilize surface interactions between the inorganic interfaces, as well as with other organic moieties present in the crystal (D and E) (Mercier N, 2009).

Mercier and co-workers have performed many other studies on the effect of the presence of the sulphur atom in the cationic moiety (these structures are reported in table 2.7) and taken into account the work established primarily by Krauschied, and put forward a mechanism for hybrid formation as seen in figure 2.27. The diagram illustrates the interactions that need to be considered in order to generate the various inorganic motifs that have been observed thus far. Firstly cases A and B are the general 2D cases in which inorganic units may be added or subtracted for the simple single layer 2D hybrid or the multilayer hybrid formation. Incorporation of a “solvent/(anionic and cationic included)” molecule may give rise to a newly defined inorganic subunit (A and C). Furthermore intermolecular interactions need to be considered in order to stabilize surface interactions between the inorganic interfaces, as well as with other organic moieties present in the crystal (D and E). A further example not included in the mechanism above, is the incorporation of solvent into the hybrid, and still be able to maintain the <100> 2D single layer motif. This was successfully accomplished by (Mitzi D. B, *et al*, 2002b) by investigating fluoroaryl type interactions with  $(\text{PEA})_2\text{SnI}_4 \cdot (\text{C}_6\text{F}_6)$ , and  $(\text{F}_5\text{-PEA})_2\text{SnI}_4 \cdot (\text{C}_6\text{H}_6)$ .

## 2.5 Optical properties and Photoluminescence of <100> 2D hybrids

Photoluminescence is a useful tool used when studying the electronic properties of semiconducting materials. Generally highly efficient luminescence for device applications is restricted to the Group (IV/V) metal halide hybrids. However the transition metal hybrids, which are better known for their low dimensional magnetism, have also shown luminescent properties in the Mn based hybrids. The aliphatic hybrids of  $(\text{C}_n\text{H}_{2n+1}\text{NH}_3)_2\text{MnX}_4$  for  $n = 1, 2$  and  $3$ , have displayed a red emission for the octahedrally coordinated  $(\text{MnCl}_6)$  systems which is a resultant transition from  ${}^4T_1$  to  ${}^6A_1$  electronic state. Because  $\text{Mn}^{2+}$  is a  $3d^5$  compound, it experiences a strong crystal field splitting, giving rise to this transition. The luminescence emissions for  $n = 1, 2$  and  $3$  have been reported at room temperature to be  $597\text{nm}$ ,  $588\text{nm}$  and  $602\text{nm}$  respectively (Morita M, and Kaeyama M, 1981; Tsuboi T, *et al*, 1995). The  $\text{MnI}_4$  hybrids don't form octahedrally coordinated systems, but rather isolated tetrahedral complexes. This is due to the weak crystal field and the weaker ligand field strength, and the larger  $\text{I}^-$  anion over  $\text{Cl}^-$ . A green luminescence results from the tetrahedral coordinated  $\text{MnI}_4$  hybrid.

Although luminescence has been reported in the transition Mn hybrids, more efficient luminescence for device application has really been restricted to the group (IV) metal (II) halides.

From the three metal halide systems (GeI, SnI and PbI) the lead hybrid has been shown to display the narrowest and most intense luminescence emissions out of the group (IV) metal halide hybrids. This is due to the lead hybrids ability to increase the excitons binding energy ( $E_b$ ) and oscillator strength compared to that of the tin and germanium iodide hybrids (Mitzi D. B, 1996). An example in which this phenomenon was demonstrated was for the Sn and Pb hybrids of  $(C_6H_5C_2H_4HH_3)_2MI_4$ , where the reported binding energies were 220meV and 160-190meV for Pb and Sn hybrids respectively (Papavassiliou G. C, 1996).

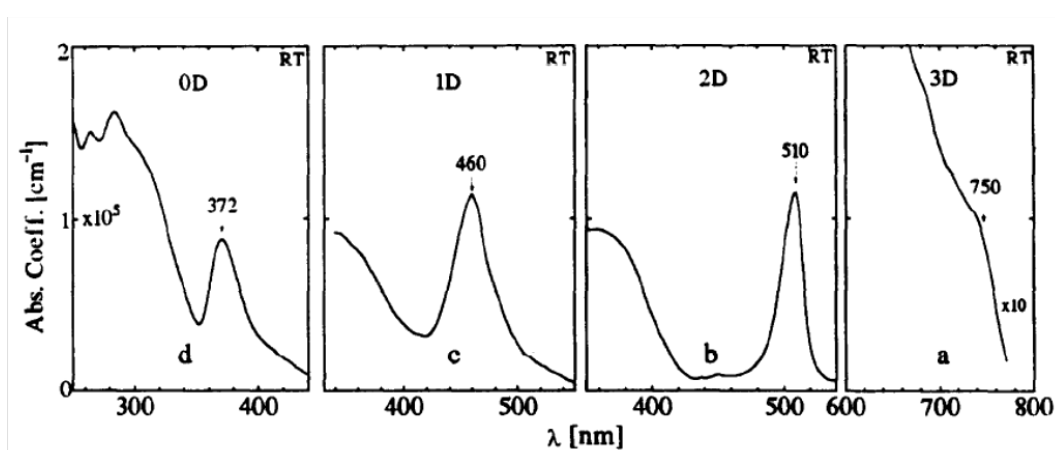


**Figure 2.28:** The Optical absorption for a) 3D  $(CH_3NH_3)PbI_3$ , b) 2D  $(C_9H_{19}NH_3)_2PbI_4$ , c) 1D  $(NH_2C(I)=NH_2)_3PbI_5$  and d) 0D  $(CH_3NH_3)_4PbI_6 \cdot H_2O$  crystals (Papavasiliou G. C, 1997).

As discussed in chapter 1, dimensional reduction results in two types of enhancements experienced by a material. Firstly, is the widening of the band gap of the material as the dimensionality is decreased (3D to 0D) as explained through the density of states calculations. This may simply be observed by the colour of the crystal, which specifically for the lead iodide systems, is observed to undergo a transition from black (3D) to colourless (0D) upon dimensional reduction. Furthermore the absorption peaks at room temperature for the 3D  $(CH_3NH_3)PbI_3$ , 2D  $(C_9H_{19}NH_3)_2PbI_4$ , 1D  $(NH_2C(I)=NH_2)_3PbI_5$  and 0D  $(CH_3NH_3)_4PbI_6 \cdot H_2O$  are 750nm, 510nm, 460nm and 372nm respectively further illustrating this phenomenon (Papavassiliou G. C, 1996) (figure 2.28).

The second enhancement that is observed is the increased exciton binding energy with the decrease in dimensionality. A large increase in oscillator strength is also observed with the decrease in dimensionality as displayed in the lead iodide hybrids (0.7 per formula unit for  $(C_{10}H_{21}NH_3)_2PbI_4$  compared to 0.02 per formula unit for  $(CH_3NH_3)PbI_3$ ) (Ishihara T, 1994). These enhancements are important as they result in highly efficient photoluminescence emissions at

room temperature. As discussed in the theory section, a decrease from 3D to 2D should result in a fourfold increase in the excitons binding energy. The binding energy enhancement argument becomes less trivial for the 1D and 0D cases, so we are just going to discuss the 2D cases here. For the 3D to 2D case in lead Iodide the binding energy has been measured to be  $\sim 45\text{meV}$  (as three papers have reported different values which lie between  $40 - 50\text{meV}$ , the average value is simply quoted, (Ishihara T, 1994; Hirasawa M, *et al*, 1994; and Tanaka T, *et al*, 2003). For the 2D system  $(\text{C}_6\text{H}_5\text{C}_2\text{H}_4\text{HH}_3)_2\text{PbI}_4$  the binding energy was measured to be  $\sim 220\text{meV}$  (Papavassiliou G. C, 1996), which is consistent with the theoretical binding energy for a 2D system being four times greater than the 3D analogue.

**Table 2.8:** The binding energies, optical absorption and Photoluminescence emissions at various temperatures, of some Pbl based hybrids.

Metal Halide	Amine	Dimensionality	Exciton (nm)	OA	PL (nm)	Binding energy	Reference
<b>Pbl<sub>4</sub></b>	C1	3D	753 <sup>a</sup> , 759 <sup>c</sup>		753 <sup>a</sup>	$\sim 45\text{meV}$	
	C4	2D	484 <sup>d</sup>		490 <sup>d</sup>	300meV	Ishihara T, <i>et al</i> , 1990
	C6	2D	516 <sup>a</sup> , 530 <sup>c</sup>			361meV	Tanaka K, Kondo T, 2003a
	H <sub>3</sub> NC <sub>6</sub> NH <sub>3</sub>	2D	483			150meV	Papavassiliou G. C, 1997
	C8	2D	484 <sup>d</sup>		490 <sup>d</sup>	380meV	Ishihara T, <i>et al</i> , 1990
	C9	2D	514 <sup>a</sup> , 484 <sup>d</sup>		490 <sup>d</sup>	300meV	Ishihara T, <i>et al</i> , 1990
	C10	2D	512 <sup>a</sup> , 484 <sup>d</sup>		517 <sup>a</sup> , 490 <sup>d</sup>	370meV	Ishihara T, <i>et al</i> , 1989
	C12	2D	484 <sup>d</sup>		490 <sup>d</sup>	300meV	Ishihara T, <i>et al</i> , 1990
	PEA	2D	517 <sup>a</sup> , 527 <sup>e</sup>		520 <sup>b</sup>	220meV	Ishihara T, <i>et al</i> , 1990
	C9	2D (2L)	562-564 <sup>a</sup>			181meV	Papavassiliou G. C, 1997
	C9	2D (4L)	630 <sup>a</sup>				Papavassiliou G. C, 1997
	C10	2D (2L)	556-564 <sup>a</sup>		575 <sup>a</sup>		Papavassiliou G. C, 1997
	C10	2D (3L)	600 <sup>a</sup>		612 <sup>a</sup>		Papavassiliou G. C, 1997
	C10	2D (4L)	632 <sup>a</sup>		652 <sup>a</sup>		Papavassiliou G. C, 1997
	PEA	2D (2L)	564 <sup>a</sup> , 576 <sup>e</sup>		574 <sup>a</sup> , 580 <sup>b</sup>	170meV	Hong X, <i>et al</i> , 1992
	C5	2D (2L)	557 <sup>a</sup>		569 <sup>a</sup>	230meV	Elleuch S, <i>et al</i> , 2010
	C <sub>4</sub> H <sub>3</sub> SCH <sub>2</sub> NH <sub>3</sub>	2D (2L)	562 <sup>a</sup>				Zhu X. H, <i>et al</i> , 2002
	C6	2D (2L)	580			260meV	Tanaka K, Kondo T, 2003a
	C6	2D (3L)	614			150meV	Tanaka K, Kondo T, 2003a
	C6	2D (4L)	646			100meV	Tanaka K, Kondo T, 2003a
<b>Pbl<sub>6</sub></b>	C1	0D	372 <sup>a</sup> , 364 <sup>c</sup>		372 <sup>a</sup>	545meV	Papavassiliou G. C, 1997
<b>Pbl<sub>4</sub></b>	4-F-PEA		528 <sup>a</sup>		530 <sup>a</sup>	540meV	Dammak T, <i>et al</i> , 2009

Cn = aliphatic, PEA = phenylethyl ammonium, a = RT, b = LNT, c = 4.2K, d = 2K, e = 10K

It should be noted that for the single layer 2D lead iodide hybrids, the binding energy has also been shown to be much larger than  $220\text{meV}$  (beyond  $320\text{meV}$  for  $(\text{C}_{10}\text{H}_{21}\text{NH}_3)_2\text{PbI}_4$ ). It should be noted that the binding energy of  $(\text{C}_{10}\text{H}_{21}\text{NH}_3)_2\text{PbI}_4$  is nearly eight times larger than that of its three dimensional analogue. Hence dimensional reduction is not the only contributor to the enhancement of the binding energy. As discussed in the theory section, the excitons binding energy may be further enhanced from the reduction in the screening for excitons in the layers. This occurs because the barrier (organic) has a much lower dielectric constant than that of the well (inorganic) (Dielectric Confinement effect) (Tanaka K, *et al*, 2005; Ishihara T, *et al*, 1990; Hong X, *et al*, 1992b). Hence the larger enhancement of the binding energy would be expected for the aliphatics as they experience a lower dielectric constant  $\sim 2.1$  from that observed for an aromatic  $\sim 3.32$  ( $\text{C}_6\text{H}_5\text{C}_2\text{H}_4\text{NH}_2$ ).

It has also been observed that an increase in well thickness decreases the excitons binding energy  $(\text{C}_6\text{H}_5\text{C}_2\text{H}_4\text{NH}_3)_2(\text{CH}_3\text{NH}_3)\text{Pb}_2\text{I}_7$   $E_b = 170\text{meV}$  from  $220\text{meV}$  of the single layered system (Hong X, *et al*, 1992). An investigation into the effect of increase/decrease in interlayer spacing has been investigated for  $\text{C}_n\text{H}_{2n+1}\text{NH}_3$  for  $n = 4, 6, 8, 9, 10, \text{ and } 12$  and it was concluded that this does not affect the binding energy much  $330 - 420\text{meV}$  (fluctuation attributed to the dielectric constant only) for  $n = 4 - 12$  (Ishihara T, *et al*, 1990).

To fully describe the binding energy dependence on the well and barrier (Elleuch S, *et al*, 2010), we need to describe the definitions of well thickness  $l_w$  and barrier lengths  $l_b$ , which describes the interlayer spacing. Furthermore the dielectric constants of the inorganic (well)  $\epsilon_w$  and the organic (barrier)  $\epsilon_b$  are defined in order to calculate the overall dielectric constant of the hybrid material  $\epsilon_\infty$  as originally described by Ishihara T, *et al*, (1990).

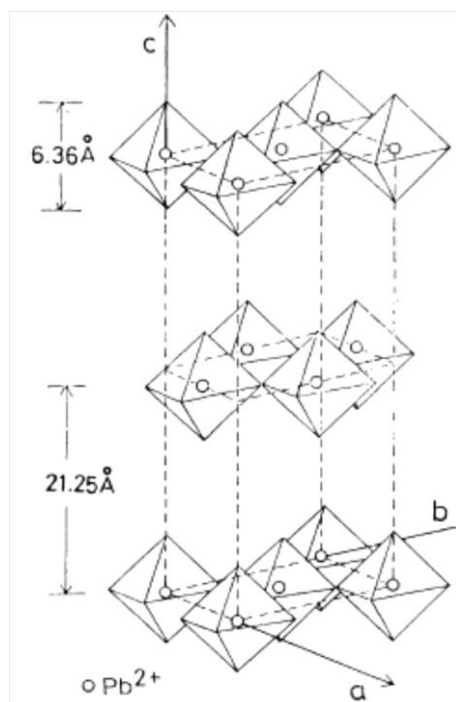


**Figure 2.29:** Height of Inorganic layer = 6.36 Å ; interlayer spacing  $c/2 = 21.25 \text{ Å}$  of  $(\text{C}_{10}\text{H}_{21}\text{NH}_3)_2\text{PbI}_4$  (Ishihara T, *et al*, 1990).

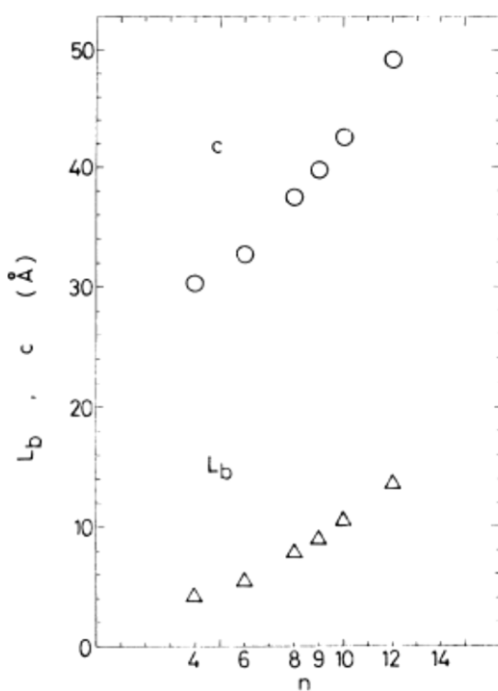


**Figure 2.30:** Lattice constant  $c$  (○) and barrier width ( $\Delta$ ) as a function of chain length of  $(\text{C}_n\text{H}_{2n+1}\text{NH}_3)_2\text{PbI}_4$  where the interlayer distance is  $c/2$  (Ishihara T, *et al*, 1990).

Assuming that the  $c$  axis is the longest unit cell axis and the inorganic layers lie perpendicular to this axis (in the  $ab$  plane), we will define the two geometrical parameters,  $l_b$  (the barrier length) and  $l_w$  (the well length) that the binding energy is dependent upon. The well length  $l_w$  is a function of the height of the inorganic layer or the octahedra, which is generally  $\sim 6.36 \text{ Å}$  from



apical iodine to apical iodine for a single layer  $(\text{RNH}_3)_2\text{PbI}_4$  2D hybrid perovskite. However the well length must also include the ionic diameter of the apical halogen ions, i.e.  $2R_I$ ; therefore  $l_w = \text{Inorganic height} + 2R_I$  and therefore the barrier length  $l_b$  may be defined as a difference of,  $l_b = \frac{c}{2} - l_w$  where  $c$  is the longest unit cell axis (figure 2.29 and 2.30).

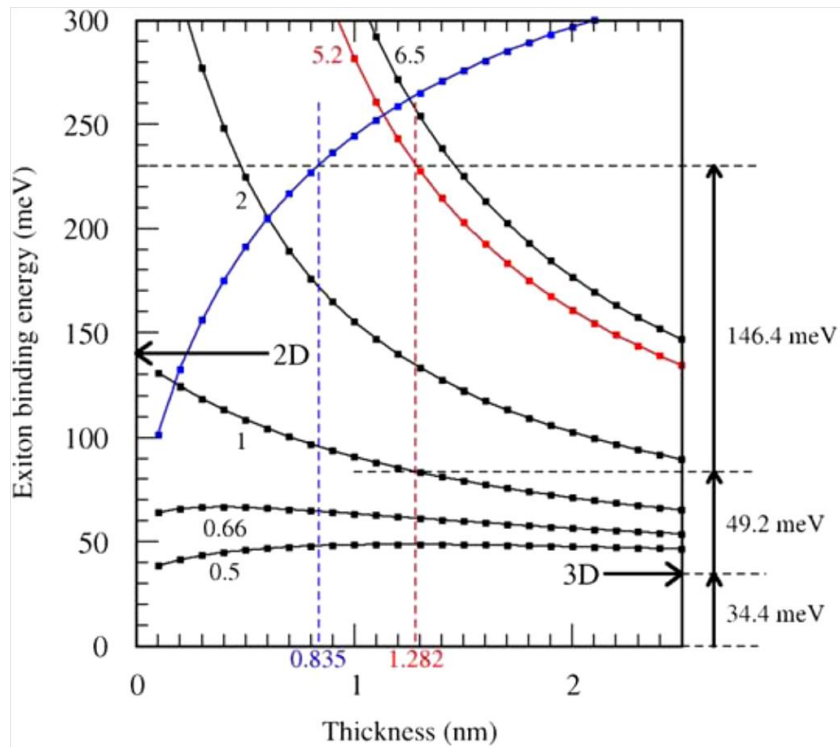


**Figure 2.31:** The calculated exciton binding energies for lead iodide. (Elleuch S, *et al*, 2010) Blue curve is the increase in well thickness as the barrier is kept constant; conversely the red and black curves are constant inorganic well thickness as a function of the barrier length i.e.  $\frac{\epsilon_w}{l_b}$  as  $l_w$  is kept constant.

The dielectric constant of the entire inorganic-organic hybrid  $\epsilon_\infty$  also needs to be defined as the binding energy is dependent on the dielectric constants of the well and barrier. Thus  $\epsilon_\infty = (\epsilon_w l_w + \epsilon_b l_b) / (l_w + l_b)$  where  $\epsilon_\infty$  is the overall dielectric constant of the hybrid,  $\epsilon_b$  is the dielectric constant of the barrier (organic ammonium cation), and  $\epsilon_w$  is the dielectric constant of the well (inorganic layer). The parameters  $l_w$  and  $l_b$  are as previously defined. Recalling from the theory section, for a 2D system the binding energy of an exciton is calculated from the energy eigenvalues of the following equation:

$$E_v^{(2)} = E_n^{(2)} = -\frac{E_R^*}{\left(n - \frac{1}{2}\right)^2}.$$

Where  $E_R^* = \frac{\mu e^4}{2\varepsilon_\infty^2}$  uses the overall dielectric constant of the hybrid material (please refer to the theory section for further details). Hence the relationship of the binding energy verses well thickness as defined by (Elleuch S, *et al*, 2010). In the calculations completed by (Elleuch S, *et al*, 2010 and references therein) they used the reduced excitonic mass of  $\mu = 0.105m_0$  which is obtained from band structure calculations, and the dielectric constant of Pbl was obtained from (Koutselas I. B, *et al*, 1996) of  $\varepsilon_w = 6.5$ . As mentioned earlier, if there is no dielectric mismatch i.e.  $\frac{\varepsilon_w}{\varepsilon_b} = 1$ , then the excitons binding energy is only related to the quantum confinement parameter i.e.  $E_b = 45meV$  for 3D Pbl and should be at least  $135meV$  for the 2D system. However since there is always a dielectric mismatch, there will be an enhancement of the excitonic binding energy.

Figure 2.31 above uses the ratio of  $\frac{\varepsilon_w}{\varepsilon_b} = 5.2$  and  $\frac{\varepsilon_w}{\varepsilon_b} = 6.5$  respectively as it varies the inorganic well thickness (red and black curves) and the barrier layer thickness for  $\frac{\varepsilon_w}{l_b} = 0.5, 0.66, 1, 2, 5.2, 6.5$  (blue curve). The two vertical dashed lines on the graph represent one (red), and two (blue), inorganic layers respectively. In simplified terms, the graph shows that as the dielectric constant of the barrier is increased, the binding energy is increased (with a constant well thickness). If the barrier is held constant and the well thickness is increases, the binding energy decreases accordingly (increasing 3D character of the material).

In a recent paper by (Dammak T *et al*, 2009), the authors measured the largest binding energy of an exciton found in a single layered lead iodide hybrid perovskite thus far (table 2.8). The binding energy was found to be  $540meV$ , which implies this material would be a great candidate for an electroluminescent device. The large increase in excitons binding energy was simply attributed to the large dielectric mismatch between the barrier and the well. The amine cation was however not an aliphatic, but 4-FPEA (4-F-Phenylethylammonium), whose dielectric constant lies within the range  $1.04 < \varepsilon_b < 1.24$ , which is significantly reduced from the parent PEA cation whose dielectric constant is  $\varepsilon_b = 3.32$ . Clearly the large decrease in the dielectric constant has been attributed to the presence of the fluorine atom on the PEA ring (Dammak T, *et al*, 2009). The binding energy was calculated using the modified Arrhenius model using the integrated intensities obtained from the variable temperature photoluminescence measurements.

The ability to enhance dielectric confinement with the use of a more rigid organic amine, other than an aliphatic is of great importance technologically, because the aliphatic chains are prone to phase changes which result in reordering in the crystal packing and sometimes may result in a thermochromic phase transition. Some phase changes observed result in the crystal itself to completely shatter (Ishihara T, et al, 1990; Billing D. G, Lemmerer A, 2007b, 2008; Lemmerer A, 2011). However if the phase transition does not physically damage the crystal, one may observe crystallographically the change in the distortions of the inorganic sheets. This property may be exploited as a temperature tuneable optical device. Recently this was explored by (Pradeesh K, *et al*, 2009b) for  $(C_{12}H_{25}NH_3)_2PbI_4$  investigating the high temperature phase change of  $(C_{12}H_{25}NH_3)_2PbI_4$  at 60°C. The optical absorption and photoluminescence before and after the phase change may be seen in figure 2.32.

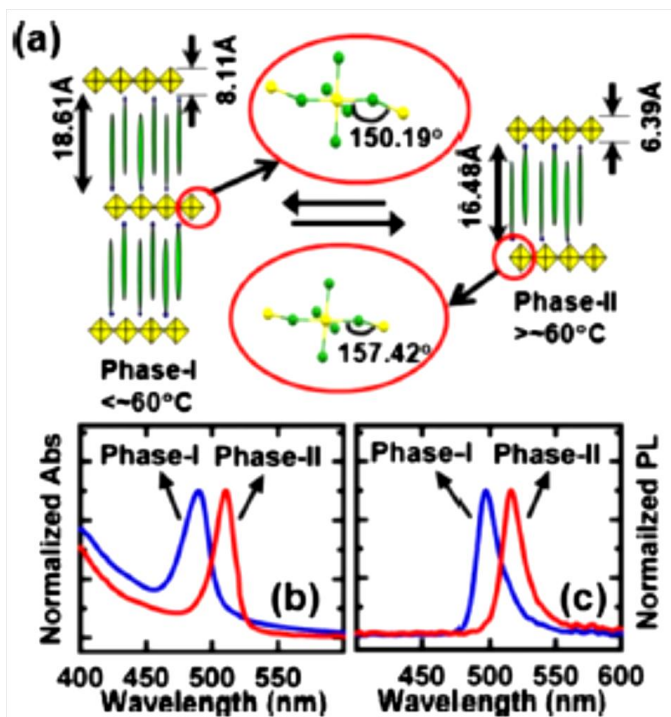


**Figure 2.32:** The optical absorption and photoluminescence emission of  $(C_{12}H_{25}NH_3)_2PbI_4$  a) displays the inorganic distortion as a result of the phase change, the reason for the optical shift. B) optical absorption, c) photoluminescence emission (Pradeesh K, *et al*, 2009b).

### 2.5.1 Optical properties of Lead Bromide and Chloride 2D hybrids

We have discussed mainly the lead iodide family up to now, however the other halogenated 2D lead hybrid perovskites have also been investigated. The substitution of the halogen from iodine to bromine and or then chlorine in the 2D perovskite has the ability to significantly blue shift the optical absorption and or photoluminescence observed. Hence a wide spectrum of colours may be achieved, by a simple halogen substitution of the hybrid i.e.  $\sim 510\text{nm} - 350\text{nm}$  for the single layer 2D hybrids. Work completed by (Kitazawa N, 1997) displays a fractional substitution of the halogen in the single layer hybrids, by only varying Br and I and Br and Cl respectively. Sharp photoluminescence emissions were also reported for these compounds despite the non-uniform halogen occupation as seen in figure 2.33 (Kitazawa N, 1997; Kitazawa N, *et al*, 2004). A larger list of fractional hybrids has been completed in a review by (Papavassiliou G. C, *et al*, 1999) as well as more recent studies completed by (Dammak T, *et al*, 2009b).

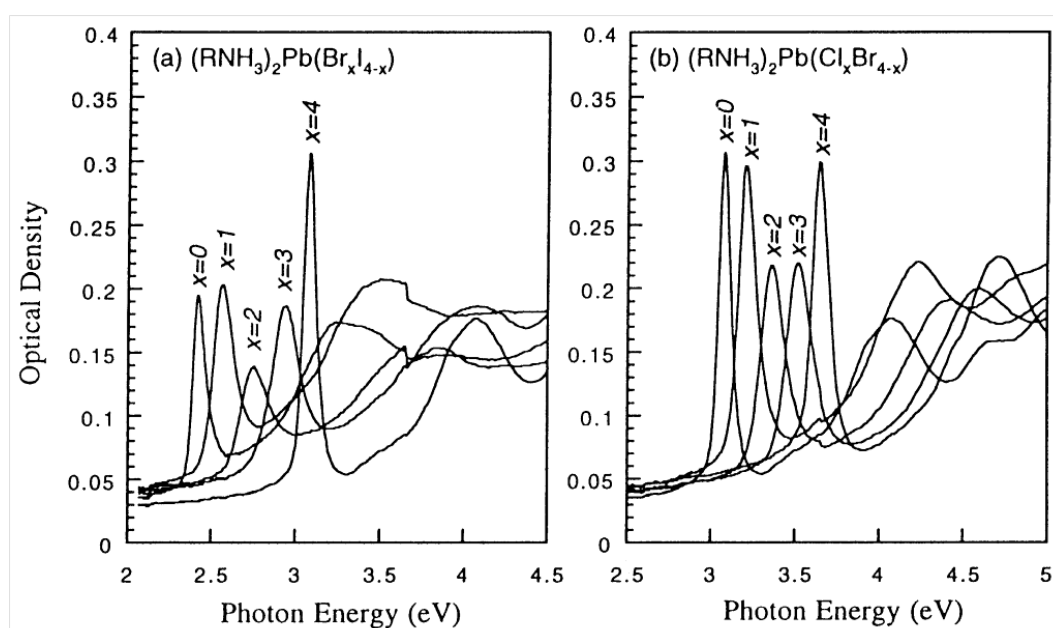


**Figure 2.33:** Optical density measurements of  $(\text{RNH}_3)_2\text{Pb}(\text{Br}_x\text{I}_{4-x})$  and  $(\text{RNH}_3)_2\text{Pb}(\text{Cl}_x\text{Br}_{4-x})$  with  $x = 0, 1, 2, 3, 4$ , displaying the optical shift with the change in halogen (Kitazawa N, 1997).

The Lead Bromide compounds are understudied by comparison with the iodide analogues. This is the case as the lead bromide hybrids were thought to display fundamentally similar optical properties, only blue shifted relative to the iodide analogues. However after further investigation, it was discovered that they display a more intricate emission spectra as seen for the simple aliphatic type compounds (Kato Y, *et al*, 2003; Ema K, *et al*, 2006; Kitazawa N, *et al*, 2010). In addition, it should be noted that, there are very few crystal structures reported for the

<100> 2D lead bromide hybrids; however the compounds whose properties have been investigated spectroscopically have confirmed the 2D structural motif through two methods. Firstly the UV-Vis absorption spectra which displays the compounds absorption peak in the expected absorption region, and secondly the unit cell and 2D interlayer spacing which are estimated and or confirmed through thin film P-XRD (Kitazawa N, *et al*, 2010; Kitazawa N, *et al*, 2010b). A summary of the reported 2D lead bromide hybrids and the optical properties and excitonic binding energies were reported may be seen in table 2.9.

Due to inconsistencies in the literature regarding the quoted values of the binding energies of the excitons, it should be brought to the reader's attention of the three methodologies employed for the measurement of this parameter i.e. from low temperature (<10K) optical absorption measurements, electro-absorption experiments, and activation energy measurements obtained through variable temperature integrated luminescence intensity measurements (Kitazawa N, *et al*, 2010). The activation energy experiments have been shown to give the most reproducible and reliable results from the various publications investigating these excitonic properties, however experiments performed by (Kitazawa N, *et al*, 2010b) displayed the optical absorption method gave more realistic results when compared with the activation energy approach also employed for that specific set of compounds.

**Table 2.9:** The binding energies, optical absorption and Photoluminescence emissions at various temperatures, of some PbBr based hybrids.

Metal Halide	Amine	Dimensionality	Exciton OA (nm)	PL (nm)	Binding energy	Reference
PbBr <sub>3</sub>	C1	3D	532 <sup>a</sup>	534 <sup>a</sup>	76meV	Tanaka K, <i>et al</i> , 2003
PbBr	C9	2D	393 <sup>a</sup>			Papavassiliou G. C, 1997
	C10	2D	396 <sup>a</sup> , 397 <sup>d</sup>			Papavassiliou G. C, 1997
	PEA	2D	402 <sup>a</sup> ,	406 <sup>a</sup>	290meV	Papavassiliou G. C, 1997; Kitazawa N, <i>et al</i> , 2005
PbBr <sub>6</sub> ·2H <sub>2</sub> O	C1	0D	312 <sup>a</sup>			Papavassiliou G. C, 1997
PbBr	C4	2D		3.03eV	330meV/430m ev	Kitazawa N, <i>et al</i> , 2010; Tanaka K, <i>et al</i> , 2005c
	C5	2D		3.06eV	290meV	Kitazawa N, <i>et al</i> , 2010
	C7	2D		3.09eV	280meV	Kitazawa N, <i>et al</i> , 2010
	C12	2D		3.19eV	310meV	Kitazawa N, <i>et al</i> , 2010
	C8	2D		3.20eV	240meV	Kitazawa N, <i>et al</i> , 2009
	C9	2D (2L)	430 <sup>a</sup>			Papavassiliou G. C, 1997
		2D (3L)	450 <sup>a</sup>			Papavassiliou G. C, 1997
		2D (4L)	472 <sup>a</sup>			Papavassiliou G. C, 1997
		2D (5L)	490 <sup>a</sup>			Papavassiliou G. C, 1997
	C10	2D (2L)	434 <sup>a</sup>	442 <sup>a</sup>		Papavassiliou G. C, 1997
		2D (3L)	450 <sup>a</sup>	456 <sup>a</sup>		Papavassiliou G. C, 1997
		2D (4L)	472 <sup>a</sup>	482 <sup>a</sup>		Papavassiliou G. C, 1997
	C6	2D	395 <sup>a</sup>			Tabuchi Y, <i>et al</i> , 2000
	C6	2D (2L)	431 <sup>a</sup>			Tabuchi Y, <i>et al</i> , 2000
	C6	2D (3L)	450 <sup>a</sup>			Tabuchi Y, <i>et al</i> , 2000
	C2	2D	402 <sup>a</sup>			Tabuchi Y, <i>et al</i> , 2000
	C3	2D	390 <sup>a</sup>			Tabuchi Y, <i>et al</i> , 2000
	C4	2D	390 <sup>a</sup> , 405 <sup>a</sup>	430 <sup>a</sup>	330meV	Tabuchi Y, <i>et al</i> , 2000; Mitzi D. B, <i>et al</i> , 2001c; Kitazawa N, <i>et al</i> , 2010
	C10	2D	390 <sup>a</sup>			Tabuchi Y, <i>et al</i> , 2000
*	H <sub>3</sub> NC6NH <sub>3</sub>	2D	380 <sup>a</sup>	402 <sup>a</sup>	180meV	Dammak T, <i>et al</i> , 2007; Papavassiliou G. C, <i>et al</i> , 1999
*	PhCH <sub>2</sub> NH <sub>3</sub>	2D	397 <sup>a</sup> , 3.08eV <sup>c</sup>	3.05eV <sup>c</sup>		Kitazawa N, <i>et al</i> , 2010b; Papavassiliou G. C, <i>et al</i> , 1999
	PhC <sub>2</sub> H <sub>4</sub> NH <sub>3</sub>	2D	3.06eV <sup>c</sup>	3.06eV <sup>c</sup>		Kitazawa N, <i>et al</i> , 2010b
	PhC <sub>3</sub> H <sub>6</sub> NH <sub>3</sub>	2D	3.11eV <sup>c</sup>	3.10eV <sup>c</sup>		Kitazawa N, <i>et al</i> , 2010b
	PhC <sub>4</sub> H <sub>8</sub> NH <sub>3</sub>	2D	3.13eV <sup>c</sup>	3.08eV <sup>c</sup>	230meV	Kitazawa N, <i>et al</i> , 2010b
*	CH <sub>3</sub> PhCH <sub>3</sub> NH <sub>3</sub>	2D	Multiple lines <sup>c</sup>	3.176eV <sup>c</sup>		Makino H, <i>et al</i> , 2005; Papavassiliou G. C, <i>et al</i> , 2000
	NMA	2D	380 <sup>a</sup>			Papavassiliou G. C, <i>et al</i> , 1999
*	2-AMP	2D	431 <sup>a</sup>	467 <sup>a</sup>		Li Y. Y, <i>et al</i> , 2007

Cn = aliphatic, PEA = phenylethyl ammonium, a = RT, b = LNT, c = 4.2K, d = 2K, \*single crystal structure reported, NMA = Naphthylmethylammonium, AMP = Aminomethylpyridine,

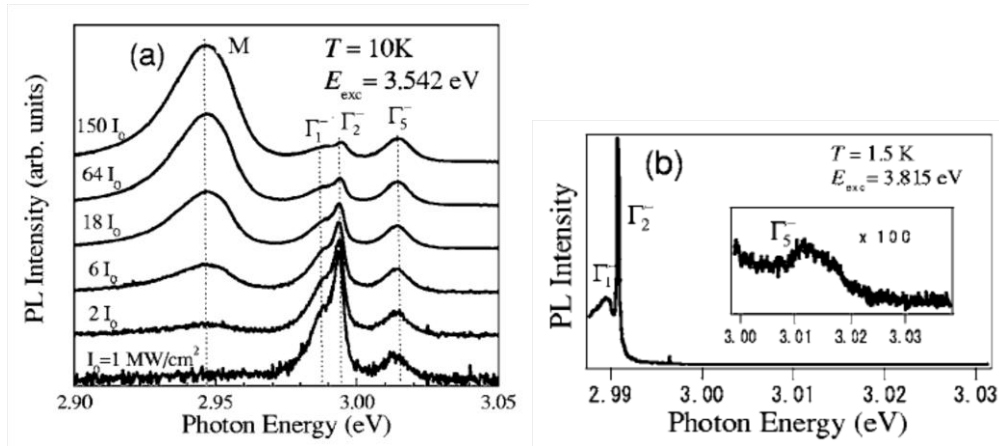


**Figure 2.34:** Photoluminescence of (C4)<sub>2</sub>PbBr<sub>4</sub> displaying the biexciton emission generated from a pulsed excitation source at 10 K (Kato Y, *et al*, 2003) a) and the continuous wave excitation luminescence displaying the excitonic fine structure at 1.5 K (no biexciton emission is observed with CW excitation) (Ema K, *et al*, 2006).

It has been shown that the excitonic binding energy tends to increase as the halogen is changed from I to Br. This may be specifically seen in the 3D (CH<sub>3</sub>NH<sub>3</sub>)PbX<sub>3</sub> case where  $E_b = 45\text{ meV}$  for the I structure, and  $E_b = 76\text{ meV}$  for the Br structure. In addition, the most studied 2D case (PEA)<sub>2</sub>PbX<sub>4</sub> illustrates this phenomenon as well, where  $E_b = 220\text{ meV}$  and  $E_b = 290\text{ meV}$  for the I and Br cases respectively (refer to table 2.8 and 2.9 for references).

Recent investigations involving the lead bromide systems have revealed further detail into the excitonic fine structure in the luminescence emissions. Figure 2.34 displays the luminescence emissions of (C4)<sub>2</sub>PbBr<sub>4</sub> for a pulsed excitation source at 10 K (figure 2.34a) in which a biexciton emission is observed with the largest binding energy (60 meV) (Kato Y, *et al*, 2003) recorded for a quantum well thus far. In addition to the biexcitonic peak in the pulsed excitation experiment, excitonic fine structure was also observed. The fine structure was also observed in the continuous wave excitation luminescence as seen in figure 2.34 b) (Ema K, *et al*, 2006). The excitonic assignments are labels derived from the FBZ critical points in the direct gap of the band structure. From previous sections we know that the 2D lead halide hybrids are direct gap semiconductors. In the case of (C4)<sub>2</sub>PbBr<sub>4</sub> the direct gap transition occurs at the FBZ critical point  $\Gamma$ .

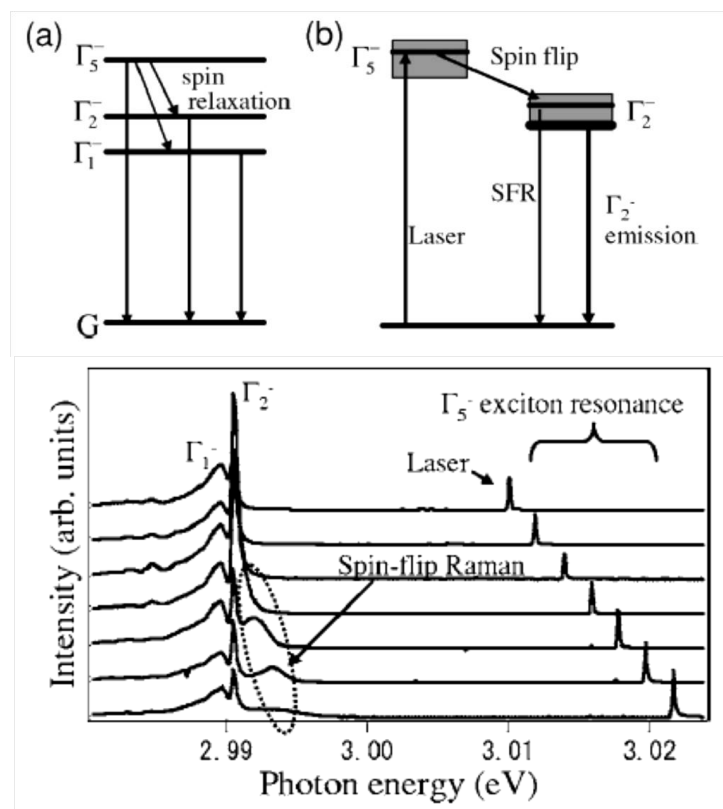


**Figure 2.35:** The 1s exciton energy level has a fine structure which is split into three fine structure energy levels. These are the purely triplet state  $\Gamma_1^-$ , the triplet dominant  $\Gamma_2^-$  and the singlet dominant state  $\Gamma_5^-$ . As may be seen in a)  $\Gamma_5^-$  decays into  $\Gamma_2^-$  and  $\Gamma_1^-$  through a spin relaxation, as well as a spin flip decay b) as may be seen in c) (Ema K, *et al*, 2006).

From the luminescence emissions it is observed that the 1s exciton energy level has a fine structure which is split into three fine structure energy levels, which are labelled accordingly. These states are the purely triplet state  $\Gamma_1^-$ , the triplet dominant  $\Gamma_2^-$  and the singlet dominant  $\Gamma_5^-$ . An aside, the  $\Gamma_5^-$  state has recently been shown to also display exciton polariton coupling, however this is of less importance to the assignment of the fine structure (Tamaki R, *et al*, 2008). The mechanism of the excitonic fine structure decay may be seen in figure 2.35 a) i.e.  $\Gamma_5^-$  decays into  $\Gamma_2^-$  and  $\Gamma_1^-$  through a spin relaxation, as well as a spin flip decay figure 2.35 b). The spin flip Raman experiments, as seen in fig 2.35 c) proved the spin flip decay mechanism and hence the proposed mechanism in figure 2.35 a) and b) (Ema K, *et al*, 2006). Further investigations into the longer chain length derivatives (C5, C7, C12) also displayed the excitonic fine structure, however, it only became evident below 40K for C4, C5 and C7, and below 80K for C12. It should be noted that C7 displays very little fine structure at low temperature in comparison with its cousins. The luminescence emissions at these temperatures display intersystem crossing between the singlet and triplet states upon cooling, and the varying of the



alkyl chain length appears to affect this process, however no real explanation as to why this occurs was proposed in this paper (Kitazawa N, *et al*, 2010).

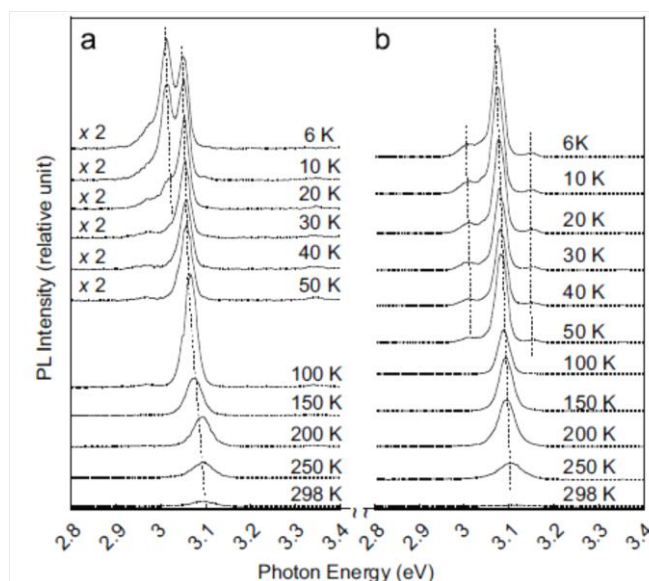


**Figure 2.36:** The temperature dependant PL spectra for a)  $\text{PhCH}_2\text{NH}_3$  displaying fine structure splitting at low temperature. b)  $\text{PhC}_4\text{H}_8\text{NH}_3$  displaying very little fine structure splitting at low temperature (Kitazawa N, *et al*, 2010b).

Further investigation of the lead bromide 2D hybrids with the templates ( $\text{PhC}_n\text{H}_{2n}\text{NH}_3$ ) where  $n = 1, 2, 3$ , and 4 have been investigated to further ascertain the effect of the organic template on the fine structure of the 2D excitons at low temperature (Kitazawa N, *et al*, 2010b). It was found that the  $n = 4$  analogue displayed very little fine structure splitting at low temperature whereas the  $n = 1, 2$  and 3 compounds displayed almost identical splitting (figure 2.36). The authors did conclude that the triplet states are formed at the interface of the organic and inorganic components. Moreover the triplet states have been shown to be dependant of the carbon chain length (Kitazawa N, *et al*, 2010; 2010b). This in itself may be due to the fact that some organic templates increase the crystallinity of the compound (i.e. grow better crystals), which has been shown to have a direct impact on the increase of PL intensity the compound displays. It should also be noted that the singlet and triplet states display different decay times, with the triplet state invariably the slower of the two thus supporting the mechanism found in figure 2.35.

The lead chloride compounds are largely understudied when compared with their bromide and iodide analogues. Table 2.10 displays the electronic properties of the various lead chloride layered hybrid perovskites reported.

**Table 2.10:** 2D lead chloride hybrids optical properties.

Metal Halide	Amine	Dimensionality	exciton OA	PL	Binding energy	Reference
<b>PbCl *</b>	H <sub>3</sub> NC <sub>6</sub> NH <sub>3</sub>	2D	332	342		Papavassiliou G. C, 1997
	N <sub>6</sub> AHMC	2D	329			Wu G, <i>et al</i> , 2009
	NMA	2D	327		240-320	Papavassiliou G. C, <i>et al</i> , 1999
<b>PbCl<sub>3</sub></b>	MeNH <sub>3</sub>	3D	397a	408a		Papavassiliou G. C, 1997
<b>PbCl<sub>4</sub></b>	C6	2D	332	342	230	Papavassiliou G. C, <i>et al</i> , 1999
	C9	2D	330a			Papavassiliou G. C, 1997
	C10	2D	331a; 330d	336a		Papavassiliou G. C, 1997
	PEA	2D	330a; 340d	347b		Papavassiliou G. C, 1997

*Cn* = aliphatic, PEA = phenylethyl ammonium, a = RT, b = LNT, c = 4.2K, d = 2K, \*single crystal structure reported, NMA = Naphthylmethylammonium, N6AHMC = N-6aminohexymethylcabazole.

Table 2.11 displays, to my knowledge, the remaining list of lead hybrids, in which only the structure has been investigated (1D compounds will be dealt with in later sections), with the exception of (XC<sub>2</sub>H<sub>4</sub>NH<sub>3</sub>)PbI<sub>4</sub> where X = I, Br, Cl, or OH, series of compounds which investigated the halogen effect on the overall band gap of the compound. These compounds will be further discussed in chapter 4 as they were a subject of great interest.

**Table 2.11:** Remaining lead halide crystal structures.

Lead Halide	Amine	X/M	Dimensionality	Reference
<b>PbI</b>	C <sub>6</sub> H <sub>5</sub> C*(H)(CH <sub>3</sub> )(NH <sub>3</sub> ) (R, S, and R&S')	4	2D (p)	Billing D. G, Lemmerer A, CrystEngComm, (2006e) 8, 686; 'Billing D. G, Acta Crystallogr., Sect A: Found Crystallogr., (2002) E58, m669
<b>PbI</b>	C <sub>6</sub> H <sub>5</sub> C*(H)(CH <sub>3</sub> )(NH <sub>3</sub> ) (R, S)	3	1D	Billing D. G, Lemmerer A, CrystEngComm, (2006e) 8, 686
<b>PbBr</b>	C <sub>6</sub> H <sub>5</sub> C*(H)(CH <sub>3</sub> )(NH <sub>3</sub> ) (R, S')	3	1D	Billing D. G, Lemmerer A, CrystEngComm, (2006e) 8, 686; 'Billing D. G, Lemmerer A, Acta Cryst., (2003) E59, m381
<b>PbBr</b>	C <sub>6</sub> H <sub>5</sub> C*(H)(CH <sub>3</sub> )(NH <sub>3</sub> ) (R&S)	5	1D	Billing D. G, Lemmerer A, CrystEngComm, (2006e) 8, 686
<b>PbCl</b>	C <sub>6</sub> H <sub>5</sub> C*(H)(CH <sub>3</sub> )(NH <sub>3</sub> ) (R)	3	1D	Billing D. G, Lemmerer A, CrystEngComm, (2006e) 8, 686
<b>PbCl</b>	C <sub>6</sub> H <sub>5</sub> C*(H)(CH <sub>3</sub> )(NH <sub>3</sub> ) (R&S)	5	1D	Billing D. G, Lemmerer A, CrystEngComm, (2006e) 8, 686
<b>PbI</b>	C <sub>6</sub> H <sub>11</sub> C*(H)(CH <sub>3</sub> )(NH <sub>3</sub> ) (R, S)	4.67	1D	Lemmerer A, PhD Thesis, (2007)
<b>PbBr</b>	C <sub>6</sub> H <sub>11</sub> C*(H)(CH <sub>3</sub> )(NH <sub>3</sub> ) (R, S)	3	1D	Lemmerer A, PhD Thesis, (2007)
<b>PbBr</b>	C <sub>6</sub> H <sub>11</sub> C*(H)(CH <sub>3</sub> )(NH <sub>3</sub> ) (R&S)	4	2D (p)	Lemmerer A, PhD Thesis, (2007)
<b>PbCl</b>	C <sub>6</sub> H <sub>11</sub> C*(H)(CH <sub>3</sub> )(NH <sub>3</sub> ) (R, S, R&S)	4	2D (p)	Lemmerer A, PhD Thesis, (2007)
<b>PbI</b>	C <sub>3</sub> H <sub>5</sub> NH <sub>3</sub>	4	2D (p)	Billing D. G and Lemmerer A, 2006f
<b>PbI</b>	C <sub>4</sub> H <sub>7</sub> NH <sub>3</sub>	4	2D (p)	Billing D. G and Lemmerer A, 2006f
<b>PbI</b>	C <sub>5</sub> H <sub>9</sub> NH <sub>3</sub>	4	2D (p)	Billing D. G and Lemmerer A, 2006f
<b>PbI</b>	C <sub>6</sub> H <sub>11</sub> NH <sub>3</sub>	4	2D (p)	Billing D. G and Lemmerer A, 2006f
<b>PbI</b>	C <sub>7</sub> H <sub>13</sub> NH <sub>3</sub>	5	1D	Billing D. G and Lemmerer A, 2006f
<b>PbI</b>	C <sub>8</sub> H <sub>15</sub> NH <sub>3</sub>	3	1D	Billing D. G and Lemmerer A, 2006f

<b>PbBr</b>	$C_3H_5NH_3$	4	2D (p)	Billing D. G and Lemmerer A, 2009
<b>PbBr</b>	$C_4H_7NH_3$	4	2D (p)	Billing D. G and Lemmerer A, 2009
<b>PbBr</b>	$C_5H_9NH_3$	4	2D (p)	Billing D. G and Lemmerer A, 2009
<b>PbBr</b>	$C_6H_{11}NH_3$	4	2D (p)	Billing D. G and Lemmerer A, 2009
<b>PbBr</b>	$C_7H_{13}NH_3$	5	1D	Billing D. G and Lemmerer A, 2009
<b>PbBr</b>	$C_8H_{15}NH_3$	4.5	1D	Billing D. G and Lemmerer A, 2009
<b>PbCl</b>	$C_3H_5NH_3$	4	2D (p)	Billing D. G and Lemmerer A, 2009
<b>PbCl</b>	$C_4H_7NH_3$	4	2D (p)	Billing D. G and Lemmerer A, 2009
<b>PbCl</b>	$C_5H_9NH_3$	4	2D (p)	Billing D. G and Lemmerer A, 2009
<b>PbCl</b>	$C_6H_{11}NH_3$	4	1D	Billing D. G and Lemmerer A, 2009
<b>PbCl</b>	$C_7H_{13}NH_3$	4.428	1D	Billing D. G and Lemmerer A, 2009
<b>PbCl</b>	$C_8H_{15}NH_3$	3.636	1D	Billing D. G and Lemmerer A, 2009
<b>Pbl</b>	$IC_nH_{2n}NH_3$ (2', 3, 4, 5, 6)	4	2D (p)	Lemmerer A and Billing D. G, 2010; 'Sourisseau S, <i>et al</i> , 2007a
<b>Pbl(Br')</b>	$HOC_nH_{2n}NH_3$ (2', 3)	4	2D (p)	Lemmerer A and Billing D. G, 2010; Mercier N, <i>et al</i> , 2004; "Sourisseau S, <i>et al</i> , 2007a
<b>Pbl</b>	$BrC_2H_4NH_3$	4	2D (p)	Lemmerer A and Billing D. G, 2010; 'Sourisseau S, <i>et al</i> , 2007a; "Sourisseau S, <i>et al</i> , 2007b
<b>Pbl</b>	$H_3NC_nH_{2n}NH_3$ (n = 4, 6, 8, 10, 12)	4	2D (p)	Lemmerer A, PhD Thesis, (2007)
<b>Pbl</b>	$H_3NC_5H_{10}NH_3$	3.33	1D	Billing D. G and Lemmerer A, 2004
<b>Pbl</b>	$H_3NC_7H_{14}NH_3$	4.67	1D	Lemmerer A, PhD Thesis, 2007
<b>PbBr</b>	$H_3NC_4H_8NH_3$	4	2D (p)	Lemmerer A, PhD Thesis, 2007
<b>PbBr</b>	$H_3NC_2H_4NH_3$	6	1D	Lemmerer A, PhD Thesis, 2007
<b>Pbl</b>	$H_3NC_{10}H_6NH_3$	4	2D (p)	Lemmerer A, PhD Thesis, 2007
<b>Pbl</b>	$H_3NPhCH_2PhNH_3$	3	1D	Lemmerer A, PhD Thesis, 2007
<b>Pbl</b>	$C_nH_{2n+1}NH_3$ n = 4, 5, 6	4	2D (p)	Billing D. G and Lemmerer A, 2007b
<b>Pbl</b>	$C_nH_{2n+1}NH_3$ n = 7, 8, 9, 10	4	2D (p)	Lemmerer A, PhD Thesis, 2007
<b>Pbl</b>	$C_nH_{2n+1}NH_3$ n = 12, 14, 16, 18	4	2D (p)	Billing D. G and Lemmerer A, 2008
<b>Pbl</b>	$C_{10}H_7NH_3$	3	1D	Billing D. G and Lemmerer A, 2006g
<b>Pbl</b>	$PhC_3H_6NH_3$	3.33	2D	Billing D. G and Lemmerer A, 2006a
<b>Pbl</b>	$H_3NCH(CH_3)CH_2NH_3$	6	0D	Billing D. G and Lemmerer A, 2006d
<b>Pbl</b>	$C_3H_7NH_3$	3.6	2D	Billing D. G and Lemmerer A, 2006b
<b>Pbl</b>	$(CH_3)_3CNH_3$	3	1D	Billing D. G and Lemmerer A, 2006h
<b>Pbl</b>	$C_6H_7C_2H_4NH_3$	4	2D (p)	Billing D. G and Lemmerer A, 2006c
<b>Pbl</b>	$H_3NPhNH_3$	4	1D	Billing D. G and Lemmerer A, 2006i
<b>Pbl</b>	$3,5(CH_3)_2PhNH_3$	4	1D	Billing D. G and Lemmerer A, 2006i
<b>Pbl</b>	$C_6H_8N_4$	4	2D(p)	Tang Z, <i>et al</i> , 2001

## 2.6 Phase changes of <100> 2D hybrids

Thermally induced structural phase transitions are an inherent physical property of many materials. As the structure is cooled or heated the compound may either increase or decrease its

level of structural order or disorder respectively. This effect is dependent on one of a few factors. Firstly, is the level of entropy of the system, for example, the decrease in entropy which occurs from a gas to liquid to solid phases of an element or compound. The entropy inherently increases with an increase in temperature which sees an increase in thermal vibrations and atomic reordering which may now readily occur. Secondly are the electronic enhancements or changes which may occur as a result of various structural distortions or change in symmetry, i.e. centric to non-centric or polar rearrangements, as a result of a structural phase transition. This particular aspect highlights the importance of investigating structural phase transitions in material science.

Within the layered hybrid perovskite family, the solid state phase transitions occur through two mechanisms. Firstly are the displacive phase transitions, i.e. associated with conformational changes of the organic ammonium group. And secondly are the order-disorder phase transitions along the longitudinal axis of the unit cell. These mechanisms are more pronounced in the more flexible alkyl ammonium chains. Since they are so flexible, the  $(C_nH_{2n+1}NH_3)_2MX_4$  hybrids tend to undergo multiple phase transitions within a certain temperature range. This behaviour ultimately results in a quasi-melting transition of the alkyl chain at higher temperatures. This, invariably final transition, only occurs after proceeding through a few solid state conformational intermediates. The quasi-melting transition refers to only the alkyl chain melting, with the overall compound still remaining in the solid state (Chanh N. B, *et al*, 1989). Through these solid state intermediates, the inorganic layers also result in the general increase of interlayer spacing as the rotational disordering increases (Barman, 2003).

The chain melting transition (quasi-melting) is the major transition observed, and is usually the final transition that occurs upon heating. Furthermore this transition also displays the highest enthalpy and entropy change for a transition (Billing D. G, Lemmerer A, 2007; 2008; Lemmerer A, Billing D. G, 2011). An additional observation has been made regarding the alkyl chain length and the phase transitions that they undergo in the hybrid perovskite. The order disorder type transitions are the only phase transitions that occur when the organic ammonium chain length has a value of  $n \leq 2$ , however both types of transitions occur when the chain lengths have values of  $n \geq 3$  i.e. displacive and order disorder.

The organic conformational rearrangements may also change the inorganic layers orientation between the eclipsed and staggered arrangements upon heating (i.e. the monoclinic and

orthorhombic phases) with an associated decrease in octahedral bond length and angle distortions. In addition an idealization of the inter-octahedral bond angle (M-X-M) toward  $180^\circ$  and an ironing out of the corrugations in the layers occur. The higher temperature phases therefore exist in higher crystal symmetry systems. This phenomenon is well known and it has been noted that the structural phase transitions change the crystal system from monoclinic to orthorhombic and finally to tetragonal with increasing temperature (Mitzi D. B, 1999; Billing D. G, Lemmerer A, 2007; 2008; Lemmerer A, 2007; Lemmerer A, Billing D. G, 2011).

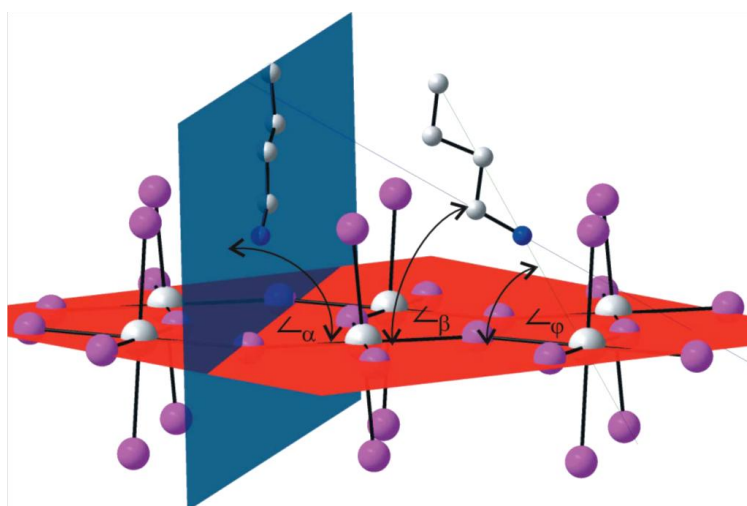


**Figure 2.37:** The geometric parameters assigned to the alkyl ammonium cation in order to describe the relevant angles associated from phase change behaviour. The angles are described in the text (Billing D. G, Lemmerer A, 2007).

In order to describe the mechanisms associated with the alkyl ammonium phase transitions, certain geometrical parameters were introduced. (Dadin B and Chapuis G, 1990) were the first to describe the necessary geometrical parameters to describe these relative angles associated with the changes of the alkyl ammonium conformations, specifically of  $C3CuCl_4$ , before and after a phase change. (Billing D. G, Lemmerer A, 2007; 2008; Lemmerer A, 2007; Lemmerer A, Billing D. G, 2011) further extended these definitions, to describe the phase changes observed in the longer alkyl ammonium chain derivatives for  $(Cn)PbI_4$  hybrid perovskites where  $n = 4-10, 12, 14, 16, 18$ . As seen in figure 2.37 above, the tilt  $\angle_\varphi$  angle of the organic chain is defined as the angle between the plane through the inorganic layers and the vector containing the first and last atom of each chain. In the case of  $C4PbI_4$  the first atom is N1 and the last is C4. Another two important geometrical parameters were used to describe the organics' motion due to the phase change. The  $\angle_\alpha$  angle, which may be defined as the torsion angle between the plane containing all of the atoms of the alkyl chain, and the plane formed by the lead atoms of the inorganic layers i.e. the vertical tilt of the organic chain. And finally the  $\angle_\beta$  angle, which is the angle between a vector

containing atoms N-C and a plane through lead atoms of the inorganic layers i.e. the tilt of the ammonium head.

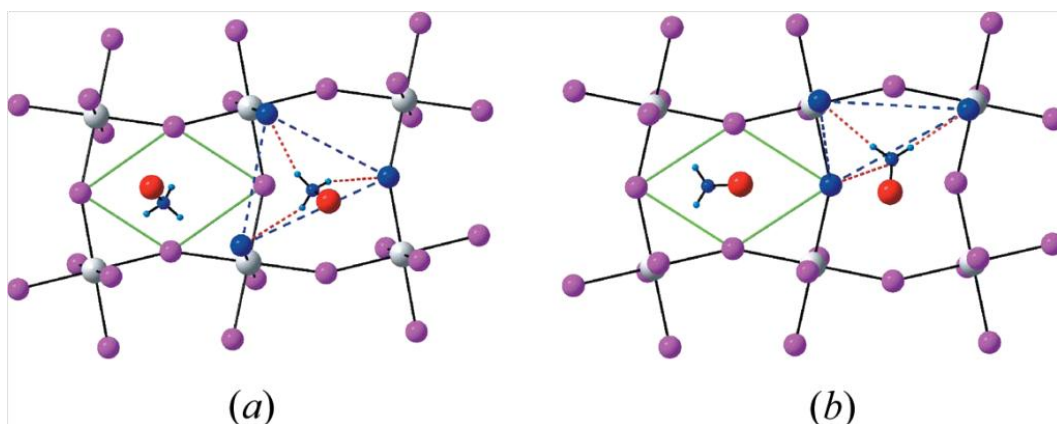


**Figure 2.38:** The two ammonium head group positions associated with the phase transformations. The green parallelogram depicts two arrangements (a) the ammonium head resides within the obtuse angle of the parallelogram and the hydrogen bonding configuration forms an equilateral triangle. The arrangement (b) situates the ammonium head in the acute angle of the green parallelogram, and the hydrogen bonding formation forms a right angled triangle. It is observed that the obtuse arrangement is associated with the low temperature phase, and the acute arrangement with the higher temperature phases. The high temperature disordered phases result in the ammonium group being in the centre of the parallelogram (Billing D. G, Lemmerer A, 2007; 2008; Lemmerer A, 2007; Lemmerer A, Billing D. G, 2011).

In addition to the tilt angles, the position of the ammonium group's hydrogen bonding configuration is also altered after a phase transition. Hence the box which contains the ammonium group is defined by the four equatorial (bridging) iodides and the four axial (terminal) iodides. In projection the ammonium group is contained within the parallelogram (figure 2.38 above) i.e. the void between the octahedra. The ammonium group may be found in the proximity of either the acute or obtuse angle of the parallelogram which further gives rise to the equilateral or right angles hydrogen bonding configuration respectively.

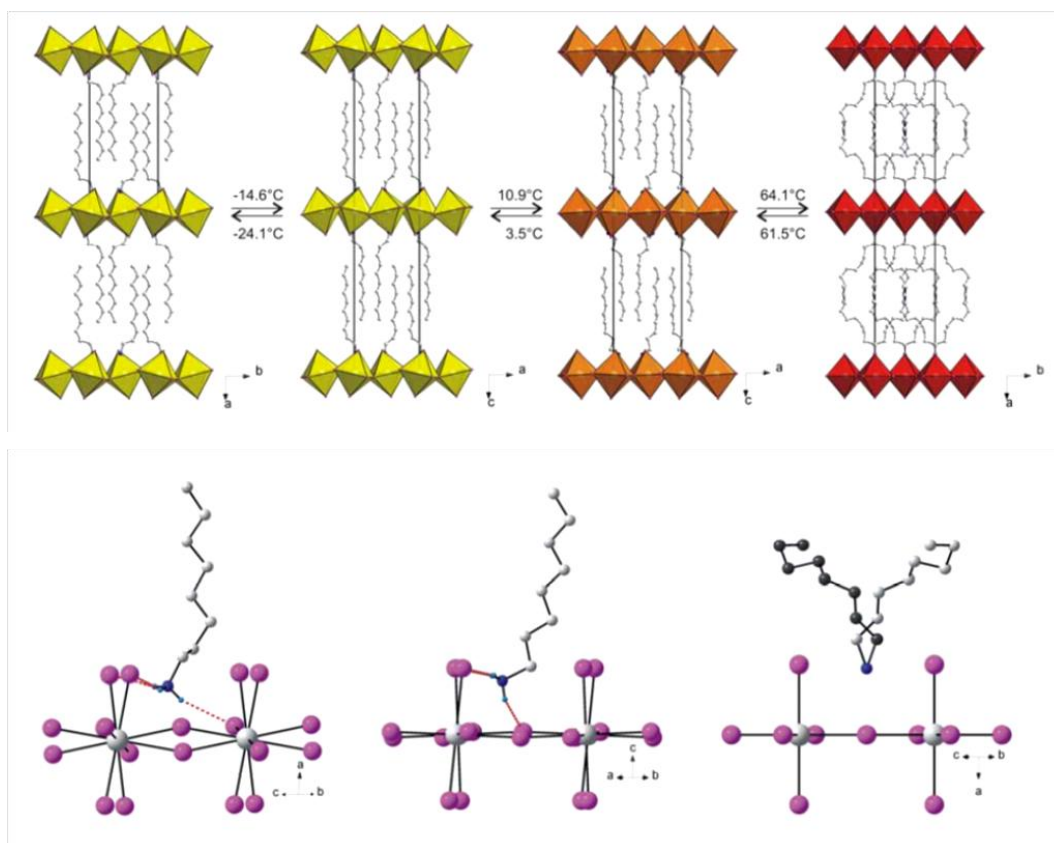


**Figure 2.39:** The top image displays the multiple phase transitions of  $C_{10}PbI_4$ , which proceeds from the low temperature monoclinic P phase to two middle orthorhombic P phases, and finally to the disordered orthorhombic C state. The bottom image of  $C_8PbI_4$  displays the same mechanism however with one less orthorhombic P phase. Both compounds highest temperature phases display the aliphatic as disordered over two position, i.e. illustrating the mechanism which suggest that the aliphatic undergoes a quasi-melting transition before the entire compound melts at a higher temperature (Lemmerer A, 2007; Lemmerer A, Billing D. G, 2011).

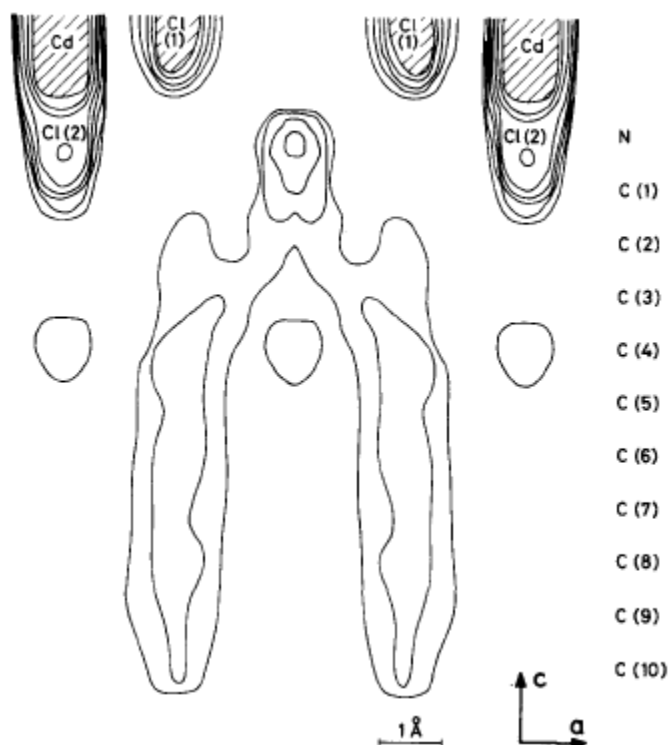


**Figure 2.40:** The high temperature phase of C10CdCl<sub>4</sub> displaying the evidence of the disordered arrangement of the decylammonium cation obtained from the electron density map (Kind R, *et al*, 1979).

In summary, the investigation of the C<sub>n</sub>PbI<sub>4</sub> hybrid perovskites reveals that the high temperature structures ammonium groups position adopts the acute angle in the parallelogram (figure 2.38b), whereas the lower temperature structures adopt the obtuse angled position, with the according hydrogen bonding configuration. The disordered high temperature phases result in the ammonium head group to now be situated in the centre of the parallelogram. Furthermore the tilt of the chains  $\angle_{\varphi}$  is an angle that decreases after each phase transition, with increasing temperature for the short chain derivatives,  $n = 4, 5$ , and  $6$ , (Billing D. G, and Lemmerer A, 2007) and increases with increasing temperature for the longer chain derivatives ( $n = 7-10, 12, 14, 16, 18$ ) (Lemmerer A, 2007; Billing D. G, and Lemmerer A, 2008). This is due to the shorter chains having fewer interactions with the chains from the opposite layer, however the longer chains are further interdigitated and hence only the first five atoms are subject to a greater freedom of motion. This may be clearly seen in the figure 2.39, where all the structures of the phases of C10PbI<sub>4</sub> are mapped with increasing temperature. Only the highest temperature phases' organic chain becomes disordered over two positions, and the chains themselves are now highly contorted and no longer interdigitated. The lead iodide octahedra also become more idealized in their geometry (Pb-I-Pb and corrugation angles) with each passing phase transition upon heating. The low temperature phase of C10PbI<sub>4</sub>, proceeds from Monoclinic P to Orthorhombic P



(two middle phases) and finally the high temperature disordered Orthorhombic C phase. The phase transition mechanism phenomenon is also observed in C8PbI<sub>4</sub> (figure 2.39) and C9PbI<sub>4</sub> (Lemmerer A, 2007; Lemmerer A, Billing D. G, 2011), however was first observed in C10CdCl<sub>4</sub> as seen in figure 2.40 (Kind R, *et al*, 1979).

Finally we should note the final two geometric parameters for the CnPbI<sub>4</sub> hybrids of  $\angle_{\alpha}$  and  $\angle_{\beta}$  which describes the angle of the plane containing the alkyl ammonium chain with the inorganic layer, and essentially the tilt of the ammonium group with the inorganic layer, respectively. The angle of the plane of the alkyl ammonium chain with the inorganic layer,  $\angle_{\alpha}$ , has been found to increase in size, with the angle limited to 90°, with increasing temperature, of each subsequent phase. The tilt of the ammonium group angle with the inorganic layer  $\angle_{\beta}$ , also increases in size with increasing temperature, of each subsequent phase. For example C5PbI<sub>4</sub> displays a  $\angle_{\beta}$  angle of 26.5° in phase III and moves to 65.7° in phase II. These two angles display this trend in all of the CnPbI<sub>4</sub> compounds investigated by Billing and Lemmerer.

Although the longer chain derivatives Cn = 12, 14, 16, 18, follow a similar phase change mechanism to that of the chains Cn where n = 4-10, an exception to the mechanism lies with the long chain aliphatics. This may be seen with the decreasing of the crystal symmetry with increasing temperature, i.e. they all proceed from the Orthorhombic low temperature form to the Monoclinic high temperature form. The inorganic octahedra still decrease in distortion with the increase in temperature; however, it is the layers that now proceed from the staggered arrangement in the low temperature phase to eclipsed arrangement in the higher temperature phase. This process also results in the unit cell to halve and the interlayer spacing to decrease, which is the opposite phase transformation behaviour observed in the shorter chain hybrid derivatives. Unfortunately the higher temperature quasi melting phases were not determined crystallographically due to the crystal shattering after this phase change. Hence the quasi melting/disordered state can only be suspected in the final phase (Billing D. G, and Lemmerer A, 2008).

Although up to now we have only discussed the CnPbI analogues, the phenomenon of the packing of the alkylammonium chains in an interdigitated fashion appears to be a unique feature observed only in the lead iodide alkyl ammonium hybrids. For instance in the hybrids C10MnCl<sub>4</sub> (Ciajolo M. R, *et al*, 1976) and C10CuCl<sub>4</sub> (Kozelj M, *et al*, 1981), the alkyl ammonium chains pack parallel all in one direction and experience a large tilting of +40° between the layers, instead of

interdigitating.  $\text{C10CdCl}_4$  (Kind R, *et al*, 1979) pack similarly however the chains on opposite sides of the layers have opposite tilts of  $+40^\circ$  and  $-40^\circ$  and do not interdigitate. The reason attributed to the lead iodides ability to template the alkyl chains into an interdigitated arrangement (which occurs from C4-C10, C12, C14, C16 and C18) is attributed to the separation of the metal centres from one another. The larger the separation the more likely interdigitation is to occur (Billing D. G, and Lemmerer A, 2008) (figure 2.41).

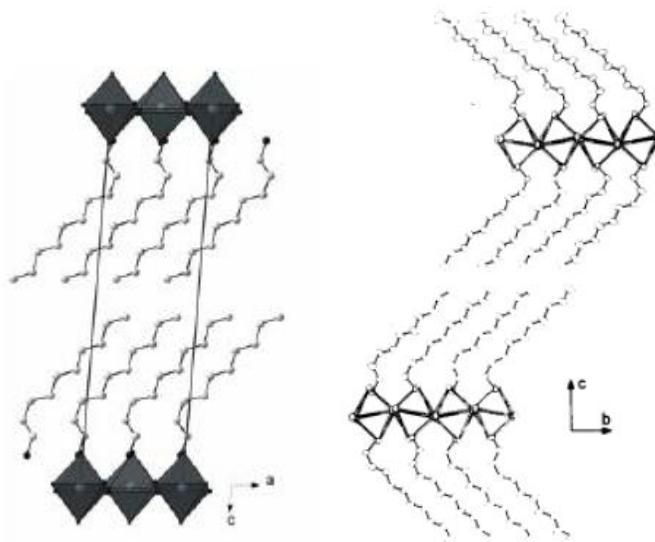


**Figure 2.41:** The above diagrams are the two types of tilting experienced from the decylammonium cation with  $\text{C10MnCl}_4$  and  $\text{C10CdCl}_4$  respectively (Ciajolo M. R, *et al*, 1976; Kind R, *et al*, 1979).

A summary of the structures of  $\text{CnCdCl}_4$ , the most well studied structures of the transition metal hybrids, is displayed in table 2.12 below as a comparison with  $\text{CnPbI}_4$  structures (table 2.13). Some of the phases only have unit cell data, obtained from powder diffraction studies, as certain intermediate and high temperature phases proved difficult to obtain any structural information due to diffuse scattering and incommensurate phases.

**Table 2.12:** Summary of the multiple phases of the alkyl ammonium cadmium chloride hybrid perovskites.

	I	II	III	IV	V	Reference
C8CdCl <sub>4</sub>	Orthorhombic T = 353 K a = 7.49(1) Å b = 7.58(1) Å c = 47.88(9) Å Z = 4 <i>Amaa</i>	Undetermined	Monoclinic T = 243 K a = 7.41(2) Å b = 7.53(2) Å c = 45.34(20) Å β = 96.55(28)° Z = 4 <i>P2<sub>1</sub>/n</i>	N/A	N/A	Chanh N. B, <i>et al</i> , 1983
C10CdCl <sub>4</sub>	Orthorhombic T = 318 K a = 7.460(2) Å b = 7.546(2) Å c = 54.64(2) Å Z = 4 <i>Amaa</i>	Orthorhombic T = 308 K a = 7.40(2) Å b = 7.54(2) Å c = 51.62(6) Å Z = 4 <i>Pmnn</i>	Monoclinic T = 294 K a = 7.354(1) Å b = 7.545(1) Å c = 51.620(3) Å β = 91.74(1)° Z = 4 <i>P2<sub>1</sub>/n</i>	N/A	N/A	Kind R, <i>et al</i> , 1979; Ricard L, <i>et al</i> , 1984
C12CdCl <sub>4</sub>	Tetragonal T = 360 K a = 5.310(1) Å b = 5.310(1) Å c = 64.31(4) Å Z = 2	Orthorhombic T = 334 K a = 7.470(7) Å b = 7.553(7) Å c = 63.50(4) Å Z = 4 <i>Amaa</i>	Monoclinic T = 293 K a = 7.463(1) Å b = 7.523(1) Å c = 59.152(8) Å β = 96.54(2)° Z = 4 <i>P2<sub>1</sub>/n</i>	N/A	N/A	Chanh N. B, <i>et al</i> , 1985
C14CdCl <sub>4</sub>	Orthorhombic T = N/A a = 7.46(1) Å b = 7.54(1) Å c = 35.77(6) Å Z = 2	Undetermined	Monoclinic T = N/A a = 7.32(3) Å b = 7.45(2) Å c = 33.60(7) Å β = 92.2(2)° Z = 2	Undetermined	Triclinic T = 298 K a = 7.329(2) Å b = 7.482(1) Å c = 33.188(5) Å α = 98.19(1), β = 92.2(2), γ = 90.04(2) Z = 2 <i>P1</i>	Schenk K. J, and Chapuis G, 1988
C16CdCl <sub>4</sub>	Tetragonal T = 360 K a = 5.298(2) Å b = 5.298(2) Å c = 80.03(7) Å Z = 2	Orthorhombic T = 354 K a = 7.383(18) Å b = 7.641(15) Å c = 76.45(11) Å Z = 4	Orthorhombic T = 348 K a = 7.437(10) Å b = 7.590(10) Å c = 75.24(8) Å Z = 4	Monoclinic T = 293 K a = 7.384(5) Å b = 7.546(11) Å c = 73.58(3) Å β = 96.27(6)° Z = 4 <i>P2<sub>1</sub>/n</i>	N/A	Chanh N. B, <i>et al</i> , 1989

**Table 2.13:** Summary of the multiple phase changes of all the alkyl ammonium Lead Iodide hybrids.

	I	II	III	IV	Reference
C4Pbl <sub>4</sub>	Orthorhombic T = 293 K a = 8.8764 (1) Å b = 8.6925 (1) Å c = 27.6014 (5) Å <i>Pbca</i>	Orthorhombic T = 223 K a = 8.428 (8) Å b = 8.6295 (1) Å c = 21.6014(5) Å <i>Pbca</i>	N/A	N/A	Billing D. G, and Lemmerer A, 2007; Mitzi D. B, 1996
C5Pbl <sub>4</sub>	Undetermined	Orthorhombic T = 333 K a = 9.0078 (10) Å b = 8.7310 (10) Å c = 29.956 (4) Å <i>Pbca</i>	Monoclinic T = 293 K a = 8.6716 (7) Å b = 8.9297 (6) Å c = 14.8805 (13) Å $\beta$ = 100.212 (2) <i>P2<sub>1</sub>/a</i>	N/A	Billing D. G, and Lemmerer A, 2007
C6Pbl <sub>4</sub>	Tetragonal T = 378 K a = 8.7632 (3) Å b = a c = 34.0586 (19) Å	Orthorhombic T = 358 K a = 8.6606 (8) Å b = 8.8215 (8) Å c = 35.2423 (36) Å	Orthorhombic T = 293 K a = 8.9413 (2) Å b = 8.6874 (2) Å c = 32.7207 (10) Å <i>Pbca</i>	Monoclinic T = 173 K a = 8.643 (4) Å b = 8.845 (4) Å c = 16.052 (7) Å $\beta$ = 91.985 (8) <i>P2<sub>1</sub>/a</i>	Billing D. G, and Lemmerer A, 2007
C7Pbl <sub>4</sub>	Orthorhombic T = 293 K a = 8.8549 (15) Å b = 8.6840 (19) Å c = 36.612 (13) Å <i>Pbca</i>	Orthorhombic T = 278 K a = 9.0126 (2) Å b = 8.7087 (2) Å c = 36.5612 (10) Å <i>Pbca</i>	Monoclinic T = 253 K a = 17.243 (9) Å b = 8.942 (4) Å c = 8.589 (4) Å $\beta$ = 96.902 (11)	N/A	Lemmerer A, 2007
C8Pbl <sub>4</sub>	Orthorhombic T = 314 K a = 40.0276 (18) Å b = 8.7440 (3) Å c = 8.7436 (3) Å <i>Cmca</i>	Orthorhombic T = 293 K a = 8.9817 (4) Å b = 8.6886 (3) Å c = 37.4821 (18) Å <i>Pbca</i>	Monoclinic T = 173 K a = 18.738 (3) Å b = 8.9916 (10) Å c = 8.4542 (9) Å $\beta$ = 96.301 (8) <i>P2<sub>1</sub>/c</i>	N/A	Lemmerer A, 2007
C9Pbl <sub>4</sub>	Undetermined	Orthorhombic T = 293 K a = 9.0232 (2) Å b = 8.7054 (2) Å c = 39.7578 (9) Å <i>Pbca</i>	Monoclinic T = 223 K a = 19.791 (3) Å b = 8.8401 (10) Å c = 8.7054 (11) Å $\beta$ = 96.376 (9) <i>P2<sub>1</sub>/c</i>	N/A	Lemmerer A, 2007; Nagapetyan S. S, <i>et al</i> , 1988.
C10Pbl <sub>4</sub>	Orthorhombic T = 343 K a = 47.479 (11) Å b = 8.7115 (19) Å c = 8.7152 (18) Å <i>Cmca</i>	Orthorhombic T = 293 K a = 8.9708 (2) Å b = 8.6733 (2) Å c = 42.5696 (12) <i>Pbca</i>	Orthorhombic T = 268 K a = 8.8314 (2) Å b = 8.4871 (2) Å c = 43.9491 (13) Å <i>Pbca</i>	Monoclinic T = 243 K a = 21.330 (9) Å b = 8.950 (4) Å c = 8.433 (3) Å $\beta$ = 96.107 (10) <i>P2<sub>1</sub>/c</i>	Lemmerer A, 2007 Ishihara T, et al, 1990.

	I	II	III	IV	Reference
C12Pbl <sub>4</sub>	Undetermined	Monoclinic T = 319 K a = 8.6882 (6) Å b = 9.0031 (6) Å c = 23.8647 (16) Å β = 92.487 (2) <i>P2<sub>1</sub>/a</i>	Orthorhombic T = 293 K a = 8.8645 (2) Å b = 8.5149 (1) Å c = 49.0253 (9) Å <i>Pbca</i>	N/A	Billing D. G, and Lemmerer A, 2008; Ishihara T, et al, 1990.
C14Pbl <sub>4</sub>	Undetermined	Monoclinic T = 335 K a = 8.6774 (16) Å b = 9.0143 (19) Å c = 26.421 (6) Å β = 92.492 (13) <i>P2<sub>1</sub>/a</i>	Orthorhombic T = 293 K a = 8.8474 (1) Å b = 8.5167 (1) Å c = 54.1561 (7) Å <i>Pbca</i>	N/A	Billing D. G, and Lemmerer A, 2008
C16Pbl <sub>4</sub>	Undetermined	Monoclinic T = 335 K a = 8.673 (2) Å b = 9.012 (3) Å c = 28.846 (8) Å β = 91.816 (6) <i>P2<sub>1</sub>/a</i>	Orthorhombic T = 293 K a = 8.8167 (1) Å b = 8.5222(1) Å c = 59.2906 (9) Å <i>Pbca</i>	N/A	Billing D. G, and Lemmerer A, 2008
C18Pbl <sub>4</sub>	Undetermined	Monoclinic T = 348 K a = 8.6917 (9) Å b = 9.0456 (10) Å c = 31.424 (4) Å β = 91.586 (8) <i>P2<sub>1</sub>/a</i>	Orthorhombic T = 293 K a = 8.7825 (1) Å b = 8.5401 (1) Å c = 64.4472 (11) Å <i>Pbca</i>	N/A	Billing D. G, and Lemmerer A, 2008

### 2.6.1 Enthalpy and entropy energies from the CnMX<sub>4</sub> phase transitions

The phase changes of the CnMX<sub>4</sub> compounds have an associated energy of transformation given by the enthalpy and entropy values which are readily acquired through thermal analysis techniques, such as, differential scanning calorimetry (DSC). This enables one to determine the magnitude of the phase change, from the scale of the enthalpy and the entropy values. Since the most recent work in literature on the phase transitions of the aliphatic CnMX<sub>4</sub> compounds has been on the lead iodide hybrids, they will be discussed first followed by the background information from the historical aliphatic transition metal hybrids.

Below, table 2.14 display's the enthalpy values obtained for the heating and cooling runs from the DSC experiments on all the CnPbl<sub>4</sub> compounds (n = 4-10, 12, 14, 16, 18, with the references at the bottom of the table). The table displays one prominent trend, which is specifically related to the quasi melting phase transition for each compound. This enthalpy value is the highest value in the series of phase transitions occurring in each compound. Furthermore this quasi melting enthalpy value significantly increases as the chain length increases particularly from C8. A plot of the chain length against quasi-melting enthalpy, as seen in figure 2.42, does show the quasi melting enthalpy increase in a linear fashion with increasing chain length.

**Table 2.14:** Phase Change enthalpies for the various phase changes for the aliphatic (Cn)PbI<sub>4</sub> hybrids.

Chain length	T1 (K)	H1/Kj.mol <sup>-1</sup>	T2 (K)	H2/Kj.mol <sup>-1</sup>	T3 (K)	H3/Kj.mol <sup>-1</sup>	Number of Phases
<b>n = 4</b>							2
Heating	274	9.5					
Cooling	256.2	12.5					
<b>n = 5</b>							3
Heating	318.6	6	391.2	0.56			
Cooling	315.4	7.8	390	0.71			
<b>n = 6</b>							4
Heating	269-265	0.435	*354.9	*13.5	371.3	1.1	
Cooling	257-251	0.539	*349.3	*12.7	367.2	1.2	
<b>n = 7</b>							3
Heating	270.7	6.7	*285.8	*8.4	310.1	2.8	
Cooling	251.6	8.9	*283.6	*8	309.1	2.8	
<b>n = 8</b>							3
Heating	241	14.6	*311.2	*21.2			
Cooling	235.6	15.1	*308.6	*20.8			
<b>n = 9</b>							3
Heating	252.1	7.1	*314	*23.7			
Cooling	240.9	7.8	*312.8	*22.9			
<b>n = 10</b>							4
Heating	258.6	10.1	284	8.4	*337.21	*32.4	
Cooling	249.1	8.2	276.6	9.6	*334.65	*28.8	
<b>n = 12</b>							3
Heating	314.9	10.9	*349.7	*44.2			
Cooling	32.9	9.2	*345.1	*41.9			
<b>n = 14</b>							3
Heating	328.6	10.6	*360.1	*54.6			
Cooling	320.9	9.6	*352.0	*51.7			
<b>n = 16</b>							3
Heating	340	11.6	*369.1	*62.7			
Cooling	332.4	10	*363.2	*61.7			
<b>n = 18</b>							3
Heating	346.3	13.4	*373.3	*79.5			
Cooling	340.8	12.1	*366.4	*75.9			

n = 4-6 (Billing D. G, and Lemmerer A, 2007); n = 7-10 (Lemmerer A, 2007; 2011); n =12, 14, 16, 18 (Billing D. G, and Lemmerer A, 2007). \*Quasi-melting transitions

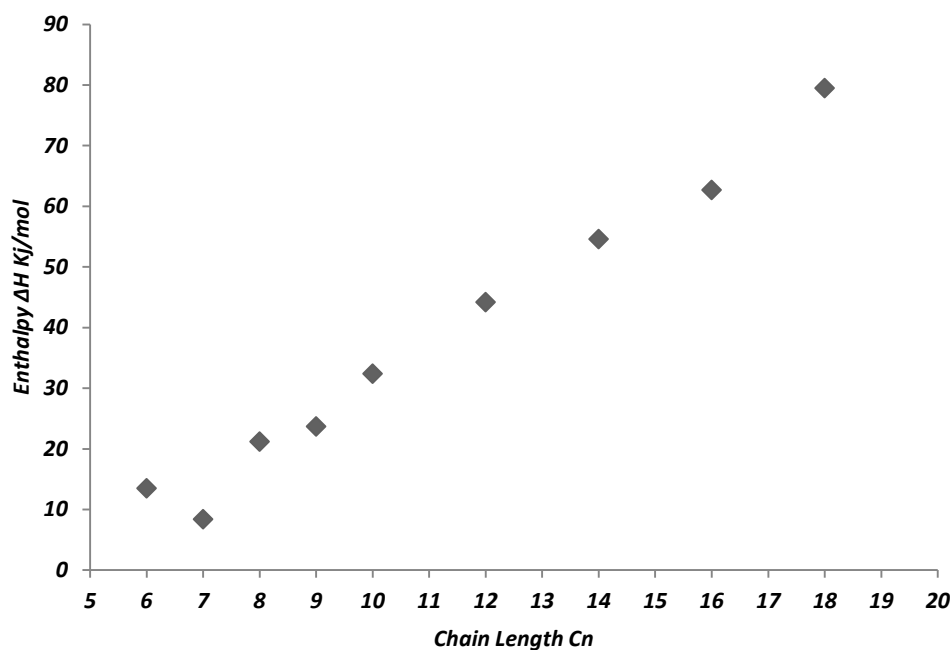


**Figure 2.42:** Chain length of  $C_nPbI_4$  vs the quasi melting phase change enthalpy for the heating run. This quasi-melting enthalpy generally increases in a linear fashion with increasing chain length.  $n = 6$  (Billing D. G, and Lemmerer A, 2007);  $n = 7-10$  (Lemmerer A, 2007);  $n = 12, 14, 16, 18$  (Billing D. G, and Lemmerer A, 2007).

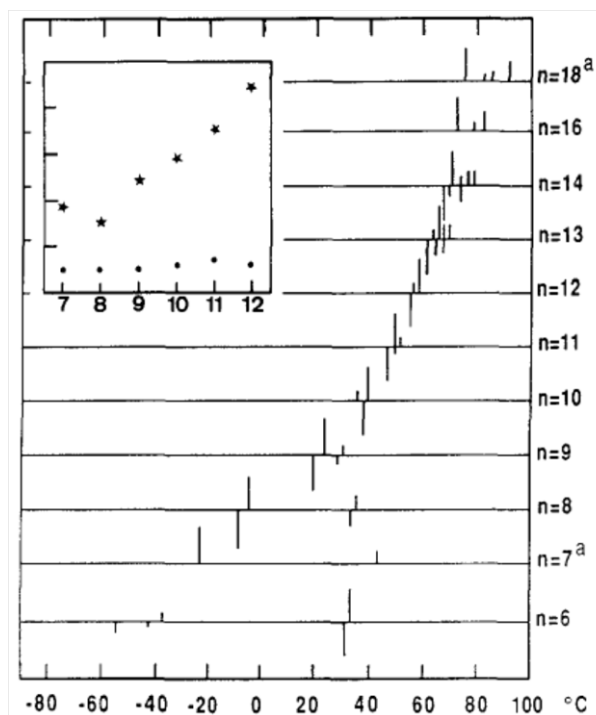


**Figure 2.43:** The DSC results from  $(C_n)CdCl_4$ . The general graph represents a schematic of the DSC phase transition runs, where the lines pointing up are the endotherms for the increasing temperature run, and the lines pointing down are the exotherms for the decreasing temperature run. The insert in the top left is the enthalpies for the quasi-melting transitions for increasing chain lengths (Shenk K. J and Chapuis G, 1988).

Although the transition metal hybrids display no interdigitation of the alkyl chains, as seen previously in figure 2.41, in which the metal centre spacing has been shown (Nagapetyan, S. S, *et. al*, 1988) to be the determining factor associated with this packing phenomenon, they display similar phase transition behaviour due to the alkyl ammonium chains. As seen in figure 2.43, the DSC results displayed show the same trend in the quasi-melting enthalpies with the increasing chain length as in their  $C_nPbI_4$  counterparts (Shenk K. J and Chapuis G, 1988). One other important phenomenon mentioned by the authors (Shenk K. J and Chapuis G, 1988) concerning the structure determination of  $C_{14}CdCl_4$  and its high temperature phase. They comment that the characterization of the structures of higher temperature phases were unsuccessful as the Bragg peaks begin to disappear, and only diffuse scattering may be observed. It was also observed that the longer chain derivatives exhibit the diffuse scattering phenomenon to a greater extent, so much so that even the powder diffraction experiments yield almost no diffraction peaks (Shenk K. J and Chapuis G, 1988).

### **2.6.2 Unusual phase behaviour of the short alkyl ammonium hybrids of $(C_3)MCl_4$**

As previously mentioned the short alkyl ammonium chains only undergo order-disorder phase transformations. However in the case of  $C_3MCl_4$ , where  $M = Mn$ , and  $Cd$ , one encounters intermediate modulated or incommensurate phases which occur as the compound moves through the phase transformations upon heating. An incommensurate modulated phase is a structure that is no longer periodic, but quasi periodic, i.e. it gives rise to compressions and rarefactions in the crystal which slightly distorts the periodicity of the material resulting in a superstructure (definition adapted from the IUCr online dictionary).

In the  $C_3CdCl_4$  case, there exists three phases. Firstly is the disordered low temperature orthorhombic phase III (Chapuis, G, 1978), which displays a simple disorder of the  $C_2$  carbon atom over two positions. The high temperature phase I (Chapuis, G, 1978) also displays a simple disorder model; however the disorder model now includes  $C_1$  and  $C_2$ . Phase II is an intermediate modulated/incommensurate phase (Doudin B, and Chapuis G, 1988). This phase displays large displacement amplitudes of the  $Cl$  and  $Cd$  atoms along the  $c$ -axis which is evidence of the modulation occurring through the crystal (Doudin B, and Chapuis G, 1988).



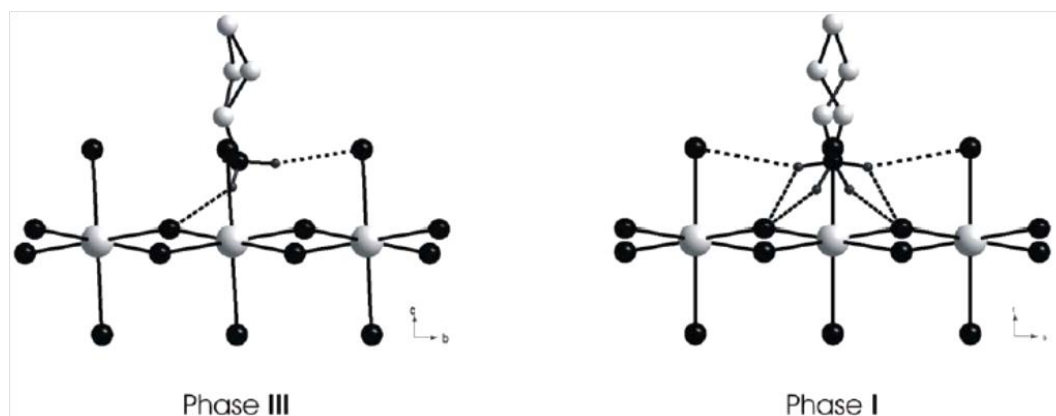


**Figure 2.44:** The  $\text{C3CdCl}_4$  disordered low temperature phase III and high temperature phase I (Chapuis, G, 1978).

III	158 K	II	180 K	I
(Z = 4)		(Z = 2)		(Z = 2)
orthorhombic		orthorhombic		orthorhombic
<i>Pbca</i>		<i>Abma</i>		<i>Abma</i>
$a = 7.568(5)$		$a = 7.585(5)$		$a = 7.607(3)$
$b = 7.359(1)$		$b = 7.359(1)$		$b = 7.370(3)$
$c = 25.515(8)$		$c = 25.053(6)$		$c = 25.184(6)$

**Figure 2.45:** The unit cell information for the phases of  $\text{C3CdCl}_4$  and the relevant phase transformation temperatures (Chapuis, G, 1978; Doudin B, and Chapuis G, 1988).

In the  $\text{C3MnCl}_4$  analogue the crystal displays six distinct phases over a wide temperature range. These phases were investigated over a number of years due to the complexity of the phases (Depmeier W and Mason S. A, 1978; 1983; Harris, *et al*, 1994). Phases V and III are incommensurate with phase V being a supercell i.e. with the three fold increase of the b axis. The remaining four phases are commensurate. Hence the sequence follows from (VI) commensurate to (V) incommensurate to (IV) commensurate to (III) incommensurate to the final two which are the commensurate high temperature phases. A recent review article of the  $\text{CnMCl}_4$  hybrids where  $M = \text{Mn, Cd, and Cu}$ , with an overview of the modulated phases of  $\text{C3MnCl}_4$  are further discussed by (Depmeier W, 2009)

VI	110 K	V	165 K	IV	344 K	III	396 K	II	446 K	I
(Z = 2)		(Z = 4)		(Z = 4)		(Z = 4)		(Z = 4)		(Z = 2)
$\zeta$		$\epsilon$		$\delta$		$\gamma$		$\beta$		$\alpha$
monoclinic		orthorhombic		orthorhombic		orthorhombic		orthorhombic		tetragonal
<i>P2<sub>1</sub>/b</i>		<i>Pbna</i>		<i>Abma</i>		<i>Abma</i>		<i>Abma</i>		<i>I4/mmm</i>
$a = 7.437(8)$		$a = 7.443$		$a = 7.458(9)$		$a = 7.39(1)$		$a = 7.40(1)$		$a = 10.465$
$b = 7.082(5)$		$b = 21.426$		$b = 7.169(9)$		$b = 7.25(1)$		$b = 7.34(1)$		$b = 10.465$
$c = 13.096(8)$		$c = 25.422$		$c = 25.61(5)$		$c = 26.72(5)$		$c = 27.45(10)$		$c = 27.500$

**Figure 2.46:** The phase sequence of  $\text{C3MnCl}_4$  (Depmeier and Mason S. A, 1978; 1983; Harris, *et al*, 1994).

## 2.7 1D hybrids and their optical properties

A large amount of work has been completed on the <100> 2D hybrids, and the other various structural orientations, including the 1D ribbons, chains, and the 0D clusters. It is necessary to discuss the few papers covering the optical properties of the single chain 1D hybrids. The main advantage of growing hybrids in lower dimensions is the ability to obtain the lower size limit of the well, wire or dot, with greater ease, when compared to the traditional lithographic top down approaches. An additional problem of fabricating the 1D wires from lithographic techniques is obtaining well defined wire lengths, barriers with wire lattice mismatch problems and difficulties in obtaining high quality multiple quantum wires for fundamental study (Wang X. L, Voliotis V, 2006).

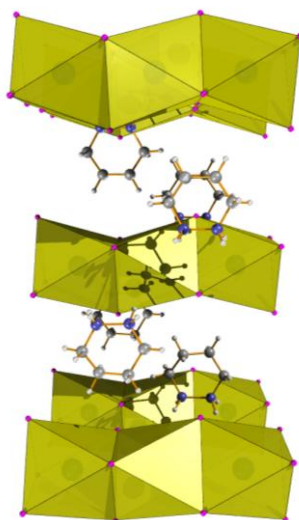


**Figure 2.47:** The room temperature structural diagram of (piperdium)PbI<sub>3</sub> displaying the face sharing octahedral chains of lead iodide.

The first 1D lead hybrid to be thoroughly studied was the single chain face sharing octahedral wires of (piperdium)PbI<sub>3</sub> (referred to as (PD)PbI<sub>3</sub> from here onwards) which was first reported by (Gridnova G. V, *et al*, 1984; Nagami A, *et al*, 1996) structurally and then optically. Above in figure 2.47 is the room temperature structural diagram of the 1D chains of (PD)PbI<sub>3</sub>. The initial paper by Nagami and co workers sparked more papers to be published on similar compounds, as the nature of the photoluminescence emission was originally not fully understood.

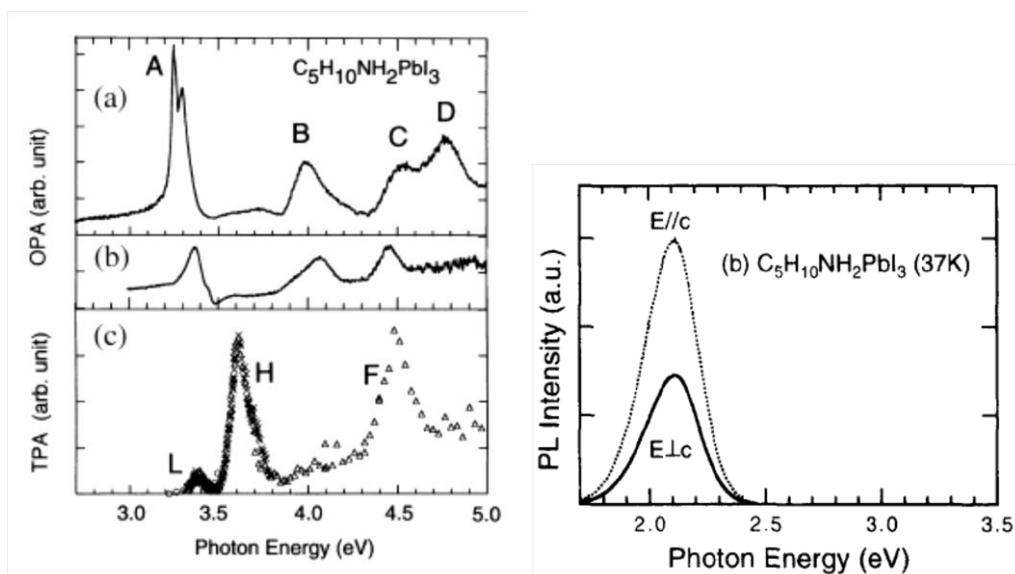


**Figure 2.48:** a) One photon absorption spectrum of  $(PD)PbI_3$   $E \perp c$ , and b)  $E//c$ . c) The two photon absorption spectrum of  $(PD)PbI_3$  displaying the odd parity absorbed exciton state (H). (Fukumoto T, *et al*, 2000) d) Photoluminescence emission of  $(PD)PbI_3$  at 37K with the peak centred at 2.1eV (Nagami A, *et al*, 1996).

The electronic structure of  $(PD)PbI_3$  was first investigated by (Nagami A, *et al*, 1996). They observed that the first exciton absorption peak of the compound was at 3.3eV which is  $\sim 1eV$  larger than its  $\langle 100 \rangle$  2D analogues. This is purely because of the exchange energy associated with the decrease of dimensionality. A substructure peak was also found at 3.25eV, which disappears above 150K and has not been assigned to this date. What was of greater interest however was the photoluminescence emission of the 1D compound which was  $\sim 1eV$  Stokes shifted from the absorption peak, i.e. the PL emission was at 2.1eV at 37K. Initial PL decay kinetics studies suggested that the PL emission arises from a self trapped exciton (STE) state and not from a separately trapped electron and hole. If this was the case the PL emission should then decay with the relationship of  $1/t$ , however this not the case. The PL emission also revealed the anisotropic nature of the excitons recombination, as the relative intensities of the  $E//c$  and  $E \perp c$  are different (figure 2.48 d).

Further work was then carried out by (Fukumoto T, *et al*, 2000) to investigate the low dimensional nature of this material, i.e. to find the conduction band edge, as well as the excitons binding energy. What was observed through the TPA (two photon absorption) experiments as seen in figure 2.48 c) was that a new TPA absorption peak was observed at 3.61eV. This peak was assigned as an exciton absorption with an odd parity envelope. The selection rules associated with 1D excitons agree with these findings (Ogawa T, Kanemitsu Y, 1995). Since this odd exciton peak should be much closer to the conduction band edge, the band gap was

estimated to be  $\sim 3.61\text{eV}$ , with the binding energy estimated from the subtraction of the first exciton and the exciton of odd parity, giving a binding energy value of  $\sim 360\text{meV}$ . The large binding energy observed is expected as a result of the Coulomb enhancement expected for 1D structures.

Fukumoto T, *et al*, 2000 further investigated the STE luminescence under hydrostatic pressure. This was done in order to study the exciton lattice interactions. The results are shown in figure 2.49. What was observed was that the exciton lattice relaxation energy decreases with increasing pressure, i.e. the luminescence blue shifts at a rate of  $36\text{meV/GPa}$ . The luminescence peak also broadens as pressure increases; which was attributed to the hardening of the crystal lattice (Fukumoto T, *et al*, 2000).

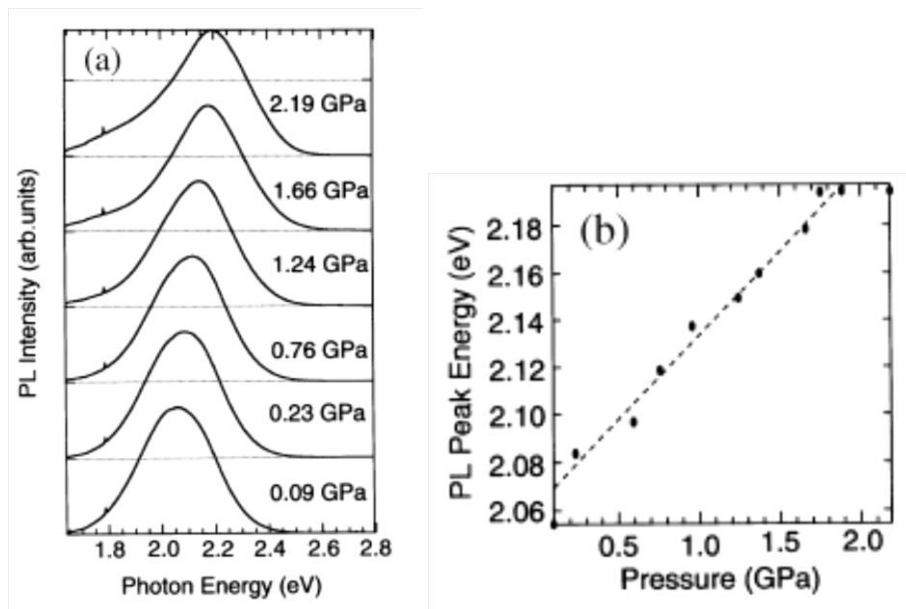


**Figure 2.49:** a) The PL emission as the hydrostatic pressure, b) a plot of the PL peak blue shift with an increase in pressure, which is due to exciton phonon coupling increasing with increasing pressure (Fukumoto T, *et al*, 2000).

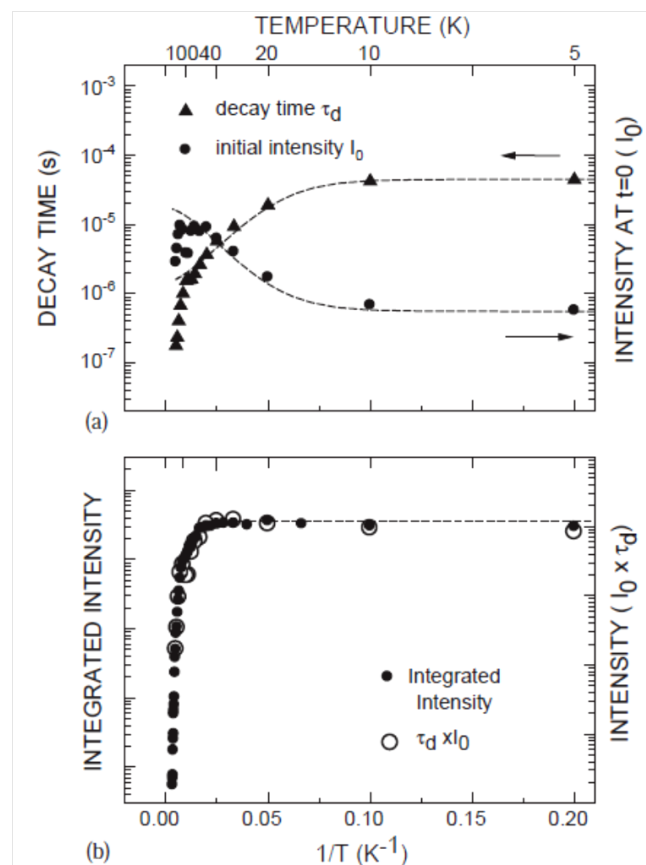


**Figure 2.50:** The luminescence decay time vs  $1/T$  a) and the plot of the luminescence integrated intensity vs  $1/T$  b) (Akimoto I, *et al*, 2004).

As the origin of the luminescence emission became clearer, (Akimoto I, *et al*, 2004) revisited the luminescence decay kinetics originally looked at by (Nagami A, *et al*, 1996) to better understand the STE emission. The luminescence decay kinetics are displayed in figure 2.50. What was observed was that the integrated luminescence intensity is almost constant from 5 – 70K and then decreases by nearly four orders of magnitude by 300K. However the most intriguing feature was the varying luminescence decay time constants from 5 – 70K, where  $\tau_d$  was  $44\mu s$  at 5K and  $2\mu s$  at 70K. These varying decay time constants suggested that the photo excited STE exists in a triplet state, with different radiative transition rates for the three triplet sub levels. What the authors discovered was that there are two energy sub levels, *a* and a nearly doubly degenerate energy level *b*. The energy level *a* is lower in energy than *b*, and has a slower luminescence decay time constant than that of *b*. As the temperature is increased, there is a thermally assisted phonon transition from *a* to *b*, and now the luminescence decays through the faster energy sub-level *b*. There is a weighting function which the authors calculated as a function of temperature for the STE energy sub-levels to give the overall decay times  $\tau_d$ . This

was done in order to match the integrated luminescence intensities as a function of temperature with  $I_0 \cdot \tau_d$  (figure 2.50b)).

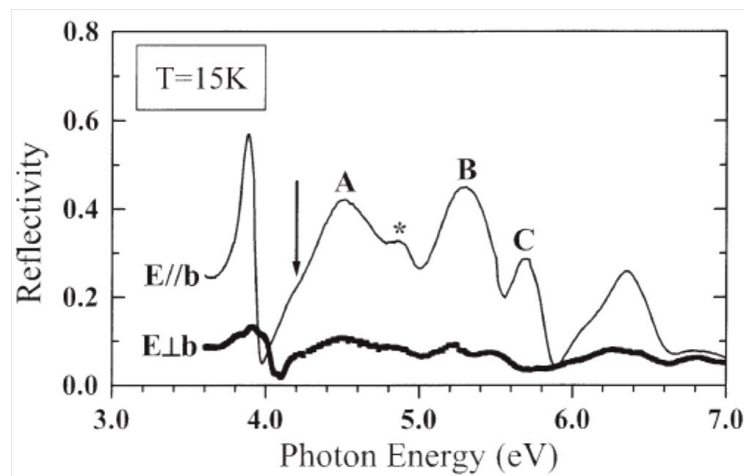


**Figure 2.51:** Reflectivity measurement of (PD)PbBr<sub>3</sub>. The first exciton peak arises at 3.9eV. Band assignments are explained in the text (Azuma J, *et al*, 2002a).

Azuma J, *et al*, 2002a; 2002b investigated the valence band structures of (PD)PbI<sub>3</sub> and of (PD)PbBr<sub>3</sub> as well as the optical properties of (PD)PbBr<sub>3</sub>, which gave further insights into the nature of the optical emissions associated with the 1D nature of these compounds. As in the (PD)PbI<sub>3</sub> case the polarized reflectance spectra showed strong optical anisotropy where the  $E//b$  (parallel to the wires) has a much stronger oscillator strength than the  $E \perp b$  reflectance spectra. This is caused from the 1D character of the compounds (Azuma J, *et al*, 2002a). As no specific band assignments for the one photon absorption experiments were given in the (PD)PbI<sub>3</sub> literature, (Azuma J, *et al*, 2002a) did the band assignments for (PD)PbBr<sub>3</sub> using the Seitz model for atomic Lead. From the reflectance spectra shown in figure 2.51 the first band is assigned as the first exciton absorption peak at 3.9eV. The first transition that is expected for the Pb<sup>2+</sup> ion is the  $6s^2 \rightarrow 6s6p$  transition which is assigned as the A band at 4.5eV i.e. the  $^1S_0$  ground state to the  $^3P_1$  excited multiplet transition. The B and C bands at 5.3eV and 5.7eV are the other excited multiplet transitions to  $^3P_2$  (B band) and  $^3P_3$  (C band) respectively. As described already the first peak at 3.9eV has also been assigned as the A exciton  $^1S_0 \rightarrow ^3P_1$  transition. Hence the direct band to band transition is expected to be between the A band and the A exciton peak. As seen in figure 2.51 the reflectance spectrum has a small bump on the A band, indicated by the arrow (4.2eV), which has been assigned as the direct band to band transition ( $E_g$ ). This assignment is confirmed through the luminescence excitation experiments performed by Azuma. An estimate to the excitons binding energy may be made by a subtraction of the band to band transition and the first exciton emission, hence  $E_b = 300\text{meV}$ , which is comparable with the (PD)PbI<sub>3</sub> value of

360 meV (Fukumoto T, *et al*, 2000). The first exciton absorption of (PD)PbBr<sub>3</sub> is 0.6 eV higher than that of (PD)PbI<sub>3</sub>, this phenomenon is also evident in the 2D and 3D cases. The red shift of the band gap as we proceed down the group (Cl → I) is due to the increase in covalent character of the halogen bonding with the lead. The band assignments are expected to remain the same for each of the halogenated systems, and should experience the same red shift as we proceed down the group (Cl → I) (Azuma J, *et al*, 2002a).

As already discussed in the (PD)PbI<sub>3</sub> case (Nagami A, *et al*, 1996; Fukumoto T, *et al*, 2000; Akimoto I, *et al*, 2004) the photo excited state is a relaxed state i.e. a self trapped state formed from the free exciton state. These photo excited states have also been investigated for 1D Peierls insulators (Kuroda N, *et al*, 1987; Tanino H, *et al*, 1988; Tomimoto S, *et al*, 1999) and have shown multi-stability with regards to the ground state after the Peierls transition has occurred (A Peierls transition is essentially a phase change of a material to a larger space group which in turn has an associated folding of the FBZ which causes a periodic fluctuation of the electron density i.e. zone folding (Kittel C, 1996)). However in the 1D band insulators of (A)PbI<sub>3</sub> systems have displayed instability in the photo excited states and not the ground states as is the case with the Peierls transition. These unstable photo excited states are caused from the multi excited states which relax into varying types of self trapped excitons, which in turn recombine to produce multi wavelength luminescence bands (Azuma J, *et al*, 2002a).

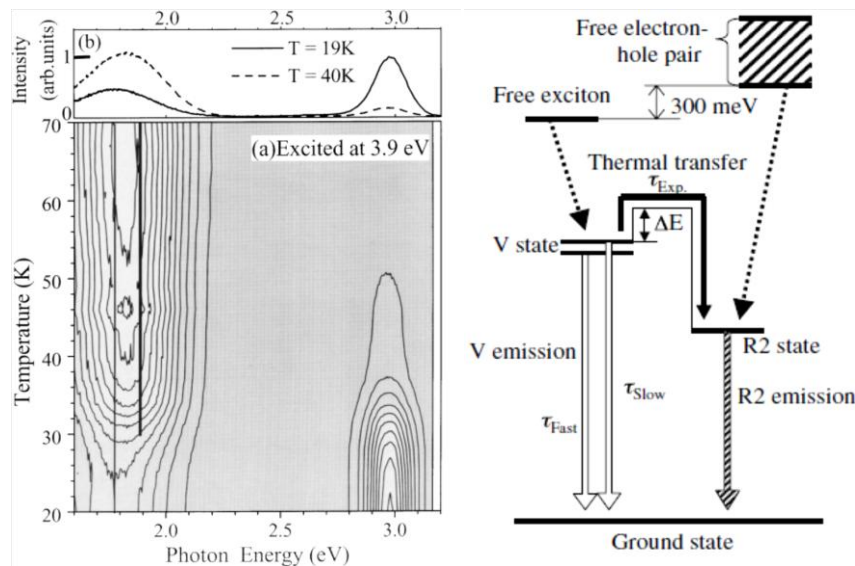


**Figure 2.52:** a) The contour map of the luminescence of (PD)PbBr<sub>3</sub> with increasing temperature. The temperature dependence of the luminescence may be seen in the luminescence intensity plot of b). The mechanism of the emission may be seen in c) as the temperature increases, the V state flows into the R2 state through thermal transfer. The V state is generated from a free exciton, and the R state is generated through the polaron formation (explained in text). Adapted from (Azuma J, *et al*, 2002a).

The photoluminescence of (PD)PbBr<sub>3</sub> has more of a complicated emission spectrum than that of its (PD)PbI<sub>3</sub> analogue. At 19K (PD)PbBr<sub>3</sub> displays two emission profiles, one at 3.0eV the violet emission (V emission) and a second emission at 1.78eV the red emission (R emission). The decay kinetics of the V emission display two exponential decay time constants as seen in (PD)PbI<sub>3</sub> (Akimoto I, *et al*, 2004). This showed that the emission was from a triplet state STE with one lower energy sub-band energy level with a fast decay time constant, and two nearly degenerate higher energy sub-bands with a slower decay time constant (figure 2.52c). The V emission is most efficiently generated when the luminescence excitation energy is around the first exciton absorption band at 3.9eV. Hence the V emission appears to be directly generated from the free exciton relaxation (Azuma J, *et al*, 2002a). The R emission however is best generated when the luminescence excitation energy is around the band to band transition at 4.2eV. The R emission has a non exponential time decay constant, which implies that it is not a STE emission. Hence R's photo excited state is suspected to be formed from an electron hole pair, which forms hole polarons, which are situated on the halogen atoms, and electron polarons which are situated on the lead atoms. These polarons may randomly move up and down the wire, and when the hole polarons and electron polarons come into close contact they annihilate to produce the emission R (Azuma J, *et al*, 2002a).

Azuma and co-workers further investigated the temperature dependence of the luminescence emissions of (PD)PbBr<sub>3</sub>. The contour map displaying the temperature dependant luminescence with the relative luminescence intensities of the two peaks at 19K and 40K are displayed in figure 2.52a) and b) respectively. We notice the temperature increases the quantum efficiency of the V emission which decreases with increasing temperature and the R emission increases accordingly. This suggests that the V emission feeds the R emission through thermal population as the temperature increases. The full mechanism for the absorption and emission processes is displayed in (figure 2.52 c). As the self trapped excitons and polaron emissions do not appear in the 2D, and 3D organic inorganic hybrids the STE emissions appear to be purely due to the 1D character of the compound (Azuma J, *et al*, 2002a). It should also be noted that (PD)PbBr<sub>3</sub> wires are crystallographically disordered over two positions, and may be a structural cause for the polaron pair generation.

The calculated DOS and band structures of (PD)PbI<sub>3</sub> and (PD)PbBr<sub>3</sub> were completed by (Azuma J, *et al*, 2002b) using the LCAO to form the basis function approximation and extended Hückel method for calculation. They also completed UPS and XPS measurements in order to correlate



the calculated and experimental band structures. The calculations and experiment were found to be in good agreement with one another. From figure 2.53 the calculated DOS may be observed for (PD)PbX<sub>3</sub>, where the bonding (B), non bonding (N.B), anti bonding (A.B), and the conduction band (C.B) may be seen. Firstly the non bonding states of the halogen's *np* orbitals are shifted closer to the top of the valence band from Bromine to Iodine because of the increase in covalent character of the halogen bonding with the lead. At the top of the valence band is the Pb 6s anti bonding lone pair of electrons. The conduction bands of both halogenated compounds appear in a similar energy region, as the vacant Pb 6*p* orbital's have little influence in the bonding of the structure. One final note is the broad band dispersion in the band structure of the compound. This is purely due to the 1D nature of these compounds (Azuma J, *et al*, 2002b).

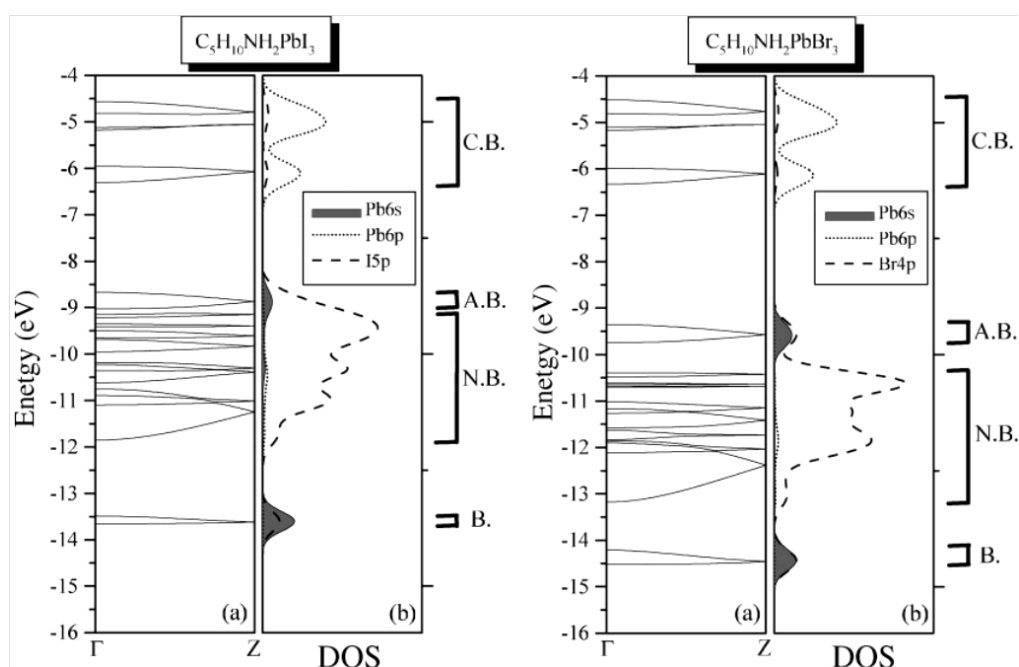


**Figure 2.53:** Calculated band structures and DOS of both (PD)PbX<sub>3</sub> where X = I and Br. The notations for C.B, A.B, N.B, B, are conduction band, antibonding, nonbonding, and bonding, respectively.

The octahedral edge sharing perovskite type 1D chains derived from the <110> orientation, have also been investigated. The electronic structures investigated by (Tanaka K, *et al*, 2005b) originally reported by (Wang S, *et al*, 1995) and (Mousdis G. A, *et al*, 1998) for [NH<sub>2</sub>C(I)=NH<sub>2</sub>]<sub>3</sub>PbI<sub>5</sub> and [CH<sub>3</sub>SC(=NH<sub>2</sub>)NH<sub>2</sub>]<sub>3</sub>PbI<sub>5</sub> respectively, have made opposing statements as to the origins of the STE luminescence to their 1D face sharing counterparts (Nagami A, *et al*, 1996). In figure 2.54 the optical absorption spectra and PL emissions at 5K may be seen. The absorption peak for [NH<sub>2</sub>C(I)=NH<sub>2</sub>]<sub>3</sub>PbI<sub>5</sub> is at ~2.5eV and the peak for [CH<sub>3</sub>SC(=NH<sub>2</sub>)NH<sub>2</sub>]<sub>3</sub>PbI<sub>5</sub> ~3.0eV. One of the reasons for the large shift between the two compounds was attributed to the increased stereo

chemical activity of the lone pair on lead for the undistorted  $[\text{NH}_2\text{C}(\text{I})=\text{NH}_2]_3\text{PbI}_5$  octahedra. However the Pb-I-Pb bond angles are essentially linear for  $[\text{NH}_2\text{C}(\text{I})=\text{NH}_2]_3\text{PbI}_5$  whereas  $[\text{CH}_3\text{SC}(=\text{NH}_2)\text{NH}_2]_3\text{PbI}_5$  displays a zig-zag of  $175^\circ$  in this angle, which could not cause such a large shift in the absorption spectrum. The large shift in the absorption band between  $[\text{NH}_2\text{C}(\text{I})=\text{NH}_2]_3\text{PbI}_5$  and  $[\text{CH}_3\text{SC}(=\text{NH}_2)\text{NH}_2]_3\text{PbI}_5$  was therefore attributed to the large distortion of the Pb-I bond lengths (down the length of the wire) which range from 3.04-3.88 Å for  $[\text{CH}_3\text{SC}(=\text{NH}_2)\text{NH}_2]_3\text{PbI}_5$ .

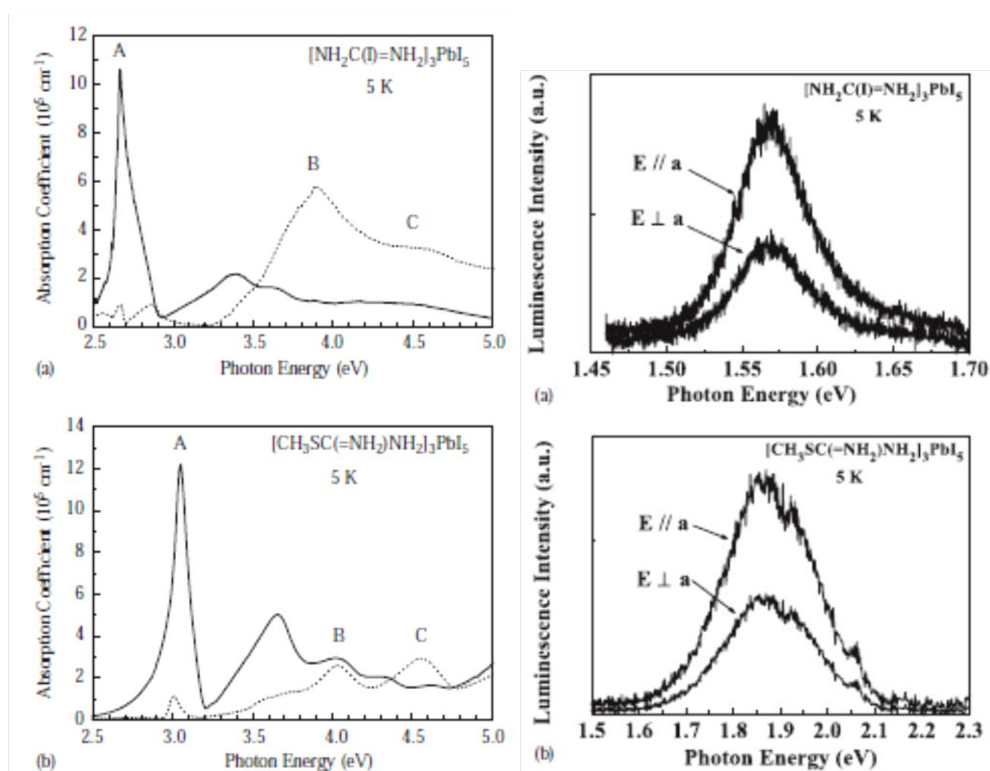


**Figure 2.54:** a) The optical absorption and photoluminescence of  $[\text{NH}_2\text{C}(\text{I})=\text{NH}_2]_3\text{PbI}_5$  respectively b) The optical absorption and photoluminescence of  $[\text{CH}_3\text{SC}(=\text{NH}_2)\text{NH}_2]_3\text{PbI}_5$  respectively. The large shift in optical absorption of the two compounds is due to the large distortions experienced in  $[\text{CH}_3\text{SC}(=\text{NH}_2)\text{NH}_2]_3\text{PbI}_5$  compared with the idealized wires in  $[\text{NH}_2\text{C}(\text{I})=\text{NH}_2]_3\text{PbI}_5$ .

As the luminescence emissions for both compounds are 1.57 eV and 1.87 eV, which are 1 eV and 1.2 eV Stokes shifted away from the optical absorption peaks for  $[\text{NH}_2\text{C}(\text{I})=\text{NH}_2]_3\text{PbI}_5$  and  $[\text{CH}_3\text{SC}(=\text{NH}_2)\text{NH}_2]_3\text{PbI}_5$  respectively. The exciton was now suggested to be Frenkel type with strong 1D character (Tanaka K, *et al*, 2005b). This reasoning is flawed as the authors do not consider the two photon absorption experiments (TPA) done on (PD) $\text{PbI}_3$  (Fukumoto T, *et al*, 2000) (this paper is even cited by Tanaka) and later work by (Azuma J, *et al*, 2002a; 2002b) on the photo excited states of the 1D compounds of (PD) $\text{PbX}_3$ . Fukumoto and co-workers further discuss the parity of the 1D Wannier exciton states obtained from the TPA experiments and

**Table 2.15:** Reference of single chain 1D lead hybrids investigated structurally, and the few papers investigating the optical and electronic properties.

Metal halide	Cation	Structure reported	Property investigated
<b>PbI</b>	C <sub>5</sub> H <sub>10</sub> NH <sub>2</sub>	Gridnova G. V, <i>et al</i> , 1984	Nagami A, <i>et al</i> , 1996; Fukumoto T, <i>et al</i> , 2000; Akimoto I, <i>et al</i> , 2004; Azuma J, <i>et al</i> , 2002b
<b>PbBr</b>	C <sub>5</sub> H <sub>10</sub> NH <sub>2</sub>	Azuma J, <i>et al</i> , 2002a	Azuma J, <i>et al</i> , 2002a; 2002b
<b>PbI</b>	NH <sub>2</sub> CINH <sub>2</sub>	Wang S, <i>et al</i> , 1995	Koutselas I. B, <i>et al</i> , 1997; Tanaka K, <i>et al</i> , 2005b
<b>PbI</b>	CH <sub>3</sub> SCNH <sub>2</sub> NH <sub>2</sub>	Mousdis G. A, <i>et al</i> , 1998	Tanaka K, <i>et al</i> , 2005b
<b>PbI</b>	(But) <sub>4</sub> N	Krautsheid H and Vielsack F, 1995	Koutselas I. B, <i>et al</i> , 1997;
<b>PbI</b>	(MV)	Tang Z and Guloy A. M, 1999	Tang Z and Guloy A. M, 1999; Fujisawa J and Ishihara T, 2004; Fujisawa J and Tajima N, 2005; Fujisawa J, <i>et al</i> , 2007
<b>PbI</b>	(EtV)	Pradeesh K, <i>et al</i> , 2010	Pradeesh K, <i>et al</i> , 2010
<b>PbI</b>	EDT-TTF-I <sub>2</sub>	Devic T, <i>et al</i> , 2004	Devic T, <i>et al</i> , 2004
<b>PbBr</b>	C <sub>6</sub> H <sub>11</sub> N <sub>2</sub>	Thirumurugan A and Rao C. N. R, 2008	
	C <sub>6</sub> H <sub>30</sub> N <sub>4</sub>	Thirumurugan A and Rao C. N. R, 2008	
<b>PbI</b>	NO <sub>2</sub> PhCH <sub>2</sub> NHPy	Zhoa H. R, <i>et al</i> , 2010	Zhoa H. R, <i>et al</i> , 2010
	BrPhCH <sub>2</sub> NHPy	Zhoa H. R, <i>et al</i> , 2010	Zhoa H. R, <i>et al</i> , 2010
	ClPhCH <sub>2</sub> NHPy	Zhoa H. R, <i>et al</i> , 2010	Zhoa H. R, <i>et al</i> , 2010
	FPhCH <sub>2</sub> NHPy	Zhoa H. R, <i>et al</i> , 2010	Zhoa H. R, <i>et al</i> , 2010
<b>PbBr</b>	C <sub>16</sub> H <sub>19</sub> N <sub>2</sub>	Papavassiliou G. C, <i>et al</i> , 2003	Papavassiliou G. C, <i>et al</i> , 2003
<b>PbI</b>	C <sub>16</sub> H <sub>19</sub> N <sub>2</sub> (DMSO)	Guloy A. M, <i>et al</i> , 2001	Guloy A. M, <i>et al</i> , 2001
<b>PbI</b>	Methyl Blue	Li M. T, <i>et al</i> , 2005	(charge transfer not investigated)
<b>PbI</b>	Hexamine	Miyamae H, <i>et al</i> , 1988	
<b>PbI</b>	C <sub>6</sub> H <sub>14</sub> N	Elleuch S, <i>et al</i> , 2008	Elleuch S, <i>et al</i> , 2008
<b>PbI</b>	C <sub>10</sub> H <sub>16</sub> N	Li H. H, <i>et al</i> , 2004	
<b>PbI</b>	C <sub>14</sub> H <sub>18</sub> N <sub>2</sub>	Huang C. C, <i>et al</i> , 2004	
<b>PbI</b>	C <sub>18</sub> H <sub>19</sub> N <sub>4</sub>	Sarker K. K, <i>et al</i> , 2006	
<b>PbI</b>	C <sub>8</sub> H <sub>17</sub> NO	Sun L. G, <i>et al</i> , 2009	
<b>PbI</b>	Me <sub>4</sub> N	Contreras, J. G, <i>et al</i> , 1983	
<b>PbBr</b>	(PhCH <sub>2</sub> ) <sub>4</sub> P	Groger H, <i>et al</i> , 2001	
<b>PbI</b>	Ph <sub>4</sub> P	Krautsheid H, <i>et al</i> , 1996	
<b>PbI</b>	Pr <sub>4</sub> N	Krautsheid H and Vielsack F, 1999b	
<b>PbBr</b>	CH <sub>3</sub> C <sub>5</sub> H <sub>4</sub> NCH <sub>3</sub>	Raptopoulou C. P, <i>et al</i> , 2002	Raptopoulou C. P, <i>et al</i> , 2002
<b>PbI</b>	Naphthylmethylammonium	Papavassiliou G. C, <i>et al</i> , 1999	Papavassiliou G. C, <i>et al</i> , 1999
<b>PbI</b>	Et <sub>4</sub> N	Papavassiliou G. C and Koutselas I. B, 1995	Papavassiliou G. C and Koutselas I. B, 1995
<b>PbBr</b>	Et <sub>4</sub> N	Papavassiliou G. C and Koutselas I. B, 1995	Papavassiliou G. C and Koutselas I. B, 1995
<b>PbI</b>	C <sub>10</sub> H <sub>7</sub> N(C <sub>4</sub> H <sub>9</sub> )	Li H. H, <i>et al</i> , 2007	Li H. H, <i>et al</i> , 2007

further deduce the binding energy of the lowest exciton. Furthermore the papers reported on (PD)PbX<sub>3</sub> work is in good agreement with what is predicted theoretically about excitonic behaviour in a 1D system (Ogawa T, Kanemitsu Y, 1995). Other 1D compounds like (PD)PbX<sub>3</sub>, have been reported and are listed in the table 2.15.

### 2.7.1 Charge transfer effects between wires and spacers.

Optical and electronic interactions between the wires and spacers have been of little concern while the nature of the STE luminescence was under investigation. The organic cations employed thus far have had a small dielectric constant with a deep UV absorption band, therefore ensuring the electronic interactions remain within the wires. However in the case where the organic cation employed is able to readily accept or donate charge, a charge transfer interaction between the wires and spacers may occur. The first reported case of a charge transfer interaction in the 1D lead hybrids, used the redox active organic cation methyl viologen which successfully grew the face sharing single chain octahedra similar to (PD)PbI<sub>3</sub>, to produce (MV)Pb<sub>2</sub>I<sub>6</sub> and was structurally characterized by (Tang Z and Guloy A. M, 1999).

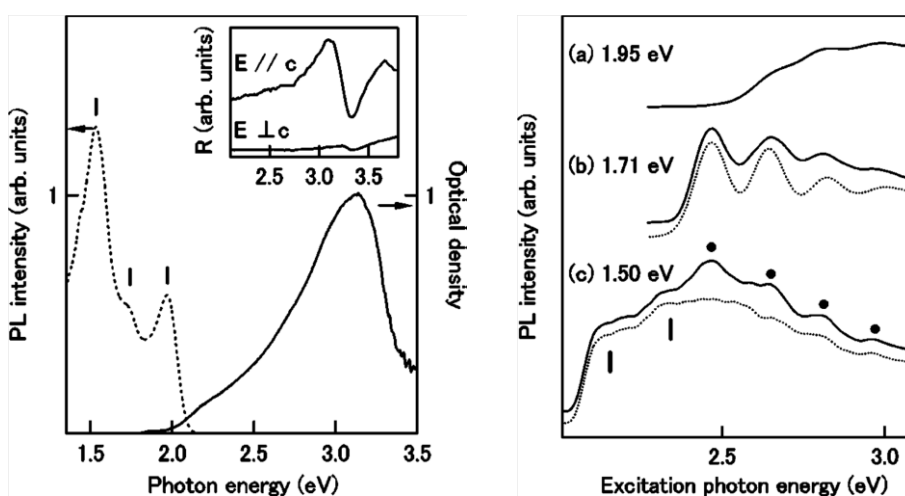


**Figure 2.55:** Optical absorption and photoluminescence spectra at 4K. Photoluminescence spectra at various excitation wavelengths (Fujisawa J and Ishihara T, 2004).

The optical properties of (MV)Pb<sub>2</sub>I<sub>6</sub> were later investigated by (Fujisawa J and Ishihara T, 2004). The reflectance spectra of (MV)Pb<sub>2</sub>I<sub>6</sub>, measured at 4K, displayed two absorption bands, i.e. one band with a strong oscillator strength at 3.1eV and a broad absorption band from 2.0 – 2.8eV, as seen in figure 2.55 I). The polarized reflectance spectrum of  $E \perp c$  (perpendicular to the wire direction) confirms the 3.1eV peak from the  $E // c$  as the first exciton absorption peak (Fujisawa J and Ishihara T, 2004), as observed for (PD)PbI<sub>3</sub> case (Nagami A, *et al*, 1996; Fukumoto T, *et al*,

2000; Akimoto I, *et al*, 2004), as a result of the strong optical anisotropy experienced from the compound. Because methyl viologen has an absorption, or electronic transition, in the UV region ( $> 4.0\text{eV}$ ), the broad absorption band of  $(\text{MV})\text{Pb}_2\text{I}_6$  from  $2.0 - 2.8\text{eV}$  cannot be directly assigned as the absorption from the organic cation. This absorption peak has been assigned as a result of a charge transfer transition from the negatively charged wires to the positively charged organic cations. Furthermore the broad absorption peak has not been assigned as a result of interwire transfers, as the first exciton absorption only occurs at  $3.1\text{eV}$ . The resultant photoluminescence emission spectrum obtained at  $4\text{K}$  is displayed in figure 2.55 I, which shows three emission bands, i.e. two peaks at  $1.95\text{eV}$  and  $1.5\text{eV}$ , and a shoulder at  $1.71\text{eV}$ . The  $1.95\text{eV}$  peak matches the emission reported for  $(\text{PD})\text{PbI}_3$  (Nagami A, *et al*, 1996; Fukumoto T, *et al*, 2000), and has also been attributed as the STE emission characteristic to the 1D wires (Fujisawa J and Ishihara T, 2004).

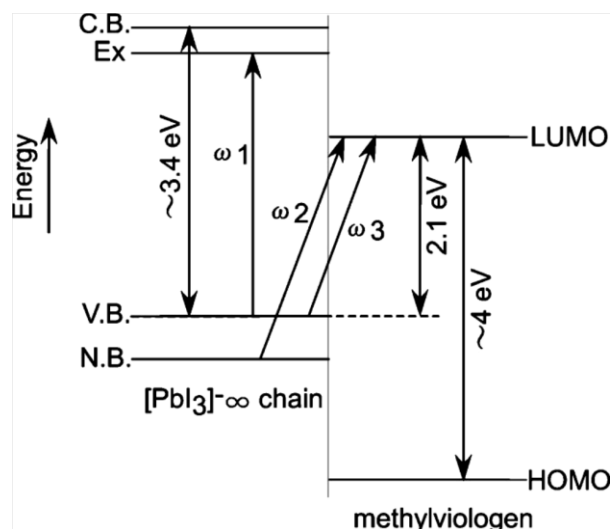


**Figure 2.56:** Charge transfer mechanism for  $(\text{MV})\text{Pb}_2\text{I}_6$  as proposed by (Fujisawa J and Ishihara T, 2004), details explained in the text.

The multiple luminescence emission bands were studied using the photoluminescence excitation technique (Figure 2.55 II). The excitation spectrum of the emission peak of  $1.95\text{eV}$ , displayed an increase in luminescence intensity in the energy absorption region  $> 2.6\text{eV}$ . This has been interpreted as a nonradiative relaxation from vibrationally excited electron hole pair states which become STE's in the wires themselves (Fujisawa J and Ishihara T, 2004).

The luminescence band origins of the bands of  $1.71\text{eV}$  and  $1.50\text{eV}$  are not the same as the self trapped exciton emission at  $1.95\text{eV}$ . These peaks arise as a result of a charge transfer from the wires to the methyl viologen. The luminescence intensity of these two peaks increased when the

excitation energy for the emission process occurred within the visible region, (below the first exciton absorption). This suggests that the charge transfer mechanism is a result of an electron being transferred from the wires valence band, to the LUMO of the methyl viologen. The emission peak at  $1.71\text{eV}$  shows an absorption edge in the PLE spectrum (b) at  $2.4\text{eV}$  (which is  $0.7\text{eV}$  Stokes shifted from the emission) and the emission peak at  $1.5\text{eV}$  displayed an absorption edge at  $2.05\text{eV}$  (Stokes shifted  $\sim 0.6\text{eV}$ ). These two PL emissions are attributed to polaron pairs generated through lattice relaxation (Fujisawa J and Ishihara T, 2004). This is likely from the large resultant Stokes shifted emissions. Furthermore the difference in these two bands absorption edges, suggest that there are two origins of the charge transfer to the LUMO of methyl viologen.

The differences in the PLE absorption edges of the two band emission bands ( $1.50\text{eV}$  and  $1.71\text{eV}$ ) with a difference of  $\sim 0.4\text{eV}$ , implies that the two charge transfer transitions occur from the top of the valence band (the antibonding lone pair electrons of Pb  $6s$ ) and the valence bands nonbonding electrons (I  $5p$  electrons). This notion is confirmed through the electronic structure calculations performed by (Azuma J, *et al*, 2002b). The calculations give the nonbonding electrons band to be  $\sim 0.5\text{eV}$  below the top of the valence band edge. The full mechanism proposed for the charge transfer absorptions are displayed in Figure 2.56 (Fujisawa J and Ishihara T, 2004). From figure 2.56  $\omega_1$  is the first exciton absorption,  $\omega_2$  is the charge transfer absorption for the  $1.71\text{eV}$  emission, and  $\omega_3$  is the charge transfer absorption for the  $1.50\text{eV}$  emission. Hence the onset of the charge transfer is  $2.1\text{eV}$  from the valence band absorption (PLE) experiments.

An aside note on 1D systems is that they are important materials in terms of electronic transport properties. As we have already discussed, after the charge carriers (excitons/electron hole pairs) are generated, they immediately relax into polarons through electron lattice interactions. The polarons then behave like a soliton (single wave packet moving down the wire). These soliton like polarons, display large carrier mobility even at room temperature ( $10^5\text{cm}^2/\text{V.s}$ ) (Fujisawa J and Tajima N, 2005). Photoconductivity measurements were also completed on  $(\text{MV})\text{Pb}_2\text{I}_6$  by (Fujisawa J and Tajima N, 2005) and displayed that the photoconductivity of this compound is predominantly induced due to the charge transfer interaction from the wires to the spacers. Furthermore the photoconductivity measurements have confirmed the energy transfer from the valence band to the LUMO of methyl viologen to be  $2.1\text{eV}$  (Fujisawa J and Tajima N, 2005).

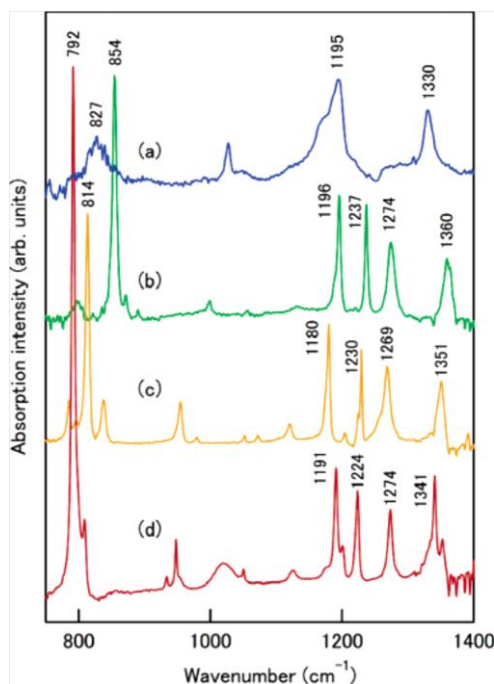


**Figure 2.57:** Infrared spectra recorded for a) (MV)Cl, b) (MV)Cl<sub>2</sub> c) (MV)I<sub>2</sub>, d) (MV)Pb<sub>2</sub>I<sub>6</sub> (Fujisawa J, *et al*, 2007).

A final investigation of the vibrational (IR) spectra of (MV)Pb<sub>2</sub>I<sub>6</sub> was completed by (Fujisawa J, *et al*, 2007) in order to investigate any weak interactions present between the wires and spacers. Infra Red spectra were collected for the following compounds: the radical compound MVCl, and the two known charge transfer compounds of MVCl<sub>2</sub> and MVI<sub>2</sub> which were used as a comparison with MVPb<sub>2</sub>I<sub>6</sub>. The reported IR spectra of all four compounds may be seen in figure 2.57. Since the lead iodide wires phonon vibrations are only expected below 200cm<sup>-1</sup> the IR spectra would still result in useful weak interactions information. Although the molecular vibrations between 1200 and 1400cm<sup>-1</sup> are fairly similar the vibrational peaks around 800cm<sup>-1</sup> significantly shift to the low energy side by 40 and 62cm<sup>-1</sup> for MVI<sub>2</sub> and MVPb<sub>2</sub>I<sub>6</sub> respectively, compared with MVCl<sub>2</sub>. In addition to the shift the oscillator strength of this peak for MVPb<sub>2</sub>I<sub>6</sub> is twice that of the other compounds, as well as having a 7% increase of the vibrational energy compared with MVCl<sub>2</sub>. This peak in the IR spectra has been attributed to the molecular vibrations of the nitrogen cations.

Hence the following conclusions have been made. Because of the peak shift and increase in oscillator strength for the nitrogen cation in MVPb<sub>2</sub>I<sub>6</sub> is observed, an increase in covalent character between the nitrogen cation and the negatively charged lead iodide wires via the charge transfer interaction is expected (Fujisawa J, *et al*, 2007).

More recently ethylviologen was incorporated with lead iodide and formed 1D ribbons/coulombs (Pradeesh K, *et al*, 2010) in preference over the single face sharing octahedral wires of (MV)Pb<sub>2</sub>I<sub>6</sub>. The first exciton absorption was also observed at 3.1eV for the ethylviologen derivative, however the STE luminescence was blue shifted and was now observed at 2.35eV with a shoulder at 2.19eV. The major difference in the photoluminescence spectrum from that reported for MVPb<sub>2</sub>I<sub>6</sub> (Fujisawa J and Ishihara T, 2004) was the emission peak at 3eV for the ethylviologen lead iodide which was not assigned (Pradeesh K, *et al*, 2010). This phenomenon will be further dealt with in chapter 5.3.

Lastly it is worth mentioning the use of an organic metal (etylenedithio-1,2-diiodotertathiafluvalene) (EDT-TTF-I<sub>2</sub>) which has also been incorporated with lead iodide to form 1D face sharing octahedral wires of ((EDT-TTF-I<sub>2</sub>)<sub>2</sub>PbI<sub>3</sub>.H<sub>2</sub>O). This compound has shown improved conductivity for an anionic  $\beta'$  type salt at ambient pressure (Devic T, *et al*, 2004). These authors also reported a similar finding for other compounds (Devic T, *et al*, 2003). Other recent work by (Zhao H, R, *et al*, 2010) has investigated the ferroelectric behaviour of some compounds like (PD)PbI<sub>3</sub>, because of their inherent crystal polarizability due to the large optical anisotropy and the 1D nature of these compounds.

## **2.8 Optical non-linearity in organic inorganic hybrids**

A brief discussion on the nonlinear optical properties of hybrids will be discussed here as this section is covered more in depth in chapter 6. As optical nonlinearity is a large field of study in its own right the ability of low dimensional hybrids to be tailored for this purpose has shown favourable results. Firstly a brief mention that second harmonic generation  $\chi^2$  (SHG) is a property of noncentrosymmetric crystals, and not dependant on the material under study. However the material may increase the SHG response recorded due to an increase in hyperpolarizability of the crystal (Nye J. F, 1957). Third harmonic generation  $\chi^3$  (THG) is different as it occurs in isotropic media, and or crystals with a centre of inversion, i.e.  $\chi^2$  is suppressed in the crystal and the non vanishing  $\chi^3$  term now predominates (Fox M, 2008). Quantum wells in general display good inherent resonant third order nonlinearity.

Compounds C10PbI<sub>4</sub> and C6PbI<sub>4</sub> 2D quantum wells have been probed for resonant third order non linearity's (Calabrese J, *et al*, 1991; Xu C. Q, *et al*, 1991; Kondo T, *et al*, 1998) and more recently for (PEA)<sub>2</sub>PbI<sub>4</sub> (Shimizu M, *et al*, 2007). The  $\chi^{(3)}(-3\omega, \omega, \omega, \omega)$  of a highly oriented film



of C10PbI<sub>4</sub> displayed a large (THG) three photon resonance at 1.53 $\mu$ m (considering the  $E_g = 2.43\text{eV}, 511.8\text{nm}$ ). This was caused from the lowest energy exciton which is known to have a large oscillator strength and sharp well defined emission profile. It was also surmised that since both  $\chi^{(3)}(-3\omega, \omega, \omega, \omega)$  and  $\chi^{(3)}(-\omega, \omega, \omega, -\omega)$  follow the same transition rule, a resonance enhancement due to the lowest energy exciton can also be expected for  $\chi^{(3)}(-\omega, \omega, \omega, -\omega)$  for C10PbI<sub>4</sub>. Moreover the magnitude of the  $\chi^{(3)}(-3\omega, \omega, \omega, \omega)$  reaches a very large value of  $0.7 \times 10^{-9}\text{esu}$  at incoming beam 1.53 $\mu$ m, THG = 511nm, which is comparable to the largest reported value of organic materials with one-dimensional structures. The result was reported to be very promising suggesting that the lead halide quantum well structures are very promising as nonlinear optical materials (Xu C. Q, *et al*, 1991). The  $\chi^{(3)}(-\omega, \omega, \omega, -\omega)$  was also investigated for C6PbI<sub>4</sub> where the nonlinear optical susceptibility was recorded as  $1.6 \times 10^{-6}\text{esu}$  also measured at the lowest exciton resonance (measured at 8K). Kondo T, *et al*, 1998 further commented that because the excitons are stable at room temperature, large nonlinear optical responses are therefore also expected at room temperature, and hence remain a class of materials with promising resonant nonlinear optical potential.

More recently an investigation of these three compounds was completed in order to study the effect of the dielectric confinement caused from the large dielectric mismatch between the well and the barrier and discovered the exciton bleaching and blue shift are larger in the (C6)<sub>2</sub>PbI<sub>4</sub> than in (PEA)<sub>2</sub>PbI<sub>4</sub> (Shimizu M, *et al*, 2005), which is advantageous for practical application.

Traditionally only organic or inorganic compounds crystallising in noncentrosymmetric space groups and have some degree of polarisability, have been investigated for their SHG responses. Hybrids are an alternative approach to finding NLO crystals with a large SHG response, as the anionic nature of the hybrids should automatically increase the (hyper)polarizability of the crystal, thereby giving larger SHG responses for hybrid type materials (Giffard M, *et al*, 2005).

In other studies the compound  $\{[\text{NH}_3(\text{CH}_2)_2\text{SS}(\text{CH}_2)_2\text{NH}_3]\text{PbI}_5\}\text{H}_3\text{O}$ , which has been reported to form 1D corner sharing chains, and crystallize in a chiral space group  $P2_1$  was shown to be a good candidate for (SHG) investigation (Mercier N, *et al*, 2006). In addition, this compound underwent a reversible phase change at 75°C. The high temperature form shifted into the space group  $P2_1/n$ . The centre of inversion generated from the phase change then suppressed the SHG response. The phase change occurred as a result of a conformational change in the organic

cation, which induced a mirror plane in the crystal above 75°C as seen in figure 2.58. Thus this material was observed to behave as a Second Harmonic Generation (SHG) switch driven by temperature. It was reported that even after 20 temperature cycles the crystal remained intact, and continued to oscillate with temperature between the chiral and non-chiral space groups (Mercier N, *et al*, 2006). A similar investigation was also completed for a bismuth iodide hybrid with the same disulphide cation, and reported the same chiral to nonchiral phase change upon temperature increase (Bi W, *et al*, 2008).

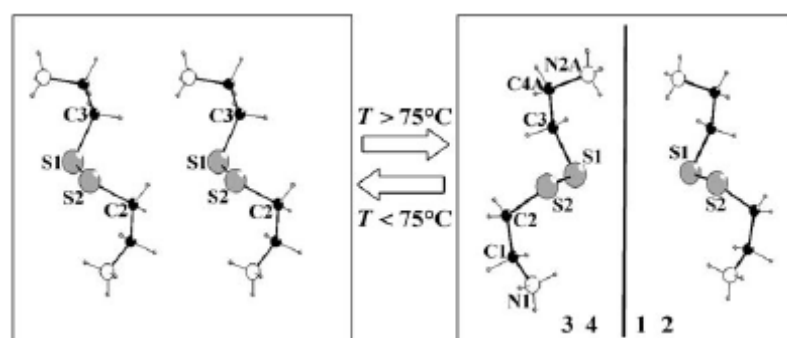


**Figure 2.58:** Schematic representation of the conformational change of the organic diamine in the  $\{[\text{NH}_3(\text{CH}_2)_2\text{SS}(\text{CH}_2)_2\text{NH}_3]\text{PbI}_3\}\text{H}_3\text{O}$  hybrid system at 75°C (Mercier N, *et al*, 2006).

The use of the highly efficient (SHG) organic cation (trans-4-[4-dimethylamino-styryl]-1-methylpyridinium), DAMS<sup>+</sup> has been reported to form 1D chains with lead iodide and dimethyl sulphoxide i.e. (DAMS)PbI<sub>3</sub>·2DMSO which crystallized in the noncentrosymmetric space group *Ic* (Guloy A. M, *et al*, 2001). The thought process behind combining these two components was firstly, to use the low dimensional nature of lead iodide to template (DAMS) into a polarized configuration, and increasing its polarizability by creating a charge on the organic molecule. Secondly the 1D wires are highly polarisable down one of the crystallographic directions, and was hypothesized that this ability may further enhance the SHG response of the crystal. It was then reported that (DAMS)PbI<sub>3</sub>·2DMSO crystal displayed a SHG response 15 times greater than that of KTP (potassium tantalum phosphate) when probed at 1390nm (Guloy A. M, *et al*, 2001). However it was also reported that when the crystal was probed at 1032nm, the 532nm SHG response also displayed a luminescence peak at 620nm (Guloy A. M, *et al*, 2001). Since the direct gap absorption from the wires should only occur around 380nm (Nagami A, *et al*, 1996) the reported red luminescence response should be due to a charge transfer mechanism occurring from the wires to the spacers or originate from the STE response as are experienced in these wires. The 532nm excitation generated from the SHG response should be sufficient to populate the LUMO of the organic cation with the electrons from the valence band of the wires,

and hence display a luminescence response at 620nm (however this was not reported in the paper, but the red colour of the crystal, and the short intermolecular distances of  $\sim 3.4\text{\AA}$  of DAMS molecules does suggest that this should be the case (Guloy A. M, *et al*, 2001)).

Other investigations of the halogen substituted (DAMS)PbBr<sub>3</sub> SHG response was also reported (Papavassiliou G. C, *et al*, 2003). This compound also displayed the red luminescence with the 532nm SHG response. Interestingly the Bromide analogue crystallized in a centrosymmetric space group *I2/a* and still displayed a large SHG response. This is thought to be due to the large anisotropic effect of the 1D wires over the centre of inversion generated by the organic cation (Papavassiliou G. C, *et al*, 2003). Other NLO studies on similar compounds have also been completed by (Papavassiliou G. C, *et al*, 1999; 1999b; 2001; Goto T, *et al*, 2002). Furthermore DAMS has been successfully investigated with the transition metal hybrids, and displayed large SHG responses specifically with the Copper Iodide analogue (Cariati E, *et al*, 2001).

## **2.9 Electroluminescent devices and the use of chromophores in 2D hybrids**

The first attempt at creating an electroluminescent device from a hybrid perovskite was with (PEA)<sub>2</sub>PbI<sub>4</sub> and (cyclohexylethylammonium)<sub>2</sub>PbI<sub>4</sub> which was investigated by (Hong X, *et al*, 1992; Era M, *et al*, 1994; 1995). They showed electroluminescence at LNT of 10 000 cd/m<sup>2</sup> at 2A.cm<sup>-2</sup> and 24V, however could not get any EL at room temperature. It was suggested that the rapid drop off in EL efficiency was due to thermal quenching of the excitons. More recently however (Pradeesh K, *et al*, 2009a) investigated a novel in situ-intercalation method to fabricate device quality hybrid inorganic organic self assembled quantum wells of the unsaturated cyclohexylethylamine (C<sub>6</sub>H<sub>9</sub>C<sub>2</sub>H<sub>4</sub>NH<sub>3</sub>)<sub>2</sub>PbI<sub>4</sub>. Pradeesh K, *et al*, 2009a showed promising results, displaying in particular the increasing in room temperature photoluminescence intensity with increasing film thickness.

Mitzi D. B, *et al*, 2001c, investigated the incorporation of a chromophore 5,5'''-bis(aminoethyl)-2,2':5',2'':5'',2'''-quaterthiophene (AEQT) with lead halide to form 2D (AEQT)PbX<sub>4</sub> where X = Cl, Br, or I. The reason for incorporating AEQT into the perovskite layers, is that the chromophore itself displays better room temperature electroluminescence than the semiconducting perovskite layers on their own (PbX<sub>4</sub><sup>2-</sup>). So then why is it necessary to have the inorganic component present in the system? The inorganic component adds thermal stability to the

organic compound (Mitzi D. B, *et al*, 2001c), and therefore the incorporation of the Dye (AEQT), as seen in figure 2.59 (the crystal structure of (AEQT)PbBr<sub>4</sub>).

From the three halogenated 2D systems investigated the (AEQT)PbCl<sub>4</sub> hybrid displayed a greater room temperature electroluminescence efficiency (20-30 times) than that of its bromide and iodide analogues. It was found that the wider the band gaps of the inorganic component the greater the electroluminescence efficiency shown. This was further supported from the investigations of an even wider band gap hybrid (AEQT)CdCl<sub>4</sub> which displayed ever better EL efficiency compared to (AEQT)PbCl<sub>4</sub>. Mitzi D. B, *et al*, 2001c suggested this phenomenon was due to better carrier injection, transport and electron hole recombination in the wider band gap systems. The UV-Vis spectrum of (AEQT)PbCl<sub>4</sub> and the EL device manufactured from this material may be seen in figure 2.60.

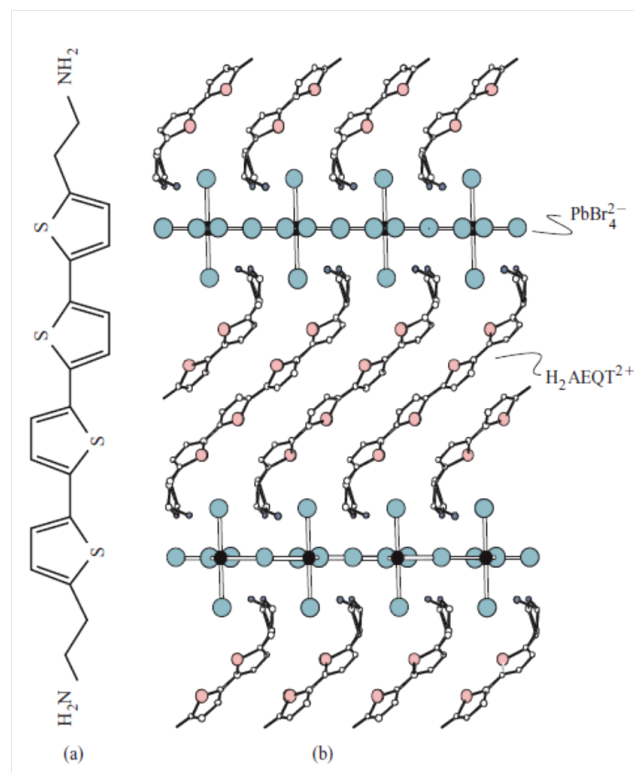


**Figure 2.59:** The use of the Chromophore 5,5'''-bis(aminoethyl)-2,2':5',2'':5'',2'''-quaterthiophene (AEQT) with in (AEQT)PbX<sub>4</sub>, where X = Cl, Br, and I (Mitzi D. B, *et al*, 2001c).

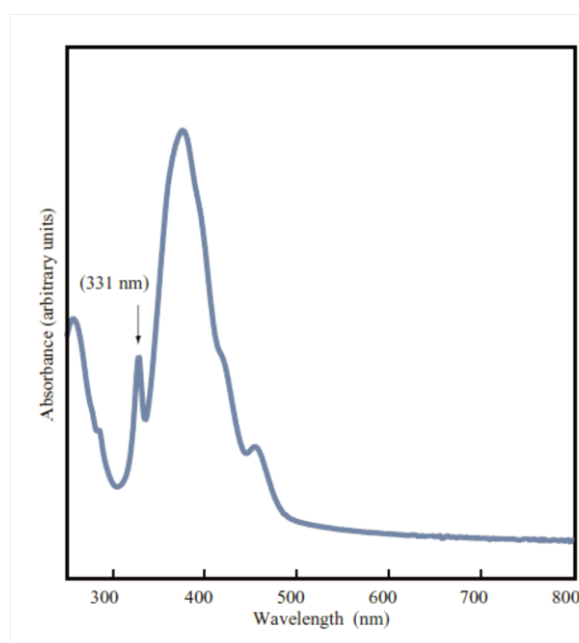
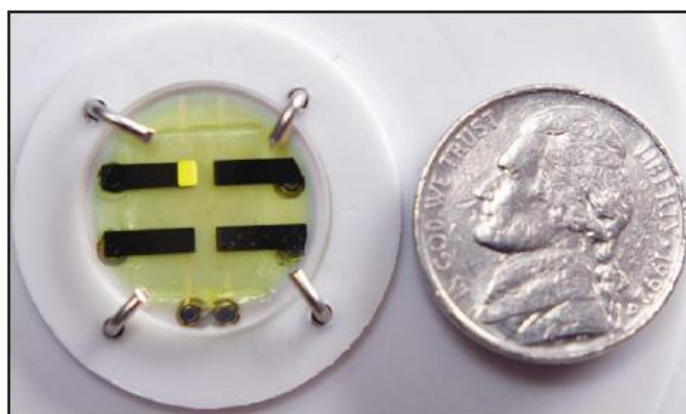


**Figure 2.60:** (Top) Electroluminescent device of the chromophore hybrid (AEQT)PbCl<sub>4</sub>, (Bottom) the UV-Vis absorption spectrum of (AEQT)PbCl<sub>4</sub>. The 331nm peak associated with the PbCl<sub>4</sub> layers and the broad 400nm peak with the AEQT dye (Mitzi D. B, *et al*, 2001c).

The other contributing papers to the above set of work should also be mentioned, namely (Chondroudis K and Mitzi D. B, 1999), in their investigations in the electroluminescence from an organic inorganic perovskite incorporating a quaterthiophene dye within lead halide perovskite layers (PbX<sub>4</sub>); design structure and optical properties of organic inorganic perovskites containing an Oligothiophene chromophore (Mitzi D. B, *et al*, 1999b); the effect of thermal annealing on the optical and morphological properties of (AETH)PbX<sub>4</sub> (Chondroudis K, *et al*, 2000b); and the use of ionic salt dyes as amorphous, thermally stable emitting layers in organic LED's (Chondroudis K and Mitzi D. B, 2000a).

Other more recent developments have investigated the incorporation of naphthalene into organic inorganic hybrid quantum well materials and shown nearly perfect triplet-triplet energy

transfer from wannier excitons (Ema K, *et al*, 2008). Also an interesting development has been the fabrication and characterization of organic inorganic perovskite films containing fullerene derivatives (Kikuchi K, *et al*, 2005). Although device fabrication is not the focus of the work in this thesis it is worth mentioning the other developments in this field. Various methodologies have been employed in the light emitting diode (LED) and organic light emitting diode (OLED) communities for their use of these materials for highly efficient displays. The review article on Inorganic organic Hybrid structured LED's (Gebauer T and Schmid G, 1999) give broader insights into this field. Spin-Coating preparation of highly ordered photoluminescent films of layered Pbl<sub>2</sub> aminoalkyloxysilane perovskites have also shown promise for further development (Cheng Z. Y, *et al*, 2005). And finally is the synthesis of liquid crystalline poly(1-pentyne)s and fabrication of polyacetylene-perovskite hybrids (Hua J, *et al*, 2006) and functional perovskite hybrid of polyacetylene ammonium lead bromide (Xu H, *et al*, 2006) for more robust device quality operation.

## **2.10 Summary and Conclusions**

In summary, in this chapter we have covered the origin of the organic inorganic hybrid perovskites specifically from the three dimensional motif. The concept of dimensional reduction and its impact on the electronic properties of the material was also illustrated. We have also shown the two mechanisms that can be used to create low dimensional systems. Namely, the traditional method developed from cutting various slices from the 3D perovskite motif, and the various inorganic motif types that can arise through altering I/M ratio's, organic weak interaction effects, and solvent effects. More attention has been focussed on the excitonic behaviour in the 2D and 1D systems with discussions of the phase transitions that may arise through temperature fluctuations as this forms the basis for the results we discuss in chapters 4 and 5. We have only briefly touched on the literature on the nonlinear optics of hybrid materials as this topic's background is developed more thoroughly in chapter 6. Lastly, a brief summary of electroluminescent devices developed from hybrid organic inorganic systems allows us to see the applicability of the research for further device development.

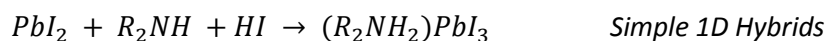
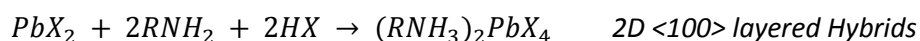
## Chapter 3: Experimental

### 3. Experimental:

Herein we report the synthesis and characterization techniques used to prepare and analyze the inorganic-organic hybrids investigated. The simple synthesis techniques will first be explained followed by a description of the characterization techniques used.

#### 3.1 Synthesis:

Two methodologies were employed in order to synthesize and grow single crystals of the hybrid materials. They follow the general equations given below.



##### 3.1.1 Slow cooling method:

The slow cooling method was employed whereby a stoichiometric amount of  $PbX_2$  salt (generally 0.1g of the metal halide salt) (where  $X = I$  or  $Br$ ) was added to a 10 or 20ml sample vial. Stoichiometric amounts of  $RNH_2$  was then added followed by the addition of an excess amount of either 47% aqueous Hydro-iodic acid or 48% aqueous Hydro-Bromic acid depending on the metal halide salt used. Approximately 2-8ml of acid was added depending on the solubility which is largely governed by the ammonium cation. A precipitate usually formed, initial dissolution was usually assisted by ultrasonication, which assisted in adequately dispersing the precipitate and hence dissolution. The precipitate usually only dissolved after heating to  $90^\circ\text{C}$ , therefore the sample vial was heated to  $90^\circ\text{C}$  and subsequently refluxed at this temperature for ~6hours (this was a critical step for the alcohol based amines, as they substituted the alcohol for the halide, compounds in chapter 4). The sample was then slow cooled in a controlled manner at a rate of  $1-2^\circ\text{C}/\text{min}$  to room temperature. If the crystals formed were not large enough or not of high enough quality the heating cycle was repeated until suitably sized crystals of adequate quality could be harvested for SC-XRD. It was generally found that the more saturated solutions produced better crystals, and that complete dissolution of the precipitate at  $90^\circ\text{C}$  is crucial. The following compounds were synthesized and crystals grown using this methodology. For the 2D layered perovskites (where  $C_n = C_nH_{2n+1}NH_3$ ):  $(C_n)_2PbBr_4$  where  $n = 4-7$ ;  $(XC_n)_2PbBr_4$  where  $X = OH$  for  $n = 2$  and  $Br$  for  $n = 3-5$ ;  $(C_n)_2PbI_4$  where  $n = 4-7$ ; and the 1D chains in 5.3 of  $(H_3NPhCH_2PhNH_3)Pb_2I_6$ ; and  $(H_3NPhPhNH_3)Pb_2I_6 \cdot 2H_2O$ .

### **3.1.2 Slow evaporation method:**

In the case where the slow cooling method did not work or was not attempted due to reactivity concerns, slow evaporation was used instead. Due to solubility issues and reactivity with the solvent (DMF) or the organic cation, only a stoichiometric amount of the halide acid was added to a  $\text{MX}_2 + z\text{RNH}_2$  reaction mixture. A suitable organic solvent was used to dissolve the reaction mixture. The dissolution of the reaction mixture was generally assisted by placing the sample vial in an ultrasound bath. The dissolved mixture was then allowed to evaporate to grow suitably sized crystals.

Dimethyl formamide (DMF) was used in the synthesis of the 1D chains of 5.1 and 5.2 as seen in the schemes below.

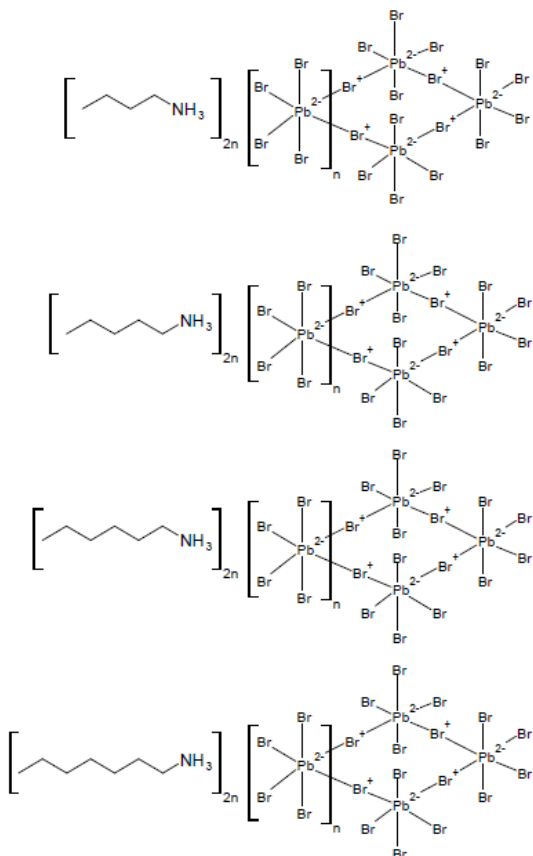
Dimethyl sulphoxide (DMSO) was used for the following compounds: the 1D chains of (5.3)  $\text{DMSO} \cdot (4,4'\text{-Bipyridine})\text{Pb}_2\text{I}_6$ ;  $\text{DMSO} \cdot (4,4'\text{-propane-1,3-dipyridine})\text{Pb}_2\text{I}_6$  and  $(4,4'\text{-(E)-ethene-1,2-dipyridine})\text{Pb}_2\text{I}_6$ .

Acetonitrile was used for the following compounds: The 2D layered perovskites of  $(\text{BrC}_2\text{H}_4\text{NH}_3)_2\text{PbI}_4$  and  $(\text{HOC}_2\text{H}_4\text{NH}_3)_2\text{PbI}_4$  in which slow evaporation was carried out at  $4^\circ\text{C}$  in order to obtain the kinetic product. The 2D layered perovskites of  $(\text{IC}_n\text{H}_{2n}\text{NH}_3)_2\text{PbI}_4$  where  $n = 2-6$  were first refluxed at  $100^\circ\text{C}$  for 1-2 hours, then allowed to slowly evaporate. In order to obtain the halogenated aliphatics  $(\text{IC}_n\text{H}_{2n}\text{NH}_3)_2\text{PbI}_4$  where  $n = 2-6$ , the respective alcohol starting materials  $(\text{HOC}_n\text{H}_{2n}\text{NH}_2)$  where  $n = 2-6$ , were used. The reflux step in the synthesis is necessary to convert the alcohol group to the halogenated group.

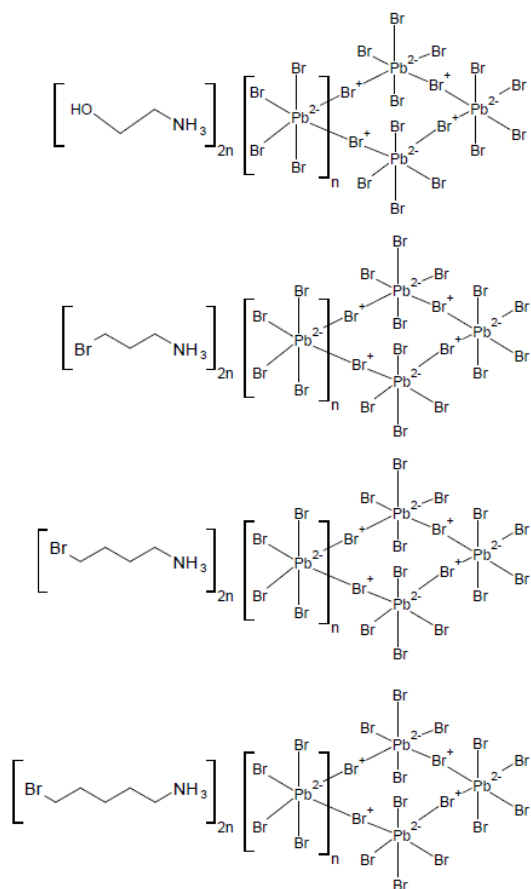


### 3.1.3 Schemes of compounds investigated with relevant chapter numbers:

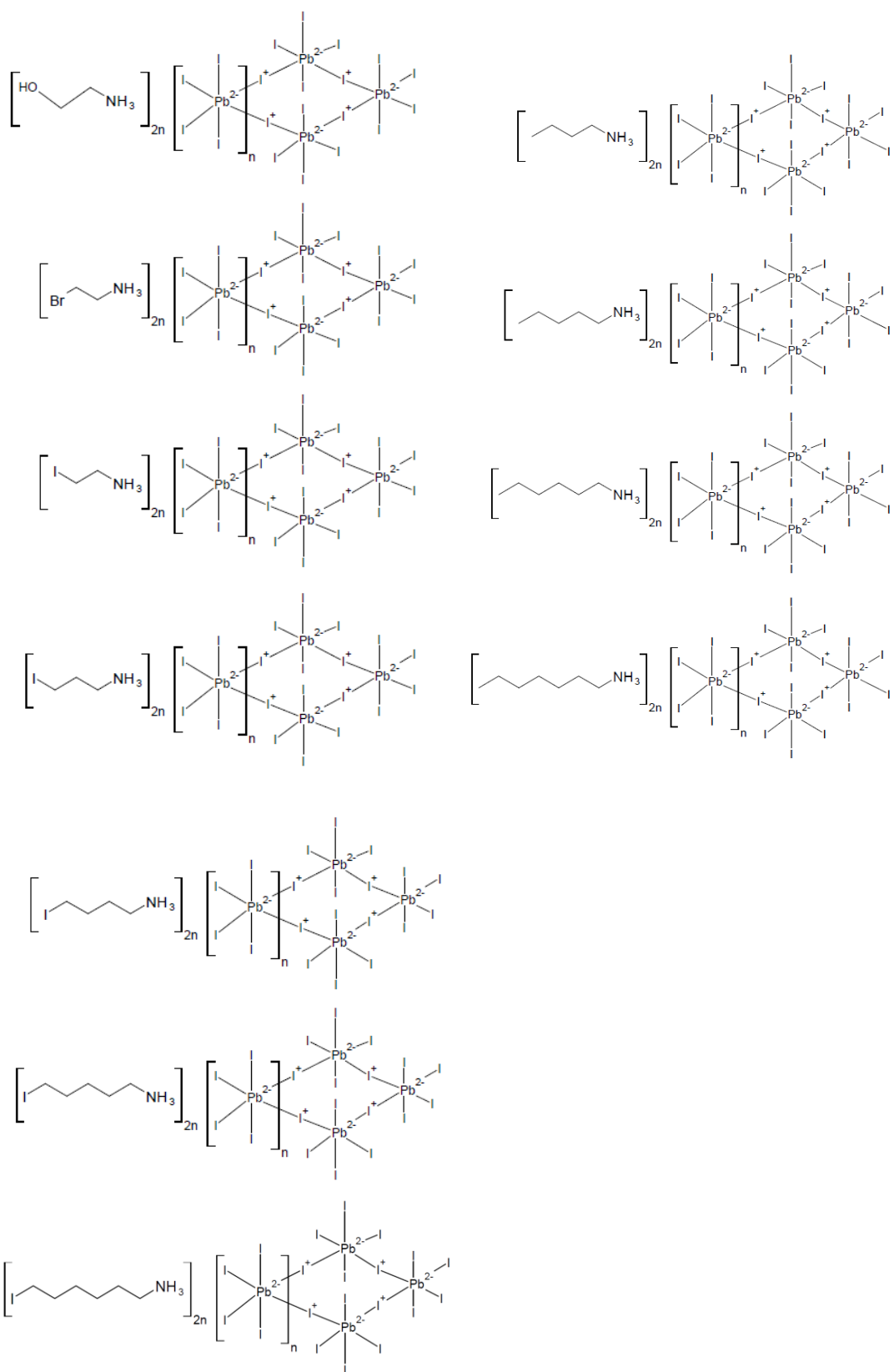
4.1



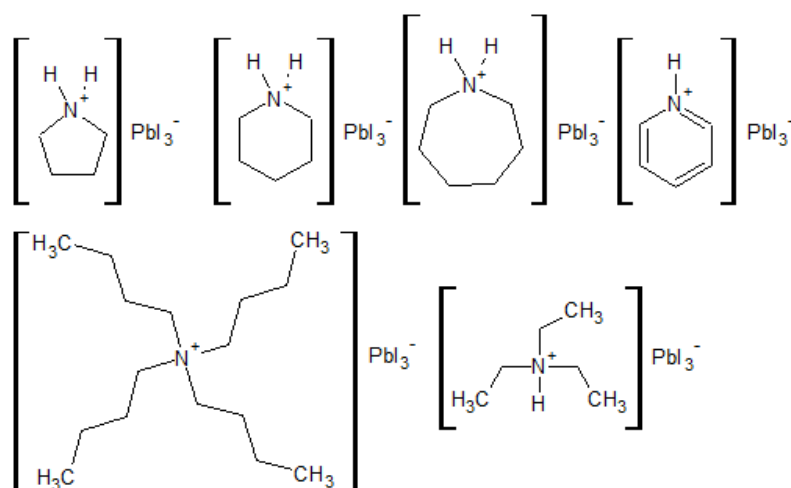
4.2



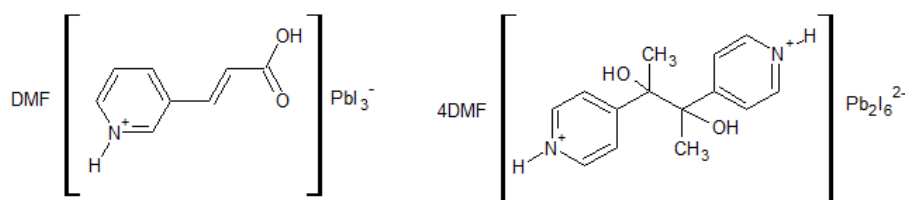
### 4.3



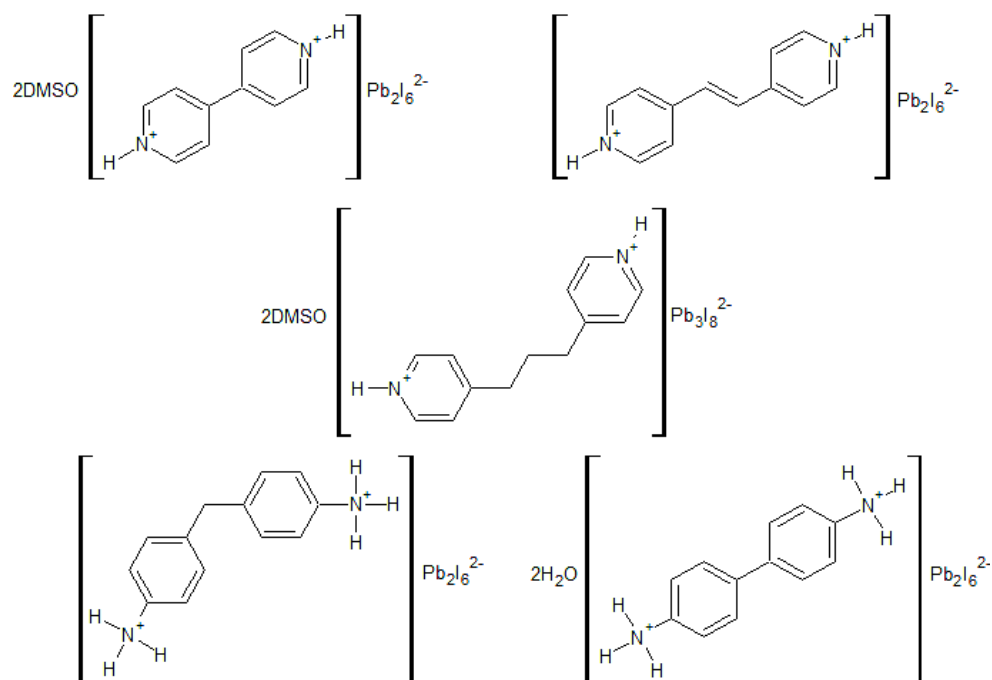
## 5.1



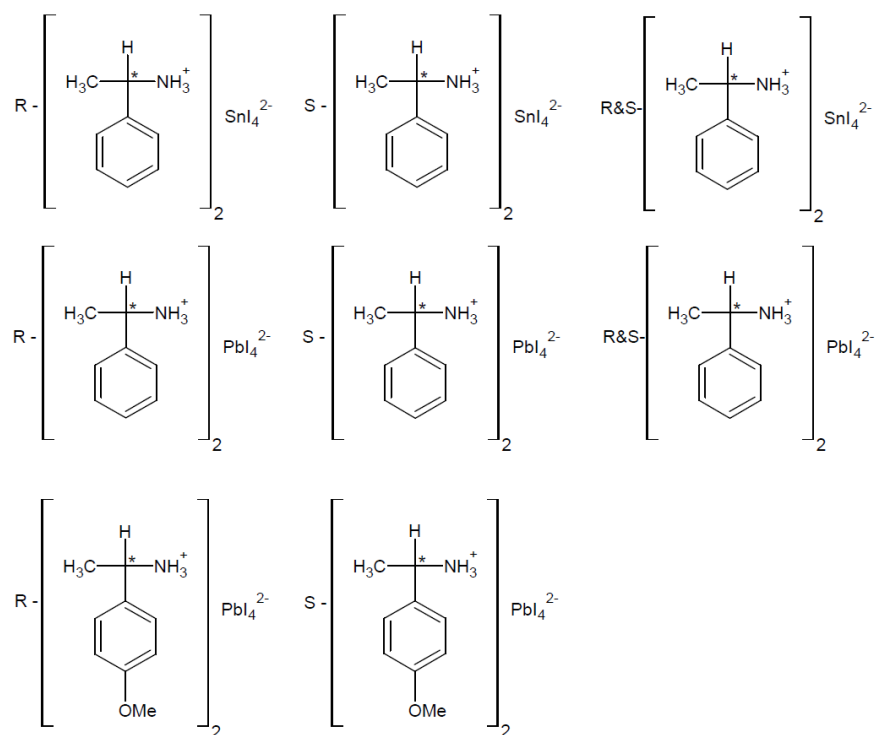
## 5.2



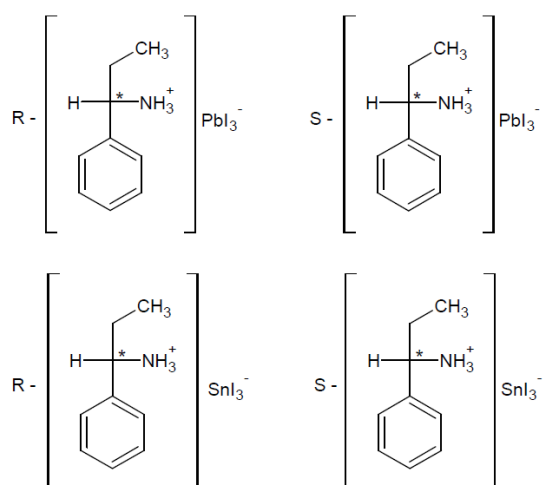
## 5.3



## 6.2



## 6.3



### 3.2 Single crystal X-ray diffraction (SC-XRD):

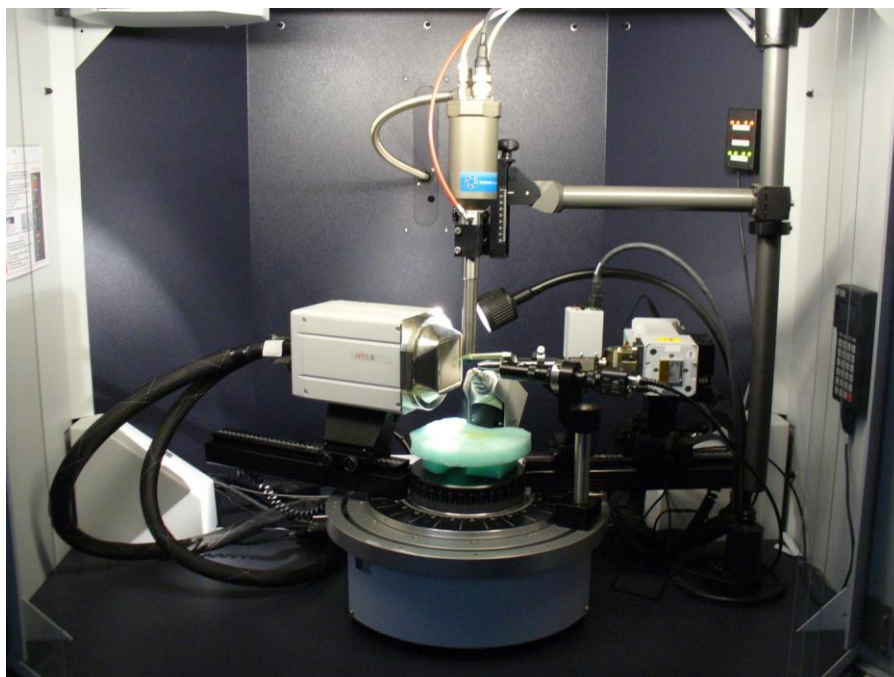


**Figure 3.1:** The Bruker Apex II single crystal diffractometer with Mo  $K_{\alpha}$  radiation, with attached Oxford cryostream cooler Series 700.

Intensity data were collected on a Bruker APEX II CCD area detector diffractometer with graphite monochromated Mo  $K_{\alpha}$  radiation (50kV, 30mA) using the APEX 2 (Bruker, 2005a) data collection software. The collection method involved  $\omega$ -scans of width  $0.5^{\circ}$  and 512x512 bit data frames. Data reduction was carried out using the program *SAINT+* (Bruker, 2005b) and face indexed absorption corrections were made using *XPREF* (Bruker, 2005b).

The crystal structures were solved by direct methods using *SHELXS* (Sheldrick G. M, 2008) and WinGX (Farrugia, 1999). Non-hydrogen atoms were first refined isotropically followed by anisotropic refinement by full matrix least-squares calculations based on  $F^2$  using *SHELXL* (Sheldrick G. M, 2008). Hydrogen atoms were first located in the difference map then positioned geometrically and allowed to ride on their respective parent atoms. Diagrams and publication material were generated using *SHELXL*, *PLATON* (Spek A. L, 2009) and *ORTEP-3* (Farrugia L. J, 1997). Temperature was controlled using the Oxford cryostream cooler Series 700, with variable temperature capabilities with a temperature range of (100-400K). Most of the hybrid materials, data collections, were obtained at various temperatures. Specifically the hybrids of chapter 4.1; 4.2; and 5.1. The remaining structures were all collected at 173K for higher resolution, and 293K to ascertain if the compounds underwent any further low temperature phase transitions unable to be detected from the DSC experiments.

### 3.2.1 References:

Brandenburg K, *Diamond version 3.1f. Crystal impact GbR Bonn, Germany.* (1997)

Bruker, *APEX2. Version 2.0-1. Bruker AXS Inc., Madison, Wisconsin, USA.* (2005a)

Bruker, *SAINT+. Version 6.0. (Includes XPREP and SADABS) Bruker AXS Inc., Madison, Wisconsin, USA.* (2005b)

Bruker, *SHELXTL. Version 5.1. (Includes XL, XS, XP and XSHELL) Bruker AXS Inc., Madison, Wisconsin, USA.* (1999)

Farrugia L.J, *J. Appl. Cryst.*, (1997) **30**, 565

Farrugia L.J, *J. Appl. Cryst.*, (1999) **32**, 837

Sheldrick G. M, *Acta. Cryst.*, (2008) **A64**, 112

Spek A. L, *Acta. Cryst.*, (2009) **D65**, 148

### 3.3 Powder X-ray Diffraction (P-XRD):

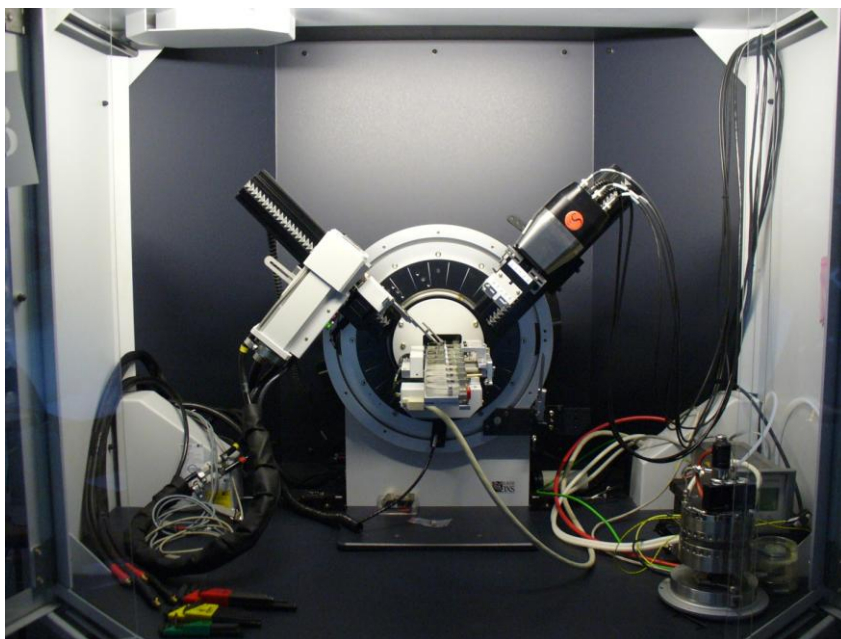


**Figure 3.2:** The Bruker D8 Advance powder diffractometer with the Vantec super-speed MIKROGAP™ detector, and Cu  $K_{\alpha 1}$ ,  $K_{\alpha 2}$  spectral lines, as  $K_{\beta}$  was suppressed using a Ni filter.

X-ray powder diffraction data were collected on a Bruker-AXS *D8 ADVANCE* diffractometer equipped with a Cu tube and Ni-filter. The diffractometer was operated in the parallel beam geometry with the data collected using a Vantec super-speed MIKROGAP™ detector. Each sample was dispersed as a finely ground powder onto a zero-background silicon wafer sample holder. All data collections were performed over the range  $5^{\circ}$  -  $90^{\circ}$   $2\theta$  using a step size of  $2\theta = 0.01^{\circ}$  and a counting time of 2 sec/step, and in reflection mode. Cell and rietveld refinements were carried out using the *TOPAS V4.2* package (Coelho A. A, 2000). Samples were also measured on the Bruker-AXS *D2 PHASER* which is in the Bragg-Brentano geometry, with a Lynx-eye detector. Similar scanning parameters used with the *D8 ADVANCE* were used to obtain powder diffraction data.

#### 3.3.1 References:

Coelho A. A, *TOPAS v4.2: General Profile and Structure Analysis Software for Powder Diffraction Data* Karlsruhe. (2000)

### 3.4 Photoluminescence:



**Figure 3.3:** The experimental set up used for the photoluminescence measurements. The UV laser had to pass outside the original optics, as the instrument was not UV optics capable. Hence a set of mirrors redirected the beam to avoid the internal optics, and onto the sample to excite the compound in order to measure the photoluminescence response. The sample is mounted in the cryostat and cooled down with liquid nitrogen to 77K through a temperature controller.

Photoluminescence spectra were acquired with the multiline UV (333.6 – 363.8nm) of an argon ion laser as the excitation source. Light emission was undertaken through the temperature controlled Linkam (THMS350V) cryostat mounted onto the spectrograph stage of a Jobin-Yvon T64000 Raman spectrometer. The power at the sample was kept very low ( $\sim 0.20$  mW) so as to not cause sample degradation, whereas the laser-beam diameter at the sample was about 1  $\mu\text{m}$ . The samples were generally measured at both 77K and 293K.

### 3.5 UV-Vis:

For the UV-vis spectral analysis, a small portion of solvent containing the product was slow evaporated off a circular sapphire disc (0.1X10mm) in order to deposit the crystals evenly on the surface. The samples were inserted into a custom built nitrogen bath cryostat, where scans were performed at 77K and room temperature. The scanned range was 200–800 nm, and carried out using a Varian Cary 500 digital spectrophotometer.



### **3.6 Thermal analysis (DSC):**

Differential Scanning Calorimetry (DSC) was used to determine the transition temperatures of the phase transitions and their enthalpies under atmospheric conditions. All DSC experiments were carried out on a Mettler Toledo 822e calorimeter, which was fitted with a cryostream in order to cool to 213K. The temperature range of the instrument is from 213-773K. Our measurements were performed from 213K-443K. This temperature range was sufficient to monitor all the phase transitions of the hybrid materials under investigation. Measurements were both heated and cooled through the above mentioned temperature range, at a heating and cooling rate of 10K/min respectively. All the compounds reported in this project were investigated for any thermal events in the above mentioned temperature range.

### **3.7 Elemental analysis:**

Elemental analysis of the compounds in 5.1 and 5.2 were performed by the Institute of Soil, Climate and Weather (Pretoria, South Africa). The instrument used was a Carlo Erba Instruments, model NA 1500, Nitrogen/Carbon/Sulphur Analyser. The instrument was modified to do CHN elemental analyses as well (Philpott, 2002).

## **Chapter 4: The structure and optical properties of <100> 2D lead halide quantum wells**

### **4.1 The Structure and Phase transitions of $(C_nH_{2n+1}NH_3)_2PbBr_4$ where $n = 4-7$**

#### **4.1.1 Introduction:**

The 2D layered aliphatic  $(C_nH_{2n+1}NH_3)_2PbX_4$  hybrid perovskite compounds, represented as  $(Cn)PbX_4$  from here, have been thoroughly investigated over the years. The Lead Bromide 2D hybrids are understudied by comparison with their iodide analogues. This is the case as the lead bromide hybrids were thought to display fundamentally similar optical properties, only the band gap was blue shifted relative to the iodide analogue (Papavassiliou G. C, 1997). The red shift of the band gap experienced as we proceed down the group ( $Cl \rightarrow I$ ) is due to the increase in covalent character of the halogen bonding with the lead. The band assignments are expected to remain the same for each of the halogenated systems, and should experience the same red shift as we proceed down the group ( $Cl \rightarrow I$ ) (Azuma J, *et al*, 2002a). However after further investigation, it was discovered that the PbBr hybrids specifically, display a more intricate emission spectra as seen for the simple aliphatic type compounds (Kato Y, *et al*, 2003; Ema K, *et al*, 2006; Kitazawa N, *et al*, 2009; 2010).

It should be noted that there are very few crystal structures reported for the <100> type 2D lead bromide hybrids. The crystal structures have been challenging to obtain through SC-XRD techniques, largely due to diffuse scattering issues, and therefore other methodologies have been employed to confirm the two dimensional nature of the lead bromide hybrids. Powder diffraction studies have been employed to obtain the interlayer spacing of the hybrid, in conjunction with optical absorption measurements to confirm the compounds two dimensional nature (Lee S. J, *et al*, 2000; Tabuchi Y, *et al*, 2000; Kitazawa N, *et al*, 2010; 2010b). The alternate methodologies have been employed as a result of the importance of investigating the optical properties associated with these compounds.

Success with determining the crystal structures of the  $(Cn)PbI_4$  layered hybrids, where  $n = 4-10, 12, 14, 16$ , and  $18$ , (Billing D. G, Lemmerer A, 2007; 2008; Lemmerer A, 2007; Lemmerer A, Billing D. G, 2011; Nagapetyan S. S, *et al*, 1988; Ishihara T, *et al*, 1990; Mitzi D. B, 1996) have been achieved. Furthermore the multiple phase transitions associated with the aliphatic templates have been categorically investigated for each of the abovementioned systems by (Billing D. G, Lemmerer A, 2007; 2008; Lemmerer A, 2007). The importance of the phase transitions on the optical properties has been realized and investigated recently for  $(C12)PbI_4$  by (Pradeesh K, *et al*,

2009b). Simple conformational changes in the aliphatic have negligible impact on the band gap of the hybrid (Ishihara T, *et al*, 1989; 1990) however, certain phase changes for example, upon heating result in the inorganic layers decreasing the degree of distortion of the layers, specifically the corrugation tilt  $\psi$  and Pb-X-Pb bridging angles which move toward their ideal  $0^\circ$  and  $180^\circ$ , respectively. These two parameters have been shown to have the largest impact on the band gap of the material (Knutson J. L, *et al*, 2005). The red shift of the band gap, as these angles move toward ideallity, is due to an increase of the stereochemical activity of lead's lone pair of electrons (Mitzi D. B, 1996; Knutson J. L, *et al*, 2005). Other phase transition mechanisms present in these systems include the inorganic layers rearranging between the eclipsed and staggered arrangements upon heating (i.e. the monoclinic and orthorhombic phases) with an associated and correlated decrease in inorganic octahedral distortions. These high temperature phases in conjunction with the decrease in overall distortions further lead to an increase in crystal symmetry. This phenomenon is well known and noted that the structural phase transitions change the crystal system from monoclinic to orthorhombic and finally to tetragonal with increasing temperature (Mitzi D. B, 1999; Billing D. G, Lemmerer A, 2007; 2008; Lemmerer A, 2007).

Billing and Lemmerer observed that the longer chain aliphatics  $n = 12, 14, 16$  and  $18$ , in  $(Cn)PbI_4$  hybrids display a decrease in crystal symmetry with increasing temperature, i.e. they move from the orthorhombic low temperature (staggered layers) to a monoclinic (eclipsed layers) at high temperature, however still observing the decrease in octahedral distortions with the increase in temperature (Billing D. G, and Lemmerer A, 2009). They were also able to confirm the structural details of the phase transformations with changing temperature of the  $(Cn)PbI_4$  series, and confirm the similarity of the phase transformation mechanisms of the originally investigated  $(Cn)MCl_4$  hybrids where  $M = Mn, Cu, Cd$ , but most comprehensively studied structurally in the  $(Cn)CdCl_4$  hybrids (Chanh N. B, *et al*, 1983; 1985; 1989; Kind R, *et al*, 1979; Ricard L, *et al*, 1984; Shenk K. J, and Chapuis G, 1988). Although the packing of the aliphatic chains in the transition metal hybrids are non-interdigitated unlike the lead iodide hybrids where the chains pack in an interdigitated fashion, the phase transformation mechanism proceed through a similar path. It has been proposed that the reason for the chains to pack in an interdigitated fashion regards the separation of the metal centres of the corner sharing octahedra from one another, i.e. the farther away the metal centres are from one other the more likely the chains will interdigitate (Nagapetyan S. S, *et al*, 1988).

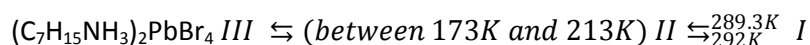
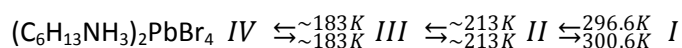
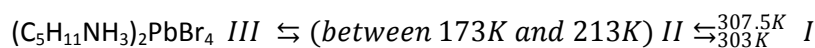
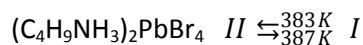
Within the layered hybrid perovskites, the changes in the organic conformations result in the solid state phase transitions to occur through one of two mechanisms. Firstly are the displacive phase transitions, i.e. associated with conformational changes of the organic ammonium group. And secondly is the order-disorder phase transition along the longitudinal axis of the unit cell. Since the alkyl ammonium chains are so flexible the  $(C_nH_{2n+1}NH_3)_2MX_4$  hybrids undergo multiple phase transitions. The phase transition progression ultimately results in a quasi-melting transition of the organic chain at higher temperatures.

This, invariably final transition, only occurs after proceeding through a few solid state conformational intermediates. These conformational intermediates proceed through the following generally accepted mechanisms. The chains may exist in an all trans conformation or kinks may arise within the chain. A kink consists of two gauche conformations of opposite signs, separated by an odd number of all trans conformations. At higher temperatures the various conformations become mobile. When two kinks of opposite sign meet each other they can annihilate. Conversely kinks may form spontaneously in sections of the chain with the all trans conformations. The combination of these conformational changes results in the quasi melting transition to occur (Depmeier W, 2009; Kind R, 1980). The quasi melting transition also displays the highest enthalpy and entropy change for a transition. In addition the quasi-melting transition refers to only the alkyl chain melting, with the overall compound still remaining in the solid state (Chanh N. B, *et al*, 1989). As the temperature increases and the alkyl ammonium hybrid moves through the series of solid state intermediates, the inorganic layers result in an increase in interlayer spacing as the rotational disordering of the chains increases (Barman S, *et al*, 2003).

An observation regarding the alkyl chain length and the phase transitions that they undergo was made by (Mitzi D. B, 1999). The order disorder type transitions are the only phase transitions that occur when the organic ammonium chain length is  $n \leq 2$ , however both types of transitions occur when the chain length  $n \geq 3$  i.e. displacive and order disorder. Incommensurate phases have also been observed, however only for  $(C3)MCl_4$  where  $M = Cd, Mn$  and  $Cu$  hybrids. The  $Cd$  hybrid has three phases, a disorder and displacive phase III and I, respectively, and an incommensurate phase II (Chapuis, G, 1978; Doudin B and Chapuis G, 1988). The  $Mn$  hybrid has six phases and proceeds through commensurate and incommensurate phases all the way to the last two high temperature commensurate phases (Depmeier W and Mason S. A, 1978; 1983; Harris, *et al*, 1994; Depmeier W, 2009). Interestingly the  $(C3)PbI_4$  hybrid investigated does not form a 2D layered hybrid perovskite but rather a 2D net type motif (Billing D. G and Lemmerer A, 2006b). The importance of the presence of modulated phases in

semiconducting hybrids may influence the emission profile experienced for that compound. As modulation, or even certain phase transitions may result in localized physical defects and or promote exciton-phonon type coupling giving rise to sub-energy levels and split emission lines, because. These split emission profiles at low temperature have been observed the 2D lead bromide's thus far, specifically in the aliphatics (Cn)PbBr<sub>4</sub> (n = 4, 5, 7, 12) (Kitazawa N, *et al*, 2010), and n = 8 (Kitazawa N, *et al*, 2009), but also in (PhCnH<sub>2</sub>nNH<sub>3</sub>)PbBr<sub>4</sub> where n = 1-4 (Kitazawa N and Watanabe Y, 2010b).

This is the underlying reason for the investigation into the well known aliphatic hybrids and their phase transitions. Herein we discuss the crystal structures and the phase transitions of the lead bromide (Cn)PbBr<sub>4</sub> family, where n = 4-7, compounds **1-4** respectively, and the associated mechanism as previously discussed by (Billing D. G, Lemmerer A, 2007) for the short chain derivatives of (Cn)PbI<sub>4</sub>. Thermal analysis studies (DSC) have been previously reported on (C4)PbBr<sub>4</sub> and (C6)PbBr<sub>4</sub>, however no further structural studies, besides powder diffraction investigations, were completed (Tabuchi Y, *et al*, 2000). A scheme summarising the phase changes in the above mentioned compounds may be seen in scheme 4.1.1.



**Scheme 4.1.1:** A summary of the phase transitions and the relative phase transformation temperatures for both heating and cooling runs for (Cn)PbBr<sub>4</sub>. Estimates of the phase transformation temperatures were made for the transitions that occurred below the measuring capability of the differential scanning calorimeter, which were examined via SC-XRD cooling experiments.

#### 4.1.2 Results and Discussion

In order to describe the mechanisms associated with a phase transition, certain geometrical parameters were introduced. (Doudin B and Chapuis G, 1990) were the first to describe the necessary geometrical parameters to describe these relative angles associated with the changes of the alkyl ammonium conformations, specifically of (C3)CuCl<sub>4</sub>, before and after a phase change. (Billing D. G, Lemmerer A, 2007; 2008; Lemmerer A, 2007, Lemmerer A, Billing D. G, 2011) further extended these definitions, to describe the phase changes observed in the longer alkyl ammonium chain derivatives for (C<sub>n</sub>)PbI<sub>4</sub> hybrid perovskites where n = 4-10, 12, 14, 16, 18. From figure 4.1.1, the tilt  $\angle_{\varphi}$  angle of the organic chain is measured by the angle between the plane through the inorganic layers and the vector containing the first and last atom of each chain. In the case of (C4)PbI<sub>4</sub> the first atom is N1 and the last is C4 (Billing D. G, Lemmerer A, 2007). Another two important geometrical parameters were used to describe the organics motion due to the phase change. The  $\angle_{\alpha}$  angle, which may be defined as the torsion angle between the plane containing all of the atoms of the alkyl chain, and the plane formed by the lead atoms of the inorganic layers i.e. the vertical tilt of the organic chain. And finally the  $\angle_{\beta}$  angle, which is the angle between a vector containing atoms N-C and a plane through lead atoms of the inorganic layers i.e. the tilt of the ammonium head.

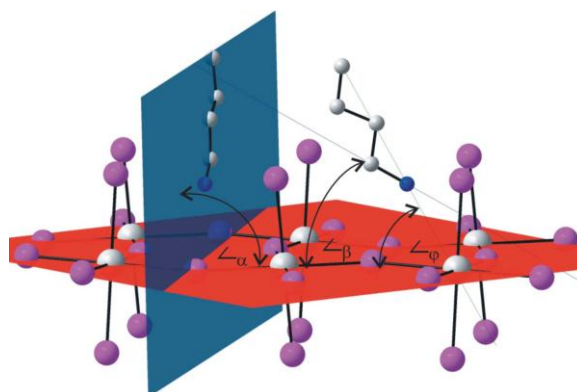


**Figure 4.1.1:** The geometric parameters assigned to the alkyl ammonium cation in order to describe the relevant angles associated from phase change behaviour. The angles are described in the text, adapted from (Billing D. G, Lemmerer A, 2007).

In addition to the alkyl ammoniums tilt angles, the position of the ammonium group's hydrogen bonding configuration may also be altered after a phase transition. Hence the "box" which contains the ammonium group is defined by the four equatorial (bridging) halogens and the four axial (terminal) halogens. In projection view of the layers, the ammonium group is contained

within the parallelogram (figure 4.1.2) i.e. the void between the octahedra. The ammonium group may be found in the proximity of either the acute or obtuse angle of the parallelogram which further gives rise to the equilateral or right angled hydrogen bonding configuration respectively. The inorganic components also undergo distortions, in which the perovskite type distortions were first described by (Hatch D. M, *et al*, 1989). Two main parameters are used to describe the octahedral type distortions. Firstly is the bridging angle, Pb-Br-Pb which deviates from  $180^\circ$ , between adjacent octahedra, this angle describes the horizontal tilt of the octahedra in the plane of the lead atoms. This angle is of the greatest importance as it has the largest impact on the stereo-chemical activity of lead's lone pair (Mitzi D. B, 1996; Knutson J. L, *et al*, 2005). Secondly is the corrugation angle,  $\psi$  tilt angle, or the vertical tilt of the octahedra, which describes the deviation of the angle of the vector which passes through the axial halogens of the octahedra, perpendicular to the plane of the lead atoms (deviation from  $0^\circ$ ). In this study we crystallized and structurally characterized the various phases of  $(\text{Cn})_2\text{PbBr}_4$  where  $n = 4 - 7$ . Table 4.1.1 summarizes the structural results.

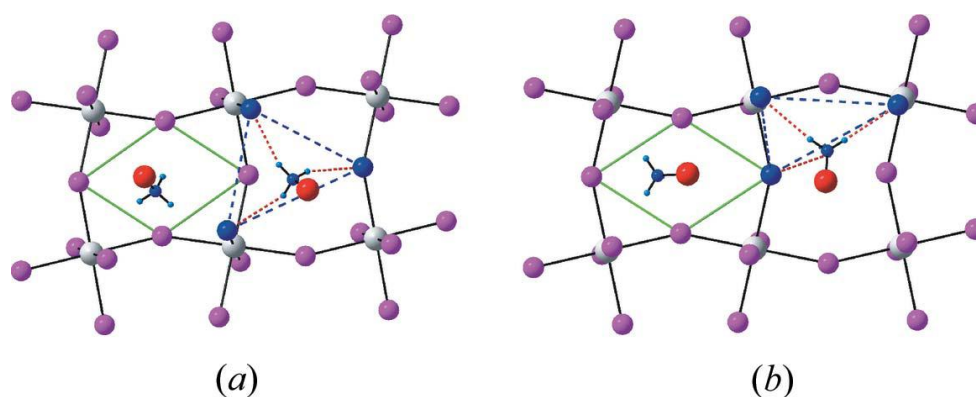


**Figure 4.1.2:** The two ammonium head group positions associated with the phase transformations. The green parallelogram depicts two arrangements (a) the ammonium head resides within the obtuse angle of the parallelogram and the hydrogen bonding configuration forms an equilateral triangle. The arrangement (b) situates the ammonium head in the acute angle of the green parallelogram, and the hydrogen bonding formation forms a right angled triangle. It is observed that the obtuse arrangement is associated with the low temperature phase, and the acute arrangement with the higher temperature phases. The high temperature disordered phases result in the ammonium group being in the centre of the parallelogram. (Billing D. G, Lemmerer A, 2007; 2008; Lemmerer A, 2007)

**Table 4.1.1:** Crystallographic structural tables of (Cn)<sub>2</sub>PbBr<sub>4</sub> where n = 4 – 7 which were completed in this study.Experiments were carried out with Mo K $\alpha$  radiation using a Bruker APEX-II CCD diffractometer.

	1_II_173K	1_II_293K	1_I_378K	2_III_173K	2_II_223K
Crystal data					
Chemical formula	2(C <sub>4</sub> H <sub>12</sub> N)·Br <sub>4</sub> Pb	2(C <sub>4</sub> H <sub>12</sub> N)·Br <sub>4</sub> Pb	2(C <sub>4</sub> H <sub>12</sub> N)·Br <sub>4</sub> Pb	2(C <sub>3</sub> H <sub>14</sub> N)·Br <sub>4</sub> Pb	2(C <sub>3</sub> H <sub>14</sub> N)·Br <sub>4</sub> Pb
<i>M<sub>r</sub></i>	675.12	675.12	675.12	703.17	703.17
Crystal system, space group	Orthorhombic, <i>Cmca</i>	Orthorhombic, <i>Cmca</i>	Tetragonal,	Monoclinic, <i>P2<sub>1</sub>/c</i>	Monoclinic, <i>P2<sub>1</sub>/c</i>
Temperature (K)	173	293	378	173	223
<i>a</i> , <i>b</i> , <i>c</i> (Å)	27.4848 (12), 8.2745 (3), 8.1631 (3)	27.5868 (10), 8.3399 (3), 8.2187 (3)	5.8461 (9), 5.8461 (9), 28.941 (5)	14.4591 (12), 8.2742 (7), 8.3360 (7)	15.938 (11), 8.264 (4), 8.232 (5)
$\alpha$ , $\beta$ , $\gamma$ (°)	90, 90, 90	90, 90, 90	90, 90, 90	90, 95.109 (3), 90	90, 95.56 (3), 90
<i>V</i> (Å <sup>3</sup> )	1856.48 (13)	1890.89 (12)	989.1 (3)	993.34 (14)	1079.1 (11)
<i>Z</i>	4	4	2	2	2
$\mu$ (mm <sup>-1</sup> )	17.68	17.36	16.59	16.52	15.21
Crystal size (mm)	0.32 × 0.14 × 0.04	0.72 × 0.61 × 0.05	0.56 × 0.13 × 0.05	0.31 × 0.10 × 0.03	0.3 × 0.08 × 0.03
Data collection					
Absorption correction	Integration <i>Bruker XPREP</i> (Bruker, 1999a)	Integration <i>Bruker XPREP</i> (Bruker, 1999a)	–	Integration <i>Bruker XPREP</i> (Bruker, 1999a)	Integration <i>Bruker XPREP</i> (Bruker, 1999a)
<i>T<sub>min</sub></i> , <i>T<sub>max</sub></i>	0.211, 0.793	0.032, 0.742	–	0.369, 0.936	0.092, 0.693
No. of measured, independent and observed [ <i>I</i> > 2 $\sigma$ ( <i>I</i> )] reflections	16463, 1155, 948	7726, 1165, 971	2211, 666, 444	7616, 2395, 1650	5970, 2526, 732
<i>R<sub>int</sub></i>	0.060	0.052	0.038	0.076	0.121
Refinement					
<i>R</i> [ <i>F</i> <sup>2</sup> > 2 $\sigma$ ( <i>F</i> <sup>2</sup> )], <i>wR</i> ( <i>F</i> <sup>2</sup> ), <i>S</i>	0.028, 0.072, 1.10	0.031, 0.075, 0.98	0.038, 0.111, 0.95	0.048, 0.111, 1.03	0.119, 0.272, 1.1
No. of reflections	1155	1165	666	2395	2526
No. of parameters	57	57	19	81	80
No. of restraints	4	4	0	0	84
H-atom treatment	H-atom parameters constrained	H-atom parameters constrained	-	H-atom parameters constrained	H-atom parameters constrained
	$w = 1/[\sigma^2(F_o^2) + (0.0267P)^2 + 25.902P]$ where $P = (F_o^2 + 2F_c^2)/3$	$w = 1/[\sigma^2(F_o^2) + (0.0263P)^2 + 26.5362P]$ where $P = (F_o^2 + 2F_c^2)/3$	$w = 1/[\sigma^2(F_o^2) + (0.0696P)^2]$ where $P = (F_o^2 + 2F_c^2)/3$	$w = 1/[\sigma^2(F_o^2) + (0.0464P)^2]$ where $P = (F_o^2 + 2F_c^2)/3$	$w = 1/[\sigma^2(F_o^2) + (0.0585P)^2 + 19.6478P]$ where $P = (F_o^2 + 2F_c^2)/3$
$\Delta_{\max}$ , $\Delta_{\min}$ (e Å <sup>-3</sup> )	0.001	0.014	0.001	0.001	0.023
	1.85, -1.14	1.23, -1.78	0.77, -0.36	4.06, -1.59	0.96, -0.72
Absolute structure	–	–	-	-	-
Flack parameter	–	–	-	-	-
	3_IV_173K	3_III_208K	3_II_273K	3_I_313K	4_III_173K
Crystal data					
Chemical formula	2(C <sub>6</sub> H <sub>16</sub> N)·Br <sub>4</sub> Pb	2(C <sub>6</sub> H <sub>16</sub> N)·Br <sub>4</sub> Pb	2(C <sub>6</sub> H <sub>16</sub> N)·Br <sub>4</sub> Pb	2(C <sub>6</sub> H <sub>16</sub> N)·Br <sub>4</sub> Pb	2(C <sub>7</sub> H <sub>18</sub> N)·Br <sub>4</sub> Pb
<i>M<sub>r</sub></i>	731.23	731.23	731.23	731.23	759.28
Crystal system, space group	Monoclinic, <i>P2<sub>1</sub>/c</i>	Monoclinic, <i>P2<sub>1</sub>/c</i>	Orthorhombic, <i>Pbca</i>	Tetragonal,	Monoclinic, <i>P2<sub>1</sub>/c</i>
Temperature (K)	173	208	273	313	173
<i>a</i> , <i>b</i> , <i>c</i> (Å)	16.6250 (8), 8.2298 (3), 8.3937	16.6562 (5), 8.2344 (2), 8.4195	34.758 (5), 8.2703 (12), 8.1998 (11)	5.5640 (16), 5.5640 (16),	18.879 (2), 8.1862 (8), 8.1829 (9)



	(4)	(2)		38.022 (15)	
$\alpha, \beta, \gamma$ (°)	90, 104.636 (2), 90	90, 104.608 (2), 90	90, 90, 90	90, 90, 90	90, 102.200 (6), 90
$V$ (Å <sup>3</sup> )	1111.16 (9)	1117.44 (5)	2357.1 (6)	1177.1 (7)	1236.1 (2)
$Z$	2	2	4	2	4
$\mu$ (mm <sup>-1</sup> )	14.78	14.69	13.93	13.95	26.58
Crystal size (mm)	0.41 × 0.05 × 0.01	0.41 × 0.05 × 0.01	0.30 × 0.08 × 0.01	0.30 × 0.21 × 0.05	0.3 × 0.25 × 0.06
Data collection					
Absorption correction	Multi-scan Absorption corrections were done using <i>SADABS</i> as incorporated in the Apex2 software (Bruker, 2005)	Multi-scan Absorption corrections were done using <i>SADABS</i> as incorporated in the Apex2 software (Bruker, 2005)	Integration <i>Bruker XPREP</i> (Bruker, 1999a)	—	Integration <i>Bruker XPREP</i> (Bruker, 1999a)
$T_{\min}, T_{\max}$	0.540, 0.746	0.487, 0.746	—	—	0.047, 0.299
No. of measured, independent and observed [ $I > 2\sigma(I)$ ] reflections	10808, 2680, 2002	11128, 2691, 1922	20153, 2404, 808	1962, 1405, 997	9055, 2897, 1582
$R_{\text{int}}$	0.050	0.057	0.175	0.057	0.396
Refinement					
$R[F^2 > 2\sigma(F^2)], wR(F^2), S$	0.033, 0.102, 1.06	0.035, 0.087, 0.98	0.345, 0.780, 2.60	0.346, 0.672, 4.66	0.087, 0.252, 1.10
No. of reflections	2680	2691	2404	1405	2897
No. of parameters	154	152	48	6	37
No. of restraints	48	50	10	0	2
H-atom treatment	H-atom parameters constrained	H-atom parameters constrained	—	—	—
	$w = 1/[\sigma^2(F_o^2) + (0.0571P)^2]$ where $P = (F_o^2 + 2F_c^2)/3$	$w = 1/[\sigma^2(F_o^2) + (0.043P)^2 + 0.1445P]$ where $P = (F_o^2 + 2F_c^2)/3$	$w = 1/[\sigma^2(F_o^2) + (0.2P)^2]$ where $P = (F_o^2 + 2F_c^2)/3$	$w = 1/[\sigma^2(F_o^2) + (0.1P)^2]$ where $P = (F_o^2 + 2F_c^2)/3$	$w = 1/[\sigma^2(F_o^2) + (0.0822P)^2 + 58.910P]$ where $P = (F_o^2 + 2F_c^2)/3$
	0.003	0.001	2.945	5.142	0.006
$\Delta_{\text{max}}, \Delta_{\text{min}}$ (e Å <sup>-3</sup> )	1.45, -1.20	1.40, -0.81	14.26, -5.05	—	3.30, -2.93
Absolute structure	—	—	—	—	—
Flack parameter	—	—	—	—	—

#### 4\_II\_223K

Crystal data	
Chemical formula	2(C <sub>7</sub> H <sub>18</sub> N)·Br <sub>4</sub> Pb
$M_r$	759.28
Crystal system, space group	Monoclinic, $P2_1/c$
Temperature (K)	223
$a, b, c$ (Å)	19.1176 (5), 8.1950 (2), 8.1972 (2)
$\alpha, \beta, \gamma$ (°)	90, 102.373 (2), 90
$V$ (Å <sup>3</sup> )	1254.42 (5)
$Z$	4
$\mu$ (mm <sup>-1</sup> )	26.19
Crystal size (mm)	0.28 × 0.28 × 0.06
Data collection	
Absorption correction	Integration <i>Bruker XPREP</i> (Bruker, 1999a)
$T_{\min}, T_{\max}$	—

No. of measured, independent and observed [ $I > 2\sigma(I)$ ] reflections	10407, 3037, 2011
$R_{\text{int}}$	0.042
Refinement	
$R[F^2 > 2\sigma(F^2)]$ , $wR(F^2)$ , $S$	0.091, 0.293, 1.09
No. of reflections	3037
No. of parameters	54
No. of restraints	7
H-atom treatment	-
	$w = 1/[\sigma^2(F_o^2) + (0.2P)^2]$ where $P = (F_o^2 + 2F_c^2)/3$
	< 0.001
$\Delta\rho_{\text{max}}, \Delta\rho_{\text{min}}$ (e Å <sup>-3</sup> )	11.35, -2.51
Absolute structure	-
Flack parameter	-

Computer programs: Bruker APEX2, Bruker SAINT, SHELXS97 (Sheldrick, 2008), SHELXL97 (Sheldrick, 2008), Bruker SHELXTL.

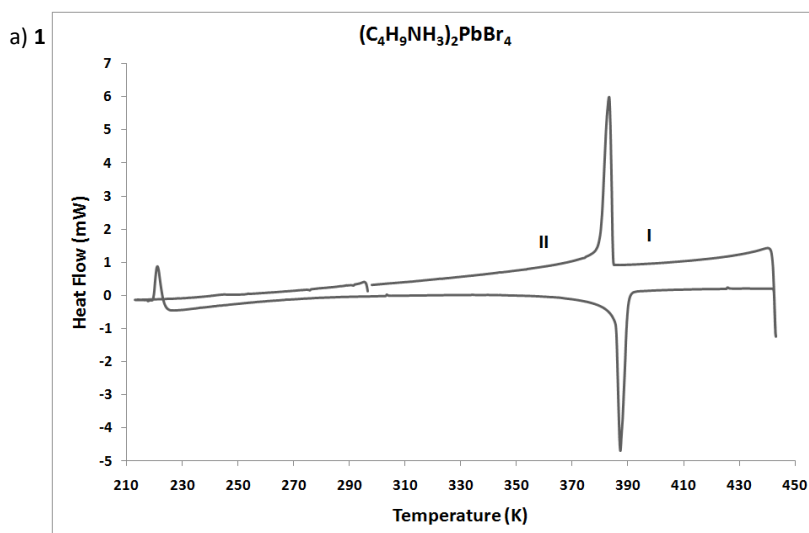
#### **(Cn)PbBr<sub>4</sub> n = 4-7.**

The aliphatic series of (Cn)PbBr<sub>4</sub>, display a unique trend that is not observed in its (Cn)PbI<sub>4</sub> counterparts. For n = 4 and 6, the alkyl ammonium chains are arranged in the disordered pre-quasi melting arrangement in the low temperature (173K) form. Our DSC experiments have a lower temperature measurement capability of 213K. However the DSC experiments carried out by (Tabuchi Y, *et al*, 2000) on (C4)PbBr<sub>4</sub> and (C6)PbBr<sub>4</sub> were measured with a lower temperature limit of 123K, which displayed no additional phase transitions at low temperature for (C4)PbBr<sub>4</sub>; however (C6)PbBr<sub>4</sub> displayed an additional two phase transitions (~213K and ~183K). The higher temperature phases of both (C4)PbBr<sub>4</sub> and (C6)PbBr<sub>4</sub> show the alkyl chain being irresolvable in the single crystal refinement although the inorganic layers were still able to be resolved crystallographically. This same phenomenon is observed for all of the phases of the (C7)PbBr<sub>4</sub> alkyl ammonium chain. However the inorganic component in phase III and II are well resolved with relevant geometrical information able to be gleaned from the structural data. The main cause for the inability to locate the alkyl chain in a phase, is a result of the Bragg diffraction disappearing, with diffuse X-ray scattering predominating due to the large amount of disorder in the alkyl chain (Schenk K. J, and Chapuis G, 1988). The alkyl chain (C5)PbBr<sub>4</sub> was the exception, as it displayed two well-resolved well-ordered phases III, and II, with only one irresolvable phase I. The crystal structures of phase III and II for (C5)PbBr<sub>4</sub> were determined and collected on the same crystal. Only one phase transition exists for (C4)PbBr<sub>4</sub> however the structures at 173K and 293K were collected, with only the unit cell being obtained for phase I. In (C6)PbBr<sub>4</sub> the full

structures of phase IV and III were obtained, whereas only the inorganic component was well resolved in the structure for phase II, with only the unit cell for phase I being obtained. For (C7)PbBr<sub>4</sub> we report the crystal structures of phase III and II however only the inorganic component is well resolved. The high temperature phase I was unresolvable. A summary of the important geometrical parameters of (Cn)PbBr<sub>4</sub> structures are given in table 4.1.3-4.1.5.

#### 4.1.3 Thermal analysis studies of the (Cn)PbBr<sub>4</sub> where n = 4-7

The DSC experiments display thermal hysteresis in the reversibility of the phase changes. The DSC graphs only display the final quasi-melting transition for each of the compounds. Hence only the enthalpy measurements for the final transition could be determined. Table 4.1.2 displays the summary of the phase transition temperatures, and enthalpies of the aliphatic compounds. The DSC experiments completed by (Tabuchi Y, *et al*, 2000) shown in figure 4.1.4, display the thermal stability of (C4)PbBr<sub>4</sub>, showing no further phase transitions below -60°C to -150°C (213-123K). However (C6)PbBr<sub>4</sub> displays an additional two phase transitions, one at ~223K and the second one at ~193K. This gives further evidence of the existence of the four phases present in (C6)PbBr<sub>4</sub>. No further comment on the enthalpies of these transitions were made by the authors.



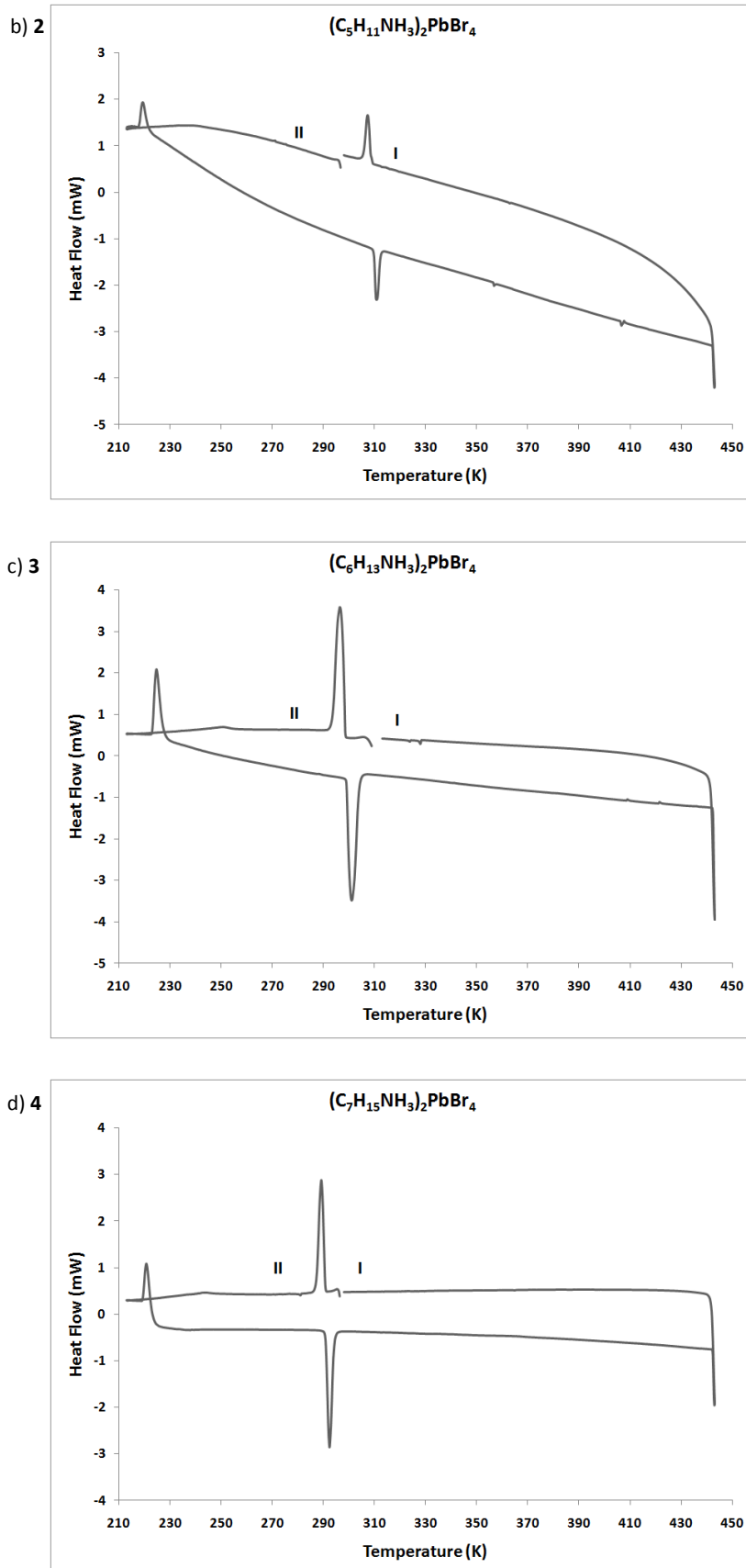


**Figure 4.1.3:** The DSC graphs displaying the reversible high temperature phase transitions for compounds 1 a), 2 b), 3 c), and 4 d).

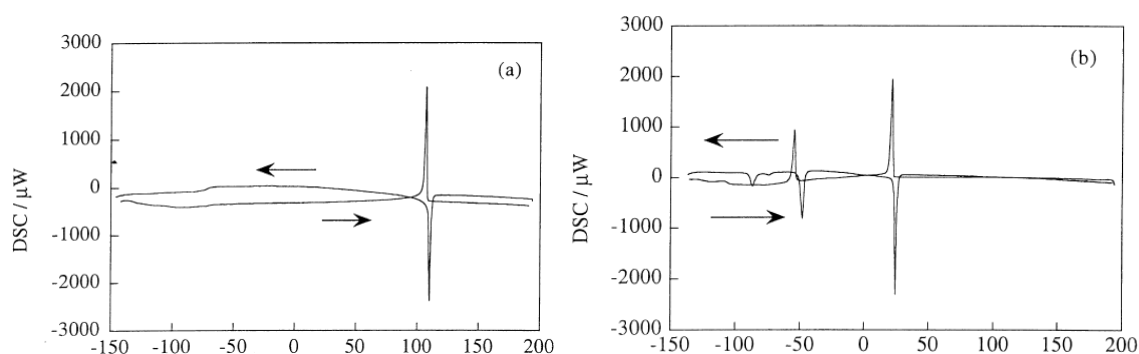


**Figure 4.1.4:** The DSC thermal graphs for (C4)PbBr<sub>4</sub> a) and (C6)PbBr<sub>4</sub> b) run between 123K and 473K, displaying the low temperature thermal stability of (C4)PbBr<sub>4</sub>, however b) displays all four phases present in (C6)PbBr<sub>4</sub>, the additional two low temperature phases are evidenced here (Tabuchi Y, *et al*, 2000).

**Table 4.1.2:** The enthalpy measurements from the DSC experiment of the phase transitions.

Enthalpy of the Phase transitions for the Heating Runs only						
Compound	T1	$\Delta H1/KJ.mol^{-1}$	T2	$\Delta H2/KJ.mol^{-1}$	T3	$\Delta H3/KJ.mol^{-1}$
C4PbBr <sub>4</sub>	387K	8.73	N/A	N/A	N/A	N/A
C5PbBr <sub>4</sub>	303K	6.08	173-123K	?	N/A	N/A
C6PbBr <sub>4</sub>	300.6K	6.75	~213K	?	~183K	?
C7PbBr <sub>4</sub>	292K	4.5	173-123K	?	N/A	N/A

Table 4.1.2 displays the enthalpy values calculated from the heating run's of the DSC experiments. The labelled temperatures T1, T2, and T3 represent the phase transition temperature from phase I to II, II to III, and III to IV, respectively. Only minor thermal hysteresis is seen in all the compounds final phase transitions. Unfortunately, all the full crystal structures obtained were all below the final phase change, and the low temperature phases were below the measurement capabilities of our instrument, therefore no enthalpy values are reported for T2 and below. It is assumed that the last phase change is the final quasi-melting transition, as the enthalpy values are comparable with the short chain (Cn)PbI<sub>4</sub> derivatives (Billing D. G, and Lemmerer A, 2007). Below is a graph (figure 4.1.5) depicting the quasi-melting enthalpies as a function of chain length for the (Cn)PbI<sub>4</sub> hybrids. The irregularities of the change of the enthalpy values of the short chain derivatives with increasing chain length, for the lead bromide hybrids, are equally seen in the lead iodide derivatives as a function of increasing chain length. However as the chain length reaches longer values (8) the quasi-melting enthalpy increases in a linear fashion. This behaviour was also first observed in the (Cn)CdCl<sub>4</sub> hybrids (Schenk K. J and Chapuis G, 1988).

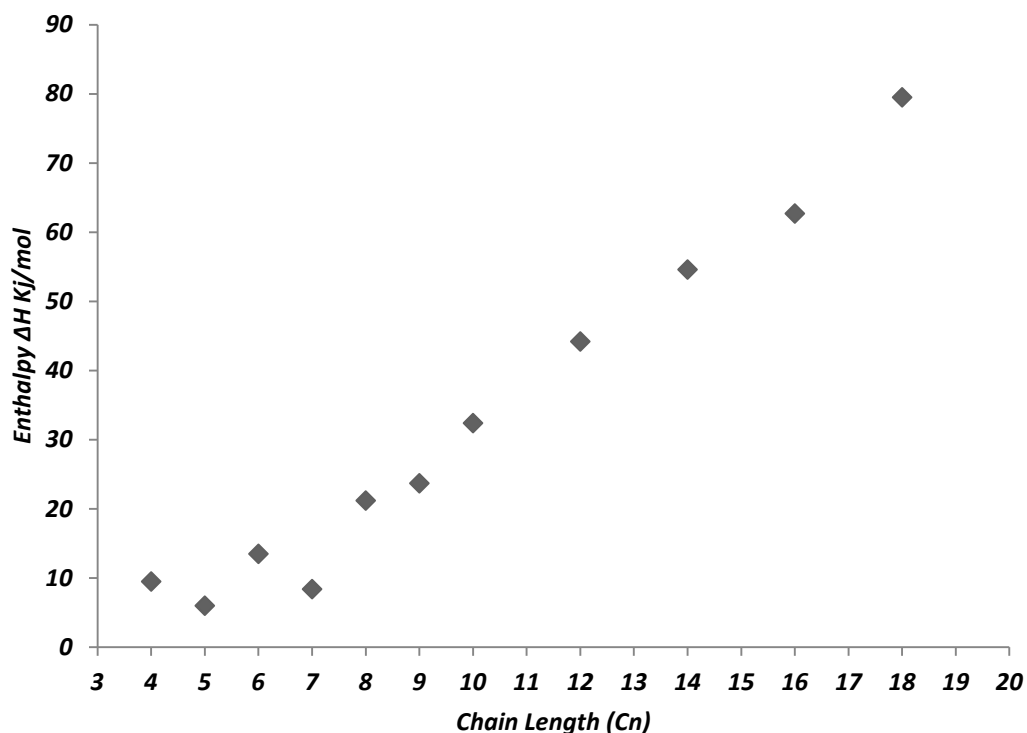


**Figure 4.1.5:** Chain length of (Cn)PbI<sub>4</sub> Vs the quasi melting phase change enthalpy for the heating run. This quasi-melting enthalpy generally increases in a linear fashion with increasing chain length. Values obtained from n = 4-6 (Billing D. G, and Lemmerer A, 2007); n = 7-10 (Lemmerer A, Billing D. G, 2011); n =12, 14, 16, 18 (Billing D. G, and Lemmerer A, 2007).

#### 4.1.4 The structures and phases of (Cn)PbBr<sub>4</sub> where n = 4-7

##### The structures and phases of (C5)PbBr<sub>4</sub>

An increase in the interlayer spacing of (C5)PbBr<sub>4</sub> between phase III and II is the only example in which both structures, before and after the phase change for this (Cn)PbBr<sub>4</sub> series was obtained. Moreover (C5)PbBr<sub>4</sub> displays the second largest increase in interlayer spacing of ~1.5Å between two consecutive phases. This large increase has been attributed to a number of factors, namely the torsion angle at the end of the alkyl chain i.e. C2-C3-C4-C5, which changes dramatically between phase III and II, from 68(1)° and 142(5)° respectively. The end of the alkyl chain essentially unfolds from the *gauche* conformation to the *anti-clinal* conformation. This conformational change results in an increase of the overall chain length i.e. the distance between N1 and the last atom in the chain C5, which is 5.5440(16)Å and 5.8981(7)Å for phase III and II respectively. These two major changes further result in the alkyl chains altering from the marginally interdigitated phase III to the non-interdigitated phase II as seen in figure 4.1.6. The alpha  $\angle_{\alpha}$  tilt angle of the plane containing the chains also increases from 82.725(3)° to 88.187(23)° as well as the  $\angle_{\phi}$  tilt of the chains which experiences an increase from 24.961(15)°

to  $31.801(56)^\circ$ . However the position of the ammonium group remains in the obtuse and equilateral configurations, with a small decrease in the  $\angle_\beta$  tilt angle from phase III to II. The hydrogen bonding distances however only experience minor changes. This in turn results in the inorganic layers experiencing only a minor decrease in the corrugation  $\psi$  tilt with an almost negligible change in the Pb-Br-Pb bridging angle. There are also negligible changes in the inorganic Pb-Br bond distances between phase III and II and the inorganic layers further remain in the monoclinic eclipsed state after the phase change.

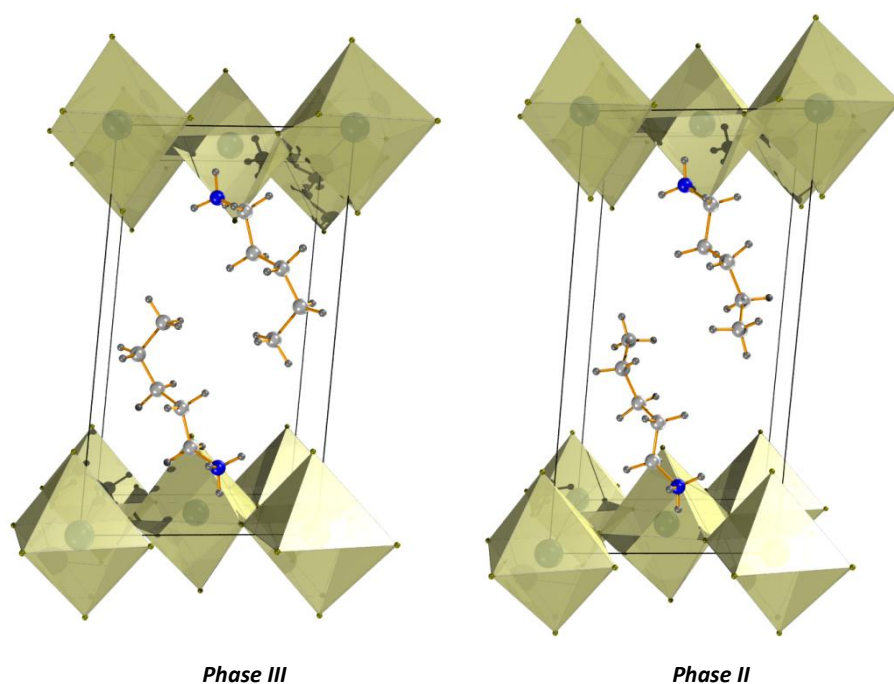


**Figure 4.1.6:** Conformational change of the alkyl ammonium chain C5, from the gauche to anti-clinal, between phase III and II. This conformational change and the increase in the alpha and phi tilts account for the large increase of interlayer spacing between phase III and II.

#### ***The structures and phases of (C4)PbBr<sub>4</sub> and (C6)PbBr<sub>4</sub>.***

The hybrids (C4)PbBr<sub>4</sub> and (C6)PbBr<sub>4</sub> both have two main similarities structurally. Firstly, is the disordered axial bromide's over two positions, and secondly, is the disordered alkyl ammonium chain over two positions. Disorder experienced in the inorganic layer is not a commonly reported phenomenon for hybrids, however the quaterthiophene dye hybrid, (AEQT)PbBr<sub>4</sub> also experiences both a disordered ammonium group, as well as the disordered bridging halogens, over two positions (Mitzi D. B, *et al*, 1999b). The disordered axial bromides corrugation  $\psi$  tilt angle is identical for the two disordered axial Br atoms in the orthorhombic C cell of (C4)PbBr<sub>4</sub>,

of  $5.79(3)^\circ$ . However the  $\psi$  tilt angle in  $(C6)PbBr_4$ , monoclinic P cell are  $9.520(43)^\circ$  and  $20.583(29)^\circ$  for phase IV, and changes marginally in phase III to  $9.424(31)^\circ$  and  $20.651(29)^\circ$ . The Br axial disorder disappears in phase II in the now orthorhombic P cell for  $(C6)PbBr_4$  and the  $\psi$  tilt angle becomes comparable ( $6.498(2)^\circ$ ) with phase II of  $(C4)PbBr_4$  ( $5.79(3)^\circ$ ). Only minor alkyl ammonium conformational changes are experienced from phase IV to III for  $(C6)PbBr_4$ , with the most notable being the  $\angle_\beta$  tilt of the ammonium group decreasing from  $62.582(8)^\circ$  to  $60.825(8)^\circ$ , and a small increase in  $\angle_\alpha$  tilt angle. Only phases IV and III were fully resolved structurally, however phase II and I still gave some important structural information relating to the inorganic component. The interlayer spacing displays a large increase from phase III to II to I, with a notable increase in the bridging Pb-Br-Pb angle from  $155.774(25)^\circ$  to  $158.5(7)^\circ$  for phase III to II respectively. Furthermore the unit cell progression through the phases matches the generally observed trend of the (eclipsed) monoclinic P phases IV and III to the (staggered) orthorhombic P phase II and finally to the tetragonal high temperature phase I.  $(C4)PbBr_4$  also obeys the generally observed trend, with the (staggered) orthorhombic C phase II which transforms to the high temperature tetragonal phase I and also experiences a large increase in interlayer spacing from phase II to I. The disordered  $(C4)PbBr_4$  alkyl ammonium chain effectively resides within the alpha plane created to measure  $\angle_\alpha$  tilt angle (figure 4.1.7).

The hexyl ammonium chains first few atoms only reside within this plane, N1-C1-C2-C3, where atoms C4-C5-C6, tilt out of the alpha plane. The torsion angle C1-C2-C3-C4 of  $163(3)^\circ$  for phase IV displays the tilt of the chain out of the alpha plane. Where the respective A and B disordered parts of  $(C4)PbBr_4$  exists in the all trans conformation,  $(C6)PbBr_4$  contains a kink (*anti-clinal*) conformation in its respective disordered chains (figure 4.1.8). This torsion angle displays a minor change between phases IV and III. These phases were all measured with the same crystal, however the experiments were repeated on a different crystal to ensure the absence of a crystallographic twinning. The best data from both experiments were combined and reported here (for both compounds).



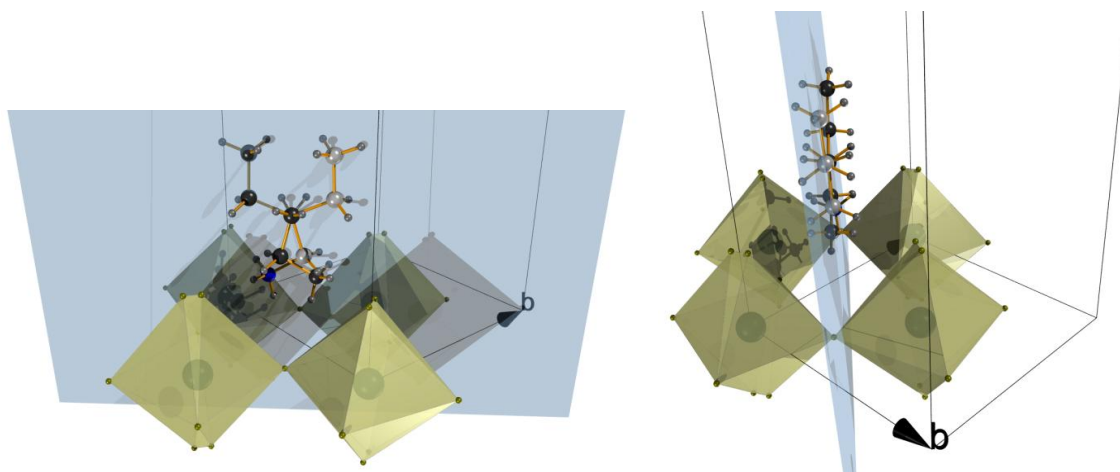


**Figure 4.1.7:** The disordered phase II of (C4)PbBr<sub>4</sub>, a) a front view of the disordered C4 alkyl ammonium chain where the dark shaded atoms represent the disordered component of the alkyl chain. The disordered alkyl chains are both coplanar for the measurement of the  $\angle_{\alpha}$  tilt angle. b) The side view of the disordered chain, displaying the low degree of distortion out of the alpha (blue) plane.

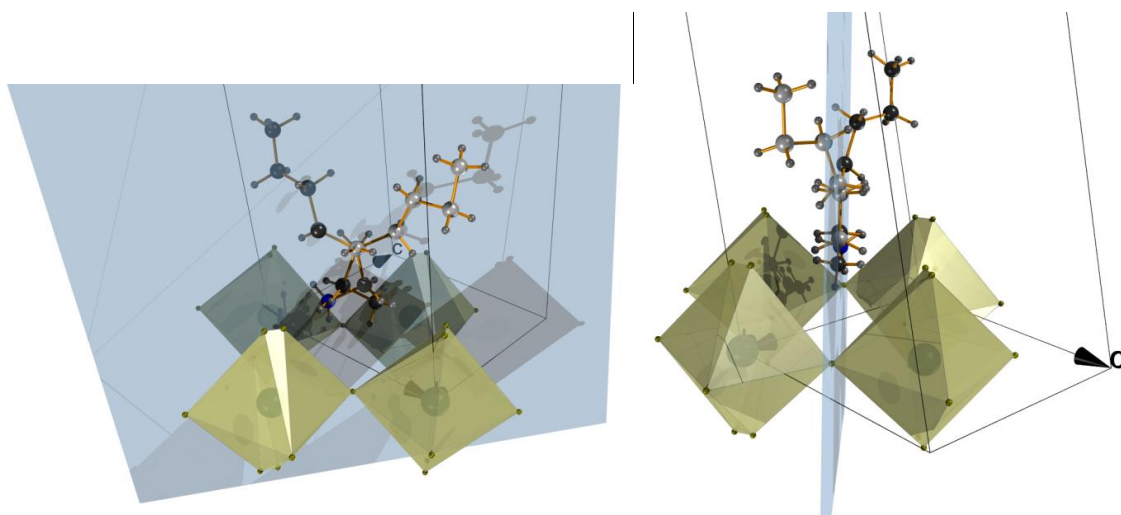


**Figure 4.1.8:** The disordered phase IV of (C6)PbBr<sub>4</sub>, a) a front view of the disordered C6 alkyl ammonium chain with the where the dark shaded atoms represent the disordered component of the alkyl chain. b) The side view of the disordered chain, displays the plane only passing through N1-C1-C2-C3, with atoms C4-C5-C6 tilting out of the alpha plane.

### **The phases of (C7)PbBr<sub>4</sub>**

The quasi-melting enthalpy for (C7)PbBr<sub>4</sub> is 4.5KJ/mol, which is the lowest enthalpy value reported for the quasi-melting transition measured for this series of compounds. This trend is mirrored in the (Cn)PbI<sub>4</sub> analogues as seen from figure 4.1.5. For phase III and II the inorganic component is well resolved, however the organic component was unable to be resolved crystallographically. Phase III is in a monoclinic P (eclipsed) arrangement and remains in this

arrangement in phase II. It is suspected that the alkyl ammonium conformation and relative tilt angles only change marginally as only a small interlayer spacing increase is observed. Only minor inorganic bridging and corrugation  $\psi$  tilt angle changes are observed from phase III to II. For the final phase I, we were only able to glean the interlayer spacing, which matches the reported value obtained through powder diffraction measurements completed by (Kitazawa N, *et al*, 2010). Table 4.1.4 displays the previously reported interlayer spacing of our series of compounds. The room temperature powder diffraction experiments do confirm the phase change from monoclinic to orthorhombic, as the lattice constant doubles, which is characteristic of this change. This is also observed for (C5)PbBr<sub>4</sub>.

**Table 4.1.3:** Summary of the important geometrical parameters for the multiple phases of the (Cn)PbBr<sub>4</sub> series of compounds.

Geometric parameter	1, II	1*, I	2, III	2, II	3, IV	3, III	3*, II	3*, I	4*, III	4*, II	4*, I
Interlayer Spacing (Å)	13.74 24(12)	14.4 70(5) )	14.45 91(12)	15.93 8(11)	16.6250(8)	16.6562(5)	17.3 74(5) )	19.01 1(15)	18.8 79(2) )	19.11 76(5)	19.39 87(12) )
Bridging angle Pb-Br-Pb (°)	153.4 0(3)	-	155.3 16(37)	153.0 46(92)	155.430(25) )	155.774(25) )	158. 5(7)	-	151. 57(8) )	151.4 96(5)	-
Corrugation $\psi$ tilt (°)	5.79(3) )	-	10.43 6(18)	9.531(60)	20.583(38); 9.520(43)	20.651(29); 9.424(31)	6.49 8(2)	-	12.2 51(7) )	12.57 3(6)	-
Tilt of Chains $\angle_{\phi}$ (°)	27.50 7(2)	-	24.96 1(15)	31.80 1(56)	34.762(3)	34.582(2)	-	-	-	-	-
Tilt of plane $\angle_{\alpha}$ (°)	89.79 6(2)	-	82.72 5(3)	88.18 7(23)	89.562(7)	89.811(7)	-	-	-	-	-
Tilt of NH <sub>3</sub> group $\angle_{\beta}$ (°)	59.44 0(3)	-	67.51 3(5)	60.31 3(19)	62.582(8)	60.825(8)	-	-	-	-	-
Position of ammonium group	acute	-	obtuse	obtuse	obtuse	obtuse	-	-	-	-	-
Hydrogen bonding configuration	Right Angled	-	Equilateral	Equilateral	Equilateral	Equilateral	-	-	-	-	-
Non coplanar torsion angles (°)	-	-	C1-C2-C3-C4 164(1)	C1-C2-C3-C4 150(4)	C1A-C2A-C3A-C4A 163(3)	C1A-C2A-C3A-C4A 164(2)	-	-	-	-	-
	-	-	C2-C3-C4-C5 68(1)	C2-C3-C4-C5 142(5)	C3A-C4A-C5A-C6A 176(3)	C3A-C4A-C5A-C6A 174(3)	-	-	-	-	-

\* Unit cells only/only inorganic resolvable in the crystal structure.

**Table 4.1.4:** The interlayer spacing and lattice constants for (Cn)PbBr<sub>4</sub> where n =4-7, obtained through thin film powder diffraction measurements.

Chain length	Interlayer spacing(Å)	Reference	lattice constant (Å)	Temperature
4	13.8	Tabuchi Y, <i>et al</i> , 2000	13.8	room Temp
5	16.45	Kitazawa N, <i>et al</i> , 2010	32.9	assumed room
6	18.02	Tabuchi Y, <i>et al</i> , 2000	18.02	room Temp
7	19.33	Kitazawa N, <i>et al</i> , 2010	38.66	assumed room

**Table 4.1.5:** The lead bromide octahedral bond lengths and angles, displaying the distortions around metal centre.

Compound	1 (II) 173K	1 (II) 293K	2 (III)	2 (II)	3 (IV)	3 (III)	3 (II)	4 (III)	4 (II)
Parameter	C4	C4	C5	C5	C6	C6	C6	C7	C7
Pb-Br <sub>eq</sub>	2.9818 (8)	3.0057 (9)	3.0028 (9)	2.998 (3)	3.004 (2)	3.0045 (6)	2.899 (14)	2.9831 (19)	2.9881 (14)
Pb-Br <sub>eq</sub>	2.9901 (8)	2.9936 (8)	3.0088 (10)	2.999 (3)	3.0140 (6)	3.0180 (6)	3.027 (11)	2.987 (2)	2.9915 (13)
Pb-Br <sub>eq</sub>	2.9818 (8)	3.0057 (9)	3.0028 (9)	2.998 (3)	3.004 (2)	3.0045 (6)	2.899 (14)	2.9831 (19)	2.9881 (14)
Pb-Br <sub>eq</sub>	2.9901 (8)	2.9936 (8)	3.0088 (10)	2.999 (3)	3.0140 (6)	3.0180 (6)	3.027 (11)	2.987 (2)	2.9915 (13)
Pb-Br <sub>ax</sub> (X2)	3.0098 (11)	3.0055 (14)	3.0055 (11)	3.068 (8)	3.002 (2); 3.0013 (6)	3.001 (2); 3.005 (2)	2.96 (2)	2.986 (2)	2.990 (2)
Br-Pb-Br	90.739 (7)	90.787 (7)	90.442 (10)	90.23 (4)	91.077 (6)	91.218 (5)	91.00 (8)	90.040 (19)	90.001 (13)
Br-Pb-Br	89.261 (7)	89.213 (7)	89.558 (10)	89.77 (4)	88.923 (6)	88.782 (5)	89.00 (8)	89.960 (19)	89.999 (13)
Br-Pb-Br	90.739 (7)	90.787 (7)	90.442 (10)	90.23 (4)	91.077 (6)	91.218 (5)	91.00 (8)	90.040 (19)	90.001 (13)
Br-Pb-Br	89.261 (7)	89.213 (7)	89.558 (10)	89.77 (4)	88.923 (6)	88.782 (5)	89.00 (8)	89.960 (19)	89.999 (13)
Br-Pb-Br <sub>ap</sub>	84.21 (2)	83.69 (2)	83.78 (3)	85.22 (14)	90.47 (4); 96.44 (4)	90.46 (4); 96.59 (4)	92.8 (6)	90.10 (8)	90.13 (6)
Br-Pb-Br <sub>ap</sub>	89.72 (3)	89.67 (3)	89.74 (3)	89.57 (14)	89.53 (4); 83.56 (4)	89.54 (4); 83.41 (4)	87.2 (6)	89.90 (8)	89.87 (5)
Br-Pb-Br <sub>ap</sub>	90.28 (3)	90.33 (3)	90.26 (3)	90.43 (14)	90.46 (4); 96.47 (4)	90.51 (4); 96.61 (4)	91.9 (6)	90.10 (8)	90.15 (7)
Br-Pb-Br <sub>ap</sub>	95.79 (2)	96.31 (2)	96.22 (3)	94.78 (14)	89.54 (4); 83.53 (4)	89.49 (4); 83.39 (4)	88.1 (6)	89.90 (8)	89.85 (7)
Br-Pb-Br	180	180	180	180	180	180	180	180	180
Br-Pb-Br	180	180	180	180	180	180	180	180	180
Br <sub>ap</sub> -Pb-Br <sub>ap</sub>	180; 168.42 (4)	180; 167.38 (5)	180	180	180; 167.07 (3)	180; 166.78 (3)	180	180	180
Pb-Br-Pb	153.40 (3)	154.77 (4)	155.32 (4)	153.06 (10)	155.43 (3)	155.78 (3)	158.6 (7)	151.60 (8)	151.50 (6)

#### 4.1.5 Conclusions

The large increase in interlayer spacing in (C5)PbI<sub>4</sub>, between phase III and II is attributed to the conformational change at the end of the alkyl chain from *gauche* to *anti-clinal*, which results in a

geometrical increase of the chain length. In addition the increase and decrease of the  $\angle_{\alpha}$  and  $\angle_{\varphi}$  tilt angles respectively, contribute to this increase. The disorder observed in the apical bromines of (C6)PbBr<sub>4</sub> disappears in phase II. The quasi-melting transitions of the alkyl chains occur at lower temperatures than their Iodide analogues; however the enthalpies associated with this phase transformation remain comparable. All four compounds follow the general increase in symmetry through each respective phase transition upon heating. Both (C5)PbBr<sub>4</sub> and (C6)PbBr<sub>4</sub> have kinks in the alkyl chains, whereas (C4)PbBr<sub>4</sub> exist in the all *trans* conformation, despite the disorder of the alkyl chains. (C4-C6)PbBr<sub>4</sub> all exhibit a  $\angle_{\alpha}$  tilt close to 90° in phase II and III, which is geometrically characteristic of the pre-chain melting arrangement which is also observed in the (Cn)PbI<sub>4</sub> analogues. In the inorganic octahedra, axial compression of the apical halide is almost insignificant by comparison with the (Cn)PbI<sub>4</sub> hybrids. Furthermore the bridging angles (Pb-Br-Pb) of all the phases are similar for each respective temperature phase, as well as over the entire temperature and chain length range. Relatively small inorganic distortions are experienced in the lower temperature phase transitions, this is a result of the alkyl chain conformational changes occurring further up the chain, where the ammonium head's position is relatively unchanged, creating stability in the inorganic sheet, through the phase transformation. The metal centred octahedra distortions also remain highly idealized, besides the disordered phases of (C4)PbBr<sub>4</sub> and (C6)PbBr<sub>4</sub>.

## **4.2 The Structure and Phase transitions of (HOC2, BrC3, BrC4, BrC5)<sub>2</sub>PbBr<sub>4</sub>**

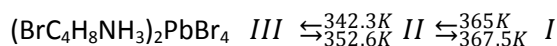
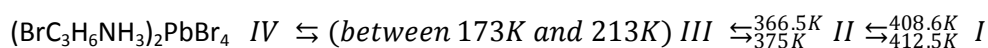
### **4.2.1 Introduction**

Various functionalisations have been added to the organic ammonium template, in order to further enhance the thermal stability, stereochemical control over crystal symmetry (Mercier N, *et al*, 2005), and to fine tune the optical properties associated with the layered organic inorganic hybrid perovskites (Mercier N, *et al*, 2004; Sourisseau S, *et al*, 2007a; 2007b). This has included the use of the aliphatic diamines, however the rigidity this template places on the system, has been shown to form other organic-inorganic motif types in preference to the layered perovskite motif (Lemmerer A, 2007). Functionalizing the organic ammonium cation with an alcohol and or carboxylic acid to provide further stability and control over the octahedral distortions have also been employed (Mercier N, 2005; Mercier N, *et al*, 2004; Lemmerer A, Billing D. G, 2010). Further examples of a diamine with a sulphide bridge (H<sub>3</sub>NC<sub>2</sub>H<sub>4</sub>SSC<sub>2</sub>H<sub>4</sub>NH<sub>3</sub>) have been incorporated as a means of the disulphide bridge supplying additional weak interaction stability

into the crystal. However this disulphide bridge gives rise to no less than five structural isomers (Mercier N, *et al*, 2006; Louvain N, *et al*, 2007; 2008b; Lemmerer A, Billing D. G, 2010). Only one of which forms the layered hybrid perovskite structure (Lemmerer A, Billing D. G, 2010). In particular functionalizing the organic cation with a halogen, specifically the halogenated aliphatics  $(X-C_nH_{2n}NH_3)_2PbI_4$  where  $n = 2-6$  and  $X = I$  and  $Br$  (for  $n = 2$ ), has proved to enhance certain aspects of the optical properties (Sourisseau S, *et al*, 2007a; 2007b) as well as providing further weak interactions between the inorganic layers and the organic ammonium cation, offering further thermal stability to the hybrid (as no structural phase transitions were reported, appendix A), while maintaining a high insulating ability, and not too high a rigidity to form a different structural motifs (Mercier N, *et al*, 2004; Lemmerer A, Billing D. G, 2010).

Further investigations into other halogenated and substitution position of aromatic hybrids, specifically in the tin iodide hybrids of  $(2-Cl,Br,F-PEA)_2SnI_4$  (Xu Z, *et al*, 2003c; d),  $(3$  and  $4-PEA)_2SnI_4$  (Mitzi D.B, 2001b) and other solvated variants (Mitzi D. B, *et al*, 2002b), have also been investigated. Furthermore, thorough optical investigation on the compound  $(4-F-PEA)_2PbI_4$  recently investigated by (Dammak T *et al*, 2009), measured the largest binding energy of an exciton found in a single layered lead iodide hybrid perovskite thus far. The binding energy was found to be  $540\text{meV}$ , which implies this material would be a great candidate for an electroluminescent device. The large increase in the excitons binding energy was simply attributed to the large dielectric mismatch between the barrier and the well. The halogenated organic templates dielectric constant lies within the range  $1.04 < \epsilon_b < 1.24$ , which is significantly reduced from the parent PEA cation whose dielectric constant is  $\epsilon_b = 3.32$ . Clearly, the large decrease in the dielectric constant has been attributed to the presence of the fluorine atom on the PEA ring (Dammak T, *et al*, 2009).

Here we report the structures and phase transitions of the functionalized aliphatic hybrids of  $(HOC_2H_4NH_3)_2PbBr_4$  and  $(X-C_nH_{2n}NH_3)_2PbBr_4$ , where  $n = 3-5$  and  $X = Br$ , compounds **5-8** respectively, in order to discuss firstly the structure and increased thermal stability of the phase transition as compared with their simple aliphatic counterparts. And secondly, the structure and optical property relationships which will be discussed further in the next section 4.3 of the chapter. We discuss the multiple phase transitions present in all four compounds despite the added stability of the alcohol and the terminal halogen on the end of the alkyl chain. Scheme 4.2.1 displays the phase transition summary of the compounds investigated.



**Scheme 4.2.1:** A summary of the phase transitions and the relative phase transformation temperatures for both heating and cooling runs for  $(\text{BrC}_n)\text{PbBr}_4$  where  $n = 3-5$  and  $(\text{HOC}_2)\text{PbBr}_4$ . Estimates of the phase transformation temperatures were made for the transitions that occurred below the measuring capability of the differential scanning calorimeter, which were examined via SC-XRD cooling experiments.

#### 4.2.2 Results and Discussion

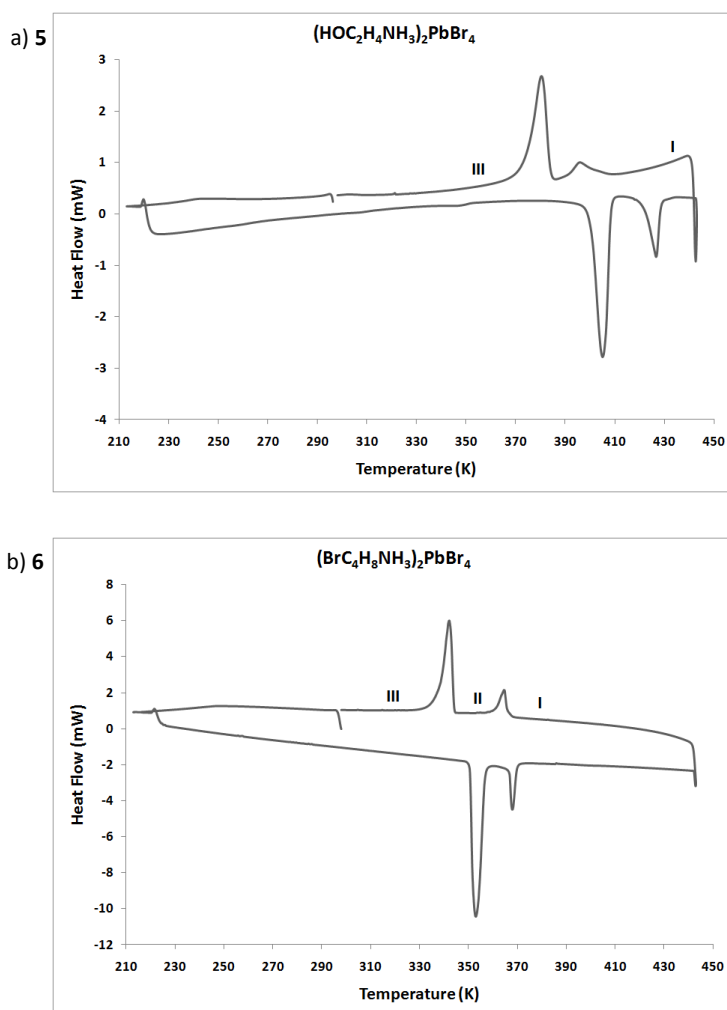
The general geometrical parameters as described in the previous section, relating to the hydrogen bonding configurations, and the relative tilts of the chains and planes will be used here again to describe the geometrical parameters related to describing the phase transition behaviour of these compounds. In addition we describe the organic halogen bonding interactions present between the terminal halogen on the aliphatic chain, and the apical halogen of the layers of the lead bromide octahedra. The nature of halogen bonding in general, is through attractive and repulsive electrostatic interactions (Dumas J. M, *et al*, 1983; Lommerse J. P, *et al*, 1996). This may be seen in the anisotropy of the organic halogen in the direction of the C-X bonding axis. This weak interaction is able to generate an electron deficient region within the region of the halogen atom, which further provides a maximum attractive electrostatic interaction toward an electron rich region, or an available Lewis base, in this case the negatively charged inorganic layers. The strength of an organic halogen (C-X) lewis base interaction, may be measured by the distance of the X...B interaction. The shorter the distance the stronger the halogen bond; however this should be coupled with an ideally linear C-X...B interaction angle.

The phase transformations observed in  $(\text{BrC}_n)\text{PbBr}_4$ , where  $n = 3-5$ , follow the general increase of symmetry trend with increasing temperature. The low temperature monoclinic (eclipsed) form is however only observed in the longer chain  $(\text{BrC}_5)\text{PbBr}_4$  compound. Both  $(\text{BrC}_3; \text{BrC}_5)\text{PbBr}_4$  undergo order-disorder phase transitions as well as displacive transitions. This is observed through the increase in interlayer spacing with each successive phase change. Only the final phase of  $(\text{BrC}_3)\text{PbBr}_4$  and  $(\text{BrC}_5)\text{PbBr}_4$  was undetermined, as phase I for  $(\text{BrC}_3)\text{PbBr}_4$  was beyond the heating capabilities of our instrument, and phase I of  $(\text{BrC}_5)\text{PbBr}_4$  did not diffract sufficiently well to allow for the measurement of any diffraction, as thermal diffuse scattering

predominated. The compound  $(\text{BrC4})\text{PbBr}_4$  is stable between 173K and room temperature, phase III, in which the aliphatic chain is in an ordered state (structures at 173K and 293K confirm this). The structure of phase II was unable to be obtained, however the unit cell dimensions and a well resolved inorganic component were found for the high temperature phase I. Phase II and I of  $(\text{HOC2})\text{PbBr}_4$  were undetermined from our analysis as the phase transitions were beyond the heating capabilities of our instrument.

#### 4.2.3 Thermal analysis

The DSC experiments display thermal hysteresis in the reversibility of the phase changes. Figure 4.1.3 the DSC graphs only display the phase transitions in the measured temperature range of 213-443K. The enthalpy measurements and phase transition temperatures for the heating runs only are reported below in table 4.2.1 for  $(\text{BrCn})\text{PbBr}_4$  where  $n = 3-5$  and  $(\text{HOC2})\text{PbBr}_4$ .



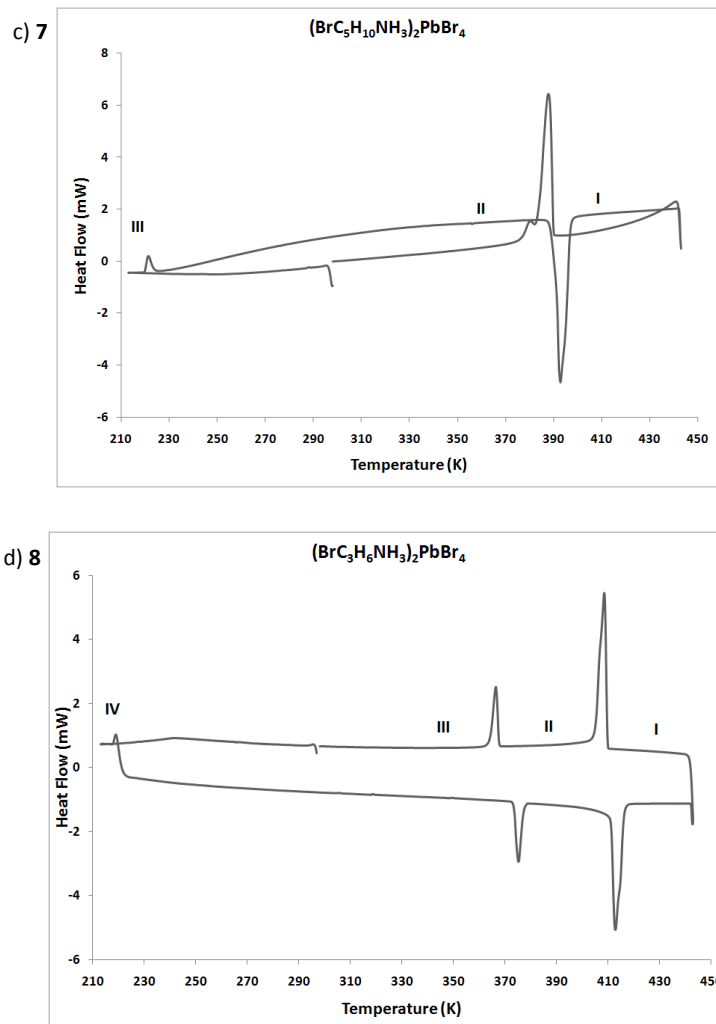


**Figure 4.2.1:** The DSC graphs displaying the reversible high temperature phase transitions for compounds 5 a), 6 b), 7 c), and 8 d).

**Table 4.2.1:** The enthalpy measurements from the DSC experiment of the phase transitions of  $(\text{HOC}2)\text{PbBr}_4$  and  $(\text{BrCn})\text{PbBr}_4$  where  $n = 3-5$ , and  $(\text{Cn})\text{PbBr}_4$  where  $n = 4-7$ .

Enthalpy of the Phase transitions for the Heating Runs only						
Compound	$T1$	$\Delta H1/\text{KJ.mol}^{-1}$	$T2$	$\Delta H2/\text{KJ.mol}^{-1}$	$T3$	$\Delta H3/\text{KJ.mol}^{-1}$
$\text{C4PbBr}_4$	387K	8.73	N/A	N/A	N/A	N/A
$\text{C5PbBr}_4$	303K	6.08	173-123K	?	N/A	N/A
$\text{C6PbBr}_4$	300.6K	6.75	~213K	?	~183K	?
$\text{C7PbBr}_4$	292K	4.5	173-123K	?	N/A	N/A
$\text{HOC2PbBr}_4$	426K	3.84	404.5K	12.55	N/A	N/A
$\text{BrC3PbBr}_4$	412.5K	9.48	375K	2.96	173-213K	?
$\text{BrC4PbBr}_4$	367.5K	4.01	352.6K	24.35	N/A	N/A
$\text{BrC5PbBr}_4$	392.5K	29.27	173-213K	?	N/A	N/A



The enthalpy change from phase III to II of (BrC3)PbBr<sub>4</sub> (T<sub>2</sub> = 375K; 2.96KJ.mol<sup>-1</sup>) is an order disorder phase transformation. The small enthalpy value is associated with a minor conformational change as described in detail for the order disorder phase transformation of (C2)CdCl<sub>4</sub> (2.0KJ.mol<sup>-1</sup>) (Tello M. J, *et al*, 1977) and (Busico V, *et al*, 1979; Kind R, *et al*, 1979) for the longer chain derivatives (Cn)MCl<sub>4</sub> where M = Hg and Cd respectively. For T<sub>1</sub> (9.48KJ.mol<sup>-1</sup>) we may only speculate that this transition, is the quasi-melting transition as phase I's structure was not determined. For the compounds (BrC4)PbBr<sub>4</sub> and (BrC5)PbBr<sub>4</sub> the T<sub>2</sub> and T<sub>1</sub> values respectively, have displayed remarkably high enthalpy values of 24.35KJ.mol<sup>-1</sup> and 29.27KJ.mol<sup>-1</sup> respectively for these phase transformations. This may explain the inability to obtain Phase II's structure for (BrC4)PbBr<sub>4</sub>, as this may be the quasi melting transition. However as Phase I of (BrC5)PbBr<sub>4</sub> was unable to be determined this is only speculative. Below in table 4.2.2 are the structures and various phases of the compounds investigated in this study.

**Table 4.2.2:** Crystallographic structural tables of (BrCn)<sub>2</sub>PbBr<sub>4</sub> where n = 3 – 5 and (HOC<sub>2</sub>)<sub>2</sub>PbBr<sub>4</sub> which where completed in this study. Experiments were carried out with Mo K $\alpha$  radiation using a Bruker APEX-II CCD diffractometer.

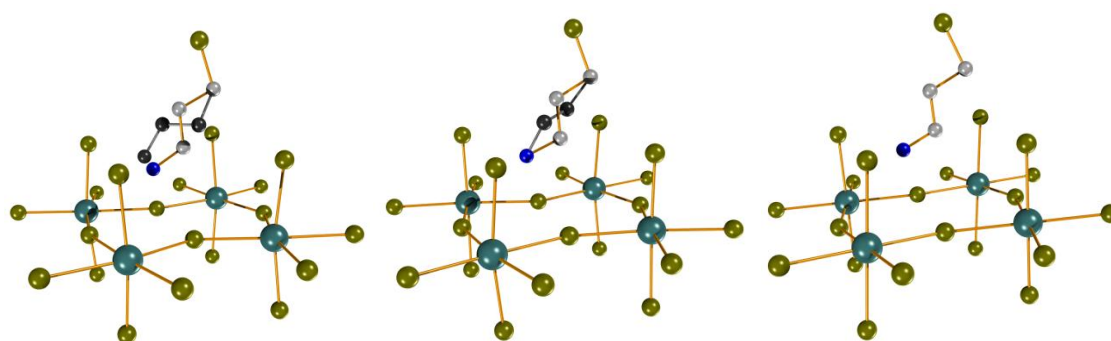
	5_II_rt	5_II_173	6_II_390K	6_III_293K	6_IV_173K
Crystal data					
Chemical formula	Br <sub>4</sub> Pb·2(C <sub>2</sub> H <sub>8</sub> NO)	Br <sub>4</sub> Pb·2(C <sub>2</sub> H <sub>8</sub> NO)	Br <sub>4</sub> Pb·2(C <sub>3</sub> H <sub>9</sub> BrN)	Br <sub>4</sub> Pb·2(C <sub>3</sub> H <sub>9</sub> BrN)	2(C <sub>3</sub> H <sub>9</sub> BrN)·Br <sub>4</sub> Pb
<i>M<sub>r</sub></i>	651.02	651.02	804.87	804.87	804.87
Crystal system, space group	Orthorhombic, <i>Pbcn</i>	Orthorhombic, <i>Pbcn</i>	Orthorhombic, <i>Pbca</i>	Orthorhombic, <i>Cmc2<sub>1</sub></i>	Orthorhombic, <i>Cmc2<sub>1</sub></i>
Temperature (K)	293	173	390	293	173
<i>a</i> , <i>b</i> , <i>c</i> (Å)	8.4523 (2), 8.6463 (2), 19.9071 (5)	8.4404 (1), 8.6068 (1), 19.8082 (3)	8.4084 (2), 8.2165 (2), 27.3662 (9)	27.2345 (6), 8.3588 (2), 8.1325 (2)	27.0655 (10), 8.4265 (3), 7.9674 (3)
$\alpha$ , $\beta$ , $\gamma$ (°)	90, 90, 90	90, 90, 90	90, 90, 90	90, 90, 90	90, 90, 90
<i>V</i> (Å <sup>3</sup> )	1454.83 (6)	1438.96 (3)	1890.67 (9)	1851.35 (8)	1817.10 (12)
<i>Z</i>	4	4	4	4	4
$\mu$ (mm <sup>-1</sup> )	22.56	22.81	21.58	22.04	22.46
Crystal size (mm)	0.95 × 0.42 × 0.09	0.26 × 0.26 × 0.03	0.70 × 0.46 × 0.09	0.82 × 0.49 × 0.07	0.30 × 0.27 × 0.03
Data collection					
Absorption correction	Integration <i>Bruker XPREP</i> (Bruker, 1999a)	Integration <i>Bruker XPREP</i> (Bruker, 1999a)	Integration <i>Bruker XPREP</i> (Bruker, 1999a)	Integration <i>Bruker XPREP</i> (Bruker, 1999a)	Integration <i>Bruker XPREP</i> (Bruker, 1999a)
<i>T<sub>min</sub></i> , <i>T<sub>max</sub></i>	0.017, 0.241	0.035, 0.625	0.008, 0.334	0.006, 0.293	0.087, 0.648
No. of measured, independent and observed [ <i>I</i> > 2 $\sigma$ ( <i>I</i> )] reflections	26275, 1753, 1322	24169, 1738, 1505	18257, 2286, 1101	13350, 2276, 1961	10260, 2232, 1759
<i>R<sub>int</sub></i>	0.056	0.050	0.082	0.051	0.066
Refinement					
<i>R</i> [ <i>F</i> <sup>2</sup> > 2 $\sigma$ ( <i>F</i> <sup>2</sup> )], <i>wR</i> ( <i>F</i> <sup>2</sup> ), <i>S</i>	0.033, 0.085, 1.19	0.020, 0.051, 1.09	0.077, 0.173, 1.09	0.032, 0.073, 1.06	0.039, 0.102, 1.04
No. of reflections	1753	1738	2286	2276	2232
No. of parameters	63	63	70	80	103

No. of restraints	0	0	28	7	65
H-atom treatment	H-atom parameters constrained $w = 1/[\sigma^2(F_o^2) + (0.0373P)^2 + 3.4255P]$ where $P = (F_o^2 + 2F_c^2)/3$ 0.001	H-atom parameters constrained $w = 1/[\sigma^2(F_o^2) + (0.0229P)^2 + 1.5268P]$ where $P = (F_o^2 + 2F_c^2)/3$ 0.001	H-atom parameters constrained $w = 1/[\sigma^2(F_o^2) + (0.0443P)^2 + 35.5995P]$ where $P = (F_o^2 + 2F_c^2)/3$ 0.001	H-atom parameters constrained $w = 1/[\sigma^2(F_o^2) + (0.0364P)^2]$ where $P = (F_o^2 + 2F_c^2)/3$ 0.001	H-atom parameters constrained $w = 1/[\sigma^2(F_o^2) + (0.0485P)^2]$ where $P = (F_o^2 + 2F_c^2)/3$ 0.001
$\Delta_{\max}, \Delta_{\min}$ (e Å <sup>-3</sup> )	1.35, -1.69	0.99, -1.08	0.92, -0.91	0.90, -1.17	1.48, -2.20
Absolute structure	—	—	—	Flack H D (1983), Acta Cryst. A39, 876-881	Flack H D (1983), Acta Cryst. A39, 876-881
Flack parameter	—	—	—	0.005 (13)	-0.007 (16)
	7_III_173K	7_III_293K	7_I_380K	8_III_173K	8_III_293K
Crystal data					
Chemical formula	2(C <sub>4</sub> H <sub>11</sub> BrN)·Br <sub>4</sub> Pb	2(C <sub>4</sub> H <sub>11</sub> BrN)·Br <sub>4</sub> Pb	2(C <sub>4</sub> H <sub>11</sub> BrN)·Br <sub>4</sub> Pb	2(C <sub>5</sub> H <sub>13</sub> BrN)·Br <sub>4</sub> Pb	2(C <sub>5</sub> H <sub>13</sub> BrN)·Br <sub>4</sub> Pb
<i>M<sub>r</sub></i>	832.93	832.93	832.93	860.98	860.98
Crystal system, space group	Orthorhombic, <i>Pbca</i>	Orthorhombic, <i>Pbca</i>	Orthorhombic, <i>Pbca</i>	Monoclinic, <i>P2<sub>1</sub>/c</i>	Orthorhombic, <i>Pbca</i>
Temperature (K)	173	293	380	173	293
<i>a</i> , <i>b</i> , <i>c</i> (Å)	8.2686 (2), 8.4437 (2), 27.7923 (6)	8.3133 (2), 8.4995 (3), 27.9491 (10)	8.192 (3), 32.939 (14), 8.182 (3)	15.902 (2), 8.4219 (11), 8.2012 (10)	8.452 (5), 8.197 (5), 32.589 (5)
α, β, γ (°)	90, 90, 90	90, 90, 90	90, 90, 90	90, 91.302 (6), 90	90, 90, 90
<i>V</i> (Å <sup>3</sup> )	1940.39 (8)	1974.85 (11)	2207.9 (14)	1098.1 (3)	2257.8 (19)
<i>Z</i>	4	4	—	2	4
μ (mm <sup>-1</sup> )	21.04	20.67	—	18.59	18.08
Crystal size (mm)	0.23 × 0.11 × 0.03	0.19 × 0.12 × 0.04	0.19 × 0.12 × 0.04	0.35 × 0.3 × 0.04	0.30 × 0.28 × 0.05
Data collection					
Absorption correction	Integration <i>Bruker XPREP</i> (Bruker, 1999a)	Integration <i>Bruker XPREP</i> (Bruker, 1999a)	—	Integration <i>Bruker XPREP</i> (Bruker, 1999a)	Integration <i>Bruker XPREP</i> (Bruker, 1999a)
<i>T<sub>min</sub></i> , <i>T<sub>max</sub></i>	0.545, 1	0.069, 0.611	—	0.068, 0.605	0.021, 0.525
No. of measured, independent and observed [ <i>I</i> > 2σ( <i>I</i> )] reflections	24092, 2339, 1699	11024, 2381, 1487	3562, 3315, 809	13326, 2649, 2162	28815, 2728, 1720
<i>R<sub>int</sub></i>	0.092	0.071	0.052	0.069	0.063
Refinement					
<i>R</i> [ <i>F</i> <sup>2</sup> > 2σ( <i>F</i> <sup>2</sup> )], <i>wR</i> ( <i>F</i> <sup>2</sup> ), <i>S</i>	0.032, 0.066, 1.03	0.042, 0.095, 1.01	0.079, 0.265, 0.92	0.068, 0.212, 1.08	0.043, 0.094, 1.17
No. of reflections	2339	2381	3315	2649	2728
No. of parameters	80	80	56	91	108
No. of restraints	0	0	1	5	8
H-atom treatment	H-atom parameters constrained $w = 1/[\sigma^2(F_o^2) + (0.020P)^2 + 2.3617P]$ where $P = (F_o^2 + 2F_c^2)/3$ < 0.001	H-atom parameters constrained $w = 1/[\sigma^2(F_o^2) + (0.0418P)^2]$ where $P = (F_o^2 + 2F_c^2)/3$ < 0.001	— $w = 1/[\sigma^2(F_o^2) + (0.1019P)^2]$ where $P = (F_o^2 + 2F_c^2)/3$ 0.318	H-atom parameters constrained $w = 1/[\sigma^2(F_o^2) + (0.1243P)^2 + 32.6847P]$ where $P = (F_o^2 + 2F_c^2)/3$ < 0.001	H-atom parameters constrained $w = 1/[\sigma^2(F_o^2) + (0.0236P)^2 + 11.607P]$ where $P = (F_o^2 + 2F_c^2)/3$ < 0.001
$\Delta_{\max}, \Delta_{\min}$ (e Å <sup>-3</sup> )	1.29, -1.11	0.79, -1.93	1.63, -0.86	7.48, -2.77	0.98, -0.73
Absolute structure	—	—	—	—	—
Flack parameter	—	—	—	—	—
Computer programs: Bruker <i>APEX2</i> , Bruker <i>SAINT</i> , <i>SHELXS97</i> (Sheldrick, 2008), <i>SHELXL97</i> (Sheldrick, 2008),					

#### **4.2.4 The structure and phases of (HOC2, BrC3, BrC4, BrC5)PbBr<sub>4</sub>**

The three halogenated alkyl chain hybrids of (BrC3, BrC4, BrC5)PbBr<sub>4</sub>, show a similar phase transition trend with increasing temperature. All three compounds' higher temperature phases form the orthorhombic staggered arrangements. However as the compounds cool down, only (BrC5)PbBr<sub>4</sub> undergoes a phase change to the monoclinic (eclipsed) phase. Both (BrC3)PbBr<sub>4</sub> and (BrC4)PbBr<sub>4</sub> remain in the orthorhombic staggered phase at low temperature. The hybrid (BrC4)PbBr<sub>4</sub> does not undergo a low temperature phase change between 173K and 293K (structures determined at these two temperatures support this). However (BrC3)PbBr<sub>4</sub> undergoes two low temperature phase transitions but still remains in the orthorhombic unit cell. Both low temperature phases IV and III of (BrC3)PbBr<sub>4</sub> contain a disordered alkyl ammonium chain in the non-centrosymmetric orthorhombic *Cmc2<sub>1</sub>*, where phase II reverts to an ordered orthorhombic *Pbca* state. The higher temperature phase II of (BrC5)PbBr<sub>4</sub> however, is a disordered orthorhombic *Pbca* phase whereas the low temperature phase III is a well ordered monoclinic *P2<sub>1</sub>/c* state. All the phases adopt the terminal halogen configuration where the ammonium head resides in the acute and right-angled position in the "box" (Billing D. G, Lemmerer A, 2007). Each structure and the differences in the respective phases will now be discussed separately.

### The structure and phases of (BrC3)PbBr<sub>4</sub>



**Phase IV**  
Orthorhombic  
*Cmc2<sub>1</sub>*  
a = 27.0655(10) Å  
b = 8.4265(3) Å  
c = 7.9674(3) Å  
T = 173K

**Phase III**  
Orthorhombic  
*Cmc2<sub>1</sub>*  
a = 27.2345(6) Å  
b = 8.3588(2) Å  
c = 7.9674(3) Å  
T = 293K

**Phase II**  
Orthorhombic  
*Pbca*  
a = 8.4084(2) Å  
b = 8.2165(2) Å  
c = 27.3662(9) Å  
T = 390K

**Scheme 4.2.2:** The phases of (BrC3)PbBr<sub>4</sub>, moving from the disordered Phase IV, and increasing in order of the aliphatic proceeding to the less disordered phase II, and finally the ordered phase I. The disordered atoms have been shaded in dark grey to enhance clarity.

The compound (BrC3)PbBr<sub>4</sub> displays four distinct phases, although only phases IV-II were able to be characterized, as phase I was beyond the heating capabilities of our instrument. The three phases are depicted in scheme 4.2.2 above. In (BrC3)PbBr<sub>4</sub> the terminal halogen behaves as an anchor, as it halogen bonds to the opposite layer to the ammonium group which is hydrogen bonded in the terminal halogen configuration. The C-Br...Br bonding angle is 171.4(4)° for phase IV, and increases marginally to 171.6(4)° for phase III. However the main change occurs after the transformation into phase II where the angle decreases to 166.8(9)°. The Br...Br halogen bonding distance also decreases as the temperature increases, increases from 3.586(2)Å to 3.620(2)Å and finally to 3.709(5)Å from phase IV to II respectively. Bromine has a Van der Waals radius of 1.85Å, and if two bromine atoms were just “touching” the bromine centres would be 3.7 Å apart. Hence phase IV and III have relatively strong halogen bonds compared to phase II, as the Br...Br halogen interatomic distances have considerable overlap and the C-Br...Br bond angle is much closer to 180°. The change in relative interlayer spacing increase is minor from phase IV to II. In phase IV and III the alkyl chain’s dynamic disorder exists in two potential wells, where the disordered atoms with the label A, reside within the alpha plane, created to measure the  $\angle_{\alpha}$  tilt

angle, of the plane of the chains relative to the plane containing the lead atoms, as previously described. The disordered atoms with the label B, form the non-coplanar atoms, which are described through the torsion angle Br4-C1-C2B-C3B which is  $67.733(1)^\circ$  and  $68.789(2)^\circ$  for phase IV and III respectively. This angle shows an increase between phase IV and III due to the disappearance of disorder of the nitrogen atom. Phase II displays no disorder and now only the coplanar atoms predominate with the chain residing in the all trans conformation. The disorder of the nitrogen atom in phase IV still lead to both disordered ammonium groups to hydrogen bond in the terminal halogen configuration, however, N1A sits closer to the bridging halides (Br2 and Br3) with a borderline bridging halogen configuration. This is a result of the bifurcated hydrogen bond of N1A-H1A...Br2, Br3, and the closer proximity to the bridging halides than N1B. However N1B displays the same bridging halogen bifurcated hydrogen bond N1B-H1F...Br2, Br3, but weaker than its counterpart. In Phase III, the nitrogen disorder is quenched with the nitrogen atom positioned closer to the apical halogens than the bridging halogens, i.e. it resembles N1B from phase IV.

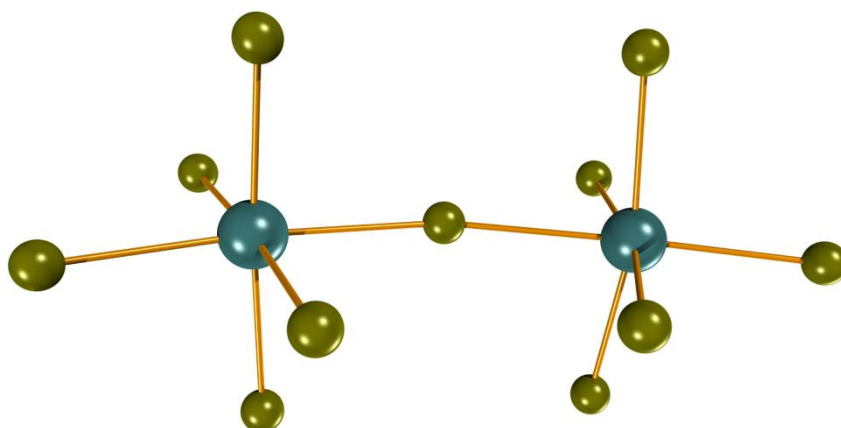


**Figure 4.2.2:** The lead bromide octahedra, depicting the distortion angles around the lead atom. The  $\text{Br}_{\text{ap}}\text{-Pb-Br}_{\text{ap}}$  and  $\text{X}_{\text{eq}}\text{-Pb-X}_{\text{eq}}$  angles which deviate significantly from  $180^\circ$ . The adjacent angles of the equatorial  $\text{X}_{\text{eq}}\text{-Pb-X}_{\text{eq}}$ 's which deviate from  $90^\circ$ . And the bridging angle Pb-Br-Br which deviate from  $180^\circ$ .

In the  $(\text{BrC3})\text{PbBr}_4$  layered hybrid the inorganic distortions are manifest in a slightly different way from that of the longer chain counterparts. The first type of distortion is the well accepted bridging Pb-Br-Pb angle and its effect on the stereochemical activity of leads lone pair. The second distortion is seen in the corrugation tilt  $\psi$  angles of the layers. Thirdly the distortion is also generally seen in the axial compression of the Pb-X bond length, and in turn one sees an elongation of the Pb-X bond lengths (axial increase or decrease of the Pb-X bond length has little

effect on the band structure as the Pb  $P_z$  orbital shows effectively no band dispersion as a result of the separation of the inorganic layers from the 3D motif, however the compression or elongation of the bridging halides does). However this effect is hardly seen in the PbBr hybrids. Lastly is the overall geometry around the lead centre, i.e. does it maintain an ideal octahedral geometry or distort considerably? This distortion is observed in the adjacent angles of the equatorial cis  $X_{ap}\text{-Pb-}X_{eq}$  and  $X_{eq}\text{-Pb-}X_{eq}$  angles respectively, and the expected linear trans bond angles of  $X_{ap}\text{-Pb-}X_{ap}$  and  $X_{eq}\text{-Pb-}X_{eq}$  respectively (figure 4.2.2 above). These angles give a greater indication as to the distortion around the metal centre to accommodate leads lone pair. Although the lead iodide octahedra experience similar distortions, these angles are distorted to a much lesser extent specifically seen comparatively with (IC3)PbI<sub>4</sub>, and that series of compounds as reported by (Lemmerer A, Billing D. G, 2010). In phase IV the Pb atom sits on a mirror plane, which includes the equatorial halogens. The  $Br_{ap}\text{-Pb-}Pb_{ap}$  is  $169.00(6)^\circ$  and the  $X_{eq}\text{-Pb-}X_{eq}$  of  $169.29(5)^\circ$ , and  $175.34(6)^\circ$  respectively, with the adjacent angles of  $Br_{ap}\text{-Pb-}X_{eq}$   $84.54(3)^\circ$  and  $88.66(4)^\circ$  respectively, and with  $X_{eq}\text{-Pb-}X_{eq}$  ranging  $83.44(4)^\circ$  -  $101.21(5)^\circ$  respectively. These bond angles are highly distorted considering the ideal angles are  $180^\circ$  and  $90^\circ$  respectively. The Pb-Br-Pb bridging angles are  $140.92(7)^\circ$  and  $157.29(6)^\circ$  which further depict the large distortion of the octahedra and the large influence of the lone pair of electrons.

The lead atom and equatorial halogens still reside on a mirror plane in phase III. However after the phase change all of the above mentioned angles display notable changes. Firstly reflected in the Pb-Br-Pb bridging angle which becomes  $144.66(6)^\circ$  and  $156.34(5)^\circ$  respectively, with the octahedral distortion decreasing as seen in the linear trans  $Br_{ap}\text{-Pb-}Br_{ap}$  and  $Br_{eq}\text{-Pb-}Br_{eq}$  angles of  $168.41(4)^\circ$ ,  $171.40(4)^\circ$  and  $176.93(5)^\circ$  respectively. The large distortion experienced in phase IV in the equatorial plane now move toward the ideal  $90^\circ$  angle in phase III, which now range  $85.61(4)^\circ$  -  $97.30(4)^\circ$ . Phase II undergoes greater octahedral idealizations, with the bridging angle now  $154.72(8)^\circ$  and the linear  $Br_{ap}\text{-Pb-}Br_{ap}$  and  $Br_{eq}\text{-Pb-}Br_{eq}$  now  $180^\circ$  respectively. In addition the equatorial cis angles  $Br_{eq}\text{-Pb-}Br_{eq}$  move close to  $90^\circ$  being  $88.64(5)^\circ$ , and  $91.36(5)^\circ$  respectively. The corrugation  $\psi$  tilt stays relatively the same through all three phases, with minor increases upon heating.

### The structure and phases of $\text{BrC4PbBr}_4$

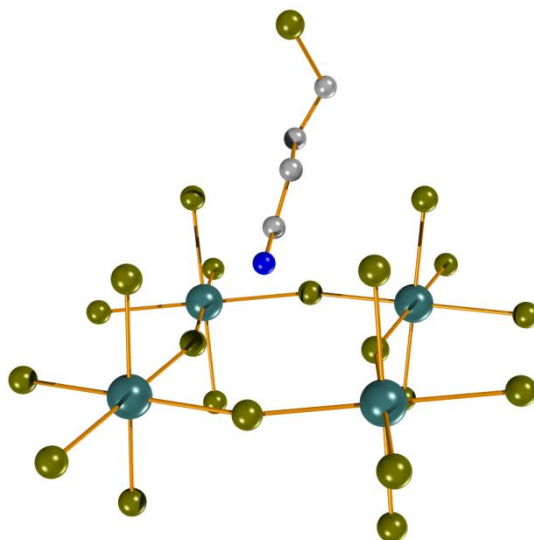


**Figure 4.2.3:** Phase III of  $(\text{BrC4})\text{PbBr}_4$  displaying the all trans conformation of N1-C4, and the kink of the Br atom out of the alpha plane of the alkyl ammonium chain.

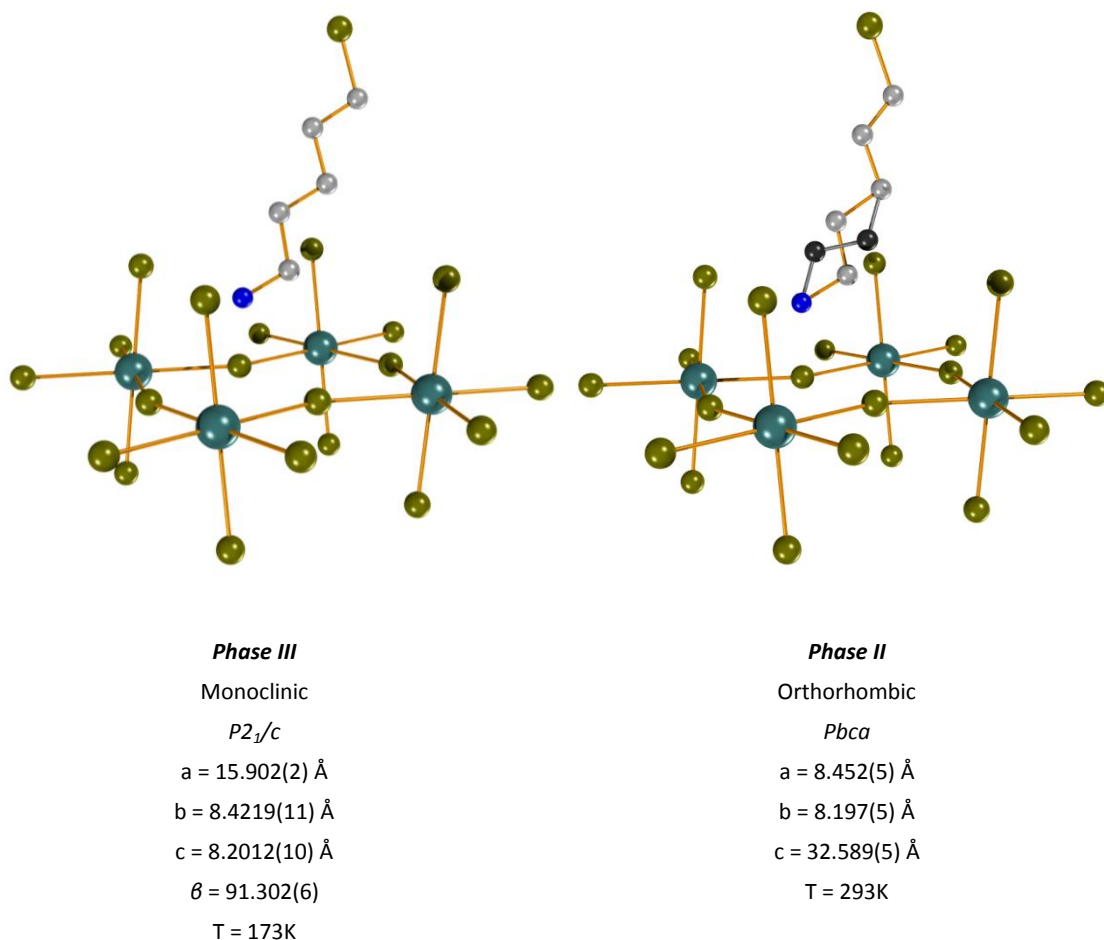
Phase III of  $(\text{BrC4})\text{PbBr}_4$  displays a reasonably strong halogen bonding interaction with a  $\text{Br}\cdots\text{Br}$  distance of  $3.6063(8)\text{\AA}$  with a  $\text{C-Br}\cdots\text{Br}$  angle of  $169.6(2)^\circ$ . The alkyl chains conformation from N1-C4, is all trans, however there exists a kink (*syn-clinal*)  $\text{Br4-C4-C3-C2}$  of  $67.321(6)^\circ$  as seen in figure 4.2.3. The tilts of the chains ( $\angle_\alpha$  and  $\angle_\varphi$ ) resemble those found in the ordered phase III of  $(\text{BrC5})\text{PbBr}_4$ . Furthermore the corrugation  $\psi$  tilt and bridging angle ( $7.803(10)^\circ$  and  $156.19(2)^\circ$  respectively) also strongly resemble those of phase III of  $(\text{BrC5})\text{PbBr}_4$ . However  $(\text{BrC4})\text{PbBr}_4$  does display a large  $\angle_\beta$  tilt of the ammonium group, leading to the N1-C1 bond angle to be considerable within the apical halogen plane. Unfortunately phase II was not able to be determined, however phase I did give a well resolved inorganic component. There is a large increase in interlayer spacing from phase III to phase I  $\sim 2.57\text{\AA}$ . We may speculate that this increase may be caused by, firstly, the conformational change in the chain to all trans, and secondly the  $\angle_\alpha$  and  $\angle_\varphi$  tilts of the chain to increase to  $\sim 90^\circ$  and decrease to its lowest value respectively. The inorganic layers further show a decrease in corrugation  $\psi$  tilt angle from phase III to I (from  $7.803(10)^\circ$  to  $0^\circ$ ), with a minor decrease in Pb-Br-Br bridging angle ( $156.19(2)^\circ$  to  $152.6(4)^\circ$ ). However the decrease in bridging angle with increasing temperature is not a commonly observed trend, usually Pb-X-Pb increases toward  $180^\circ$ . The octahedra themselves experience minor distortions unlike phase IV of  $(\text{BrC3})\text{PbBr}_4$ . Where the trans angles  $X_{\text{ap}}\text{-Pb-}X_{\text{ap}}$

and  $X_{eq}-Pb-X_{eq}$  are both linear, and only minor distortions of the cis angles of  $Br_{ap}-Pb-X_{eq}$  and  $X_{eq}-Pb-X_{eq}$  of  $83.43(2)^\circ$ ,  $89.48(2)^\circ$ , and  $88.79(2)^\circ$ ,  $91.21(2)^\circ$ , are experienced.

### ***The structure and phases of (BrC5)PbBr<sub>4</sub>***

The halogen bonding interaction of (BrC5)PbBr<sub>4</sub> is seen in the angle C-Br...Br of  $172.7(5)^\circ$  for phase III, which decreases to  $169.7(4)^\circ$  for phase II. The Br...Br halogen bonding distance however decreases marginally as the temperature increases, from  $3.843(3)\text{\AA}$  to  $3.833(2)\text{\AA}$  from phase III to II respectively. Both phase III and II have a much weaker halogen bonding interaction compared to the phases of (BrC3)PbBr<sub>4</sub>, however phase III does have a marginally stronger halogen bonding interaction as the C-Br...Br angle is closer to  $180^\circ$  than in phase II. In phase III the alkyl chain, and the bromine atom exist in the all trans configuration. In phase II the alkyl chain's dynamic disorder exists in two potential wells, where the disordered atoms with the label A, reside within the alpha plane, created to measure the  $\angle_\alpha$  tilt angle. The disordered atoms with the label B, form the non-coplanar atoms, which are described through the torsion angle N1-C1B-C2B-C3 which is  $73.053(3)^\circ$  which is the *syn-clinal* conformation. Unlike (BrC3)PbBr<sub>4</sub> the disorder of the chain of (BrC5)PbBr<sub>4</sub> increases as the temperature increases. The interlayer spacing also exhibits an increase from phase III to II by  $\sim 0.3\text{\AA}$  as the disorder increases. In addition the  $\angle_\alpha$  tilt of the chain decreases, and the  $\angle_\varphi$  tilt of the plane containing the chain increases from  $73.597(2)^\circ$  to  $88.820(9)^\circ$  and  $88.726(10)^\circ$  (accounting for the disorder). These changes follow the general trend observed for the aliphatic metal 2D layered halide hybrids. The inorganic layers are eclipsed at the low temperature phase III and staggered in phase II, and experiences a decrease in corrugation  $\psi$  tilt angle (from  $7.915(3)^\circ$  to  $6.161(19)^\circ$ ), with a minor decrease in Pb-Br-Br bridging angle ( $155.88(6)^\circ$  to  $155.12(3)^\circ$ ). The octahedra themselves only experience minor distortions unlike (BrC3)PbBr<sub>4</sub>. Where the  $X_{ap}-Pb-X_{ap}$  and  $X_{eq}-Pb-X_{eq}$  are both linear, with only minor distortions of the cis  $Br_{ap}-Pb-X_{eq}$  and  $X_{eq}-Pb-X_{eq}$  angles as seen in phase III of (BrC4)PbBr<sub>4</sub>.





**Scheme 4.2.3:** The phases of  $(\text{BrC5})\text{PbBr}_4$ , moving from the ordered Phase III, to the disordered phase II. The disordered atoms have been shaded in dark grey to enhance clarity.

### The Structure of $(\text{HOC2})\text{PbBr}_4$

The room temperature structure of  $(\text{HOC2})\text{PbBr}_4$  was previously reported by (Mercier N, *et al*, 2004). We briefly discuss the important structural features here for later comparison for the optical experiments. As described by Mercier, the  $\text{HOC}_2\text{H}_4\text{NH}_3$  cation has two hydrogen bond donors and one hydrogen bond acceptor. This cation forms a dimer between the layers, forming a  $R^2_2(10)$  hydrogen bonded ring as seen in Fig 4.2.4. This interaction causes further adhesion between the layers themselves, which drastically decreases the interlayer spacing, to  $9.9041(3)\text{\AA}$ , with an interlayer  $\text{Br}\cdots\text{Br}$  contact distance of only  $4.632(1)\text{\AA}$ . The ammonium's hydrogen bonding to the oxygen alters the usual hydrogen bonding configurations observed. The inorganic tilt distortions are minimal, where the bridging angle  $\text{Pb}-\text{Br}-\text{Pb}$  of  $171.951(15)^\circ$  which is the lowest reported in a lead bromide structure thus far. It also experiences a minor corrugation  $\Psi$  tilt angle of  $5.144(1)^\circ$ . The small distortion in the bridging angle means a reduced influence of the lone pair's stereo chemical activity. However as observed in  $(\text{BrC3})\text{PbBr}_4$  the

octahedral distortions are more pronounced. The  $X_{ap}-Pb-X_{ap}$  and  $X_{eq}-Pb-X_{eq}$  are no longer linear,  $177.94(2)^\circ$  and  $174.83(2)^\circ$  respectively, with only minor distortions of the adjacent cis angles  $Br_{ap}-Pb-X_{eq}$  from  $90^\circ$ , however more notable distortions in the  $X_{eq}-Pb-X_{eq}$  cis angles ranging  $83.74(2)^\circ - 94.07(2)^\circ$  which is comparable with phase II of  $(BrC4)PbBr_4$ . The high temperature phases were undetermined from our analysis as they exceeded the heating capability of our instrument.

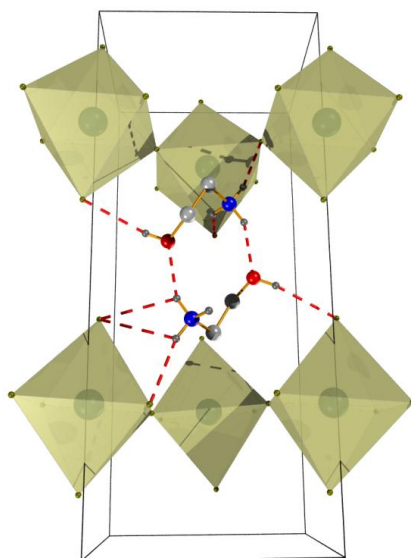


**Figure 4.2.4:** The packing diagram of  $(HOC2)PbBr_4$  displaying the dimer between the layers, forming an  $R^2_2(10)$  hydrogen bonded ring.

**Table 4.2.3:** Important geometrical parameters associated with the phase transitions, and halogen bonding interactions.

Geometric parameter	5, II	6, IV	6, III	6, II	7, III	7*, II	7*, I	8, III	8, II
Interlayer Spacing (Å)	9.9041 (3)	13.5327 (10)	13.6172 (6)	13.6831 (9)	13.8961(6 )	undet ermin ed	16.46 9 (19)	15.902 (2)	16.294 (5)
Bridging angle Pb-Br-Pb (°)	171.95 1 (15)	140.92 (7); 157.29 (6)	144.66 (6); 156.34 (5)	154.72 (5)	156.19 (2)		152.6 (4)	155.88 (6)	155.12 (3)
Corrugation $\Psi$ tilt (°)	5.144 (1)	5.500 (3)	5.797(23)	6.012 (5)	7.803 (10)		-	7.915 (3)	6.161 (19)
Compression Pb-Br bond lengths	axial	axial	axial	axial	axial			none	axial
Conformation of the hydrocarbon chain		flat (A); bent (B)	flat (A); bent (B)	flat	bent		-	flat	flat (A); bent (B)
Non coplanar torsion angles (°)		Br4-C1-C2B-C3B (67.733(1) )	Br4-C1-C2B-C3B (68.789(2))	-	Br3-C1-C2-C3 (67.321(6) )		-	-	C2-C3-C4B-C5B (73.053(3) )
Interdigitation		Br(4)	Br(4)	Br(4)	C(1)			C(2)	C(2)
Tilt of Chains $\angle_{\varphi}$ (°)		27.192(3); 21.724(2)	23.820(8)	23.144(3)	26.460(4)		-	28.869(8)	16.592(5)
Tilt of plane $\angle_{\alpha}$ (°)		84.942(3); 86.390(3)	86.587(2); 87.530(2)	86.354(5)	62.920(2) ex Br;		-	73.597(2)	88.820(9); 88.726(10) )
Tilt of NH <sub>3</sub> group $\angle_{\beta}$ (°)		60.064(9); 38.747(10) )	67.995(6); 29.055(12)	65.797(1)	73.291(3)		-	65.209(7)	63.900(6); 30.295(11) )
Position of ammonium group		acute	acute	acute	acute		-	acute	acute
Hydrogen bonding configuration		Right angled	Right angled	Right angled	Right angled		-	Right angled	Right angled
C-Br...Br (Å)		3.586(2)	3.620(2)	3.709(5)	3.6063(8)		-	3.8430(3)	3.833(2)
C-Br...Br (°)		171.4(4)	171.6(4)	166.8(9)	169.6(2)			172.7(5)	169.7(4)

\* Unit cells only/only inorganic resolvable in the crystal structure.

**Table 4.2.4:** Inorganic distortions of the bond lengths and angles for the respective compounds and their phases.

Compound	5 (II) 173K	5 (II) 293K	6 (IV)	6 (III)	6 (II)	7 (II) 173K	7 (II) 293K	8 (III)	8 (II)
Parameter	HOC2	HOC2	BrC3	BrC3	BrC3	BrC4	BrC4	BrC5	BrC5
Pb-Br <sub>eq</sub>	3.0408 (3)	3.0149 (6)	3.0443 (17)	2.9807 (13)	3.0091 (17)	3.0148 (6)	3.0352 (8)	2.9960 (14)	3.0088 (16)
Pb-Br <sub>eq</sub>	3.0015 (3)	3.0462 (6)	3.0658 (14)	2.9852 (17)	3.0150 (16)	3.0241 (6)	3.0261 (8)	3.0143 (14)	3.0198 (16)
Pb-Br <sub>eq</sub>	3.0408 (3)	3.0149 (6)	2.974 (2)	3.0402 (14)	3.0091 (17)	3.0148 (6)	3.0352 (8)	2.9960 (14)	3.0088 (16)
Pb-Br <sub>eq</sub>	3.0015 (3)	3.0462 (6)	2.9810 (17)	3.0710 (12)	3.0150 (16)	3.0241 (6)	3.0261 (8)	3.0143 (14)	3.0198 (16)
Pb-Br <sub>ax</sub> (X2)	2.9824 (4)	2.9874 (8)	2.9797 (13)	2.9846 (9)	2.980 (2)	2.9852 (6)	2.9836 (10)	3.0019 (18)	2.9983 (11)
Br-Pb-Br	94.217 (15)	94.08 (3)	101.21 (6)	91.31 (2)	88.638 (14)	88.787 (5)	91.257 (6)	88.536 (14)	91.75 (4)
Br-Pb-Br	90.9150 (10)	91.093 (3)	84.84 (5)	97.29 (5)	91.362 (14)	91.213 (5)	88.743 (6)	91.464 (14)	88.25 (4)
Br-Pb-Br	90.915 (2)	83.74 (3)	83.446 (16)	85.781 (13)	88.638 (14)	88.787 (5)	91.257 (6)	88.536 (14)	91.75 (4)
Br-Pb-Br	83.955 (14)	91.093 (3)	90.50 (3)	85.61 (4)	91.362 (14)	91.213 (5)	88.743 (6)	91.464 (14)	88.25 (4)
Br-Pb-Br <sub>ap</sub>	91.118 (10)	89.85 (2)	90.22 (4)	84.21 (2)	85.94 (7)	90.515 (16)	90.90 (2)	89.54 (5)	88.81 (3)
Br-Pb-Br <sub>ap</sub>	89.892 (10)	91.55 (2)	95.50 (3)	89.29 (3)	94.06 (7)	89.485 (16)	89.10 (2)	90.46 (5)	91.19 (3)
Br-Pb-Br <sub>ap</sub>	89.121 (10)	89.76 (2)	88.67 (4)	89.84 (3)	91.23 (7)	83.425 (17)	96.40 (3)	95.46 (5)	85.38 (3)
Br-Pb-Br <sub>ap</sub>	89.776 (10)	88.71 (2)	84.54 (3)	95.79 (2)	88.77 (7)	96.575 (17)	83.60 (3)	84.54 (5)	94.62 (3)
Br-Pb-Br	174.863 (14)	174.83 (3)	168.29 (5)	176.93 (5)	180	180	180	180	180
Br-Pb-Br	174.863 (14)	174.83 (3)	175.34 (6)	171.40 (4)	180	180	180	180	180
Br <sub>ap</sub> -Pb-Br <sub>ap</sub>	178.517 (15)	177.94 (3)	169.00 (6)	168.41 (4)	180	180	180	180	180
Pb-Br-Pb	171.952 (15)	171.80 (3)	157.29 (6)	156.34 (5)	154.72 (8)	156.19 (2)	157.48 (4)	155.88 (6)	155.12 (3)
Pb-Br-Pb	-	-	140.92 (7)	144.66 (6)	-	-	-	-	-

#### 4.2.5 Conclusions

In the (BrC3)PbBr<sub>4</sub> layered hybrid the inorganic distortions manifest in a slightly different way from that of the longer chain derivatives. With the combination of the strong halogen bonding interaction and the disordered aliphatic in Phase IV and III, and the general high inorganic distortion trend for low temperature phases results in an increased octahedral distortion experienced in phase IV and III of (BrC3)PbBr<sub>4</sub>. These distortions are highly reduced in phase II. At low temperature the metal centred octahedral distortions are large, as a result there is an increase of the stereochemical activity of the lone pair on the metal centre (Mitzi D. B, 1996), also partially due to the decreased covalent character of the Br-Pb bond (bond length) compared to the lead iodide counterpart. Conversely, the trend of the order disorder phases are observed in (BrC3)PbBr<sub>4</sub> where the low temperature phase IV is the most disordered, and increases in order through each progressive phase to become the ordered phase II. In addition the halogen

bonding interaction decreases with increasing temperature. The octahedral distortions decrease in (BrC4)PbBr<sub>4</sub> however are still comparatively large, and also experiences a fairly strong Br...Br, halogen bonding interaction. The halogen bonding interaction becomes much weaker in (BrC5)PbBr<sub>4</sub>, and now experiences a highly reduced distortion of the metal centres octahedra. The phase transformations of (BrC5)PbBr<sub>4</sub> proceed in the expected way of the disordered (monoclinic) low temperature phase III to the ordered (orthorhombic) phase II. Essentially one may say that the strength of the halogen bonding interaction decreases as temperature increases, and with increasing chain length. In addition the octahedral distortion increases with increasing halogen bonding strength. This is reiterated in (HOC2)PbBr<sub>4</sub>, where the short interlayer spacing results in some metal centred octahedral distortions, however drastically decreasing the Pb-Br-Pb bridging angles distortion. Table 4.2.4 displays the bond lengths and angles of the inorganic octahedra in order to readily compare the distortions experienced in the different compounds and their respective phases. Axial compression is more predominant in the (XCn)PbBr<sub>4</sub> compounds than its aliphatic counterparts; however it is still very small in comparison with the iodide derivatives. Lastly the halogen bonding interaction has drastically increased the thermal stability of the lead bromide hybrids, as the quasi-melting temperatures are drastically increased by halogen bonding interaction, compared with the simple aliphatic (Cn)PbBr<sub>4</sub> compounds.

**4.3 Optical properties of (C<sub>n</sub>H<sub>2n</sub>NH<sub>3</sub>)<sub>2</sub>PbX<sub>4</sub> where n = 4-7, and (HOC<sub>2</sub>H<sub>4</sub>NH<sub>3</sub>)<sub>2</sub>PbX<sub>4</sub>, where X = Br and I and (BrC<sub>n</sub>H<sub>2n</sub>NH<sub>3</sub>)<sub>2</sub>PbBr<sub>4</sub> where n = 3-5 and (IC<sub>n</sub>H<sub>2</sub>NH<sub>3</sub>)<sub>2</sub>PbI<sub>4</sub> where n = 2-6 and (BrC<sub>2</sub>H<sub>4</sub>NH<sub>3</sub>)<sub>2</sub>PbI<sub>4</sub>.**

**4.3.1 Introduction**

The distortions of the inorganic layer have been attributed to the arrangement of the hydrogen bonding between the inorganic layers and the position of the ammonium head within the void or the “box”. This conclusion arose through the study of the thermochromic phase transitions of (Cn)MX<sub>4</sub> hybrids, where the ammonium head alters from the acute to obtuse positions, and or vice versa, through thermal cycling. This interaction appears to have the largest impact on the bridging angle (M-X-M) of the layers and hence was dubbed the main cause for the distortions (Willet R. D, *et al*, 1974; Ishihara T, *et al*, 1989; Billing D. G, Lemmerer A, 2007; 2008; Lemmerer A, 2007). This was further confirmed by our studies in 4.1 and 4.2. Therefore employing other functionalizations on the (RNH<sub>3</sub>) ammonium R group to anchor and or create greater octahedral idealization through weak interactions have also been attempted in order to create greater

stabilizations (thermal and structural idealizations) within the inorganic layers. This has included the use of the aliphatic diamines, however the rigidity this template places on the system, has been shown to form other organic-inorganic motif types in preference to the layered perovskite motif (Lemmerer A, 2007). Less rigid templates have been successfully used to achieve greater stability with the use of an alcohol, carboxylic acid and a halogen terminally substituted at the end of an aliphatic chain (Mercier N, *et al*, 2004; 2005; Sourisseau S, *et al*, 2007a; Lemmerer A, Billing D. G, 2010).

As these other weak interactions have been employed in order to create various inorganic stabilizations within the layers, the authors (Knutson J. L, *et al*, 2005) have completed a series of extended Hückel tight binding band structure calculations for the tin iodide hybrids, in order to explain the distortions of the inorganic octahedra and the impact on the band gap of the material. They investigated the undistorted 2D (A)<sub>2</sub>SnI<sub>4</sub> lattice, the in-plane only distortions, (the M-X-M distortions only), out of plane distortions (corrugations) and the combination of the in and out of plane distortions. Their key findings will be described here as we attempt to further investigate these parameters experimentally for the lead halogenated compounds. In the undistorted tin iodide lattice, the anti-bonding interactions from the I  $p_x$  and  $p_y$  bands are the main cause for the significant dispersion in the Sn  $p_x$  and  $p_y$  bands in the conduction band. The Sn  $p_z$  band does not significantly contribute to the bottom of the conduction band and it shows no dispersion because of the separation of the layers in the vertical direction. When the in-plane distortions do occur, it results in the loss of anti-bonding interaction from the I  $p_x$  and  $p_y$  band, which results in a lowering of the top of the valence band, or the Sn 5s band, which ultimately results in the band gap to increase. Furthermore the loss of anti-bonding interaction between Sn  $p$  and I  $p$  orbital's as a result of larger in plane distortions lowers the top of the conduction band, however it is the bottom of the conduction band which results in the band gap to be altered. In addition the in-plane distortions do break the overall symmetry, and hence the degeneracy of the Sn  $p_x$  and  $p_y$  bands of the crystal which causes a large amount of anti-bonding interactions between the Sn  $p$  and the hybrid I  $s/p$  orbital in the bottom of the conduction band are disturbed. The extent to which the I  $s/p$  hybrid orbital is mixed into the bottom of the conduction band is directly proportional to the M-X-M bonding angles deviation from 180°. This mixing increases and raises the bottom of the conduction band as the distortion of the M-X-M bonding angle deviation from 180°. These two main factors are the main reason for the increasing band gap, i.e. the decreasing and increasing of the valence and conduction bands respectively due to the loss of antibonding interactions with I  $p$  orbital's, and the increased mixing of the hybrid I  $s/p$  orbital's. The exclusively out of plane distortions also influence the top

of the valence band (Sn 5s orbital's) which are stabilized by the out plane distortions. The stabilizations of the valence band caused from the out of plane distortions are only half of that caused through the in-plane distortions however the calculations only distorted one Sn-I-Sn bond angle  $p_x$  where  $p_y$  was still idealized as creating only out of plane distortions requires the M-X<sub>y</sub>-M angle to remain idealized. Furthermore it has also been suggested that that a distortion mechanism that yields mainly the out-of plane distortions, should support the smallest band gaps (Knutson J. L, *et al*, 2005). Lastly the shorter Sn-I bonding distances in the equatorial bonds result in the destabilization of the top of the valence band, due to the increase in Sn-I anti-bonding, which raises the top of the valence band (reducing the band gap), however has no effect on the conduction band. Hence axial bond compression in the MX<sub>6</sub> octahedra does affect the band gap as it creates elongations in the equatorial M-X bond lengths.

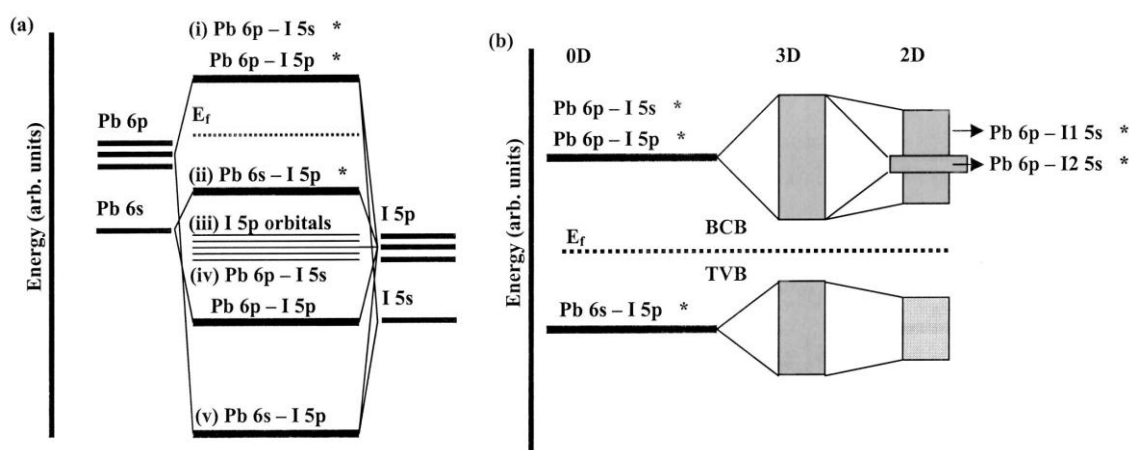


**Figure 4.3.1:** a) The molecular orbital diagram of an isolated lead iodide Pbl<sub>6</sub> cluster (0D), displaying the anti-bonding orbital's of the  $\pi$ -antibonding Pb 6p – I 5p and the  $\sigma$ -antibonding Pb 6p – I 5s at the bottom of the conduction band (BCB). The top of the valence band (TVB) is comprised of the Pb 6s – I 5p  $\sigma$ -antibonding (nonbonding) orbitals, below which are the nonbonding I 5p states. Further below are the  $\pi$ -bonding Pb 6p – I 5p and the  $\sigma$ -bonding Pb 6p – I 5s orbitals in the bottom state. b) The 3D and 2D states are extrapolated from the 0D case, where the 3D case remains similar to the 0D system. However the 2D system the I1 and I2 states split due to the two dimensional nature, where the (I1)  $\pi$ -antibonding Pb 6p – I 5p and the  $\sigma$ -antibonding Pb 6p – I 5s show greater dispersion than the (I2)  $\sigma$ -antibonding Pb 6p – I 5s orbital. This is due to the loss of  $\pi$  character as a result of the separation of the layers. The top of the valence band still remains with mainly the Pb 6s, as well as the I 5p  $\sigma$ -antibonding orbital's (Umebayashi T, *et al*, 2003).

In addition to the work completed by Knutson and co-workers, calculations obtained of the 3D (CH<sub>3</sub>NH<sub>3</sub>)PbI<sub>3</sub> and 2D (C<sub>4</sub>)PbI<sub>4</sub> hybrid perovskite compounds, where the electronic band structure and DOS were investigated (Umebayashi T, *et al*, 2003). Their calculations for the lead iodide hybrids also agree with the band assignments allocated for 2D tin iodide compounds. Figure 4.3.1 displays the molecular orbital bonding diagram of a lead iodide Pbl<sub>6</sub> cluster, a zero

dimensional case in a) and the extrapolation into the 3D and 2D systems in b). This diagram enables us to picture the band structure arguments given by Knutson and co-workers. The lack of dispersion of the Pb- $p_z$  hybrid  $\sigma$ -antibonding orbital (I2) only may be seen from the reduction of dimensionality from 3D to 2D, where the hybrid Pb  $p_x$  and  $p_y$  orbital's display the much larger dispersion (I1), as a result of the  $\pi$ -antibonding interaction still being present.

Substitution of the metal centre of the group IV metals, of  $(C_4H_9NH_3)_2MI_4$  where M = Ge, Sn and Pb were investigated in order to ascertain the impact the  $ns^2$  lone pair has on the inter and intra octahedral geometry and distortions experienced in order to accommodate the lone pair on the metal centre (Mitzi D. B, 1996). Larger metal centred octahedral distortions were experienced in the following order Pb < Sn < Ge, which was mainly attributed to the increase in covalent character between the metal and the halogen. However the M-I-M bridging angle between the  $MI_6$  octahedra where  $166.27(8)^\circ$ ,  $159.61(5)^\circ$ , and  $155.19(6)^\circ$  for Ge, Sn and Pb respectively, which displays an alternate manifestation of a distortion mechanism through the M-I-M bridging angle, which becomes apparent as we move down the group. However the distortions around the metal centre have been said to display the greater impact on the lone pair's stereo chemical activity. Furthermore, although the bridging angle of the germanium compound is closer to  $180^\circ$  the layers themselves were shown to display larger corrugations than its Sn and Pb counterparts (Mitzi D. B, 1996).

In addition, although these calculations generally do not take into account the influence of the organic cation, they do give a healthy background to the predominant effects associated with chains and altering of the band structure. The organic cation may greatly enhance the excitons binding energy, creating much greater excitonic stability for highly efficient luminescence emissions at room temperature (Hong X, *et al*, 1992). However the low dielectric constants of the alkyl ammonium cations have one drawback as the chains are prone to phase transitions due to their high flexibility. Never the less it does make them great candidates for study, as we may have greater control over the influence attributed by the organic as they only have simple or no functionalizations, and we are able to obtain optical data from more than one phase, which adds to the data points we have, which we are able to explain more readily. The distortions mechanisms due to phase transitions of the inorganic components have been described in the previous sections (and references cited therein), in this section however we attempt to rationalize the optical properties with the structural aspects where possible, such as the in and out of plane distortions, the metal centred octahedral distortions themselves, the influence of the terminal halogen on the band structure, and finally the issue of short interlayer spacing.



Herein we report the optical properties of the structures of 4.1 and 4.2 and the optics and structural summary of the iodide analogues (XCn)PbI<sub>4</sub> where n = 2-6 and X = I, (ZCn)PbI<sub>4</sub> where n = 2 and Z = OH and Br, and (Cn)PbI<sub>4</sub> where n = 4-7 as the structures have been previously reported (Lemmerer A, Billing D. G, 2010; Mercier N, *et al*, 2004; Sourisseau S, *et al*, 2007a; Billing D. G, Lemmerer A, 2007).

#### **4.3.2 Results and discussion**

The important structural aspects of the lead iodide series of compounds will be briefly summarised and discussed here as they have been previously published. Furthermore the (Cn)PbI<sub>4</sub> series where n = 4-7, structures and phase behaviour has been previously published by (Billing D. G, Lemmerer A, 2007; Lemmerer A, 2007) and the optical properties of the aliphatic (Cn)PbI<sub>4</sub> have also been extensively investigated, where the general optical and luminescence properties were investigated by (Hong X, *et al*, 1989; Ishihara T, *et al*, 1990), dielectric confinement/image charge effect (Hong X, *et al*, 1992b; Tanaka K, *et al*, 2005; Shimizu M, 2005) and magneto optical properties of the excitons (Xu C.Q, *et al*, 1991; Kataoka T, *et al*, 1993) for the lead iodide compounds. The lead bromide aliphatics have been investigated for their optical properties (Tabauchi, *et al*, 2000) biexciton generation (Kato Y, *et al*, 2003), exciton polariton interactions (Tamaki R, *et al*, 2008) and the excitonic fine structure displayed (Ema K, *et al*, 2006; Kitazawa N, *et al*, 2009; 2010; 2010b). However herein we wish to highlight the important inorganic and structural distortions that occur, and to further correlate a direct structure to optical property relationship, as this has not been previously reported (with the exception of (C12)PbI<sub>4</sub> by Pradeesh K, *et al*, 2009b). In addition the aliphatic lead iodide series serves as a literature benchmark for the optical properties on which we are reporting.

### 4.3.3 Structural summary of the lead iodide analogues

**The (ZCn)PbI<sub>4</sub> series where Z = I for n = 2-6, and where Z = OH and Br for n = 2.**

**Table 4.3.1:** Important geometrical parameters of the (X-Cn)PbI<sub>4</sub> series where X = I for n =2-6 and X = OH and Br for n = 2. (This data is from our own structural (SC-XRD) experiments however the structures previously reported by (Mercier N, *et al*, 2004 (9); Sourisseau S, *et al*, 2007a 10-11; Lemmerer A, Billing D. G, 2010 9-15).

Geometric parameter	9 (HOC2)	10 (BrC2)	11 (IC2)	12 (IC3)	13 (IC4)	14 (IC5)	15 (IC6)
Interlayer Spacing (Å)	10.1370 (2)	10.3086(6)	12.5683(3)	13.9916(14 )	15.3616(3 )	16.272(4)	15.9526(5)
Bridging angle Pb-I-Pb (°)	159.09 (1)	174.38(2); 176.92(2)	147.242 (15)	148.633 (13)	147.051 (9)	154.39 (4)	161.076 (16)
Corrugation $\Psi$ tilt (°)	13.30(1)	2.08(1)	15.31(1)	12.70(1)	12.06(1)	5.64(2)	9.94(1)
Compression Pb-I bond lengths	Axial	Axial	Axial	Axial	-	Bridging	Axial
Conformation of the hydrocarbon chain	Bent	Bent	Flat	Bent	Flat	Flat	Bent
Non coplanar torsion angles (°)	N1-C1-C2-O1 59.7(3)	Br1-C1-C2-N1 68.9(6)	-	C1-C2-C3-I1 73.3(6)	-	-	C1-C2-C3-C4 68.9 (9); C4-C5-C6-I2 67.7(9)
Interdigitation	-	-	I1	C3	C4	C4	C4
Tilt of Chains $\angle_{\varphi}$ (°)	-	-	36.075(6)	19.775(5)	31.090(3)	31.191(8)	25.373(4)
Tilt of plane $\angle_{\alpha}$ (°)	-	-	60.608(2)	63.954(3)*	77.861(2)	68.829(2)	33.938(4)^
Tilt of NH <sub>3</sub> group $\angle_{\beta}$ (°)	-	-	29.197(3)	25.596(3)	26.282(2)	64.125(7)	55.610(4)
Position of ammonium group	-	-	Obtuse	Obtuse	Obtuse	Acute	Acute
Hydrogen bonding configuration	-	-	Equilateral	Equilateral	Equilateral	Right-angled	Right-angled
C-X...I (Å)	-	3.6715(7)	3.8276(7)	3.8038(6)	3.9313(4)	3.840(2)	3.8700(7)
C-X...I (°)	-	160.8(2)	176.4(2)	167.3(2)	163.1(1)	177.5(4)	161.3(2)
Interlayer I...I (Å)	4.2204 (3)	4.8892(6)	6.6694(7)	7.928(1)	9.2300(4)	9.907(3)	10.7170(7)

\*excluding the terminal iodine. ^plane only contains N1-C1-C2-C3

Table 4.3.1 displays the important structural aspects of compounds **9-15** for easy comparison. Included are the tilts of the chains ( $\angle_{\varphi}$  and  $\angle_{\alpha}$ ) the position of the ammonium group and the relative hydrogen bonding configuration, with more importantly the short interlayer contacts, as well as the terminal halogen bonding interactions, as described for the lead bromide analogues in 4.1 and 4.2. Table 4.3.2 show the inorganic octahedral distortions, for the Pb-I bond lengths in the axial and equatorial directions, as well as the I-Pb-I cis bond angles which deviate from 90° in the axial and equatorial directions respectively. Furthermore the trans I-Pb-I bond angles, which may display deviation from 180° of the axial to axial, and equatorial to equatorial bond angles also give further indications to the distortions in the octahedra. Lastly the bridging angle is also quoted for the overall comparison of the inorganic distortions. From both of these tables, what becomes immediately apparent, are how the Pb-I bond lengths (3.193Å average bond length, averaged over all the structures) between structures. Specifically the large axial compression

experienced in all the structures with the exception of (IC4)PbI<sub>4</sub> and (IC5)PbI<sub>4</sub>, where (IC4)PbI<sub>4</sub> displays an axial bond length comparable with two of the bridging halides, and (IC5)PbI<sub>4</sub> which shows a bridging compression where the axial bond length is elongated. However the hybrid (BrC2)PbI<sub>4</sub> displays the largest Pb-I bond distance distortions, where the Pb-I<sub>ax</sub> is 3.1590(4)Å and Pb-I<sub>eq</sub> range from (3.0854(6)-3.3612(6)Å). The cis I-Pb-I bond angles also experience a fairly large distortion for each compound. However the compounds (HOC2)PbI<sub>4</sub>, (BrC2)PbI<sub>4</sub> and (IC2)PbI<sub>4</sub> only experience a minor cis I-Pb-I<sub>ax</sub> angled distortion whereas (IC3-IC6)PbI<sub>4</sub> observe the larger bond angle distortions ranging from 84-95°.

**Table 4.3.2** The important geometrical parameters relating to the inorganic distortions for the Pb-I bond distances (Å) and the relevant octahedral angles (°).

Compound	9	10	11	12	13	14	15
Parameter	HOC2	BrC2	IC2	IC3	IC4	IC5	IC6
Pb-I <sub>eq</sub>	3.2199 (2)	3.0854 (6)	3.2104 (4)	3.1997 (4)	3.1840 (3)	3.1788 (11)	3.2318 (4)
Pb-I <sub>eq</sub>	3.2199 (2)	3.3612 (6)	3.2141 (4)	3.2196 (4)	3.1973 (2)	3.1823 (11)	3.2475 (4)
Pb-I <sub>eq</sub>	3.2273 (2)	3.1689 (6)	3.2104 (4)	3.1997 (4)	3.1840 (3)	3.1788 (11)	3.2318 (4)
Pb-I <sub>eq</sub>	3.2273 (2)	3.2829 (6)	3.2141 (4)	3.2196 (4)	3.1973 (2)	3.1823 (11)	3.2475 (4)
Pb-I <sub>ax</sub> (X2)	3.1736 (2)	3.1590 (4)	3.1687 (5)	3.1714 (5)	3.1844 (3)	3.2081 (12)	3.1703 (4)
I-Pb-I	89.049 (2)	94.573 (17)	93.157 (5)	89.582 (10)	86.852 (3)	88.472 (17)	92.749 (3)
I-Pb-I	90.951 (2)	91.934 (16)	86.843 (5)	90.418 (10)	93.148 (3)	91.528 (17)	87.251 (3)
I-Pb-I	90.951 (2)	82.445 (15)	93.157 (5)	92.271 (10)	93.148 (3)	88.472 (17)	92.749 (3)
I-Pb-I	89.049 (2)	91.048 (16)	86.843 (5)	87.729 (10)	86.852 (3)	91.528 (17)	87.251 (3)
I-Pb-I <sub>ap</sub>	90.278 (5)	88.919 (9)	88.604 (11)	95.041 (8)	88.344 (7)	90.50 (3)	88.913 (12)
I-Pb-I <sub>ap</sub>	89.722 (5)	88.310 (9)	91.396 (11)	84.959 (8)	94.073 (7)	89.50 (3)	91.087 (12)
I-Pb-I <sub>ap</sub>	87.589 (5)	91.802 (9)	90.366 (12)	95.041 (8)	85.927 (7)	85.38 (3)	84.914 (12)
I-Pb-I <sub>ap</sub>	92.411 (5)	91.276 (9)	89.634 (12)	84.959 (8)	91.656 (7)	94.62 (3)	95.086 (12)
I-Pb-I	180	174.38 (2)	180	180	180	180	180
I-Pb-I	180	173.493 (11)	180	180	180	180	180
I <sub>ap</sub> -Pb-I <sub>ap</sub>	180	175.831 (18)	180	180	180	180	180
Pb-I-Pb	159.092 (8)	176.92 (2)	147.242 (15)	148.633 (13)	147.051 (9)	154.39 (4)	161.076 (16)
Pb-I-Pb	-	174.38 (2)	-	-	-	-	-

More importantly are the I<sub>eq</sub>-Pb-I<sub>eq</sub> cis angles which display a slightly smaller distortion range than I-Pb-I<sub>ax</sub> however the only notable distortions are experienced in (BrC2)PbI<sub>4</sub>, (IC2)PbI<sub>4</sub> and (IC4)PbI<sub>4</sub> which range (82.445(15)-94.573(17)°); (86.843(5)-93.157(5)) and (86.852(3)-93.148(3)°) respectively. Most notably the (BrC2)PbI<sub>4</sub> hybrid experiences the largest distortion, which translates into the deviation of the trans I-Pb-I bond angles from 180°. This is the only structure that displays a deviation from 180° out of the entire lead iodide series investigated. Although the

(BrC2)PbI<sub>4</sub> hybrid displays the largest metal centred octahedral distortions, it displays the smallest bridging angle deviation, where the Pb-I-Pb angles are 174.38(2)<sup>°</sup>; 176.92(2)<sup>°</sup> respectively. This is the lowest reported bridging angle of a single layered 2D hybrid to date with the exception of the (2,2'-biimidazolium)PbI<sub>4</sub> which has a bridging angle of 173.687(17)<sup>°</sup> and also experiences trans I-Pb-I bond angle distortions (Tang Z, *et al*, 2001). In addition (BrC2)PbI<sub>4</sub> also displays only a minor corrugation tilt angle of 2.08(1)<sup>°</sup>. Only the compounds (HOC2)PbI<sub>4</sub> and (IC6)PbI<sub>4</sub> display a bridging angle closer to 180<sup>°</sup> however still experience a fair deviation from 180<sup>°</sup> of 159.092(8)<sup>°</sup> and 161.076(16)<sup>°</sup> respectively. In addition these two compounds also experience a larger corrugation tilt than (BrC2)PbI<sub>4</sub> of 13.30(1)<sup>°</sup> and 9.94(1)<sup>°</sup> for (HOC2)PbI<sub>4</sub> and (IC6)PbI<sub>4</sub> respectively. The compound (IC5)PbI<sub>4</sub> displays the next most idealized bridging angle, of 154.39(4)<sup>°</sup>, however out of this series, (IC5)PbI<sub>4</sub> shows a much smaller corrugation tilt angle of 5.64(2)<sup>°</sup>. The compounds (IC2-IC4)PbI<sub>4</sub> all experience large distortions of the bridging angle of 147.051(9)<sup>°</sup>, 148.633(13)<sup>°</sup> and 147.242(15)<sup>°</sup> respectively, and the larger corrugation angles of 12.06(1)<sup>°</sup>, 12.70(1) and 15.31(1)<sup>°</sup> respectively. The corrugation tilt increases as the chain length decreases, which also results in the strength of the terminal halogen bonding interaction to increase. The halogen bonding interaction is defined by the linearity by the C-X...X bonding angle, and by the overlap of the X...X van der Waals radii (Dumas J. M, *et al*, 1983; Lommerse J. P, *et al*, 1996). The I...I van der Waals distance for the atoms to be “touching” is 3.96Å, and the Br...I interaction vdW distance is 3.83Å. Hence (IC2)PbI<sub>4</sub> displays a stronger halogen bonding interaction, (3.8276(7)Å; 176.4(2)<sup>°</sup>) in comparison with (IC3)PbI<sub>4</sub> (3.8038(6)Å; 167.3(2)<sup>°</sup>) and (IC4)PbI<sub>4</sub> (3.9313(4); 163.1(1)<sup>°</sup>). Compound (IC5)PbI<sub>4</sub> also displays a strong halogen bonding interaction (3.840(2)Å; 177.5(4)<sup>°</sup>) which may explain the decreased corrugation angle compared with (IC6)PbI<sub>4</sub> which displays a weaker halogen bonding interaction (3.8700(7)Å; 161.3(2)<sup>°</sup>). However (IC6)PbI<sub>4</sub>, has a smaller interlayer spacing than (IC5)PbI<sub>4</sub> ((IC5)PbI<sub>4</sub> has an all trans conformation), where the (IC6)PbI<sub>4</sub>'s chain displays two gauche kinks, which results in the chain to have a much smaller  $\angle_{\varphi}$ ,  $\angle_{\alpha}$  and  $\angle_{\beta}$  tilt angles which should result in larger layer corrugations tilts due to increased penetration of the N1-C1 bond into the void of the octahedra, as well as resulting in a shorter interlayer spacing. Compounds (IC2, IC3, IC4)PbI<sub>4</sub> display the largest cis I-Pb-I bond angle distortions out of (XCn)PbI<sub>4</sub> series. Compound (IC4)PbI<sub>4</sub> manifests the distortions in both the axial and equatorial I-Pb-I cis angles, (IC2)PbI<sub>4</sub> only displays the larger distortions in the equatorial cis I-Pb-I angles, and (IC3)PbI<sub>4</sub> only manifests it's distortion in the axial cis angles.

### The (Cn)PbI<sub>4</sub> series where n = 4-7.

**Table 4.3.3:** Important geometrical parameters of (Cn)PbI<sub>4</sub> where n = 4-7 (Values obtained exclusively from Billing D. G and Lemmerer A, 2007 16-18; Lemmerer A, 2007 19) Only low temperature and phases close to room temperature are quoted below, as our optical experiments did not investigate the high temperature forms.

Geometric parameter	16 (C4) (II) (223K)	16 (C4) (I) (293K)	17 (C5) (III) (173K)	17 (C5) (III)* (293K)	17 (C5) (II) (333K)	18 (C6) (IV) (173K)	18 (C6) (III) (293K)	19 (C7) (III) (253K)	19 (C7) (I) (293K)
Interlayer Spacing (Å)	13.117 (5)	13.800 7(5)	14.784 (3)	14.881 (1)	14.978(4)	16.052(7 )	16.351(1 )	17.243(9)	18.306(13)
Bridging angle Pb-I-Pb (°)	149.24 (10)	155.07 (5)	150.22 (2)	153.68 (3)	159.01 (11)	155.13(3 )	155.65(5 )	149.61(10 )	154.96(16)
Corrugation $\Psi$ tilt (°)	12.92 (4)	5.78 (2)	12.83 (1)	12.59 (2)	7.30(7)	5.68(2)	5.85(3)	13.60(5)	5.75(1)
Compression Pb-I bond lengths	Axial	Bridging	Axial	Axial	Bridging	Bridging	Bridging	Axial	Bridging
Conformation of the hydrocarbon chain	Flat	Flat	Flat	Flat	Bent	Flat	Flat	Bent	Bent
Non coplanar torsion angles (°)	-	-	-	-	C1-C2-C3-C4 138(9); C2-C3-C4-C5 89(8)	-	-	C1-C2-C3-C4 98(5)	C2-C3-C4-C5 118(11); C4-C5-C6-C7 112(11)
Interdigitation	C4	C4	C4	C4	C4	C3	C4	C4	C4
Tilt of Chains $\angle_{\varphi}$ (°)	39.8(5)	29.2(3)	30.8(1)	29.0(2)	19.2(1)	32.6(2)	21.1(3)	16.7(5)	7.88(7)
Tilt of plane $\angle_{\alpha}$ (°)	55.9(1)	88.4(7)	67.5(3)	70.2(8)	87.4(1)	75.1(5)	89.7(7)	88.3(8)	84.34(8)
Tilt of NH <sub>3</sub> group $\angle_{\beta}$ (°)	33.2(2)	62.7(6)	27.6(5)	26.5(1)	65.7(1)	66.0(8)	66.9(1)	30.8(2)	46.52(3)
Position of ammonium group	Obtuse	Acute	Obtuse	Obtuse	Acute	Acute	Acute	Obtuse	Acute
Hydrogen bonding configuration	Equilateral	Right-Angled	Equilateral	Equilateral	Right-angled	Right-angled	Right-angled	Equilateral	Right-angled

As the aliphatic compounds undergo multiple phase transitions, here we only report on the room temperature (293K) and the low temperature forms of this series, as these structures have been used for the optical experiments. Tables 4.3.3 and 4.3.4 summarize the important geometrical parameters of these compounds. All of the low temperature forms of this series display the greatest inorganic distortions, with the exception of phase IV of (C6)PbI<sub>4</sub>. Compounds (C4)PbI<sub>4</sub>, (C5)PbI<sub>4</sub> and (C7)PbI<sub>4</sub> all display a highly distorted bridging angle of 149.24(10)<sup>o</sup>, 150.22(2)<sup>o</sup> and 149.71(11)<sup>o</sup> respectively, as well as all experiencing axial compression accompanying the equatorial bond elongations. The room temperature phases of (C4)PbI<sub>4</sub> and (C7)PbI<sub>4</sub> however show bridging compression where the room temperature phase of (C5)PbI<sub>4</sub> still maintains, axial compression, however the 333K phase also reverts to the bridging compression. All of the room temperature phases of these compounds, bridging angles move closer toward the idealized 180<sup>o</sup> however still maintain a fairly large distortion of 155.08(2)<sup>o</sup>; 153.68(3)<sup>o</sup>, 155.65(5)<sup>o</sup> and 154.99(12)<sup>o</sup> for (C4-C7)PbI<sub>4</sub> respectively. The low temperature phase of (C6)PbI<sub>4</sub> however does maintain a more idealized bridging angle of 155.11(3)<sup>o</sup> and also

experiences bridging compression in both phases. The cis I-Pb-I bond angle distortions experienced in these compounds are more pronounced in the low temperature phases than in the room temperature ones. However only (C5)PbI<sub>4</sub> and (C7)PbI<sub>4</sub> display greater equatorial cis bond angle distortions ranging (84.535(17)<sup>o</sup>-95.465(17)<sup>o</sup>) and (85.71(4)<sup>o</sup>-94.29(4)<sup>o</sup>) respectively, and (C6)PbI<sub>4</sub> displayed the largest axial cis I-Pb-I bond angle distortions ranging (85.39(3)<sup>o</sup>-94.61(3)<sup>o</sup>). The trans I-Pb-I bond angles all maintain a 180<sup>o</sup> bonding angles for all of the (C4-C7)PbI<sub>4</sub> phases reported here.

**Table 4.3.4:** The important geometrical parameters relating to the inorganic distortions for the Pb-I bond distances (Å) and the relevant octahedral angles (°).

Compound	16 (II) 223K	16 (I) 293K	17 (III) 173K	17 (II) 293K	17 (I) 333K	18 (IV) 173K	18 (III) 293K	17 (III) 253K	17 (I) 293K
Parameter	C4	C4	C5	C5	C5	C6	C6	C7	C7
Pb-leq	3.190 (2)	3.1781 (5)	3.1923 (7)	3.1940 (6)	3.188 (2)	3.1608 (13)	3.1835 (11)	3.206 (3)	3.174 (2)
Pb-leq	3.199 (2)	3.1836 (5)	3.2052 (7)	3.1975 (6)	3.191 (2)	3.1712 (13)	3.1932 (11)	3.216 (3)	3.178 (3)
Pb-leq	3.190 (2)	3.1781 (5)	3.1923 (7)	3.1940 (6)	3.188 (2)	3.1608 (13)	3.1835 (11)	3.206 (3)	3.174 (2)
Pb-leq	3.199 (2)	3.1836 (5)	3.2052 (7)	3.1975 (6)	3.191 (2)	3.1712 (13)	3.1932 (11)	3.216 (3)	3.178 (3)
Pb-lax (X2)	3.170(3)	3.2029 (7)	3.1743 (9)	3.1720 (8)	3.200 (4)	3.2069 (17)	3.2062 (15)	3.202 (4)	3.214 (9)
I-Pb-I	88.52 (3)	91.256 (4)	95.465 (17)	93.399 (8)	92.095 (19)	88.70 (3)	91.695 (9)	85.71 (4)	91.27 (3)
I-Pb-I	91.48 (3)	88.744 (4)	84.535 (17)	86.601 (8)	87.91 (2)	91.30 (3)	88.305 (9)	94.29 (4)	88.73 (3)
I-Pb-I	88.52 (3)	91.256 (4)	95.465 (17)	93.399 (8)	92.095 (19)	88.70 (3)	91.695 (9)	85.71 (4)	91.27 (3)
I-Pb-I	91.48 (3)	88.744 (4)	84.535 (17)	86.601 (8)	87.91 (2)	91.30 (3)	88.305 (9)	94.29 (4)	88.73 (3)
I-Pb-lap	86.15 (7)	91.077 (18)	89.177 (16)	92.01 (2)	92.76 (9)	90.22 (3)	88.50 (4)	91.92 (8)	92.86 (17)
I-Pb-lap	93.85 (7)	88.922 (18)	90.823 (16)	87.99 (2)	87.24 (9)	89.78 (3)	93.64 (4)	88.08 (8)	88.64 (18)
I-Pb-lap	90.26 (7)	93.576 (19)	92.585 (17)	90.16 (2)	87.77 (10)	85.39 (3)	86.36 (4)	94.29 (4)	91.36 (18)
I-Pb-lap	89.74 (7)	86.424 (19)	87.415 (17)	89.84 (2)	92.23 (10)	94.61 (3)	91.50 (4)	85.71 (4)	87.14 (17)
I-Pb-I	180	180	180	180	180	180	180	180	180
I-Pb-I	180	180	180	180	180	180	180	180	180
Iap-Pb-Iap	180	180	180	180	180	180	180	180	180
Pb-I-Pb	149.24 (10)	155.08 (2)	150.22 (2)	153.68 (3)	159.01 (11)	155.11 (3)	155.65 (5)	149.71 (11)	154.99 (12)

#### 4.3.4 Optical absorption and photoluminescence of (Cn)PbX<sub>4</sub> and (ZCn)PbX<sub>4</sub> compounds

The optical absorption and continuous wave excitation photoluminescence emissions of all of the investigated compounds were measured at both 77K and 293K. This was done in order to ascertain if any phase transitions relating to major inorganic distortions had occurred, as the minor intermediate conformational changes in the aliphatic chains do not result in any major

inorganic distortions. Photoluminescence emissions were however only obtained on compounds (ZC2)PbI<sub>4</sub> and (ICn)PbI<sub>4</sub> where Z = HO and Br, and n = 2-6. This was to investigate the possibility of charge transfer interactions between the alkyl terminal halogen and the inorganic layers. A broad stokes shifted PL emission relative to the free exciton emission of the compounds was observed for all of the (ICn)PbI<sub>4</sub> compounds, however this peak was shown to be largely sample dependant, as it shifted in both photon emission energy and intensity after measuring different crystals of the same compound. The higher quality crystals PL spectra displayed this emission at much lower intensities, and hence this emission is assigned as an emission derived from a crystal lattice defect. The assignment is further supported from the PL emissions observed in (BrC2)PbI<sub>4</sub> where the initial sample investigated displayed a broad stokes shifted emission relative to the free exciton emission, however this emission vanished when a higher crystal quality crystal used for a full SC-XRD data collection was then also used for the PL experiment. Furthermore the UV-Vis optical absorption experiments did not yield any further support for charge transfer interaction in any of the above mentioned compounds. Although as seen in figure 4.3.2 the optical absorption does display two minor peaks between 1.95-2.05eV, however these peaks were common to all of the lead halide compounds measured in the entire series, even after background correction, and hence these peaks cannot be directly assigned as anything. The compound (IC6)PbI<sub>4</sub> free exciton emission is stokes shifted by 26meV from the optical absorption which supports the assignment of the PL band as a free exciton. The shorter chain (XCn)PbI<sub>4</sub> derivatives displayed minor or no stokes shift from the optical absorption. From the band assignments of the optical absorption experiments of the (Cn)PbI<sub>4</sub> (Ishihara T, *et al*, 1989; 1990), the approximate binding energies of the compounds were obtained from the 77K optical absorption measurements. The difference between the free exciton absorption and the first band, as seen in figure 4.3.2, gives a good approximation to the exciton binding energy  $E_b$ . The values obtained from our experiments were in good agreement for the previously published values obtained for the (Cn)PbX<sub>4</sub> compounds and within range of all the chain aliphatic's shown in table 4.3.5 and 4.3.6 at the end of the chapter, for the lead iodide and lead bromide series respectively where the optical absorption and structural distortions are also displayed. The functionalized aliphatic's display a binding energy slightly larger but comparable to the (PEA)PbX<sub>4</sub> compounds for the Br (290meV) (Papavassiliou G. C, 1997; Kitazawa N, *et al*, 2005) and I (220meV) (Ishihara T, *et al*, 1990) compound respectively.

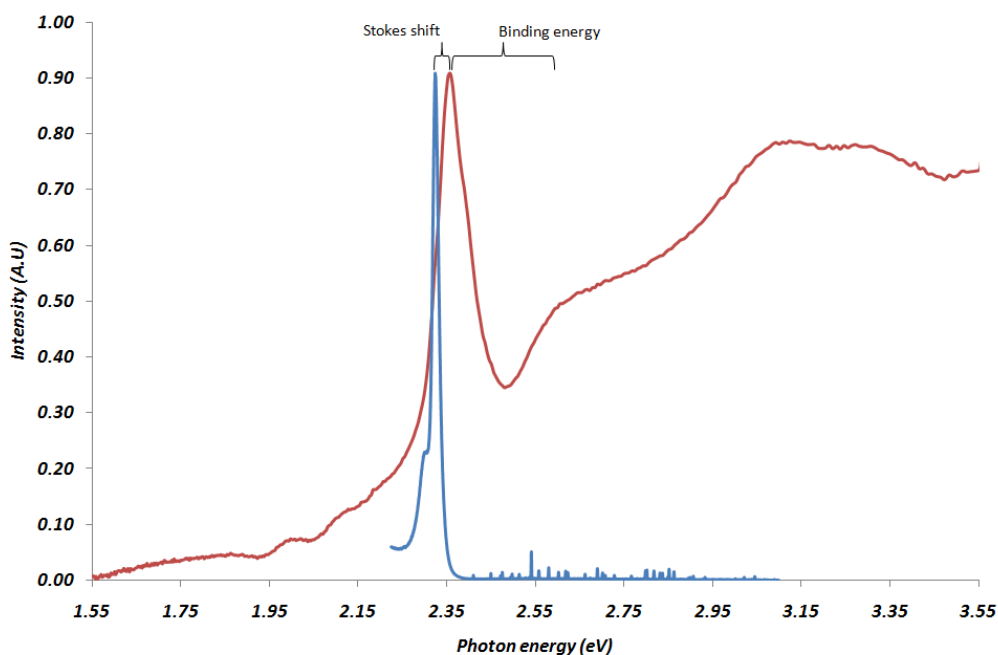


**Figure 4.3.2:** The photoluminescence (Blue) Stokes shifted (26meV) from the exciton absorption peak (Red). Both spectra were measured at 77K, and were able to obtain the approximated binding energy for (IC6)PbI<sub>4</sub> of (260meV).

The fine excitonic structure of the luminescence emissions found in (C4)PbBr<sub>4</sub> using a continuous wave excitation source (Ema K, *et al*, 2006) as in our experiments, found multiple emission lines in the emission spectrum, however the emission lines were only separated by a few tenths of meV. Multiple emission lines are also observed in the luminescence emission spectra of some of the hybrids in this series, but we will discuss only (IC5)PbI<sub>4</sub> and (IC4)PbI<sub>4</sub>. The PL spectra are seen in figure 4.3.3, where (IC5)PbI<sub>4</sub> displays the multiple emission lines. The main peak corresponds to the free exciton absorption in the optical absorption measurements. The shoulder on the peak may be a shallow bound exciton (Ishihara T, *et al*, 1990) or part of the excitonic fine structure (Ema K, *et al*, 2006), however further experimentation would be needed in order to ascertain the origin of this peak. In addition the small peak 2.520eV may be due to a direct band to band transition, as the difference between the free exciton emission and this peak is 179meV which is comparable with the binding energy. However further investigations would also be needed to further ascertain the origin of the peak. Lastly the PL emission spectrum of (IC4)PbI<sub>4</sub> displays two emission lines, where the main peak at 2.531eV corresponds to the free exciton absorption peak, however the second peak at 2.402eV is assigned as a deeply bound exciton at an impurity centre as the peak shape and intensity was shown to be sample dependant. The optical absorption and PL emissions of the entire series may be found in appendix A, where the multiple emission lines found in their spectra correspond to the assignments described here.



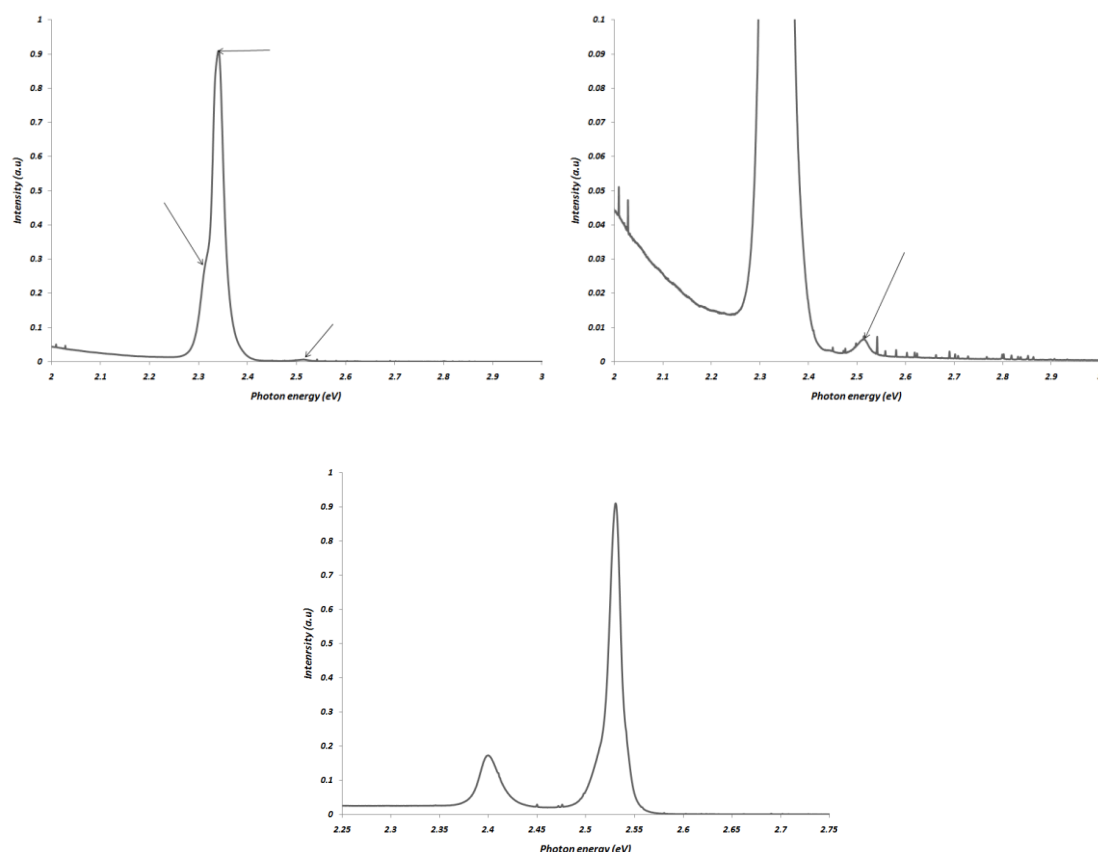


**Figure 4.3.3:** The continuous excitation photo-luminescence emissions at 77K of (IC5)PbI<sub>4</sub> (left) displaying the multiple emission lines. The main peak (2.341eV) corresponds to the free exciton absorption at 77K, however the small peak at 2.520eV (right) may be the direct band to band recombination, as the separation of the main peak and the blue shifted emission are 179meV apart, however decay kinetics experiments would need to be carried out to further ascertain the origin of the peak. The photoluminescence emission of (IC4)PbI<sub>4</sub> (77K) also displays two emission peaks, where the main peak (2.531eV) corresponds to the free exciton optical absorption peak at 77K. The pronounced but secondary peak (2.402eV) which is still present in the 293K spectra may be assigned as a deeply bound exciton trapped at an impurity centre (Ishihara T, *et al*, 1990).

#### 4.3.5 Structure and optical property correlation of the lead iodide series

In figure 4.3.4 a plot of the first exciton absorption against the bridging angle (Pb-I-Pb) may be seen. The general trend displays the largely distorted bridging angles with a much higher absorption energy, than the almost idealized bridging angles of (BrC2)PbI<sub>4</sub>. This trend follows the curve observed for the calculated and experimental tin iodide analogues (Knutson J. L, *et al*, 2005). We wish to rationalize the outliers on this scatter plot in terms of the observed structural distortions within the layers. Firstly the highly distorted bridging angled compounds all with similar exciton absorptions give us some insight as to why the larger bridging angle of (C5)PbI<sub>4</sub>'s low temperature phase (150.22(2)°) gives slightly larger exciton absorption (2.545eV) to the

most distorted bridging angle compound of (IC4)PbI<sub>4</sub> (147.05(9)°) of (2.530eV) which is a 15meV difference. Although this angle change may appear small, consider (HOC2)PbI<sub>4</sub> with a bridging angle of 159.092(8)° with an exciton absorption of 2.269eV compared with a ~4° change in bridging angle of RT C4 (155.07(5)°) 2.317eV. This is a difference of 48meV red shifted. In addition the Pb-I bond length bridging compression experienced in (C4)PbI<sub>4</sub>, should lead to a further red shift as a result of the increased Pb-I anti bonding interaction which raises the top of the valence band, while (HOC2)PbI<sub>4</sub> experiences an axial compression (resulting in equatorial bond elongations) resulting in a blue shift, as a consequence of the loss of Pb-I antibonding interaction.

In addition the corrugation angles of (HOC2)PbI<sub>4</sub> and RT (C4)PbI<sub>4</sub> are 13.30(1)° and 5.78(2)° respectively. Hence the difference between the bridging angles should result in a larger separation of the respective exciton absorptions if only the bridging angle is considered. Furthermore both RT (C4)PbI<sub>4</sub> and (HOC2)PbI<sub>4</sub> display similar equatorial cis I-Pb-I bond distortions. Consequently this red shift caused through an increased bridging angle of (C5)PbI<sub>4</sub> should also be observed between exciton absorptions of (IC4)PbI<sub>4</sub> and (C5)PbI<sub>4</sub> respectively. Similarly, both compounds experience similar bond length distortions of (0.0073 and 0.015) as well as both compounds displaying similar corrugation tilt angles of 12.06(1)° and 12.83(1)° for (IC4)PbI<sub>4</sub> and (C5)PbI<sub>4</sub> respectively. However (IC4)PbI<sub>4</sub> does display marginally shorter equatorial bond lengths (3.1840(3)Å; 3.1973(2)Å) than C5 (3.1923(7)Å; 3.2052(7)Å) which should increase the σ-antibonding Pb-I interaction which will marginally raise the top of the valence band, which contributes to an increase in the band gap; the converse will apply for (C5)PbI<sub>4</sub>. However the cis I<sub>eq</sub>-Pb-I<sub>eq</sub> bond angles display larger distortion angles for (C5)PbI<sub>4</sub> (95.465(17)°; 84.535(17)°) than for (IC4)PbI<sub>4</sub> (93.148(3)°; 86.852(3)°). Hence a combination of increased antibonding in the equatorial bond lengths of (IC4)PbI<sub>4</sub> causing a marginal red shift, and the greater metal centred octahedral distortions and the equatorial Pb-I<sub>eq</sub> bond length elongations of (C5)PbI<sub>4</sub> blue shifting the exciton absorption, should account for (C5)PbI<sub>4</sub> displaying a marginally larger band gap than (IC4)PbI<sub>4</sub>, despite the larger bridging angle.

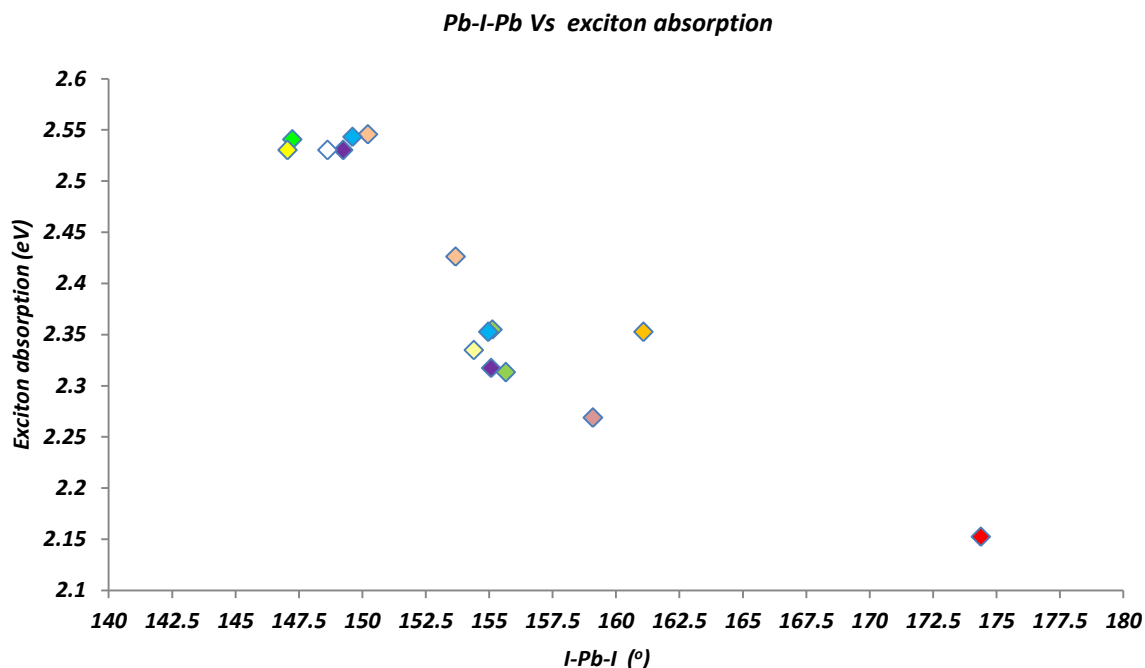


**Figure 4.3.4:** A plot of the exciton absorption against the Br-Pb-Br bridging angle. The compounds are coloured accordingly: red (BrC2), light red (HOC2), bright green (IC2), white (IC3), yellow (IC4), Light yellow (IC5), orange (IC6), purple (C4), light orange (C5), olive green (C6), and light Blue (C7).

The low temperature form of (C7)PbI<sub>4</sub> also displays comparable cis I<sub>eq</sub>-Pb-I<sub>eq</sub> bond angle distortions (85.71(4)°, 94.29(4)°), Pb-I<sub>eq</sub> bond lengths (3.206(3)Å, 3.216(3)Å), and a comparable bridging and corrugation angle (149.61(10)°; 13.60(5)°) with an exciton absorption of 2.543eV, to (C5)PbI<sub>4</sub>. This correlation further supports the idea that the larger cis I<sub>eq</sub>-Pb-I<sub>eq</sub> bond angle distortions decrease σ-antibonding interactions from the I 5p orbital's resulting in less repulsion of the Pb 6s<sup>2</sup> lone pair, which may lower the top of the valence band, which offset the higher bridging angles of (C5)PbI<sub>4</sub> and (C7)PbI<sub>4</sub> compared with (IC4)PbI<sub>4</sub>, to give larger (marginally) band gaps. The compounds (IC3)PbI<sub>4</sub> and LT (C4)PbI<sub>4</sub> have comparable exciton absorptions to (IC4)PbI<sub>4</sub>, as they experience similar bond Pb-I<sub>eq</sub> lengths and I<sub>eq</sub>-Pb-I<sub>eq</sub> bond angle distortions, as well as similar corrugation and bridging angles, which further supports this hypothesis.

One general trend should be highlighted of the inorganic distortions, found from the multiple phases of the (Cn)PbI<sub>4</sub> compounds previously published (Billing D. G, Lemmerer A, 2007; Lemmerer A, 2007). Firstly the room temperature phases display more idealized structures, where (C4-C7)PbI<sub>4</sub> show similar inorganic distortions with highly comparative inorganic bond angles and bond lengths as well as exciton absorptions. In addition, as the compounds undergo their low temperature phase transitions, the compounds display highly distorted inorganic bond angles and bond lengths, with the exception of (C6)PbI<sub>4</sub>, whose inorganic component only

undergoes minor distortions from the room temperature form. Importantly the corrugation tilt angles further increase in distortion, namely from  $\sim 5^\circ$  at 293K to  $12.5^\circ$  at 173K. Furthermore the room temperature forms generally show much larger interlayer spacing's with the exception of (C4)PbI<sub>4</sub> as it displays a larger interlayer spacing at low temperature than at room temperature. The comparison of interlayer spacing and exciton absorption of the lead iodide series may be seen in figure 4.3.5.

In the scatter plot of figure 4.3.4 an outlier is found at  $161.076(16)^\circ$ , the bridging angle of (IC6)PbI<sub>4</sub>. The outlier is a result of the higher exciton absorption energy experienced for (IC6)PbI<sub>4</sub> than expected for that particular bridging angle. As a comparison, both compounds (IC6)PbI<sub>4</sub> and (HOC2)PbI<sub>4</sub> display similar bridging angles of  $161.076(16)^\circ$  and  $159.092(8)^\circ$  respectively, however experience a large difference in exciton absorption energy of 84meV (2.353eV and 2.269eV respectively). Unfortunately there is no obvious explanation as to why (IC6)PbI<sub>4</sub> displays such a large blue shift in comparison to (HOC2)PbI<sub>4</sub>, as both compounds experience highly comparable bond length and bond angle distortions with one another. Specifically both compounds observed a large axial compression resulting in the largest Pb-I<sub>eq</sub> bond length elongations experienced in this series of compounds (3.2318(4)Å; 3.2475(4)Å) and (3.2199(2)Å; 3.2273(2)Å) for (IC6)PbI<sub>4</sub> and (HOC2)PbI<sub>4</sub> respectively. This may explain why (IC6)PbI<sub>4</sub> displays a blue shift, but then why does (HOC2)PbI<sub>4</sub> not exhibit the same behaviour?

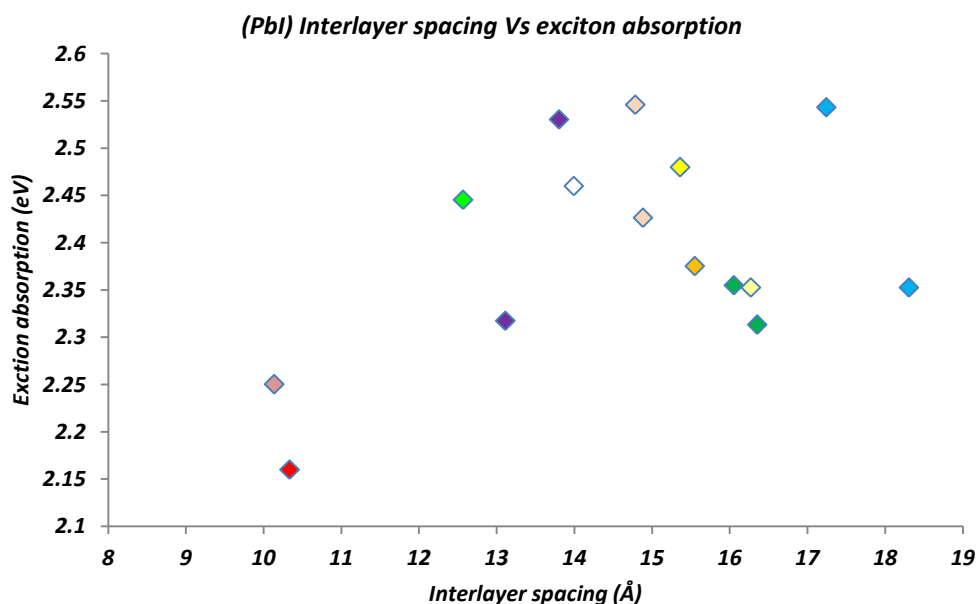


**Figure 4.3.5:** A plot of the exciton absorption against the interlayer spacing. The compounds are colored accordingly: red (BrC2), light red (HOC2), bright green (IC2), white (IC3), yellow (IC4), Light yellow (IC5), orange (IC6), purple (C4), light orange (C5), olive green (C6), and light Blue (C7).

There are several factors influencing the exciton absorption in a 2D layered hybrid, which have been discussed in the literature. Firstly is the concept of the short interlayer spacing being responsible for red shifts experienced in the hybrids due to the increase of 3 dimensional character of the hybrid (Tabuchi Y, *et al*, 2000). The authors suggested that the small separation of the layers does not give enough distance to neglect the percolation of the electronic wave function. However this is not entirely the case as the luminescence emission for (HOC2)PbI<sub>4</sub> is intense and sharp (fwhm of 15 meV of the main peak), at 77K, with weaker but still visible emissions at 293K, which still illustrates the strong 2D character of this compound as a result of the smaller band dispersion from dimensional reduction (Umebayashi T, *et al*, 2003). The peak width of the emission of (HOC2)PbI<sub>4</sub> is comparable with the longer chain derivatives (Table 4.3.5). Furthermore the (HOC2)PbI<sub>4</sub> compound lies very close to the trend line of the other experimentally observed exciton absorptions verses the Pb-I-Pb bridging angle, and the one calculated by Knutson and co-workers for the tin iodide hybrids. Another possible reason for the increased exciton energies may be due to the cation penetration of the ammonium head. However the hydrogen bonding, must strongly influence the bridging halides, as the axial halides only contain the I *p<sub>z</sub>* orbital's which have very little influence on the valence or conduction bands. Hence a fair amount of corrugation tilt is needed for significant bridging hydrogen bonding to take place. (IC6)PbI<sub>4</sub> does experience a fairly large cation penetration; however it is difficult to assign a value to the increase in exciton absorption it would experience. In addition the room temperature (C7)PbI<sub>4</sub> and (IC5)PbI<sub>4</sub> also experience a large cation penetration, however they do not experience the large exciton shifts as (IC6)PbI<sub>4</sub> does, and therefore I am reluctant to cite this as the reason for (IC6)PbI<sub>4</sub>'s increased exciton absorption. The halogen bonding interaction may also influence the exciton absorption energy, however, as the I...I interaction occurs with the I *p<sub>z</sub>* orbital this cannot be directly assigned as the reason based on the current data. In addition as (IC6)PbI<sub>4</sub> optical absorption at 293K and 77K are very similar, an unforeseen phase transition below 173K cannot be envisaged. Hence further studies into (IC6)PbI<sub>4</sub>'s optical properties are needed.

Finally the compound (BrC2)PbI<sub>4</sub> with the most ideal bridging angle of (174.38(2)<sup>o</sup>, 176.92(2)<sup>o</sup>) displays the lowest exciton absorption energy, in this series. As in the (2,2'-biimidazolium)PbI<sub>4</sub> compound which has a bridging angle of 173.687(17)<sup>o</sup> (Tang Z, *et al*, 2001), both compounds required additional weak interactions to create such an idealized bridging angle. In the biimidazolium compounds additional hydrogen bond donors are available in the rigid template in order to force the idealizations of the inorganic layers. However in the (BrC2)PbI<sub>4</sub> case, a much weaker halogen bonding interaction was still robust enough to create the idealizations within

the layers. Although the bridging angle is now almost linear, a certain amount of space is still needed for the lone pair on the lead atom, and thus both of these compounds, experience much larger metal centred octahedral distortion than the remaining lead iodide series discussed here, in order to accommodate the lone pair. In addition the halogen bonding interaction between the axial iodine and bromine was found to undergo a solid state reaction at higher temperatures, in this reaction the bromine and bridging iodine effectively trade places, and the Iodine is then placed on the alkyl chain and the bromine gets intercalated through a suspected two step mechanism into the equatorial positions in the layers (Sourisseau S, *et al*, 2007). This raised two immediate questions, firstly, is there a charge transfer interaction that occurs between the layers and the alkyl bromine atom? Secondly what are the orbital contributions from the bromine atom into the band structure and the density of states and where do they lie? The photoluminescence emission spectrum as seen in figure 4.3.6 displays no immediate evidence that a charge transfer interaction has taken place, as no broad secondary peaks arise. The luminescence emission of the main peak has a fwhm of 15meV at 77K which is comparable with the other longer chain compounds in this series. Furthermore it also shows a sharp weaker secondary peak, which is a sample dependant emission, whose intensity largely decreased in the room temperature emission spectrum, and is assigned as a shallow bound exciton in the lattice (Ishihara T, *et al*, 1990). The stronger main peak, is the free exciton emission characteristic of the 2D nature of the lead iodide hybrid and corresponds to the optical absorption measurements.

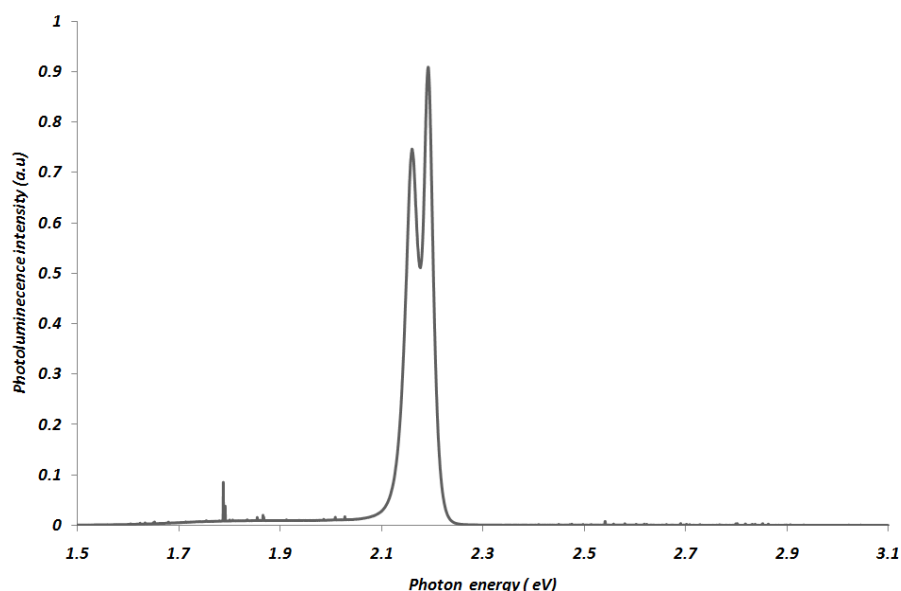


**Figure 4.3.6:** Photoluminescence emission of a single crystal of (BrC2)PbI<sub>4</sub> at 77K with a FWHM of the main peak 15meV. The main peak is from the usual exciton recombination, the smaller peak is sample dependant, and is hence assigned as a shallow bound exciton emission. (Sharp lines at ~1.8eV are plasma lines)

Electronic structure calculations were further done for  $(\text{BrC2})\text{PbI}_4$  and  $(\text{IC2})\text{PbI}_4$  for comparison. The methodology behind the DFT calculations was as follows. A structure optimization was first completed on both  $(\text{BrC2})\text{PbI}_4$  and  $(\text{IC2})\text{PbI}_4$ , which gave a good agreement with our experimental results, where the calculated unit cell parameters for the orthorhombic system of  $(\text{BrC2})\text{PbI}_4$  were  $a = 12.965 \text{ \AA}$ ,  $b = 20.8885 \text{ \AA}$ ,  $c = 6.4839 \text{ \AA}$

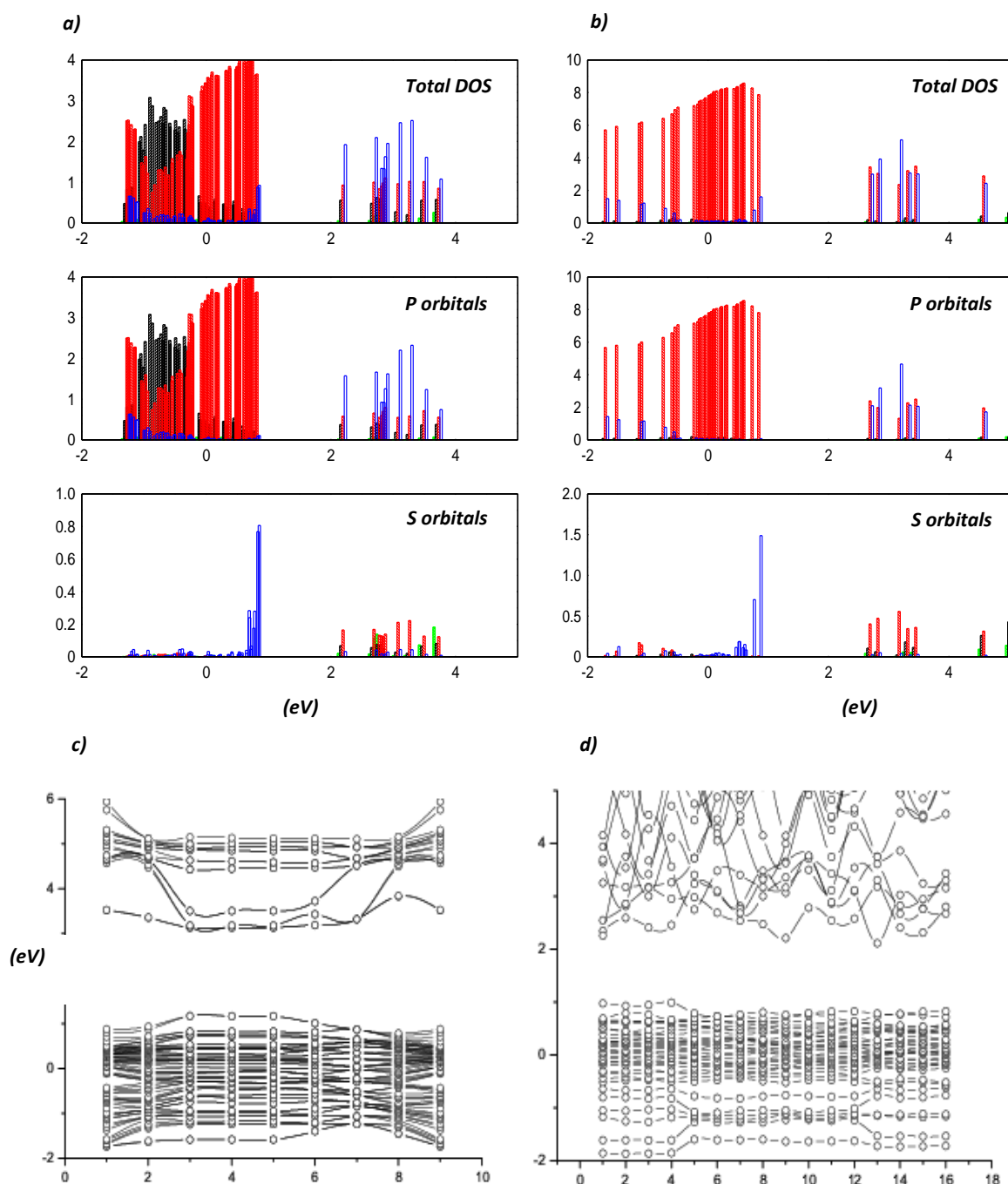


**Figure 4.3.7:** a) The total and partial density of states, of  $(\text{BrC2})_2\text{PbI}_4$  b)  $(\text{IC2})_2\text{PbI}_4$ . The band structure plots of  $(\text{BrC2})_2\text{PbI}_4$  c) and  $(\text{IC2})_2\text{PbI}_4$  d). The atomic contributions in the DOS are as follows: Blue Pb, Red I, Black Br, Green N.

and the experimental cell parameters were  $a = 12.8669(3) \text{ \AA}$ ,  $b = 20.6712(6) \text{ \AA}$ ,  $c = 6.4440(1) \text{ \AA}$  respectively. The calculated cell volume was 2.4% larger than the experimentally observed cell volume. For IC2 the calculated monoclinic unit cell parameters were  $a = 12.60125 \text{ \AA}$ ,  $b = 8.89252 \text{ \AA}$ ,  $c = 8.65653 \text{ \AA}$ ,  $\beta = 97.80790^\circ$  and the experimental unit cell were  $a = 12.5683(3) \text{ \AA}$ ,  $b = 8.7743(2) \text{ \AA}$ ,  $c = 8.6592(2) \text{ \AA}$ ,  $\beta = 97.957(2)^\circ$  respectively. The calculated unit cell volume was 1.6% larger than the experimental results. Furthermore the Pb-I bond lengths were 0.68%, and 0.57% larger than the experimental values for (BrC2)PbI<sub>4</sub> and (IC2)PbI<sub>4</sub> respectively. Importantly the halogen bonding weak interactions of Br...I distance was 0.46% longer than the experimental, and the I...I interaction was 0.03% shorter than the experimental value.

As the structurally optimized results were satisfactory, we then continued with the electronic structure calculations, in order to obtain the (density of states) DOS and the band structure calculations along high symmetry lines. The DOS plots (figure 4.3.7) for both compounds display the partial density of states contributions from the relative atomic  $p$  and  $s$  orbital contributions respectively. The lead's orbital contributions are shown in blue, where the Pb 6s character may be readily seen at the top of the valence band in both compounds. The Iodine orbital contribution shown in red, displays the large amount of  $p$  orbital contribution in the valence band with both significant  $s$  and  $p$  antibonding character in the conduction band. In the less distorted (BrC2)PbI<sub>4</sub> compound shows a large amount of I 5p character at the top of the valence band, however in (IC2)PbI<sub>4</sub> the decrease in antibonding I 5p character, results in the a large amount of this contribution to move toward lower energies, and away from the top of the valence band, and hence widening the band gap as there is now less repulsion with the Pb 6s<sup>2</sup> band and the band is lowered. The bottom of the conduction band in (BrC2)PbI<sub>4</sub> displays the essentially degenerate Pb  $p_x$  and  $p_y$  band, with the Pb  $p_z$  contribution at a higher energy. The DOS of (IC2)PbI<sub>4</sub>, displays a split the degeneracy of the pseudo 1D Pb  $p_x$  and  $p_y$  bands due to the large amount of distortion in the inorganic layers, and the loss of symmetry which is readily seen at the bottom of the conduction band. The band structure plot of (BrC2)PbI<sub>4</sub> does display the slightly split degeneracy of the Pb  $p_x$  and  $p_y$  bands, at the bottom of the conduction band, but then display the usual dispersion of the band as the we move away from the direct gap at point 3, along the in plane high symmetry lines. No dispersion is seen for the movement in the vertical direction, along the Pb  $p_z$  band, due to the 2D nature of the compound and hence the hybrid I 5p/Pb  $p_z$  band shows little dispersion at 5eV as expected. However the new unexpected band at the bottom of the conduction band which shows little dispersion in any direction needs further clarification. The partial density of states reveals this band to belong to Br with both  $p$  and  $s$  character. The fact that the band shows little dispersion indicates the spatial confinement of the



band further confirming the contribution of this band to be from the organic bromine atom. In addition the Br atom behaves as an n-doping atom with the band structure, however further experiments would be required in order to confirm this. The “n-doping” character in addition to the highly idealized bridging angle further explains the highly reduced band gap of (BrC2)PbI<sub>4</sub>, and the observance of the solid state reaction this compound undergoes at elevated temperatures.

**Table 4.3.5:** The lead iodide series summary of inorganic distortions, exciton optical absorptions, and estimated binding energies from the low temperature optical absorption measurements.

Cation	Exciton energy (nm, eV)	Pb-I-Pb	in-/out of plane distortion	eq/axial (Å) (averaged)	Distortion of PbI <sub>6</sub> octahedra (°)	Cation penetration (Å) (°)	Binding energy (meV)	FWHM Of PL emission
<b>C4 (77K)</b>	490, 2.53	149.24	15.40/12.9 2	3.195/3.17 0	0.0107	0.5323	300 (300 <sup>1</sup> )	
<b>C4 (RT)</b>	535, 2.32	155.07	12.47/5.78	3.181/3.20 3	0.0114	0.5893		
<b>C5 (77K)</b>	487, 2.55	150.22	14.86/12.8 3	3.199/3.17 4	0.0105	0.5775	320	
<b>C5 (RT)</b>	511, 2.43	153.68	13.17/12.5 9	3.196/3.17 2	0.0088	0.5915		
<b>C6 (77K)</b>	526.5, 2.35	155.13	12.47/5.68	3.166/3.20 7	0.0226	0.6035	330(361 <sup>2</sup> )	
<b>C6 (RT)</b>	536, 2.31	155.65	12.19/5.85	3.188/3.20 6	0.0076	0.6256		
<b>C7 (77K)</b>	487.5, 2.54	149.61	15.17/13.6 0	3.211/3.20 2	0.0150	0.4889	330	
<b>C7 (RT)</b>	527, 2.35	154.99	12.51/5.75	3.176/3.21 4	0.0183	0.7432	-	
<b>HOC2 (77K)</b>	545, 2.28	159.09	10.44/13.3 0	3.224/3.17 4	0.0269	0.3625	-	15meV
<b>BrC2 (77K)</b>	565, 2.19	174.38	2.86/2.08	3.244/3.15 9	0.0763	-0.3655	-	15meV
<b>IC2 (77K)</b>	507, 2.44	147.24	16.37/15.3 1	3.212/3.16 9	0.0209	0.4508	-	20meV
<b>IC3 (77K)</b>	504, 2.46	148.62	15.73/12.7 0	3.210/3.16 9	0.0183	0.4858	270	14meV
<b>IC4 (77K)</b>	500, 2.48	147.05	16.51/12.0 6	3.191/3.18 4	0.0073	0.4885	250	18meV
<b>IC5 (77K)</b>	527, 2.35	154.26	12.81/5.64	3.181/3.20 8	0.0133	0.5991	250	27meV
<b>IC6 (77K)</b>	522, 2.38	161.08	9.49/9.94	3.240/3.17 0	0.0387	0.6309	260	17meV

[1] Ishihara T, *et al*, 1990 [2] Tanaka K, Kondo T, 2003a. (a) Bond length distortion is defined as  $\sum \text{abs}(d_i - \langle d \rangle)/6$ , where  $d_i$  is the summation over the six Pb-I distances and  $\langle d \rangle$  represents the average bond length. (b) Cation penetration is defined by the distance between the planes of the N atoms of the cation and the planes of the axial I atoms of the perovskite sheet.

#### 4.3.6 Lead halide substitution and the effect on the exciton absorption.

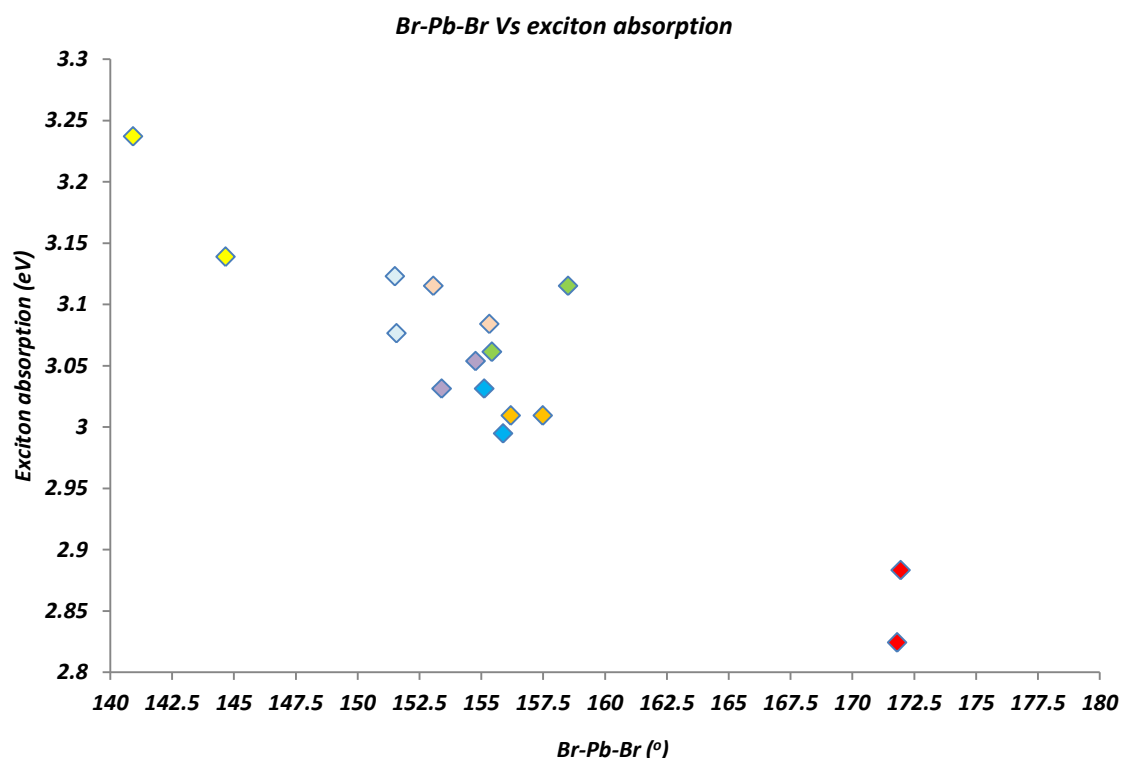


**Figure 4.3.8:** A plot of the exciton absorption against the Br-Pb-Br bridging angle. The compounds are colored accordingly: red (HOC2), yellow (BrC3), orange (BrC4), Sky Blue (BrC5), purple (C4), light orange (C5), green (C6), and light Blue (C7).

As has already been established, the blue shift in the optical absorption from lead iodide to the lead bromide is due to the decrease in covalent character of the Pb-X bond. Furthermore the bridging angle correlation with the lead iodide series is also expected. In the scatter plot (figure 4.3.8) of the lead bromide analogues' bridging angles against exciton absorption energies, we see the direct correlation of the increase in distortion on the increase in exciton absorption energies as in the lead iodide series. The distortions of the lead bromide octahedra measured by the Pb-Br bond lengths deviation from the average Pb-Br bond length show much smaller distortions than its lead iodide counterparts. In general the lead bromide series does display more idealized octahedra than the lead iodide compounds. However the short chain derivatives of (HOC2)PbBr<sub>4</sub> and (BrC3)PbBr<sub>4</sub> display much larger cis/trans Br-Pb-Br bond angle distortions than its respective iodide analogues. The immediate outliers in the scatter plot may be seen with (BrC5)PbBr<sub>4</sub>, (C7)PbBr<sub>4</sub> and (HOC2)PbBr<sub>4</sub> where there exists a vertical separation of exciton absorption energies with a minor change in bridging angle. In all three cases the higher energy exciton absorption are from the room temperature experiment. Although all three compounds follow the general trend there is unfortunately no further structural evidence at 77K to

substantiate if a new low temperature phase occurs at that temperature, more over it may suggest that the exciton has a greater temperature dependence, and some other exciton-lattice interactions may be occurring. The variable temperature photoluminescence experiments carried out by (Kitazawa N, *et al*, 2010) also displayed a stokes shifted emission with decreasing temperature, of (C4,C6,C7)PbBr<sub>4</sub>. This stokes shift is also observed on the scatter plot with the phases of (C6)PbBr<sub>4</sub> (green) compound, however it manifests as a large blue shift as the bridging angle increases from the low temperature to the room temperature phase. This same phenomenon is observed in (C4)PbBr<sub>4</sub> (purple). Furthermore the increase in bridging angle with no decrease in exciton absorption observed for (BrC4)PbBr<sub>4</sub> cannot be readily rationalized from a structure and property correlation as no phase transition occurs, however normal thermal contractions do occur on cooling, and hence the decreased in bridging angle observed in the low temperature crystal structure. These stokes shifts of the absorption observed with decreasing temperature is counterintuitive to the structurally observed parameters. This is less evident in the lead iodide analogues with the exception of (IC6)PbI<sub>4</sub> which obeys the trend observed in the bromide analogues. The only two compounds in the lead bromide series that do follow the increase in exciton absorption energy with a decrease in the Pb-Br-Pb bridging angle, are (BrC3)PbBr<sub>4</sub> and (C5)PbBr<sub>4</sub>. We do suspect that the large amount of disorder in the aliphatic and inorganic components of (C4, C6, C7)PbBr<sub>4</sub> at low temperature may directly influence the interaction of the exciton with the lattice, however further experiments to correlate this would need to be carried out. Figure 4.3.9 does also illustrate another trend, which shows an increase in interlayer spacing observed between low and room temperature phases, accompanied by an increase in exciton optical absorption energy.

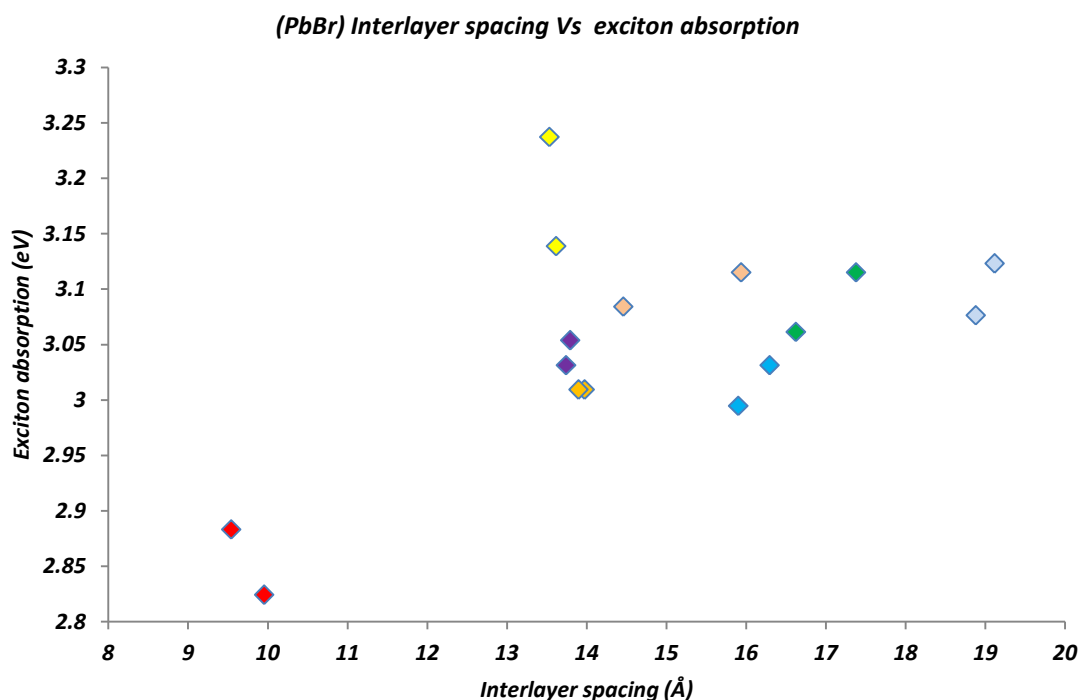


**Figure 4.3.9:** A plot of the exciton absorption against the interlayer spacing. The compounds are coloured accordingly: red (HOC2), yellow (BrC3), orange (BrC4), Sky Blue (BrC5), purple (C4), light orange (C5), green (C6), and light Blue (C7).

#### 4.3.7 Conclusions

The metal centred distortions do display some impact on the band gap, the greater the distortion experienced in the  $I_{eq}$ -Pb- $I_{eq}$  cis bond angles, the wider the band gap, as we suspect a decrease in  $I$  5p antibonding character which lowers the top of the valence band. The terminal halogen interaction specifically in  $(BrC2)PbI_4$ , clearly displayed some Br 4p/s character at the bottom of the conduction band, which may further explain the reduction of the band gap of this compound. This, in conjunction with the shorter interlayer spacing serve to stabilize more idealized bridging angles, as seen in both the lead iodide and bromide analogues. In addition, the short interlayer spacing compounds show large idealizations of the Pb-X-Pb bridging angle however display a large metal centred octahedral distortion in order accommodate the spatial occupation of the lone pair on lead, in both the bromide and iodide analogues. The lead bromide analogues appear to have a greater sensitivity to exciton lattice interactions, which give rise to red shifted emissions and absorptions with decreasing temperature. Structurally this behaviour is counterintuitive; as the structures increase in inorganic distortions as a temperature decrease a blue shift in the exciton absorption is expected. However the compounds displaying this

phenomenon the most, (C4, C6, C7)PbBr<sub>4</sub> do display a large amount of structural disorder in their lower temperature phases.

**Table 4.3.6:** The lead iodide series summary of inorganic distortions, exciton optical absorptions, and estimated binding energies from the low temperature optical absorption measurements.

Cation	Exciton energy (nm, eV)	Pb-Br-Pb	in-/out of plane distortion	eq/axial (Å) (averaged)	Distortion of PbBr <sub>6</sub> octahedra (Pb-Br)	Cation penetration (Å)	Binding energy (meV)
C4 (77K)	409, 3.03	153.4	13.29/5.79	2.986/3.01	0.013	0.518	350 (330 <sup>1</sup> /430 <sup>2</sup> )
C4 (RT)	406, 3.05	154.77	12.59/6.31	2.999/3.006	0.006	0.513	
C5 (77K)	402, 3.08	155.32	12.33/10.44	3.006/3.006	0.005	0.525	320 (290 <sup>1</sup> )
C5 (RT)	398, 3.12	153.06	13.48/9.53	2.998/3.068	0.024	0.032	
C6 (77K)	405, 3.06	155.43	12.26/20.58(9.52)	3.009/3.002	0.006	0.588/0.547	270
C6 (RT)	398, 3.12	158.5	10.50/6.50	2.963/2.963	0.056	Undetermined	
C7 (77K)	403, 3.07	151.57	14.19/12.25	2.985/2.986	0.016	Undetermined	350 (280 <sup>1</sup> )
C7 (RT)	397, 3.12	151.5	14.26/12.57	2.990/2.990	0.011	Undetermined	
HOC2 (77K)	430, 2.88	171.95	4.00/5.14	3.021/2.982	0.020	0.177	-
HOC2 (RT)	439, 2.82	171.8	4.08/5.62	3.031/2.987	0.024	0.182	
BrC3 (77K)	383, 3.24	140.92	19.52/5.50	3.016/2.980	0.033	0.149/0.620	330
BrC3 (RT)	395, 3.14	144.66	17.66/5.78	3.019/2.985	0.030	0.415	
BrC4 (77K)	412, 3.01	156.19	11.89/7.80	3.019/2.985	0.018	0.429	340
BrC4 (RT)	412, 3.01	157.48	11.28/8.04	3.031/2.984	0.026	0.425	
BrC5 (77K)	414, 2.99	155.88	12.10/7.92	3.005/3.002	0.006	0.577	280
BrC5 (RT)	409, 3.03	155.12	12.46/6.16	3.014/3.002	0.010	0.534	

[1] Kitazawa N, *et al*, 2010 [2] Tanaka K, *et al*, 2005c. (a) Bond length distortion is defined as  $\sum \text{abs}(d_i - \langle d \rangle)/6$ , where  $d_i$  is the summation over the six Pb-I distances and  $\langle d \rangle$  represents the average bond length. (b) Cation penetration is defined by the distance between the planes of the N atoms of the cation and the planes of the axial I atoms of the perovskite sheet.

## **Chapter 5: Structure and optical properties of lead iodide quantum wires**

### **5.1 The structures, phase transitions and optical properties of the natural 1D organic inorganic quantum wire hybrids of (A)PbI<sub>3</sub>**

#### **5.1.1 Introduction**

Through the mechanism of dimensional reduction of the tin and lead organic inorganic metal halide hybrids, preferential 1D wire formation may be generated through the correct choice of a bulky organic ammonium template and synthesized with an excess of aqueous halide acid (Mercier N, *et al*, 2009). The formation of the 1D band insulators of the face sharing octahedral wires of (A)PbX<sub>3</sub> have shown unstable photo-excited states which relax into self trapped excitons (STE's) and display a large broad stokes shifted photoluminescence emissions of  $\sim 1\text{eV}$  (Nagami A, *et al*, 1996; Fukumoto T, *et al*, 2000; Azuma J, *et al*, 2002a; Akimoto I, *et al*, 2004). This phenomenon has led these compounds to be of great fundamental interest as to the excited state dynamics of the wires, and the compounds inherent electronic properties. Electronic structure investigations have been reported for (piperdium)PbX<sub>3</sub>, from here (PD)PbX<sub>3</sub>, for both the bromide and iodide analogues. The calculations revealed the expected bonding, nonbonding, and anti-bonding orbital's pertaining to the valence and conduction bands, and the wide band gaps associated with these 1D band insulators. Moreover, the resultant band structure calculations also displayed a lack of band dispersion. This further supported the UPS and XPS experimental findings as to the strong 1D nature of these compounds (Azuma J, *et al*, 2002b; Tanaka K, *et al*, 2005b). It should be noted that the emission spectra of the (PD)PbBr<sub>3</sub> compound has been shown to only display the expected triplet state STE emission at much lower temperatures than its (PD)PbI<sub>3</sub> analogue. A distinct polaron based emission dominates at higher temperatures (Azuma J, *et al*, 2002a). Although the emission origin was investigated and the luminescence decay kinetic mechanisms ascertained, questions relating to the structural dynamics of the compound while undergoing the temperature cycles still remains unclear. Emissions related to defects of the lattice or inorganic type distortions caused from the phase transitions may influence the instability of the photo-excited states, which give rise to alternate emission pathways.

Very few studies have been reported on the structural aspects of the 1D compounds which include a direct structure to property relationship description. The exception lies with the work completed on the corner-shared perovskite type 1D wires of [NH<sub>2</sub>C(I)=NH<sub>2</sub>]<sub>3</sub>PbI<sub>5</sub> and [CH<sub>3</sub>SC(=NH<sub>2</sub>)NH<sub>2</sub>]<sub>3</sub>PbI<sub>5</sub> where the structures were reported by (Wang S, *et al*, 1995 and Mousdis G. A, *et al*, 1998) respectively, and the structure to optical property correlation was reported by

(Tanaka K, *et al*, 2005b). Tanaka discovered a large energy difference between the optical absorption of the first exciton peak of the two compounds. A minor structural correlation with the Pb-I-Pb bridging angle distortion was established as the stereo chemical activity of lead's lone pair is most influenced by the bridging angle in the 2D <100> orientation (Knutson J. L, *et al*, 2005). Much larger distortions of the respective trans Pb-I<sub>eq</sub> bond length elongations and compressions (3.882(2) Å and 3.037(2) Å) along the length of the wire, were observed in the [CH<sub>3</sub>SC(=NH<sub>2</sub>)NH<sub>2</sub>]<sub>3</sub>PbI<sub>5</sub> structure (Tanaka K, *et al*, 2005b). This distortion resulted in a large blue shift relative to [NH<sub>2</sub>C(I)=NH<sub>2</sub>]<sub>3</sub>PbI<sub>5</sub> optical absorption. The structural distortions impact on the first exciton absorption shifts were also manifest in the respective PL STE emissions.

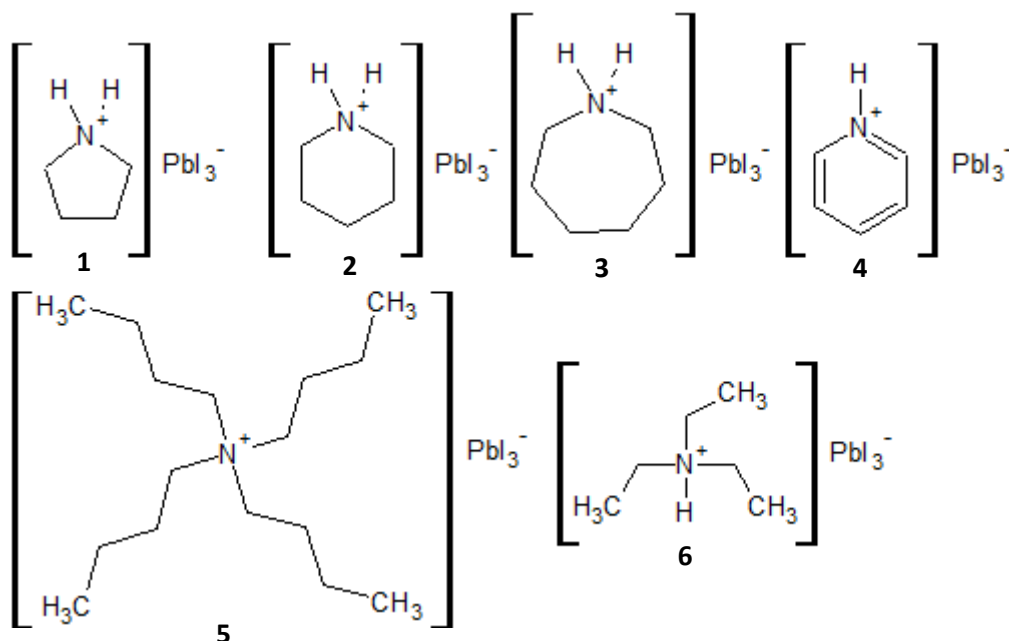
Optical property investigations are generally completed at low temperature (< 77K) in order to observe the exciton emission as in most semiconductors the excitonic binding energy is small and is only observed at room temperature if the binding energy is >  $k_bT$ . The structures of the 1D band insulators in particular are generally only determined at room temperature, with the 1D band insulators STE emission having a strong electron lattice interaction which largely suppresses the PL emission at room temperature despite the large binding (360meV) energy (Fukumoto T, *et al*, 2000). This does, to some degree, make it difficult to make direct structure to optical property correlations at room temperature as structural phase transitions may occur on heating or cooling of the crystal. This prompted a thorough investigation into the 1D band insulators structures and their thermal tendencies toward phase transitions in a series of (A)PbI<sub>3</sub> compounds. In addition correlations between the structures their respective optical properties have been attempted.

Of the six compounds investigated in this section, the room temperature structures of (PD)PbI<sub>3</sub> and [(But)<sub>4</sub>N]PbI<sub>3</sub> have been previously reported by (Gridnova G. V, *et al*, 1984; Krautschied and Vielsack, 1995) respectively. Additionally, the room temperature optical absorption measurements of [(But)<sub>4</sub>N]PbI<sub>3</sub> were previously reported by (Koutselas I. B, *et al*, 1997). These two compounds have been revisited via both variable temperature structure determination as well as optical absorption and PL measurements. The optical properties of (PD)PbI<sub>3</sub> have been thoroughly investigated (Nagami A, *et al*, 1996; Fukumoto T, *et al*, 2000; Azuma J, *et al*, 2002a; Akimoto I, *et al*, 2004) and shall be used as the bench mark for the remaining optical property experiments carried out on this series of compounds. Further attempts to correlate the contributions of the organic component on the optical absorption and STE emissions have also been empirically investigated.

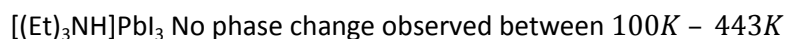
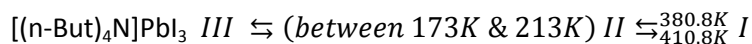
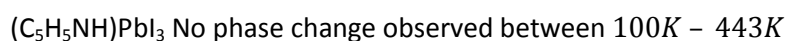
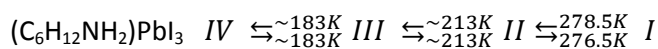
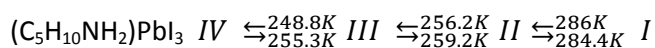
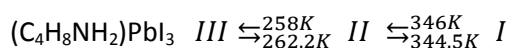
### 5.1.2 Results and discussion

The alkyl ammonium templates of the layered  $(C_nH_{2n}NH_3)_2MX_4$  hybrid perovskites have displayed a propensity to undergo phase transitions due to the flexibility of the alkyl chain. The conformational rearrangements of the alkyl chain may result in thermochromic phase transitions occurring (specifically in the lead iodide analogues), if the hydrogen bonding positions altered from acute to obtuse positions within the defined “box” or parallelogram (Billing D. G, and Lemmerer A, 2007). The flexibility of the organic templates of the 1D compounds investigated, specifically of the first three compounds which have cyclic aliphatic templates, i.e. pyrrolidine, piperidine, and azepane, denoted (Py)PbI<sub>3</sub>, (PD)PbI<sub>3</sub> and (Az)PbI<sub>3</sub>, compounds **1-3** respectively, display multiple phase transitions on cooling. The next 1D compound investigated used the rigid template of pyridine, denoted (Pyr)PbI<sub>3</sub>, **4** which suppressed any organic based phase transition behaviour. It was also used to ascertain if any inorganic based phase transitions would occur. Finally the last two 1D structures used the quaternary and tertiary ammonium aliphatics, of tetrabutylammonium, and triethylamine, denoted **5** [(n-But)<sub>4</sub>N]PbI<sub>3</sub> and **6** [(Et)<sub>3</sub>NH]PbI<sub>3</sub> respectively. Compounds **1-3**, and **5** undergo phase transitions upon cooling, however all the compounds’ structures were determined at both 293K and 173K in addition to the other phases present for standardized structural comparisons. Additionally, unit cell measurements were carried out at 20K intervals on all of the compounds down to 100K (the limit of the cooling device) to ensure no additional phases were present, for direct structure to property correlations. A summary of the phase transitions present in all of the compounds investigated (scheme 5.1.1) may be seen in scheme 5.1.2 below.





**Scheme 5.1.1:** The chemical diagrams of the crystal structures of compounds **1-6**. The compounds follow the number sequence from left to right.



**Scheme 5.1.2:** A summary of the phase transitions and the relative phase transformation temperatures for both heating and cooling runs of the (A)Pbl<sub>3</sub> compounds. Estimates of the phase transformation temperatures were made for the transitions that occurred below the measuring capability of the differential scanning calorimeter, and were examined via VT-SC-XRD cooling experiments.

**Table 5.1.1:** The experimental crystal structure data of compounds **1-6**, and their respective phases. Structures at both 173K and 293K are reported even if no phase transition was observed. Experiments were carried out with Mo K $\alpha$  radiation using a Bruker APEX-II CCD diffractometer. H-atom parameters were constrained.

	1_III	1_II	2_IV	2_III	2_II
Crystal data					
Chemical formula	I <sub>3</sub> Pb·C <sub>4</sub> H <sub>10</sub> N	C <sub>4</sub> H <sub>10</sub> N·I <sub>3</sub> Pb	C <sub>5</sub> H <sub>12</sub> N·I <sub>3</sub> Pb	C <sub>5</sub> H <sub>12</sub> N·I <sub>3</sub> Pb	C <sub>5</sub> H <sub>12</sub> N·I <sub>3</sub> Pb
$M_r$	660.02	660.02	674.05	674.05	674.05
Crystal system, space group	Orthorhombic, <i>Pnma</i>	Hexagonal, <i>P6<sub>3</sub>/m</i>	Monoclinic, <i>P2<sub>1</sub>/c</i>	Orthorhombic, <i>C2<sub>2</sub>2<sub>1</sub></i>	Orthorhombic, <i>C2<sub>2</sub>2<sub>1</sub></i>
Temperature (K)	173	293	173	252	273
$a, b, c$ (Å)	16.1474 (4), 8.0870 (2), 8.9569 (2)	16.0374 (3), 16.0374 (3), 8.0767 (2)	19.316 (2), 8.2486 (7), 17.4130 (15)	8.6537 (5), 18.1219 (11), 8.2071 (9)	8.6769 (7), 18.3267 (16), 8.1629 (7)
$\alpha, \beta, \gamma$ (°)	90, 90, 90	90, 90, 120	90, 116.717 (4), 90	90, 90, 90	90, 90, 90
$V$ (Å <sup>3</sup> )	1169.63 (5)	1799.00 (7)	2478.3 (4)	1287.05 (18)	1298.06 (19)
$Z$	4	6	8	4	4
$\mu$ (mm <sup>-1</sup> )	22.29	21.73	21.04	20.26	20.08
Crystal size (mm)	0.12 × 0.05 × 0.05	0.69 × 0.09 × 0.08	0.56 × 0.08 × 0.06	0.30 × 0.08 × 0.04	0.26 × 0.07 × 0.04
Data collection					
Absorption correction	Integration <i>Bruker XPREP</i> (Bruker, 2005)	Integration <i>Bruker XPREP</i> (Bruker, 2005)	Integration <i>Bruker XPREP</i> (Bruker, 2005)	Integration <i>Bruker XPREP</i> (Bruker, 2005)	Integration <i>Bruker XPREP</i> (Bruker, 2005)
$T_{\min}, T_{\max}$	0.174, 0.427	0.179, 0.844	0.235, 0.746	0.268, 0.849	0.214, 0.717
No. of measured, independent and observed [ $I > 2\sigma(I)$ ] reflections	15380, 1513, 1323	23995, 1556, 914	18302, 5978, 4709	6355, 1553, 1025	4418, 1576, 1018
$R_{\text{int}}$	0.049	0.050	0.058	0.061	0.044
Refinement					
$R[F^2 > 2\sigma(F^2)], wR(F^2), S$	0.023, 0.052, 1.07	0.059, 0.200, 1.08	0.063, 0.179, 1.08	0.058, 0.120, 1.07	0.040, 0.079, 1.00
No. of reflections	1513	1556	5978	1553	1576
No. of parameters	49	69	177	45	40
No. of restraints	0	45	9	7	0
	$w = 1/[\sigma^2(F_o^2) + (0.0242P)^2 + 2.1793P]$ where $P = (F_o^2 + 2F_c^2)/3$	$w = 1/[\sigma^2(F_o^2) + (0.0819P)^2 + 41.0983P]$ where $P = (F_o^2 + 2F_c^2)/3$	$w = 1/[\sigma^2(F_o^2) + (0.0878P)^2 + 92.1911P]$ where $P = (F_o^2 + 2F_c^2)/3$	$w = 1/[\sigma^2(F_o^2) + (0.P)^2 + 100.4405P]$ where $P = (F_o^2 + 2F_c^2)/3$	$w = 1/[\sigma^2(F_o^2) + (0.0257P)^2 + 3.2483P]$ where $P = (F_o^2 + 2F_c^2)/3$
$\Delta_{\text{max}}, \Delta_{\text{min}}$ (e Å <sup>-3</sup> )	1.19, -1.25	4.64, -3.74	4.27, -4.29	5.03, -3.07	0.85, -1.10
Absolute structure	-	-	-	Flack H D (1983), Acta Cryst. A39, 876-881	Flack H D (1983), Acta Cryst. A39, 876-881
Flack parameter	-	-	-	0.52 (5)	0.47 (4)
	2_I	3_IV	3_III	3_II	3_I
Crystal data					
Chemical formula	C <sub>5</sub> H <sub>12</sub> N·I <sub>3</sub> Pb	I <sub>6</sub> Pb <sub>2</sub> ·3(C <sub>6</sub> H <sub>14</sub> N)·I <sub>3</sub> Pb	C <sub>6</sub> H <sub>14</sub> N·I <sub>3</sub> Pb	C <sub>6</sub> H <sub>14</sub> N·I <sub>3</sub> Pb	C <sub>6</sub> H <sub>14</sub> N·I <sub>3</sub> Pb
$M_r$	674.05	2064.22	688.07	688.07	688.07
Crystal system, space group	Orthorhombic, <i>C2<sub>2</sub>2<sub>1</sub></i>	Monoclinic, <i>P2<sub>1</sub>/n</i>	Monoclinic, <i>P2<sub>1</sub>/n</i>	Orthorhombic, <i>C2<sub>2</sub>2<sub>1</sub></i>	Orthorhombic, <i>C2<sub>2</sub>2<sub>1</sub></i>
Temperature (K)	293	173	203	263	293
$a, b, c$ (Å)	8.7050 (3), 18.4332 (7), 8.1359 (4)	16.0387 (6), 8.2494 (3), 30.4561 (11)	10.5885 (4), 8.2362 (2), 16.1736 (4)	8.7092 (4), 19.5158 (8), 8.2160 (4)	8.7474 (3), 19.5951 (7), 8.1982 (3)

$\alpha, \beta, \gamma$ (°)	90, 90, 90	90, 93.879 (1), 90	90, 102.477 (1), 90	90, 90, 90	90, 90, 90
$V$ (Å <sup>3</sup> )	1305.49 (9)	4020.4 (3)	1377.17 (7)	1396.45 (11)	1405.22 (9)
$Z$	4	4	4	4	4
$\mu$ (mm <sup>-1</sup> )	19.97	19.46	18.93	18.67	18.56
Crystal size (mm)	0.22 × 0.1 × 0.04	0.49 × 0.08 × 0.08	0.27 × 0.06 × 0.04	0.27 × 0.05 × 0.03	0.23 × 0.08 × 0.05
Data collection					
Absorption correction	Integration <i>Bruker XPREP</i> (Bruker, 2005)	Integration <i>Bruker XPREP</i> (Bruker, 2005)	Integration <i>Bruker XPREP</i> (Bruker, 2005)	Integration <i>Bruker XPREP</i> (Bruker, 2005)	Integration <i>Bruker XPREP</i> (Bruker, 2005)
$T_{\min}, T_{\max}$	0.097, 0.502	0.251, 0.746	0.080, 0.518	0.166, 0.659	0.124, 0.631
No. of measured, independent and observed [ $I > 2\sigma(I)$ ] reflections	4744, 1586, 1177	31735, 7886, 6474	24269, 3314, 2447	4329, 1695, 1129	13414, 1707, 1139
$R_{\text{int}}$	0.042	0.051	0.054	0.037	0.050
Refinement					
$R[F^2 > 2\sigma(F^2)], wR(F^2), S$	0.033, 0.075, 1.07	0.054, 0.109, 1.20	0.059, 0.165, 1.08	0.045, 0.102, 1.04	0.029, 0.068, 1.03
No. of reflections	1586	7886	3314	1695	1707
No. of parameters	52	298	147	40	54
No. of restraints	17	0	82	7	17
	$w = 1/[\sigma^2(F_o^2) + (0.0248P)^2 + 0.9682P]$ where $P = (F_o^2 + 2F_c^2)/3$	$w = 1/[\sigma^2(F_o^2) + (0.0051P)^2 + 194.659P]$ where $P = (F_o^2 + 2F_c^2)/3$	$w = 1/[\sigma^2(F_o^2) + (0.0659P)^2 + 43.8386P]$ where $P = (F_o^2 + 2F_c^2)/3$	$w = 1/[\sigma^2(F_o^2) + (0.0257P)^2 + 22.9129P]$ where $P = (F_o^2 + 2F_c^2)/3$	$w = 1/[\sigma^2(F_o^2) + (0.0247P)^2 + 3.2751P]$ where $P = (F_o^2 + 2F_c^2)/3$
$\Delta_{\max}, \Delta_{\min}$ (e Å <sup>-3</sup> )	0.98, -1.15	2.59, -4.45	7.78, -2.83	1.71, -1.74	0.89, -0.85
Absolute structure	Flack H D (1983), Acta Cryst. A39, 876-881	-	-	Flack H D (1983), Acta Cryst. A39, 876-881	Flack H D (1983), Acta Cryst. A39, 876-881
Flack parameter	0.49 (6)	-	-	0.47 (5)	0.44 (5)

	4_I_173K	4_I_293K	5_II	5_I	6_I_173K
Crystal data					
Chemical formula	I <sub>3</sub> Pb·C <sub>3</sub> H <sub>6</sub> N	I <sub>3</sub> Pb·C <sub>3</sub> H <sub>6</sub> N	C <sub>16</sub> H <sub>36</sub> N·I <sub>3</sub> Pb	C <sub>16</sub> H <sub>36</sub> N·I <sub>3</sub> Pb	C <sub>6</sub> H <sub>16</sub> N·I <sub>3</sub> Pb
$M_r$	668	668	830.35	830.35	690.09
Crystal system, space group	Orthorhombic, <i>Pnma</i>	Orthorhombic, <i>Pnma</i>	Tetragonal, <i>I</i> 4	Tetragonal, <i>I</i> 4 <sub>2</sub> d	Orthorhombic, <i>Pnma</i>
Temperature (K)	173	293	173	288	173
$a, b, c$ (Å)	14.9083 (5), 8.0796 (3), 9.7255 (3)	14.975 (1), 8.1071 (5), 9.9080 (7)	24.3279 (4), 24.3279 (4), 8.3560 (2)	24.5813 (17), 24.5813 (17), 8.3859 (7)	18.3989 (5), 8.0101 (2), 20.1371 (5)
$\alpha, \beta, \gamma$ (°)	90, 90, 90	90, 90, 90	90, 90, 90	90, 90, 90	90, 90, 90
$V$ (Å <sup>3</sup> )	1171.47 (7)	1202.87 (14)	4945.47 (17)	5067.1 (7)	2967.75 (13)
$Z$	4	4	8	8	8
$\mu$ (mm <sup>-1</sup> )	22.25	21.67	10.57	10.31	17.57
Crystal size (mm)	0.25 × 0.06 × 0.06	0.97 × 0.06 × 0.05	0.46 × 0.16 × 0.06	0.45 × 0.08 × 0.05	0.43 × 0.04 × 0.02
Data collection					
Absorption correction	Integration <i>Bruker XPREP</i> (Bruker, 2005)	Integration <i>Bruker XPREP</i> (Bruker, 2005)	Integration <i>Bruker XPREP</i> (Bruker, 2005)	Integration <i>Bruker XPREP</i> (Bruker, 2005)	Multi-scan Absorption corrections were done using <i>SADABS</i> as incorporated in the <i>Apex2</i> software

					(Bruker, 2005)
$T_{\min}, T_{\max}$	0.324, 0.746	0.282, 0.887	0.044, 0.641	0.516, 1.000	0.351, 0.746
No. of measured, independent and observed [ $I > 2\sigma(I)$ ] reflections	14043, 1517, 1214	7635, 1547, 1200	44355, 5953, 5273	11425, 3064, 1615	37534, 3844, 2463
$R_{\text{int}}$	0.051	0.035	0.045	0.063	0.095
Refinement					
$R[F^2 > 2\sigma(F^2)], wR(F^2), S$	0.034, 0.084, 1.07	0.028, 0.066, 1.13	0.024, 0.043, 1.02	0.052, 0.102, 1.00	0.056, 0.113, 1.14
No. of reflections	1517	1547	5953	3064	3844
No. of parameters	56	49	192	98	136
No. of restraints	6	0	18	53	70
	$w = 1/[\sigma^2(F_o^2) + (0.0464P)^2 + 3.7155P]$ where $P = (F_o^2 + 2F_c^2)/3$	$w = 1/[\sigma^2(F_o^2) + (0.0284P)^2 + 0.735P]$ where $P = (F_o^2 + 2F_c^2)/3$	$w = 1/[\sigma^2(F_o^2) + (0.0176P)^2]$ where $P = (F_o^2 + 2F_c^2)/3$	$w = 1/[\sigma^2(F_o^2) + (0.0376P)^2]$ where $P = (F_o^2 + 2F_c^2)/3$	$w = 1/[\sigma^2(F_o^2) + (0.0185P)^2 + 47.1678P]$ where $P = (F_o^2 + 2F_c^2)/3$
$\Delta_{\text{max}}, \Delta_{\text{min}}$ (e Å <sup>-3</sup> )	3.30, -1.04	0.75, -1.48	0.59, -0.54	0.55, -0.96	1.31, -2.48
Absolute structure	-	-	Flack H D (1983), Acta Cryst. A39, 876-881	Flack H D (1983), Acta Cryst. A39, 876-881	-
Flack parameter	-	-	0.012 (17)	0.00 (5)	-

	6_I_293K
Crystal data	
Chemical formula	C <sub>6</sub> H <sub>16</sub> N·I <sub>3</sub> Pb
$M_r$	690.09
Crystal system, space group	Orthorhombic, <i>Pnma</i>
Temperature (K)	293
$a, b, c$ (Å)	18.4877 (5), 8.0700 (2), 20.3607 (5)
$\alpha, \beta, \gamma$ (°)	90, 90, 90
$V$ (Å <sup>3</sup> )	3037.73 (13)
$Z$	8
$\mu$ (mm <sup>-1</sup> )	17.17
Crystal size (mm)	0.43 × 0.04 × 0.02
Data collection	
Absorption correction	Multi-scan Absorption corrections were done using <i>SADABS</i> as incorporated in the <i>Apex2</i> software (Bruker, 2005)
$T_{\min}, T_{\max}$	0.338, 0.746
No. of measured, independent and observed [ $I > 2\sigma(I)$ ] reflections	57253, 3932, 2083
$R_{\text{int}}$	0.105
Refinement	
$R[F^2 > 2\sigma(F^2)], wR(F^2), S$	0.045, 0.114, 1.01
No. of reflections	3932
No. of parameters	125
No. of restraints	94
	$w = 1/[\sigma^2(F_o^2) + (0.0362P)^2 + 21.143P]$ where $P = (F_o^2 + 2F_c^2)/3$
$\Delta_{\text{max}}, \Delta_{\text{min}}$ (e Å <sup>-3</sup> )	1.09, -1.27
Absolute structure	-

### 5.1.3 Powder Diffraction investigations

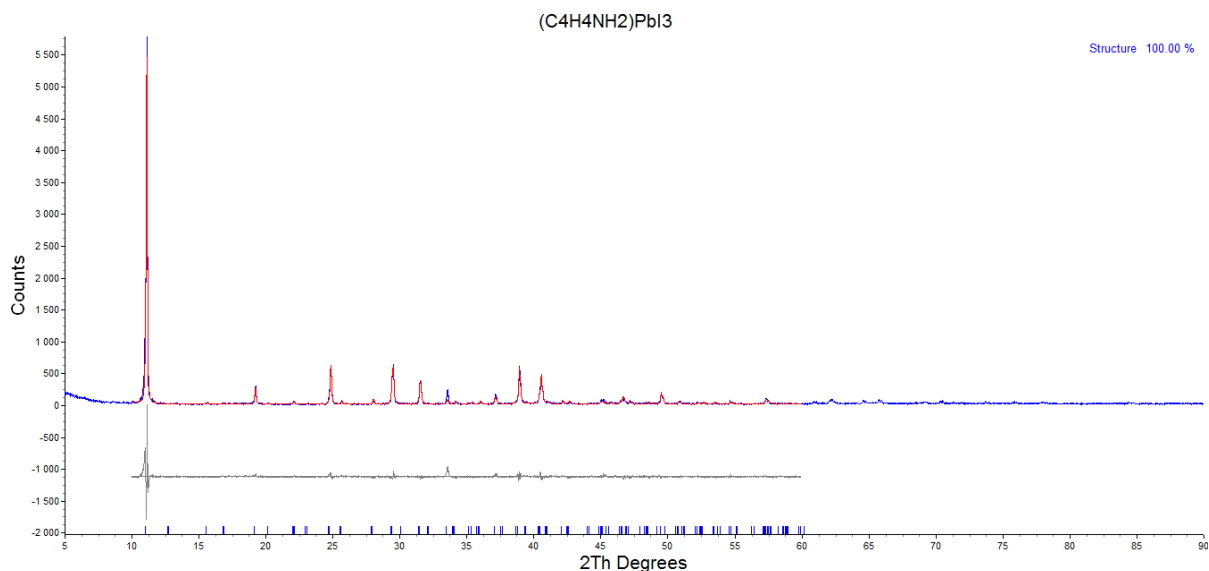


**Figure 5.1.1:** The rietveld refinement of the room temperature powder diffraction pattern of (Py)PbI<sub>3</sub>. Where  $R_{\text{Bragg}}$ : 6.586  $R_{\text{exp}}$ : 12.65,  $R_{\text{wp}}$ : 19.99,  $R_p$ : 15.62, GOF: 1.58  $R_{\text{exp}}$ : 18.65,  $R_{\text{wp}}$ : 29.47,  $R_p$ : 26.98, DW: 0.97. The remaining PXRD patterns can be found in appendix B.

Before any optical property investigations were undertaken, powder x-ray diffraction (PXRD) studies were completed in order to ascertain if the bulk sample was representative of the room temperature single crystal structures. Phase identification and rietveld refinement were carried out on the sample using the *Pseudo Voigt TCHZ* analytical peak profile function. The refinement was carried out with the use of the room temperature single crystal structure data obtained from our SC-XRD experiments. All of the PXRD patterns displayed certain levels of preferred orientation, as the crystal habit is very plate like. Therefore spherical harmonics function of order 4-8 was used to correct for this. From the difference plot and the R factors quoted above (figure 5.1.1), the refinement gave satisfactory results indicating that the bulk and single crystal phases were the same. The remaining five compounds rietveld refined room temperature PXRD patterns can be found in appendix B, along with their respective R factors and refined unit cell parameters. Although all the PXRD patterns were collected from 5-90° 2 $\theta$  the refinement was restricted to the range of 8-60° 2 $\theta$  as to reduce the amount of background parameters used, and due to the distinct lack of low angle peaks despite the longer scan times. For refinement the 2 $\theta$  low angle limit changed from sample to sample, where the high angle limit remained at 60° for

every sample. The remaining instrumental experimental details may be found in chapter 3. The refined unit cell parameters for compound **1** were found to be  $a = 16.0560(31) \text{ \AA}$  and  $c = 8.0668(16) \text{ \AA}$ ,  $V = 1800.98(78) \text{ \AA}^3$  for the hexagonal unit cell with the space group  $P6_3/m$ . The SC-XRD unit cell parameters were  $a = 16.0374(3) \text{ \AA}$  and  $c = 8.0767(2) \text{ \AA}$ ,  $V = 1799.0(7) \text{ \AA}^3$  respectively. As both lead atoms reside on special positions their atomic positions in the asymmetric unit were not refined. Furthermore, due to the large difference in the electron densities of the lead iodide octahedra and the organic component the thermal parameter  $B_{eq}$  and organic atomic positions were also not refined. This was the case for all six compounds.

#### 5.1.4 Thermal analysis studies (DSC)

The DSC experiments carried out display thermal hysteresis with respect to the reversibility of the phase changes observed. The high temperature forms I of (Py)PbI<sub>3</sub> and [(n-But)<sub>4</sub>N]PbI<sub>3</sub> were not obtained due to [(n-But)<sub>4</sub>N]PbI<sub>3</sub> phase I being beyond the heating capabilities of our instrument, and secondly, our interest lay with the lower temperature forms and their impact on the optical properties of the compounds. The phase transitions observed in **1-3** were a result of the conformational changes of the unsaturated cycloalkyl ammonium rings. Due to the lower temperature limit of the DSC instrument (-60°C) the low temperature which phase transitions which showed the largest impact on the crystal system enthalpies were not able to be obtained, however were further monitored through VT-SC-XRD and plots of the unit cell volumes against temperature may be seen in figure 5.1.3. Although very large changes in the unit cell volume are seen in compounds **1**, **2** and **3**, the enthalpy change of these phases are only seen in (Py)PbI<sub>3</sub> and (PD)PbI<sub>3</sub> which are  $2.11 \text{ kJ} \cdot \text{mol}^{-1}$  and  $5.16 \text{ kJ} \cdot \text{mol}^{-1}$  respectively. In compound **2** the peak integration to obtain the enthalpy values for the phase between II to III and III to IV was less accurate for the individual peaks, as the peaks were overlapped, hence the enthalpy value for both transitions were obtained. The enthalpy of the phase change from II to I of [(n-But)<sub>4</sub>N]PbI<sub>3</sub> was  $9.89 \text{ kJ} \cdot \text{mol}^{-1}$  which is consistent with the values of a quasi-melting enthalpy displayed in the 2D aliphatic compounds of (C4-7)PbI<sub>4</sub> (Billing D. G, Lemmerer A, 2007). The enthalpy changes for all the phase transitions within the measured temperature range of the DSC experiments are reported in table 5.1.2.

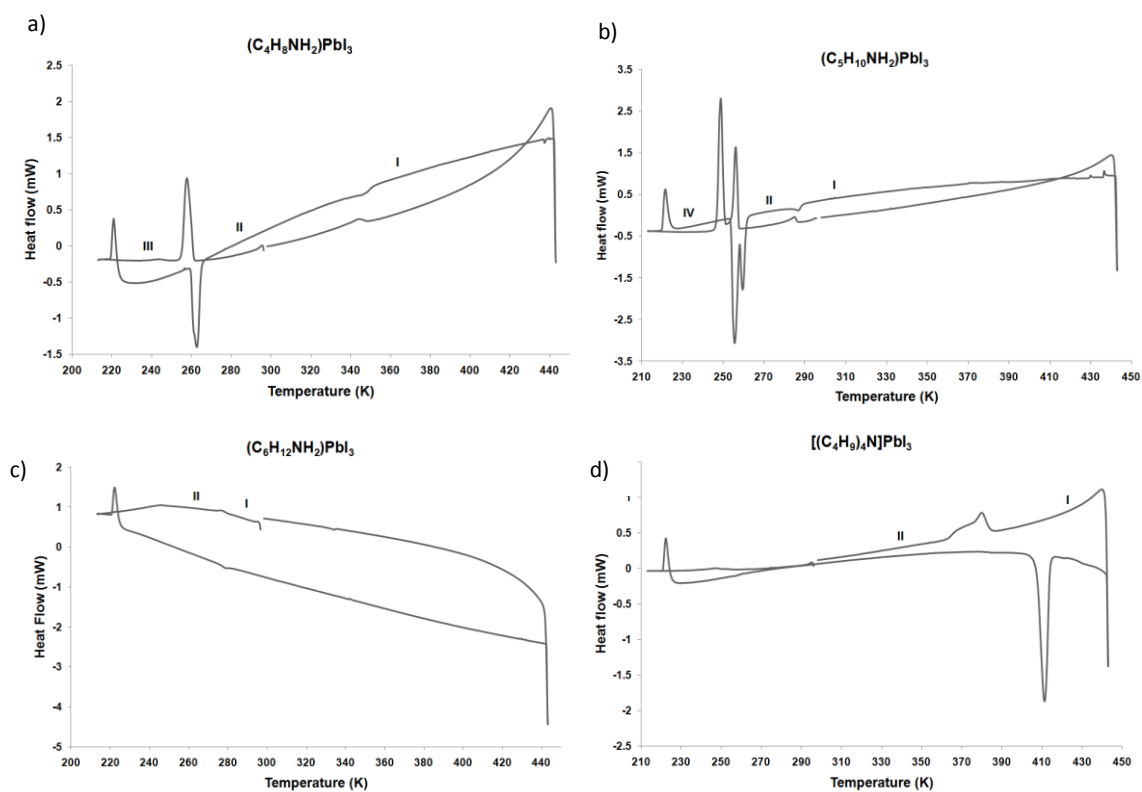


**Figure 5.1.2:** The DSC graphs displaying the reversible high temperature phase transitions for compounds **1 a)**, **2 b)**, **3 c)**, and **5 d)**. Compounds **3** and **6** displayed no thermal event within the measured temperature range and their DSC graphs may be found in appendix B.

**Table 5.1.2:** The enthalpy measurements of the phase transitions of compounds **1-3** and **5** for the heating runs only.

Compound	T1 (K)	$\Delta H1$ (KJ.mol <sup>-1</sup> )	T2 (K)	$\Delta H2$ (KJ.mol <sup>-1</sup> )	T3 (K)	$\Delta H3$ (KJ.mol <sup>-1</sup> )	$\Delta H2\&3$ (KJ.mol <sup>-1</sup> )
(Py)PbI <sub>3</sub>	344.5	0.11	262.2	2.11	-	-	-
(PD)PbI <sub>3</sub>	284.4	0.2	259.2	0.65	255.3	1.86	5.16
(Az)PbI <sub>3</sub>	276.5	0.2	~213	?	~183	?	-
[(n-But) <sub>4</sub> N]PbI <sub>3</sub>	410.8	9.89	173-213	?	-	-	-

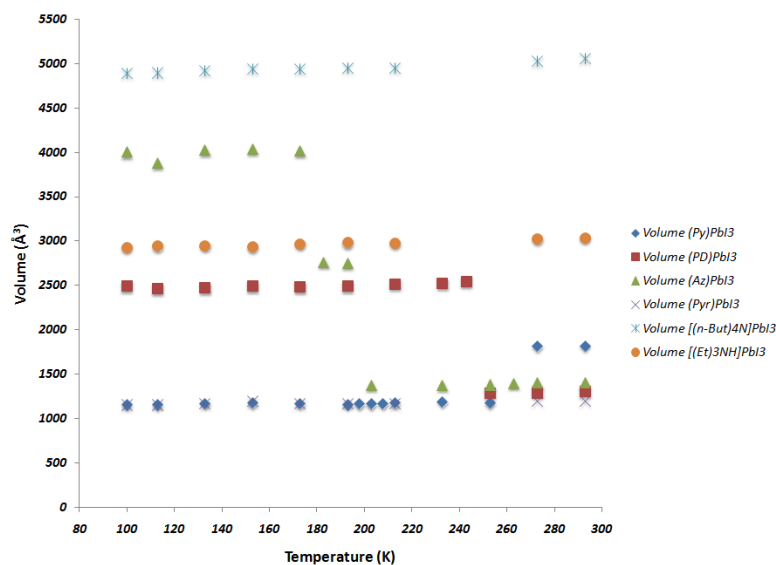


**Figure 5.1.3:** A plot of the unit cell volumes of compounds **1-6** against temperature (100-293K). Most of the volumes were obtained from only unit cells indexed from SC-XRD experiments collected on between 50-250 reflections. All new phase's volumes however, were obtained from full SC-XRD data sets which are included in the graph. The experiment displays the relative thermal stability of compounds **4-6** despite the existence of a minor phase change in **5**. Gaps in the temperature range are due to the results from the DSC experiments which showed no existence of a new phase in that temperature region. Compounds **1-3** show the large unit cell volume changes as a result of the crystal systems changing with decreasing temperature.

### 5.1.5 The structure and phase transitions of (Py)PbI<sub>3</sub>, (PD)PbI<sub>3</sub> and (Az)PbI<sub>3</sub>

There are various conformations possible for each of the ring types and we summarize them here before proceeding. The conformation of the pyrrolidinium cation (C5 ring) may only exist in two conformation types, the envelope and the half chair conformation (Pitzer K. S and Donath W. E, 1959) where the envelope conformer is the most energetically favoured. The piperidinium and azepanium rings (C6 and C7 rings) may exist in four and six conformations respectively. Where the cyclohexane ring type may exist in the twist chair, boat, twist boat and chair conformations, which are in order of increasing energetic stability (Shachse H, 1890; 1892; 1893; Mohr E, 1918; 1922; Gill G, *et al*, 2005). The cycloheptane ring type conformations may exist in the boat, twist boat, chair, twist chair, bent transition state, and the twist transition state conformers respectively. Where the twist and bent transition states are the least favoured conformations energetically, whereas the twist chair and twist boat conformations are the most favoured, however only mildly favoured over the chair and boat conformations (Bocian D. F, *et al*, 1975).



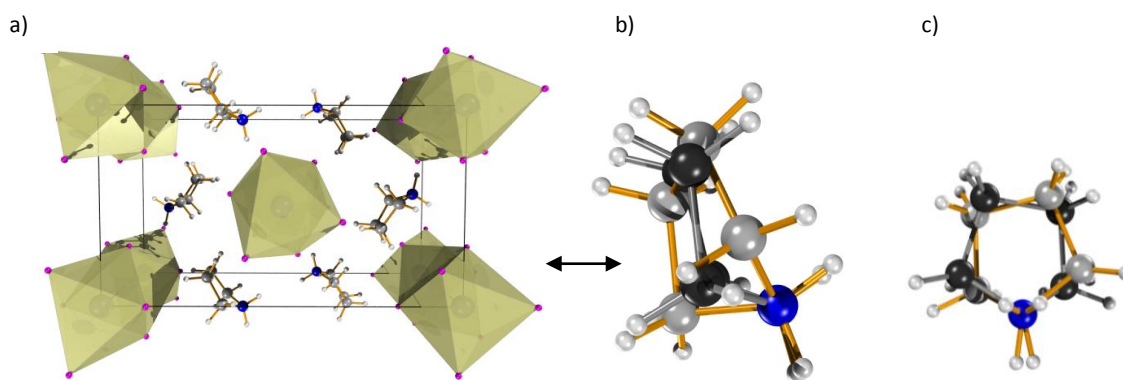


**Figure 5.1.4:** The crystal packing viewed along (010) axis of the ordered Phase III of (Py)PbI<sub>3</sub> (a) and the disordered envelope conformation shown from the side and above (b, c), where the dark grey atoms represent the disordered component.

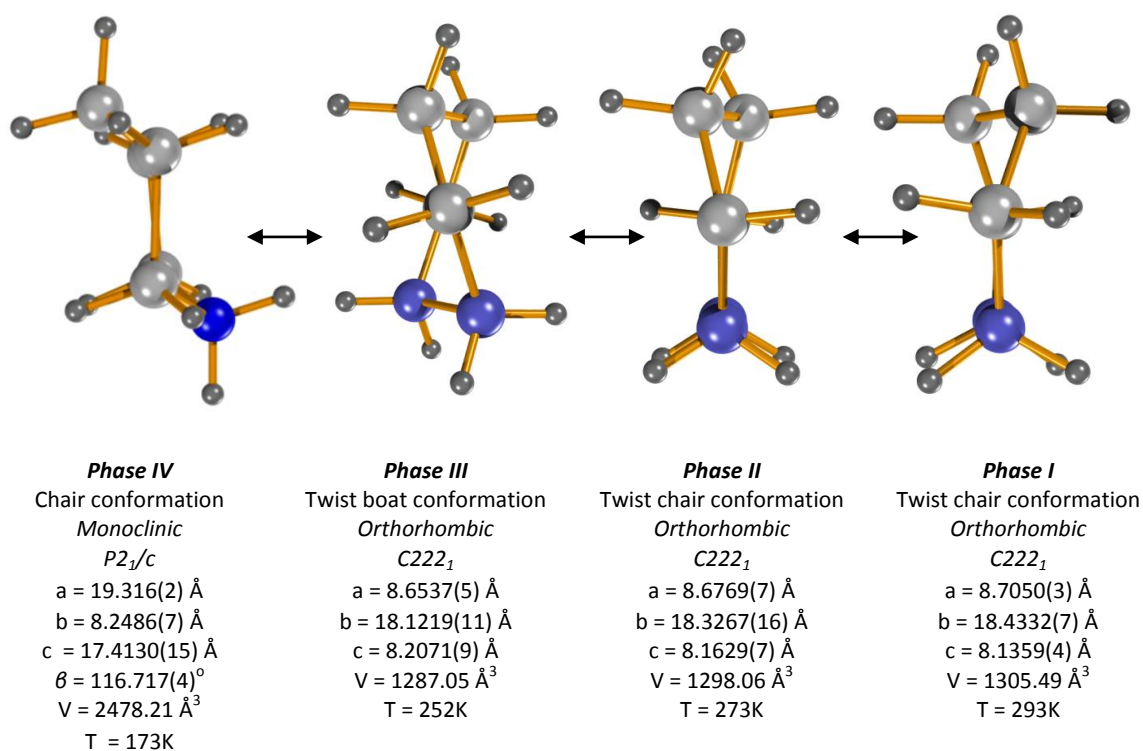


**Figure 5.1.5:** The conformations of the cyclohexane type ring of pyrrolidinium cation through the four phase changes present in the compound (PD)PbI<sub>3</sub>. The most unfavoured twist chair conformation exists in the higher temperature phases II and I, where the more idealized conformations of the twist boat and chair conformer exist in the low temperature phases III and IV respectively. Note in phase III-I the nitrogen is disordered over two positions, where in phase I the nitrogen is no longer disordered.

As in the 2D (C<sub>n</sub>H<sub>2n</sub>NH<sub>3</sub>)MX<sub>4</sub> hybrids, the cyclo-ammonium rings undergo phase changes that result in order disorder transitions (Mitzi D. B, 1999). This type of transition was observed between phase II and III of compounds **1** and **3**, respectively. Although six conformations are

possible in the azepanium ring of (Az)PbI<sub>3</sub>, only four conformational arrangements appear in the four phases of the measured temperature range, where the lowest temperature phase exists in the most favoured conformation. Additionally, only three of the four conformational arrangements of the piperdimium ring in (PD)PbI<sub>3</sub> are present whilst the boat conformation is not observed.

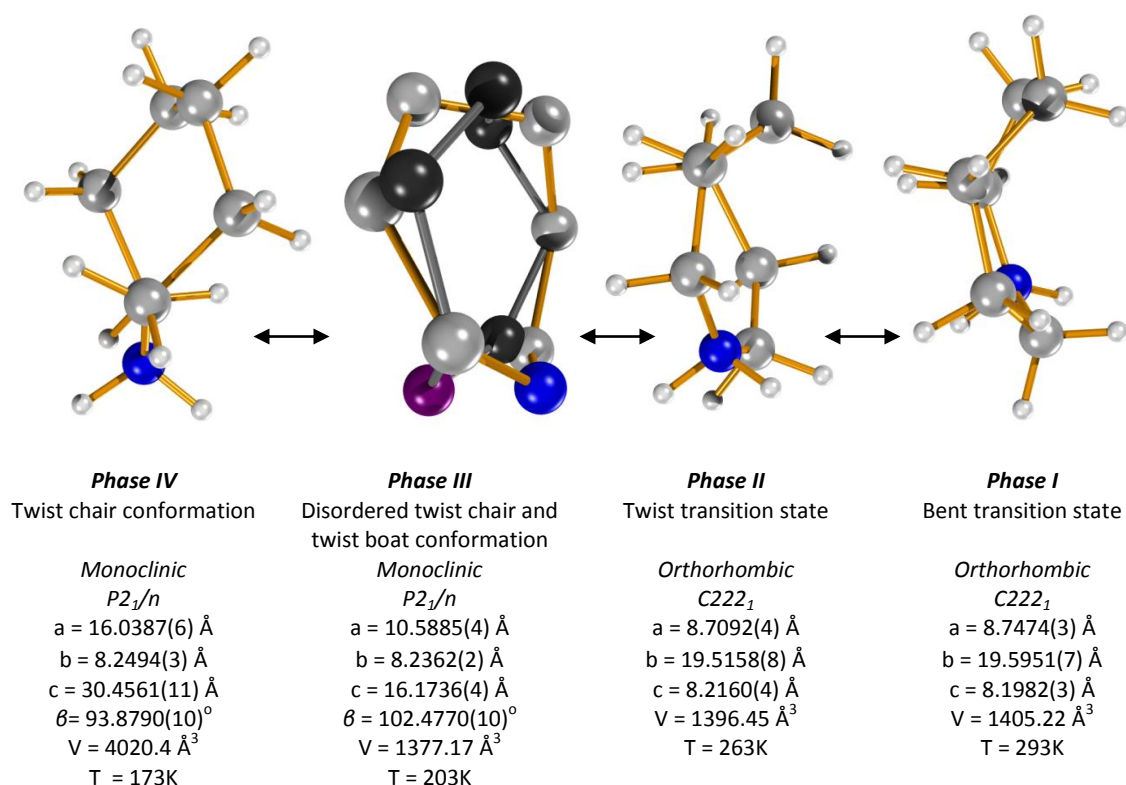


**Figure 5.1.6:** The conformations of the cycloheptane type ring of the azepanium cation through the four phases of the compound (Az)PbI<sub>3</sub>. The low temperature phases IV and III are the most thermodynamically favoured conformations, whereas the twist and bent transition states in phases II and I respectively, are the least favoured conformers.

(Py)PbI<sub>3</sub> displayed three phases where we suspect the high temperature phase to display the half chair conformation as the lower temperature phases display the disordered envelope and ordered envelope conformations which are more energetically favoured. It is interesting to note that only certain conformational changes resulted in phase transitions that showed a strong impact on the crystal system and the unit cell volume as seen in (figure 5.1.3). In (PD)PbI<sub>3</sub> the unit cell volume doubles from phase III to IV, in addition a decrease in symmetry from orthorhombic *C222<sub>1</sub>* to monoclinic *P2<sub>1</sub>/c* was observed. From phase I of (Az)PbI<sub>3</sub> to phase IV the unit cell volume was observed to increase almost four fold, in addition to the decrease in crystal symmetry from orthorhombic *C222<sub>1</sub>* to monoclinic *P2<sub>1</sub>/n*. Conversely, the compound (Py)PbI<sub>3</sub>

also displayed a decrease in crystal symmetry on cooling, which transformed from the hexagonal  $P6_3/m$  phase II to the orthorhombic  $Pnma$ , however phase III displayed a volume decrease of 66% from that of phase II. This is the expected behaviour in the quenching of dynamical disorder in crystal structures.

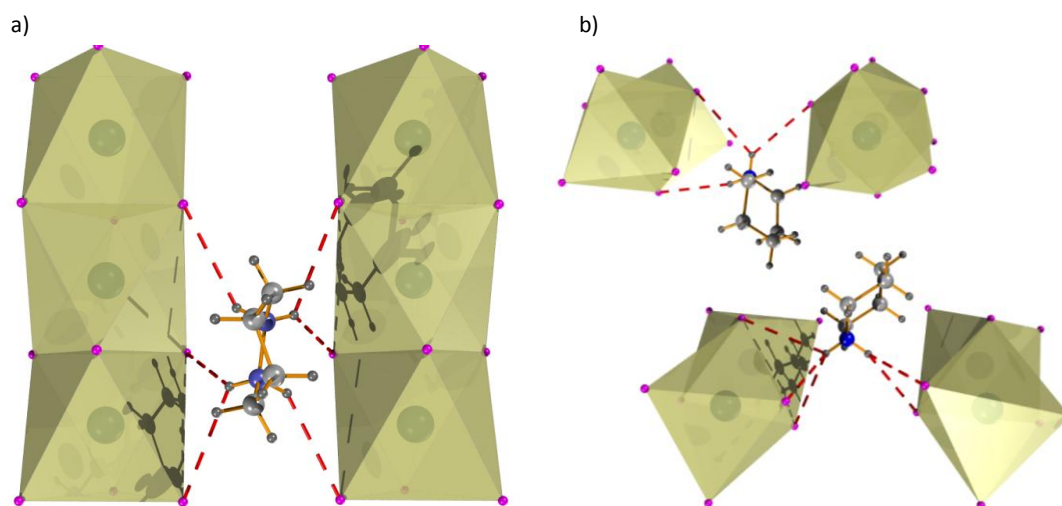


**Figure 5.1.7:** Phase I of (PD)PbI<sub>3</sub> disordered nitrogen's hydrogen bonding between the adjacent wires (a). The hydrogen bonding may be described by a hydrogen bonding interaction with the concave face generated by the octahedral face sharing of adjacent octahedra. The ammonium cation displays an N-H...I H-bond interaction with the edge and bottom of the concave face. The hydrogen bonding motif only alters in phase IV (b), where the N-H...I H-bonds now also occur with the top of the concave face in addition to the edge and bottom H-bonds. The H-bonds between the wires also become unsymmetrical in IV.

Figures 5.1.4; 5.1.5; and 5.1.6 display the conformational changes of the rings of **1-3** through their respective phases. Interestingly, the largest unit cell changes to occur upon cooling are due to all three rings types adopting their most energetically favoured conformation, i.e. being the chair and twist chair conformation for the C6 and C7 rings, and the ordered envelope conformation of the C5 ring.

The cyclopentane ring of the pyrrolidinium cations, pack in a disordered envelope conformation in phase II, where the site occupancy factors were fixed to 50% due to the N1 atom lying on a mirror plane passing through the C3A-C3B' bond, resulting in only half of the molecule to be in the asymmetric unit. In phase III an ordered envelope conformation now exists as the symmetry induced dynamical disorder has been quenched (figure 5.1.4). As the conformational arrangement remains the same in both phases the enthalpy associated with the quenching of the disorder was measured to be  $2.11 \text{ kJ} \cdot \text{mol}^{-1}$  which is within the range reported for the

quenching of the dynamical disorder found in  $\text{C}_2\text{CdCl}_4$  (Tello M. J, *et al*, 1977). In the disordered phase II both of the face sharing octahedral wires generated in the asymmetric unit contain a  $6_3$  rotation axis which passes through the centre of the wire. In addition both Pb1 and Pb2 of the two separate wires reside on special positions, with the respective I1, I2 and I3 all falling on a mirror plane. The high symmetry of the crystal is a result of the generally idealized bond lengths and angles of the lead iodide octahedra (table 5.1.3). The idealized inorganic octahedra are maintained in the lower temperature *Pnma* form of phase III.

The conformational changes of the C6 ring type of the pyrrolidinium cation changing through their respective phases may be seen in figure 5.1.5. Phase I and II display the ring in the twist chair conformation where the nitrogen is disordered over two positions (the site occupancy factor was fixed to 50% as the disorder is symmetry induced). Little appears to have changed between these two phases, however a decrease in the torsion angle C2-C3-C3'-C2' (a twofold rotation axis runs through the centre of the molecule) from  $64(3)^\circ$  to  $47(4)^\circ$  and a marginal decrease in the N-H...I hydrogen bonding distances are observed (table 5.1.4). The hydrogen bonding of the ammonium cation to the wires may be described through the interaction of the H-bonding with the concave face created between two face shared lead iodide octahedra (figure 5.1.7). We define the top and bottom of the face by the way the ring penetrates from "above" between the two adjacent wires. Therefore the top and bottom of the face are defined with this point of reference. Phases I-III display a nitrogen disordered over two positions due to the ring lying on a twofold rotation axis which passes through the centre of the (N1/C1-N1'/C1' and C3-C3') bonds. The disorder arisen through symmetry ensures the nitrogen's hydrogen bonding interactions between adjacent wires are equivalent. In phase IV the conformation of the ring adopts the marginally distorted chair conformation, where the ring itself rearranges marginally relative to the concave face of the wire. The nitrogen cation becomes the apical point of the chair conformation, and the twofold rotation symmetry seen in phase III is now broken. The hydrogen bonding of phase I and IV may be seen in figure 5.1.7, where phase I's nitrogen disorder creates an equivalent cohesive hydrogen bonding interaction between the adjacent wires (inter wire spacing I...I contacts of  $4.2690(8) \text{ \AA}$ ). Considering the concave face, the N-H...I bonds to the edge as well as the bottom of the face. The hydrogen bonding motif alters in phase IV, where now the N-H...I bonds also occur with the top of the concave face in addition to the edge and bottom. In phase IV the Pb-I bond distances in the top of the concave face display large Pb-I bond elongations, where the Pb1-I2 (N1-H1B...I2  $3.11 \text{ \AA}$ ) and Pb2-I4 (N2-H2C...I4  $3.12 \text{ \AA}$ ), bond distances become  $3.507(2) \text{ \AA}$  and  $3.504(2) \text{ \AA}$  respectively. These bond elongations in turn cause a Pb-I compression of the trans Pb-I bond length, leading to a wide range of Pb-I bond

distances from 3.045(2) – 3.507(2) Å. In addition the metal centred octahedral distortions seen in the trans I-Pb-I and cis bonds angles range between 167.66(6)-177.44(5)° and 81.21(5)-97.06(5)° for phase IV, and between 179.35(14)-179.89(10)° and 83.21(6)-96.87(6)° for phase I. These bond angles do increase in distortion progressively from phase I to IV, however the Pb-I bond distances make an abrupt change from phase III to IV. A combination of a longer inter-wire spacing (4.404(3) Å phase IV 4.2690(8) Å phase I) caused from the larger spatial occupation of the chair conformation, and increased hydrogen bonding interactions with the concave face appear to be responsible for the larger inorganic distortions observed in phase IV. In addition, we attribute the idealization of the ring conformation and its effect on the inorganic distortions, the cause of the decrease in symmetry of the crystal, and hence the large increase in unit cell volume from phase III to IV. However there is one more argument thought to be responsible for the increase in distortions experienced in the low temperature forms of both (Az)PbI<sub>3</sub> and (PD)PbI<sub>3</sub>. However we need to discuss (Az)PbI<sub>3</sub> compound first.

A similar phase transition mechanism is present involving the conformations of the Azepanium ring and the PbI<sub>3</sub><sup>-</sup> wires in the case of the (PD)PbI<sub>3</sub> compound. However the nitrogen atom does not exhibit disorder in the higher temperature phases. Phase I and II also pack in the space group C222<sub>1</sub> as for the respective phases of (PD)PbI<sub>3</sub>. Similarly a twofold rotation axis passes through the centre of the azepanium cation with the nitrogen atom lying on the twofold rotation axis which also passes through the centre of the molecule and the C1-C1' bond. The conformations of the cation through the phases may be seen in figure 5.1.6 where they proceed from the high temperature bent transition state, to the twist transition state, the disordered twist chair and twist boat conformation, and finally to the twist chair conformation in phase IV. Phase III and IV of (Az)PbI<sub>3</sub> are similar to the respective phases in (PD)PbI<sub>3</sub>, regarding the inorganic distortions which arise in the Pb-I bond lengths and I-Pb-I bond angles. The symmetrical hydrogen bonding between the adjacent wires seen in phase I and II (N1-H1C/D...I1/I1' 3.03 Å and N1-H1C/D...I1/I1' 3.01 Å for phase I and II respectively) is a result of the nitrogen atoms central position between the two adjacent wires and the N1 atom resting on a twofold rotation axis. The N-H...I interactions are to the bottom of the concave face in both phases. In phase III, the nitrogen becomes disordered over two positions, however maintains the hydrogen bonding interaction between the adjacent wires. Each respective nitrogen hydrogen bonds to both the top and bottom of each concave face, however the N1A and N1B hydrogen bonding interactions are no longer equivalent (N1A-H1E...I3 2.98 Å, N1A-H1F...I2 2.82 Å; N1B-H1G...I3 3.01 Å, N1B-H1H...I1 2.76 Å). In phase IV the hydrogen bonding motif alters significantly. There is a large decrease in symmetry, where three full azepanium cations are present in the asymmetric unit.

Two different hydrogen bonding motifs arise in this phase. Firstly the N1 hydrogen bonds to adjacent wires, i.e. to the top and bottom of one concave face (N1-H1D...I2, I3), and the bottom of the other (N1-H1C...I6). And secondly the N2 and N3 atoms only hydrogen bond on one face of one wire, where the H-bond forms to the bottom and the edge of the face respectively. The Pb2-I2 (N1-H1D...I2 2.8 Å) and the Pb3-I9 (N2-H2C...I9 2.91 Å) bond distances are distorted to 3.452(1) Å and 3.454(1) Å respectively, and the trans axial compression experienced are 3.103(1) Å and 3.132(1) Å respectively. It should be noted that the Pb-I bond distances in all the phases of compound **1-3** with the exception of phase IV of compound **2** and phase IV and III of **3**, display Pb-I bond lengths within 3.2  $\pm$  0.06 Å range (table 5.1.4). In addition the I-Pb-I trans angles of the octahedra are only idealized in phase III of compound **1**, however the distortion experienced in the other phases are all > 177° with the exceptions of phase IV and III of **2** and **3** respectively.

**Table 5.1.3:** Summary of the ranges of inorganic bond angles and bond lengths experienced in each compound.

Compound	1 III	1 II	2 IV	2 III	2 II	2 I	3 IV	3 III	3 II	3 I
<b>Pb-I (Å)</b>	3.2161 (4) - 3.2407 (4)	3.244 (2)	3.045 (2) - 3.507(2)	3.154 (3) - 3.299 (3)	3.197 (2) - 3.258 (2)	3.214 (4) - 3.2442 (7)	3.0991 (12) - 3.3914 (12)	3.1555 (13) - 3.3329 (11)	3.186 (4) - 3.256 (4)	3.198 (3) - 3.2522 (5)
<b>I-Pb-I (°)</b>	83.026 (11) - 96.974 (11)	84.85 (5) - 96.62 (9)	81.21 (5) - 97.06 (5)	84.25 (5) - 98.05 (6)	82.70 (4) - 96.22 (5)	83.21 (6) - 96.87 (6)	82.99 (3) - 104.10 (3)	81.98 (3) - 101.24 (4)	82.06 (7) - 97.76 (8)	82.43 (4) - 97.58 (5)
<b>I<sub>eq</sub>-Pb-I<sub>eq</sub> (°)</b>	180	177.74 (12) - 180	167.66(6) - 177.44 (5)	176.82 (12) - 179.96 (8)	178.43 (9) - 179.84 (8)	179.35 (14) - 179.89 (10)	170.50 (3) - 178.20 (4)	174.89 (3) - 176.49 (4)	178.85 (19) - 179.74 (9)	178.98 (12) - 179.99 (7)
<b>Pb-I-Pb (°)</b>	77.199 (11) - 77.897 (11)	76.98 (6) - 77.67 (6)	77.31(5) - 80.07 (4)	78.56 (4) - 78.94 (3)	78.02 (2) - 78.434 (18)	77.652 (19) - 78.195 (12)	77.39(3) - 79.97 (3)	78.58 (2) - 79.47 (3)	78.29 (2) - 79.23 (2)	79.007 (13) - 78.130 (16)
<b>Inter wire spacing I...I (Å)</b>	4.5446(7)	4.629(8)	4.404(3)	4.274(2)	4.249(1)	4.2690(8)	4.654(2)	4.283(2)	4.300(1)	4.3330(8)

Therefore as the C6 and C7 ring types of **2** and **3** obtain their ideal conformation upon cooling, a general decrease in crystal symmetry occurs. In phase I and II of both (PD)PbI<sub>3</sub> and (Az)PbI<sub>3</sub> the rings are symmetrically hydrogen bonded between adjacent wires. This in turn sees regularized Pb-I bond distances. In phase III of (Az)PbI<sub>3</sub> the disordered cation still maintains an adjacent hydrogen bonding interaction between the wires, however the hydrogen bonding interactions are no longer equivalent, and Pb-I bond distance deviations begin to arise. In phase IV of both (PD)PbI<sub>3</sub> and (Az)PbI<sub>3</sub> the hydrogen bonding interactions now lack the symmetry of the hydrogen bonding interactions of phase I and II, and form unsymmetrical hydrogen bonding interactions with the wires. This results in the greatest Pb-I bond distance and I-Pb-I bond angle distortions.

### 5.1.6 Structures of (Pyr)PbI<sub>3</sub>, [(n-But)<sub>4</sub>N]PbI<sub>3</sub> and [(Et)<sub>3</sub>NH]PbI<sub>3</sub>

As in the higher temperature phases of (PD)PbI<sub>3</sub> and (Az)PbI<sub>3</sub> the rigid pyridinium cation displays a disordered nitrogen atom due the mirror plane which passes through the centre of the N1/C1-N1'/C1' and C3-C3' bonds of the pyridinium cation. This also creates a symmetrical disordered hydrogen bonding interaction as found in compounds **2** and **3**. Small Pb-I bond length elongations occur where the N1-H1...I3 (3.14 Å) H-bond interaction occurs, where the Pb-I bond lengths range 3.2090 (6) Å – 3.2637 (6)Å. The rigidity of the template does create a thermally stable structure, as no phase transitions are observed in the 100-443K range (figure 5.1.3).

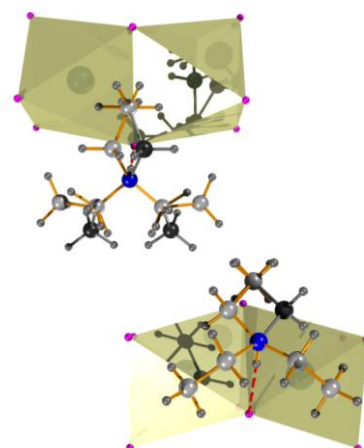


**Figure 5.1.8:** Disorder of [(Et)<sub>3</sub>NH]PbI<sub>3</sub> shown in black

The compound [(Et)<sub>3</sub>NH]PbI<sub>3</sub> also does not display any phase transitions in the 100-443K temperature range despite the flexible ethyl arms. However the template itself is disordered. With two templates in the asymmetric unit, both nitrogen atoms reside on a mirror plane which passes through the N1-C2 and N2-C6 atoms respectively. Therefore the CH<sub>2</sub> atoms of C1 and C5 are disordered through the mirror plane (fixed site occupancy factor of 50%) (figure 5.1.8). The ethyl arm of C7 and C8 (N2) generate the final ethyl arm through the mirror plane. However the C3 C4A/B ethyl arm (N1) is further disordered in the C4A/B methyl (refined site occupancy of C4A 62%) which disorders over two positions. The mirror plane translates this disorder to the final ethyl arm. The methyl disorder is not visible at room temperature.

Compound **5** [(n-But)<sub>4</sub>N]PbI<sub>3</sub> is the only compound in this series to have no clearly identifiable hydrogen bonding interactions. The crystal is stabilized only through the ionic interaction between the negatively charged wires, and the positively charge quaternary ammonium cation. The flexible butyl arms of the cation make the compound susceptible to phase transitions. In this respect, a decrease in symmetry was observed in the low temperature structure, where phase III's tetragonal space group was found to be *I*-4 and the room temperature phase II's space group was determined to be *I*-4<sub>2</sub>*d*. In phase II the nitrogen cation sits on a special position, where only two of the four butyl arms are in the asymmetric unit. The atoms C1-C2-C3-C4, exist in the all trans conformation where C5-C6-C7-C8 displays a gauche kink of 58(3)°. The symmetry of the crystal dictates the trans butyl arms to be in identical conformations. In addition the gauche kink creates enough space for a solvent molecule to reside between the adjacent cations, with a void volume of (87.6 Å<sup>3</sup>) (Spek A. L, 2009). Upon cooling, the phase transition



results in the conformations of the butyl arm to alter, where two of the butyl arms trans to each other C1-C2-C3-C4 and C9-C10-C11-C12 respectively, remain with the all trans conformation as in phase II. However C5-C6-C7-C8 torsion angle becomes  $157(1)^\circ$  and C13-C14-C15-C16 remains close to phase II's torsion angle of  $61(1)^\circ$ . The change in the torsion angle of C5-C6-C7-C8 results in the butyl arm to extent into the void between the cations, and hence the void volume now decreases to  $72.2 \text{ \AA}^3$  as seen in figure 5.1.9. The inorganic bond lengths and angles remained reasonably similar between the two phases, only the inter-wire spacing decreased from  $8.043(1)$  to  $7.7804(6) \text{ \AA}$  from phase II to III respectively.

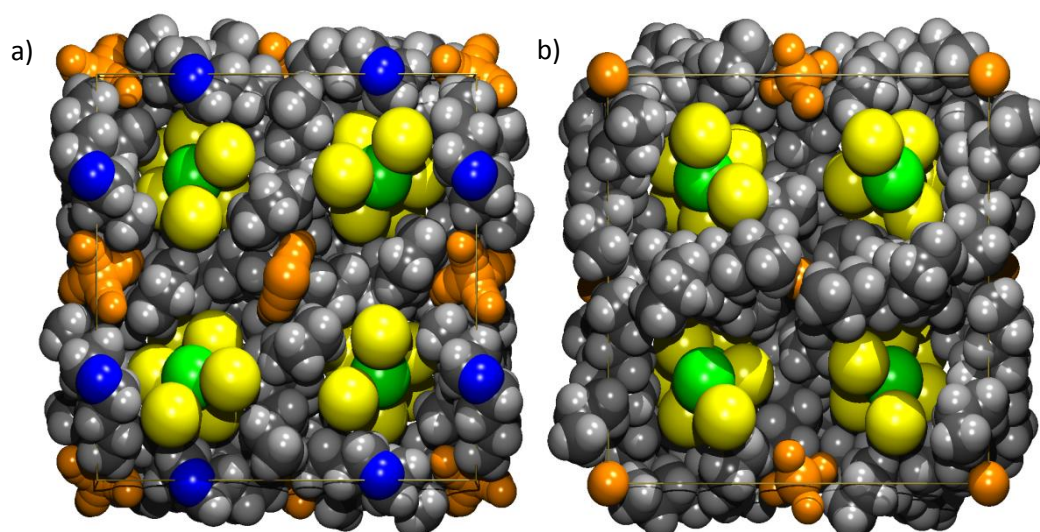


**Figure 5.1.9:** The space filling view of Phase II (a) void shown in orange, which decreases in volume in phase III (b) as the C5-C6-C7-C8 torsion angle changes.

**Table 5.1.4:** Summary of inorganic bond angles and bond length ranges experienced in each compound.

Compound	4 I 173K	4 I 293K	5 III	5 II	6 I 173K	6 I 293K
Pb-I ( $\text{\AA}$ )	3.2090 (6) - 3.2637 (6)	3.2204 (5) - 3.2663 (5)	3.2222 (6) - 3.3092 (6)	3.2294 (10) - 3.2757 (10)	3.2077 (10) - 3.2577 (10)	3.2167 (10) - 3.2647 (10)
I-Pb-I ( $^\circ$ )	84.471 (16) - 95.529 (16)	84.279 (14) - 95.721 (14)	82.298 (17) - 97.122 (11)	81.69 (2) - 98.83 (4)	83.88 (3) - 95.60 (3)	83.47 (3) - 95.59 (3)
$I_{eq}$ -Pb- $I_{eq}$ ( $^\circ$ )	180	180	178.85 (2) - 179.75 (2)	179.22 (3) - 179.86 (2)	177.12 (3) - 179.05 (3)	177.03 (3) - 179.15 (2)
Pb-I-Pb ( $^\circ$ )	76.472 (16) - 78.019 (17)	76.706 (14) - 78.006 (15)	79.174 (8) - 80.824 (10)	79.64 (3) - 80.263 (18)	75.05 (3) - 78.80 (3)	75.56 (3) - 79.01 (3)
Inter wire spacing I...I ( $\text{\AA}$ )	4.239(1)	4.324(1)	7.7804(6)	8.043(1)	5.011(2)	5.111(2)

### 5.1.7 Structural conclusions

The lead iodide octahedral wires are largely stable with respect to the distortions of bond angles and bond lengths caused from phase transitions. The relative stability of the wires regardless of the presence of hydrogen bonding further supports their independence and stability. As the wires are formed from the use of either secondary, tertiary or quaternary amines in this study,



the hydrogen bonding that does occur, is highly symmetrical, with the wires themselves supporting disordered nitrogen atoms to form this type of interaction. However when the symmetry of the hydrogen bonding does decrease and the hydrogen bonding interactions are no longer equivalent, mainly Pb-I bond length elongations and compressions are observed. In addition the conformations of the heterocyclic rings through the phase transitions are strongly correlated with the relative energies of the isolated conformers themselves, i.e. they observe the predicted energetically favoured conformations through the phases.

**Table 5.1.5:** Hydrogen bonding tables of compounds **1-4**, and **6**.

<i>D</i> —H... <i>A</i>	<i>D</i> —H (Å)	H... <i>A</i> (Å)	<i>D</i> ... <i>A</i> (Å)	<i>D</i> —H... <i>A</i> (°)
<b>1 III</b>				
N1—H1A...I2 <sup>i</sup>	0.92	2.77	3.660 (8)	163.4
N1—H1B...I3	0.92	2.74	3.572 (8)	150.6
<b>1 II</b>				
N1—H1A...I3 <sup>ii</sup>	0.90	2.81	3.44 (4)	128.4
N1—H1B...I1 <sup>iii</sup>	0.90	3.16	3.99 (4)	153.9
<b>2 IV</b>				
N1—H1A...I2 <sup>iv</sup>	0.90	3.15	3.85 (2)	136.2
N1—H1A...I3 <sup>v</sup>	0.90	3.25	3.89 (3)	130.3
N1—H1A...I1 <sup>iv</sup>	0.90	3.28	3.80 (3)	119.7
N1—H1B...I2 <sup>vi</sup>	0.90	3.11	3.85 (2)	140.8
N1—H1B...I3 <sup>vii</sup>	0.90	3.23	3.92 (3)	135.1
N2—H2C...I4 <sup>viii</sup>	0.90	3.12	3.74 (2)	128.4
N2—H2C...I5 <sup>ix</sup>	0.90	3.27	3.87 (2)	126.7
N2—H2D...I6 <sup>ix</sup>	0.90	2.87	3.71 (3)	156.0
<b>2 III</b>				
N1—H1B...I2 <sup>x</sup>	0.9	3.17	4.0596 (3)	169.2
<b>2 II</b>				
N1—H1A...I1 <sup>xi</sup>	0.9	3.2	3.9096 (9)	137.1
N1—H1B...I1 <sup>x</sup>	0.9	3.31	3.9693 (10)	131.7
<b>2 I</b>				
N1—H1A...I2 <sup>xii</sup>	0.970	3.233	4.0007 (10)	137.39
N1—H1A...I2 <sup>xiii</sup>	0.970	3.408	4.038 (4)	124.58
N1—H1B...I2 <sup>x</sup>	0.970	3.296	4.100 (4)	141.53
N1—H1B...I2 <sup>xiv</sup>	0.970	3.436	4.0900 (12)	126.65
<b>3 IV</b>				
N1—H1C...I6 <sup>i</sup>	0.92	2.96	3.765 (16)	146.9
N1—H1D...I2	0.92	2.8	3.649 (16)	154.1
N1—H1D...I3	0.92	3.25	3.693 (14)	111.7

N2—H2C...I9 <sup>xv</sup>	0.92	2.91	3.733 (14)	150.2
N2—H2D...I7 <sup>xv</sup>	0.92	2.88	3.663 (13)	143.8
N3—H3C...I4 <sup>xvi</sup>	0.92	2.84	3.703 (14)	157.1
N3—H3D...I1 <sup>xvii</sup>	0.92	2.8	3.531 (13)	137.6
<b>3 III</b>				
N1B—H1G...I3	0.91	3.01	3.82 (3)	148.6
N1B—H1H...I1 <sup>xxiii</sup>	0.91	2.76	3.48 (3)	136.5
N1A—H1E...I3 <sup>xxiv</sup>	0.91	2.98	3.84 (4)	157.6
N1A—H1F...I2 <sup>xxiv</sup>	0.91	2.82	3.55 (4)	139
<b>3 II</b>				
N1—H1D...I1	0.9	3.01	3.821 (16)	151.4
N1—H1C...I1 <sup>xviii</sup>	0.9	3.01	3.821 (16)	151.4
<b>3 I</b>				
N1—H1D...I1 <sup>xi</sup>	0.9	3.03	3.855 (11)	153
N1—H1C...I1 <sup>xx</sup>	0.9	3.03	3.855 (11)	153
<b>4 I 173K</b>				
N1—H1...I3	0.88	3.14	3.8533 (4)	139.3
<b>4 I 293K</b>				
N1—H1...I2 <sup>xxi</sup>	0.86	3.18	3.8825 (4)	139.9
<b>6 I 173K</b>				
N1—H1...I5 <sup>xvii</sup>	0.93	2.74	3.666 (19)	175.5
N2—H2...I1 <sup>xxii</sup>	0.93	3.14	4.05 (3)	167
<b>6 I 293K</b>				
N1—H1...I5 <sup>xv</sup>	0.91	2.72	3.627 (18)	177.8
N2—H2...I4 <sup>xv</sup>	0.91	3.05	3.96 (4)	179.5

---

Symmetry code(s): (i)  $-x+1, -y, -z$ ; (ii)  $x-y, x-1, -z+2$ ; (iii)  $-x+y, -x, z$ ; (iv)  $x, y+1, z-1$ ; (v)  $-x+1, y+1/2, -z+1/2$ ; (vi)  $-x+1, -y+1, -z+1$ ; (vii)  $x, -y+3/2, z-1/2$ ; (viii)  $-x+2, -y+1, -z+2$ ; (ix)  $x, y-1, z$ ; (x)  $x-1/2, y-1/2, z$ ; (xi)  $-x+5/2, y-1/2, -z+1/2$ ; (xii)  $-x+1/2, -y+3/2, z+1/2$ ; (xiii)  $-x+1/2, y-1/2, -z-1/2$ ; (xiv)  $x-1/2, -y+3/2, -z$ ; (xv)  $x, y+1, z$ ; (xvi)  $x-1, y+1, z$ ; (xvii)  $x-1, y, z$ ; (xviii)  $-x+1, y, -z+1/2$ ; (xix)  $x-1/2, y+1/2, z$ ; (xx)  $-x+1/2, y+1/2, -z+3/2$ ; (xxi)  $-x+1/2, -y, z-1/2$ ; (xxii)  $-x+3/2, -y+1, z+1/2$ ; (xxiii)  $-x+1, -y, -z+1$ ; (xxiv)  $x-1/2, -y+1/2, z-1/2$ .

### 5.1.8 Optical properties of compounds 1-6

#### Optical Absorption Experiments

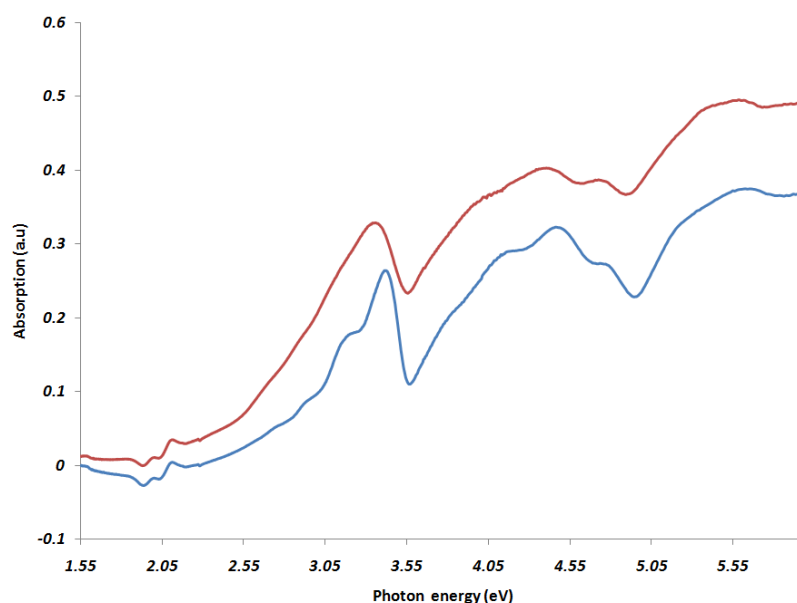


**Figure 5.1.10:** Optical absorption of (PD)PbI<sub>3</sub> at room temperature (red) and 77K (blue). The first excitation peak at 3.324 eV at room and displays a minor blue shift upon cooling to 3.397 eV at 77K. The remaining optical absorption of **1**, **5**, and **6**, may be found in appendix B.

For all of the compounds investigated the UV-Vis optical absorption experiments were collected at both room temperature and 77K, using a cold bath cryostat. The first exciton absorption of (PD)PbI<sub>3</sub> was readily seen at 3.324 eV at 77K in figure 5.1.10. From the absorption measurements, a substructure peak at 3.2 eV became apparent at 77K, which is not visible in the room temperature spectrum. The first exciton absorption band assignment is in good agreement with the previously reported value (Nagami A, *et al*, 1996; Fukumoto T, *et al*, 2000). In addition the substructure peak at 3.2 eV was also observed by (Nagami A, *et al*, 1996; Fukumoto T, *et al*, 2000) however was not assigned to a specific transition. Furthermore the peak does not appear to be a sample dependant phenomenon. Much stronger substructure peaks were observed in both the room temperature and 77K absorption spectra of (Az)PbI<sub>3</sub> and (Pyr)PbI<sub>3</sub>. The substructure absorption peak was observed at ~2.7 eV in both compounds and may be seen in figure 5.1.11. As the optical absorption of the pyridine  $\pi \rightarrow \pi^*$  transition is only observed at 4.59 eV, the peak of **4** cannot be ascribed as a direct transition from pyridine or the organic component in general. As this substructure peak is also present for **3** the peak cannot be due to a charge transfer interaction as the azepanium cation would be unable to accept any charge at such low energy from the wires as it is a saturated heterocyclic compound. Therefore

further investigations would need to be carried out in order to ascertain the origin of this absorption peak.

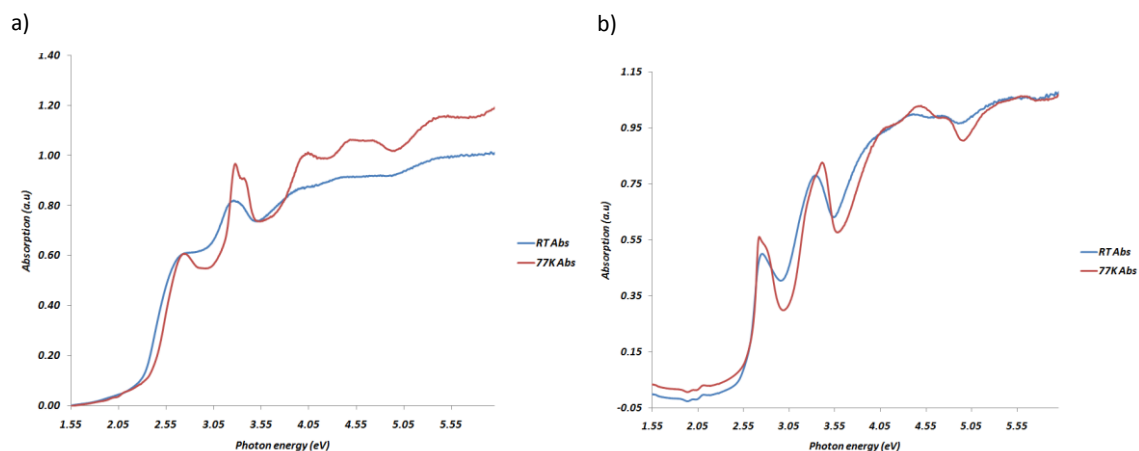


**Figure 5.1.11:** The optical absorption of (Az)PbI<sub>3</sub> (a) and (Pyr)PbI<sub>3</sub> (b), displaying the large substructure peak at 2.7 eV.

### Photoluminescence experiments

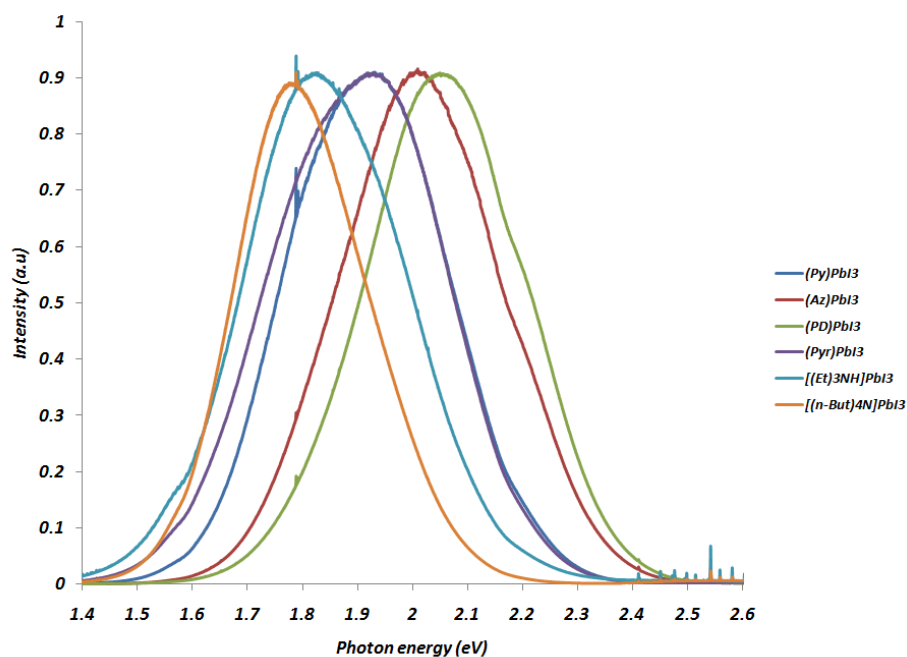


**Figure 5.1.12:** The photoluminescence emission from the self trapped exciton generated from the 1D photo-excited states of compounds 1-6.

The photoluminescence emission of (PD)PbI<sub>3</sub> was assigned as a self trapped exciton, as the large stokes shift (1.3 eV) and broad PL emission profile ( $\sim 0.3$  eV FWHM) supporting the assignment as a STE emission (Nagami A, *et al*, 1996; Fukumoto T, *et al*, 2000). The remaining compounds

emission profiles correlate with the assignments for (PD)PbI<sub>3</sub>, and are also assigned as STE emissions. The photoluminescence emission of compounds **1-6** may be seen in figure 5.1.12, where the PL emission energy varies quite considerably between the compounds which range from 1.730 – 2.075 eV. From a kinetics standpoint the PL decay time constants have been reported to be exponential, which further supports the assignment of the emissions as a STE rather than a Frenkel exciton. Furthermore the STE has been shown to exist in a triplet exciton state, which displays two different decay time constants in the recombination processes. The triplet excitation is separated into a single lower energy sub-band with slower time decay constant, and a doubly degenerate sub-band at a higher energy level with a faster decay time constant. At low temperatures (5K) the singlet state is the dominant emission, however as the temperature increases, phonon assisted transitions into the doubly degenerate sub-band with the faster decay time constant becomes dominant (Akimoto I, *et al*, 2004). In addition the STE luminescence intensity decreases by four orders of magnitude from 70K to 300K which gives evidence of a large exciton lattice coupling interaction. It has also been shown that the 1D compounds have large excitonic binding energies (360 meV) which should allow for strong room temperature emissions. The strong exciton lattice coupling was confirmed from investigations of (PD)PbI<sub>3</sub> under hydrostatic pressure, where the PL emission blue shifts with increasing pressure. The STE emission was also reported to display strong exciton lattice coupling even at ambient pressure. The hardening of the crystal due to the increasing pressure was shown to decrease the exciton lattice interaction, hence the blue shift in the emission observed (Fukumoto T, *et al*, 2000).

### **Structure to Property correlation**

Table 5.1.6 summarizes the important geometrical and optical aspects for compounds **1-6**. The structures of **1-6** have been investigated in the temperature range of 293 – 100K. The lowest temperature full crystal structure determination was obtained at 173K for all of the compounds. A reasonable assumption that no further structural phase transitions take place below 173K was made as the conformations of the compounds were in their lowest energy states, and was further supported through the lack of any observable unit cell changes between 173 – 100K (figure 5.1.3). Therefore the crystal structures obtained at 173K are used as a good approximation for the correlation of the geometrical parameters with the optical experiments completed at 77K. In this series investigated the 173K structures of (PD)PbI<sub>3</sub> and (Az)PbI<sub>3</sub>, displayed the largest inorganic structural distortions displayed in the Pb-I bond lengths and I<sub>eq</sub>-Pb-I<sub>eq</sub> bond angles. However only marginal shifts in the first exciton absorption energy's between room temperature and 77K are observed, where a blue shift of 73 meV and 60 meV,

for (PD)PbI<sub>3</sub> and (Az)PbI<sub>3</sub>, are observed between phase I and IV respectively. However negligible inorganic distortions occur in (Pyr)PbI<sub>3</sub> as no phase transitions occur upon cooling, and yet a blue shift of 91 meV was experienced between room temperature and 77K. Therefore the observed optical absorption shifts due to temperature cannot be assigned to the structural distortions observable in the wires. However the relative PL emission shifts of the compounds do appear to be quantifiable, as the STE emission has been shown to display changes with increasing pressure which was attributed to the exciton lattice coupling interaction (Fukumoto T, *et al*, 2000). A correlation of the inter-wire spacing, and the organic dielectric constant, against the STE emission was investigated as seen in figure 5.1.13.

**Table 5.1.6** The optical absorption and photoluminescence emissions summarized with the most important structural aspects of the compounds.

Compound	OA (eV)	PL (eV) (77K)	Inter Wire spacing (Å)	Organic Dielectric constant	Phase	Structure Temp (K)	Stokes Shift (eV)	Crystal density $\rho$ (g/cm <sup>3</sup> )
(Py)PbI <sub>3</sub>	3.054		4.629(8)	2.082	II	293		3.655
(Py)PbI <sub>3</sub>	3.123	1.931	4.5446(7)	2.082	III	173	1.192	3.748
(PD)PbI <sub>3</sub>	3.324		4.2690(8)	2.108	I	293		3.252
(PD)PbI <sub>3</sub>	3.397	2.075	4.404(3)	2.108	IV	173	1.322	3.613
(Az)PbI <sub>3</sub>	3.212		4.3330(8)	2.149	I	293		3.252
(Az)PbI <sub>3</sub>	3.271	2.030	4.654(2)	2.149	IV	173	1.241	3.41
(Pyr)PbI <sub>3</sub>	3.306		4.324(1)	2.277	I	293		3.689
(Pyr)PbI <sub>3</sub>	3.397	1.941	4.239(1)	2.277	I	173	1.456	3.788
[(n-But) <sub>4</sub> N]PbI <sub>3</sub>	3.271		8.043(1)	1.963'	II	293		2.177
[(n-But) <sub>4</sub> N]PbI <sub>3</sub>	3.351	1.843	7.7804(6)	1.963'	III	173	1.508	2.23
[(Et) <sub>3</sub> NH]PbI <sub>3</sub>	3.204		5.111(2)	1.960	I	293		3.018
[(Et) <sub>3</sub> NH]PbI <sub>3</sub>	3.237	1.730	5.011(2)	1.960	I	173	1.507	3.089

\*The optical absorption measurements were carried out at room temperature and 77K respectively. The low temperature structures (173K) were used and compared with the 77K OA and PL measurements. 5.1.4 Established no additional phases were present down to 100K. 'The dielectric constant was taken from (n-But)<sub>4</sub>NOH.

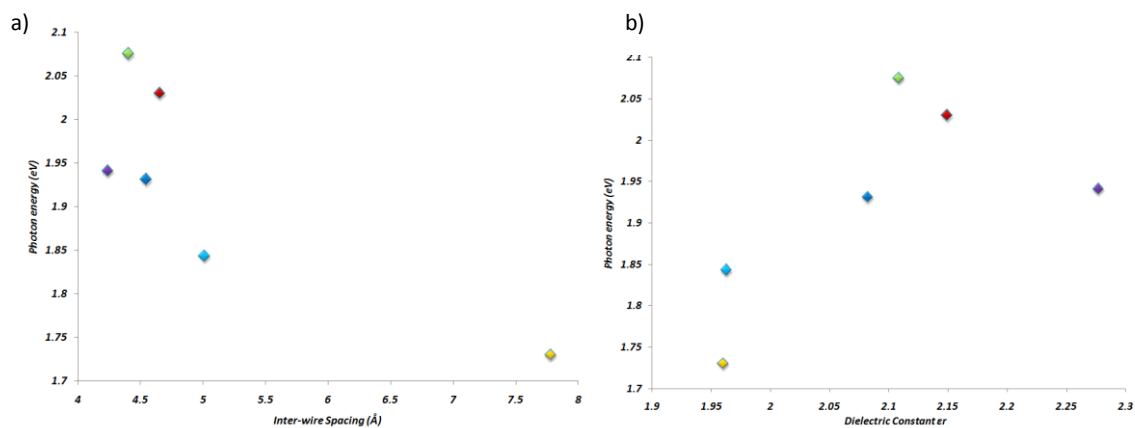


**Figure 5.1.13:** The photoluminescence emission against the inter-wire spacing defined by the closet I...I contact (a), and the organic dielectric constant against the photoluminescence emission (b). Orange [(n-But)<sub>4</sub>N]PbI<sub>3</sub>, Light Blue [(Et)<sub>3</sub>NH]PbI<sub>3</sub>, Blue (Py)PbI<sub>3</sub>, Purple (Pyr)PbI<sub>3</sub>, Red (Az)PbI<sub>3</sub>, Green (PD)PbI<sub>3</sub>.

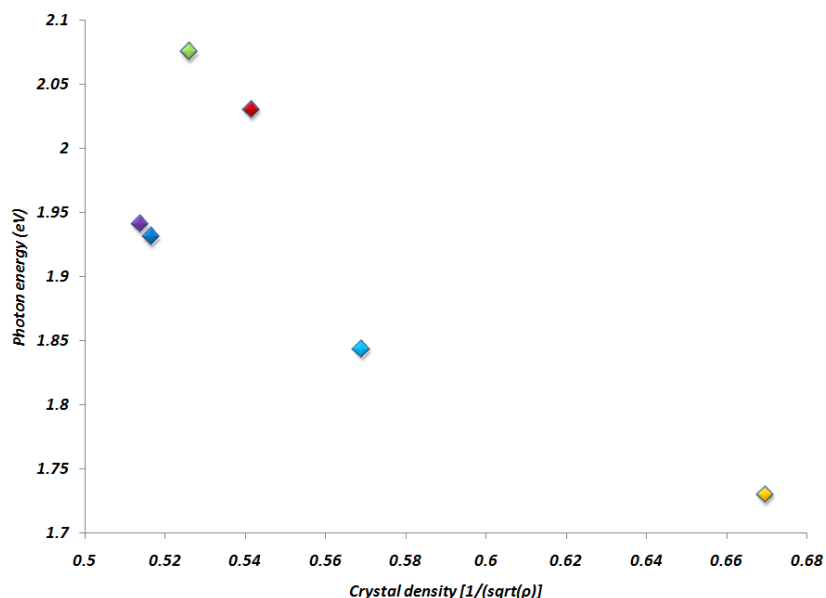


**Figure 5.1.14:** The STE emission against the crystal density. The decreasing crystal density increases exciton lattice interactions. This sees an associated red shift of the STE emission. Orange [(n-But)<sub>4</sub>N]PbI<sub>3</sub>, Light Blue [(Et)<sub>3</sub>NH]PbI<sub>3</sub>, Blue (Py)PbI<sub>3</sub>, Purple (Pyr)PbI<sub>3</sub>, Red (Az)PbI<sub>3</sub>, Green (PD)PbI<sub>3</sub>.

It was observed that as the inter-wire spacing increases as the STE emission energy generally decreases (red shifts). In addition the lowest dielectric constants of the cations which display the largest inter-wire spacing are directly related to the lowest energy STE emission. To correlate to some degree the “hardness” of the crystal, a plot of the crystal density against the STE emission also yielded an interesting correlation. We know that a direct correlation between the refractive index and the density of various materials are not directly related. However, as the heavy

elements are the same throughout the series, and simple organic cations have been used, the correlation may be used as a point of reference in this case. Furthermore the bulk and shear modulus of crystals are related to the density of a material for measurement of the pressure and shears wave through the crystal. Therefore the plot of the STE emission against  $\frac{1}{\sqrt{\rho}}$  was completed as seen figure 5.1.14. Again, the general trend observed supports the correlations of the same materials found in figure 5.1.13, which relates the STE emission which red shifts with decreasing crystal density. Therefore with some degree of certainty we may say that the STE emission is red shifted due to the increase in exciton-lattice interactions, which increase with increasing inter-wire spacing, decreasing organic dielectric constant, and decreasing crystal density. The experiments correlating exciton lattice coupling with increasing pressure (Fukumoto T, *et al*, 2000) indirectly supports the hypothesis of increasing crystal density decreasing exciton lattice coupling, as increasing pressure decreases the volume of the material, and therefore increases the materials density. In all three of the plots, (Az)PbI<sub>3</sub> and (PD)PbI<sub>3</sub> are to some degree outliers. The large phase transitions observed in **2** and **3** may impact the way in which the STE interacts with the lattice, however further investigations would be needed in order to ascertain the underlying reasons for this.

#### **5.1.9 Structure and optical property conclusions**

Unlike the corner-shared perovskite type 1D wires of [NH<sub>2</sub>C(I)=NH<sub>2</sub>]<sub>3</sub>PbI<sub>5</sub> and [CH<sub>3</sub>SC(=NH<sub>2</sub>)NH<sub>2</sub>]<sub>3</sub>PbI<sub>5</sub> the first exciton absorption of the octahedral face sharing wires of (A)PbI<sub>3</sub> appear to be largely insensitive to the inorganic structural distortions experienced as a result of the low temperature phase transitions. However links between the STE luminescence emissions the inter-wire spacing, organic dielectric constant, and the density of the crystal, have been shown to influence the exciton lattice interactions. The exciton lattice interactions are increased from a decrease in crystal density, organic dielectric constant, and an associated increase in the inter-wire spacing. Therefore as the exciton lattice interactions increase, a red shift in the STE emission will be observed.



## **5.2 The structures and phases of the solvated 1D xDMF.(A)PbI<sub>3</sub> compounds, where distortions of the periodicity of the wire generates an alternative PL emission pathway.**

### **5.2.1 Introduction**

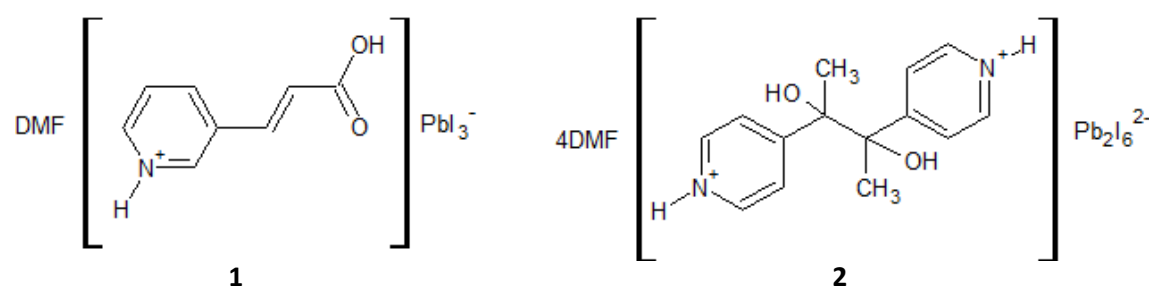
As established in the previous section (5.1), the distortions experienced in the face sharing octahedral wires of (A)PbI<sub>3</sub> relating to the Pb-I bond lengths and I<sub>eq</sub>-Pb-I<sub>eq</sub> bond angles, display almost no correlation to the shifts observed in the optical properties of the compound. The predominant effects on the PL shifts experienced in the STE emissions were however related to fluctuations in exciton lattice interactions. This was primarily due to the variations caused from the organic dielectric constant, crystal density, and inter-wire spacing.

Variations in the inorganic motif types (0D clusters, 1D ribbons/sheets, 2D nets) may occur when more complex organic templates are utilized in addition to multi-solvent crystallization techniques (Mercier N, *et al*, 2009 and references cited therein). However if an excess of the halide acid is used during the synthesis, even the complex organic cations produce single chain face sharing octahedral wires, where solvent inclusion into the lattice adds the remaining stabilization required for the crystal to pack in this motif type (Krautschild H, *et al*, 1996; 1997; 1998; 1999; 2000; 2001; Guloy A. M, *et al*, 2001). Due to the low solubility of the reaction mixtures of 1D compounds dimethyl formamide (DMF) and dimethyl sulphoxide (DMSO) are the common solvents for producing the low order dimensional inorganic motifs where these solvents are often incorporated into the lattice of the compound. Therefore the predictability of producing the face sharing octahedral wires has led to the use of the more complex organic templates for the added templating effect the 1D wires have on the hyperpolarizability of non-linear optically susceptible organic compounds for (SHG) (Guloy A. M, *et al*, 2001; Giffard M, *et al*, 2005; Papavassiliou G. C, *et al*, 1999; 1999b; 2001; 2003; Goto T, *et al*, 2002) ferroelectric behavior of polar chiral 1D compounds due to the optical anisotropy the wires provide within the crystal (Zhao H, R, *et al*, 2010) and organic molecules with metallic conductivity have also been incorporated into a face sharing octahedral wire systems of lead iodide, in order to further improve the conductivity of the template by promoting  $\pi - \pi$  interactions between adjacent organic molecules (Devic T, *et al*, 2004). Moreover charge transfer effects between the wires and spacers have also been investigated (Tang Z and Guloy A. M, 1999; Fujisawa J and Ishihara T, 2004; Fujisawa J, *et al*, 2007; Pradeesh K, *et al*, 2010), for improved carrier mobility along the wires (Fujisawa J and Tajima N, 2005). Transition metal complexes have also been incorporated into 1D lead iodide wire systems in order to further investigate the magnetic properties of the crystals (Zhang Z. J, *et al*, 2006b). Recently various functionalized pyridine based templates have

also been employed in order to create coordinated templates to lead and still create 1D wires. Investigations of the optical and electronic properties showed the coordinated wires displayed reduced and indirect band gaps (Li H. H, *et al*, 2010; Zhu H. G, 1999).

Most of these systems have used the inorganic wires as templates to preferentially arrange the organic molecules to induce a desired property. Herein we wished to investigate functionalized pyridine based templates with increased hydrogen bonding donor sites in order to study their influence on the electronic and physiochemical properties. Both templates produced face sharing octahedral wires in which the additional hydrogen bond donors created further stabilizations for solvent inclusion into the crystal. However, we also encountered a low temperature phase transition which gives rise to a new photoluminescence emission peak, which will also be briefly described here.

### 5.2.2 Results and discussion



**Scheme 5.2.1:** The chemical diagrams of the crystal structures of **1** and **2** respectively.

**Table 5.2.1:** The crystal structure data of the compound **1** and **2** completed at various temperatures. Experiments were carried out with Mo Ka radiation. H-atom parameters were constrained.

	1_I_293K	1_I_173K	1_II_100K	1_II_30K	2_I_293K
Crystal data					
Chemical formula	'C <sub>14</sub> H <sub>18</sub> N <sub>2</sub> O <sub>2</sub> ·2(I <sub>3</sub> Pb)·4(C <sub>3</sub> H <sub>7</sub> NO)'	C <sub>14</sub> H <sub>18</sub> N <sub>2</sub> O <sub>2</sub> ·2(I <sub>3</sub> Pb)·4(C <sub>3</sub> H <sub>7</sub> NO)	C <sub>14</sub> H <sub>18</sub> N <sub>2</sub> O <sub>2</sub> ·I <sub>6</sub> Pb <sub>2</sub> ·4(C <sub>3</sub> H <sub>7</sub> NO)	C <sub>14</sub> H <sub>18</sub> N <sub>2</sub> O <sub>2</sub> ·I <sub>6</sub> Pb <sub>2</sub> ·4(C <sub>3</sub> H <sub>7</sub> NO)	C <sub>8</sub> H <sub>8</sub> NO <sub>2</sub> ·I <sub>3</sub> Pb·C <sub>3</sub> H <sub>7</sub> NO
<i>M<sub>r</sub></i>	1714.47	1714.47	1714.47	1714.47	811.14
Crystal system, space group	Triclinic, <i>P</i> <sup>-</sup> 1	Triclinic, <i>P</i> <sup>-</sup> 1	Triclinic, <i>P</i> <sup>-</sup> 1	Triclinic, <i>P</i> <sup>-</sup> 1	Monoclinic, <i>P</i> 2 <sub>1</sub> / <i>c</i>
Temperature (K)	291	173	100	30	293
<i>a</i> , <i>b</i> , <i>c</i> (Å)	7.9012 (4), 12.5473 (5), 13.5221 (6)	7.8741 (2), 12.5100 (2), 13.2024 (3)	12.9494 (14), 13.0905 (14), 15.6888 (17)	12.9441 (17), 13.0454 (16), 15.676 (2)	8.6325 (11), 29.845 (4), 8.0038 (12)
<i>α</i> , <i>β</i> , <i>γ</i> (°)	68.929 (2), 82.261 (2), 74.381 (2)	69.273 (1), 82.358 (1), 75.037 (1)	97.621 (2), 111.250 (2), 104.991 (2)	97.904 (4), 111.339 (4), 104.669 (4)	90, 98.108 (5), 90
<i>V</i> (Å <sup>3</sup> )	1203.67 (9)	1173.84 (4)	2317.4 (4)	2306.4 (5)	2041.5 (5)
<i>Z</i>	1	1	2	2	4
<i>μ</i> (mm <sup>-1</sup> )	10.87	11.15	11.29	11.34	12.81
Crystal	0.35 × 0.23 × 0.08	0.60 × 0.17 × 0.13	0.34 × 0.08 × 0.04	0.25 × 0.10 × 0.10	0.32 × 0.07 × 0.05

size (mm)					
Data collection					
Diffraction eter	Bruker <i>APEX</i> -II CCD diffractometer	Bruker <i>APEX</i> -II CCD diffractometer	'CCD area detector 3- circle diffractometer'	'CCD area detector 3- circle diffractometer'	Bruker <i>APEX</i> -II CCD diffractometer
Absorption correction	Integration <i>Bruker XPREP</i> (Bruker, 2005)	Multi-scan Absorption corrections were done using <i>SADABS</i> as incorporated in the <i>Apex2</i> software (Bruker, 2005)	Integration <i>SADABS2008/1</i> - Bruker AXS area detector scaling and absorption correction	Multi-scan <i>SADABS</i> - Bruker Nonius area detector scaling and absorption correction - V2.10	Integration <i>Bruker XPREP</i> (Bruker, 2005)
$T_{\min}, T_{\max}$	0.072, 0.434	0.246, 0.746	0.107, 0.644	0.407, 1.000	0.170, 0.779
No. of measured, independent and observed [ $I$ $> 2\sigma(I)$ ] reflections	27361, 5812, 4589	23420, 5112, 4553	50204, 13009, 10278	18505, 8801, 7623	21343, 4947, 2218
$R_{\text{int}}$	0.030	0.036	0.046	0.035	0.106
Refinement					
$R[F^2 > 2\sigma(F^2)]$ , $wR(F^2)$ , $S$	0.023, 0.057, 1.02	0.026, 0.064, 1.07	0.030, 0.054, 1.02	0.033, 0.085, 1.06	0.054, 0.112, 0.99
No. of reflections	5812	5112	13009	8801	4947
No. of parameters	217	217	430	424	179
No. of restraints	0	0	0	0	28
	$w = 1/[\sigma^2(F_o^2) + (0.024P)^2 + 0.8831P]$ where $P = (F_o^2 + 2F_c^2)/3$	$w = 1/[\sigma^2(F_o^2) + (0.0217P)^2 + 3.9767P]$ where $P = (F_o^2 + 2F_c^2)/3$	$w = 1/[\sigma^2(F_o^2) + (0.0158P)^2 + 1.0765P]$ where $P = (F_o^2 + 2F_c^2)/3$	$w = 1/[\sigma^2(F_o^2) + (0.0342P)^2 + 4.8849P]$ where $P = (F_o^2 + 2F_c^2)/3$	$w = 1/[\sigma^2(F_o^2) + (0.0335P)^2]$ where $P = (F_o^2 + 2F_c^2)/3$
$\Delta_{\max}, \Delta_{\min}$ ( $e \text{ \AA}^{-3}$ )	0.80, -0.54	1.44, -1.67	0.93, -1.21	1.51, -1.83	1.51, -1.07

2_I_173K	
Crystal data	
Chemical formula	$\text{C}_8\text{H}_8\text{NO}_2 \cdot \text{I}_3\text{Pb} \cdot \text{C}_3\text{H}_7\text{NO}$
$M_r$	811.14
Crystal system, space group	Monoclinic, $P2_1/c$
Temperature (K)	173
$a, b, c$ ( $\text{\AA}$ )	8.5288 (2), 29.3961 (8), 7.9683 (2)
$\alpha, \beta, \gamma$ ( $^\circ$ )	90, 98.878 (2), 90
$V$ ( $\text{\AA}^3$ )	1973.83 (9)
$Z$	4
$\mu$ ( $\text{mm}^{-1}$ )	13.25
Crystal size (mm)	$0.31 \times 0.08 \times 0.04$
Data collection	
Diffractometer	Bruker <i>APEX</i> -II CCD diffractometer
Absorption correction	Integration <i>Bruker XPREP</i> (Bruker, 2005)
$T_{\min}, T_{\max}$	0.194, 0.770
No. of measured, independent and observed [ $I > 2\sigma(I)$ ]	20262, 4775, 2910

reflections	
$R_{\text{int}}$	0.082
Refinement	
$R[F^2 > 2\sigma(F^2)], wR(F^2), S$	0.044, 0.085, 1.01
No. of reflections	4775
No. of parameters	185
No. of restraints	46
	$w = 1/[\sigma^2(F_o^2) + (0.0242P)^2 + 4.3742P]$ where $P = (F_o^2 + 2F_c^2)/3$
$\Delta\rho_{\text{max}}, \Delta\rho_{\text{min}}$ (e Å <sup>-3</sup> )	1.49, -1.48

Computer programs: Bruker *APEX2*, *SMART* V5.049 (Bruker, 1999), Bruker *SAINT*, *SAINT* v6.45A (Bruker, 2003), *SHELXS97* (Sheldrick, 2008), *SHELXL97* (Sheldrick, 2008), *SHELXL97* (Sheldrick, 1997).

### 5.2.3 Photoluminescence and optical absorption

The multiple temperature single crystal structure determinations of the solvated 4.DMF.(2,3-di(pyridin-4-yl)butane-2,3-diol)Pb<sub>2</sub>I<sub>6</sub>, (DPBD)Pb<sub>2</sub>I<sub>6</sub> from here and DMF.(2(E)-3-(pyridine-3-yl)prop-2-enoic acid)PbI<sub>3</sub>, (EPPA)PbI<sub>3</sub> from here, were investigated at both room temperature and 173K (table 5.2.1). No phase transitions were observed in this temperature range as the structures were essentially the same for each compound. The low temperature (77K) photoluminescence emissions of (DPBD)PbI<sub>3</sub> however revealed an additional blue shifted Gaussian shaped emission (2.33eV; FWHM 0.353eV) next to the STE luminescence emission (1.90eV; FWHM 0.342eV) (figure 5.2.1). This prompted further structural investigations at 100K and 30K, as the PL emission at 123K displayed the expected STE emission (1.88eV; FWHM 0.357eV) with no additional peaks. Furthermore the relative intensities of the STE emission at 77K had decreased in intensity from the 123K spectra (experimental set up and laser power were the same for both temperatures). The curiosity as to whether the new emission was due to a structural distortion was indeed enough reason for further low temperature structural investigations.

The PL emission spectra of (EPPA)PbI<sub>3</sub> displayed the STE emission at (1.86eV; FWHM 0.287eV), however also displayed an additional weak blue shifted emission at 2.45eV. This peak is thought to be lattice defect related, as the (EPPA)PbI<sub>3</sub> crystals decomposed at room temperature (~30min) when not stored in the crystallization mother liquor. Therefore special precautions for both the PL and optical absorptions measurements were taken. After mounting the (EPPA)PbI<sub>3</sub> crystals into the low temperature LINKAM cryostat for PL measurements, the samples were cooled quickly to 77K to ensure the sample longevity. The optical absorption measurements

were completed in a custom built low temperature bath cryostat, which was kept under a moderate vacuum from a turbo molecular pump ( $10^{-5}$  torr). The samples were kept “wet” while mounting in order to ensure the longevity of the samples. In addition the room temperature spectra were obtained while the vacuum in the cryostat was pumping down. As DMF was included in the lattice the absorption spectra of the “wet” samples was thought to be accounted for. After the room temperature measurements were collected and the correct vacuum was obtained, the samples were cooled rapidly for measurement of the 77K spectra. As seen in figure 5.2.2, both samples display a substructure peak at ( $2.97\text{eV}$ ) and ( $3.04\text{eV}$ ) which is more resolved at 77K for (DPBD) $\text{Pb}_2\text{I}_6$  and (EPPA) $\text{PbI}_3$  respectively. Therefore the first exciton absorption peaks were assigned as ( $3.28\text{eV}$ ) and ( $3.24\text{eV}$ ) for (DPBD) $\text{Pb}_2\text{I}_6$  and (EPPA) $\text{PbI}_3$  respectively.

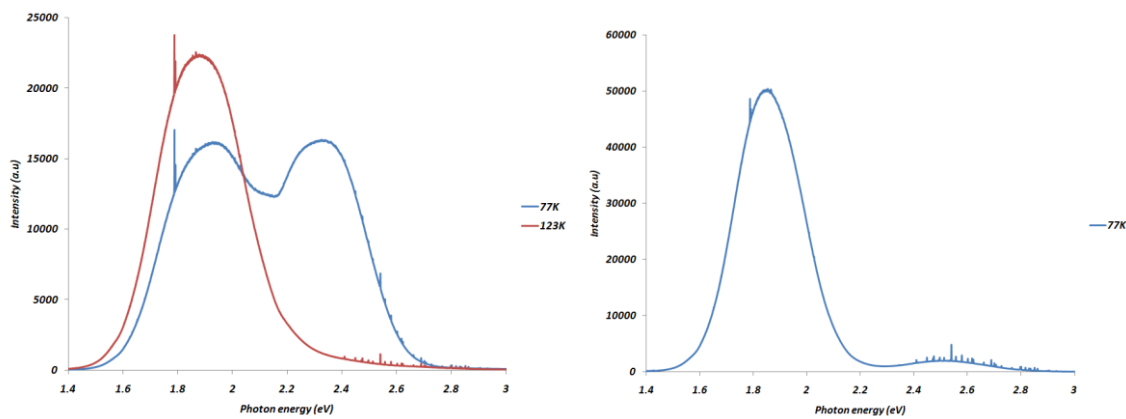


**Figure 5.2.1:** Photoluminescence spectra of (DPBD) $\text{Pb}_2\text{I}_6$  and (EPPA) $\text{PbI}_3$  displaying the STE luminescence at 123K and 77K respectively. However at 77K (DPBD) $\text{Pb}_2\text{I}_6$  displays and additional emission blue shifted to the STE emission. The excitation energy laser power were maintained at both 77K and 123K.

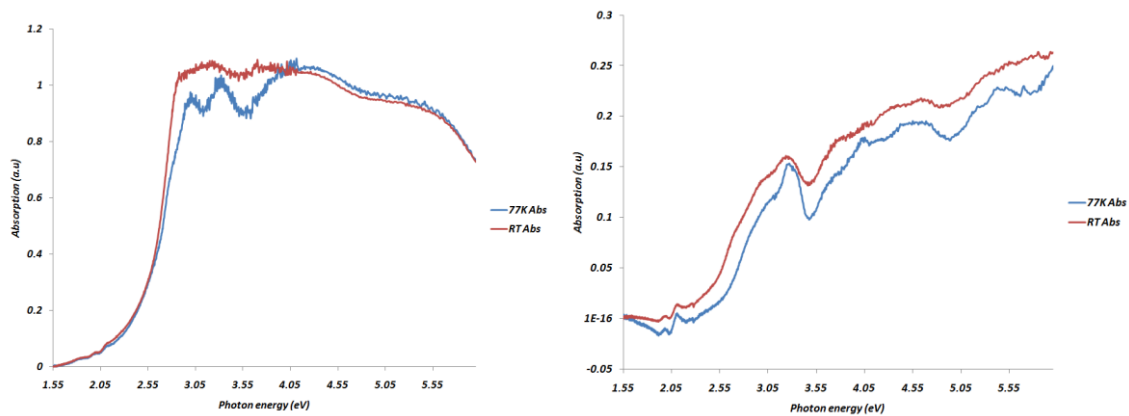


**Figure 5.2.2:** Optical absorption spectra of (DPBD) $\text{Pb}_2\text{I}_6$  and (EPPA) $\text{PbI}_3$  at both room temperature and 77K.

#### 5.2.4 The variable temperature structures of (DPBD)Pb<sub>2</sub>I<sub>6</sub> and (EPPA)PbI<sub>3</sub>

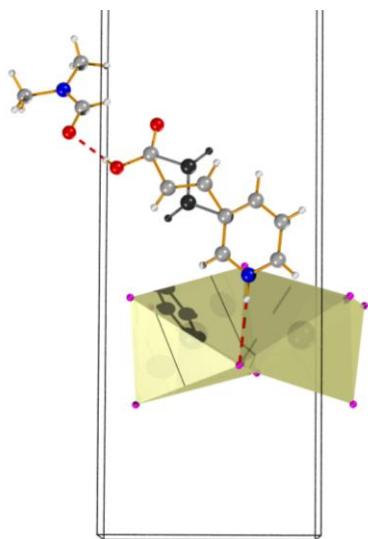


**Figure 5.2.3:** The hydrogen bonding and disorder (dark grey) of (EPPA)PbI<sub>3</sub> viewed along the (100) axis.

The structures of (DPBD)Pb<sub>2</sub>I<sub>6</sub> and (EPPA)PbI<sub>3</sub> both have additional hydrogen bond donors, however only (EPPA)PbI<sub>3</sub> hydrogen bonds to the lead iodide wires. The nitrogen is in the 3 position of the pyridine ring which forms a hydrogen bond to the bottom of the concave face generated between the adjacent face sharing octahedra, where the wires propagate along the (001) axis. In addition the N-H...I interaction is bifurcated to the same position of the adjacent wire (N1-H1A...I1 and N1-H1A...I3 (2.97 Å and 3.16 Å) respectively). This directly relates to the short inter-wire spacing observed (I...I 4.2046(9) Å). The inorganic bond lengths and angle ranges may be seen in table 5.2.2. The alcohol of the carboxylic acid group, additionally hydrogen bonds to the carbonyl of DMF (O2-H2A...O3 (1.81Å)), and hence a ratio of one solvent molecule per EPPA molecule are found in the crystal. The list of hydrogen bonding interactions may be found in table 5.2.3. Interestingly, despite the double bond of C6A/B-C7A/B, the atoms are disordered over two positions (shown in dark grey fig 5.2.3) where the final site occupancy factors were 0.492(18) for the A/B components. In addition, the delocalization of electrons through the carbonyl, double bond and the pyridine ring should result in the planarity of the (EPPA) molecule. However the O1-C8-C7B-C6B torsion angle of 164(2)° displays the deviation from planarity. This may be due to the strain induced by the O2-H2A...O3 hydrogen bond to DMF (figure 5.2.3).

Phase I (173K) and II (100K) of (DPBD)Pb<sub>2</sub>I<sub>6</sub> may be seen in figure 5.2.4. a) and b) respectively. The (DPBD) template has four hydrogen bond donors on the molecule. The nitrogen of the pyridine ring is on the 4 position unlike (EPPA)PbI<sub>3</sub>. The (DPBD) template therefore forms no hydrogen bonding interactions with the lead iodide wires. However does experience I...π interactions with the pyridine ring of N1...I1 and C1...I1 of 3.958(6) Å and 3.982(6) Å respectively (phase I). In addition the N1...I1 interaction should also be strongly columbic as the iodine's are negatively charged, and the nitrogen positively charged. As in (EPPA)PbI<sub>3</sub> the alcohol groups hydrogen bond with the carbonyls of the DMF solvent. However the nitrogen's also hydrogen bond to the carbonyls of the DMF solvent (table 5.2.3), and therefore four DMF solvent molecules are present for every one DPBD molecule. Upon cooling, the phase transition

results in the unit cell volume to double. The packing motif of the organic component remains almost identical, with the exception of the pyridine rings of molecule to no longer arrange parallel with one another, but are now tilted by  $10.601(2)^\circ$ . Additionally the  $N2...I2$  and  $C12...I2$  interactions contract to  $3.723(5)$  Å and  $3.890(5)$  Å respectively.

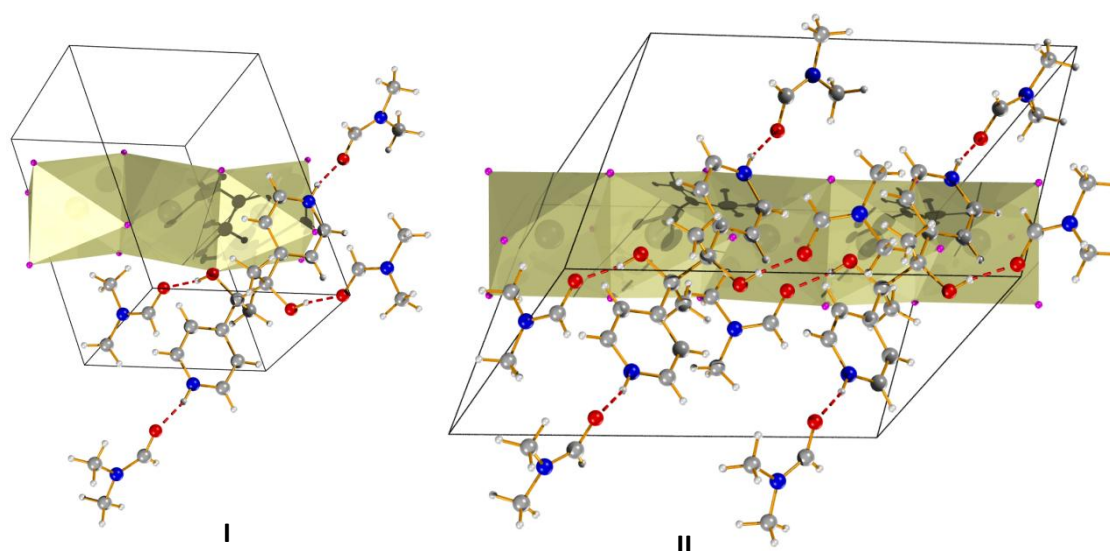


**Figure 5.2.4:** The packing motif of phase I and II of  $(DPBD)Pb_2I_6$  which shows the organic packing motif which remains the same in both phases, however the unit cell volume has doubled from phase I to II.

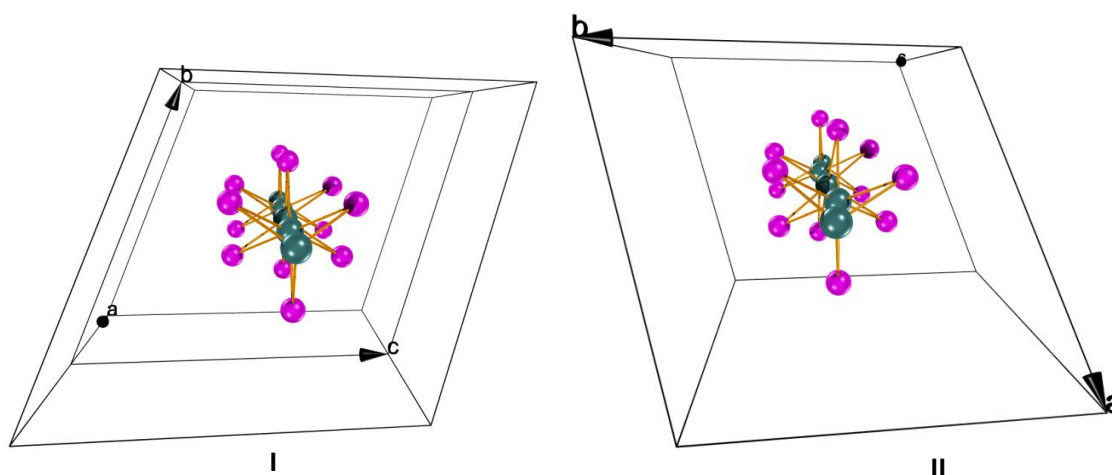


**Figure 5.2.5:** Phase I and II of  $(DPBD)Pb_2I_6$  the lead iodide wire viewed down the (100) direction in phase I, shows the regularity of the wire, in phase II the unit cell origin shifts, and the lead atoms now arrange in a wave like fashion in the (001) direction. This distortion has been attributed to the new PL emission at 77K.

Moreover, an increase in the inter-wire spacing is experienced, from  $7.5831(6)$  Å to  $8.728(1)$  Å, from phase I (173K) to phase II (100K). The Pb-I bond lengths, and I-Pb-I and Pb-I-Pb bond angles only marginally change between the phases (table 5.2.2). However the  $I_{eq}-Pb-I_{eq}$  angles distort significantly from  $180^\circ$  in phase II. As these distortions have been shown to display

a very minor impact on the optical properties (chapter 5.1), these distortions cannot be attributed to the new PL emission peak found at 77K. Interestingly, as seen in figure 5.2.5 where the wires are viewed along their respective axis, the lead centers all line up (collinear) in phase I however in phase II the lead centers appear like a wave propagating along the wire. This wave created the periodic discontinuity, and therefore resulted in the unit cell volume to double. Therefore we attribute the new blue shifted emission in the PL spectra to this distortion. As polarons are known to create lattice distortions as they move through the crystal lattice, we suspect this new emission to be due to polaron generation in the wires. However further luminescence decay kinetics experiments would need to be performed in order to confirm this.

### 5.2.5 Conclusions

For the first time in case of the face sharing lead halide 1D hybrids, we have found a direct structural influence of the inorganic wires and their impact on the PL emissions. It was noted that the distortions present along the wires is a result of the lead centers arranging like a wave propagating along the wire. We now know that this causes the blue shifted emission. Furthermore we assign the emission to be polaron in nature as polarons are able to create lattice distortions within a structure. However further investigations into the decay kinetics of the emission would need to be carried out to further establish the character of the particle. A large red shifted polaron emission (relative to the STE emission) was reported for (PD)PbBr<sub>3</sub> (Azuma J, *et al*, 2002a). Although no direct property to structure correlation was made, we suspect that the polaron emission found in this compound is due to the disordered wires found in the crystals (Azuma J, *et al*, 2002b).

**Table 5.2.2:** Summary of the inorganic bond lengths and bond angles.

Compound	1   293K	1   173K	1   100K	1   30K	2   293K	2   173K
<b>Pb-I (Å)</b>	3.2165 (3) - 3.2541 (3)	3.2056 (3) - 3.2439 (4)	3.1910(3) - 3.2699(4)	3.1869 (5) - 3.2672 (6)	3.1722 (12) - 3.2894 (12)	3.1544 (8) - 3.2821 (8)
<b>I-Pb-I (°)</b>	85.437 (9) - 94.563 (9)	85.721 (10) - 94.279 (10)	83.075 (11) - 96.925 (11)	82.791 (15) - 97.209 (15)	83.60 (3) - 96.61 (3)	83.734 (19) - 96.75 (2)
<b>I<sub>eq</sub>-Pb-I<sub>eq</sub> (°)</b>	180	180	174.500 (9) - 180	173.906 (14) - 180	176.47 (4) - 179.56 (3)	176.20 (3) - 179.49 (2)
<b>Pb-I-Pb (°)</b>	74.960 (8) - 75.580 (7)	74.98(1) - 75.55(1)	74.017 (10) - 75.684 (11)	74.007 (14) - 75.654 (15)	76.30 (2) - 76.62 (2)	75.947 (16) - 76.679 (16)
<b>Lead centres (°)</b>	180	180	173.48(1)-180	172.72(1)-180	179.61(2)	179.86(1)
<b>Inter wire spacing I...I (Å)</b>	7.6381(6)	7.5831(6)	8.728(1)	8.688(1)	4.276(1)	4.2046(9)



**Table 5.2.3:** Table of hydrogen bonding interactions of compounds **1** and **2** at various temperatures.

$D-H\cdots A$	$D-H$ (Å)	$H\cdots A$ (Å)	$D\cdots A$ (Å)	$D-H\cdots A$ (°)
1_I_293K				
$N1-H1\cdots O3^i$	0.86	1.87	2.707 (5)	164.4
$O1-H1B\cdots O2^i$	0.82	1.84	2.660 (5)	172.9
1_I_173K				
$N1-H1\cdots O3^{ii}$	0.88	1.83	2.694 (6)	165.6
$O1-H1B\cdots O2^{iii}$	0.84	1.82	2.654 (10)	171
1_II_100K				
$N1-H1\cdots O6$	0.88	1.81	2.673 (5)	164.5
$N2-H2A\cdots O3$	0.88	1.84	2.697 (5)	165.4
$O1-H1B\cdots O5$	0.84	1.83	2.654 (4)	167.3
$O2-H2B\cdots O4$	0.84	1.85	2.689 (4)	172
1_II_30K				
$N1-H1\cdots O6$	0.88	1.81	2.672 (8)	164
$N2-H2A\cdots O3$	0.88	1.83	2.691 (8)	163.8
$O1-H1B\cdots O5$	0.84	1.84	2.660 (7)	164.4
$O2-H2B\cdots O4$	0.84	1.86	2.690 (7)	171.7
2_I_293K				
$N1-H1A\cdots I1$	0.86	3	3.751 (13)	147.1
$N1-H1A\cdots I3^{iii}$	0.86	3.23	3.797 (13)	125.9
$O2-H2A\cdots O3^{iv}$	0.82	2	2.58 (2)	127.4
2_I_173K				
$N1-H1A\cdots I1$	0.86	2.97	3.716 (9)	146.7
$N1-H1A\cdots I3^{iii}$	0.86	3.16	3.732 (9)	126.2
$O2-H2A\cdots O3^{iv}$	0.82	1.81	2.549 (13)	148.6

Symmetry code(s): (i)  $x+1, y, z$ ; (ii)  $-x, -y+1, -z+1$ ; (iii)  $x-1, y, z$ ; (iv)  $-x+1, -y, -z$ ;

### **5.3 Structure and optical properties of thick chain 1D lead iodide wires, and the Charge transfer effects between the wires and spacers.**

#### **5.3.1 Introduction**

Complex organic templates have been incorporated into various 1D wire systems in order to enhance the property of the organic component, such as hyperpolarizability for nonlinear optics (Guloy A. M, *et al*, 2001; Papavassiliou G. C, *et al*, 1999; 1999b; 2001; 2003; Goto T, *et al*, 2002; Cariati E, *et al*, 2001), metallic conductivity (Devic T, *et al*, 2003; 2004) and ferroelectric behavior (Zhao H, R, *et al*, 2010). Charge transfer interactions between wires and spacers, and spacer-spacer interactions have also been investigated in order to understand the nature of the electronic transitions and electrical conductivity displayed in these 1D quantum wire systems (Tang Z and Guloy A. M, 1999; Fujisawa J and Ishihara T, 2004; Fujisawa J and Tajima N, 2005; Fujisawa J, *et al*, 2007; Pradeesh K, *et al*, 2010). Most of the fundamental investigations into the 1D organic inorganic CT hybrids have used Methyl viologen (MV) as the common di-cation due to its inherent electron accepting, and redox behavior (Tang Z and Guloy A. M, 1999). Historically the behavior of MV has led to extensive studies into its biological, electrochemical, photochemical, and conductive properties in various environments. Additionally, it is well known that methyl viologen undergoes a photo induced colour change which is due to the photocatalysed electron transfer from the counter ion (Cl, Br, I, etc) to the viologen dication (Xu G, *et al*, 2007). This colour change has mainly been shown in liquid crystal systems, with only one recent report of a 1D (MV)Bi<sub>2</sub>Cl<sub>8</sub> hybrid single crystal. The single crystal system displayed a photochromic phase transition under UV irradiation, which was shown to be reversible upon heating in air (130°C) (Xu G, *et al*, 2007). The (MV)Bi<sub>2</sub>Cl<sub>8</sub> compound was yellow prior to the photochromic transition, and becomes black after irradiation, due to the formation of the MV<sup>•+</sup> radical cation. The two crystalline phases displayed comparatively little difference between them and questions arose as to where the MV radical originated. Structurally the MV molecules themselves, only showed a shortest inter ring separation distance of 5.54 Å, which largely eliminated the possibility of an electron transfer occurring between MV molecules themselves. With a shortest Cl...N distance of 3.44 Å, which is substantially shorter than the ~3.8 Å needed for an electron transfer interaction, the electron donation was attributed to the Bi<sub>2</sub>Cl<sub>8</sub> wires through a  $\sigma \rightarrow \pi$  type interaction which is a well established mechanism for these compounds (Xu G, *et al*, 2007, and references cited therein). Further confirmation as to the presence of the radical was confirmed when the compound was heated in an argon atmosphere and the

reversible transition was inhibited. The reversible transition mechanism is facilitated through oxygen ( $O_2$ ) radical surface absorption for radical back donation to reform the yellow complex.

Other charge transfer investigations between wires and spacers that have been thoroughly studied for the single chain face sharing octahedral wires of lead iodide and methyl viologen ( $(MV)Pb_2I_6$ ). The structure was first reported by (Tang Z and Guloy A. M, 1999) with the subsequent optical property investigations carried out by (Fujisawa J and Ishihara T, 2004; Fujisawa J and Tajima N, 2005; Fujisawa J, *et al*, 2007). The authors collectively ascertained the mechanisms of the charge transfer transitions, which occurred from the top of the valence band (the antibonding lone pair from Pb 6s) and the non-bonding electron band (the nonbonding electrons from I 5p) of the  $PbI_3^-$  wires to the LUMO ( $\pi^*$ ) of MV. The low temperature (4K) absorption experiments revealed a strong absorption band at 3.1eV which was assigned as the first exciton absorption, and a broad absorption band from 2.0 – 2.7eV which was attributed to the charge transfer from the negatively charged  $PbI_3^-$  wires to the  $MV^{2+}$  dication. The red color of the crystal was attributed to the broad CT absorption band. Photoconductivity measurements were also completed on  $(MV)Pb_2I_6$  by Fujisawa J and Tajima N, 2005 and displayed that the photoconductivity of this compound is predominantly induced due to the charge transfer interaction from the wires to the spacers.

The photoluminescence emission spectra of  $(MV)Pb_2I_6$  at 4K revealed the usual STE luminescence emission at 2.0eV (the nonradiative relaxation from vibrationally excited electron hole pair states which become STE's in the wires themselves (Fujisawa J and Ishihara T, 2004)), however it also displayed an additional strong emission peak at 1.5eV with a shoulder at 1.7eV. The origin of the latter peaks were further investigated through photoluminescence excitation spectroscopy. These two peaks showed absorption edges arising at 2.05eV and 2.4eV respectively. This confirmed the two emissions to be from the intermediary band arising from the LUMO of  $MV^{2+}$ , however also revealed the source of the electrons for the CT interactions occurrence. This is due to the difference of the absorption edges from the PLE experiments of the two peaks which is  $\sim 0.4eV$ . The energy difference is approximately the same as the energy difference from the top of the valence band (Pb 6s) and the non-bonding electrons band arising from the I 5p orbital's, obtained from experiments and calculations performed on specifically (PD) $PbI_3$  (Azuma J, *et al*, 2002a; 2002b).

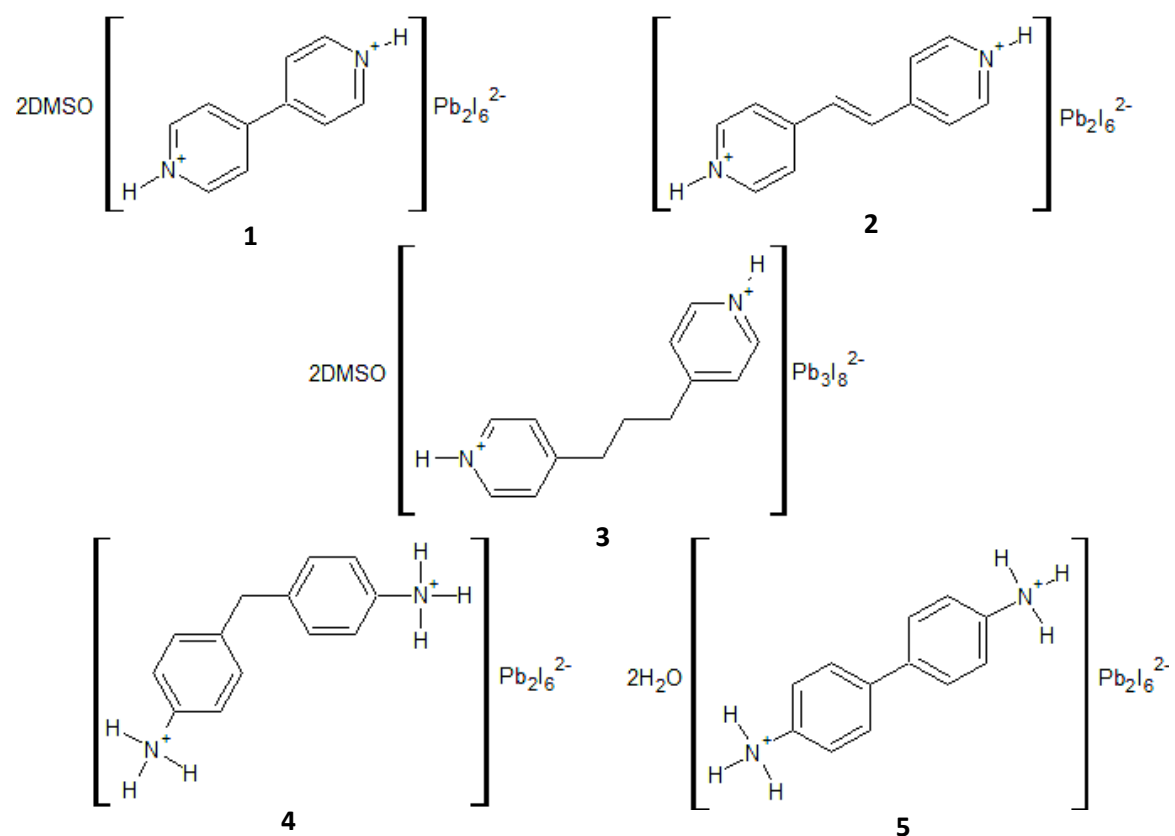
Further investigations into charge transfer interactions of various templates with the wires of thicker chain derivatives have not been thoroughly explored with possibly the exception of the recently reported case of ethylviologen (EV) and lead iodide (Pradeesh K, *et al*, 2010). The use of

ethylviologen with lead iodide also produced 1D wires except they no longer formed single chain face sharing lead iodide octahedra, but formed columns of face and edge sharing octahedra, containing six coordinated lead iodide centers (Pradeesh K, *et al*, 2010). The compound formed a similar CT type complex, with a similar absorption spectrum as (MV)Pb<sub>2</sub>I<sub>6</sub>. The first exciton absorption showed a marginal blue shift to 3.19 eV when compared with the (MV)Pb<sub>2</sub>I<sub>6</sub> with the broad CT absorption band observed between 2.4 – 2.8 eV. The PL emission spectrum however revealed three distinct emission bands, with strong emissions observed at 3.0 eV, and 2.35 eV, containing a shoulder at 2.19 eV. The newly observed PL peak at 3.0 eV was suggested to be the desired first exciton emission, with the red shifted PL emissions due to the CT emissions (Pradeesh K, *et al*, 2010).

Two distinct advances were made from this discovery. Firstly, a lead iodide wire thickness at which a first exciton emission arises in preference to the STE emission has been established. And secondly, the CT interaction has been shown to be largely similar to the MV compound, which established the relative independence of the CT emission from an STE type emission.

As the origins of the CT and STE type luminescence emissions have been well established, a semi-empirical investigation was needed in order to ascertain the effect of different templates of similar design to MV and EV would have on growing wires of various thickness with an analysis of the respective CT, first exciton emissions and absorption spectra, as predicting crystal structures and their properties in these compounds remains a challenge. Both electron accepting and non-electron accepting templates were used for the comparative study to further establish and compare the optical character. The electron accepting templates are 4,4'-bipyridine (BP) (**1**), and 4,4'-(E)-ethene-1,2-dipyridine (EEDP) (**2**), and the non CT templates of 4,4'-propane-1,3-dipyridine (PDP) (**3**), 4,4'-methylene dianilinium (MDA) (**4**), and benzidine (BD) (**5**) as seen in scheme 5.3.1 below. The first three templates were synthesized in DMSO with lead iodide, where both (BP) and (PDP) incorporated DMSO into the lattice, however (EEDP) did not. The two templates of BD and MDA only produced wires with lead iodide when grown in a supersaturated solution with 47% aqueous hydroiodic acid. The (BD) crystal incorporated water into the lattice however (MDA) did not. It should also be noted that the first three compounds are pyridine based cations, where **4** and **5** are both aniline base cations.

### 5.3.2 Results and Discussion



**Scheme 5.3.1:** The chemical diagrams of the crystal structures of **1-5** respectively.

**The structures of 2DMSO.(BP)Pb<sub>2</sub>I<sub>6</sub> (1), (EEDP)Pb<sub>2</sub>I<sub>6</sub> (2), 2DMSO.(PDP)Pb<sub>3</sub>I<sub>8</sub> (3), 2H<sub>2</sub>O.(BD)Pb<sub>2</sub>I<sub>6</sub> (4) and (MDA)Pb<sub>2</sub>I<sub>6</sub> (5).**

**Table 5.3.1:** These experiments were carried out at 173K with Mo K $\alpha$  radiation using a Bruker APEX-II CCD diffractometer. Absorption corrections were completed using the Integration method, *Bruker XPREP* (Bruker, 2005).

	(1)	(2)	(3)	(4)	(5)
Crystal data					
Chemical formula	I <sub>6</sub> Pb <sub>2</sub> ·C <sub>10</sub> H <sub>10</sub> N <sub>2</sub> ·2(C <sub>2</sub> H <sub>6</sub> OS)	C <sub>12</sub> H <sub>12</sub> N <sub>2</sub> ·2(I <sub>3</sub> Pb)	I <sub>8</sub> Pb <sub>3</sub> ·C <sub>13</sub> H <sub>16</sub> N <sub>2</sub> ·2(C <sub>2</sub> H <sub>6</sub> OS)	C <sub>13</sub> H <sub>16</sub> N <sub>2</sub> ·2(I <sub>3</sub> Pb)	C <sub>12</sub> H <sub>14</sub> N <sub>2</sub> ·2(I <sub>3</sub> Pb)·2(H <sub>2</sub> O)
<i>M<sub>r</sub></i>	1490.24	1360.02	1993.3	1376.06	1398.06
Crystal system, space group	Orthorhombic, <i>Pbca</i>	Triclinic, <i>P</i> <sup>-</sup> 1	Orthorhombic, <i>P</i> 2 <sub>1</sub> 2 <sub>1</sub> 2	Orthorhombic, <i>Fdd</i> 2	Monoclinic, <i>P</i> 2 <sub>1</sub> / <i>c</i>
<i>a</i> , <i>b</i> , <i>c</i> (Å)	8.0590 (2), 23.4644 (5), 32.9245 (6)	4.5156 (1), 11.1910 (3), 12.3922 (3)	11.830 (2), 36.177 (6), 4.5977 (8)	25.3060 (4), 42.8881 (6), 4.5113 (1)	4.4970 (4), 13.1656 (12), 22.658 (2)
$\alpha$ , $\beta$ , $\gamma$ (°)	90, 90, 90	72.079 (2), 81.961 (2), 88.598 (2)	90, 90, 90	90, 90, 90	90, 90, 90
<i>V</i> (Å <sup>3</sup> )	6226.0 (2)	589.88 (2)	1967.7 (6)	4896.23 (15)	1341.5 (2)
<i>Z</i>	8	1	2	8	2
$\mu$ (mm <sup>-1</sup> )	16.9	22.1	19.20	21.30	19.45
Crystal size (mm)	0.22 × 0.02 × 0.02	0.13 × 0.08 × 0.06	0.60 × 0.05 × 0.03	0.33 × 0.05 × 0.03	0.25 × 0.05 × 0.03
Data collection					
<i>T</i> <sub>min</sub> , <i>T</i> <sub>max</sub>	0.483, 0.746	0.264, 0.505	0.381, 0.746	0.063, 0.444	0.206, 0.749
No. of measured, independent and observed [ <i>I</i> > 2 $\sigma$ ( <i>I</i> )] reflections	52740, 7517, 4615	4164, 2310, 1944	10692, 4711, 3860	14462, 2898, 2687	12352, 2750, 1879
<i>R</i> <sub>int</sub>	0.121	0.022	0.043	0.031	0.127
Refinement					
<i>R</i> [ <i>F</i> <sup>2</sup> > 2 $\sigma$ ( <i>F</i> <sup>2</sup> )], <i>wR</i> ( <i>F</i> <sup>2</sup> ), <i>S</i>	0.043, 0.073, 1.00	0.026, 0.053, 1	0.046, 0.094, 1.05	0.019, 0.032, 0.89	0.061, 0.132, 1.03
No. of reflections	7517	2310	4711	2898	2750
No. of parameters	257	104	169	107	65
No. of restraints	0	0	0	1	4
H-atom treatment	H-atom parameters constrained	H-atom parameters constrained	H-atom parameters constrained	H-atom parameters constrained	H atoms treated by a mixture of independent and constrained refinement
	$w = 1/[\sigma^2(F_o^2) + (0.0159P)^2]$ where $P = (F_o^2 + 2F_c^2)/3$	$w = 1/[\sigma^2(F_o^2) + (0.0218P)^2]$ where $P = (F_o^2 + 2F_c^2)/3$	$w = 1/[\sigma^2(F_o^2) + (0.0336P)^2 + 10.5196P]$ where $P = (F_o^2 + 2F_c^2)/3$	$w = 1/[\sigma^2(F_o^2) + (0.0P)^2]$ where $P = (F_o^2 + 2F_c^2)/3$	$w = 1/[\sigma^2(F_o^2) + (0.0602P)^2 + 0.0258P]$ where $P = (F_o^2 + 2F_c^2)/3$
$\Delta_{\text{max}}$ , $\Delta_{\text{min}}$ (e Å <sup>-3</sup> )	1.21, -1.42	0.89, -0.86	1.92, -2.05	0.87, -0.59	1.69, -2.83
Absolute structure	—	—	Flack H D (1983), Acta Cryst. A39, 876-881	Flack H D (1983), Acta Cryst. A39, 876-881	—
Flack parameter	—	—	0.391 (9)	0.019 (4)	—

Computer programs: Bruker *APEX2*, Bruker *SAINT*, *SHELXS97* (Sheldrick, 2008), *SHELXL97* (Sheldrick, 2008), Bruker *SHELXTL*.

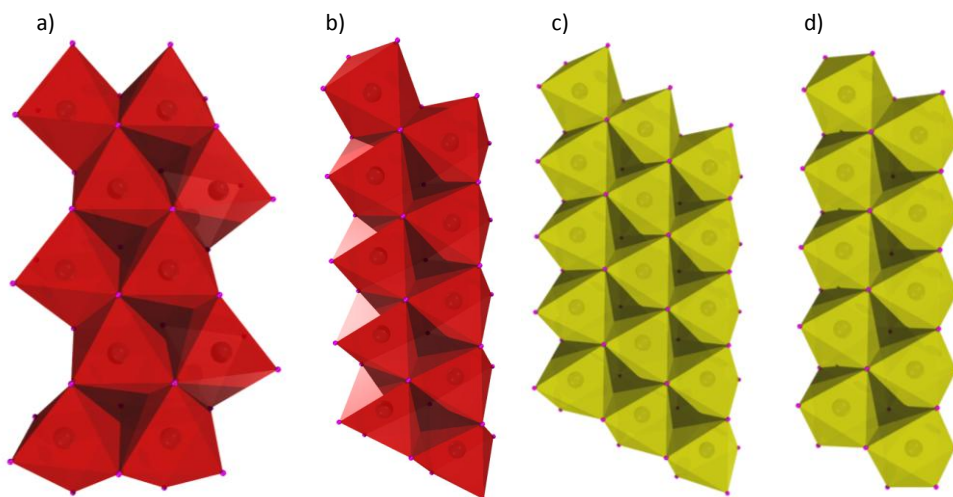


**Figure 5.3.1:** The inorganic 1D “sheets” and the arrangement of the edge sharing lead iodide octahedra for compounds **1-5**. All five compounds display a similar surface topology on the “top” of the wire. Compounds **2** (b), **4** and **5** (d) display identical wire topologies as seen in b) and d) where the wire color represents the compounds crystal color. In compound (**1**) a) the octahedra are offset from one another, unlike the remaining compounds, and compound (**3**) c) displays the same topology as **2**, **4**, and **5**, however has an additional chain of lead iodide octahedra.

### Wire Topology

For the compounds under investigation, data collection and structural information may be found in table 5.3.1. (BP) $\text{Pb}_2\text{I}_6$  (**1**) crystallizes in the space group  $Pbca$ , (EEDP) $\text{Pb}_2\text{I}_6$  (**2**) in  $P-1$ , (PDP) $\text{Pb}_3\text{I}_8$  (**3**) in the non-centro-symmetric space group  $P2_12_12$ , (MDA) $\text{Pb}_2\text{I}_6$  (**4**) in the non-centro symmetric space group  $Fdd2$ , and (BD) $\text{Pb}_2\text{I}_6$  (**5**) in  $P2_1/c$ . Despite the similarity of the templates used there are three different inorganic motif arrangements that arise (figure 5.3.1). Unlike the 1D sheet like motif of corner-sharing lead iodide octahedra discussed by (Mercier N, *et al*, 2009) the lead iodide octahedra form single layer flat 1D sheets through octahedral edge sharing (figure 5.3.1). If we consider the wires as rectangular tubes of 1D sheets propagating along one of the crystallographic axes, we may define the top and bottom of the wire from the short dimension, the sides or edges of the rectangle as the medium dimension (thickness), and the length of the wire as the direction the wire propagates through the crystal lattice. Therefore compounds **1**, **2**, **4** and **5**, display a thickness of two edge sharing lead iodide octahedra, where the top of the wire is terminated by an octahedral face and the topology along the length of the wire generates equilateral triangle holes penetrating the wire from above and below (figure 5.3.1). The edges of the wires are also terminated by the face of the octahedra. Compounds **2**, **4** and **5** display identical wire topologies as seen in figure 5.3.1 b) and d) as every  $\text{PbI}_6$  units lead centre’s arrange in a collinear fashion down the length of the wire. The only difference is the wire color which represents the compounds crystal color. In compound (**1**) a) the octahedra are offset from one

another where only every second  $\text{PbI}_6$  unit are collinear and forms a zigzag pattern down the length of the wire. Compound (3) figure 5.3.1 c) displays the same topology as 2, 4, and 5, however has an additional chain of lead iodide octahedra, which increases the thickness of the wire.

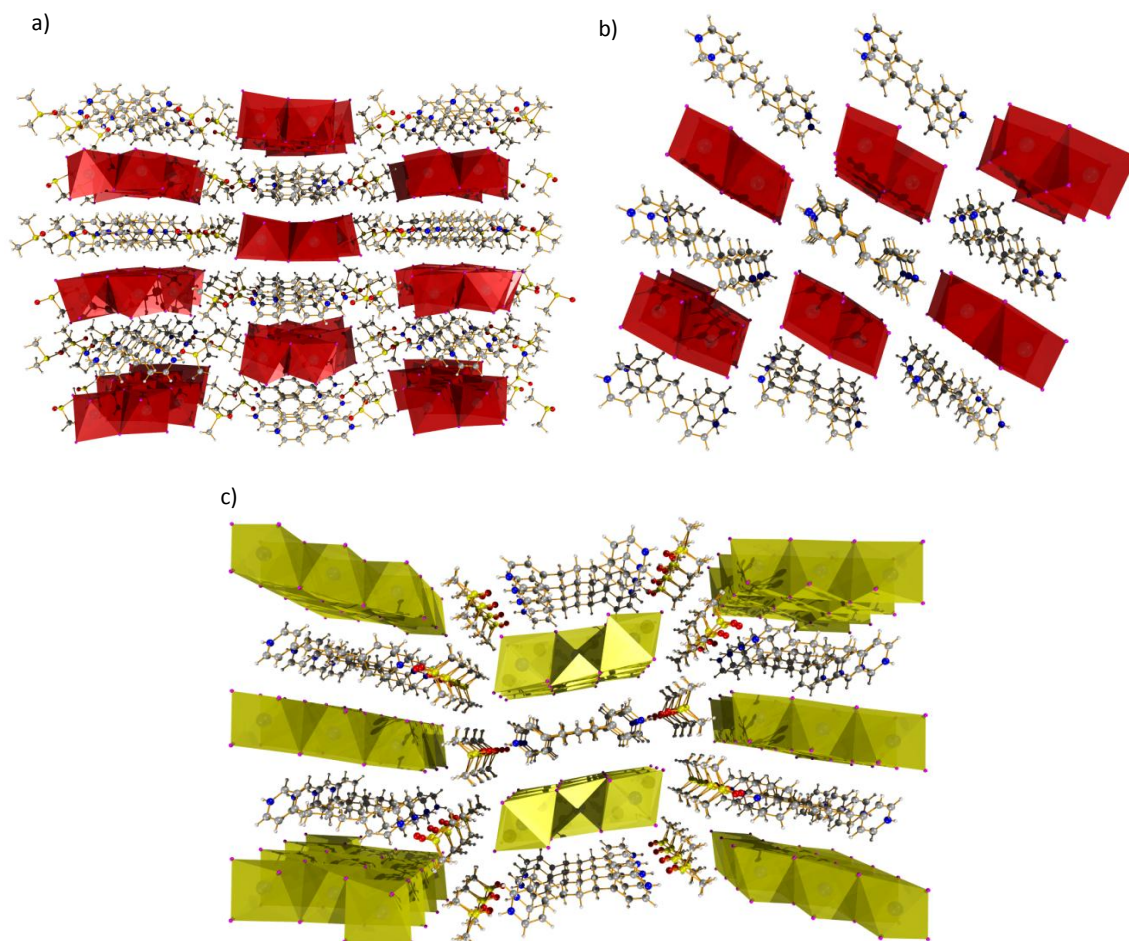


**Figure 5.3.2:** a) The packing diagram of 2.DMSO.(BP) $\text{Pb}_2\text{I}_6$  viewed along (100) axis. b) The packing diagram of (EEDP) $\text{Pb}_2\text{I}_6$  viewed along the (100) axis. c) The packing diagram of 2DMSO.(PDP) $\text{Pb}_3\text{I}_8$  viewed along the (001) axis. (The wire colors represent the crystal color).

**Table 5.3.2:** Summary of the inorganic bond length and angle distortions ranges for compounds 1-5.

Compound	1	2	3	4	5
Pb-I (Å)	3.0207 (8) - 3.5224 (8)	3.0040 (6) - 3.2835 (5)	2.9951 (12) - 3.509 (11)	3.0405 (4) - 3.4051 (4)	3.0986 (15) - 3.3417 (16)
I-Pb-I (°)	81.48 (2) - 109.69 (2)	87.270 (13) - 91.907 (14)	87.27 (4) - 99.29 (3)	87.925 (10) - 93.155 (11)	85.50 (4) - 93.61 (5)
I <sub>eq</sub> -Pb-I <sub>eq</sub> (°)	164.03 (2) - 179.44 (2)	177.335 (15) - 178.487 (17)	166.25 (3) - 178.82 (3)	176.786 (11) - 178.919 (12)	174.82 (6) - 176.90 (5)
Pb-I-Pb (°)	92.547 (18) - 99.35 (2)	87.270 (13) - 90.455 (13)	91.55 (2) - 95.43 (3)	88.945 (10) - 91.644 (9)	88.37 (4) - 94.50 (4)
Lead centers (°)	> 176.299(12), collinear	collinear	178.904(10), collinear	collinear	collinear
Inter wire spacing I...I (Å)	6.137(1)	4.1600(8)	6.699(2)	3.9818(8)	4.645(2)



### ***Intermolecular interactions (pyridine based templates)***

The packing arrangements of compounds **1-3** may be found in figure 5.3.2, where DMSO solvent molecules are included in the lattice of **1** and **3**. The presence of the solvent defers the hydrogen bonding interactions from the ammonium group and the iodine's of the wires to itself. Whereas in **2**, no solvent is present in the lattice, and N-H...I interactions are present from the EEDP dication between adjacent wires (table 5.3.3). This does result in a much shorter inter-wire spacing observed in **2** (I...I 4.1600(8) Å) whereas **1** and **3** display larger inter-wire spacing's of 6.137(1) Å and 6.699(2) Å respectively. Moreover, in compounds **1** and **2** the  $\pi$  conjugated cations of BP and EEDP experience a templating effect from the wires which promote  $\pi - \pi$  interactions between adjacent molecules, which is commonly observed in similar molecular archetypes. As the BP molecules do not hydrogen bond to the iodides, a bifurcated hydrogen bond is present between the carbonyl and sulphur atoms of DMSO, which occurs at both ends of the BP molecule. This interaction does cause the BP molecules to not align exactly parallel with one another. This was observed when comparing the relatively strong  $\pi - \pi$  interaction distances of N1...C8 (3.46 (1) Å), and C5...N1 (3.71 (1) Å) at the opposite ends of the molecule and may be seen in the tilt angle of the BP molecules away from the parallel arrangement 4.707(95)°.

In compound **2** the EEDP molecule's also display relatively strong  $\pi - \pi$  interactions of N1...C1 (3.67 (1) Å) and C6...C4 (3.67 (1) Å) respectively, which are the interactions with Py...Py rings and the ethylene bridge with the pyridine ring (only half the molecule is in the asymmetric unit). As compound **2** has no solvent included in the lattice, the EEDP molecules remain parallel with one another. In addition, it is noted that there are also  $I - \pi$  interactions present, in addition to the N-H...I hydrogen bonds experienced. This may be seen specifically with the N...I interactions of (3.928(7) Å, 4.373(7) Å) and (3.673(7) Å) for **1** and **2** respectively. Both compounds also display C...I interactions ranging (3.66(1) – 3.934(9) Å) and (3.715(9) Å and 3.971(8) Å), for **1** and **2** respectively. These N...I interactions are comparable with the reported values in (MV)Pb<sub>2</sub>I<sub>6</sub> of 3.629 Å (Tang Z and Guloy A. M, 1999), suggesting both electron transfer mechanisms may be present in **1** and **2**, namely, wire to spacer, and spacer to spacer. As has been previously established for the CT interactions observed in (MV)Bi<sub>2</sub>Cl<sub>8</sub>, for the electron transfer interaction to take place from I to N the I...N distance should be < 3.8 Å as this is the longest distance observed for a charge transfer interaction in viologen metal halide compounds (Xu G, *et al*, 2007, references cited therein). However this may not be entirely accurate as these (I...N) interactions are considerably shorter than that observed for (EtV)Pb<sub>2</sub>I<sub>6</sub> of 4.889 Å

(Pradeesh K, *et al*, 2010) which still displays charge transfer behavior, and suggests that the wire to spacer electron transfer distance may have a longer range than originally anticipated.

In compound **1** the main inorganic distortions experienced in the wire are due to the steric interaction of the two DMSO molecules with the edge of the wire. These distortions are experienced in the trans I<sub>eq</sub>-Pb-I<sub>eq</sub> bond angle of (I4-Pb2-I3) 164.03 (2)<sup>o</sup> and the cis I-Pb-I bond angle of (I6-Pb2-I3) 109.69(2)<sup>o</sup> which are both large deviations from the ideal 180<sup>o</sup> and 90<sup>o</sup> respectively. In addition the largest Pb-I bond length compression and elongations are on the same lead atom, where the distortions are Pb2-I6 3.0484(8) Å where I6 is 4.738(3) Å away from S2, and the Pb-I trans bond elongation experienced is large 3.5224(8) Å for Pb2-I2 respectively. In compound **2** the inorganic distortions experienced are minor and correlate to what is expected to compensate for the spatial occupation of the 6s<sup>2</sup> lone pair of electrons on lead. The largest Pb-I bond length compression (3.0040(6) Å) occurs where the N1-H...I4 interaction occurs (table 5.3.3) with the largest bond elongation occurring with the trans Pb-I bond (3.2835(5) Å). No substantial destabilization of the band structure is expected from the Pb-I compressions and elongations are expected for **1** as these bond distortions have been shown to have little impact in shifting of the first exciton absorption band (5.1).

In compound **3** the (PDP) molecule resides on a twofold rotation which passes through the central C7 atom of the propane bridge. The pyridine ring is offset at an angle of 123(2)<sup>o</sup> (C7-C6-C3-C2) which is primarily due to the hydrogen bonding interaction with the disordered DMSO molecule, where the methyl atoms of DMSO are not disordered however the oxygen and sulphur atoms are disordered over two positions (SOF : 0.63/0.37 between atoms labelled A and B respectively). The N-H...A interactions are bifurcated between the disordered oxygen, and disordered sulphur atoms resulting in no hydrogen bonding interactions to occur with the inorganic wires. However there are weak I – π interactions specifically with N...I (4.26(1) Å) and C...I (3.51(2) Å – 4.15(2) Å) respectively, with much stronger π – π interactions of 3.53(2) Å and 3.56(2) Å respectively. As in compound **1** the main inorganic distortions in the wires are created from DMSO's steric interaction with the edge of the wires. The methyl groups of DMSO weakly interact with I4 and I3 (4.17(2) Å and 3.89(2) Å respectively) which are adjacent (cis) iodine's on the Pb2 atom. The corresponding I4-Pb2-I3 bond angle distorts to 99.29(3)<sup>o</sup> which is the most distorted cis I-Pb-I bond angle in the wires. In addition I3-Pb2-I1 trans angle also experiences a large distortion of 166.25(3)<sup>o</sup>, with bond length distortions of Pb2-I4 experiencing the largest Pb-I bond compression (2.9951(12) Å) and in turn it's trans Pb-I

bond length the greatest elongation to 3.509(1) Å. These distortions are comparable with those seen in compound **1**.

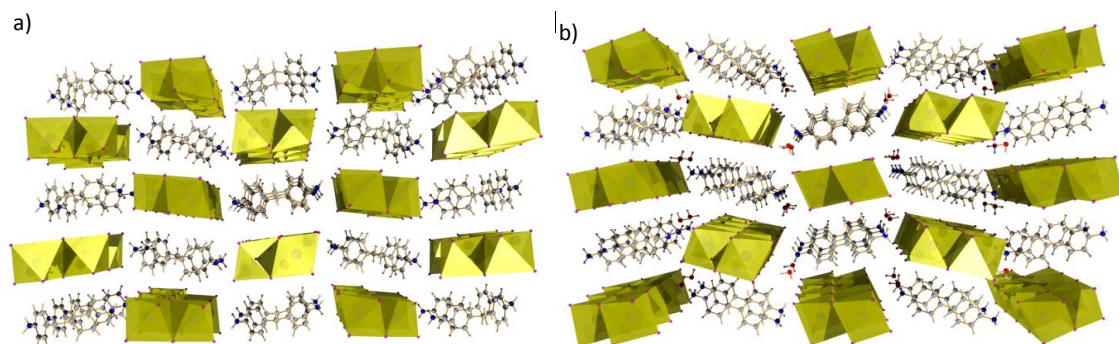


**Figure 5.3.3:** a) The packing diagram of **4** (MDA)Pb<sub>2</sub>I<sub>6</sub> viewed along (001) axis. b) The packing diagram of **5** (BD)Pb<sub>2</sub>I<sub>6</sub> viewed along the (100) axis.

### **Intermolecular interactions (aniline based templates)**

Compound **4** and **5** are both non electron accepting templates and both display mostly unremarkable intermolecular interactions. This can be seen in the lack of inorganic distortions as summarized in table 5.3.2, where **5** does display a larger I<sub>eq</sub>-Pb-I<sub>eq</sub> distortion away from 180° due to the presence of the water molecule at the edge of the wire. The benzidine template does pack cofacial with the other benzidine molecules, down the length of the wire (100) which are spaced 4.50(3) Å from one another, again due to the water molecule forming a hydrogen bonding chain with the ammonium groups of adjacent benzidine molecules, and therefore the intermolecular spacing is increased to accommodate for this. In compound **4** as in **3** the absence of a solvent molecule allows the rings to have shorter and stronger intermolecular  $\pi - \pi$  distances which range from 3.392(7) – 3.735(7) Å. The packing diagrams of both compounds may be seen in figure 5.3.3 above and hydrogen bonding interactions in table 5.3.3.

**Table 5.3.3:** Hydrogen bonding interactions for compounds **1-5**.

<i>D</i> —H... <i>A</i>	<i>D</i> —H (Å)	H... <i>A</i> (Å)	<i>D</i> ... <i>A</i> (Å)	<i>D</i> —H... <i>A</i> (°)
(1)				
N1—H1A...O1	0.88	1.67	2.525 (11)	162.5
N1—H1A...S1	0.88	2.8	3.659 (8)	166.1
N2—H2A...O2	0.88	1.74	2.617 (10)	173.3
N2—H2A...S2	0.88	2.86	3.690 (8)	158.5
(2)				
N1—H1...I4 <sup>i</sup>	0.88	2.85	3.593 (6)	143.8
N1—H1...I2 <sup>i</sup>	0.88	3.29	3.885 (6)	126.7
(3)				

N1—H1A...O1A	0.86	1.78	2.62 (2)	163.2
N1—H1A...O1B	0.86	1.85	2.67 (3)	157.3
N1—H1A...S1A	0.86	2.82	3.669 (14)	167.5
N1—H1A...S1B	0.86	2.82	3.678 (16)	171.4
(4)				
N1—H1B...I <sup>ii</sup>	0.89	2.77	3.594 (4)	154
N1—H1C...I <sup>iii</sup>	0.89	2.72	3.498 (5)	146
(5)				
O1W—H1W...I <sup>iv</sup>	0.96	2.62	3.580 (13)	179.4 (12)
O1W—H2W...I <sup>v</sup>	0.96 (12)	2.78 (13)	3.684 (16)	158 (8)
N1—H1A...O1W <sup>iv</sup>	0.89	1.93	2.74 (3)	150.6
N1—H1B...I <sup>iv</sup>	0.89	3.03	3.65 (2)	127.9
N1—H1C...O1W <sup>vi</sup>	0.89	2.01	2.85 (3)	156.4
N1—H1B...I <sup>vii</sup>	0.89	3.08	3.79(2)	137(1)

Symmetry code(s): (i)  $-x-1, -y+1, -z+1$ ; (ii)  $x+1/4, -y+1/4, z+1/4$ ; (iii)  $x+1/4, -y+1/4, z+5/4$ ; (iv)  $-x+1, y-1/2, -z+1/2$ ; (v)  $x+1, y, z$ ; (vi)  $-x, y-1/2, -z+1/2$ ; (vii)  $-x, -1/2 + y, 1/2 - z$ .

### 5.3.3 Powder diffraction investigations

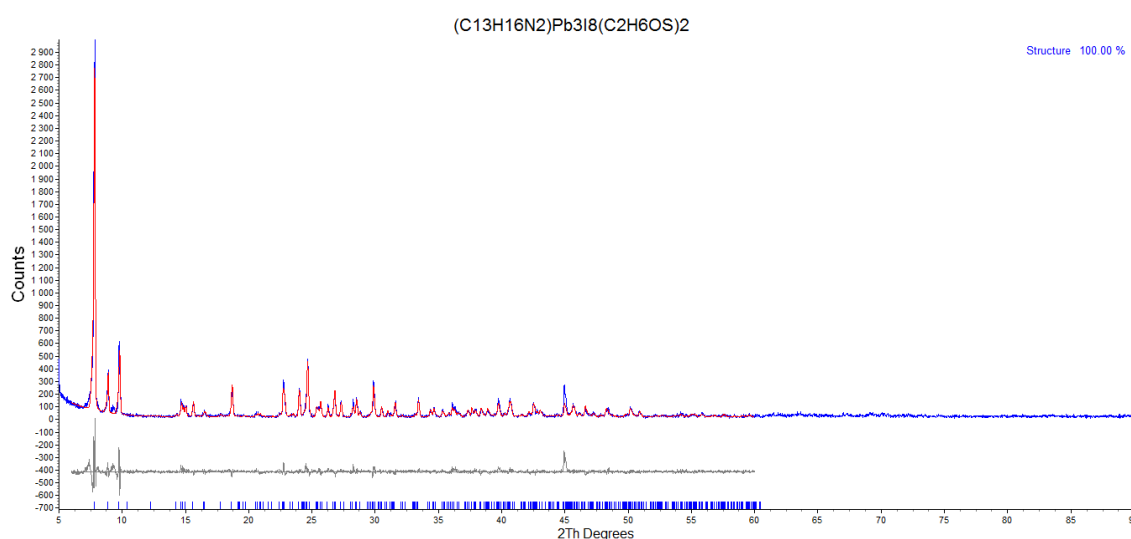


**Figure 5.3.4:** The rietveld refined P-XRD data of (PDP)Pb<sub>3</sub>I<sub>8</sub> (**3**).  $R_{\text{Bragg}}$  5.507,  $R_{\text{exp}}$  12.80,  $R_{\text{wp}}$  18.71,  $R_p$  4.50, GOF 1.46,  $R_{\text{exp}}$  19.53,  $R_{\text{wp}}$  28.55,  $R_p$  24.87, DW 1.05.

Compounds **1** and **3**, **4** and **5** room temperature powder diffraction patterns displayed the same phase though out the bulk as the 173K single crystal structure. Compound **2** did not and hence no further optical absorption experiments were run on it, however the low temperature PL was obtained on the same crystal used for the SC-XRD data collection. Figure 5.3.4 shows the rietveld refined P-XRD data of compound **1**. Compound **3**, **4** and **5** may be found in appendix B with their respective R factors and refined unit cell parameters. The phase identification and rietveld

refinements were carried out on the sample using the *Pseudo Voigt\_TCHZ* analytical peak profile function. The refinements were carried out with the use of the 173K temperature single crystal structure data obtained from our SC-XRD experiments. Both of the PXRD patterns displayed varying levels of preferred orientation, as the crystal habit was plate like. Therefore a spherical harmonics function of order 4-8 was used to correct for this. From the difference plot and the R factors quoted above (figure 5.3.3), the refinement gave satisfactory results that the bulk and single crystal phases were the same. Although all the PXRD patterns were collected from 5-90° 2 $\theta$  the refinement was ranged from 5-60° 2 $\theta$  due to the distinct lack of high angle peaks despite the longer scan times. The remaining instrumental experimental details/configurations may be found in chapter 3. The refined unit cell parameters for compound **1** were found to be  $a = 11.9674(12) \text{ \AA}$ ,  $b = 36.2811(32) \text{ \AA}$ ,  $c = 4.63193(55) \text{ \AA}$ ,  $V = 2011.15(36) \text{ \AA}^3$  for the orthorhombic unit cell with the space group  $P2_12_12$ . The SC-XRD unit parameters were  $a = 11.830(2) \text{ \AA}$ ,  $b = 36.177(6) \text{ \AA}$ ,  $c = 4.5977(8) \text{ \AA}$ ,  $V = 1967.7(6) \text{ \AA}^3$  respectively. All the inorganic atomic positions were refined, however due to the large difference in the electron densities of the lead iodide octahedra and the organic component the thermal parameter *Beq* and organic atomic positions were not refined. The same procedure was followed for the remaining compounds.

#### 5.3.4 Optical Properties

The optical properties of (PDP)Pb<sub>3</sub>I<sub>8</sub> will be discussed first as, the (PDP) molecule was not susceptible to charge transfer interactions between the wires and spacers. The wires of (PDP)Pb<sub>3</sub>I<sub>8</sub> consist of three PbI<sub>6</sub> octahedral units wide and only one octahedral unit high. The first exciton absorption peak was found at 3.27eV with a substructure peak observed at 2.72eV as seen in Figure 5.3.5 a). The first exciton absorption peak is in the characteristic position observed for the single chain (A)PbI<sub>3</sub> compounds (5.1; 5.2) however the substructure peak is not and may be due to the non-uniform wire thickness, as the wire thickness ratio is 1:3. This may impact the absorption edge due to the anisotropic nature of the wires, from that observed for 1:1 wires of (PD)PbI<sub>3</sub> (Nagami A, *et al*, 1996). The altering of the wire dimensions from square to rectangular has been shown to alter the optical absorption profiles in GaAs quantum wires, however the dimensions of the wires were much larger (~100 – 300Å) (Ogawa T and Kanemitsu Y, 1998) than the wire dimension observed in these compounds (17.9 Å X 8.55 Å). Low temperature polarization dependant absorption/reflectance spectra would be needed to further clarify this assignment. The room temperature optical absorption spectra obtained on the six lead iodide octahedral thick wires with a 3:2 packing thickness of (EV)Pb<sub>2</sub>I<sub>6</sub> may have masked the true

nature of the absorption of the wires due to the charge transfers broad absorption band between 2.4 – 2.8eV (Pradeesh K, *et al*, 2010). However this compound still displayed the characteristic first exciton absorption peak at 3.19eV. Additionally the PL emission displayed a strong emission band at 3.0eV and another strong emission and shoulder at 2.35eV and 2.19eV respectively. The emission at 3.0eV is thought to be due to the first exciton emission, 0.19eV Stokes shifted from the absorption band. As previous optical studies on (PD)PbI<sub>3</sub> and [NH<sub>2</sub>C(I)=NH<sub>2</sub>]<sub>3</sub>PbI<sub>5</sub> and [CH<sub>3</sub>SC(=NH<sub>2</sub>)NH<sub>2</sub>]<sub>3</sub>PbI<sub>5</sub> have been at the lower size limit of the wires, the STE emission was more favorable than the desired first exciton emission (Nagami A, *et al*, 1996; Fukumoto T, *et al*, 2000; Azuma J, *et al*, 2002a; Akimoto I, *et al*, 2004; Wang S, *et al*, 1995; Mousdis G. A, *et al*, 1998 and Tanaka K, *et al*, 2005b). Therefore the size dimension of the wire that allows the expected first exciton emission and suppresses the STE emission has been found with the lower energy emission peaks of (EV)Pb<sub>2</sub>I<sub>6</sub> assigned to the charge transfer emissions. The 1D sheets of (PDP)Pb<sub>3</sub>I<sub>8</sub> (figure 5.36a) also displayed two distinct PL emissions at 77K, which gave rise to a large asymmetric emission peak profile, where the asymmetric tail was found on the blue side of the main emission band. Using a Gaussian peak profile fitting function, the two overlapping peaks positions were assigned. The peak centered at 1.92eV displayed a *FWHM* of 0.3eV which is consistent with an STE emission as assigned for (PD)PbI<sub>3</sub> (Nagami A, *et al*, 1996; chapter 5.1, 5.2). The second peak was a broad peak centered at 2.11eV with a *FWHM* of 540meV. We suspect this peak may be due to the anisotropic (rectangular) shape of the wire, which is beginning to allow higher energy emissions to occur as the spatial confinement of the electron and hole begins to relax (Ogawa T and Kanemitsu Y, 1998). Although the dimensions of the GaAs wires do not obtain the low size limit as in the hybrids, and do not display an STE emission, different wire thickness ratio's have been shown to alter the photoluminescence emission profiles (Ogawa T and Kanemitsu Y, 1998). Further investigations into the band assignments are needed to confirm our hypothesis.

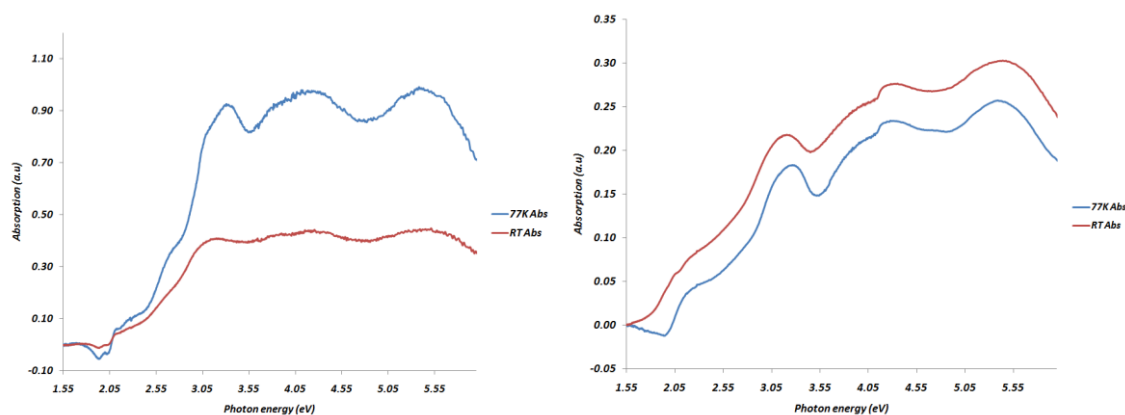


**Figure 5.3.5:** The optical absorption measurements for (PDP)Pb<sub>3</sub>I<sub>8</sub> (a) and (BP)Pb<sub>2</sub>I<sub>6</sub> (b) at both room temperature and 77K. Both compounds display the distinct first exciton absorption peak at 3.21eV and 3.27eV for a) and b) respectively. However a substructure peak at 2.7eV is present in b) and the broad CT absorption band from 2.0 – 2.8eV is present in a).

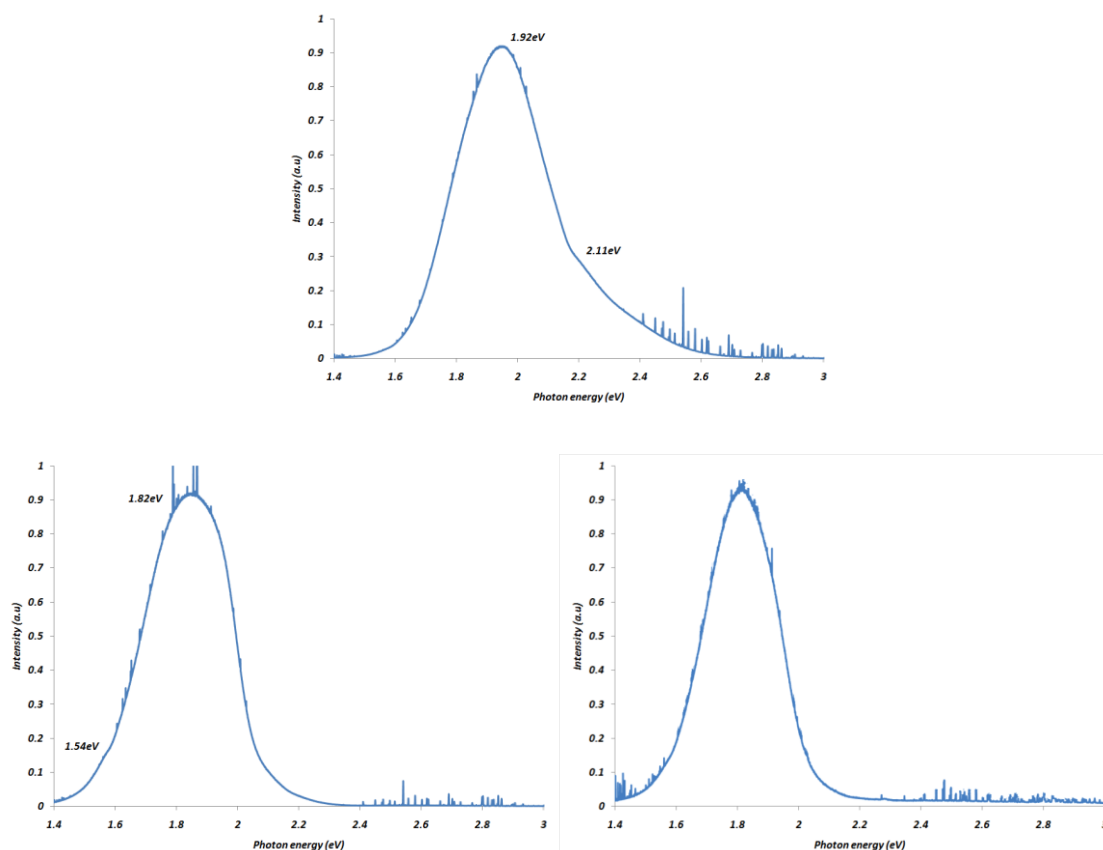


**Figure 5.3.6:** The 77K photoluminescence emission of (PDP)Pb<sub>3</sub>I<sub>8</sub> (a), (BP)Pb<sub>2</sub>I<sub>6</sub> and (EEDP)Pb<sub>2</sub>I<sub>6</sub> (c). Emission profiles are explained in the text. Plasma lines are present in all the spectra as we did not have the correct band pass filter.

The 77K optical absorption spectra of (BP)Pb<sub>2</sub>I<sub>6</sub> (figure 5.3.5 b) revealed the strong first exciton absorption peak at 3.21eV, with the broad charge transfer band from 2.0 – 2.8eV, where the

initial peak maximum occurs at  $2.2\text{eV}$ . This absorption peak is assigned to the generation of the  $\text{BP}^+$  radical cation. The peak maximum also reveals the energy level of the  $\pi^*$  LUMO band above the top of the (Pb 6s) valence band of the lead iodide wires. Furthermore the PL emission spectra also displayed an asymmetric emission peak, however it was not as pronounced as the (PDP) $\text{Pb}_3\text{I}_8$  PL emission. Using a Gaussian peak profile fitting function, three Gaussian peaks were fit for the emission. One peak was centered at  $1.82\text{eV}$  ( $FWHM$   $0.325\text{eV}$ ), and the other main peak at  $1.93\text{eV}$  ( $FWHM$   $0.115\text{eV}$ ), with a small shoulder at  $1.56\text{eV}$ . Once again the peak at  $1.82\text{eV}$  should be the STE emission as the  $FWHM$  correlates with previously assigned emissions. However the higher energy emission at  $1.93\text{eV}$  should be the STE with the peak at  $1.82\text{eV}$  and the shoulder at  $1.56\text{eV}$  from the charge transfer interactions. This is consistent with what is observed with both the MV and ET assignments. Our assignments are somewhat speculative and low temperature ( $4\text{K}$ ) PL spectra are needed to confirm if these peaks are indeed present. (EEDP) $\text{Pb}_2\text{I}_6$  displayed an even more Gaussian shaped emission, however displayed two similar size peaks overlapping at  $1.83\text{eV}$  ( $FWHM$   $0.241\text{eV}$ ) which we assign as the STE peak and a peak centered at  $1.74\text{eV}$  ( $FWHM$ :  $0.272\text{eV}$ ) which we suspect to be from the charge transfer emissions.

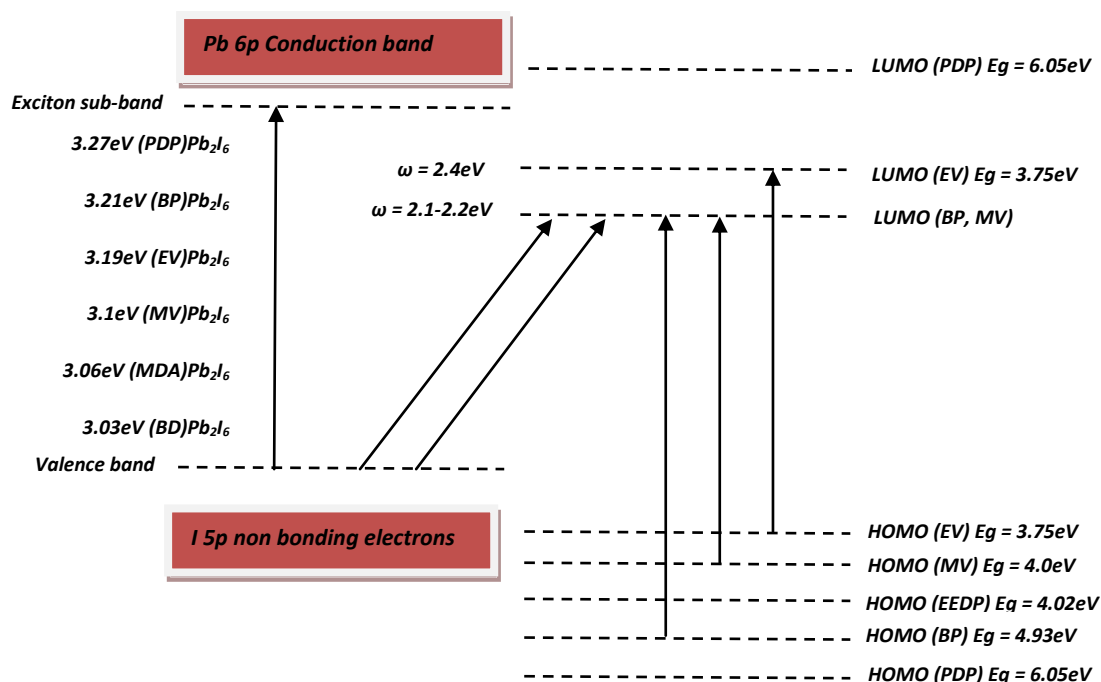


**Figure 5.3.7:** Charge transfer mechanism between the wires and spacers. Included are the previously investigated samples of (EV) $\text{Pb}_2\text{I}_6$  and (MV) $\text{Pb}_2\text{I}_6$  from which this mechanism is adapted from (Fujisawa J and Ishihara T, 2004; Fujisawa J and Tajima N, 2005; Fujisawa J, *et al*, 2007). (not to scale)



The peak assignments of our CT compounds are based upon the assignments of the charge transfer absorptions and emissions of (MV)Pb<sub>2</sub>I<sub>6</sub> (Fujisawa J and Ishihara T, 2004; Fujisawa J and Tajima N, 2005; Fujisawa J, *et al*, 2007). The mechanism of the CT interactions from the wires to the spacers may be seen in figure 5.3.7. We calculated the HOMO-LUMO gaps for BP, EEDP and PDP, on the isolated molecules, using the DFT and LCAO approach. In addition we used the hybrid exchange correlation potential B3-LYP with a medium sized basis set of 6-31-G\*. The HOMO-LUMO gap for BP was (4.93eV), EEDP (4.02eV) and PDP (6.05eV) respectively, where MV and ET have been reported to be 4.0eV and 3.75eV (Pradeesh K, *et al*, 2010) respectively. Interestingly despite the varying wire thickness the first exciton absorptions of all the compounds **1-3** and the previously reported MV and EV are similar, as seen in figure 5.3.7. In addition despite the large difference in organic HOMO-LUMO gaps, (BP) and (MV) display similar CT absorptions energies of 2.2eV and 2.1eV respectively, whereas for EV the CT absorption energy of 2.4eV is larger.

The similar CT energy experienced in MV and BP may be due to the similar N...I distances experienced in both compounds 3.629 Å and 3.928(7) Å respectively, whereas ET N...I interaction was as far as 4.889 Å, and hence the higher energy of adsorption. It was shown by (Fujisawa J, *et al*, 2007) that the CT transfer between the iodine in the PbI<sub>3</sub><sup>-</sup> wires and the nitrogen in MV is a very strong interaction as the IR spectrum of this compound showed a large increase in oscillator strength for the expected N...I interaction when compared with the CT MV halogen salts. The IR band of the N...X interactions, oscillator strength increased with the substitution of the halogen atom from chlorine to Iodine and then almost doubled in strength when observed in (MV)Pb<sub>2</sub>I<sub>6</sub>. The IR band also progressed to lower wave numbers through the halogen substitution progression. It was stated that this interaction showed a large increase in covalent character and therefore a strong CT interaction is expected. This strong covalent character may allow for a CT interaction to take place at much longer distances than originally thought.

These principles have been shown in organic conductor materials such as the oligiohetrocycles. The charge transfer process rely's mainly on two weak interactions, the first being the electron acceptor distance and orientation relative to the inorganic nano-wire, and secondly the CT interactions that may be transferred between the organic spacers themselves, which are also highly dependent on the molecular orientation and intermolecular spacing which promotes maximum intermolecular orbital overlap for electron transport. Charge transfer between the organic moieties has been shown to be highly dependent on the solid state molecular

arrangement, such as *cofacial*, *herringbone*, and *tilted* (Hutchison G. R, *et al*, 2005). The molecules in principle transfer charge when the molecules are arranged in the parallel (cofacial) stacking arrangement, and are within a certain intermolecular distance of one another. The modeling of heterocyclic dimmers showed that observable ionization energy was detectable up to 5.0 Å reaching an ionization energy (binding energy) minimum between 3.75 – 4.25 Å. It was further shown that increasing the tilt angles between the molecules increased the intermolecular orbital overlap which was favorable for intermolecular charge transfer (Hutchison G. R, *et al*, 2005). It was further stated that the cofacial distances were dependent on the number of heterocyclic units in the molecule, i.e. the more units in the molecule the further apart the molecules could be and still maintain a stable CT interaction.

### 5.3.5 Conclusions

The effect of the DMSO solvent on the inorganic distortions experienced has been investigated, although it appears to largely not affect the position of the first exciton absorption edge. Strong  $I - \pi$  and  $\pi - \pi$  interactions are present in both compounds **1** and **2**, where the wires also promote  $\pi - \pi$  interactions between the organic templates. The wire thickness appears to display a pronounced effect on the PL emission as seen in compound **3**, as it begins to allow higher energy emission's occur as the desired first exciton emission begins to become favored due to the relaxing of the wires special confinement on the electron-hole's orbit. Further investigations are needed into the thicker chain wires, to ascertain the ideal size of the wire to obtain the desired first exciton emission however the wire thickness that does give rise to the first exciton emission appears to still need at least six coordinated  $\text{PbI}_6$  octahedral units as seen with the ethyl viologen compound. In compounds **1** and **2** the CT transitions begin to largely coincide with the STE emission arising from the inorganic wire. Even though **1** and **2** have strong  $\pi - \pi$  interactions the current experiments do not ascertain to what degree this interaction assists in the electron transport. As intermolecular  $\pi - \pi$  interactions are absent in MV and Et the dominant CT interaction does show that the I...N distance functions over a large range (4.9 Å). This distance is supported from the strong covalent character of the I...N interaction observed in  $(\text{MV})\text{Pb}_2\text{I}_6$ . Additionally the position of the LUMO of the organic cation relative to the valence band of the inorganic wires appears to be largely dependent on the N...I distance and largely independent of the electron accepting templates HOMO-LUMO gap. Further experimentation into the conductivity of **1** and **2** are needed to establish the degree to which  $\pi - \pi$  interactions improve electron transport through the crystal.

## ***Chapter 6: Chiral Organic inorganic hybrid materials and their potential use for NLO applications***

### ***6.1 Theoretical background***

The results in this section began as an investigation into the use of chiral templates to ensure the symmetry condition would be met for efficient second order non linear effects to occur. As the project progressed we began to appreciate the fundamentals of excitonic behavior in quantum wells and wires. The work in this chapter is therefore presented in light of the understanding gained through the course of the project. I also wished to collate in this chapter the things I had learnt about non-linear optics (in general) in the hope that if future work was to continue then a theoretical background would have been established. The following textbooks served as the source material from which the theoretical discussion was constructed: Fox M, *Optical Properties of Solids*, 2008, Kittel C, *Introduction to Solid State Physics 7<sup>th</sup> Ed*, John Wiley & Sons, (1996), and Singleton J, *Band Theory and Electronic Properties of Solids*, Oxford University Press, (2008).

#### ***6.1.1 The physical origin of optical nonlinearities.***

In a nonlinear optical medium, optical nonlinearities may only arise from a fairly strong electric field source such as a laser. This is due to the electric field that binds an electron to an atom which is typically around  $10^{10} - 10^{11} \text{ V.m}^{-1}$ . The relationship between the intensity of a light beam and its electric field is given by the equation below:

$$I = \frac{1}{2} c \epsilon_0 n E^2$$

Where  $I$  is the intensity of the incoming beam of light,  $c$  the speed of light  $\epsilon_0$  is the electric permittivity of free space,  $n$  is the refractive index of the material, and  $E$  is the electric field that binds the electron to the atom. Assuming that the electric field strength is as specified above; the intensity of the incoming beam needed to create a non-linear effect would be of the order of  $10^{19} \text{ Wm}^{-2}$ . These types of intensities can only be achieved with very powerful lasers; however in reality optical non-linearities can be achieved at much lower intensity levels. Why is this true? It is because we can produce a sizeable macroscopic result by simply adding together all of the very small nonlinear effects from a very large number of atoms. This obviously will only work if the all nonlinear contributions from all of the atoms in the system are in phase with each other. This is known as phase matching (to be described later).

The microscopic non-linearity's can be explained in terms of the frequency of the incoming beam, i.e. whether it is close to one of the natural transition frequencies of the atoms (molecules) or not. If it is, then we are considering resonant nonlinear effects. If the frequency is not close to the natural transition frequency, the nonlinear effect may be described by non-resonant nonlinearities. Non-resonant nonlinearities can be explained by the classical oscillator model by introducing anharmonic terms in the description of the motion of an electron from the atom with the incoming beam of light, whereas the resonant nonlinearities must be described through the use quantum models.

To describe the more common non-resonant nonlinearity effects one must first describe the effect of the simple dipole oscillator model for an atom in an externally polarized electric field  $E$ . This model may be used to describe the frequency dependence of the refractive index and absorption coefficient. This will provide a simple explanation for the dispersion of the refractive index in optical materials, and subsequent nonlinear activity.

The electric field of the light wave induces forced oscillations of the atomic dipoles through the driving forces exerted on the electrons of the atom. In the atomic oscillator model we do assume that the mass of the nucleus is much greater than that of the electron  $m_N \gg m_0$  which allows us to largely ignore the motion of the nucleus. The displacement  $x$  of the electrons may then be described from the equation of motion:

$$m_0 \frac{d^2x}{dt^2} + m_0 \gamma \frac{dx}{dt} + m_0 \omega_0^2 x = -eE$$

Where  $\gamma$  is the damping rate,  $e$  is the magnitude of the electric charge of the electron,  $E$  is the electric field of the light wave, and  $\omega_0$  is the natural resonant frequency of the oscillator. The terms on the left hand side of the equation represent the acceleration, the damping and the restoring force respectively. The damping term is modeled by a frictional force which is proportional to the velocity and impedes the motion. The right hand side of the equation is the driving force due to the AC electric field of the light wave.

To further describe the interaction of the atom with the light wave an equation for  $E$  must then be derived, to describe the frequency dependence, amplitude and the phase of the incoming light beam and its subsequent time dependence, this may be seen below:

$$E(t) = E_0 \Re(\exp(-i\omega - \phi))$$

Where  $E_0$  is the amplitude of the wave,  $\phi$  is the phase of the light, and  $\omega$  is the frequency of the wave. To then find solutions to the equation of motion above, we must then look for solutions of the following from:

$$x(t) = X_0 \Re(\exp(-i\omega t - \phi'))$$

Where  $X_0$  and  $\phi'$  are the amplitude and phase of the oscillations respectively. The above two equations may then be substituted into the equation of motion to find solutions for  $X_0$

$$-m_0\omega^2 X_0 e^{-i\omega t} - im_0\gamma\omega X_0 e^{-i\omega t} + m_0\omega^2 X_0 e^{-i\omega t} = -eE_0 e^{-i\omega t}$$

This can then be solved for  $X_0$  by eliminating the  $e^{-i\omega t}$  term.

$$X_0 = \frac{-eE_0/m_0}{\omega_0^2 - \omega^2 - i\gamma\omega}$$

We may now use this expression to give the resonant contribution to the macroscopic polarization (dipole moment per unit volume) of the medium. Therefore if  $N$  is the number of atoms per unit volume, the resonant polarization may be given by:

$$P_{resonant} = Np$$

Where  $p$  is the time varying dipole moment for an atom.

$$P_{resonant} = -Nex$$

We may then substitute the values of  $X_0$  in for the  $x$  term giving:

$$P_{resonant} = \frac{Ne^2}{m_0} \frac{1}{(\omega_0^2 - \omega^2 - i\gamma\omega)} E$$

This equation then gives us an indication that the magnitude of the dipole is very small unless the frequencies are close to resonance with the natural frequency of the oscillator.

To begin to relate this to the nonlinear effect we must understand that the materials properties are related to and may be described through the real and imaginary parts of the dielectric constant  $\epsilon_r$ . The dielectric constant is derived from the polarization  $P$  of the medium according to the following equation:

$$D = \epsilon_0 E + P = \epsilon_0 \epsilon_r E$$

In linear optics it is assumed that  $P$  depends linearly on the electric field  $E$  of the light wave, and so may be described as

$$P = \epsilon_0 \chi E$$

Where  $\chi$  is the electric susceptibility tensor. Through the combination of the above two equations a relationship between the dielectric constant and the electric susceptibility may be derived:

$$\epsilon_r = 1 + \chi$$

In non-linear optics the relationship between  $E$  and  $P$  is more general than that described for a linear system. We consider a system where the nonlinear medium is parallel to the polarization of the electric field so that we do not need to consider the vector nature of  $P$  and  $E$ . The polarization of  $P$  is split into the linear ( $P^{(1)}$ ) and non linear responses ( $P^{(n)}$ ).

$$P^{nonlinear} = P^{(1)} + P^{(2)} + P^{(3)} + \dots$$

The relationship to now describe the nonlinear electric susceptibility may be described as follows

$$P^{nonlinear} = \epsilon_0 \chi^{nonlinear} E = \epsilon_0 (\chi^{(1)} E + \chi^{(2)} E^2 + \chi^{(3)} E^3 + \dots)$$

Then as in the linear expression the equations may be related to the dielectric constant

$$\epsilon_r^{nonlinear} = 1 + \chi^{(1)} + \chi^{(2)} E + \chi^{(3)} E^2 + \dots$$

This dielectric relationship is important to describe as it shows that the dielectric constant is dependent on the electric field through the nonlinear susceptibilities. In addition, since the optical power is proportional to  $E^2$  this means that  $\epsilon_r$  is also dependent on the optical power. Therefore the properties such as the refractive index and the absorption coefficient become power dependant in nonlinear materials.

It should also be noted that since nonlinear crystals are not always cubic crystal systems it is important to define the nonlinear response (the direction in which the electric field is applied) through the various well defined crystal axes. For instance two optical fields could be applied in different directions and then generate a third nonlinear polarization in a resultant direction.

$$P = P_0 + \chi_{ij}^{(1)} E_j + \chi_{ijk}^{(2)} E_j E_k + \chi_{ijkl}^{(3)} E_j E_k E_l + \dots$$

This may be described by the power series above. For example in the second order term  $\chi_{ijk}^{(2)}$  two electric polarizations are allowed  $E_j E_k$ . The terms  $i, j, k$  can be directly related to the Cartesian coordinates of the crystal  $x, y$  and  $z$ .

### 6.1.2 Non-resonant nonlinearities

Now that we've established the foundation of the polarization of the incoming electric field and its impact on the electric susceptibility of the crystals of various orders, we may begin to describe the first case of non-linearity in crystals namely non-resonant non-linear effects. As we described above, we may calculate the response of a medium to electromagnetic waves by assuming that it consists of oscillators with characteristic resonant frequencies. Furthermore it is generally assumed that the electrons are bound to atoms by harmonic restoring forces such that the displacement induced by the driving field of light is linear. However, as with most systems this will only be true for small displacements. When the displacements are larger due to the driving field of light being larger (due to a laser), the displacements will be large and hence we may no longer assume that the displacement varies linearly with the driving field.

We can therefore describe non-resonant non-linearity by assuming that an electron in an atom is bound in an anharmonic potential well of the form:

$$U(x) = \frac{1}{2}m_0\omega_0^2x^2 + \frac{1}{3}C_3m_0x^3 + \frac{1}{4}C_4m_0x^4 + \dots$$

Where  $\omega_0$  is the natural resonant frequency and  $x = 0$  corresponds to the equilibrium position of the electron. It is assumed that  $\omega_0^2 \gg C_3x \gg C_4x^2 \dots$ , which will justify the use of the power series, and that the harmonic term dominates for small displacements.

As described for the simple harmonic oscillator's equation of motion, we must be able to define the restoring force for displacements of the electrons from the equilibrium position which is given by (only concentrating on the second order effects):

$$F(x) = -\frac{dU}{dx} = -(m_0\omega_0^2x + m_0C_3x^2)$$

The relationship between  $C_3$  and  $\chi^{(2)}$  can be made by finding an approximate solution to the equation of motion of the electron which will be driven by an AC electric field at a frequency  $\omega$ . We now insert the restoring force as described above into the equation of motion defined for the harmonic oscillator:

$$m_0\frac{d^2x}{dt^2} + m_0\gamma\frac{dx}{dt} + m_0\omega_0^2x + m_0C_3x^2 = -eE$$

Where  $\gamma$  is the usual damping term  $E$  is obviously the driving field of the electromagnetic wave, which is assumed to have the following time and frequency dependence:

$$E(t) = \frac{1}{2}E_0(e^{i\omega t} + e^{-i\omega t})$$

It can be readily shown that the  $C_3$  term leads to a response at frequency  $2\omega$ , in addition to the one at  $\omega$ . The electron displacements time dependence may then be written as:

$$x(t) = \frac{1}{2}(X_1 e^{i\omega t} + X_2 e^{2i\omega t} + c.c.)$$

Where the term c.c. stands for complex conjugate, and we also assume that the nonlinear term is small so that  $X_1 \gg X_2$ . I will not go through the full derivation of these two terms, but merely quote them to show their dependence on both  $\omega$  and  $2\omega$ .

$$X_1 = \frac{-eE_0}{m_0} \frac{1}{(\omega_0^2 - \omega^2) + i\gamma\omega}$$

$$X_2 = \frac{-m_0 C_3 \epsilon_0^3 \chi(\omega)^2 \chi(2\omega)}{2N^3 e^4} E_0^2$$

As previously shown for the harmonic oscillator  $X_1$  dramatically increases as the frequency approaches the fundamental frequency of the crystal. This is known as this term is the linear response of the system and the polarization at frequency  $\omega$  may be described by:

$$P(\omega, t) = \epsilon_0 \chi(t) E(t)$$

The polarization at frequency  $2\omega$  may then be described with the incorporation of the  $X_2$  term:

$$P(2\omega, t) = -\frac{Ne}{2} (X_2 e^{2i\omega t} + c.c.)$$

Now in the case where we are considering the polarization at frequency  $2\omega$  is generated by nonlinear conversion of the driving field at frequency  $\omega$ ,  $P(2\omega, t)$  can also be described in terms of the electric susceptibility

$$P(2\omega, t) = \epsilon_0 \chi^{(2)} \left(\frac{1}{2}E_0\right)^2 (e^{2i\omega t} + c.c.)$$

And thus  $\chi^{(2)}$  may then be described as a final result of the non-resonant nonlinearity (full derivation not given)

$$\chi^{(2)} = \frac{m_0 C_3 \chi(\omega)^2 \chi(2\omega) \epsilon_0^2}{N^2 e^3}$$



This final result shows that the second-order non-resonant nonlinear susceptibility is directly proportional to the  $C_3$  term, the anharmonic term from the equation of motion. It should be noted that this equation is reasonably successful in predicting the dispersion of  $\chi^{(2)}$  in a large number of crystals. This has been found empirically to be due to the anharmonic constant  $C_3$  not varying by much from material to material.

### 6.1.3 Resonant nonlinearities

The off-resonant nonlinear effects discussed in the previous section are known as virtual processes. This means that there are no real transitions that take place because the photon energy does not coincide with any of the transition frequencies of the atoms. In the case of resonant nonlinearity's the laser frequency is in resonance with an atomic transition of the medium. In this case the atoms may now absorb photons and make transitions to the transition states as the wave propagates through the medium.

The absorption rate may be determined from the matrix element of the transition, and the density of states according to Fermi's golden rule (giving the transition rate between energy levels 1 and 2 in terms of the matrix element  $M_{12}$ ) as seen below:

$$W_{1 \rightarrow 2} = \frac{2\pi}{\hbar} |M_{12}|^2 \delta(E_2 - E_1 - h\nu)$$

This equation allows us to determine the absorption coefficient for a particular material at a particular frequency. However this does assume that the intensity of light on the sample is still small. If the intensity increases it will be found that the absorption coefficient becomes intensity dependent. Ultimately we know that the absorption coefficient is related to the dielectric constant, and therefore the dielectric constant is related to intensity. This implies that we are dealing with an optical nonlinearity.

To assess the absorption rate we must consider the three processes which occur when a laser propagates through the medium at the crystals resonant frequency  $E_2 - E_1 = h\nu$ . The first two processes are the absorption of a photon from  $E_1 \rightarrow E_2$  and the spontaneous emission from level 2 to level 1. There is also a third emission type called the stimulated emission from level 2 to 1. The Einstein  $A$  coefficients are able to describe the spontaneous emission process sufficiently, whereas Einstein's  $B$  coefficients' describe the absorption rate and the interrelated stimulated emission rate. If we consider that absorption is from level 1 to 2 and the stimulated emission is obviously then from level 2 to 1. We also then must assume that there are  $N_1$  atoms

per unit volume in level 1 and  $N_2$  atoms per unit volume in level 2. The total number of atoms per unit volume will then be described as  $N_0 = N_1 + N_2$ .

When the laser propagates through the medium at its resonant frequency, photons are absorbed, however are also added to the beam through the stimulated emission process. At low power the amount of photons added are generally not considered as there is almost a negligible effect, however when the laser power is higher, one must then consider the stimulated emission process, as the absorption transitions into the upper level will be substantial, and therefore also giving rise to a significant stimulated emission rate, which reduces the mediums overall absorption coefficient. To illustrate this concept one must consider an incremental beam slice of thickness  $dz$  passing through an area  $A$  of a cylinder. The number of photons absorbed per unit time may be described through

$$\delta N_{absorbed} = B_{12}N_1u_v \times Adz$$

Where  $B_{12}$  is the Einstein coefficient and  $u_v$  is the energy density of the beam at position  $z$ . The stimulated emission may similarly be described

$$\delta N_{stimulated} = B_{21}N_2u_v \times Adz$$

Therefore the total number of photons per unit time is then given by

$$\delta N_{total} = \delta N_{absorbed} - \delta N_{stimulated} = (B_{12}N_1 - B_{21}N_2)u_vAdz$$

This equation describes the net absorption rate. However to adequately relate this to the intensity of the incoming beam we must consider the intensity of the beam at position  $z$  to be  $I(z)$ , where the reduction in intensity as the beam propagates through the medium as the incremental slice  $dI$ . It can therefore be said

$$AdI = \delta N_{total} \times hv = -(B_{12}N_1 - B_{21}N_2)u_vhvAdz$$

We can further simplify this equation and relate it to the refractive index of the crystal and assuming that the two  $B$  coefficients are equal, we then obtain:

$$\frac{dI}{dz} = \frac{-(B_{12}N_1 - B_{21}N_2)h\nu n}{c}I = -\alpha I$$

This shows that the absorption coefficient is proportional to the population difference between the lower and upper energy levels. The decrease of the absorption with the laser power may be characterized through the introduction of the saturation intensity term  $I_s$ . The absorption

coefficient is found experimentally to depend on the intensity  $I$  according to the following relationship:

$$\alpha(I) = \frac{\alpha_0}{1 + I/I_s}$$

Where  $\alpha_0$  is the absorption measured in the linear regime when  $I \ll I_s$ . A medium which illustrated the behavior as outlined in the above equation is called a saturable absorber. Obviously the saturation intensity measured for a particular absorption line for a medium will also depend on the detailed rate constants for the transitions of the atoms, however at low intensity levels the above equations may be expanded to obtain:

$$\alpha(I) = \alpha_0 - \left(\frac{\alpha_0}{I_s}\right)I$$

This form of the equation shows that absorption decreases linearly with  $I$ . In addition, we know that  $\alpha$  is proportional to the imaginary part of  $\epsilon_r$  and  $I$  is proportional to  $E^2$  (as described in the first equation). Therefore  $\epsilon_r$  varies in proportion to  $E^2$  and as we know of the nonlinear relationship between these two quantities making this equivalent to a  $\chi^{(3)}$  process. Hence resonant nonlinearities are third order processes. This description of absorption related to intensity is based on the discrete energy levels of atoms. In a material with inter-band absorption it is better to base the approach based on Pauli's exclusion principle. For further derivation using this approach see (Fox M, 2008), we merely used this expression to adequately describe resonant non-linearity's.

#### **6.1.4 Phase matching and optical birefringence (briefly)**

As will be described later with chromophore systems, nonlinear effects are generally small, and therefore a long length of nonlinear medium is needed to obtain useful nonlinear conversion efficiency. In addition, to then obtain a quantifiable result all of the nonlinear waves generated in the medium must be identical, so that as the wave fields are added together, and they do so coherently. When this condition has been achieved, we are in the regime known as phase matching. Due to the multiple frequencies being generated in a nonlinear crystal phase matching becomes a problem if the incident beam only propagates through the crystal parallel to the extraordinary axis. This is because the refractive index will be different for the incident beam  $\omega$  as it is for the frequency doubled beam  $2\omega$ , and therefore both beams exit the crystal out of phase from one another, causing destructive interference. If our non-linear crystal is biaxial, the

crystal may be oriented at an angle, that the refractive indices of the ordinary and extraordinary axes, cause the incident beam, and the frequency doubled beam to exit the crystal in phase so that ultimately the condition  $n^{2\omega} = n^\omega$  is met.

### 6.1.5 Symmetry conditions for second order effects

It should be noted that there is an additional constraint for second order non-linear optical process to occur. We must consider the systems crystal symmetry (or just symmetry in the case of polymer systems). I will not rigorously cover this section, but will describe the necessity of a noncentrosymmetric system to satisfy the condition for second order nonlinear effects to occur. In the simplest case, we consider a centrosymmetric crystal. Suppose a nonlinear polarization is generated in the crystal by using a single applied field  $E$ . The components of  $P^{(2)}$  is described below, with the consideration of a reversal in the direction of the electric field.

$$\begin{aligned} P_i^{(2)}(-E) &= \epsilon_0 \sum_{j,k} \chi_{ijk}^{(2)} (-E_j)(-E_k) \\ &= \epsilon_0 \sum_{j,k} \chi_{ijk}^{(2)} (E_j)(E_k) \\ &= P_i^{(2)}(+E) \end{aligned}$$

Since the crystal has inversion symmetry, we know that from Neumann's principle that we must get the same physical result by keeping the field in the original direction and inverting the crystal. In terms of the coordinate axes of the inverted crystal, all of the components of  $E$  and  $P^{(2)}$  change sign. Therefore for the inverted crystal we have:

$$-P_i^{(2)} = \epsilon_0 \sum_{j,k} \chi_{ijk}^{(2)} (-E_j)(-E_k)$$

The only way for this condition to be valid is for the  $\chi_{ijk}^{(2)} = 0$  for all permutations of  $i, j, k$ . Therefore we must conclude that second order nonlinear susceptibility of centrosymmetric crystals is zero. The same conclusion may be drawn in analysing the anharmonic potential of the harmonic oscillator for a centrosymmetric system the following condition should also be met  $U(x) = U(-x)$ . This implies that the physical properties of the crystal cannot alter on inverting the crystal. This means that the anharmonic term  $C_3 = 0$ , and therefore the  $\chi^{(2)}$  will also equal zero (from our earlier proof).

### 6.1.6 Brief literature survey of NLO hybrid materials

As we have now covered the background theory for nonlinear optics, we now describe some of the composite materials which are being currently researched for nlo susceptibility. To recap our theoretical findings, we now know that in the field of non-linear optics, a non-linear optical response of a material is induced by the charge displacement generated by an externally applied field. In the applied oscillatory field, electrons will oscillate at the applied frequency. At low field strengths the magnitude of the induced polarization is proportional to the applied field; however at high field strengths (when using lasers as an excitation source) the polarization will no longer be linear (Nye J. F, 1957). Industrially non-linear optical systems have been confined to inorganic non-centrosymmetric single crystals. Attempts over the past few decades has been on finding organic (chromophores), polymer composites and hybrid organic inorganic systems which would be able to surpass the performance of these inorganic systems in terms of optical response and robustness for practical application. We will first describe here the physical components necessary for NLO generation in these systems with our theoretical background in mind, and the parameters in which one may enhance, and or alter to give the desired response, specifically on a molecular and then a macroscopic or crystal level. As we have already covered the theory of non-linear optics I thought it pertinent to string together some practical examples from a very diverse and current field which highlights some of the research endeavors in the non-linear optical field.

In the case of organic chromophore molecules, we first consider the isolated molecule and its molecular dipole moment  $\mu$  which may be represented by the power series, as seen below:

$$\mu = \mu_0 + \alpha_{ij}E_j + \beta_{ijk}E_jE_k + \gamma_{ijkl}E_jE_kE_l + \dots$$

Where  $E$  is the applied electric field,  $\mu_0$  is the permanent dipole moment of the molecule,  $\alpha$  is the linear polarizability, and  $\beta$  and  $\gamma$  are the molecule's first and second hyperpolarizability factors, respectively (Innocenzi P and Lebeau B, 2005; Verbiest T, *et al*, 1997).

As shown on the macroscopic scale already the above equation strongly resembles the macroscopic materials dipole moment, which may also be described by a power series:

$$P = P_0 + \chi_{ij}^{(1)}E_j + \chi_{ijk}^{(2)}E_jE_k + \chi_{ijkl}^{(3)}E_jE_kE_l + \dots$$

where  $P_0$  is any permanent polarization of the material. A molecule will experience a non-linear response if its hyperpolarizability factors ( $\beta$  and  $\gamma$ ) are non zero. This may in turn allow the nonlinear terms  $\chi^{(2)}$  and  $\chi^{(3)}$  to be non-vanishing in the crystal, and therefore allow for the

crystal to have a non-linear response. However, in a macroscopic system to generate a non-vanishing  $\chi^{(2)}$  value, the space group of the crystal (material) must be non-centrosymmetric (polar) as previously described. Therefore the polarisable molecules must pack in a non-centrosymmetric crystal system (or arrangement in the case of polymers) for second order effects to occur. However, it should be noted that second-order effects may occur in the absence of a polarizable molecule; nevertheless molecular polarizability does substantially aid the second-order response from the crystal. Therefore second order effects may be described by  $\chi^{(2)}$  and  $\beta$  values, which may manifest through second harmonic generation (SHG), the Pockels effect, optical rectification, non-degenerate three wave mixing, and parametric oscillation. Several applications may be based on these effects, such as: self-frequency doubling lasers, light sources which are tunable by optical parametric oscillators (OPO) and optical switching at high temperatures. Third order non-linear effects described by  $\chi^{(3)}$  and  $\gamma$  are responsible for the dc-Kerr effect, third harmonic generation (THG), self focusing, optical limiting, stimulated Brillouin scattering and Raman scattering (Innocenzi P, and Lebeau B, 2005, Fox M, 2008).

To establish the factors influencing the  $\beta$  component of an isolated molecule in an applied electric field  $E$ , its value may be described as follows:

$$\beta(-2\omega, \omega, \omega) = \frac{3}{2\varepsilon_0 \hbar^2} \frac{\omega_{ge}^2 \Delta\mu_{ge} \mu_{ge}^2}{[(\hbar\omega_{ge})^2 - (\hbar\omega)^2][(\hbar\omega_{ge})^2 - (2\hbar\omega)^2]}$$

$$\beta(-2\omega, \omega, \omega) = \beta(0) \frac{\omega_{ge}^4}{[(\hbar\omega_{ge})^2 - (\hbar\omega)^2][(\hbar\omega_{ge})^2 - (2\hbar\omega)^2]}$$

where  $\hbar\omega_{ge}$  being the energy difference of the charge transfer between the ground and excited state,  $\hbar\omega$  the energy of the incident photon,  $\Delta\mu_{ge}$  the difference in the dipole moments of the ground and excited states and  $\mu_{ge}$  the transition dipole moment between the ground and excited states. It is clear from this equation that the hyperpolarizability will be enhanced when the fundamental excitation frequency  $\hbar\omega$  and or the doubled frequency  $2\hbar\omega$  are close to the molecules charge transfer absorption band. In addition,  $\beta(0)$  is an inherent property of the molecule, and is the relevant parameter in comparing the potential nonlinearity's of different molecules (Verbiest T, *et al*, 1997).

In the generation of second order effects, a subtle interplay exists between tuning of the hyperpolarizability of a molecule, whilst attempting to ensure that the molecule itself will crystallize in a non-centrosymmetric space group. Research for materials possessing strong hyperpolarizabilities and thus strong non-linear optical responses has given rise to numerous

sets of work (Giffard M, *et al*, 2005; references cited therein). Most of the work has however been focused on the inorganic compounds, KTP (Potassium Titanyl Phosphate) or neutral organic molecular compounds such as Urea and POM (3-methyl-4-nitropyryne-1 oxide). Reports of organic inorganic systems are less common, but have been growing in literature more recently (Bi W, *et al*, 2008; Cariati E, *et al*, 2001; Goto T, *et al*, 2002; Guloy A. M, *et al*, 2001; Mercier N, *et al*, 2006; Papavassiliou G. C, *et al*, 1999; 1999b; 2001; 2003).

The macroscopic non-linear properties may be directly related to the molecular nonlinearity by local field factors, density of the molecules (chromophores) and an appropriate coordinate transformation. In addition to these factors the non-centrosymmetry requirement must be met for second order effects to occur on a macroscopic level. Several other requirements need to be met for a material to be of use in practical applications, such as phase matching possibilities (for SHG specifically), mechanical strength, thermal stability, and environmental stability (Verbiest T, *et al*, 1997). Due to chromophores high hyperpolarizabilities they have been incorporated in a variety of ways to generate macroscopic NLO properties. Probably one of the most widely used techniques is the incorporation of dipolar chromophores into a polymer host. This occurs through the simple dissolution of the respective chromophore and polymer (guest host scenario), covalently bonding the chromophore to the polymer backbone (side chain polymers) or by incorporating the chromophores into the backbone of the polymer, (main chain polymers). To then generate a noncentrosymmetric system for nlo effects to occur, the polymer and chromophores need to be poled, which is prepared though heating the polymer to its glass transition temperature in order to allow the material to become rubbery and amenable to deformation. A strong orienting electric field is subsequently applied to the field to polarize the chromophores. The material is then allowed to cool in the applied field freezing it in a polarized arrangement. Since the chromophores are oriented by their static dipole moment, the materials macroscopic nonlinearity is proportional to the chromophores  $\mu\beta$  value. The advantage of this method is the solution processability of these polymer systems into thin films which is compatible for use in the semiconducting industry (Verbiest T, *et al*, 1997). The only disadvantage with this approach is the thermodynamically unstable solid state system. Over time the chromophores in the polymer relax and the material loses its polarization and becomes centrosymmetric and subsequently losses its NLO ability (Burland D. M, *et al*, 1994; Marks T. J and Ratner M. A, 1995). Crosslinking and using polymers with a high glass transition temperatures have also been attempted to hinder the relaxation process. The poled polymer approach has matured sufficiently to be of use in the electro-optic market. However the development of polymer systems for SHG applications has been less successful, mainly due to

absorption losses, phase matching problems, and low non-linearity's (Innocenzi P, and Lebeau B).

Another approach has been to arrange NLO chromophores into Langmuir-Blodgett films. The advantage of this process is its ability to better align the dipole moments of the chromophores as well as having a higher chromophore density. However, the disadvantage of the LB films is the low optical quality of the films due to micro domain formation; the films are extremely fragile and have a low consistency in NLO response over time. However, some very good responses from these films have shown cause for further research. A related approach is the generation of self assembled super-lattices by covalently bonding different layers of the superlattice, thereby solving the problem of fragile films. Since each layer of the superlattice involves a chemical reaction. The question still remains as to its ability to generate sufficiently thick layers with the desired optical quality.

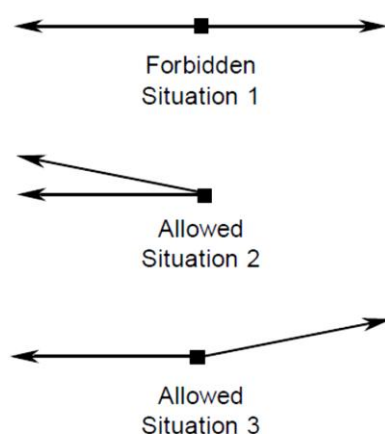
The last "hybrid" approach is the generation of single crystals. Single crystals themselves solve many of the abovementioned problems, such as phase matching which is achieved through optical birefringence type I and II (critical and non-critical phase matching), providing a high degree of ordering, a large concentration of chromophores per unit volume, as well as a stable structure. However, the inherent problem with single crystals is the fabrication of high quality crystals which is often a painstaking and a time consuming procedure. Moreover, is the problem of crystallizing the non-linear chromophores, and or the necessary elements, into a non-centrosymmetric spacegroup.

Recently Giffard M, *et al*, 2005 attempted to solve the noncentrosymmetric crystallization problem through the co-crystallization of anionic thiolate molecules and related anionic species with either of the chiral cationic amines of (1R, 2S)-ephedrine or (R)- $\alpha$ -methylbenzyl amine. It is expected from theoretical models that, with a comparable noncentrosymmetric structure, organic anions will possess much higher intrinsic polarizabilities than neutral molecules. After calculating the high theoretical polarizabilities of the anions having narrowed down the potential anionic molecular candidates the experimental hurdle arose with the crystallization step. Although crystallization in the noncentrosymmetric space group was no longer an issue (Situation 1, scheme 6.1), two other situations could arise with respect to the alignment of the anions  $\beta$  tensor, which can be represented by the vector situation as seen in scheme 6.1 below. Situation 3 is the most desirable, where the neighbouring molecules  $\beta$  tensor is almost fully aligned with itself. However, situation 2 is also symmetry allowed where almost complete cancellation of the neighbouring molecules  $\beta$  tensor can occur. In such cases the NLO response



practically, will lead to a very small, if any, observable second order NLO effect (Giffard M, *et al*, 2005).

An additional question arose as to why there was a lack of NLO response from thiolate anions that crystallized in situation 3 however still suffered from a reduced response from the predicted values. Giffard postulated that the further reduction in nlo response was due to the incomplete dissociation of the (acidic) S-H hydrogen bond to the (basic) N-H, alternatively this effect could be explained from the presence of a hydrogen bonding interaction from the cationic amine to the anionic thiolate reducing the anionic charge to a partial value.



**Scheme 6.1:** The  $\beta$  tensor vector possibilities of neighbouring polarizable molecules (Giffard M, *et al*, 2005).

Further developments in this field have made use of the highly efficient chromophore (SHG) organic cation (trans-4-[4-dimethylamino-styryl]-1-methylpyridinium), DAMS<sup>+</sup> which has been reported to form 1D chains with lead iodide and dimethyl sulphoxide i.e. (DAMS)PbI<sub>3</sub>.2DMSO which crystallized in the noncentrosymmetric space group *Ic* (Guloy A. M, *et al*, 2001). Due to the ability of the lead halide systems to readily form 1D wires in the presence of a bulky cation and excess halide acid, it was thought that the use of the low dimensional nature of lead iodide would template (DAMS) into a polarized configuration. Moreover the 1D wires themselves are highly polarisable down one of the crystallographic directions, and it was hypothesized that this ability may further enhance the SHG response of the crystal. Subsequent experimentation showed that the (DAMS)PbI<sub>3</sub>.2DMSO crystal displayed a SHG response 15 times greater than that of KTP (potassium tantalum phosphate) when probed at 1390nm (Guloy A. M, *et al*, 2001). However it was also reported that when the crystal was probed at 1032nm, the 532nm SHG response also displayed a luminescence peak at 620nm (Guloy A. M, *et al*, 2001). Since the direct gap absorption from the wires should only occur around 380nm (Nagami A, *et al*, 1996) the reported red luminescence response should be due to a charge transfer mechanism

occurring from the wires to the spacers or originate from the STE response as are experienced in these wires (Fujisawa J and Tajima N, 2005). The 532nm excitation generated from the SHG response should be sufficient to populate the LUMO of the organic cation with the electrons from the valence band of the wires, and hence display a luminescence response at 620nm (however this was not reported in the paper, but the red colour of the crystal, and the short intermolecular distances of  $\sim 3.4\text{\AA}$  of DAMS molecules does suggest that this should be the case (Guloy A. M, *et al*, 2001)). Other investigations of the halogen substituted (DAMS)PbBr<sub>3</sub> SHG response was also reported (Papavassiliou G. C, *et al*, 2003). This compound also displayed the red luminescence with the 532nm SHG response. Interestingly the Bromide analogue crystallized in a centrosymmetric space group *I2/a* and still displayed a large SHG response (value not quoted). This is thought to be due to the large anisotropic effect of the 1D wires over the centre of inversion generated by the organic cation (Papavassiliou G. C, *et al*, 2003).

Lastly (C10)PbI<sub>4</sub> and (C6)PbI<sub>4</sub> 2D quantum wells have been probed for resonant third order non linearity's (Xu C. Q, *et al*, 1991; Kondo T, *et al*, 1998). The  $\chi^{(3)}(-3\omega, \omega, \omega, \omega)$  of a highly oriented film of (C10)PbI<sub>4</sub> displayed a large (THG) three photon resonance at  $1.53\mu\text{m}$  (considering the  $E_g = 2.43\text{eV}$ ,  $511.8\text{nm}$ ). This was caused from the lowest energy exciton which is known to have a large oscillator strength and sharp well defined emission profile. It was also surmised that since both  $\chi^{(3)}(-3\omega, \omega, \omega, \omega)$  and  $\chi^{(3)}(-\omega, \omega, \omega, -\omega)$  follow the same transition rule, a resonance enhancement due to the lowest energy exciton can also be expected for  $\chi^{(3)}(-\omega, \omega, \omega, -\omega)$  for (C10)PbI<sub>4</sub>. Moreover the magnitude of the  $\chi^{(3)}(-3\omega, \omega, \omega, \omega)$  reaches a very large value of  $0.7 \times 10^{-9}\text{esu}$  at incoming beam  $1.53\mu\text{m}$ ,  $\text{THG} = 511\text{nm}$ , which is comparable to the largest reported value of organic materials with one-dimensional structures. The result was reported to be very promising suggesting that the lead halide quantum well structures are very promising as nonlinear optical materials (Xu C. Q, *et al*, 1991). The  $\chi^{(3)}(-\omega, \omega, \omega, -\omega)$  was also investigated for (C6)PbI<sub>4</sub> where the nonlinear optical susceptibility was recorded as  $1.6 \times 10^{-6}\text{esu}$  also measured at the lowest exciton resonance (measured at 8K). Kondo T, *et al*, 1998 further commented that because the excitons are stable at room temperature, large nonlinear optical responses are therefore also expected at room temperature, and hence remain a class of materials with promising resonant nonlinear optical potential.

## 6.2 Introduction:

Our studies have focused on the synthesis, crystallization, structural investigations, as well as temperature dependent luminescence responses of the 1D and 2D noncentrosymmetric metal

iodide systems. This work was initial explorative test work in order to assess the validity for further investigations into the NLO properties of these materials. Therefore this work is presented in light of the potential properties that these materials possess for future work to potentially continue. This after a theoretical basis and brief literature survey has now been established for the generation of optical nonlinearities (second or third order) in crystalline and or polymeric hybrid materials.

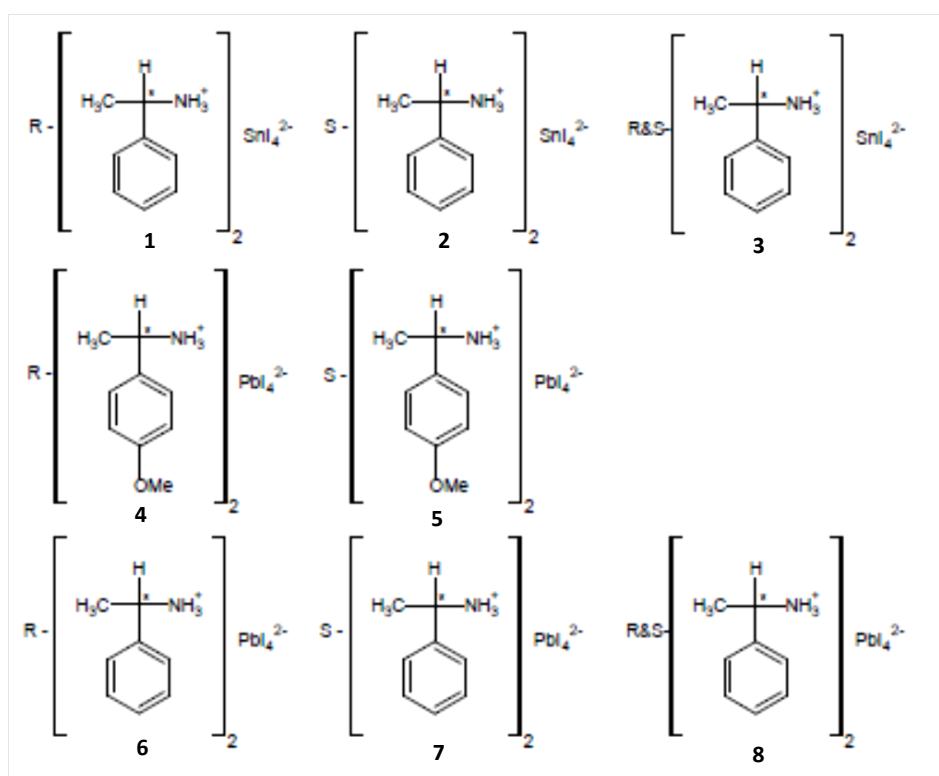
In order to generate the noncentrosymmetric crystal systems needed for second order effects to occur, we used chiral amine templates, much like Giffard M, *et al*, 2005, to produce 12 different compounds. The templates investigated were all similar, and were only marginally modified to promote secondary interactions, to alter crystal symmetry, and perhaps alter the inorganic's dimensionality. In addition, we investigated both enantiomer amines, as well as their racemates, however not all of the racemate crystal structures formed. The following templates produced eight 2D <100> single layer quantum wells (scheme 6.2): R, S, R&S - PhMetNH<sub>3</sub> producing (A)<sub>2</sub>MI<sub>4</sub> where M = Sn (**1-3**) and Pb (**7-8**) where the Pb structures have been previously published by (Billing D. G, 2002; Billing D. G, Lemmerer A, 2006e). And R, S - MeOPhMetNH<sub>3</sub> which we were only able to produce the lead compounds (A)<sub>2</sub>PbI<sub>4</sub> (**4** and **5**). The remaining enantiomer templates (R, S - PhEtNH<sub>3</sub>) produced four 1D ribbons, (A)MI<sub>3</sub> where M = Sn and Pb compounds **9 - 12** respectively. Both sets of 1D systems displayed the characteristic self trapped exciton (STE) emission known for these systems (Chapter 5, Nagami A, *et al*, 1996; Fukumoto T, *et al*, 2000; Azuma J, *et al*, 2002a; Akimoto I, *et al*, 2004; Tanaka K, *et al*, 2005b; Wang S, *et al*, 1995; Mousdis G. A, *et al*, 1998).

One of the core ideas behind the analysis of these compounds was to characterize each compound's crystal structure to assess possible structure to optical property relationships; this was achieved through investigating the luminescence emission's temperature dependence. This in itself had a threefold purpose, firstly, we could ascertain if the main excitonic emission behaved as expected, and may be mapped according to Varshni's model which illustrates a band gap decrease in a material with increasing temperature (Damak T, *et al*, 2009; Cheng C, Yan H, 2009; Gilliland G. D, 1997). Secondly, the *FWHM* of the emission peaks which would give an indication of the exciton lattice coupling contribution with temperature (Damak T, *et al*, 2009; Li T, *et al*, 1992). Any secondary peaks present in the emission could then be classed using the above two techniques, and an initial assessment of an emission being part of the excitonic fine structure (Ema K, *et al*, 2006), or as being an impurity based emission, where the exciton is trapped at an impurity/defect centre before radiatively recombining (Ishihara T, *et al*, 1990;

Hong X, *et al*, 1992; Kitazawa N, *et al*, 2010; Kitazawa N, Watanabe Y, 2010b). We measured the luminescence responses of both enantiomer crystals in all cases, which assisted in the final assignment of which emissions were sample dependant, and which emissions are inherent properties of the crystalline material.

Here we present the previously unknown crystal structures of compounds **1-5** along with the structures of the previously published compounds **6-8** used for structural comparison. An initial structure to optical property comparison with the 2D systems will be completed, as well as a brief structural description and discussion. This is followed by a discussion of the variable temperature photoluminescence of the 2D lead compounds only. Due to the nature of the emissions from the 1D compounds their structure and optical properties will be discussed together as a separate section at the end of this chapter.

### 6.2.1 Results and discussion (2D)



**Scheme 6.2** Polymeric schemes of the chiral crystal structures and respective racemate structures of compounds **1-8**.

**Table 6.1:** Crystal structure data of compounds **1-5**, and their respective phases. Structures at both 173K and 243K are reported even if no phase transition was observed. Experiments were carried out with Mo  $K\alpha$  radiation using a CCD area detector diffractometer. Integration, *Bruker XPREP* (Bruker, 2005). H-atom parameters were constrained.

	<b>1(a)</b>	<b>1(b)</b>	<b>2(a)</b>	<b>2(b)</b>	<b>3(a)</b>
Crystal data					
Chemical formula	2(R-C <sub>8</sub> H <sub>12</sub> N)·I <sub>4</sub> Sn	2(R-C <sub>8</sub> H <sub>12</sub> N)·I <sub>4</sub> Sn	2(S-C <sub>8</sub> H <sub>12</sub> N)·I <sub>4</sub> Sn	2(S-C <sub>8</sub> H <sub>12</sub> N)·I <sub>4</sub> Sn	2(C <sub>8</sub> H <sub>12</sub> N)·I <sub>4</sub> Sn
$M_r$	870.66	870.66	870.66	870.66	870.66
Crystal system, space group	Orthorhombic, $P2_12_12_1$	Orthorhombic, $P2_12_12_1$	Orthorhombic, $P2_12_12_1$	Orthorhombic, $P2_12_12_1$	Orthorhombic, $Pnma$
Temperature (K)	173	243	173	243	173
$a, b, c$ (Å)	8.8448 (4), 9.2821 (4), 28.5464 (13)	8.9069 (14), 9.3572 (14), 28.730 (4)	8.8549 (3), 9.2789 (2), 28.5401 (9)	8.922 (2), 9.369 (2), 28.769 (8)	8.7324 (2), 28.5705 (8), 9.3481 (3)
$\alpha, \beta, \gamma$ (°)	90, 90, 90	90, 90, 90	90, 90, 90	90, 90, 90	90, 90, 90
$V$ (Å <sup>3</sup> )	2343.61 (18)	2394.4 (6)	2344.96 (12)	2404.7 (11)	2332.25 (11)
$Z$	4	4	4	4	4
$\mu$ (mm <sup>-1</sup> )	6.36	6.23	6.36	6.20	6.39
Crystal size (mm)	0.44 × 0.09 × 0.01	0.74 × 0.36 × 0.04	0.43 × 0.06 × 0.004	0.62 × 0.22 × 0.02	0.33 × 0.05 × 0.04
Data collection					
$T_{\min}, T_{\max}$	0.235, 0.831	0.090, 0.781	0.242, 0.778	0.084, 0.779	0.378, 0.804
No. of measured, independent and observed [ $I > 2\sigma(I)$ ] reflections	22578, 5665, 4308	25593, 5787, 4841	21582, 5655, 3742	14971, 5804, 3837	20878, 2873, 2107
$R_{\text{int}}$	0.073	0.109	0.076	0.102	0.074
Refinement					
$R[F^2 > 2\sigma(F^2)], wR(F^2), S$	0.033, 0.061, 0.91	0.032, 0.077, 1.09	0.036, 0.054, 0.83	0.050, 0.119, 0.96	0.028, 0.048, 0.88
No. of reflections	5665	5787	5655	5804	2873
No. of parameters	210	208	208	208	109
No. of restraints	0	0	0	0	0
$\Delta_{\text{max}}, \Delta_{\text{min}}$ (e Å <sup>-3</sup> )	0.92, -0.82	0.69, -1.53	0.89, -1.18	1.31, -1.69	1.32, -1.36
Absolute structure	Flack H D (1983), Acta Cryst. A39, 876-881	Flack H D (1983), Acta Cryst. A39, 876-881	Flack H D (1983), Acta Cryst. A39, 876-881	Flack H D (1983), Acta Cryst. A39, 876-881	—
Flack parameter	0.02 (5)	-0.01 (4)	-0.09 (5)	0.01 (8)	—

Computer programs: Bruker *APEX2*, Bruker *SMART*, Bruker *SAINT*, *SHELXS97* (Sheldrick, 2008), *SHELXL97* (Sheldrick, 2008).

	3(b)	4(a)	4(b)	5(a)	5(b)
Crystal data					
Chemical formula	2(C <sub>8</sub> H <sub>12</sub> N)·I <sub>4</sub> Sn	I <sub>4</sub> Pb·2(R-C <sub>9</sub> H <sub>14</sub> NO)	I <sub>4</sub> Pb·2(R-C <sub>9</sub> H <sub>14</sub> NO)	I <sub>4</sub> Pb·2(S-C <sub>9</sub> H <sub>14</sub> NO)	I <sub>4</sub> Pb·2(S-C <sub>9</sub> H <sub>14</sub> NO)
<i>M<sub>r</sub></i>	870.66	1019.21	1019.21	1019.21	1019.21
Crystal system, space group	Orthorhombic, <i>Pnma</i>	Monoclinic, <i>P2<sub>1</sub></i>	Monoclinic, <i>P2<sub>1</sub></i>	Monoclinic, <i>P2<sub>1</sub></i>	Monoclinic, <i>P2<sub>1</sub></i>
Temperature (K)	243	173	243	173	243
<i>a</i> , <i>b</i> , <i>c</i> (Å)	8.8187 (19), 28.783 (6), 9.436 (2)	9.1530 (5), 8.7172 (5), 17.2804 (10)	9.1530 (5), 8.7172 (5), 17.2804 (10)	9.1250 (2), 8.6968 (2), 17.2301 (4)	9.1600 (2), 8.7185 (2), 17.2832 (4)
$\alpha$ , $\beta$ , $\gamma$ (°)	90, 90, 90	90, 103.481 (3), 90	90, 103.481 (3), 90	90, 103.407 (1), 90	90, 103.467 (1), 90
<i>V</i> (Å <sup>3</sup> )	2395.2 (9)	1340.79 (13)	1340.79 (13)	1330.09 (5)	1342.31 (5)
<i>Z</i>	4	2	2	2	2
$\mu$ (mm <sup>-1</sup> )	6.22	10.91	10.91	11.00	10.90
Crystal size (mm)	0.44 × 0.14 × 0.1	0.76 × 0.09 × 0.07	0.75 × 0.1 × 0.07	0.37 × 0.08 × 0.03	0.37 × 0.08 × 0.03
Data collection					
<i>T<sub>min</sub></i> , <i>T<sub>max</sub></i>	0.212, 0.550	0.044, 0.520	0.045, 0.511	0.106, 0.720	0.107, 0.736
No. of measured, independent and observed [ <i>I</i> > 2σ( <i>I</i> )] reflections	10421, 2944, 2156	12959, 5430, 5273	14931, 6255, 5822	19985, 6174, 5690	15883, 6273, 5556
<i>R<sub>int</sub></i>	0.083	0.026	0.043	0.029	0.030
Refinement					
<i>R</i> [ <i>F</i> <sup>2</sup> > 2σ( <i>F</i> <sup>2</sup> )], <i>wR</i> ( <i>F</i> <sup>2</sup> ), <i>S</i>	0.039, 0.095, 1.05	0.037, 0.094, 1.10	0.043, 0.110, 1.04	0.019, 0.032, 0.84	0.024, 0.043, 0.90
No. of reflections	2944	5430	6255	6174	6273
No. of parameters	109	251	251	251	250
No. of restraints	0	1	1	1	1
$\Delta_{\text{max}}$ , $\Delta_{\text{min}}$ (e Å <sup>-3</sup> )	1.10, -1.47	6.54, -1.90	4.93, -2.56	1.19, -0.63	1.64, -0.51
Absolute structure	—	Flack H D (1983), Acta Cryst. A39, 876-881	Flack H D (1983), Acta Cryst. A39, 876-881	Flack H D (1983), Acta Cryst. A39, 876-881	Flack H D (1983), Acta Cryst. A39, 876-881
Flack parameter	—	0.084 (8)	0.133 (7)	0.005 (3)	0.009 (4)
Computer programs: Bruker <i>APEX2</i> , Bruker <i>SMART</i> , Bruker <i>SAINT</i> , <i>SHELXS97</i> (Sheldrick, 2008), <i>SHELXL97</i> (Sheldrick, 2008).					

As has been well established in literature, and mentioned in chapter four, the parameters which influence the structural arrangements of the inorganic layers and which affects the electronic properties of the compound the most will briefly be redefined here for clarity. The 2D <100> orientated hybrids inorganic layers may adopt one of two arrangements within the crystal structure. The metal atom may be arranged directly over one another in each adjacent layer (eclipsed conformation), or they may be offset from one another giving the staggered arrangement. The position of the ammonium group's hydrogen bonding configuration may also be defined by the "box" which contains the ammonium group which is defined by the four equatorial (bridging) halogens and the four axial (terminal) halogens (Mitzi D. B, 1999; Billing D.

G, Lemmerer A, 2007). In projection view of the layers, the ammonium group is contained within the parallelogram (Figure 6.1) i.e. the void between the octahedra. The ammonium group may be found in the proximity of either the acute or obtuse angle of the parallelogram which further gives rise to the equilateral or right angled hydrogen bonding configuration respectively. The inorganic components undergo distortions depending on the position of the organic ammonium group within the parallelogram's void.

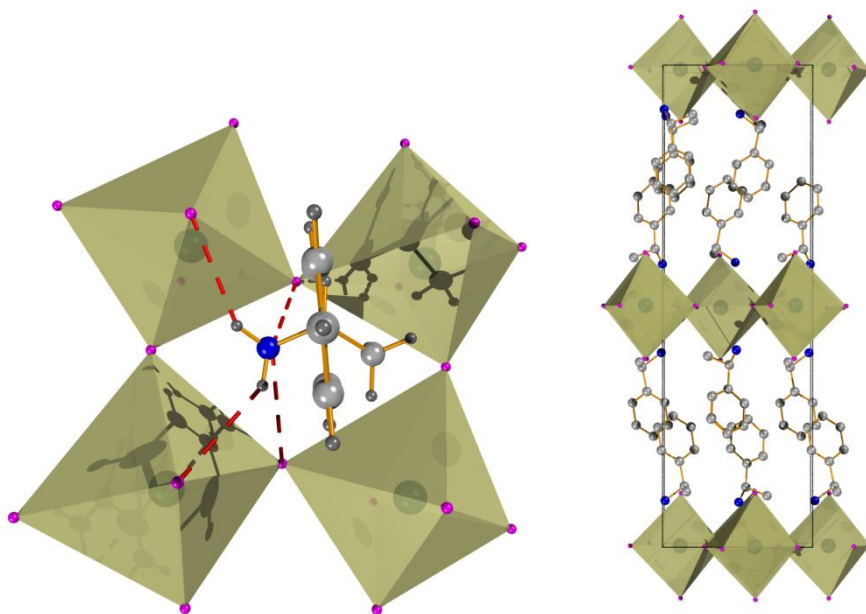


**Figure 6.1:** a) A view of compound **1** along the 001 axis. The hydrogen bonding of the compound adopts the acute right angled hydrogen bonding configuration within the void of the parallelogram formed between the four metal iodide octahedral. We notice for this compound an elongation of the sides of the parallelogram where the methyl group is positioned. This coincides with Sn-I<sub>eq</sub> bond length elongations (methyl position) and compressions (ammonium position) along the length of the obtuse angled side of the parallelogram. b) The view of **1** in its space group  $P2_12_12_1$  along the 010 axis showing the staggered arrangement of the inorganic layers.

Two main parameters are used to describe the octahedral type distortions. Firstly is the bridging angle, M-I-M which deviates from 180°, between adjacent octahedra, this angle describes the horizontal tilt of the octahedra in the plane of the metal atoms (in plane distortion). This angle has been shown to have the largest impact on the stereo-chemical activity of lead/tin's lone pair, and thus the band gap of the material (Mitzi D. B, 1996; Knutson J. L, *et al*, 2005). Secondly is the corrugation angle,  $\psi$  tilt angle (out of plane distortion), other wise known as the vertical tilt of the octahedra, which describes the deviation of the angle of the vector which passes through the axial halogens of the octahedra, perpendicular to the plane of the lead atoms (deviation

from 0°). These values have been summarized in tables 6.2 and 6.3 for lead and tin, and are compared with previously published compounds.

It should be noted that the enantiomer crystals having the R handed template **1**, **4** and **6** are isomorphous with **2**, **5** and **7** respectively, but have the opposite handedness S. Within the asymmetric unit of the crystal all of the chiral crystals have two full cations in the asymmetric unit, whereas in the racemate compounds only one full cation molecule is found in the asymmetric unit. The bond lengths and angles of the R handed crystals are therefore similar to those in their respective S handed crystals. Compounds **1-5** were structurally investigated at both 243K and 173K. This was because the tin compounds could not be studied at room temperature because of their oxidation/decomposition in air and hence the highest temperature that a stable nitrogen cryostream flow would reduce crystal decomposition was thought to be 243K. In addition, we wished to ensure no low temperature phase transitions occurred upon cooling. Our DSC experiments showed no phase transitions occurred from room temperature to 213K, (Appendix C).

Figure 6.1 shows a view of compound **1** along the 001 axis. The hydrogen bonding of the compound adopts the acute right angled hydrogen bonding configuration within the void of the parallelogram formed between the four metal iodide octahedral. This hydrogen bonding motif is adopted in all of the eight compounds studied, with a bifurcated hydrogen bond to the two bridging (axial) halogens (longer hydrogen bonds), and two separate hydrogen bonds to the two terminal (axial) halogens (shorter hydrogen bonds). The hydrogen bonding table may be found in table 6.5. We notice for compound **1** (and the remaining tin compounds) an elongation of the sides of the parallelogram where the methyl group is positioned. This coincides with Sn-I<sub>eq</sub> bond length elongations (methyl position) and compressions (ammonium position) along the length of the obtuse angled side of the parallelogram. The Sn-I bond length elongations are very large resulting in bond lengths of ~3.72Å and ~3.58Å for compound **1b** and **2b**, which also results in the opposite Sn-I<sub>eq</sub> compressions of ~2.96 Å and ~3.01 Å. Table 6.2 illustrates the structurally important parameters that influence the optical properties of the compounds (a decrease in temperature does show a decrease in octahedral distortion as seen in structures **1a** and **2a**). We also notice the optical results for compounds **1-3** have a largely red shifted room temperature PL emission of ~710nm (1.75eV) in comparison with the other reported compounds.



**Table 6.2:** Summary of excitonic emissions, and the relevant structural parameters for compounds **1-3**, which are compared with literature (references cited in the table), adapted from (Knutson J. L, *et al*, 2005).

Cation	OA exciton energy eV RT	PL RT	Sn-I- Sn (°)	In and out of plane distortion	eq/ax Sn-I bond length	Distortion of SnI <sub>6</sub> octahedon	Cation penetration	Reference
R- PhMetNH <sub>3</sub>		716, 1.73 4	153	13.3/4.31	3.296/3.150	0.247	0.504	This work
S- PhMetNH <sub>3</sub>		709, 1.75	153	13.4/4.28	3.297/3.151	0.247	0.507	This work
R&S- PhMetNH <sub>3</sub>		706, 1.75 8	153. 3	14.0/4.36	3.286/3.153	0.238	0.453	This work
C4	2.04, 607	625, 1.98 6	159. 3	19.4/6.4	3.136/3.160	0.011	0.76	Mitzi D. B, 1996
C10	2.13, 583	603, 2.05 8	155. 7	16.7/11.2	3.138/3.152	0.007	0.52	Xu, Z, Mitzi D. B, 2003d
PEA	2.093, 593	620, 2.00 2	156. 5	23.5/<1	3.136 / 3.161	0.012	0.57	Papavassillou
4-CIPEA	2.02, 615		157	22.9/<1	3.139/3.176	0.017	0.58	Mitzi D. B, et al, 2001b; Xu Z, et al, 2003b
4-FPEA	2.04, 609		156. 4	23.7/<1	3.135/3.181	0.020	0.56	Mitzi D. B, et al, 2001b; Xu Z, et al, 2003b
NEA	2.06, 602		156. 6	23.4/<1	3.152/3.204	0.023	0.58	Xu Z, et al, 2003b
3-FPEA	2.07, 599		154. 2	25.8/<1	3.136/3.207	0.033	0.57	Mitzi D. B, et al, 2001b; Xu Z, et al, 2003b
N5FPEA	2.11, 588		154. 5	25.5/<1	3.161/3.184	0.020	0.51	Xu Z, Mitzi D. B, 2003c
2-FPEA	2.11, 588		153. 3	26.7/<1	3.149/3.178	0.013	0.47	Mitzi D. B, et al, 2001b; Xu Z, et al, 2003b
2-CIPEA	2.12, 586		154. 8	25.2/<1	3.169/3.156	0.006	0.48	Mitzi D. B, et al, 2001b; Xu Z, et al, 2003b
5FPEA	2.17, 572		152. 4	27.6/<1	3.169/3.173	0.041	0.46	Xu Z, Mitzi D. B, 2003c
2-BrPEA	2.23, 557		148. 7	25.1/11.3	3.145/3.155	0.005	0.37	Mitzi D. B, et al, 2001b; Xu Z, et al, 2003b
2-CF <sub>3</sub> PEA	2.23, 556		149. 6	23.2/12.3	3.147/3.162	0.007	0.4	Knutson J. L, et al, 2005
1-PYREA	2.28, 545		144. 1	28.5/12.3	3.124/3.170	0.020	0.28	Xu Z, Mitzi D. B, 2003c
TMAEA	1.97, 630		166. 9	0.8/11.8	3.162/3.127	0.015	0.99/-1.22	Xu Z, et al, 2003a

PEA: Phenylethyl amine; NEA: 2-Napthalenethylamine; N5FPEA: A mixture of 2-Napthalenethylamine and pentafluorophenylethylamine; 5FPEA: pentafluorophenylethylamine; 1-PYREA: 1-Pyreneethylamine; TMAEA: 2-Trimethylammonioethylamine; XPEA: halogen substituted onto the respective position on the Phenylethyl amine ring.

If we continue to compare compounds **1-3** with the previously published compounds, we notice that most of the parameters investigated such as the in and out of plane distortions, the Sn-I-Sn bridging angle and cation penetration, are all within the range of the other compounds shown in table 6.2. The factor that affects the band gap the most has been shown to be the Sn-I-Sn

bridging angle, i.e. the closer this angle is to 180° the more red shifted the band gap (Xu Z, et al, 2003a).

**Table 6.3:** Summary of excitonic emissions, and the relevant structural parameters for the lead iodide compounds **4-8**, which are compared with work completed in chapter 4.

Cation	Exciton energy (nm, eV)	Pb-I-Pb (average d)	in-/out of plane distortion	eq/axial (Å) (average d)	Distortion of Pbl <sub>6</sub> octahedra (°)	Cation penetration (Å) (°)	Binding energy (meV)	FWHM Of PL emission	E0,ex (eV)
<b>C4 (77K)</b>	490, 2.53	149.24	15.40/12.92	3.195/3.170	0.0107	0.5323	300 (300 <sup>1</sup> )		
<b>C4 (RT)</b>	535, 2.32	155.07	12.47/5.78	3.181/3.203	0.0114	0.5893			
<b>C5 (77K)</b>	487, 2.55	150.22	14.86/12.83	3.199/3.174	0.0105	0.5775	320		
<b>C5 (RT)</b>	511, 2.43	153.68	13.17/12.59	3.196/3.172	0.0088	0.5915			
<b>C6 (77K)</b>	526.5, 2.35	155.13	12.47/5.68	3.166/3.207	0.0226	0.6035	330(361 <sup>2</sup> )		
<b>C6 (RT)</b>	536, 2.31	155.65	12.19/5.85	3.188/3.206	0.0076	0.6256			
<b>C7 (77K)</b>	487.5, 2.54	149.61	15.17/13.60	3.211/3.202	0.015	0.4889	330		
<b>C7 (RT)</b>	527, 2.35	154.99	12.51/5.75	3.176/3.214	0.0183	0.7432	-		
<b>HOC2 (77K)</b>	545, 2.28	159.09	10.44/13.30	3.224/3.174	0.0269	0.3625	-	15meV	
<b>BrC2 (77K)</b>	565, 2.19	174.38	2.86/2.08	3.244/3.159	0.0763	-0.3655	-	15meV	
<b>IC2 (77K)</b>	507, 2.44	147.24	16.37/15.31	3.212/3.169	0.0209	0.4508	-	20meV	
<b>IC3 (77K)</b>	504, 2.46	148.62	15.73/12.70	3.210/3.169	0.0183	0.4858	270	14meV	
<b>IC4 (77K)</b>	500, 2.48	147.05	16.51/12.06	3.191/3.184	0.0073	0.4885	250	18meV	
<b>IC5 (77K)</b>	527, 2.35	154.26	12.81/5.64	3.181/3.208	0.0133	0.5991	250	27meV	
<b>IC6 (77K)</b>	522, 2.38	161.08	9.49/9.94	3.240/3.170	0.0387	0.6309	260	17meV	
<b>R-PhMetNH<sub>3</sub> (77K)</b>	506, 2.452	153.60	11.80 (14.61)/5.39	3.292/3.192	0.067	0.49	-	32.7meV	2.4412
<b>S-PhMetNH<sub>3</sub> (77K)</b>	508, 2.444	153.56	11.76 (14.69)/6.02	3.286/3.183	0.070	0.5055	-	22.6meV	
<b>R&amp;S-PhMetNH<sub>3</sub> (77K)</b>	512, 2.425	155.43	12.29/8.70	3.292/3.190	0.051	0.473	-	45.9meV	2.4242
<b>R-MeOPhMetNH<sub>3</sub> (77K)</b>	501, 2.477	152.14	12.46 (15.41)/14.17	3.257/3.192	0.039	0.453	-	19meV	
<b>S-MeOPhMetNH<sub>3</sub> (77K)</b>	500, 2.481	152.16	12.40 (15.45)/14.14	3.248/3.184	0.039	0.459	-	13.9meV	

TMAEA produces the most ideal bridging angle of 166.9° with a respective excitonic absorption of 630nm (1.97eV). The compounds **1** and **2** display an averaged bridging angle of 153° with the racemic compound **3** displaying an averaged bridging angle of 153.3°. We do notice that the octahedral distortion factor for these three compounds 0.247 (**1&2**) and 0.238 (**3**) are largely

distorted in comparison with the most distorted previously published structure (0.04). Therefore we can attribute the large red shift to the large equatorial Sn-I bond length distortions found in **1-3**. Knutson J. L, *et al*, 2005 did show that equatorial Sn-I bond distortions effect the Sn  $P_x$  and  $P_y$  orbital's at the top of the valence band. The shorter Sn-I distances result in the destabilization of the top of the valence band because of the increased anti-bonding while the nonbonding crystal orbital's of the bottom of the conduction band are not really affected by the variations of the Sn-I bond distances. This results in a red shifted band gap.

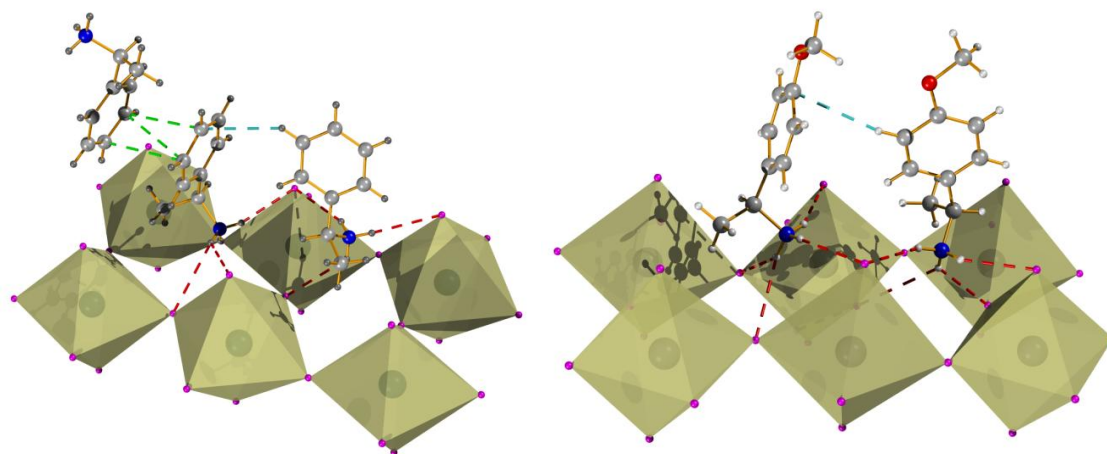


**Figure 6.2:** The weak interactions present in compound **7** (left) are representative of compounds **1-3** and **6-8** and compound **5b** (right) weak interactions, which is representative of compounds **4** and **5**.  $\pi - \pi$  interactions shown in green,  $\sigma - \pi$  interactions shown in light blue.

The large octahedral distortion experienced in the  $\text{SnI}_6$  octahedra however does not translate to the previously published lead iodide compounds (**6-8**) (Billing D. G, 2002; Billing D. G, Lemmerer A, 2006e) and the new structures of **4** and **5** containing the same functionality at the cationic end of the organic template as **1-3 6-8**, as seen from the bond lengths and angles tables of Tables 6.3 and 6.4. It should be noted that the racemic compound **3** does display marginally less distorted octahedra than its enantiomerically pure counterparts **1** and **2**, however experiences a marginally increased distortion in the bridging angle, and in and out of plane distortions. This same trend is observed with compound **8** showing a greater octahedral distortion than its enantiomer counterparts **6** and **7**. Nevertheless the racemic compounds overall are not that dissimilar from the enantiomerically pure compounds hence the similar optical emissions experienced. The most significant difference between the enantiomerically pure compounds **1** and **2** and the racemate compound **3** is the centrosymmetric orthorhombic space group  $Pnma$  where **1** and **2** crystallize in the chiral space group  $P2_12_12_1$ . Interestingly the lead iodide

racemate compound crystallizes in the monoclinic space group  $P2_1/a$ , where compounds **6** and **7** also crystallize in the chiral orthorhombic space group  $P2_12_12_1$  much like **1** and **2**. The centrosymmetric monoclinic unit cell of compound **8** causes the inorganic layers to now arrange in the eclipsed conformation, whereas compounds **1-3**, **6** and **7**'s orthorhombic unit cells arrange in the staggered arrangement as previously mentioned.

**Table 6.4:** Relevant inorganic bond lengths and angles and crystallographic data.

Compound	1a	1b	2a	2b	3a	3b	4a	4b	5a	5b	6	7	8
Chirality	R	R	S	S	R&S	R&S	R	R	S	S	R	S	R&S
Space group	$P2_12_12_1$	$P2_12_12_1$	$P2_12_12_1$	$P2_12_12_1$	$Pnma$	$Pnma$	$P2_1$	$P2_1$	$P2_1$	$P2_1$	$P2_12_12_1$	$P2_12_12_1$	$P2_1/a$
<i>a</i> (Å)	8.448 (4)	8.9069 (14)	8.8549 (3)	8.922 (2)	8.7324 (2)	8.8187 (19)	9.1530 (5)	9.1530 (5)	9.2150 (2)	9.1600 (2)	8.868 (5)	8.8531 (17)	8.7935 (11)
<i>b</i> (Å)	9.2821 (4)	9.3572 (14)	9.2789 (2)	9.369 (2)	28.570 5 (8)	28.783 (6)	8.7172 (5)	8.7172 (5)	8.6968 (2)	8.7185 (2)	9.247 (5)	9.2312 (18)	9.3913 (11)
<i>c</i> (Å)	28.546 4 (13)	28.730 (4)	28.540 1 (9)	28.769 (8)	9.3481 (3)	9.436 (2)	17.280 4 (10)	17.280 4 (10)	17.230 1 (4)	17.283 2 (4)	28.729 (5)	28.650 (6)	14.642 8 (18)
$\beta$ (°)	-	-	-	-	-	-	103.48 1 (3)	103.48 1 (3)	103.40 70 (10)	103.46 70 (10)	-	-	-
Vol (Å <sup>3</sup> )	2343.6 1	2394.4 6	2344.9 6	2404.8 1	2332.2 5	2395.1 3	1340.7 9	1340.7 9	1330.0 9	1342.3 1	2355.8 5	2341.4 1	1190.5 2
Temp (K)	173	243	173	243	173	243	173	243	173	243	173	173	293
M-I <sub>eq</sub>	2.9502 (5)	2.9612 (6)	2.9521 (5)	2.9669 (10)	2.9376 (6)	2.9525 (10)	3.2654 (8)	3.2625 (9)	3.2620 (3)	3.2655 (5)	3.190 (2)	3.1807 (7)	3.2609 (4)
M-I <sub>eq</sub>	2.9975 (5)	3.0090 (5)	2.9977 (5)	3.0122 (10)	3.0098 (6)	3.0259 (10)	3.2716 (7)	3.2680 (8)	3.2775 (3)	3.2691 (4)	3.344 (2)	3.3403 (7)	3.3226 (4)
M-I <sub>eq</sub>	3.6821 (5)	3.7207 (6)	3.6845 (5)	3.729 (1)	3.6584 (6)	3.705 (1)	3.2047 (9)	3.2003 (9)	3.1957 (4)	3.2005 (5)	3.346 (2)	3.3440 (1)	3.2609 (4)
M-I <sub>eq</sub>	3.5525 (5)	3.5829 (6)	3.5541 (5)	3.586 (1)	3.5395 (6)	3.580 (1)	3.2865 (7)	3.2858 (8)	3.2574 (4)	3.2889 (4)	3.346 (2)	3.2797 (7)	3.3226 (4)
M-I <sub>ax</sub>	3.1425 (11)	3.1564 (9)	3.1427 (15)	3.1610 (19)	3.1531 (3)	3.1710 (8)	3.2135 (6)	3.2048 (7)	3.2074 (3)	3.2087 (4)	3.212 (1)	3.200 (1)	3.1896 (5)
M-I <sub>ax</sub>	3.1574 (11)	3.1722 (9)	3.1577 (15)	3.1754 (19)	3.1531 (3)	3.1710 (8)	3.1707 (6)	3.1646 (7)	3.1609 (3)	3.1628 (4)	3.171 (1)	3.166 (1)	3.1896 (5)
I-M-I	177.63 (2)	177.51 (2)	177.54 (3)	177.49 (3)	176.25 (2)	176.53 (3)	175.43 (2)	175.53 (3)	178.22 1 (13)	178.26 4 (15)	177.94 (2)	177.93 (2)	180.00 (1)
I-M-I	177.43 (2)	177.54 (2)	177.53 (3)	177.63 (3)	178.77 (2)	178.54 (3)	178.28 (3)	178.32 (3)	175.29 5 (10)	175.36 6 (14)	175.07 (2)	174.90 (2)	180.00 (1)
I <sub>ax</sub> -M-I <sub>ax</sub>	171.34 7 (15)	171.31 5 (13)	171.35 0 (16)	171.29 (3)	171.32 2 (18)	171.27 (3)	167.03 (2)	166.93 (2)	166.92 8 (8)	166.81 0 (11)	167.72 (3)	167.48 (3)	180.00 (1)
M-I-M	153.39 (2)	153.10 (2)	153.27 (3)	153.07 (3)	152.02 (2)	152.58 (3)	149.17 (3)	149.64 (3)	149.10 6 (13)	149.51 2 (16)	156.41 (3)	156.62 (2)	155.43 (1)
M-I-M	152.67 (2)	153.59 (2)	152.70 (2)	153.52 (3)	154.55 (2)	154.59 (2)	155.09 (3)	155.44 (3)	155.19 4 (13)	155.50 4 (15)	150.78 (3)	150.62 (2)	155.43 (1)

The modification of the  $C_6H_5C^*HCH_3NH_3$  cation to include a OMe group in the para position, reduces the 2D inorganic organics' crystal symmetry in compounds **4** and **5** to a chiral monoclinic space group  $P2_1$  and experience eclipsed inorganic layers like the monoclinic racemic compound **8**. The introduction of the additional functionality also decreased the presence of the weak  $\pi - \pi$  interactions ranging from 3.3 – 3.4 Å present between the rings of **1-3**, and **6-8**, as seen in figure 6.2. Compounds **4** and **5** only possess the  $\sigma - \pi$  weak interactions which are present in all eight compounds ranging from 2.8 – 2.9 Å. Compounds **4** and **5** also experience a marginal

decrease in octahedral distortion when compared with **6** and **7**, otherwise the compounds bond lengths and angles are similar with **6-8**.

**Table 6.5:** The hydrogen bonding table of compounds **1-5**.

<i>D</i> —H... <i>A</i>	<i>D</i> —H (Å)	H... <i>A</i> (Å)	<i>D</i> ... <i>A</i> (Å)	<i>D</i> —H... <i>A</i> (°)
<b>1a</b>				
N1—H1A...I1	0.91	3.08	3.745 (7)	131.4
N1—H1A...I3 <sup>i</sup>	0.91	3.23	3.842 (7)	126.6
N1—H1B...I2	0.91	2.68	3.521 (8)	153.7
N1—H1C...I4 <sup>i</sup>	0.91	2.79	3.643 (8)	157.5
N2—H2A...I3	0.91	2.9	3.658 (8)	142.1
N2—H2B...I2	0.91	2.74	3.523 (9)	144.6
N2—H2C...I4 <sup>ii</sup>	0.91	2.91	3.715 (8)	148.6
N2—H2A...I1 <sup>ii</sup>	0.91	3.28	3.717 (8)	112.1
<b>1b</b>				
N1—H1A...I3 <sup>iii</sup>	0.9	3.28	3.910 (5)	129
N1—H1A...I4	0.9	3.14	3.782 (5)	130
N1—H1B...I2	0.9	2.68	3.531 (5)	157.2
N1—H1C...I1 <sup>iii</sup>	0.9	2.84	3.689 (6)	158.7
N2—H2A...I2 <sup>iv</sup>	0.9	2.84	3.542 (6)	135.8
N2—H2B...I1 <sup>v</sup>	0.9	3.01	3.751 (6)	140.6
N2—H2B...I4 <sup>v</sup>	0.9	3.2	3.741 (5)	120.8
N2—H2C...I3 <sup>iv</sup>	0.9	2.86	3.666 (5)	149.3
<b>2a</b>				
N1—H1A...I1	0.89	3.09	3.735 (8)	131.4
N1—H1A...I4 <sup>vi</sup>	0.89	3.24	3.848 (9)	127.3
N1—H1B...I3 <sup>vi</sup>	0.89	2.83	3.671 (8)	158.7
N1—H1C...I2	0.89	2.69	3.519 (9)	155.5
N2—H2A...I2	0.89	2.81	3.507 (9)	136.3
N2—H2B...I4	0.89	2.85	3.645 (9)	149
N2—H2B...I1	0.89	3.32	3.736 (9)	111.1
N2—H2C...I3 <sup>vii</sup>	0.89	2.99	3.723 (9)	141.4
N2—H2C...I1 <sup>vii</sup>	0.89	3.2	3.725 (9)	120.1
<b>2b</b>				
N1—H1A...I2	0.9	3.11	3.773 (11)	132
N1—H1A...I3 <sup>vi</sup>	0.9	3.28	3.887 (11)	126.7
N1—H1B...I4 <sup>vi</sup>	0.9	2.85	3.704 (11)	158.2
N2—H16A...I3 <sup>viii</sup>	0.9	2.91	3.677 (12)	144.2
N2—H16B...I4 <sup>ix</sup>	0.9	2.96	3.749 (12)	147.9
N2—H16B...I2 <sup>ix</sup>	0.9	3.29	3.754 (11)	114.3
N2—H16C...I1 <sup>viii</sup>	0.9	2.77	3.532 (11)	143.1
<b>3a</b>				
N1—H1A...I1	0.89	2.78	3.594 (4)	152.9
N1—H1B...I2	0.89	3	3.695 (4)	136.2
N1—H1B...I3 <sup>x</sup>	0.89	3.28	3.818 (4)	121.1
N1—H1C...I1 <sup>x</sup>	0.89	2.78	3.614 (3)	157.4

**3b**

N1—H1A...I2	0.90	3.08	3.724 (5)	129.8
N1—H1A...I1 <sup>xi</sup>	0.90	3.24	3.854 (6)	127.1
N1—H1B...I3	0.90	2.78	3.629 (6)	158.7
N1—H1C...I3 <sup>xi</sup>	0.90	2.79	3.656 (5)	161.1

**4a**

N1—H1A...I5 <sup>xii</sup>	0.91	2.77	3.629 (9)	157.7
N1—H1B...I3 <sup>xiii</sup>	0.91	3.14	3.809 (7)	132.2
N1—H1B...I2	0.91	3.11	3.738 (8)	128.1
N1—H1C...I4	0.91	2.68	3.533 (8)	156.1
N2—H2A...I3 <sup>xiv</sup>	0.91	3.11	3.706 (9)	125.3
N2—H2A...I2 <sup>xv</sup>	0.91	3.08	3.772 (9)	133.8
N2—H2B...I4 <sup>xvi</sup>	0.91	2.62	3.491 (10)	159.5
N2—H2C...I5 <sup>xv</sup>	0.91	2.83	3.702 (9)	160.6

**4b**

N1—H1A...I5 <sup>xii</sup>	0.89	2.78	3.619 (9)	158.7
N1—H1B...I3 <sup>xiii</sup>	0.89	3.12	3.820 (9)	137.4
N1—H1B...I2	0.89	3.19	3.761 (9)	123.7
N1—H1C...I4	0.89	2.69	3.542 (10)	160.1
N2—H2A...I3 <sup>xiv</sup>	0.89	3.05	3.722 (11)	134.2
N2—H2A...I2 <sup>xv</sup>	0.89	3.18	3.770 (10)	125.6
N2—H2B...I4 <sup>xvi</sup>	0.89	2.68	3.510 (11)	156.2
N2—H2C...I5 <sup>xv</sup>	0.89	2.87	3.691 (11)	155

**5a**

N1—H1A...I4 <sup>xv</sup>	0.91	2.66	3.517 (3)	156.2
N1—H1B...I3 <sup>xv</sup>	0.91	3.11	3.741 (3)	128.6
N1—H1B...I2 <sup>xvii</sup>	0.91	3.14	3.809 (3)	132.1
N1—H1C...I5 <sup>xvii</sup>	0.91	2.77	3.629 (4)	157.2
N2—H2A...I5	0.91	2.86	3.693 (3)	153.4
N2—H2B...I4 <sup>xviii</sup>	0.91	2.65	3.489 (4)	154
N2—H2C...I2 <sup>xviii</sup>	0.91	2.97	3.688 (3)	137
N2—H2C...I3	0.91	3.18	3.749 (3)	122.2

**5b**

N1—H1A...I4 <sup>xix</sup>	0.89	2.68	3.520 (4)	157.5
N1—H1B...I2 <sup>xx</sup>	0.89	3.13	3.752 (5)	128.4
N1—H1B...I3 <sup>xx</sup>	0.89	3.18	3.839 (5)	132.7
N1—H1C...I5 <sup>xxi</sup>	0.89	2.8	3.641 (5)	158
N2—H2A...I5	0.89	2.92	3.710 (5)	149.6
N2—H2B...I4 <sup>xxii</sup>	0.89	2.7	3.506 (5)	150.8
N2—H2C...I3 <sup>xxii</sup>	0.89	2.95	3.700 (6)	142.5
N2—H2C...I2	0.89	3.27	3.765 (5)	117.4

Symmetry code(s): (i)  $x+1/2, -y+3/2, -z$ ; (ii)  $x-1/2, -y+3/2, -z$ ; (iii)  $x-1/2, -y+1/2, -z+2$ ; (iv)  $-x+2, y+1/2, -z+3/2$ ; (v)  $-x+3/2, -y+1, z-1/2$ ; (vi)  $x+1/2, -y+3/2, -z+2$ ; (vii)  $x-1/2, -y+3/2, -z+2$ ; (viii)  $-x, y-1/2, -z+3/2$ ; (ix)  $-x+1/2, -y+1, z-1/2$ ; (x)  $x+1/2, y, -z+3/2$ ; (xi)  $x-1/2, y, -z+3/2$ ; (xii)  $-x+2, y-1/2, -z+1$ ; (xiii)  $x-1, y, z$ ; (xiv)  $x-2, y, z-1$ ; (xv)  $x-1, y, z-1$ ; (xvi)  $-x+1, y-1/2, -z$ ; (xvii)  $-x+1, y+1/2, -z+1$ ; (xviii)  $-x+2, y+1/2, -z+2$ ; (xix)  $x+1, y, z+1$ ; (xx)  $x, y, z+1$ ; (xxi)  $-x+2, y+1/2, -z+1$ ; (xxii)  $-x+1, y+1/2, -z$ .

### 6.2.2 Variable temperature photoluminescence of compounds 4-8:

Before describing the photoluminescence data we need to describe Varshni's empirical model. This enables us to map the band gap drift with temperature, in our case the excitonic emission, which is described by the equation below (Damak T, *et al*, 2009; Cheng C, Yan H, 2009; Gilliland G. D, 1997):

$$E_{ex}(T) = E_{0,ex} - \frac{\alpha T^2}{\beta + T}$$

Where  $E_{ex}$  is the exciton energy gap,  $E_{0,ex}$  is the excitonic energy gap at 0K,  $\alpha$  is responsible for the linear shift of  $E_{ex}(T)$ , and the value  $\beta$  is near the Debye temperature ( $\theta_D$ ) of the material. Ultimately  $\alpha$  is of the order of  $10^{-4}T$ , and the Debye temperature ranges anywhere from 50 – 1000K for elements across the periodic table (Singleton J, 2008). Although  $\beta$  is not exactly the Debye temperature, it is necessary to understand the origin of it, which is described by the following functional relationship:

$$\theta_D = \frac{hc_s}{2k_B} \sqrt{\frac{6N}{\pi V}}$$

Where  $c_s$  is the speed of sound through the medium,  $h$  is Planck's constant,  $k_B$  is Boltzmann's constant,  $N$  is the number of atoms present in the unit cell, and  $V$  is the volume of the unit cell. It should be noted that this is a simple expression for a cubic system, which is to simply illustrate the relationship of the materials physical properties to the Debye temperature. The Debye temperature is unique to each material, and is largely used in the description of electron phonon relationships. This relationship allows us to see that the Varshni model is material dependant (Singleton J, 2008, Fox M, 2008). In four of the five lead iodide compounds investigated, the main excitonic emission peak, follow Varshni's model within the measured temperature range (the details will be described later) (figure 6.3 – 6.5). The empirical fitting parameters of  $\alpha$  and  $\beta$  may be seen in table 6.6. A quadratic polynomial was fit to the experimental data, in order to obtain the  $E_{0,ex}$  value for the fitting of Varshni's model. Reasonable fits to the experimental data were found with comparable  $\alpha$  and  $\beta$  values, with those obtained for the similar (F-PEA)<sub>2</sub>PbI<sub>4</sub> compound investigated by (Damak T, *et al*, 2009). It should also be noted that deviations from Varshni's model which lead to S-shaped temperature variations from the model are indicative of exciton localization on defects or impurities within the crystal lattice (Damak T, *et al*, 2009). In addition, it should be noted that the variation of the  $\beta$  values specifically for such similar

compounds (table 6.6), does show the empirical nature of this model, and indicates secondary effects are at play.

**Table 6.6:** The refined  $\alpha$  and  $\beta$  values for the empirical parameters of Varshni's model, for the 2D lead iodide compounds.

Compound ((A) <sub>2</sub> PbI <sub>4</sub> )	$\alpha$	$\beta$	Comment	Reference
R-PhMtNH <sub>3</sub> (77K)	2.80E-04	780		This work
S-PhMtNH <sub>3</sub> (77K)	-	-	Impurity/defect not mapped	This work
R&S-PhMtNH <sub>3</sub> (77K)	3.19E-04	780		This work
R-MeOPhMtNH <sub>3</sub> (77K)	2.94E-04	500		This work
S-MeOPhMtNH <sub>3</sub> (77K)	3.26E-04	500		This work
F-PhC <sub>2</sub> H <sub>4</sub> NH <sub>3</sub>	8.00E-04	858		Damak T, <i>et al</i> , 2009

In addition to the description required to map the drift in exciton emission with increasing temperature, we wished to understand the emissions *FWHM* broadening with temperature. To understand this phenomenon we must consider the exciton-phonon coupling, which we described for the 1D system in chapter 5.1. Exciton-phonon interactions are known to increase the PL line width, and may be described through the following relationship (Damak T, *et al*, 2009; Li T, *et al*, 1992):

$$\Gamma_{ex}(T) = \Gamma_{0,ex} + A_{ac}T + \frac{B_{op}}{\exp\left(\frac{\hbar\omega_{op}}{kT}\right) - 1}$$

Where  $\Gamma_{0,ex}$  is the line width at 0K,  $A_{ac}$  is the coupling strength of acoustic phonons to the excitons via deformation potential and piezoelectric interactions. The term  $B_{op}$  is the parameter describing the interaction between the polar optical phonons of energy  $\hbar\omega_{op}$  and the excitons. From the above equation we notice that the linear contribution to the PL linewidth broadening is predominantly due to the acoustical phonon contribution. From all of the experiments conducted on the 2D systems (figure 6.3-6.5; 6.8), we notice a linear increase in linewidth with increasing temperature within the measured temperature range (77K-293K).

We therefore must assign the increase in linewidth as due to the acoustical phonon contribution, however further experimentation would need to be completed to fully quantify this contribution. Moreover, the second term should not be neglected, the contribution of the optical phonon's should be very low due to the vibrations of Pb-I modes to be in the 10 – 30 $cm^{-1}$  area. This does imply that the energy contribution from  $\frac{\hbar\omega_{op}}{kT} < 1$ , within our measured temperature range. As stated from Damak T, *et al*, 2009 this relationship should then lead to a



“quasilinear asymptotic contribution” to the PL line broadening with increasing temperature. It should also be noted that CdTe/Cd<sub>1-x</sub>Zn<sub>x</sub>Te strained single layer quantum wells also display a similar linewidth increases with temperature within the above mentioned temperature range, however as the temperature continues to decrease, the linewidth becomes constant at temperatures less than 60K (Li T, *et al*, 1992).

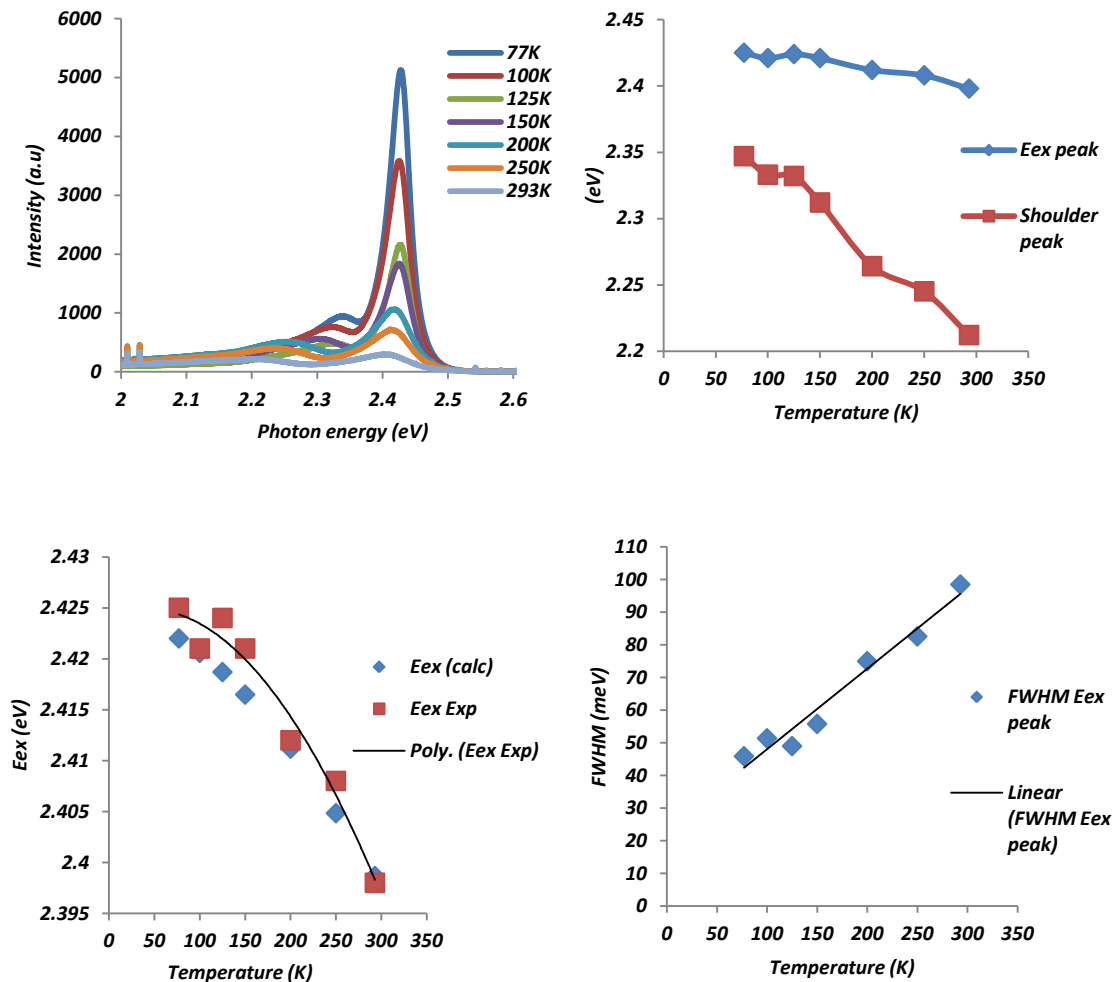


**Figure 6.3:** The variable temperature photoluminescence of (R&S-PhMetNH<sub>3</sub>)<sub>2</sub>PbI<sub>4</sub>. Two peaks are present at low temperature, the main excitonic emission, and a shoulder peak which displays much greater temperature dependence than the excitonic emission. The excitonic shift with temperature may be modeled using the varshni model as described in the test, with a  $\beta$  value of 780 and an alpha value of  $3.19 \times 10^{-4}$ . The FWHM of the main Eex peak has also been plotted against temperature and displays the expected liner increase with temperature (although not shown here the shoulder peak displays a similar linear increase with temperature). It should be noted that the main excitonic peak was fitted with a Gaussian peak profile with a minor amount of lorentzian character, while the shoulder peak showed a more lorentzian peak profile.

It should be noted that although the *FWHM* of the main excitonic emission is linear between each compound the straight line fits are however different from compound to compound suggesting that this parameter is to some degree sample dependant (as we will now explain).

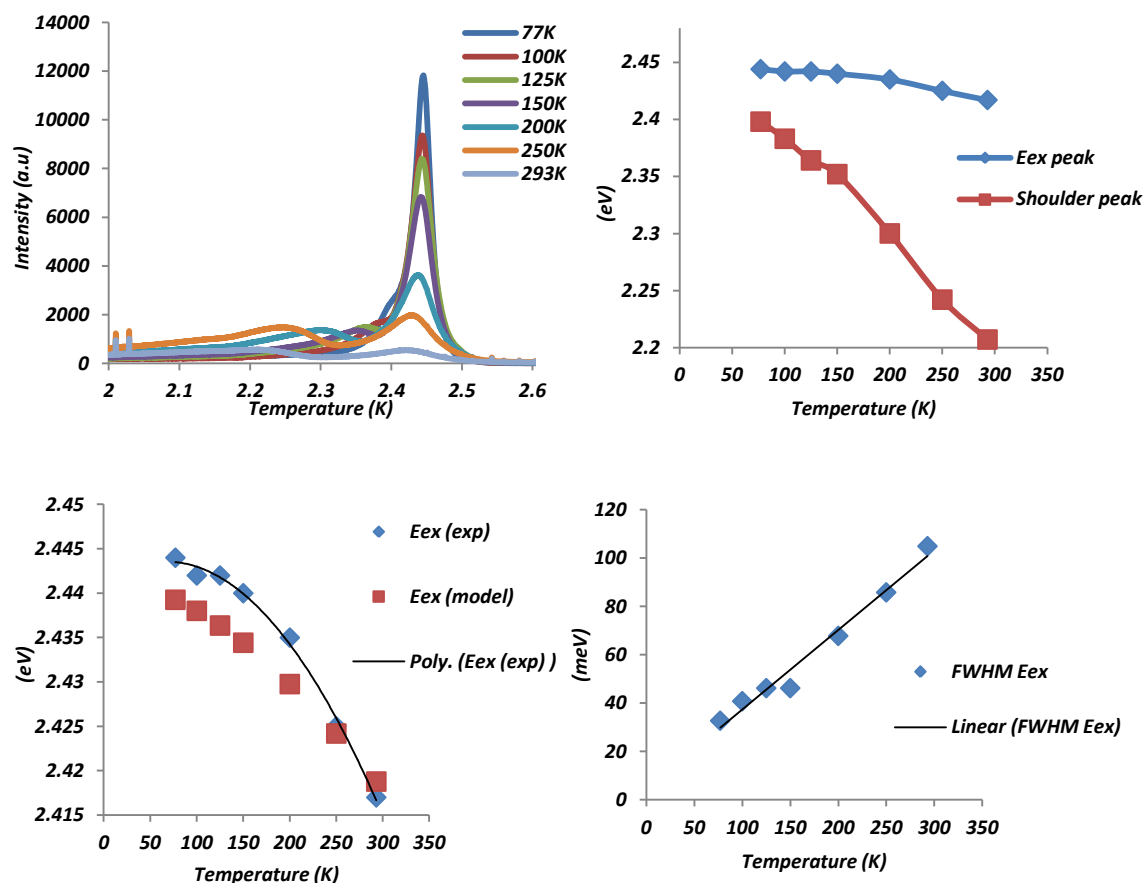


**Figure 6.4:** The variable temperature photoluminescence of (R-PhMetNH<sub>3</sub>)<sub>2</sub>PbI<sub>4</sub>. Two peaks are present at low temperature, the main excitonic emission, and a shoulder peak which displays much greater temperature dependence than the excitonic emission. The excitonic shift with temperature may be modeled using the varshni model as described in the test, with a  $\beta$  value of 780 and an alpha value of  $2.8 \times 10^{-4}$ . The FWHM has also been plotted against temperature and displays the expected liner increase with temperature (although not shown here the shoulder peak displays the same linear increase with temperature). It should be noted that the main excitonic peak was fitted with a Gaussian peak profile with a minor amount of lorentzian character, while the shoulder peak showed a more lorentzian peak profile.

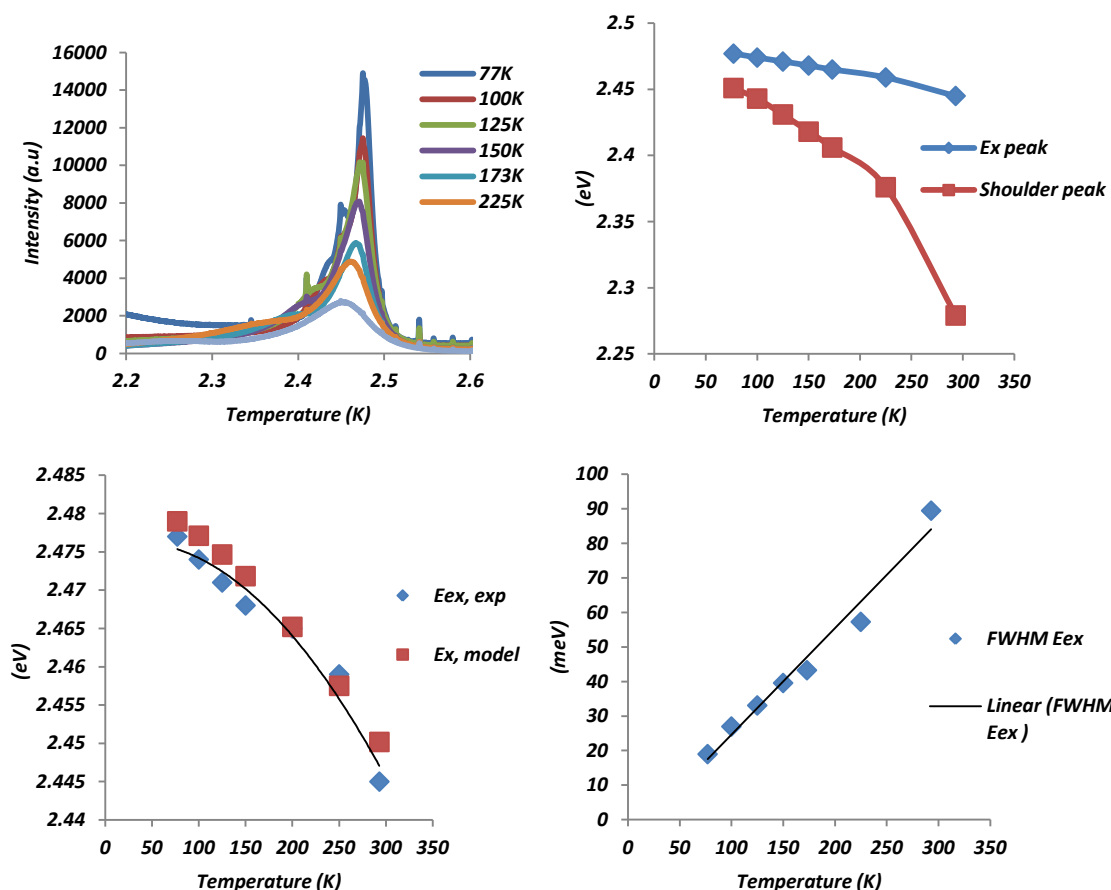


**Figure 6.5:** The variable temperature photoluminescence of  $(\text{R-MeOPhMtNH}_3)_2\text{PbI}_4$ . Two peaks are present at low temperature, the main excitonic emission, and a shoulder peak which displays much greater temperature dependence than the excitonic emission. The excitonic shift with temperature may be modeled using the Varshni model as described in the test, with a  $\beta$  value of 500 and an alpha value of  $2.94 \times 10^{-4}$ . The FWHM has also been plotted against temperature and displays the expected linear increase with temperature. It should be noted that the main excitonic peak was fitted with a Gaussian peak profile with a minor amount of lorentzian character, while the shoulder peak showed a more lorentzian peak profile.

### ***Fine structure or defect/impurity luminescence?***

We have successfully established that the main excitonic emission follows the expected behavior reported in the literature for similar compounds. However the question still remains as to the origin of the shoulder peak prevalent in the five 2D lead iodide compounds emission profiles. Would it not be reasonable to attribute this shoulder peak, with comparable energy differences between the main excitonic peak for each structure (figure 6.7), is due to the excitonic fine structure inherent for lead iodide 2D quantum wells? Or is it? We look to the theoretical descriptions found in literature to help ascertain the origin of this peak.

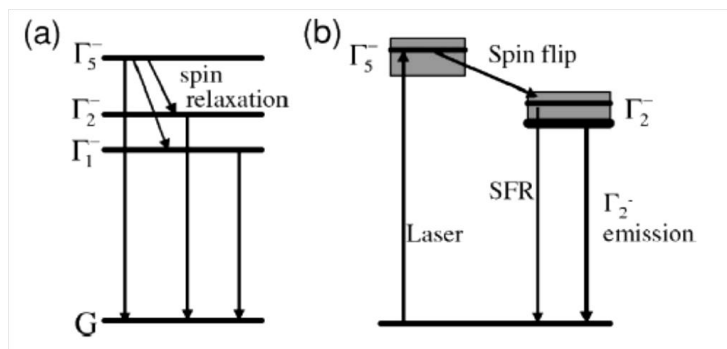


**Figure 6.6:** The 1s exciton energy level has a fine structure which is split into three fine structure energy levels. These are the purely triplet state  $\Gamma_1^-$ , the triplet dominant  $\Gamma_2^-$  and the singlet dominant state  $\Gamma_5^-$ . As may be seen in a)  $\Gamma_5^-$  decays into  $\Gamma_2^-$  and  $\Gamma_1^-$  through a spin relaxation, as well as a spin flip decay b) as may be seen in c). (Ema K, *et al*, 2006)

Recently (Ema K, *et al*, 2006) investigated the luminescence fine structure of  $(C4)_2PbBr_4$  where the 1s exciton energy level displayed an excitonic fine structure split into three energy levels. These states have been described as the purely triplet  $\Gamma_1^-$ , the triplet dominant  $\Gamma_2^-$  and the singlet dominant  $\Gamma_5^-$  states. In this compound the  $\Gamma_5^-$  state has recently been shown to also display exciton polariton coupling, however this is of less importance to the assignment of the fine structure (Tamaki R, *et al*, 2008). The mechanism of the excitonic fine structure decay may be seen in figure 6.6 a) i.e.  $\Gamma_5^-$  the singlet dominant decays into  $\Gamma_2^-$  and  $\Gamma_1^-$  through a spin relaxation process, as well as a spin flip decay (figure 6.6 b)). The main excitonic emission has been shown to be the triplet dominant  $\Gamma_2^-$  emission line and to some degree the  $\Gamma_1^-$  state. This is due to the different time decays of the respective emission lines. The  $\Gamma_5^-$  state has a much stronger emission however was shown to have a decay time of the order of picoseconds whereas the  $\Gamma_1^-$  and  $\Gamma_2^-$  states have decay times on the order of nano-seconds. The  $\Gamma_5^-$  spin state relaxes into the triplet dominant  $\Gamma_2^-$  state hence the slower decay kinetics and therefore becoming the dominant emission line.

Ema K, *et al*, 2006 performed further experiments in order to ascertain if the energy dependence of the fine structure emissions through resonant PL and SFRS experiments. They showed that the  $\Gamma_5^-$  state is energy dependant, i.e. it may shift its emission line depending on the photon energy input, whereas the  $\Gamma_1^-$  and  $\Gamma_2^-$  states were largely independent of the variance of input photon energy, due to their dependence on the spin relaxation of the  $\Gamma_5^-$  state.

Further variable temperature PL investigations into the longer chain length derivatives (C5, C7, C12) of  $PbBr_4$  also displayed the excitonic fine structure described by Ema K, *et al*, 2006,

however, it only becomes evident below 40K for C4, C5 and C7, and below 80K for C12. In addition it should be noted that C7 displayed very little fine structure at low temperature in comparison with the shorter chain derivatives. The luminescence emissions at these temperatures displayed the characteristic intersystem (spin relaxation) crossing between the singlet and triplet states upon cooling, where the varying of the alkyl chain length appears to affect this process, however no real explanation as to why this occurred was proposed (Kitazawa N, *et al*, 2010).

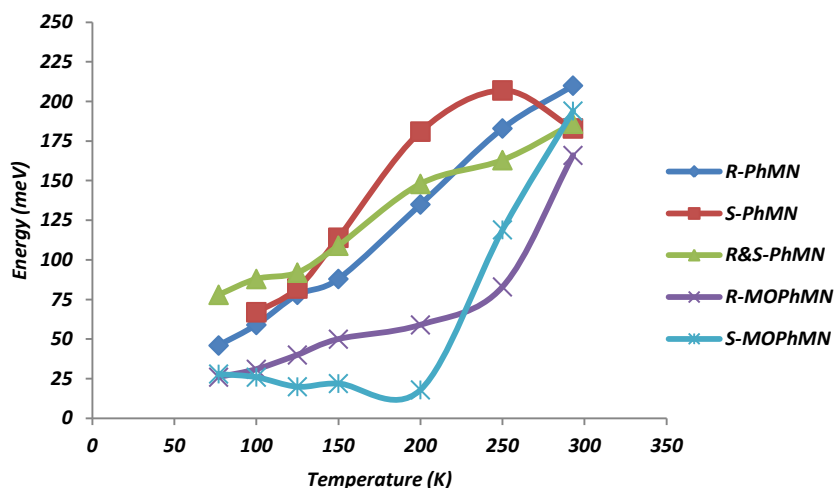


**Figure 6.7:** The energy difference between the main sharp excitonic peak, and the shoulder peak present in the emission spectrum. The shoulder peak positions have been plotted for each compound.

Further investigation of the lead bromide 2D hybrids with the templates ( $\text{PhC}_n\text{H}_{2n}\text{NH}_3$ ) where  $n = 1, 2, 3$ , and 4 investigated the effect of the organic template on the fine structure of the 2D excitons at low temperature (Kitazawa N, *et al*, 2010b). It was found that the  $n = 4$  analogue displayed very little fine structure splitting at low temperature whereas the  $n = 1, 2$  and 3 compounds displayed almost identical splitting. The authors concluded that the triplet states are formed at the interface of the organic and inorganic components. It was also proposed that the triplet states have been shown to be dependant of the carbon chain length (Kitazawa N, *et al*, 2010; 2010b). This in itself may be due to the fact that some organic templates increase the crystallinity of the compound (i.e. grow better crystals), which has been shown to have a direct impact on the increase of PL intensity the compound displays. Lastly Kitazawa N, 2010b also found that the energy difference between the singlet and triplet states of  $(\text{PhC1NH}_3)_2\text{PbBr}_4$  at 6K is of the order of 50meV, which becomes evident below 40 – 80K.

Although further experimentation is needed to ascertain the origin of the shoulder peak in our lead iodide compounds the data and literature does suggest that the decreasing emission energy

dependence with increasing temperature implies a thermal population of this state with increasing temperature, in similar fashion to the main excitonic emission (Varshni model). Furthermore the shoulder peak can be polynomially least squares fit just as the main excitonic emission. Therefore, initially one could suggest that the main excitonic emission is due to the triplet dominant  $\Gamma_2^-$  emission whereas the low energy shoulder peak should be due to the purely triplet state  $\Gamma_1^-$ .

This is in contrast to the initial suggestions from Ishihara T, *et al*, 1990, who investigated the low temperature PL (4K) of  $(\text{Cn})_2\text{PbI}_4$  where  $n = 4, 6, 8, 9, 10, 12$ . Only the compound  $\text{C10PbI}_4$  was investigated under variable temperature conditions, and Ishihara suggested that the shoulder peaks origin (similar position to the currently investigated compounds) is simply to be due to an impurity/defect centre and may be written off as a sample dependent phenomenon. The “impurity” band of  $\text{C10PbI}_4$  only becomes visible at 200K, however this is due to an the excitonic energy shift and 293K – 200K, which is due to two consecutive phase transitions in that temperature range (Lemmerer A, Billing D. G, 2011). Our latest data suggests that both mechanisms (fine structure and impurity) may be at play.

There is validity to both fine structure and impurity/arguments as we may see from figure 6.7 above, that the energy difference's between the main excitonic and shoulder peak is fairly consistent between R-PhMN, and R&S-PhMN supporting the fine structure argument. However the enantiomer crystals of R-MOPhMN and S-PhMN supports the shoulder peak having impurity band characteristics, as these two crystals should be mathematically identical in their VT-PL emissions with their enantiomer counterparts. The impurity/fine structure argument is further supported by the VT-Luminescence of S-PhMN shown in figure 6.8.

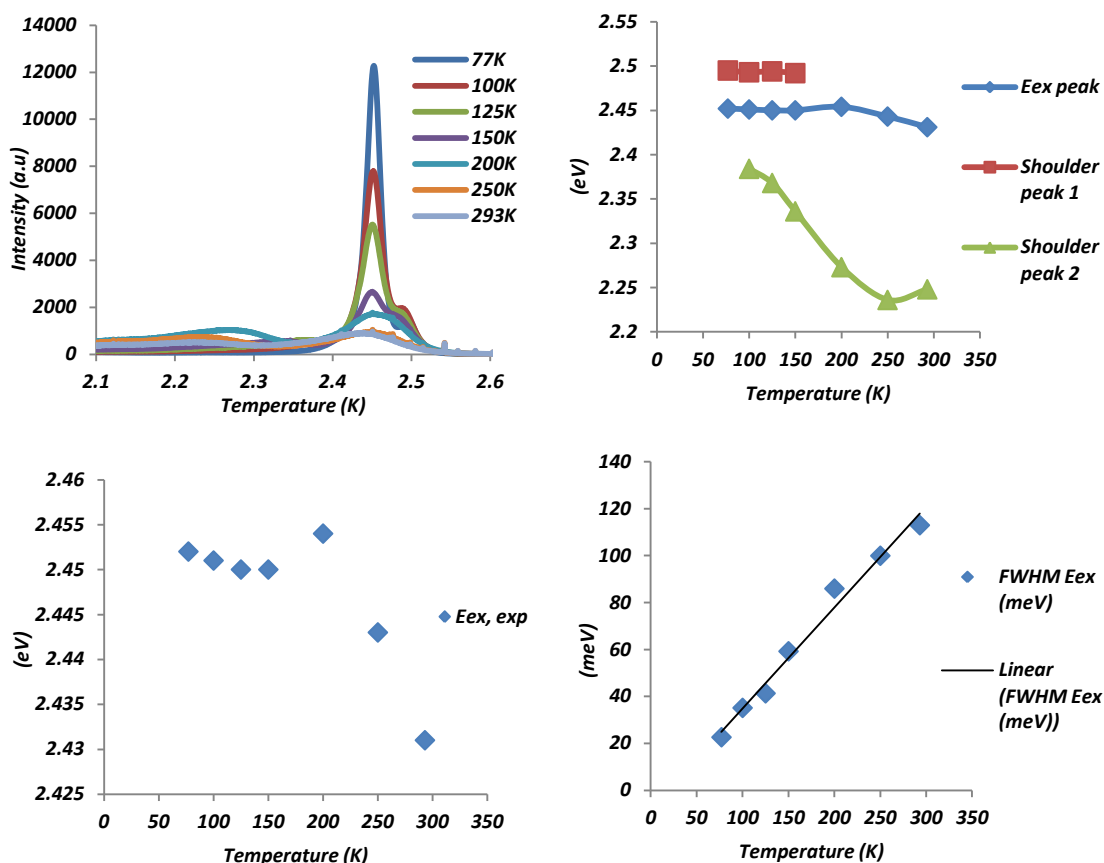


**Figure 6.8:** The variable temperature photoluminescence of  $(S\text{-MeOPhMtNH}_3)_2\text{PbI}_4$ . Three peaks are present at 100K, the main excitonic emission, the similar shoulder peak observed for the all of the 2D lead iodide systems, and a higher energy shoulder peak visible in the temperature range 77-150K. In this compound the  $E_{ex}$  could not be empirically fitted with the Varshni model, however the  $FWHM$  plotted against temperature displays the expected liner increase with temperature. It should be noted that the main excitonic peak was fitted with a Gaussian peak profile with a minor amount of lorentzian character, while the shoulder peaks showed a more lorentzian peak profile.

At 77K the emission profile of  $(S\text{-MeOPhMtNH}_3)_2\text{PbI}_4$  shows the main emission line at (2.452eV) with a higher energy shoulder at 2.495eV with an energy difference of  $\sim 43\text{meV}$ . At 100K the emergence of the Stokes shifted emission arises at 2.384eV. With increasing temperature we notice that the higher energy shoulder merges with the main band at 200K. This correlates with a minor shift of the main excitonic peak at 200K, and a marginal increase in the  $FWHM$  of the peak. Unfortunately this anomaly does cause the  $E_{ex}$  emission line plot against temperature to be unable to be fit with the Varshni model. Nevertheless the  $FWHM$  plot with temperature is similar to the one observed for the R enantiomer crystal.

The collective experimental findings and the data from  $(S\text{-MeOPhMtNH}_3)_2\text{PbI}_4$  suggests that there is fine structure present from the excitonic emissions observed. The observation of the

higher energy  $\Gamma_5^-$  may be sample dependant, meaning that an increase crystal quality will allow for this emission to be adequately observed. This was also shown by indirectly by Ema K, *et al*, 2006 findings of the  $\Gamma_5^-$  emission energy being dependant on the input photon energy. The lower energy bands  $\Gamma_2^-$  and  $\Gamma_1^-$  states presence appears to be less sample dependent, however, as seen from the oscillations of their emission profiles with temperature, these states are still susceptible to coupling to any lattice defects present in the crystal which is also supported by the increasing *FWHM* with increasing temperature. This would give rise to the varying peak emission energy's with temperature, between the mathematically identical enantiomer compounds.

### **6.2.3 Conclusions:**

The main excitonic peaks for most of the compounds are temperature dependant according to Varshni's model. The shoulder peak, present is however also temperature dependant (decreasing energy with increasing temperature) indicating thermal population with increasing temperature. This in conjunction with the low temperature emissions of all of the compounds suggest an excitonic fine structure is present, with the main emission being the triplet dominant  $\Gamma_2^-$  and the shoulder peak being the purely triplet  $\Gamma_1^-$  states respectively. As found in literature the excitonic fine structure emissions may be sample dependant, in particular with regards to the crystallinity of the compound. The fact that there is variation in the shoulder emission position between the mathematically identical enantiomer crystals also suggests that these emissions are sample dependant; however the temperature dependence supports the fine structure assignment. Therefore the collective experimental findings do suggest that there is fine structure present from the excitonic emissions; however this may vary with lattice distortions present in the crystal. This would give rise to the varying peak emission energy's with temperature, between the mathematically identical enantiomer compounds.

Structurally we have observed that the 8 compounds are not dissimilar from one another, this also manifests itself in the similar optical emissions observed. We have also found that the tin iodide compound's equatorial Sn-I bond lengths are highly distorted giving rise to a large red shifted room temperature photoluminescence emission. To our knowledge this is the largest red shifted single layer <100> 2D tin iodide hybrid published to date.



### 6.3 Structure and Optical properties of the 1D compounds

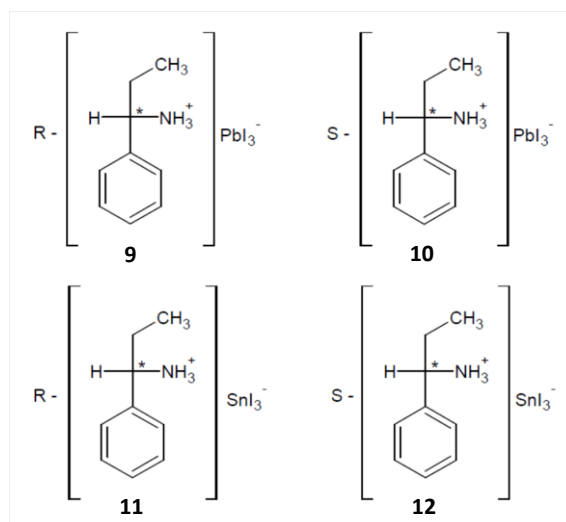
#### 6.3.1 Results and discussion (1D)

As established in chapter 5.1, the distortions experienced in the single chain face sharing octahedral wires of (A)PbI<sub>3</sub> relating to the Pb-I bond lengths and I<sub>eq</sub>-Pb-I<sub>eq</sub> bond angles, display almost no correlation to the shifts observed in the optical properties of the compound. The predominant effects on the PL shifts experienced from the Stokes shifted ( $\sim 1\text{eV}$ ) STE emissions from the unsaturated organic ammonium templates 1D lead iodide wires, were however only related to fluctuations from exciton lattice interactions. This was primarily due to the variations caused from the interrelated properties of the organic dielectric constant, crystal density, and inter-wire spacing.

Then in chapter 5.2 for the first time in the face sharing lead halide 1D hybrids we found a direct structural influence of the inorganic wires and their impact on the PL emissions. The low temperature phase change of the material observed at  $\sim 77\text{K}$  caused a distortion within the wires which resulted in the lead atom centers to arrange as a wave propagating along the wire, whereas the higher temperature phase displayed undistorted wires which have the lead centers arranging in a co-linear fashion. It was therefore surmised that the blue shifted emission observed at  $77\text{K}$  in addition to the STE emission was due to the creation of a polaron which has the ability to create lattice distortions in a crystal. However, further investigations into the decay kinetics of the emission would need to be carried out to further establish the character of the particle. A large red shifted polaron emission (relative to the STE emission) was reported for (PD)PbBr<sub>3</sub> (Azuma J, *et al*, 2002a). Although no direct property to structure correlation was made, we also suspect that the polaron emission found in this compound was due to the disordered wires found in the crystals (Azuma J, *et al*, 2002b).

#### 6.3.2 Crystal structures

In the final four 1D compounds synthesized we used the enantiomer template (R, S – C<sub>6</sub>H<sub>5</sub>C<sup>\*</sup>(H)(C<sub>2</sub>H<sub>5</sub>)NH<sub>3</sub>) where the \* represents the stereogenic centre of the template. The template produced four 1D ribbons with the general formula (A)MI<sub>3</sub> where M = Sn and Pb compounds **9** - **12** respectively. The molecular diagrams may be seen in scheme 6.3, and the crystal structures experimental data may be found in table 6.7.



**Scheme 6.3:** The polymeric schemes of the 1D crystal structures of compounds **9-12**.

From table 6.7 we notice that all four compounds crystallize in the chiral orthorhombic space group  $P2_12_12_1$ . We know that the chiral enantiomer crystals of lead and of tin respectively, are essentially isomorphous with one another with the exception of the handedness of the crystal. At first glance one would also expect the Sn and Pb crystals to be isomorphous with one another; however this is not the case. Firstly, we notice the unit cell axes of the Sn (**11**, **12**) analogue are closer to a tetragonal arrangement than the lead compounds (**9**, **10**). Secondly we notice the (100) axis of compounds **11** and **12** are elongated from  $\sim 8.1$  Å in **9** and **10** to  $\sim 8.6$  Å which is fairly significant for such similar compounds.

**Table 6.7:** For all structures: orthorhombic,  $P2_12_12_1$ ,  $Z = 4$ . Experiments were carried out with Mo  $K\alpha$  radiation using a CCD area detector diffractometer. Integration, *Bruker XPREP* (Bruker, 2005). Refinement was completed with 0 restraints. H-atom parameters were constrained. The absolute structure was obtained using Flack H D (1983), Acta Cryst. A39, 876-881.

	<b>9</b>	<b>10</b>	<b>11</b>	<b>12a</b>	<b>12b</b>
Crystal data					
Chemical formula	$C_9H_{14}N \cdot I_3Pb$	$C_9H_{14}N \cdot I_3Pb$	$C_9H_{14}N \cdot I_3Sn$	$C_9H_{14}N \cdot I_3Sn$	$C_9H_{14}N \cdot I_3Sn$
Chirality	R	S	R	R	S
$M_r$	724.1	724.1	635.6	635.6	635.6
Temperature (K)	173	173	173	173	200
$a, b, c$ (Å)	8.1016 (4), 8.7482 (4), 21.6782 (13)	8.0789 (2), 8.7214 (2), 21.6044 (6)	8.5832 (8), 8.583, 20.318 (2)	8.6135 (7), 8.614, 20.359 (2)	8.5472 (3), 8.6718 (3), 20.3785 (6)
$\alpha, \beta, \gamma$ (°)	90, 90, 90	90, 90, 90	90, 90, 90	90, 90, 90	90, 90, 90
$V$ (Å <sup>3</sup> )	1536.43 (14)	1522.23 (7)	1496.9 (2)	1510.5 (2)	1510.45 (9)
$\mu$ (mm <sup>-1</sup> )	16.98	17.14	7.87	7.79	7.79
Crystal size (mm)	$0.32 \times 0.16 \times 0.09$	$0.38 \times 0.21 \times 0.16$	$0.51 \times 0.10 \times 0.04$	$0.86 \times 0.12 \times 0.06$	$0.55 \times 0.09 \times 0.07$
Data collection					
$T_{min}, T_{max}$	0.084, 0.251	0.013, 0.086	0.132, 0.593	0.110, 0.519	0.076, 0.545
No. of measured, independent and observed [ $I > 2\sigma(I)$ ] reflections	19537, 3652, 3510	28323, 3684, 3584	42456, 3611, 3554	9299, 3621, 3544	17865, 3647, 3439
$R_{int}$	0.109	0.109	0.079	0.098	0.154
Refinement					
$R[F^2 > 2\sigma(F^2)], wR(F^2), S$	0.029, 0.069, 1.08	0.035, 0.090, 1.14	0.026, 0.063, 1.03	0.045, 0.121, 0.82	0.040, 0.091, 1.00
No. of reflections	3652	3684	3611	3621	3647
No. of parameters	127	127	127	128	128
$\Delta_{max}, \Delta_{min}$ (e Å <sup>-3</sup> )	0.80, -2.51	1.57, -3.60	1.47, -1.16	1.40, -2.28	1.44, -1.66
Flack parameter	0.005 (5)	0.006 (6)	0.00 (5)	0.13 (8)	0.05 (6)

Computer programs: Bruker *APEX2*, Bruker *SAINT*, *SHELXS97* (Sheldrick, 2008), *SHELXL97* (Sheldrick, 2008).

Let us first consider the molecular arrangement of the organic template relative to the inorganic wires, which we can observe in figure 6.9 before describing this anomaly. From figure 6.9 we notice the conformation of the ethyl chain, which may be described by the torsion angle from the ring through to the ethyl arm C6-C7-C8-C9 which is 59.8 (9)° for compound **9** with the comparative torsion angle (C5-C7-C8-C9) 175.1 (5)° in **11**. A better description of the ethyl chains conformation may be described by the conformation of the four atom alkyl chain of N1-C7-C8-C9 which is 176.5 (7)° displaying the all trans (anti) conformation of the template in **9** where this angle is 61.5 (6)° in **11** showing the gauche conformation of the alkyl chain (comparative torsion angles may be found in Table 6.9). The top two images in figure 6.9 display the embodiment of this conformational difference by the ethyl arm pointing out of the plane containing the

inorganic wires in compound **9** where the ethyl arm points down into the plane of the wires in compound **11**.

**Table 6.8:** Some selected inorganic bond lengths and angles for comparison between the structures. The labels have been rearranged for a direct comparison between each of the structures.

Compound	<b>9</b>	<b>10</b>	<b>11</b>	<b>12a</b>	<b>12b</b>
<b>M-I (1) (Å)</b>	3.1495 (6)	3.1400 (7)	3.0944 (5)	3.1039 (7)	3.1078 (7)
<b>M-I (1) (Å)</b>	3.3031 (6)	3.2920 (7)	3.2852 (5)	3.1041 (7)	3.2898 (7)
<b>M-I (2) (Å)</b>	3.0838 (5)	3.0734 (7)	2.9469 (5)	2.9564 (7)	2.9584 (7)
<b>M-I (2) (Å)</b>	3.4283 (5)	3.4194 (6)	3.5581 (5)	3.5710 (8)	3.5621 (7)
<b>M-I (3) (Å)</b>	3.2215 (5)	3.2119 (6)	2.9391 (5)	2.9467 (8)	2.9364 (7)
<b>M-I (3) (Å)</b>	3.2331 (5)	3.2236 (6)	3.6490 (5)	3.6600 (8)	3.6494 (7)
<b>M-I(1)-M (°)</b>	77.895 (12)	77.930 (13)	84.66 (1)	84.68 (2)	83.93 (2)
<b>M-I(2)-M (°)</b>	76.889 (10)	76.899 (12)	82.14 (1)	82.14 (2)	81.48 (2)
<b>M-I(3)-M (°)</b>	77.906 (10)	77.920 (12)	80.66 (1)	80.73 (2)	80.27 (2)
<b>I1-M-I1 (°)</b>	169.974 (16)	170.03 (2)	172.18 (2)	172.17 (2)	172.34 (2)
<b>I2-M-I2 (°)</b>	170.463 (14)	170.438 (18)	165.40 (1)	165.38 (2)	165.67 (2)
<b>I3-M-I3 (°)</b>	174.203 (13)	174.214 (17)	159.21 (1)	159.21 (2)	159.20 (2)
<b>M...M (Å)</b>	4.0579 (4)	4.0465 (4)	4.2982 (6)	4.3113 (8)	4.2789 (7)
<b>Interwire Spacing (I...I) (Å)</b>	4.2378 (6)	4.2250 (8)	4.2104 (5)	4.2266 (7)	4.2556 (6)

More importantly we notice that in compound **11**, the octahedral face where the ethyl arm points into the plane containing the wires, displays a large Sn-I elongation drastically distorting the shape of tin iodides octahedra. The highly distorted apical Sn-I bond length corresponding to the position from where the organic template is “inserted” into the plane containing the wires is 3.6490 (5) Å, and equatorial Sn-I bond length that is then adjacent to the organic template is distorted to 3.5581 (5) Å, creating the distorted octahedral face we observe. In compound **9** there is one elongated Pb-I bond length 3.4283 (5) Å which corresponds to the equatorial position of the octahedra which is adjacent to the organic template. The apical Sn-I’s bond length distortion also result in a substantial deviation of the I-Sn-I bond angle from 180° with the resultant angle being 159.21 (1)°. The comparable angle in **9** is 169.974 (16)°. Ultimately the elongation of octahedral face of the tin compound **11** is the reason we observe an elongation in the (100) axis from ~8.1 Å in **9** and **10** to ~8.6 Å in **11** and **12** respectively.

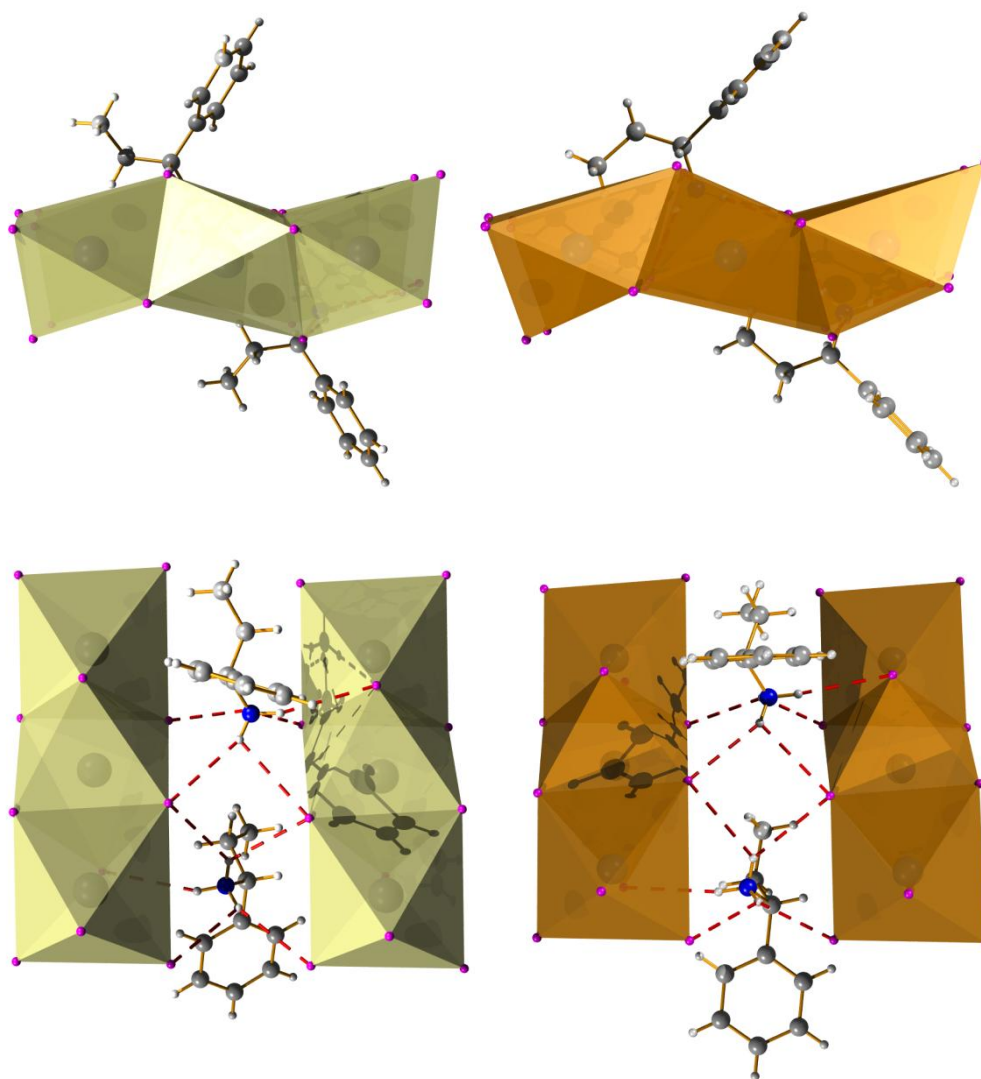


**Figure 6.9:** Compound **9** on the left with compound **11** on the right. As seen from the diagrams above we notice the difference in the arrangement of the organic template relative to the inorganic metal halide's face sharing octahedral wires of compounds **9** and **11**. In both compounds the wires propagate along the (100) axis. We also notice that the hydrogen bonding motif between both compounds is almost identical.

The last difference between compounds **9** and **11** may be seen in orientation of the phenyl rings in the tin compound (**11**), which are essentially parallel with one another, whereas in the Pb compound (**9**) they are tilted. This tilt may be described by the torsion angle between the ring and the nitrogen atom for **9** (C5-C6-C7-N1) which is  $42.6(10)^\circ$  and for **11** (C4-C5-C7-N1) being  $58.9(7)^\circ$ , the ideal being  $60^\circ$ . Despite the differences in the conformational arrangement of the rings and the ethyl arm, the hydrogen bonding motifs of **9** and **11** are almost identical (figure 6.9), with hydrogen bonds from the primary ammonium group to the iodine's of adjacent wires.

This does give rise to the short inter-wire spacing observed for both compounds ( $\sim 4.2$  Å) as seen for the 1D wires described in 5.1 and 5.2. The relevant hydrogen bonding interactions may be found in Table 6.10 below.

**Table 6.9:** Relevant organic torsion angles ( $^{\circ}$ ) for comparison between compounds.

9	10	11	12a	12b
C5—C6—C7—N1 42.6 (10)	C5—C6—C7—N1 -42.2 (13)	C4—C5—C7—N1 58.9 (7)	C5—C6—C7—N1 -58.5 (10)	C1—C6—C7—N1 -59.4 (9)
N1—C7—C8—C9 176.5 (7)	C9—C8—C7—N1 -177.3 (9)	N1—C7—C8—C9 61.5 (6)	N1—C7—C8—C9 -61.8 (10)	N1—C7—C8—C9 -63.5 (8)
C6—C7—C8—C9 -59.8 (9)	C9—C8—C7—C6 60.1 (11)	C5—C7—C8—C9 -175.1 (5)	C6—C7—C8—C9 175.5 (8)	C6—C7—C8—C9 175.8 (7)

**Table 6.10:** The hydrogen bonding table of compounds 9-12.

$D-H\cdots A$	$D-H$ (Å)	$H\cdots A$ (Å)	$D\cdots A$ (Å)	$D-H\cdots A$ ( $^{\circ}$ )
9				
N1—H1A $\cdots$ I3 <sup>i</sup>	0.89	2.99	3.653 (7)	132.2
N1—H1A $\cdots$ I2 <sup>ii</sup>	0.89	3.17	3.854 (7)	135.9
N1—H1B $\cdots$ I2 <sup>iii</sup>	0.89	2.91	3.745 (6)	156.8
N1—H1B $\cdots$ I3 <sup>iv</sup>	0.89	3.12	3.578 (6)	114
N1—H1C $\cdots$ I1 <sup>v</sup>	0.89	3	3.837 (6)	157.4
10				
N1—H1A $\cdots$ I1 <sup>vi</sup>	0.89	2.98	3.644 (8)	132.7
N1—H1A $\cdots$ I2 <sup>vii</sup>	0.89	3.16	3.847 (8)	136
N1—H1B $\cdots$ I3 <sup>viii</sup>	0.89	2.99	3.825 (8)	157.9
N1—H1C $\cdots$ I2 <sup>ix</sup>	0.89	2.9	3.728 (8)	156.1
N1—H1C $\cdots$ I1 <sup>x</sup>	0.89	3.1	3.562 (8)	114.4
11				
N1—H1A $\cdots$ I2	0.89	2.88	3.681 (5)	149.9
N1—H1A $\cdots$ I1 <sup>viii</sup>	0.89	3.09	3.623 (5)	120.5
N1—H1B $\cdots$ I3 <sup>viii</sup>	0.89	2.88	3.754 (5)	168
N1—H1C $\cdots$ I1 <sup>xi</sup>	0.89	3.05	3.761 (5)	138.4
N1—H1C $\cdots$ I2 <sup>xii</sup>	0.89	3.17	3.787 (5)	128.5
12a				
N1—H1A $\cdots$ I3 <sup>viii</sup>	0.89	2.89	3.687 (8)	150.4
N1—H1A $\cdots$ I1	0.89	3.11	3.638 (8)	120
N1—H1B $\cdots$ I1 <sup>vi</sup>	0.89	3.07	3.775 (7)	138.1
N1—H1B $\cdots$ I3 <sup>xiii</sup>	0.89	3.19	3.809 (7)	128.8
N1—H1C $\cdots$ I2	0.89	2.9	3.774 (8)	167.3
12b				
N1—H1A $\cdots$ I2 <sup>xiv</sup>	0.91	2.86	3.685 (7)	151.1
N1—H1A $\cdots$ I1 <sup>xv</sup>	0.91	3.1	3.621 (7)	117.9
N1—H1B $\cdots$ I1 <sup>xvi</sup>	0.91	3.08	3.785 (7)	135.3

N1—H1B...I2 <sup>xvii</sup>	0.91	3.16	3.810 (7)	130.4
N1—H1C...I3 <sup>xv</sup>	0.91	2.91	3.797 (7)	164.7

Symmetry code(s): (i)  $-x+1/2, -y+1, z+1/2$ ; (ii)  $-x+1/2, -y, z+1/2$ ; (iii)  $-x+1, y+1/2, -z+1/2$ ; (iv)  $-x+1, y-1/2, -z+1/2$ ; (v)  $-x, y-1/2, -z+1/2$ ; (vi)  $x+1/2, -y+3/2, -z$ ; (vii)  $x+1/2, -y+1/2, -z$ ; (viii)  $x, y-1, z$ ; (ix)  $x+1, y, z$ ; (x)  $x+1, y-1, z$ ; (xi)  $x-1/2, -y+1/2, -z+2$ ; (xii)  $x-1/2, -y-1/2, -z+2$ ; (xiii)  $x+1/2, -y+5/2, -z$ ; (xiv)  $x, y+1, z-1$ ; (xv)  $x, y, z-1$ ; (xvi)  $x-1/2, -y+3/2, -z+1$ ; (xvii)  $x-1/2, -y+1/2, -z+1$ .

### 6.3.3 Luminescence

To briefly recap from chapter 5.1 and 5.2, the origin of the photoluminescence emission of (PD)PbI<sub>3</sub> was assigned as a self trapped excitation, as the large stokes shift (1.3eV) and broad PL emission profile ( $\sim 0.36\text{eV FWHM}$ ) supporting the assignment as a STE emission (Nagami A, *et al*, 1996; Fukumoto T, *et al*, 2000). Compounds **9-12** PL emission profiles as in chapter 5.1 and 5.2 correlate with the assignment for that given for (PD)PbI<sub>3</sub>, and are therefore also assigned as STE emissions. The STE emissions from a kinetics standpoint PL decay time constants have been reported to be exponential. This further supports the assignment of the emissions as a STE rather than a frenkel exciton. Moreover the STE has been shown to exist in a triplet exciton state, which displays two different decay time constants in the recombination processes. The triplet excitation is separated into a single lower energy sub-band with slower time decay constant, and a doubly degenerate sub-band at a higher energy level with a faster decay time constant. At low temperatures (5K) the singlet state is the dominant emission, however as the temperature increases, phonon assisted transitions into the doubly degenerate sub-band with the faster decay time constant becomes dominant (Akimoto I, *et al*, 2004). In addition, it should be noted that the STE luminescence intensity decreases by four orders of magnitude from 70K to 300K which gives evidence of a large exciton lattice coupling interaction. It has also been shown that the 1D compounds have large excitonic binding energies (360meV) which should allow for strong room temperature emissions, however the strong exciton lattice coupling (STE emission) suppresses this in reality. The strong exciton lattice coupling was confirmed from investigations of (PD)PbI<sub>3</sub> under hydrostatic pressure, where the PL emission blue shifts with increasing pressure. The STE emission was also reported to display strong exciton lattice coupling even at ambient pressure. The hardening of the crystal due to the increasing pressure was shown to decrease the exciton lattice interaction, hence the blue shift in the emission observed (Fukumoto T, *et al*, 2000).

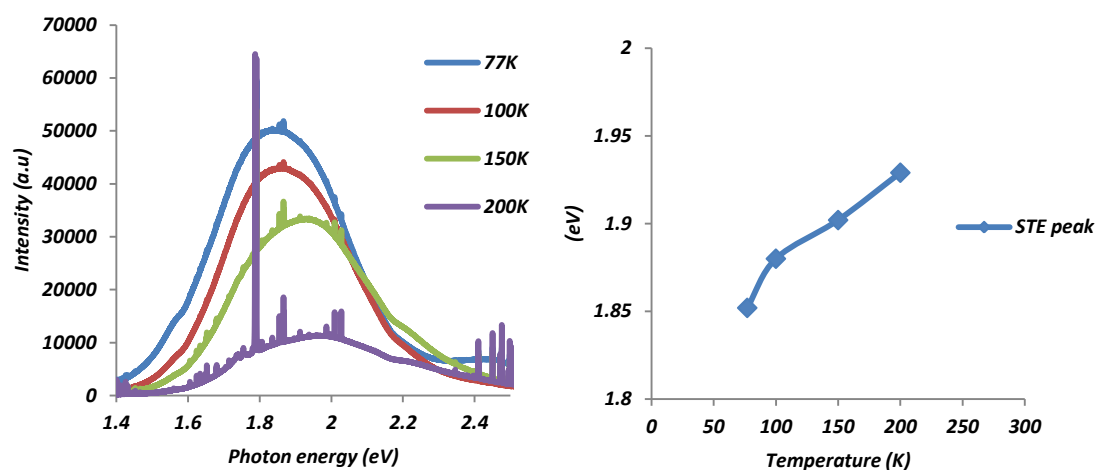


**Figure 6.10:** The Variable temperature PL spectrum is of the R enantiomer 1D PbI<sub>3</sub> wires, and follows a similar increase in temperature as observed for the PbI<sub>3</sub><sup>-</sup> wires shown in the diagram on the right. (Sharp emission lines from the plasma lines from the laser, were present as we did not have the correct band pass filter). Bad crystal quality lead to the exclusion of the luminescence data of the S enantiomer.

Initially what we wished to investigate was the temperature dependence of the STE emission and attempt to correlate any anomalies observed to structural changes. The Variable temperature photoluminescence emission of **9** may be seen in figure 6.10, in which we observe a gradual increase in the photon energy emission, with increasing temperature. We also notice the large decrease in the emission intensity with increasing temperature, as the room temperature emission was no longer visible at consistent laser power. The emission of **9** at 77K was found to be 1.852eV which is in range of the compounds investigated in 5.1 and 5.2. The increase in the emission energy with increasing temperature is once again inevitably due to an increase in the exciton lattice interaction with increasing temperature, which was also found to be true for the 2D case but is much less pronounced. We also are well aware of the strong exciton lattice interactions that are present for these systems (Fukumoto T, *et al*, 2000; Akimoto I, *et al*, 2004). The same temperature trend is observed for the lower energy emissions of compounds **11** and **12**.



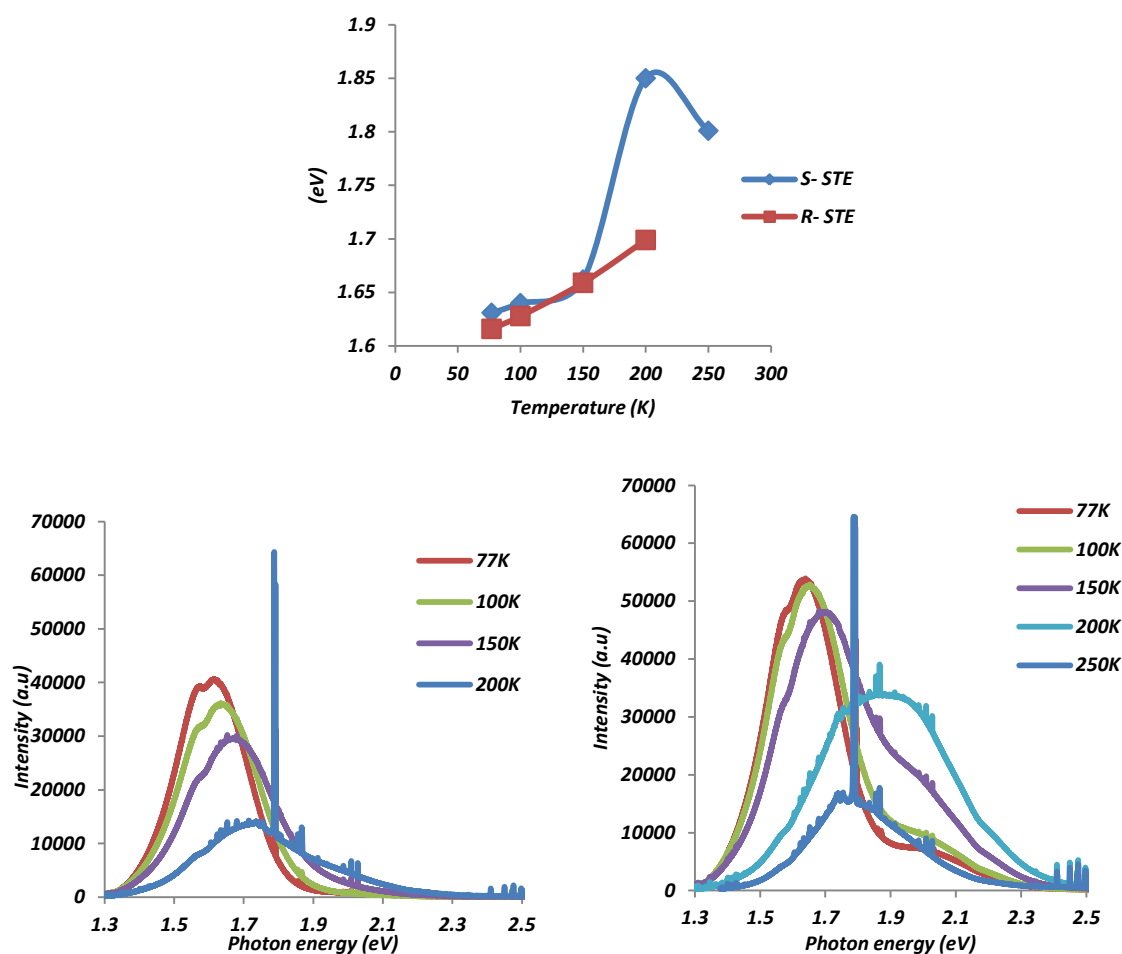


**Figure 6.11:** The characteristic STE luminescence emission found in the 1D  $\text{SnI}_3$  compounds. What is evident from the temperature dependence experiments is that both the R and S enantiomer have similar STE shifts as the temperature increases, however at 200K, the S enantiomer exhibits a large shift, whereas the R enantiomer does not. The variable temperature PL is of (R) $\text{SnI}_3$  on the left and (R) $\text{SnI}_3$  on the right. (The sharp lines are plasma lines due to the lack of a band pass filter in for the UV laser).

In the tin compounds the 77K emission of **11** and **12** were found to be 1.616eV and 1.631eV respectively. To my knowledge this the first report of the photoluminescence of  $\text{SnI}_3^-$  wires in literature. The PL shift from  $\sim 1.85\text{eV}$  to  $\sim 1.62\text{eV}$  from the lead to tin system respectively is obviously expected to due to the band gap shift. We observe the same STE emission shift in the  $\text{PbBr}_3^-$  wires which are blue shifted with respect to the  $\text{PbI}_3^-$  wires due to the band gap increase (Nagami A, *et al*, 1996; Azuma J, *et al*, 2002a; b). From the VT PL of **11** displays a good emission profile at 77K, which broadens with increasing temperature, in the expected manner. Compound **12** also displays a good emission profile at 77K; however we also notice a blue shifted shoulder at the base of the main emission. As the temperature increases this blue shifted shoulder increases in intensity where at 200K the main emission blue shifts to merge with the shoulder emission. What we found to be interesting was the main 250K emission red shifts back

to its expected position. We noticed under the microscope a wave front moving through the crystal upon heating and cooling through 200K. The emission was shown to be repeatable and reversible upon heating and cooling cycles and after performing the collection at 200K multiple times. It was suspected that the shift was due to an intermediate phase transition caused by the presence of an impurity in the crystal, as this anomaly was not observed in its enantiomer counterpart. A SC-XRD data collection on a suitable crystal from the same crystallization batch was then performed at 200K compound **12b**. There were minor structural differences between compounds **12a** and **12b** however; there was not enough evidence to suggest that the PL luminescence shift at 200K was due to a structural distortion within the wires as observed in chapter 5.2. We therefore must assign this shift in emission to the presence of an impurity present on the crystal, which is thermally activated (Gilliland G. D, 1996).

#### **6.3.4 Conclusions 1D:**

In conclusion, we have successfully crystallized and characterized two (four) chiral hybrid systems for potential SHG applications. We do however notice in both the 1D and 2D systems, crystal quality is of the utmost importance, and that lattice distortions or the presence of impurities will drastically alter the expected emission profile. As previously mentioned single crystals themselves solve many of the macroscopic problems, such as phase matching which is achieved through optical birefringence type I and II (critical and non-critical phase matching), providing a high degree of ordering, as well as a stable structure. The negatively highly polarizable 1D wires (Zhoa H. R, *et al*, 2010) further ensure a large optical anisotropy down one of the crystallographic axis. The use of the chiral template has ensured the 1D hybrid systems have potential for further SHG investigations.

## **Chapter 7: Conclusion**

### **7.1 Concluding remarks**

The synthesis, SC-XRD, and optical property investigations were carried out on 44 distinct low dimensional organic inorganic hybrids. Only 29 of the structures have not been previously reported, however these all formed the basis of the optical investigations. Below we will summarize the important findings of each chapter.

Chapter 4 investigated the structural phase transitions of the 2D <100> lead bromide hybrids of both the simple aliphatics and halogenated aliphatics. These were subsequently compared with the previously published lead iodide analogues which had also been structurally characterized. This formed the basis for the optical investigations of both the lead iodide and bromide systems. The aim of chapter 4 was to investigate octahedral distortions, short interlayer spacings, and the effect of the aliphatic's terminal halogen on idealizing or destabilizing the octahedral arrangements and their effect on the band gap. It was found that the  $\text{PbX}_6$  metal centred distortions do display some impact on the band gap, the greater the distortion experienced in the  $\text{I}_{\text{eq}}\text{-Pb-I}_{\text{eq}}$  cis bond angles, the wider the band gap, as we suspect a decrease in  $5p$  antibonding character which lowers the top of the valence band. The terminal halogen interaction specifically in  $(\text{BrC}_2)\text{PbI}_4$ , clearly displayed some  $\text{Br } 4p/s$  character at the bottom of the conduction band, which may further explain the reduction of the band gap of this compound. This in conjunction with the shorter interlayer spacing serve to stabilize more idealized bridging angles, as seen in both the lead iodide and bromide analogues. In addition the short interlayer spacing compounds show large idealizations of the  $\text{Pb-X-Pb}$  bridging angle however display a large metal centred octahedral distortions in order accommodate the spatial occupation of the lone pair on lead, in both the bromide and iodide analogues. The lead bromide analogues appear to have a greater sensitivity to exciton lattice interactions, which give rise to red shifted emissions and absorptions with decreasing temperature. Structurally this behaviour is counterintuitive; as the structures increase in inorganic distortions with a temperature decrease with a blue shift in the exciton absorption is expected. It should be noted that compounds displaying this phenomenon most,  $(\text{C}_4, \text{C}_6, \text{C}_7)\text{PbBr}_4$  do display a large amount of structural disorder in their lower temperature phases.

In chapter 5.1 we first investigated the single chain face sharing lead iodide octahedra with various simple secondary, tertiary and quaternary ammonium templates. The aim was to investigate if structural phase transitions displayed any impact on the first exciton absorption. It

was found the lead iodide octahedral wires are largely stable with respect to the distortions of bond angles and bond lengths caused from phase transitions. In addition it was found that the relative stability of the wires independent of the presence of hydrogen bonding further supported their independence the templates behaviour. The hydrogen bonding that did occur is highly symmetrical, and the wires themselves support disordered nitrogen atoms to form this type of interaction. However when the symmetry of the hydrogen bonding did decrease and the hydrogen bonding interactions are no longer equivalent, then mainly Pb-I bond length elongations and compressions were observed. In addition the conformations of the heterocyclic rings through the phase transitions are strongly correlated with the relative energies of the isolated conformers themselves, i.e. they observe the predicted energetically favoured conformations through the phases.

Optically it was found that unlike the corner-shared perovskite type 1D wires of  $[\text{NH}_2\text{C}(\text{I})=\text{NH}_2]_3\text{PbI}_5$  and  $[\text{CH}_3\text{SC}(\text{=NH}_2)\text{NH}_2]_3\text{PbI}_5$  the first exciton absorption of the octahedral face sharing wires of (A)PbI<sub>3</sub> appear to be largely insensitive to the inorganic structural distortions experienced as a result of the low temperature phase transitions. However links between the STE luminescence emissions and the inter-wire spacing, organic dielectric constant, and the density of the crystal, have been shown to influence the exciton lattice interactions. This effect is increased through a decrease in crystal density and organic dielectric constant, with an associated increase in the inter-wire spacing. Therefore as the exciton lattice interactions increase, a red shift in the STE emissions is observed.

In the following section 5.2 we did observe a direct structural influence of the single chain face sharing octahedral wires and on the STE PL emissions. As the distortion present in the wires is a result of the lead centers arranging like a wave propagating along the wire. We suspect the observed blue shifted emission is due to a polaron which creates lattice distortions. Further investigations into the decay kinetics of the emission would need to be carried out to further establish the character of the particle. A large red shifted polaron emission (relative to the STE emission) was reported for (PD)PbBr<sub>3</sub> (Azuma J, *et al*, 2002a). Although no direct property to structure correlation was made, we suspect that the polaron emission found in this compound is due to the disordered wires found in the crystals (Azuma J, *et al*, 2002b).

In section 5.3 the effect of the DMSO solvent on the inorganic distortions was investigated, although this appears to largely not affect the position of the first exciton absorption edge as was found in chapter 5.1. Strong  $I - \pi$  and  $\pi - \pi$  interactions were present in both charge

transfer compounds. It was noted that the wires promote  $\pi - \pi$  interactions between the organic templates as has also been established in literature. The increased wire thickness does appear to display a pronounced effect on the PL emission as seen in three chain wide wire. The thicker chain begins to allow higher energy emission's to occur i.e. the desired first exciton emission begins to become favored due to the relaxing of the wires spatial confinement on the electron-hole's orbit. Further investigations are needed into even thicker chain wires, in order to ascertain the ideal size of the wire to obtain the desired first exciton emission. However the wire thickness that does give rise to the first exciton emission appears to still need at least six coordinated  $\text{PbI}_6$  octahedral units as seen with the ethyl viologen compound.

It was also noted that in compounds **1** and **2** the CT transitions begin to largely coincide with the STE emission arising from the inorganic wire. Even though **1** and **2** have strong  $\pi - \pi$  interactions the current experiments do not ascertain to what degree this interaction assists in electron transport. As intermolecular  $\pi - \pi$  interactions are absent in MV and Et the dominant CT interaction does show that the I...N distance function over a large range ( $4.9\text{\AA}$ ). This long distance is substantiated from the strong covalent character of the I...N interaction observed in IR experiments completed on  $(\text{MV})\text{Pb}_2\text{I}_6$ . It was also observed that the position of the LUMO of the organic cation relative to the valence band of the inorganic wires appears to be largely dependent on the N...I distance and largely independent of the electron accepting templates HOMO-LUMO gap.

In the study of the chiral 2D  $\langle 100 \rangle$  lead iodide systems (section 6.2) it was observed that the main excitonic peaks' temperature dependence observed Varshni's empirical model. The shoulder peak luminescence emission was also observed to be temperature dependent (decreasing energy with increasing temperature) indicating thermal population of this energy level with increasing temperature. This in conjunction with the low temperature emissions of all of the compounds suggest an excitonic fine structure is present, with the main emission being the triplet dominant  $\Gamma_2^-$  and the shoulder peak being the purely triplet  $\Gamma_1^-$  state. As found in literature the excitonic fine structure emissions may be sample dependent, in particular with regards to the crystallinity of the compound. The fact that there is variation in the shoulder emission position between the enantiomerically related crystals also suggests that these emissions are sample dependent; however the temperature dependence supports the fine structure assignment. Therefore the collective experimental findings do suggest that there is fine structure present from the excitonic emissions; however this may vary with lattice distortions

present in the crystal. This would give rise to the varying peak emission energies with temperature, between the enantiomerically related compounds.

Structurally we observed that the eight compounds reported in this section are not dissimilar from one another, this also manifests itself in the similar optical emissions observed. We have also found that the tin iodide compound's equatorial Sn-I bond lengths are highly distorted giving rise to a large red shifted room temperature photoluminescence emission. To our knowledge this is the largest red shifted single layer <100> 2D tin iodide hybrid reported to date.

In section 6.3 we successfully crystallized and characterized four chiral hybrid systems for potential SHG applications. We do however notice in both the 1D and 2D systems, crystal quality is of the utmost importance, and that lattice distortions or the presence of impurities will drastically alter the expected emission profile. As previously mentioned single crystals themselves solve many of the macroscopic problems, such as phase matching which is achieved through optical birefringence type I and II (critical and non-critical phase matching), providing a high degree of ordering, as well as a stable structure. The negatively charged highly polarizable 1D wires (Zhoa H. R, *et al*, 2010) further ensure a large optical anisotropy down one of the crystallographic axis. The use of the chiral template has ensured the 1D hybrid systems have potential for further SHG investigations.

## **7.2 Future work**

It is imperative to understand the fundamentals of solid state (semiconductors) systems before one can make use of these devices industrially. There are immense opportunities in crystallographic solid state physics for the design and study of fundamental systems which could be later made use of in the industrial market.

## Chapter 8: References

### A

- Akimoto I, Sakai M, Kan'no K, *Journal of Luminescence*, (2004) **108**, 31  
Azuma J, Tanaka K, Kan'no K, *J. Phys. Soc. Jpn.*, (2002a) **71**, 971  
Azuma J, Tanaka K, Kamada M, Kan'no K, *J. Phys. Soc. Jpn.*, (2002b) **71**, 2730

### B

- Barman S, Venkatamaran N. V, Vasudevan S, Shesadri R, *J. Phys. Chem. B*, (2003) **107**, 1875  
Barman S, Vasudevan S, *J. Phys. Chem. C*, (2009) **113**, 15698  
Ben Ghazlen M. H, Daoud A, Bats J. W, *Acta Cryst.*, (1981) **B37**, 1415  
Bi W, Louvain N, Mercier N, Luc J, Rau I, Kajzar F, Sahraoui B, *Adv. Mater.*, (2008) **20**, 1013  
Billing D. G, *Acta Cryst.*, (2002) **E58**, m669  
Billing D. G, Lemmerer A, *Acta Cryst.*, (2003) **E59**, m381  
Billing D. G, Lemmerer A, *Acta Cryst.*, (2004) **C60**, m224  
Billing D. G, Lemmerer A, *Acta Cryst.*, (2006a) **C62**, m174  
Billing D. G, Lemmerer A, *Acta Cryst.*, (2006b) **C62**, m238  
Billing D. G, Lemmerer A, *Acta Cryst.*, (2006c) **C62**, m269  
Billing D. G, Lemmerer A, *Acta Cryst.*, (2006d) **E62**, m1103  
Billing D. G, Lemmerer A, *CrystEngComm*, (2006e) **8**, 686  
Billing D. G, Lemmerer A, *CrystEngComm*, (2006f) **9**, 236  
Billing D. G, Lemmerer A, *Acta. Cryst.*, (2006g) **E62**, m904  
Billing D. G, Lemmerer A, *Acta. Cryst.*, (2006h) **C62**, m264  
Billing D. G, Lemmerer A, *Acta. Cryst.*, (2006i) **C62**, m597  
Billing D. G, Lemmerer A, *CrystEngComm*, (2007) **9**, 236  
Billing D. G, Lemmerer A, *Acta. Cryst.*, (2007b) **B63**, 735  
Billing D. G, Lemmerer A, *New. J. Chem.*, (2008) **32**, 1736  
Billing D. G, Lemmerer A, *CrystEngComm*, (2009) **11**, 1549  
Bocain D. F, Pickett H. M, Rounds T. C, Strauss H. L, *J. Am. Chem. Soc.*, (1975) **97**, 687  
Burland D. M, Miller R. D, Walsh C. A, *Chem. Rev.*, (1994) **94**, 31  
Busico V, Saleno V, Vacatello M, *Gazz.Chim. Ital.*, (1979) **109**, 581

### C

- Caijolo M. R, Corradini P, Pavone V, *Gazz. Chim. Ital.*, (1976) **106**, 807  
Calabrese J, Jones N. L, Harlow R. L, Herron N, Thorn D. L, Wang Y, *J. Am. Chem. Soc.*, (1991) **113**, 2328  
Cariati E, Ugo R, Cariati F, Roberto D, Masciocchi N, Galli S, Sironi A, *Adv. Mater.*, (2001) **13**, 1665  
Chanh N. B, Haget Y, Hauw C, Meresse A, Ricard L, Rey-Lafon L, *J. Phys. Chem. Solids.*, (1983) **44**, 589  
Chanh N. B, Hauw C, Meresse A, Rey-Lafon L, Ricard L, *J. Phys. Chem. Solids.*, (1985) **46**, 1413  
Chanh N. B, Houstry J. R, Meresse A, Ricard L, Rey-Lafon L, *J. Phys. Chem. Solids.*, (1989) **50**, 829  
Chapuis G, *Acta Cryst.*, (1978) **B34**, 1506  
Cheng C, Yan H, *Physica E*, (2009) **41**, 828  
Cheng Z. Y, Shi B. L, Gao B. X, Pang M. L, Wang S. Y, Han Y. C, Lin J, *Eur. J. Inorg. Chem.*, (2005) 218

Chondroudis K, Mitzi D. B, *Chem. Mater.*, (1999) **11**, 3028  
 Chondroudis K, Mitzi D. B, *Appl. Phys. Lett.*, (2000a) **76**, 58  
 Chondroudis K, Mitzi D. B, Brock P, *Chem. Mater.*, (2000b) **12**, 169  
 Contreras J. G, Seguel G. V, Ungerer B, Maier W. F, Hollander F. J, *J. Mol. Struct.* **102**, 295  
 Corradi A. B, Ferrari A. M, Pellacani G. C, Saccani A, Sandrolini F, Sgarabotto P, *Inorg.Chem.*, (1999) **38**,716  
 Corradi A. B, Ferrari A. M, Righi L, Sgarabotto P, *Inorg.Chem.*, (2001) **40**, 218

## D

Dammak T, Fourati N, Boughzala H, Mlayah A, Abid Y, *Journal of Luminescence.*, (2007) **127**, 404  
 Dammak T, Koubaa M, Boukheddaden K, Bougzhala H, Mlayah A, Abid Y, *J. Phys. Chem. C*, (2009) **113**, 19305  
 Dammak T, Elleuch S, Bougzhala H, Mlayah A, Chtourou R, Abid Y, *Journal of Luminescence*, (2009b) **129**, 893  
 Delerue C, Lannoo M, *Nanostructures Theory and modelling*, Springer, (2004) 47  
 Depmeier W, Mason S. A, *Acta. Cryst.*, (1978) **B34**, 920  
 Depmeier W, Mason S. A, *Solid State Comm.*, (1983) **46**, 409  
 Depmeier W, *Zietschrift Fur Kristalloraphie*, (2009) **224**, 287  
 Devic T, Evain M, Moelo Y, Canadell E, Aubin-Senzier P, Fourmigue M, Batail P, *J. Am. Chem. Soc.*, (2003) **125**, 3295  
 Devic T, Canadell E, Aubin-Senzier P, Batail P, *J. Mater. Chem.*, (2004) **14**, 135  
 Dobrzycki L, Wozniak K, *Journal of Molecular Structure.*, (2009) **921**, 18  
 Doudin B, Chapuis G, *Acta. Cryst.*, (1988) **B44**, 495  
 Doudin B, Chapuis G, *Acta. Cryst.*, (1990) **B46**, 175  
 Dumas J. M, Gomel L, Guerin M, *Molecular interactions involving organic halides. The chemistry of functional groups, Supplement D*; Wiley New York., (1983), 985-1020

## E

Elleuch S, Abid Y, Damak T, Mlayah A, Boughzala H, *Journal of Raman Spectroscopy*, (2008) **39**, 786  
 Elleuch S, Damak T, Abid Y, Mlayah A, Boughzala H, *Journal of Luminescence*, (2010) **130**, 531  
 Ekimov A. I, Onushchenko A. A, *JETP Lett.*, (1981) **34**, 345  
 Ema K, Umeda K, Toda M, Yajima C, Arai Y, Kunugita H, Wolverson D, Davies J. J, *Phys. Rev. B.*, (2006) **73**, 241310  
 Ema K, Inomata M, Kato Y, Kunugita H, Era M, *Phys. Rev. Lett.*, (2008) **100**, 257401  
 Era M, Morimoto S, Tsutsi T, Saito S, *Appl. Phys. Lett.*, (1994) 65, 676  
 Era M, Morimoto S, Tsutsi T, Saito S, *Synth. Metals.*, (1995) **71**, 2013

## F

Fox. M. *Optical Properties of Solids*. (2008). Oxford University Press Inc., New York  
 Fukumoto T, Hirasawa M, Ishihara T, *Journal of Luminescence*, (2000) **87-89**, 497  
 Fujisawa J, Ishihara T, *Phys. Rev. B.*, (2004) **70**, 113203  
 Fujisawa J, Tajima N, *Phys. Rev. B.*, (2005) **72**, 125201  
 Fujisawa J, Tajima N, Tamaki K, Shimomura M, Ishihara T, *J. Phys. Chem. C.*, (2007) **111**, 1146

## G

Gebauer T, Schmid G, *Z. Anorg. Allg. Chem.*, (1999) **625**, 1124



Giffard M, Mercier N, Mabon G, Nguyen Phu X, Sylla M, Delhaes P, Soscun H, Castellano O, Hernandez J, Rodriguez L, Marcano A, Yartsev V, *Microelectronics Journal*, (2005) **36**, 933

Gill G, Pawar D. M, Noe E. A, *J. Org. Chem.*, (2005) **70**, 10726

Gilliland G. D, *Material Science and Engineering*, (1997) **R18**, 99

Goto T, Ohshima N, Mousdis G. A, Papavassiliou, *Nonlin. Opt.*, (2002) **29**, 379

Gröger H, Lode C, Vollmer H, Krautscheid H, Lebekin S, *Z. Anorg. Allg. Chem.*, (2002) **628**, 57

Geun L, Palvadeau P, Spiesser M, Tournoux M, *Rev. Chim. Miner.*, (1982) **19**, 1

Guloy A. M, Tang Z, Miranda P. B, Srdanov V. I, *Adv. Mater.*, (2001), **13**, 833

## H

Harris P, Larsen F. K, Lebech B, Achiwa N, *Acta. Cryst.*, (1994) **B50**, 676

Hatch D. M, Stokes , Aleksandrov

Hirasawa M, Ishihara T, Goto T, *J. Phys. Soc. Jpn*, (1994) **63**, 3870

Hong X, Ishihara T, Nurmikko A. V, *Solid State Commun.*, (1992) **84**, 657

Hong X, Ishihara T, Nurmikko A. V, *Phys. Rev. B.*, (1992) **45**, 6961

Hua J, Lam J. W. Y, Li Z, Qin A, Sun J, Dong Y, Dong Y, Tang B. Z, *Journal of Polymer Science: Part A: Polymer Chemistry.*, (2006) **44**, 3538

Huang C. C, Li H. H, Chen Z. R, Chen J. H, Ren Y. G, Ni Z. X, *Jiegou Huaxue(Chin.J.Struct.Chem.)*, (2004) **23**, 1013

## I

Innocenzi P, Lebeau B, *J. Mater. Chem.*, (2005) **15**, 3821

Ishihara T, Takahasi J, Goto T, *Solid State Commun.*, (1989) **69**, 933

Ishihara T, Takahasi J, Goto T, *Phys. Rev. B.*, (1990) **42**, 11099

Ishihara T, *J. Lumin.*, (1994) **60–61**, 269

## K

Kagan C. R, Mitzi D. B, Dimitrakopoulos C. D, *Science*, (1999) **286**, 945

Kataoka T, Kondo T, Ito R, Sasaki S, Uchida K, Miura N, *Phys. Rev. B.*, (1993) **47**, 2010

Kataoka T, Kondo T, Ito R, Sasaki S, Uchida K, Miura N, *Physica B*, (1994) 201, 423

Kato Y, Ichii D, Ohashi K, Kunugita H, Ema K, Tanaka K, Takahasi T, Kondo T, *Solid State Communications.*, (2003) **128**, 15

Kikuchi K, Takeoka Y, Rikukawa M, Sanui K, *Colloids and Surfaces A : Physicochem. Eng. Aspects.*, (2005) **267-258**, 199

Kind R, Plesko S, Arend H, Blinc R, Zeks B, Seliger J, Lozar B, Slak J, Levstik A, Filipic C, Zagar V, Lahajnar G, Milla F, Chapuis G, *J. Chem. Phys.*, (1979) **71**, 2118

Kind R, *Ferroelectrics*, (1980) **24**, 81

Kitazawa N, *Materials Science and Engineering B*, (1997) **B49**, 233

Kitazawa N, Enomoto K, Aono M, Watanabe Y, *Journal of Materials Science*, (2004) **39**, 749

Kitazawa N, Watanabe Y, *Surface & Coatings Technology.*, (2005) **198**, 9

Kitazawa N, Yaemponga D, Aono M, Watanabe Y, *Journal of Luminescence*, (2009) **129**, 1036

Kitazawa N, Aono M, Watanabe Y, *Thin Solid Films*, (2010) **518**, 3199

Kitazawa N, Watanabe Y, *J. Phys. Chem. Solids.*, (2010b) **71**, 797

Kittel C, *Introduction to Solid State Physics 7<sup>th</sup> Ed*, John Wiley & Sons, (1996)

Klapper H, Hahn Th, *International Tables of Crystallography*, 2002, Kluwer Academic Publishers  
 Dodrecht/Boston/London, **Vol A**, 804-807

Knop O, Wasylshen R. E, White M. A, Cameron T. S, Van Oort M. J. M, *Can. J. Chem*, (1990) **68**, 412

Knutson J. L, Martin J. D, Mitzi D. B, *Inorg. Chem.*, (2005) **44**, 4699

Kondo T, Iwamoto S, Hayase S, Tanaka K, Ishi J, Mizuno M, Ema K, Ito R, *Solid State Communications.*, (1998), **105**, 503

Koutselas I. B, Ducasse L, Papavassiliou G. C, *J. Phys.: Condens. Matter*, (1996) **8**, 1217.

Koutselas I. B, Mitzi D. B, Papavassiliou G. C, Papaioannou G. J, Krautscheid H, *Synthetic Metals*, (1997) **86**, 2171.

Kozelj M, Rutar V, Zupancic I, Blinc R, Arend H, Kind R, Chapuis G, *J. Chem. Phys.*, (1981) **74**, 4123

Krautschied H, Veilsack F, *Angew. Chem., Int. Ed. Engl.*, (1995) **34**, 2035

Krautscheid H, Lekieffre J. F, Besinger J, *Z.Anorg.Allg.Chem.*, (1996) **622**, 1781

Krautscheid H, Vielsack F, *Z.Anorg.Allg.Chem.*, (1997) **623**, 259

Krautscheid H, Vielsack F, Klaassen N, *Z. Anorg. Allg. Chem.*, (1998) **624**, 807

Krautschild H, Veilsack F, *J. Chem. Soc., Dalton Trans.*, (1999) 2731

Krautscheid H, Vielsack F, *Z.Anorg.Allg.Chem.*, (1999b) **625**, 562

Krautscheid H, Vielsack F, *Z.Anorg.Allg.Chem.*, (2000) **626**, 3

Krautscheid H, Lode C, Vielsack F, Vollmer H, *J.Chem.Soc., Dalton Trans.*, (2001) 1099

Kuroda N, Sakai M, Nishina Y, Tanaka M, Kurita S, *Phys. Rev. Lett.*, (1987) **58**, 2122

## L

Lee S. J, Kim G. Y, Oh E. J, Kim K. H, Yo C. H, *Bull. Kor. Chem.Soc.*, (2000) **21**, 317

Lee S. W, Mao C, Flynn C. E, Belcher A. M, *Science*, (2002) **296**, 892

Lemmerer A, *Phase Transitions and Structural Motifs of Inorganic-Organic lead Halide Hybrids*, PhD Thesis, 2007

Lemmerer A, Billing D. G, *CrystEngComm*, (2010) **12**, 1290

Lemmerer A, Billing D. G, *Dalton. Trans.*, (2011) DOI: 10.1039/c0dt01805h

Li T, Lozykowski H. J, Reno J. L, *Phys. Rev. B.*, (1992) **46**, 6961

Li H. H, Chen Z. R, Huang C. C, Lian Z. X, Chen J. H, *Wuji Huaxue Xuebao(Chin.)(Chin.J.Inorg.Chem.)*, (2004) **20**, 703

Li M. T, Liao Q. L, Fu X. C, Wang C. G, *Acta. Cryst.*, (2005) **E61**, m1396

Li H. H, Chen Z. R, Guo L. Q, Ding K. N, Li J. Q, Huang C. C, Cai Z. L, *Aust.J.Chem.*, (2007) **60**, 595

Li H. H, Chen Z. R, Huang, C. C, Lian Z. X, Chen J H, *Wuji Huaxue Xuebao(Chin.)(Chin.J.Inorg.Chem.)* (2004) **20**, 703

Li H. H, Chen Z, Cheng L. C, Liu J. B, Chen X. B, Li J. Q, *Cryst. Growth Des.*, (2008) **8**, 4355

Li H. H, Zheng Q. S, Cheng Z. R, Dong H. J, Wu Y. L, Wang M, *Journal of Molecular Structure.*, (2010) **982**, 28

Li Y.Y, Lin C. K, Zheng G. L, Cheng Z. Y, You H, Wang W. D, Lin J, *Chem. Mater.*, (2006) **18**, 3463

Li Y. Y, Zheng G, Lin C, Lin J, *Solid State Sciences*, (2007) **9**, 855

Li Y.Y, Zheng G. L, Lin C, Lin J, *Crystal Growth and Design*, (2008a) **8**, 1990

Li Y.Y, Zheng G. L, Lin J, *European Journal of Inorganic Chemistry*, (2008b) **10**, 1689

Lommerse J. P, Stone A. J, Taylor R, Allen F. H, *J. Am. Chem. Soc.*, (1996) **118**, 3108

Louvain N, Bi W, Mercier N, Buzare J. Y, Legein C, Corbel G, *Dalton Trans.*, (2007) 965

Louvain N, Mercier N, *Solid State Sciences*, (2008a) **10**, 1269

Louvain N, Mercier N, Luc J, Sahraoui B, *Eur.J.Inorg.Chem.*, (2008b) 3592

## M

Makino H, Goto T, Yao T, Mousdis G. A, Papavassiliou G. C, *Journal of Luminescence.*, (2005) **112**, 54

Marks T. J, Ratner M. A, *Angew Chemie., Int. Ed. Engl.*, (1995) **34**, 155

Maxcy K. R, Willett R. D, Mitzi D. B, Afzali A, *Acta Cryst.*, (2003) **59**, m364

Mitzi D. B, Field C. A, Harrison W. T. A, Guloy A. M, *Nature*, (1994) **369**, 467

Mitzi D. B, Wang S, Field C. A, Chess C. A, Guloy A. M, *Science*, (1995a) **267**, 1473

Mitzi D. B, Field C. A, Schlesinger Z, Laibowitz R. B, J. *Solid State Chem.*, (1995b) **114**, 159

Mitzi D. B, *Chem. Mater.* (1996) **8**, 791

Mitzi D. B and Liang K, *J. Solid State Chem*, (1997) **134**, 376

Mitzi D. B, Liang K, Wang S, *Inorg. Chem.*, (1998) **37**, 321

Mitzi D. B, *Prog. Inorg. Chem*, (1999) **48**, 1

Mitzi D. B, Chondroudis K, Kagan C. R, *Inorg. Chem.*, (1999b) **38**, 6248

Mitzi D. B, *J. Chem. Soc., Dalton Trans.*, (2001a) 1

Mitzi D. B, Dimitrakopoulos C. D., Kosbar, L. L, *Chem. Mater.*, (2001b) **13**, 3728

Mitzi D. B, Chondroudis K, Kagan C. R, *IBM Res. Dev.*, (2001c) **45**, 29

Mitzi D. B, Dimitrakopoulos C. D, Rosner J, Medeiros D. R, Xu Z, Noyan C, *Adv. Mater.*, (2002) **14**, 1772

Mitzi D. B, Medeiros D. R, Malenfant P. R. L, *Inorg.Chem.*, (2002b)

Mitzi D. B, *J. Mater. Chem.*, (2004) **14**, 2355

Miyamae H, Nishikawa H, Hagimoto K, Hihara G, Nagata M, *Chem. Lett.*, (1988) 1907

Mercier N, Pioroux S, Riou A, Batail P, *Inorg. Chem.*, (2004) **43**, 8631

Mercier N, *CrysEngComm*, (2005) **7**, 429

Mercier N, Barres A. L, Giffard I. R, Kajzar F, Sahrour B, *Angew. Chem. Int. Ed.*, (2006) **45**, 2100

Mercier N, Louvain N, Wenhua B, *CrystEngComm*, (2009) **11**, 720

E. Mohr, *J. Prakt. Chem.*, (1918) **98**, 315

E. Mohr, *Chem. Ber.*, (1922) **55**, 230

Morita M, Kameyama M, *Journal of Luminescence*, (1981) **24/25**, 79

Mousdis G. A, Goinis V, Papavassiliou G. C, Raptopoulou C. P, Terzis A, *J. Chem. Mater.*, (1998) **8**, 2259

## N

Nagapetyan S. S, Dolzhenko Y. L, Arakelova E. R, Koshkin V. M, Struchkov Y. T, Shklover V. E, *Zh.Neorg.Khim.(Russ.)(Russ.J.Inorg.Chem.)*, (1988) **33**, 2806

Nye J. F, *Physical Properties of Crystals*, 1957, Oxford atarendon Press, 235-273

## O

Ogawa T, Kanemitsu Y., *Optical Properties of Low-Dimensional Materials.*, World Scientific Publishing Co Pte Ltd., 1995

Ogawa T, Kanemitsu Y., *Optical Properties of Low-Dimensional Materials Volume 2.*, World Scientific Publishing Co Pte Ltd., 1998

## P

Papavassiliou G.C, Patsis A. P, Lagouvardos D J, Koutselas I. B, *Synth. Met.*, (1993) **55-57**, 3889.

Papavassiliou, G. C, Koutselas I. B, Terzis A, Whangbo M. H, *Solid State Commun.*, (1994) **91**, 695

Papavassiliou G.C, Koutselas I. B, *Synth. Met.*, (1995) **71**, 1713.

Papavassiliou G. C. *Mol. Cryst. Liq. Cryst. Sci. Technol., Sect. A*, (1996) **286**, 553

Papavassiliou G. C, *Prog. Solid. St. Chem.*, (1997) **25**, 125

Papavassiliou G. C, Mousdis G. A, Koutselas, *Adv. Mater. Opt. Electron.*, (1999) **9**, 265

Papavassiliou G. C, Mousdis G. A, Raptopoulou C. P, Terzis A, *Z.Naturforsch.*, (1999b) **54b**, 1405

Papavassiliou G. C, Mousdis G. A, Raptopoulou C. P, Terzis A, *Z.Naturforsch.*, (2000) **55b**, 536

Papavassiliou G. C, Mousdis G. A, Koutselas, *Synth. Met.*, (2001) **121**, 1339

Papavassiliou G. C, Mousdis G. A, Terzis A, Raptopoulou C. P, *Z. Naturforsch.*, (2003) **58b**, 815

Perez-Jimenez A. J, *J. Phys. Chem. B.*, (2005) **109**, 10052

Philpott, M. F. (2002). *Conversion of a N/C/S Analyser for High Precision CHN Determination on Samples of 1 Milligram or Less*, Poster Presentation, Analytika 2002, Stellenbosch.

Pitzer K. S, Donath W. E, *J. Am. Chem. Soc.*, (1959) **81**, 3213

Pradeesh K, Baumberg J. J, Prakash G. V, *Appl. Phys. Lett.*, (2009a) **95**, 033309

Pradeesh K, Baumberg J. J, Prakash G. V, *Appl. Phys. Lett.*, (2009b) **95**, 173305

Pradeesh K, Agarwal M, Rao K. K, Prakash G. V, *Solid State Sciences.*, (2010) **12**, 95

## R

Raptopoulou C. P, Terzis A, Mousdis G. A, Papavassiliou G. C, *Z.Naturforsch.*, (2002) **57b**, 645

Reed M. A, Randall J. N, Aggarwal R. J, Matyi R. J, Moore T. M, Wetsel A. E, *Phys. Rev. Lett.*, (1988) **60**, 535

Ricard L, Rey-Lafon M, Biran C, *J. Phys. Chem.*, (1984) **88**, 5614

## S

Sarker K K, Jana A. D, Mostafa G, Wu J. S, Lu T H, Sinha C, *Inorg.Chim.Acta*, (2006) **359**, 4377

Schenk K. J, Chapuis G, *J. Phys. Chem.*, (1988) **92**, 7141

Sachse H, *Chem. Ber*, (1890) **23**, 1363

Sachse H, *Z. Physik. Chem*, (1892) **10**, 203

Sachse H, *Z. Physik. Chem.*, (1893) **11**, 185

Shimizu M, Fujisawa J, Ishi-Hayase J, *Phys. Rev. B.*, (2005) **71**, 205306

Shimizu M, Fujisawa J, Ishihara T, *Journal of Luminescence.*, (2007) **122-123**, 485

Singleton J, *Band Theory and Electronic Properties of Solids*, Oxford University Press, (2008)

Sourisseau S, Louvain N, Bi W, Mercier N, Rondeau D, Boucher F, Buzare J. Y, Legien C, *Chem. Mater.*, (2007a) **19**, 600

Sourisseau S, Louvain N, Bi W, Mercier N, Rondeau D, Boucher F, Buzare J. Y, Legien C, *Inorg. Chem.*, (2007b) **46**, 6148

Sun L. G, Chen Z. R, Li J. S, Li H. H, Ou M. R, Li J. Q, *Jiegou Huaxue (Chin.J.Struct.Chem.)*, (2009) **28**, 301

## T

Tabuchi Y, Asai K, Rikukawa M, Sanui K, Ishigure K, *Journal of Physics and Chemistry of Solids*, (2000) **61**, 837

Takahashi Y, Obara R, Nakagawa K, Nakano M, Tokita J, Inabe T, *Chem. Mater*, (2007) **19**, 6312

Tamaki R, Arai Y, Ichikawa D, Inoue M, Kunugita H, Ema K, *Journal of Luminescence*, (2008) **128**, 842

Tanaka K, Kondo T, *Science and Technology of Advanced Materials*, (2003a) **4**, 599

Tanaka K, Takahashi T, Ban T, Kondo T, Uchida K, Miura N, *Solid State Communications*, (2003b) **127**, 619

Tanaka K, Takahashi T, Kondo T, Umebayashi T, Asai K, Ema K, *Phys. Rev. B.*, (2005) **71**, 045312

Tanaka K, Ozawa R, Umebayashi T, Asai K, Ema K, Kondo T, *Physica E.*, (2005b) **25**, 378

Tanaka K, Takahashi T, Kondo K, Umeda K, Ema K, Umebayashi T, Asai K, Uchida K, Miura N, *Jpn. J. Appl. Phys.*, (2005c) **44**, 5923

Tang Z, Guloy A. M, *J. Am. Chem. Soc.*, (1999) **121**, 452

Tang Z, Guloy A. M, *J. Mater. Chem.*, (2001) **11**, 479  
 Tanino H, Ruhle W. W, Takahashi K, *Phys. Rev. B.*, (1988) **38**, 12716  
 Tello M. J, Arriandiaga M. A, Fernandez J, *Solid State Commun.*, (1977) **24**, 299  
 Thiele G, Rotter H. W, Schmidt K. D, *Z. Anorg. Allg. Chem.*, (1987) **545**, 148  
 Thirumurugan A, Rao C. N. R, *Crystal Growth and Design*, (2008) **8**, 1640  
 Tomimoto S, Saito S, Suemoto T, Sakata K, Takeda J, Kurita S, *Phys. Rev. B.*, (1999) **60**, 7961  
 Tsuboi T, Matasubara A, Kato K, Iio K, Henderson B, *Phys. Status Solidi B*, (1995) **188**, K35

## U

Umebayashi T, Asai K, Kondo T, Nako A, *Phys. Rev. B*, (2003) **67**, 155405

## V

Verbiest T, Houbrechts S, Kauranen M, Clays K, Persoons A, *J. Mater. Chem.*, (1997) **7**, 2175  
 Vincent B. R, Robertson K. N, Cameron T. S, Knop O, *Can. J. Chem.*, (1987) **65**, 1042

## W

Wang S, Mitzi D. B, Field C. A, Guloy A, *J. Am. Chem. Soc.*, (1995) **117**, 5297  
 Wang X. L, Voliotis V, *Journal of Applied Physics*, (2006) **99**, 121301  
 Wu G, Cheng S, Deng M, Zheng Y, Chen H, Wang M, *Synthetic Metals*, (2009) **159**, 2425

## X

Xu C. Q, Kondo T, Sakakura H, Kumata K, Takahashi Y, Ito R, *Solid State Communications*, (1991) **79**, 245  
 Xu C. Q, Sakakura H, Kondo T, Takeyama S, Miura N, Takahashi Y, Kumata K, Ito R, *Solid State Communications*, (1991b) **79**, 249  
 Xu H, Sun J, Qin A, Hua J, Li Z, Dong, Y, Xu H, Yuan W, Ma Y, Wang M, Tang B. Z, *J. Phys. Chem. B.*, (2006) **110**, 21701  
 Xu Z, Mitzi D. B, Medeiros D. R, *Inorg. Chem.*, (2003a) **42**, 1400  
 Xu Z, Mitzi D. B, Dimitrakopoulos C. D, Maxcy K. R, *Inorg.Chem.*, (2003b) **42**, 2031  
 Xu Z, Mitzi D. B, *Chem. Mater.*, (2003c) **15**, 3632  
 Xu Z, Mitzi D. B, *Inorg. Chem.*, (2003d) **42**, 6589  
 Xu G, Guo G. C, Wang M. S, Zhang Z. J, Chen W. T, Huang J. S, *Angew. Chem. Int. Ed.*, (2007) **46**, 3249

## Z

Zhang Z. J, Guo G. C, Xu G, Fu M. L, Zou J. P, Huang J. S, *Inorg.Chem.*, (2006) **45**, 10028  
 Zhang Z. J, Xiang S. C, Zhang Y. F, Wu A. Q, Cai L. Z, Guo G. C, Huang J. S, *Inorg. Chem.*, (2006b) **45**, 1972  
 Zhang Z. J, Xiang S. C, Guo G. C, Xu G, Wang M. S, Zou J. P, Guo S. P, Huang J. S, *Angew.Chem.,Int.Ed.*, (2008) **47**, 4149  
 Zhao H. R, Li D. P, Ren X. M, Song Y, Jin W. Q, *J. Am. Chem. Soc.*, (2010) **132**, 18  
 Zheng Y. Y, Wu G, Chen H. Z, Wang M, *Acta Crystallogr.,Sect.E:Struct.Rep.Online*, (2007) **63**, m504  
 Zhu H. G, Xu Y, Yu Z, Wu Q. J, Fun H. K, You X. Z, *Polyhedron*, (1999) **18**, 3491  
 Zhu X. H, Mercier N, Riou A, Blanchard P, Frere P, *Chem.Comm.*, (2002) 2160  
 Zhu X. H, Mercier N, Frere P, Blanchard P, Roncali J, Allain M, Pasquier C, Riou A, *Inorg. Chem.*, (2003) **42**, 5330  
 Zhu X. H, Mercier N, Allain M, Frere P, Blanchard P, Roncali J, Riou A, *Journal of Solid State Chemistry*, (2004) **177**, 1067

Zyss J, Nicoud J. F, *Current opinion in Solid State and Materials Science*, (1996) **1**, 533

## Appendix A

### 4.3 Optical absorption and photoluminescence.

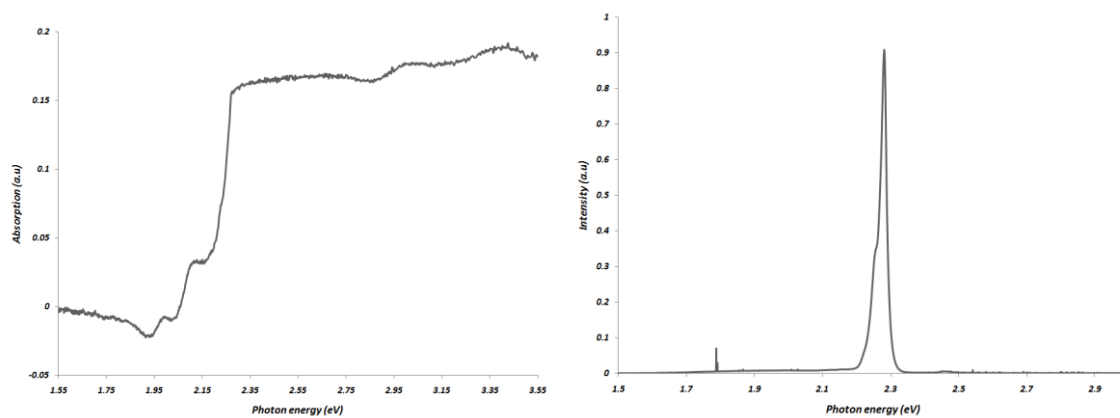


**Figure A.1:** (HOC2)PbI<sub>4</sub> the optical absorption and photoluminescence. Please note as no band pass filter was used, the plasma lines are still present in the PL spectra

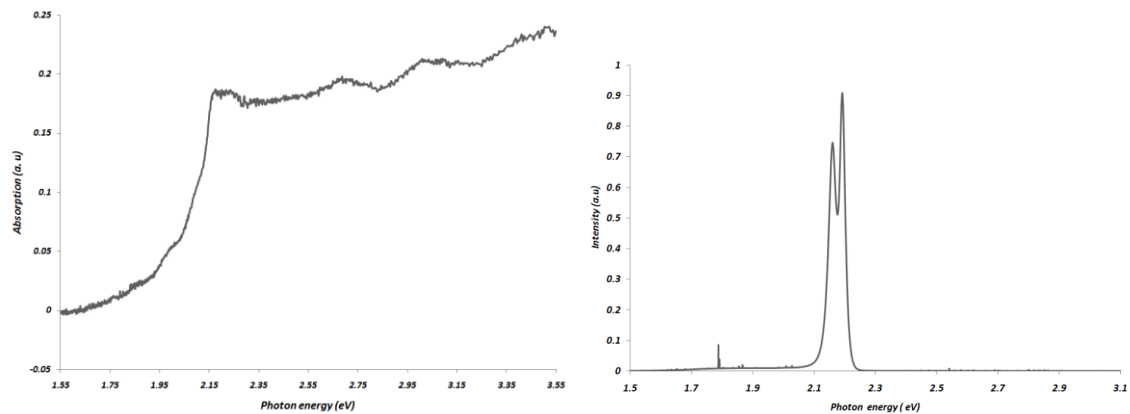


**Figure A.2:** (BrC2)PbI<sub>4</sub> the optical absorption and photoluminescence. Please note as no band pass filter was used, the plasma lines are still present in the PL spectra

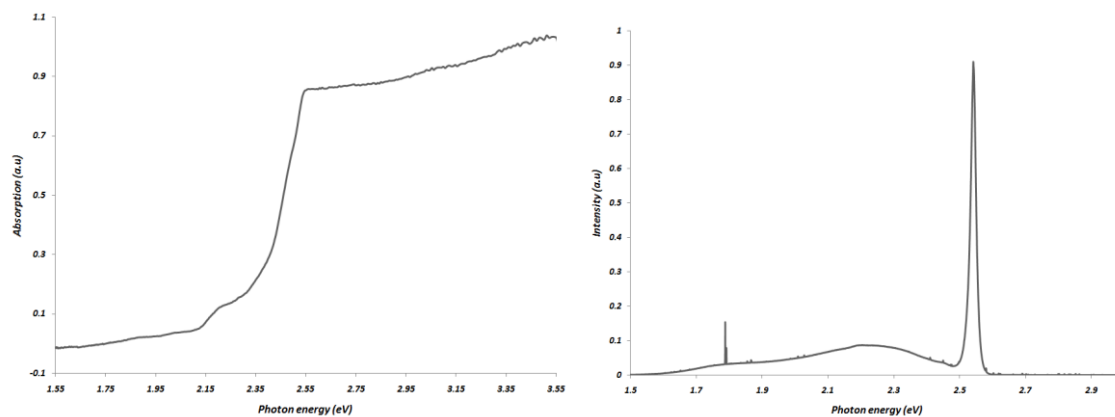


**Figure A.3:** (IC2)PbI<sub>4</sub> the optical absorption and photoluminescence at 77K. Please note as no band pass filter was used, the plasma lines are still present in the PL spectra.

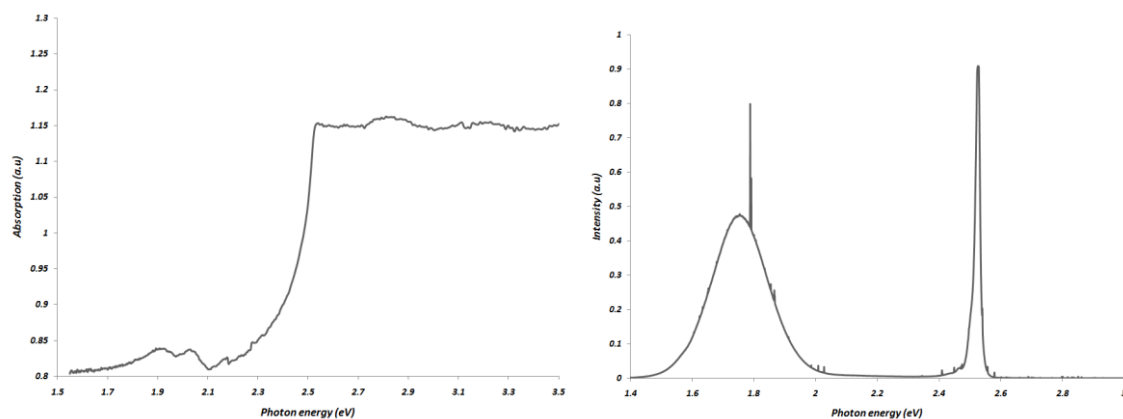


**Figure A.4:** (IC3)PbI<sub>4</sub> the optical absorption and photoluminescence at 77K. Please note as no band pass filter was used, the plasma lines are still present in the PL spectra.

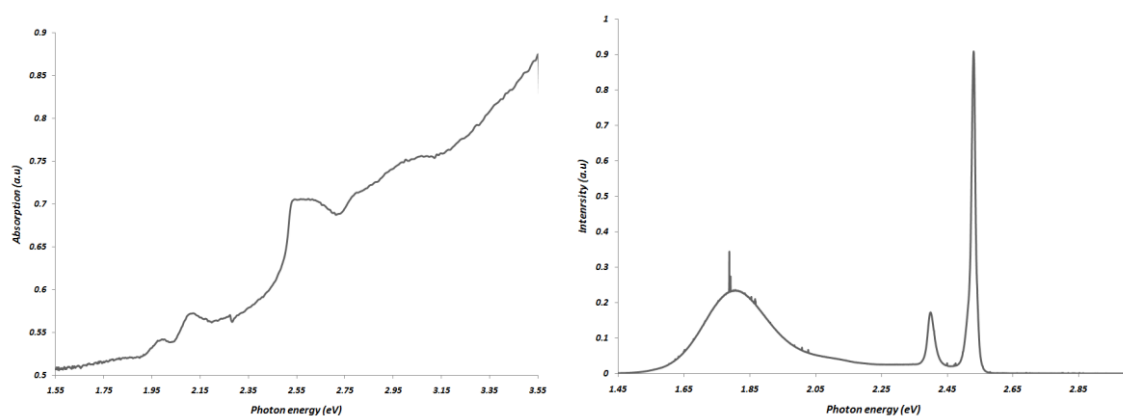


**Figure A.5:** (IC4)PbI<sub>4</sub> the optical absorption and photoluminescence at 77K. Please note as no band pass filter was used, the plasma lines are still present in the PL spectra.

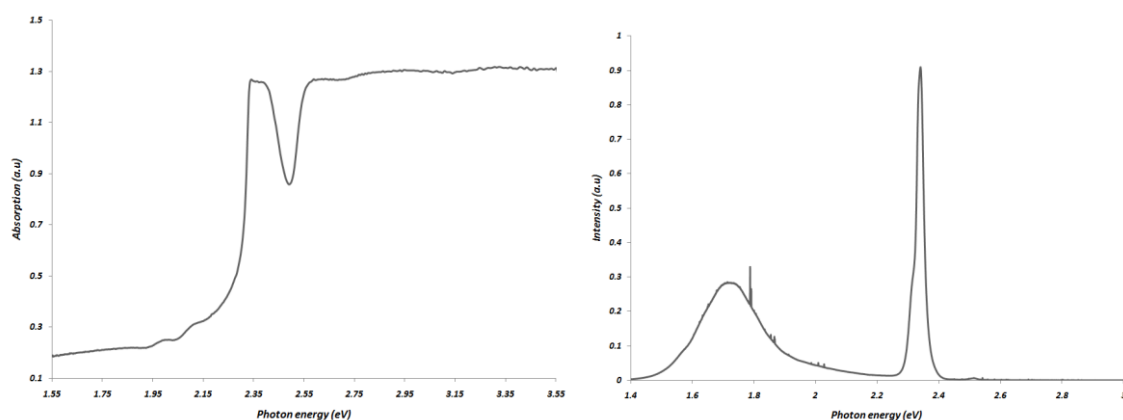


**Figure A.6:** (IC5)PbI<sub>4</sub> the optical absorption and photoluminescence at 77K. Please note as no band pass filter was used, the plasma lines are still present in the PL spectra.



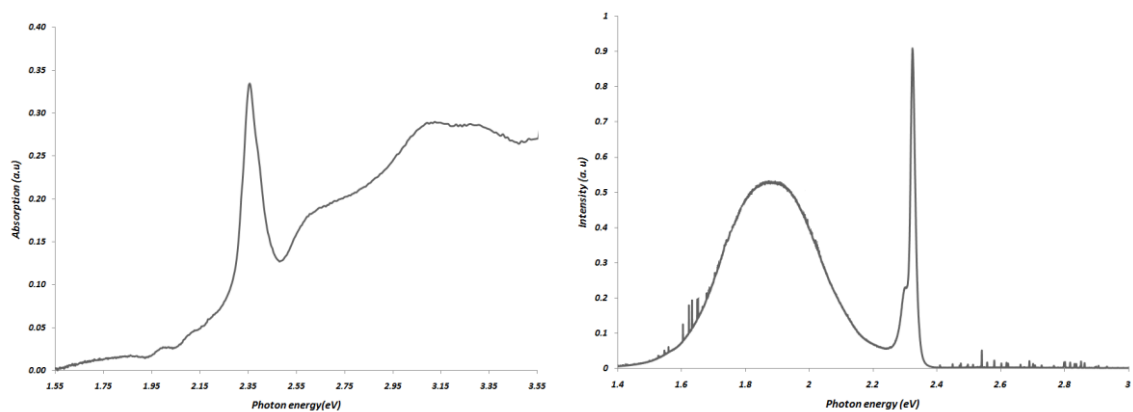


**Figure A.7:** (IC6)PbI<sub>4</sub> the optical absorption and photoluminescence at 77K. Please note as no band pass filter was used, the plasma lines are still present in the PL spectra.

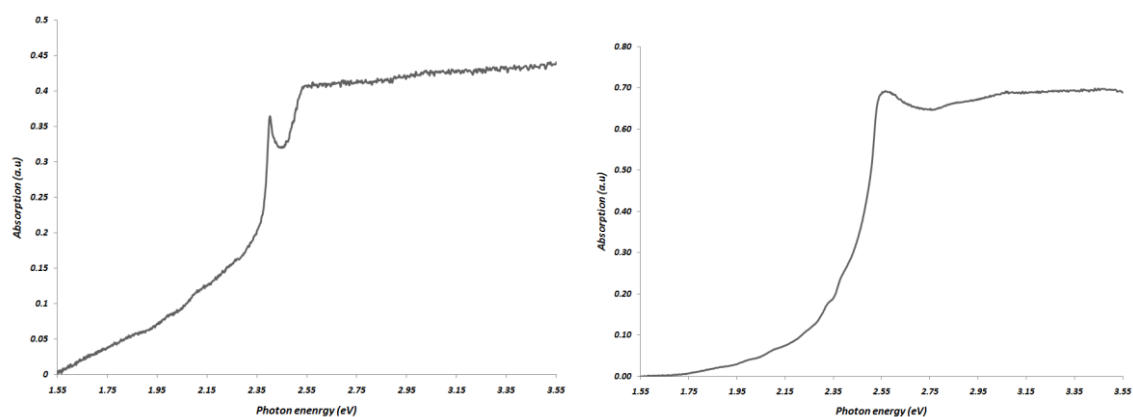


**Figure A.8:** The optical absorption of (C4)PbI<sub>4</sub> (left) and (C5)PbI<sub>4</sub> (right) at 77K

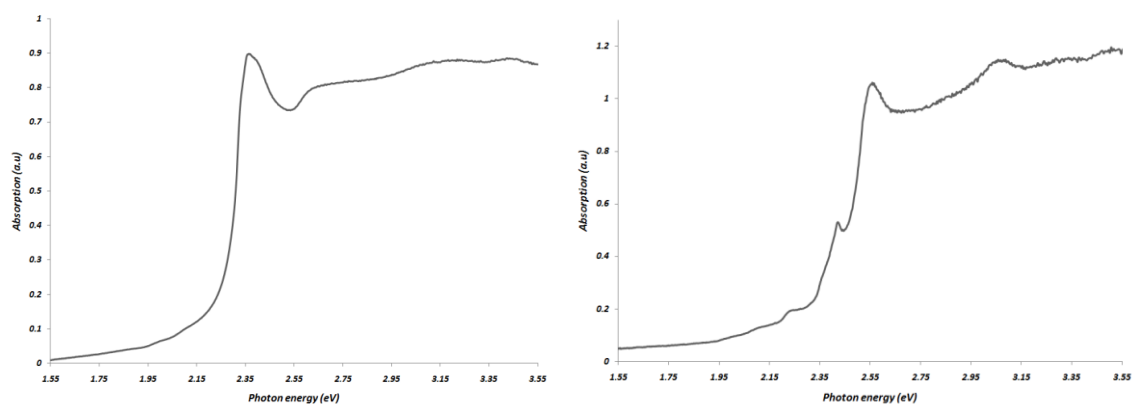


**Figure A.9:** The optical absorption of (C6)PbI<sub>4</sub> (left) and (C7)PbI<sub>4</sub> (right) at 77K

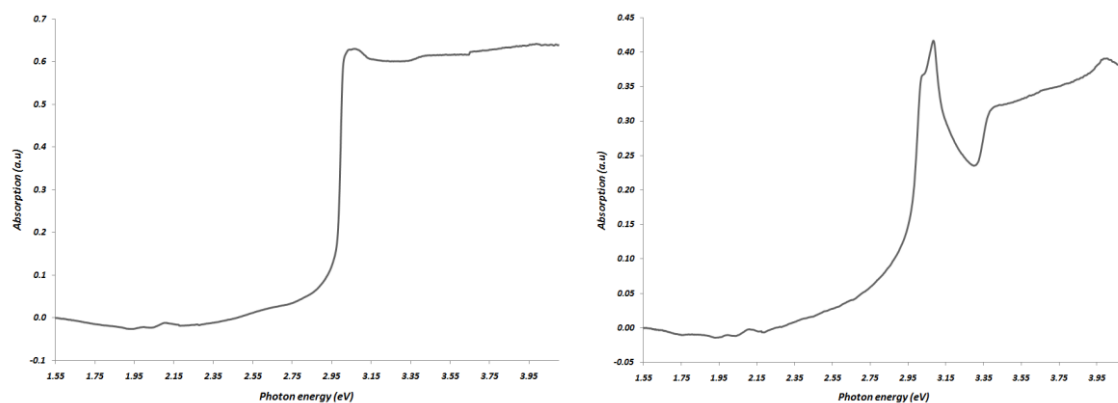


**Figure A.10:** The optical absorption of (C4)PbBr<sub>4</sub> (left) and (C5)PbBr<sub>4</sub> (right) at 77K

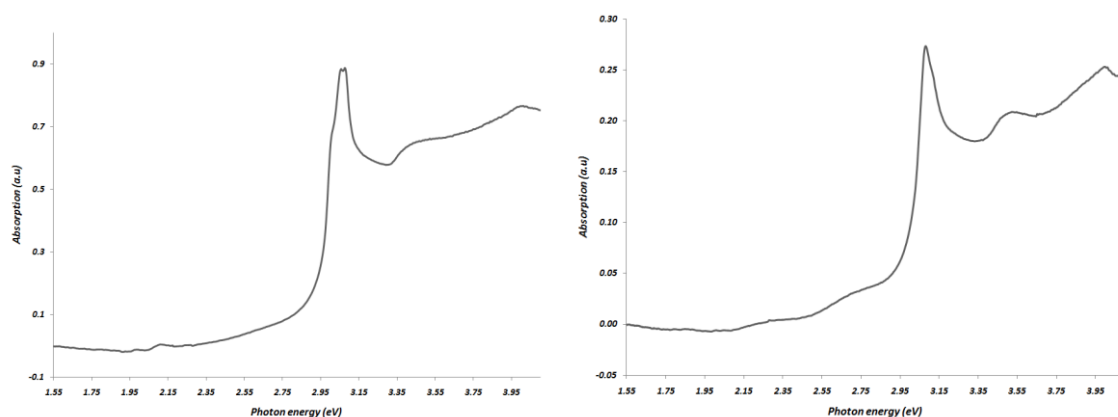


**Figure A.11:** The optical absorption of (C6)PbBr<sub>4</sub> (left) and (C7)PbBr<sub>4</sub> (right) at 77K

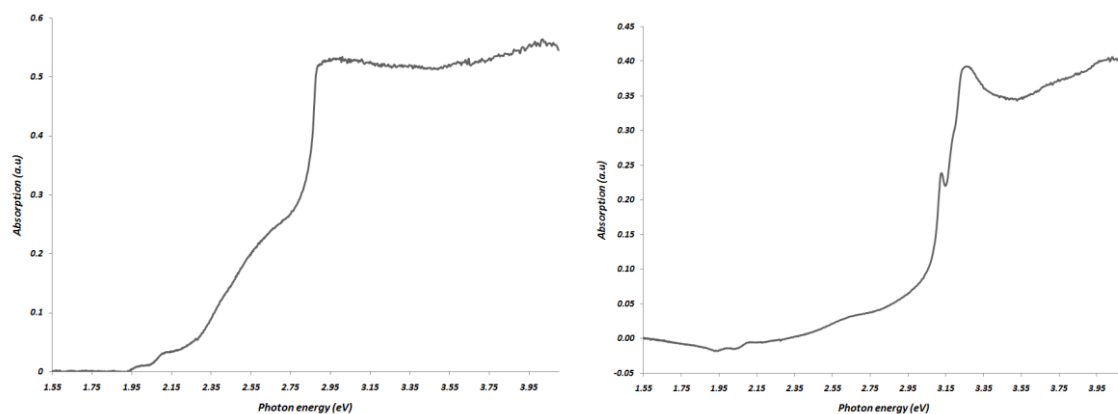


**Figure A.12:** The optical absorption of (HOC2)PbBr<sub>4</sub> (left) and (BrC3)PbBr<sub>4</sub> (right) at 77K

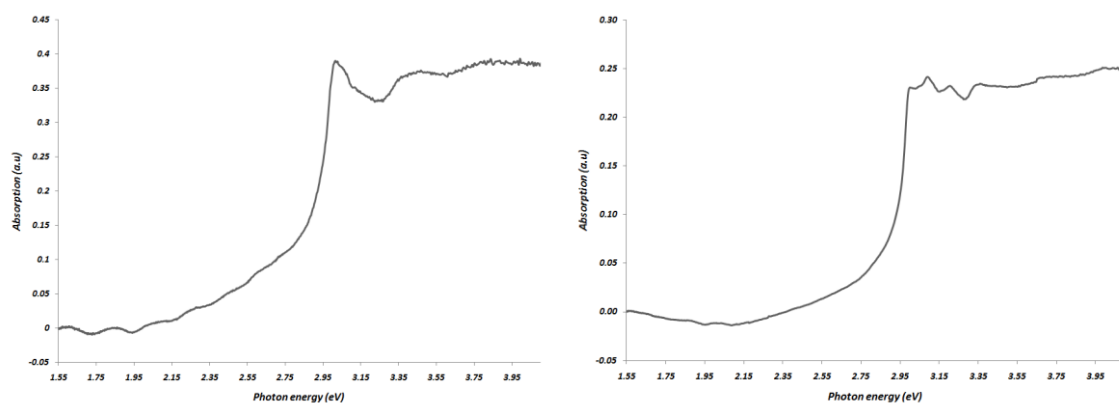


**Figure A.13:** The optical absorption of (BrC4)PbBr<sub>4</sub> (left) and (BrC5)PbBr<sub>4</sub> (right) at 77K

#### 4.3 Thermal analysis (DSC) on (XCn)PbI<sub>4</sub> where n = 2-6 and X = I and (ZC2)PbI<sub>4</sub> where Z = HO and Br.

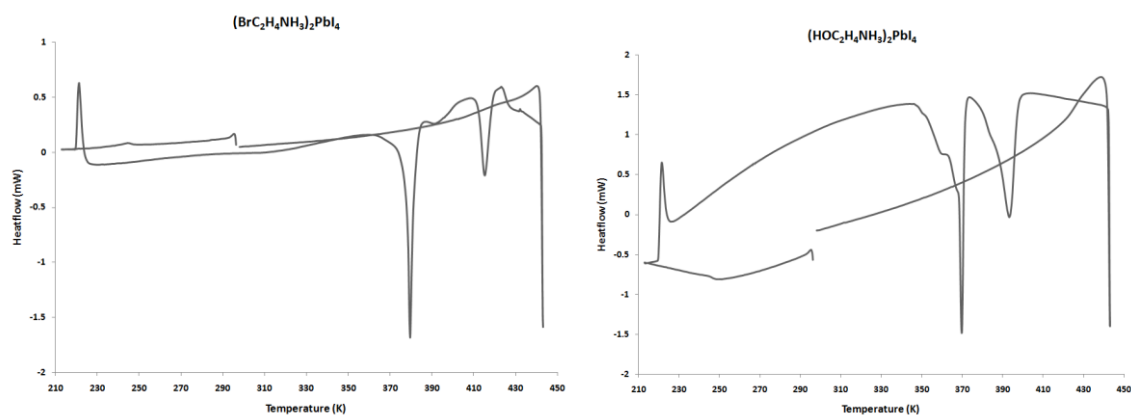


**Figure A.14:** The DSC scans of (BrC2)PbI<sub>4</sub> (left) and (HOC2)PbI<sub>4</sub> (right)

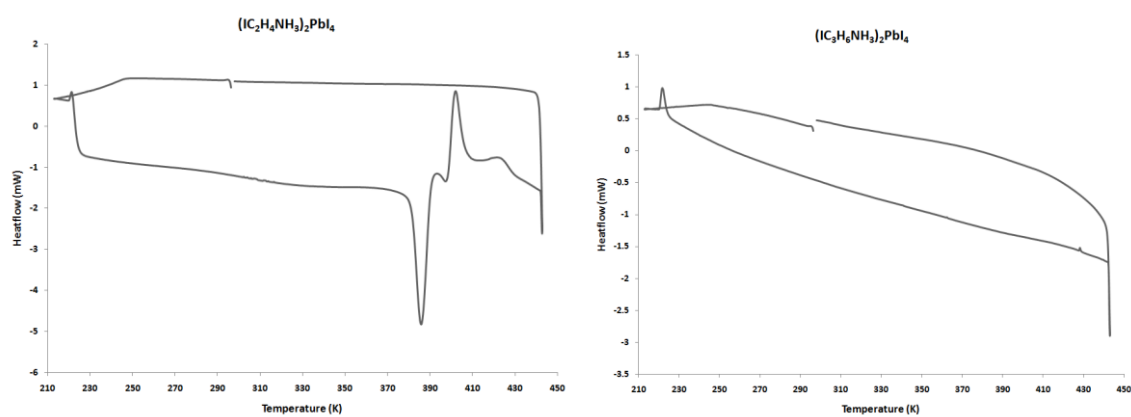


**Figure A.15:** The DSC scans of (IC2)PbI<sub>4</sub> (left) and (IC3)PbI<sub>4</sub> (right)

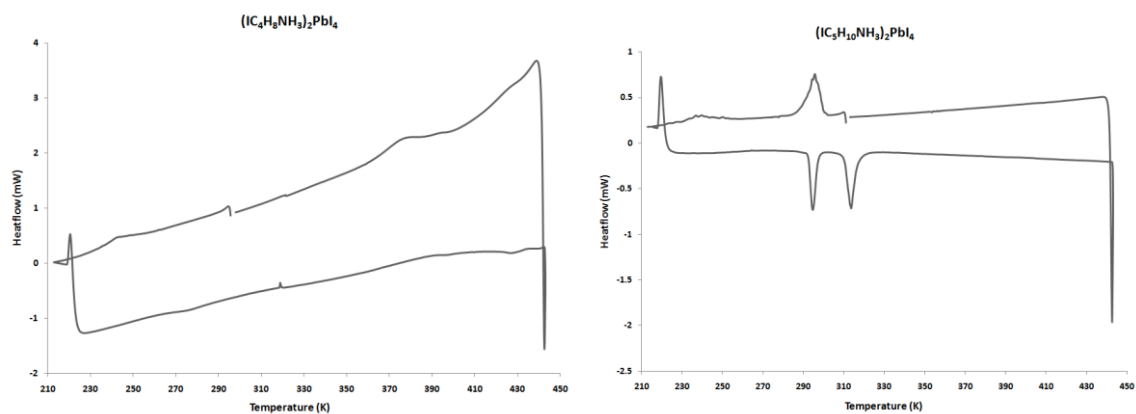


**Figure A.16:** The DSC scans of  $(\text{IC}_4)\text{PbI}_4$  (left) and  $(\text{IC}_5)\text{PbI}_4$  (right)

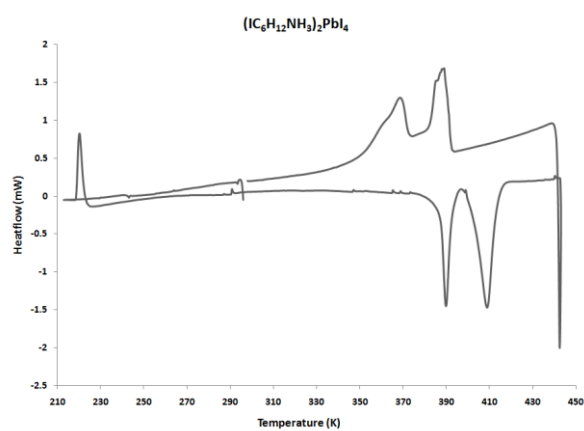


**Figure A.17:** The DSC scans of  $(\text{IC}_6)\text{PbI}_4$

## Appendix B

### 5.1 Thermal analysis (DSC) on (Pyr)PbI<sub>3</sub> and [(Et)<sub>3</sub>NH]PbI<sub>3</sub>

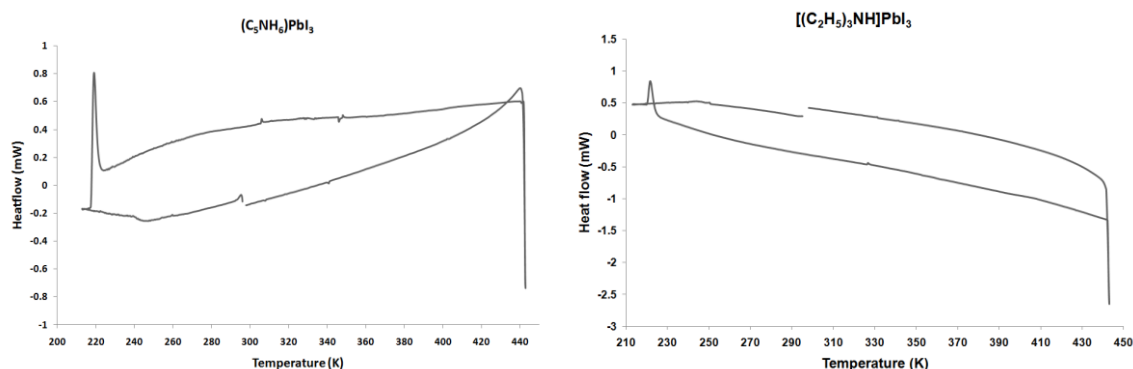


**Figure B.1:** The DSC scans of (Pyr)PbI<sub>3</sub> (left) and [(Et)<sub>3</sub>NH]PbI<sub>3</sub> (right). The small peaks in (Pyr)PbI<sub>3</sub> are sample dependant.

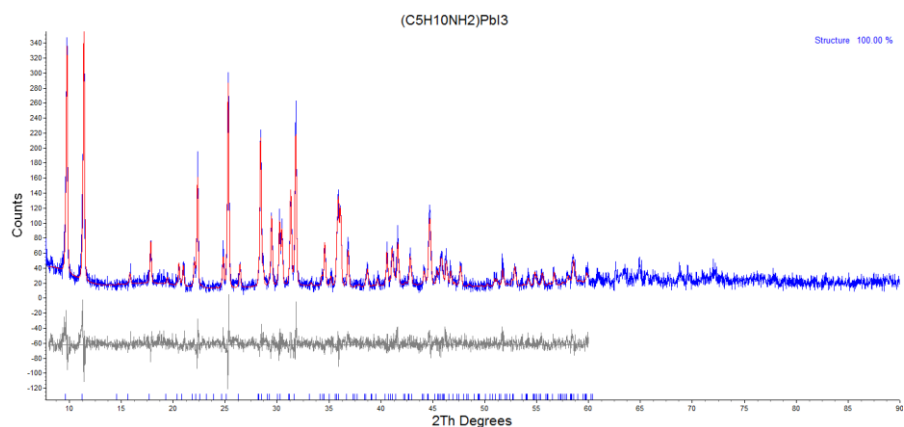


**Figure B.2:** The powder diffraction pattern and rietveld refinement of (PD)PbI<sub>3</sub> where  $R_{\text{Bragg}}$ : 3.635  $R_{\text{exp}}$ : 17.41,  $R_{\text{wp}}$ : 19.77,  $R_p$ : 15.30, GOF: 1.14,  $R_{\text{exp}}^2$ : 30.83,  $R_{\text{wp}}^2$ : 35.01,  $R_p^2$ : 31.85, DW: 1.56. Refined unit cell parameters for C222<sub>1</sub> a = 8.7083(23) Å, b = 18.4196(50) Å, c = 8.1241(22) Å, V = 1303.15(61) Å<sup>3</sup>, refinement range: 5-60° 2θ

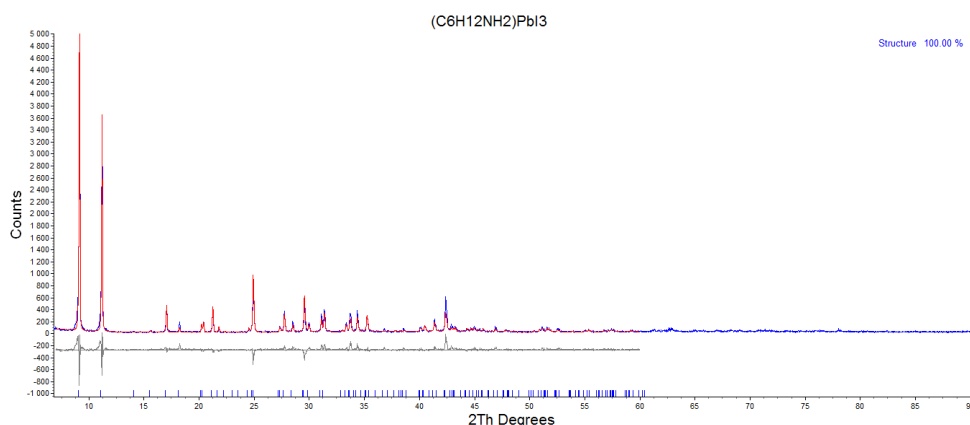


**Figure B.3:** The powder diffraction pattern and rietveld refinement of (Az)PbI<sub>3</sub> where  $R_{\text{Bragg}}$ : 8.801  $R_{\text{exp}}$ : 11.18,  $R_{\text{wp}}$ : 18.36,  $R_p$ : 14.37, GOF: 1.64,  $R_{\text{exp}}^2$ : 16.20,  $R_{\text{wp}}^2$ : 26.61,  $R_p^2$ : 23.86, DW: 0.84. Refined unit cell parameters for C222<sub>1</sub> a = 8.75506(92) Å, b = 19.6060(21) Å, c = 8.20201(93) Å, V = 1407.89(26) Å<sup>3</sup>, refinement range: 7-60° 2θ

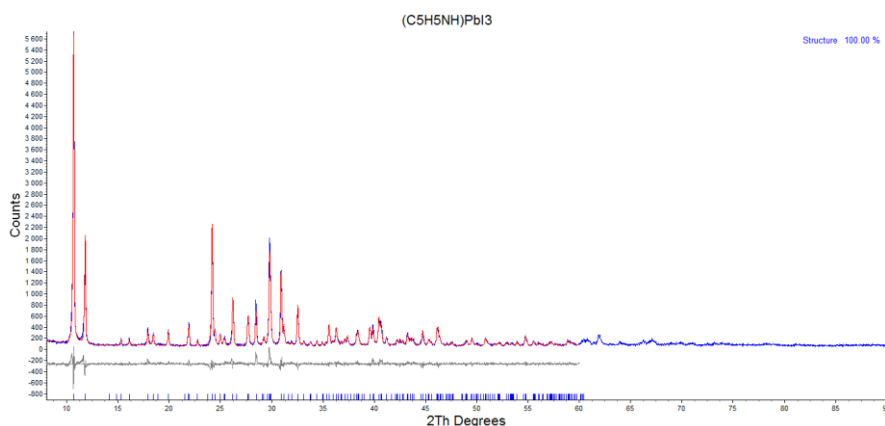


**Figure B.4:** The powder diffraction pattern and rietveld refinement of (Pyr)PbI<sub>3</sub> where  $R_{\text{Bragg}}$ : 3.502  $R_{\text{exp}}$  : 7.52,  $R_{\text{wp}}$  : 11.71,  $R_p$  : 9.04, GOF : 1.56,  $R_{\text{exp}}$ : 10.25,  $R_{\text{wp}}$ : 15.95,  $R_p$ : 13.24 DW : 0.92. Refined unit cell parameters for *Pnma*  $a = 14.9702(11)$  Å,  $b = 8.09842(60)$  Å,  $c = 9.89108(74)$  Å,  $V = 1199.15(15)$  Å<sup>3</sup>, refinement range: 8-60° 2θ

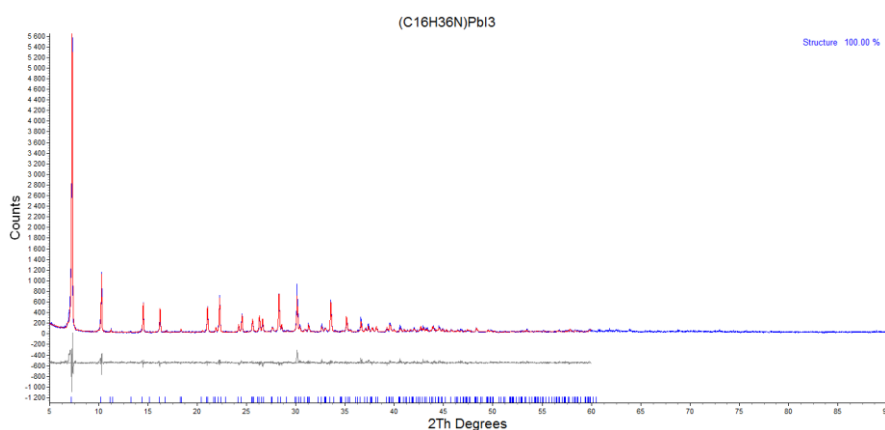


**Figure B.5:** The powder diffraction pattern and rietveld refinement of [(n-But)<sub>4</sub>N]PbI<sub>3</sub> where  $R_{\text{Bragg}}$ : 5.735,  $R_{\text{exp}}$  : 10.87,  $R_{\text{wp}}$  : 16.68,  $R_p$  : 13.01, GOF : 1.53,  $R_{\text{exp}}$ : 17.11,  $R_{\text{wp}}$ : 26.26,  $R_p$ : 24.07, DW : 1.05. Refined unit cell parameters for *I*-4<sub>2</sub>*d*  $a = 24.5855(16)$  Å,  $b = 8.38275(63)$  Å,  $V = 5066.91(76)$  Å<sup>3</sup>, refinement range: 5-60° 2θ

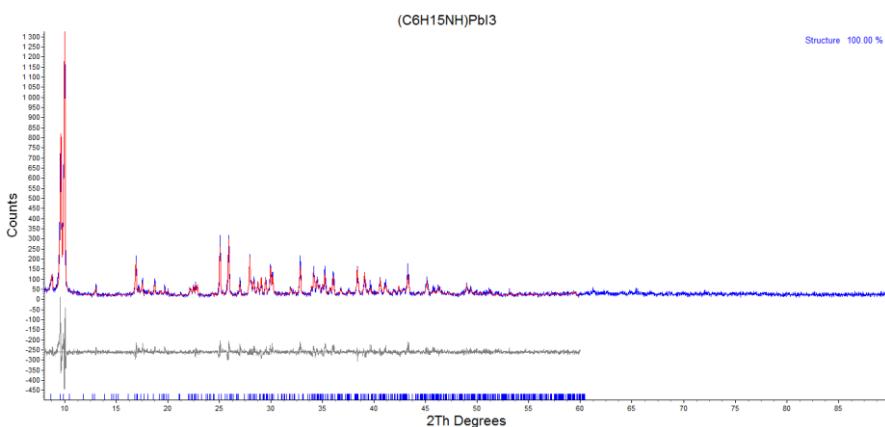


**Figure B.6:** The powder diffraction pattern and rietveld refinement of [(Et)<sub>3</sub>NH]PbI<sub>3</sub> where  $R_{\text{Bragg}}$ : 5.868,  $R_{\text{exp}}$  : 14.64,  $R_{\text{wp}}$  : 19.79,  $R_p$  : 15.90, GOF : 1.35,  $R_{\text{exp}}$ : 24.64,  $R_{\text{wp}}$ : 33.32,  $R_p$ : 30.89, DW : 1.24. Refined unit cell parameters for *Pnma*  $a = 18.4833(24)$  Å,  $b = 8.0652(11)$  Å,  $c = 20.3529(26)$  Å,  $V = 3034.01(69)$  Å<sup>3</sup>, refinement range: 8-60° 2θ

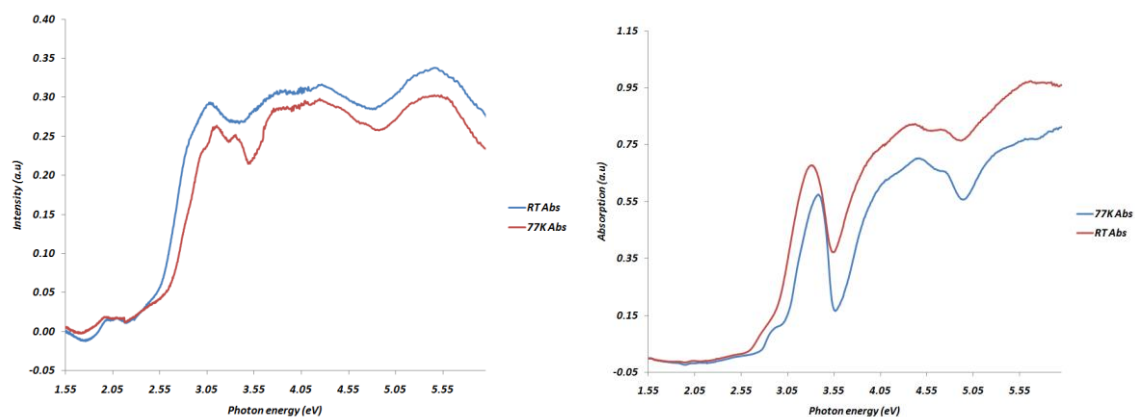


**Figure B.7:** The optical absorption of (Py)PbI<sub>3</sub> (left) and [(Et)3NH]PbI<sub>3</sub> (right) at both 77K and room temperature.

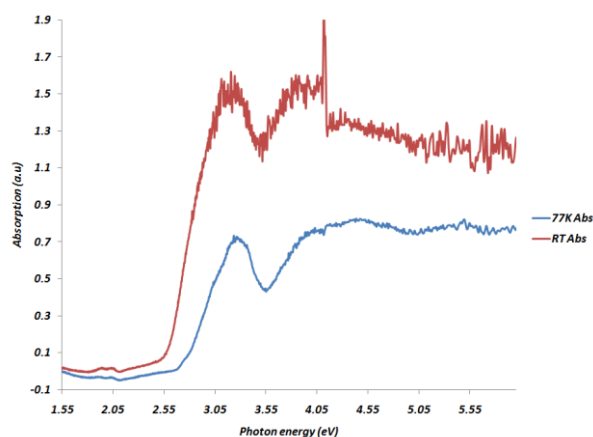


**Figure B.8:** The optical absorption of [(n-But)<sub>4</sub>N]PbI<sub>3</sub> at both 77K and room temperature.

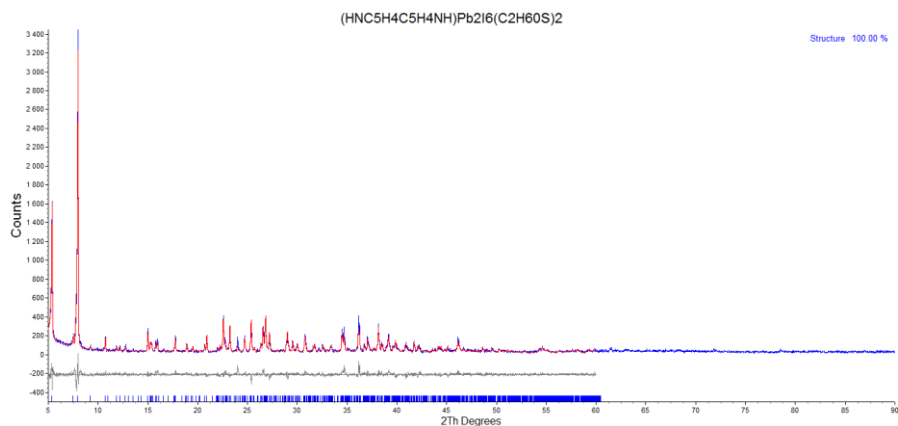


**Figure B.9:** The powder diffraction pattern and rietveld refinement of 2.DMSO(BP)Pb<sub>2</sub>I<sub>6</sub> where  $R_{\text{Bragg}}$  : 6.004,  $R_{\text{exp}}$  : 11.52,  $R_{\text{wp}}$  : 15.53,  $R_p$  : 12.01, GOF : 1.35,  $R_{\text{exp}}$  : 18.79,  $R_{\text{wp}}$  : 25.33,  $R_p$  : 22.19, DW : 1.24. Refined unit cell parameters for  $P2_12_12$   $a = 8.10947(49)$  Å,  $b = 23.6548(12)$  Å,  $c = 33.0516(16)$  Å,  $V = 6340.21(59)$  Å<sup>3</sup>, refinement range: 5-60° 2θ.

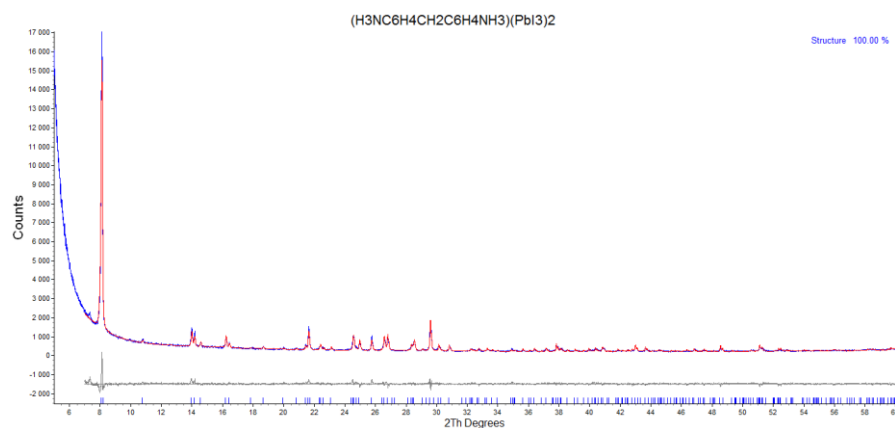


**Figure B.10:** The powder diffraction pattern and rietveld refinement of  $2\text{H}_2\text{O} \cdot (\text{BD})\text{Pb}_2\text{I}_6$  where  $R_{\text{Bragg}} : 2.318$ ,  $R_{\text{exp}} : 4.73$ ,  $R_{\text{wp}} : 7.79$ ,  $R_p : 6.12$ ,  $\text{GOF} : 1.65$ ,  $R_{\text{exp}} : 13.63$ ,  $R_{\text{wp}} : 22.46$ ,  $R_p : 26.19$ ,  $\text{DW} : 0.88$ . Refined unit cell parameters for  $Fdd2$  a =  $25.3445(17)\text{\AA}$ , b =  $43.1408(27)\text{\AA}$ , c =  $4.53537(35)\text{\AA}$ , V =  $4958.88(60)\text{\AA}^3$ , refinement range:  $5-60^\circ 2\theta$ .

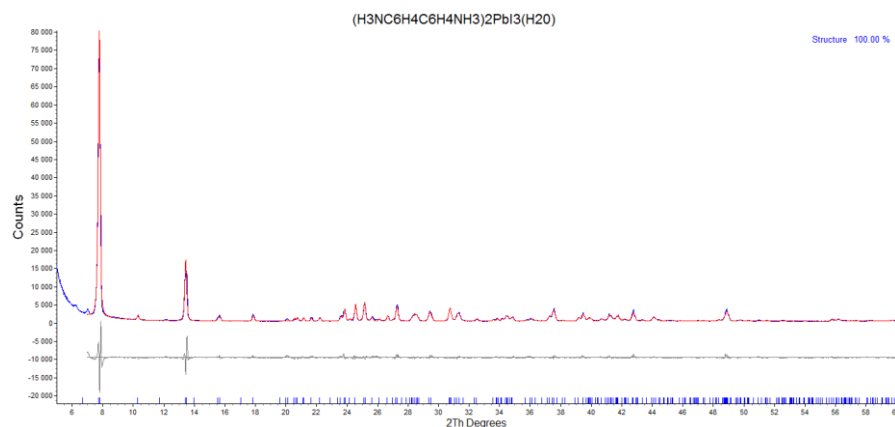


**Figure B.11:** The powder diffraction pattern and rietveld refinement of  $(\text{MDA})\text{Pb}_2\text{I}_6$  where  $R_{\text{Bragg}} : 19.447$ ,  $R_{\text{exp}} : 2.71$ ,  $R_{\text{wp}} : 12.13$ ,  $R_p : 8.72$ ,  $\text{GOF} : 4.48$ ,  $R_{\text{exp}} : 4.33$ ,  $R_{\text{wp}} : 19.41$ ,  $R_p : 16.46$ ,  $\text{DW} : 0.26$ . Refined unit cell parameters for  $P2_1/c$  a =  $4.521(67)\text{\AA}$ , b =  $13.216(65)\text{\AA}$ , c =  $22.636(11)\text{\AA}$ , V =  $1352.76(46)\text{\AA}^3$ , refinement range:  $5-60^\circ 2\theta$ .

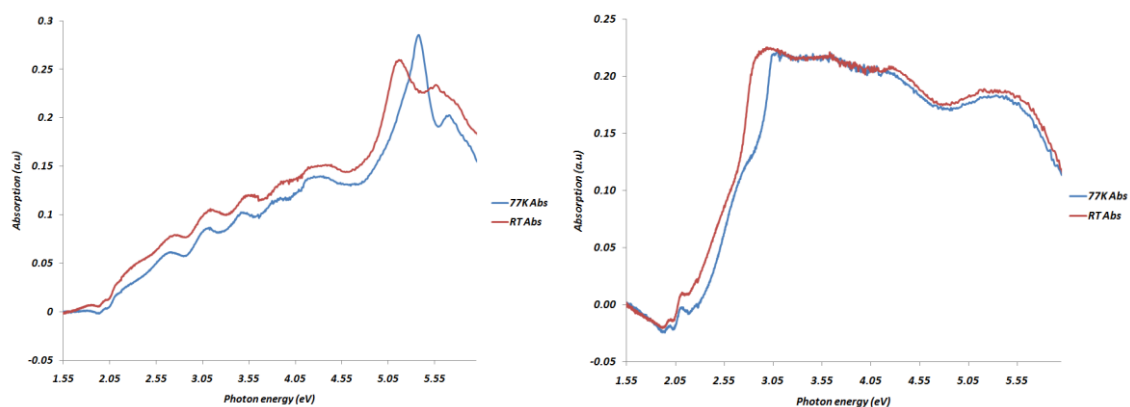


**Figure B.12:** The optical absorption of  $2\text{H}_2\text{O} \cdot (\text{BD})\text{Pb}_2\text{I}_6$  (left) and  $(\text{MDA})\text{Pb}_2\text{I}_6$  (right) at both 77K and room temperature.



## Appendix C

### 6.2 and 6.3 Thermal analysis (DSC) of compound 1-10

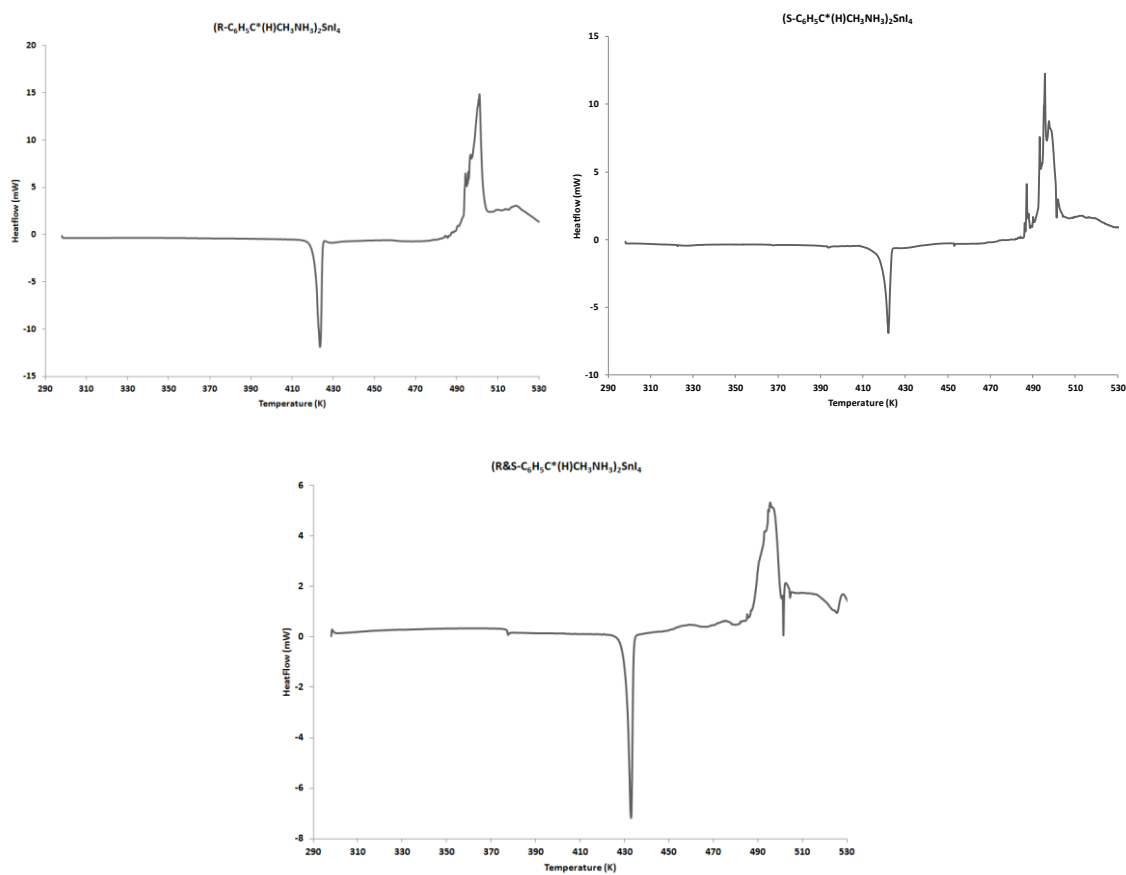


**Figure C.1:** The DSC scans of  $(R-C_6H_5C^*(H)CH_3NH_3)_2SnI_4$  (left),  $(S-C_6H_5C^*(H)CH_3NH_3)_2SnI_4$  (right) and  $(R\&S-C_6H_5C^*(H)CH_3NH_3)_2SnI_4$  (bottom), compounds **1-3** respectively.

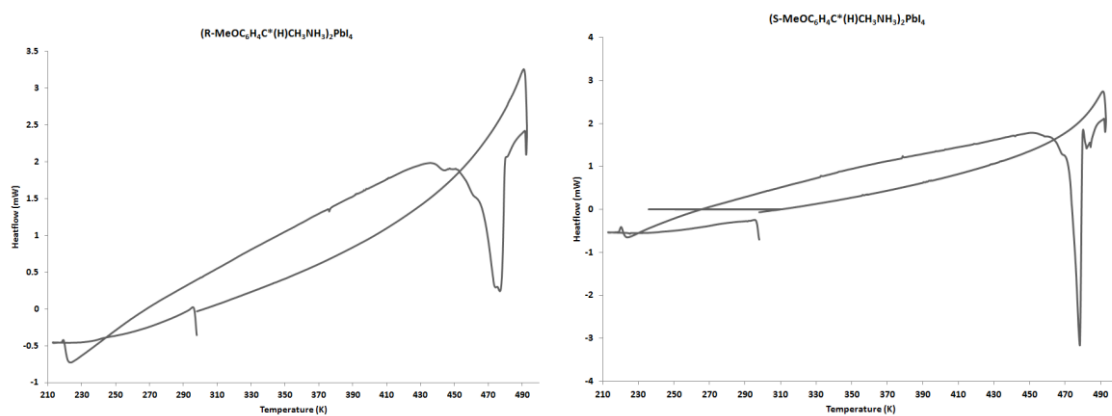


**Figure C.2:** The DSC scans of  $(R-MeOC_6H_4C^*(H)CH_3NH_3)_2PbI_4$  (left),  $(S-MeO-C_6H_4C^*(H)CH_3NH_3)_2PbI_4$  (right) compounds **4-5** respectively.

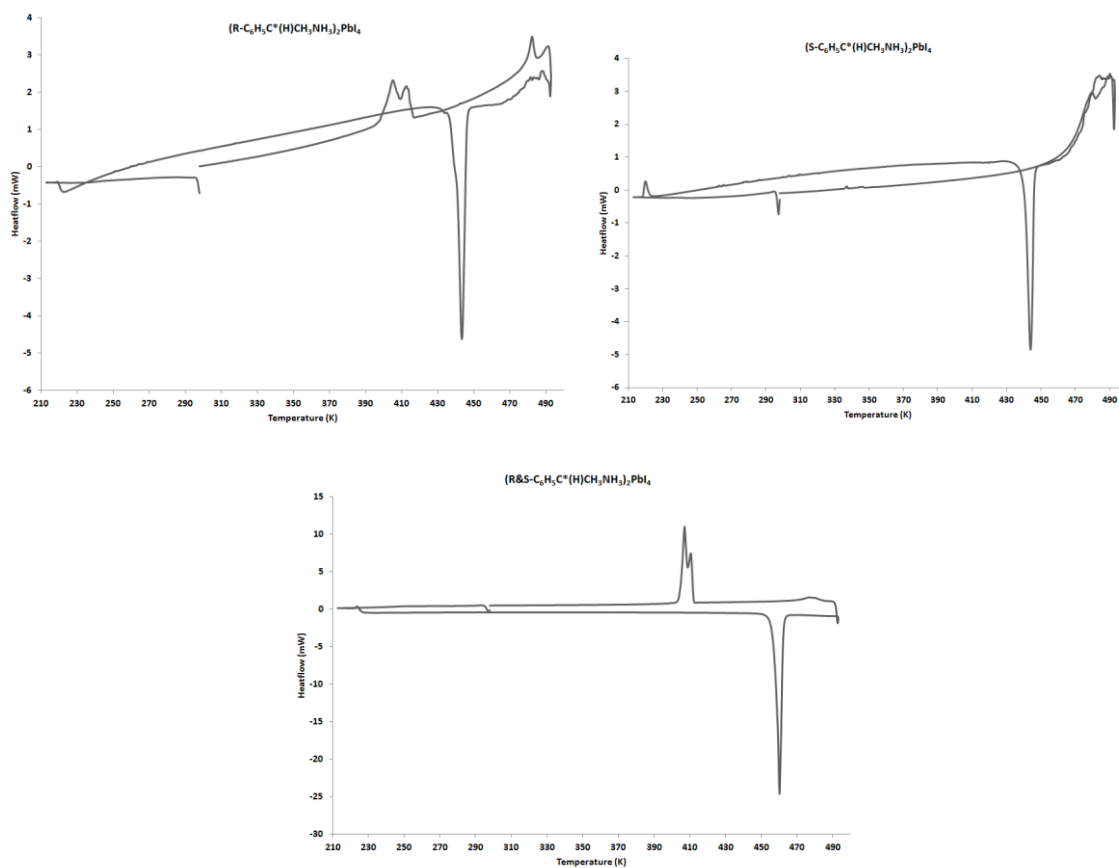


**Figure C.3:** The DSC scans of  $(R-C_6H_5C^*(H)CH_3NH_3)_2PbI_4$  (left),  $(S-C_6H_5C^*(H)CH_3NH_3)_2PbI_4$  (right) and  $(R\&S-C_6H_5C^*(H)CH_3NH_3)_2PbI_4$  (bottom), compounds **6-8** respectively.

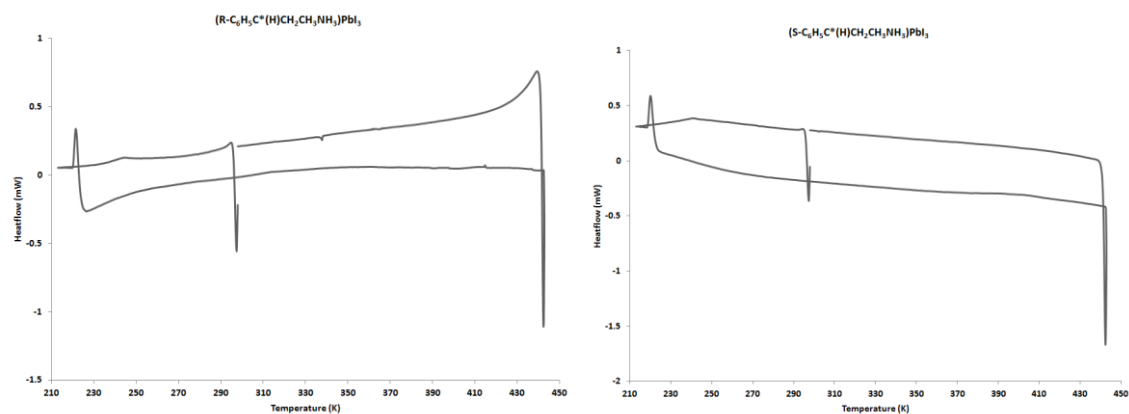


**Figure C.4:** The DSC scans of  $(R-C_6H_5C^*(H)CH_2CH_3NH_3)_2PbI_4$  (left),  $(S-C_6H_5C^*(H)CH_2CH_3NH_3)_2PbI_4$  (right), compounds **9-10** respectively.

**Table C1:** Summary of the melting point temperatures of compounds **1-10**

<b>Compound</b>	<b>Measured temperature range (K)</b>	<b>Phase transition</b>	<b>Melting point (K)</b>
<b>1</b>	298-533	No	420.82
<b>2</b>	298-533	No	419.48
<b>3</b>	298-533	No	430.51
<b>4</b>	213-491	No	476.33
<b>5</b>	213-491	No	478.33
<b>6</b>	213-491	No	443.5
<b>7</b>	213-491	No	443.83
<b>8</b>	213-491	No	460.17
<b>9</b>	213-442	No	-
<b>10</b>	213-442	No	-
<b>11</b>	N/A	N/A	N/A
<b>12</b>	N/A	N/A	N/A